Oceanologia

Official Journal of the Polish Academy of Sciences

This journal is supported by the Ministry of Science and Higher Education, Warsaw, Poland

Indexed in: ISI Journal Master List, Science Citation Index Expanded, Scopus, Current Contents, Zoological Record, Thomson Scientific SSCI, Aquatic Sciences and Fisheries Abstracts, DOAJ

IMPACT FACTOR ANNOUNCED FOR 2020 IN THE 'JOURNAL CITATION REPORTS' IS 2.427; 5-year IF is 2.671. CITESCORE ANNOUNCED FOR 2020 IS 4.3

Publisher
Elsevier B.V.
Radarweg 29
1043 NX Amsterdam
The Netherlands

Senior Publisher
Tobias Wesselius
+31 6 5370 3539

ISSN 0078-3234

Oceanologia 64 (2022) 233—243

Available online at www.sciencedirect.com

ScienceDirect

journal homepage: www.journals.elsevier.com/oceanologia

ORIGINAL RESEARCH ARTICLE

Validation of measurements of pine pollen grain concentrations in Baltic Sea waters

Magdalena M. Pawlik*, **Dariusz Ficek**

Institute of Biology and Earth Sciences, Pomeranian University in Słupsk, Słupsk, Poland

Received 2 July 2021; accepted 17 November 2021
Available online 29 November 2021

KEYWORDS
Pine pollen grains;
Particle size distribution;
Suspended particulate matter;
The Baltic Sea;
Remote sensing

Abstract Each spring, pine pollen coats considerable expanses of Baltic Sea surface waters. Measurements have shown that there are areas where its concentrations in this surface layer are so high that they are the dominant constituent of the suspended particulate matter (SPM) (Pawlik and Ficek, 2016). It then determines to a large extent the optical properties of the water surface, inter alia by modifying the sea colour. To date, however, the concentration of this constituent in the marine environment has rarely been studied, and its presence is not accounted for in the satellite algorithms used to define the composition and properties of sea water. This may well be the source of substantial errors in the remote sensing of the optical properties of the water and the measurement of concentrations of the optically important constituents it contains (chlorophyll *a*, TSM, CDOM). Measuring the concentration of pollen suspensions in Baltic Sea water, which often contains prodigious amounts of other SPM, is a daunting experimental challenge. Firstly, we characterized the pollen from pine trees growing near the southern shores of the Baltic Sea (northern Poland) using a microscope and two instruments routinely used in oceanography for measuring SPM size distributions: the LISST-100X and the Coulter counter. The measurements and analyses showed that a correct interpretation of the LISST-100X and Coulter measurements, is sufficient to count the number of pollen grains in distilled water alone. Furthermore, our laboratory analysis of the particle size distribution spectra enabled the fraction due only to pine pollen grains to be separated from the overall SPM. We then tested our method of analysing the SPM composition, which showed that the

* Corresponding author at: Institute of Biology and Earth Sciences, Pomeranian University in Słupsk, 22A Arciszewskiego Str., 76—200 Słupsk, Poland.
E-mail address: magdalena.pawlik@apsl.edu.pl (M.M. Pawlik).
Peer review under the responsibility of the Institute of Oceanology of the Polish Academy of Sciences.

Production and hosting by Elsevier

https://doi.org/10.1016/j.oceano.2021.11.001

LISST-100x instrument is both a useful and an effective means for the in situ detection of the pine pollen that one sees in spring in Baltic waters.

1. Introduction

Besides dissolved substances, suspended particulate matter (SPM) is one of the most important groups of optically important constituents in sea water. Marine SPM is formed mainly as a result of biological production, shore and bottom abrasion, and precipitation from dissolved matter. Allochthonous SPM is derived mainly from rivers, the atmosphere and subterranean waters. The SPM concentration in waters is variable both seasonally (as a result of cyclic inflows of riverine waters, pollen formation and the seasonal fluctuations of phytoplankton) and regionally. Pempkowiak et al. (2002) measured SPM concentrations in open, southern Baltic Sea waters, obtaining levels from 0.27 to 1.78 mg/dm^3. SPM levels are the highest in the coastal zone, in the lagoons and especially in river estuaries — from 0.36 to 35 mg/dm^3 (Eisma et al., 1991; Emelyanov (ed.), 2002; Krężel and Cyberski, 1993; Schiewer, 2008).

SPM exerts a major influence on the functioning of aquatic ecosystems. Suspended particles are responsible inter alia for the transport, accumulation and transformation of many chemical elements, e.g. nutrients, carbon, metals, as well as non-biodegradable organic pollutants discharged into the sea (e.g. Szefer, 2002; Turner and Millward, 2002). SPM also affects the optical properties of water, interacting as it does with light during its absorption and scattering and thus modifying the colour of the water, which is a basic source of information in the remote monitoring of water bodies. Such remote measurements of water properties have become much more common in recent years (Ficek et al., 2011; Kahru et al., 2007; Reinart and Kutser, 2006; Woźniak et al., 2011). Teledetection from aircraft or satellites enables the quantitative measurement of optically active constituents (OAC) levels, so long as the signal reaching the sensors from the water is correctly interpreted. The remote detection of these constituents requires robust algorithms that can isolate that fraction of the total signal best correlating with the constituent to be analysed. One constituent, which to date has not been taken into consideration, and which could be the source of serious errors in remote measurements, is pine pollen, vast amounts of which reach Baltic waters each spring. A preliminary study of ours showed that large pollen concentrations are found not only in the immediate vicinity of the shoreline, but also at considerable distances from it, where it can make up more than 40% of all the 1.25—250 μm SPM floating on the water (Pawlik and Ficek, 2016). Pine pollen grains are carried to Baltic waters by terrestrial run-off and winds. The latter can blow them 50—60 km out to sea (Dyakowska, 1959), a feat enabled by their structure — a waxy outer skin and air vesicles (sacci) (see Figure 1). For two-three weeks in late May and early June (the pine pollen season), these trees produce vast quantities

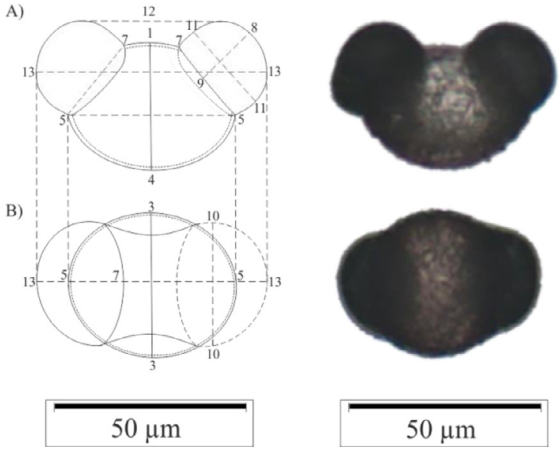

Figure 1 Magnitudes measured in pine pollen grains (after Erdtman, 1954): A — lateral position (equatorial), B — dorsal (polar); 4-12 — height of pollen grain, 13-13 — width of pollen grain; 3-3 — depth of pollen grain; 1-4 height of corpus, 5-5 — width of corpus, 9-8 — height of sacci, 10-10 — width of sacci, 11-11 — depth of sacci.

of pollen, coating the adjacent land and water with yellow dust. The Baltic coast is well wooded, the dominant tree species being the Scots pine Pinus sylvestris. According to the Polish National Forest Inventory (Bureau for Forest Management and Geodesy, 2020), this species makes up 58% of forests in the country. A single pine tree produces some 350 000 000 pollen grains, so 1 ha of a monospecific tree stand will generate as many as 12 910 095 300 (Pohl, 1937). Numerous authors have shown that pollen pine grains vary in diameter, depending on the environment the trees are growing in. For example, pine pollen grains from the state of Maine (USA) range in diameter from 60 to 75 μm (Keller and Matrai, 1998), while those from New York from 32 to 65 μm (Wodehouse, 1935).

Microscope measurements of suspended particle sizes in natural waters are unreliable, so other instruments that indirectly measure particle sizes are usually used, e.g. the LISST-100X, which operates on the basis of light scattering, or the Coulter counter, which relies on changes in permittivity. The various techniques for measuring the equivalent spherical diameter (ESD) of a particle often give different results for the same particles, particularly if these are non-spherical (Janosz, 1987; Jennings and Parslow, 1988; Karp-Boss et al., 2007). But despite these limitations, these instruments are routinely used in studies of aquatic environments for determining the size distributions of total lacustrine and marine SPM (Ahn and Grant, 2007; Bradtke, 1997; Reynolds et al., 2010), phytoplankton suspensions (Anglès et al., 2008; Karp-Boss et al., 2007; Rienecker et al., 2008; Rzadkowolski and Thornton, 2012), bacteria

(Serra et al., 2001, 2002) and sediment (Gartner et al., 2001). An attempt to analyse the concentration of pine pollen grains in sea water has also been described (Pawlik and Ficek, 2016).

The principal aim of the present study was to devise and test a method for the in vitro and in situ measurement of pine pollen grains found on Baltic Sea surface waters. Since there might be local differences in grain sizes, we first measured microscopically the grain sizes of pollen from pines growing on the southern Baltic coast in order to characterize their size distributions. Then we applied those characteristics to develop a method for estimating the in situ concentration of pine pollen grains in an aquatic environment using the LISST-100X instrument. The method was validated using suspensions of pollen in pure water and sea water.

2. Material and methods

In sea water, pollen is present along with other optically important constituents in various concentration combinations. The optical characteristics of such water are the upshot of interactions between all of its constituents and are difficult to interpret. Therefore, in order to obtain samples of maximally uncontaminated pollen for laboratory analysis, we collected pollen directly from pine tree inflorescences during the pollen season. The sizes of these grains were then measured in different planes under a CKX41 microscope (Olympus).

Pine pollen grains are irregular in shape. The parameters shown on Figure 1 were measured in order to determine grain volume (V) and surface area (S): this was done on the assumption that the various parts of a pollen grain resembled a triaxial ellipsoid (Cho et al., 2003).

As a large number of parameters have to be measured in order to determine V and S for irregular 3D shapes, the procedure is simplified, for example, by approximating an irregular particle to a sphere of volume equal to that of the irregular particle. Then we calculate ESDv, the volume-equivalent spherical diameter of a sphere, for such a sphere using the formula:

$$ESDv = \left(\frac{6}{\pi} V_{particle}\right)^{-3}$$

Better results are sometimes achieved by approximating the particle to a sphere whose surface area is equal to that of the irregular particle. In this case, we calculate ESDs, the surface-equivalent spherical diameter of a sphere (Karp-Boss et al., 2007) from the formula:

$$ESDs = \left(\frac{6}{\pi} S_{particle}\right)^{-2}$$

Jonasz (1987), Jennings and Parslow (1988) and Karp-Boss et al. (2007) showed that Coulter counter measurements were better correlated with ESDv, whereas those obtained with the LISST-100X were better correlated with ESDs. Different physical measurements are sensitive to different attributes of the particle (for example, whereas near-forward light scattering is sensitive to the particle's cross-sectional area, electrical impedance is sensitive to the particle's volume). In line with the results of those authors, we used ESDs for the LISST-100X and ESDv for the Coulter counter.

To test the feasibility of detecting pollen suspended in distilled water and multi-constituent sea water we used two instruments:

1. The LISST-100X, type B (Sequoia Scientific, Inc.), a laser instrument for measuring scattering and transmission in situ. This measures the volume concentration of particles V(D) in 32 size classes, divided logarithmically from 1.25 to 250 μm, using small angle forward-scattering laser diffraction. The scattered light is measured in 32 size bins using a red laser diode at 670 nm and a 32-ring silicon detector. At these small angles, laser diffraction is unaffected by the composition of particles, because light scattering is determined almost entirely by light diffracted by the particle. With the software provided by the manufacturers, the scattering intensities measured by the detector are mathematically inverted to obtain the particle volume concentration, assuming that the particles are spheres. A detailed description of the technology and its application is provided by Agrawal and Pottsmith (2000).
2. Multisizer 4 Coulter Counter (Beckman Coulter) equipped with a 100-μm aperture. The device uses the Coulter method, known as electrical sensing zone (ESZ), a method with high resolution and accuracy, additionally supported by digital pulse processor, which provides ultra-resolution, multi-channel analysis, and accuracy unattainable by other technologies and methods of measurement (volumetric pump precise is higher than 99.5%). The application of 100 μm aperture allows for precise designation of particles in 2—60 μm size range (treated as equivalent sphere diameter) divided into 400 size channels logarithmically spaced over the measured range. The aperture of the instrument was calibrated using microsphere standards following the manufacturer's procedure. The measurements of particle size distribution (PSD) were made in three replicates for each sample.

It should be mentioned, however, that in situ measurements in sea water are possible only with the LISST-100X instrument. The Coulter counter is suitable only for the in vitro examination of water samples in the laboratory. Moreover, as it is extremely sensitive to extraneous factors, it is usually used for measurements on land in samples conserved with Lugol's solution.

The research material consisted of pine pollen grains collected from male inflorescences directly from the trees during the pollen season (12—31.05.2018). In the laboratory, this pollen was mixed with distilled water to obtain a preliminary suspension. After 24 hours, this was used to prepare further suspensions with different concentrations of pollen. These were obtained by mixing the preliminary suspension with different proportions of distilled water. The final samples thus contained 10, 20, 25, 30, 50, 75 and 100% of the preliminary suspension. These were then examined using the LISST-100X instrument and the Coulter counter. The measurements with the LISST-100X were carried out for 10 minutes. To prevent the pollen grains from the outflow during the measurements, the samples were stirred continuously in a chamber equipped with a magnetic stirrer (Full Path Mixing Chamber for LISST-100X).

Table 1 Characteristics of ESD values of pine pollen grains (maximum, minimum, mean, median and standard deviation) measured under a microscope and regrouped into the LISST and Coulter counter classes.

equivalent spherical diameter (ESD)	range of min–max	average	median	standard deviation
Microscope and Coulter				
ESDs [μm]	27.7–67.4	44.7	45.0	4.2
ESDv [μm]	27.4–67.3	44.1	44.4	4.1
LISST-100X				
ESDs [μm]	26.7–72.2	44.7	43.9	4.8
ESDv [μm]	26.7–72.2	44.1	43.9	4.7

The next experiment was carried out using sea water. The pine pollen grains were mixed with distilled water and left to stand for 24 hours. On the following day, sea water (not containing any pollen grains) was sampled from the sea surface by the pier at Ustka. These samples were not conserved with Lugol's solution: both the conservation of sea water (Menden-Deuer et al., 2001; Zaruz and Irigoien, 2008) and its non-conservation, as well as any lengthy delay between sampling of the water and its analysis in the laboratory can modify the particle size distribution (PSD) of biological particles. As soon as the sea water was brought to the laboratory (ca 1 hour after sampling), 7 samples were prepared containing the suspension prepared 24 hours earlier (containing pine pollen grains and distilled water) and sea water. The respective samples contained 10, 20, 25, 30, 50, 75 and 100% of the distilled water suspension. The LISST-100X was then used to measure PSD in both the original sea water and in the mixtures prepared from it. The measurements were carried out under exactly the same conditions as were applied when measuring the suspensions of pollen in distilled water (see the previous paragraph).

3. Results and discussion

3.1. ESD measurements of pine pollen grains under the microscope

Because pollen grains differ in size in different parts of the world, the first step in this research involved characterizing the size distribution of pine pollen grains from southern Baltic coastal areas. To this end, pollen was collected directly from the male inflorescences of pine trees, which was then soaked in distilled water for 24 hours prior to the measurements. A total of 3353 pollen grains in this suspension were measured under an optical microscope, after which the ESDv and ESDs of each grain were determined. Table 1 lists the maximum and minimum values of ESD for pine pollen grains, along with their mean values, median and standard deviation. ESDv ranged from 27.4 to 67.3 μm with a mean of 44.1 μm, ESDs from 27.7 to 67.4 μm with a mean of 44.7 μm.

The Coulter and LISST-100X measurements were classified according to size. The Coulter diameters were allocated to 400 size bins, each of constant width. With the LISST-100X there are just 32 size bins of uneven width, which increases with increasing particle diameter. To correctly interpret the Coulter and LISST-100X diameters, the microscopically measured diameters were regrouped into the same size bins as those obtained with the instruments. Table 1 and Figure 2 show the results of the analyses of these regrouped distributions of diameters. Clearly, the grouping of diameters measured under the microscope in the Coulter size classes with respect to the ungrouped measurements does not alter the parameters describing their characteristics. The reverse is the case when diameters are regrouped according to the LISST size classes. In this case, the smaller number of bins means that we observe certain changes with respect to the ungrouped measurements. The mean value of ESDs = 44.7 and ESDv = 44.1, whereas the standard devation is 4.8 and 4.7, respectively.

3.2. PSD measurements of pine pollen grains in water

In the next experiment, we tested whether the LISST-100X and Coulter instruments could be used to measure the concentration and PSD of a suspension of pollen in water. PSD was measured in suspensions of six different concentrations of pine pollen grains in distilled water. By way of example, Figure 3 shows the results obtained for suspensions containing three different concentrations of pollen. We see that the presence of pollen grains in water is indicated by a distinct peak in the same range as that where the peak was observed in the microscope measurements (see Figure 2). We can therefore assume that this peak is due to the presence of pine pollen.

The measurements of pollen suspensions under the microscope and with the two instruments also enabled a comparison of the results. The Coulter measurements are similar to the results obtained with the microscope. On the other hand, the distribution of the LISST diameters is distinctly broader than that of the Coulter measurements. The ESD of pine pollen grains measured with the LISST ranged from 24.6 to 78.4 μm, but with the Coulter counter was from 24.62 to 60.0 μm. The wider range of ESD bins of pollen grains obtained with the LISST is due to the differences in the size bins of the two instruments: the LISST has far larger bins than the Coulter counter. Measuring the size of very large pine pollen grains using the Coulter counter was limited by the size of the diaphragm in this instrument. With a 100 μm diameter diaphragm, pollen grains from 2 to 60 μm can be measured, but the ESDs of some grains lie beyond this range. To measure such larger grains a diaphragm of wider diameter would be necessary. Despite these differences, we still get good agreement between the maxima from both in-

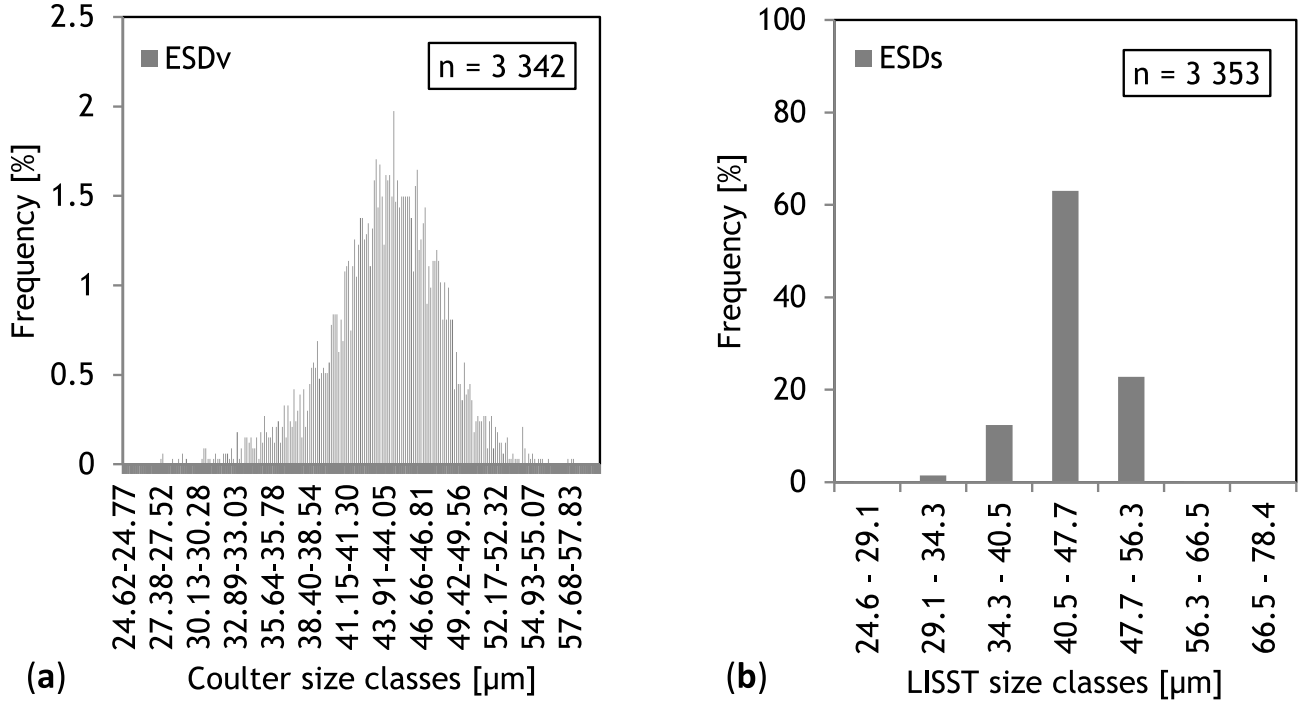

Figure 2 Equivalent spherical diameter (ESDv and ESDs) of pine pollen grains measured under the microscope in (**a**) Coulter size classes and (**b**) LISST-100X size classes.

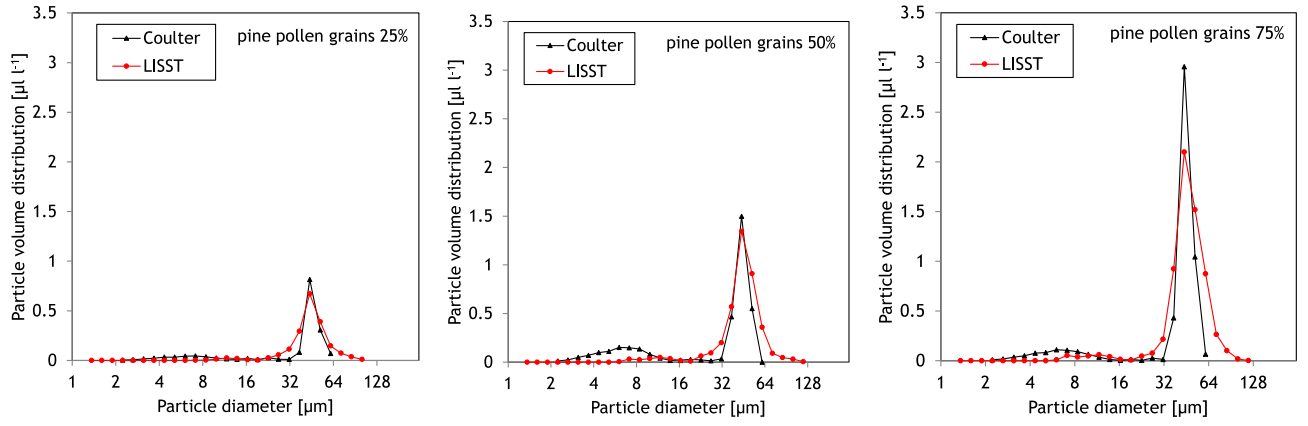

Figure 3 Particle size distribution of pine pollen grains as measured with two different instruments. Three samples with different concentrations are depicted (25, 50, 75% pollen: distilled water).

struments for the pine pollen grain size class from 40.5 to 47.7 µm. Both instruments showed a distinct peak in the diameters in the same range as the microscope measurements at ca 45 µm, albeit the local Coulter maximum displays a greater volume concentration than that obtained with the LISST. This is due to the narrower measurement range of the latter instrument.

Both instruments were also used to estimate the total number of pollen grains in the suspension. The measurements made under the microscope (Figure 2) and with the LISST and Coulter counter (Figure 3) indicate that the peak from the pollen grain size ranging from 24.6 to 78.4 µm and from 24.62 to 60 µm (Coulter) can be linked to the presence of pine pollen, and that the magnitude of that peak gives a rough indication of its concentration in water. In the subsequent calculations, therefore, it was assumed that the pollen concentration was equal to its concentration in the following ranges: LISST-100 × 24.6—78.4 µm, Coulter 24.62—60.0. To test the quality of this means of estimating pollen concentrations in water, we analysed the measurements obtained from the samples with different pollen concentrations. Here we took into account the fact that when mixing a known volume of a water-pollen grain mixture with a known volume of distilled water, we can define the relative changes in pollen concentration in the samples with respect to the concentration in the original pollen mixture. The results of these measurements confirmed the linear dependence between the instrumentally measured concentrations and the calculated ones (coefficient of determination r^2=0.99) (see Figure 4a).

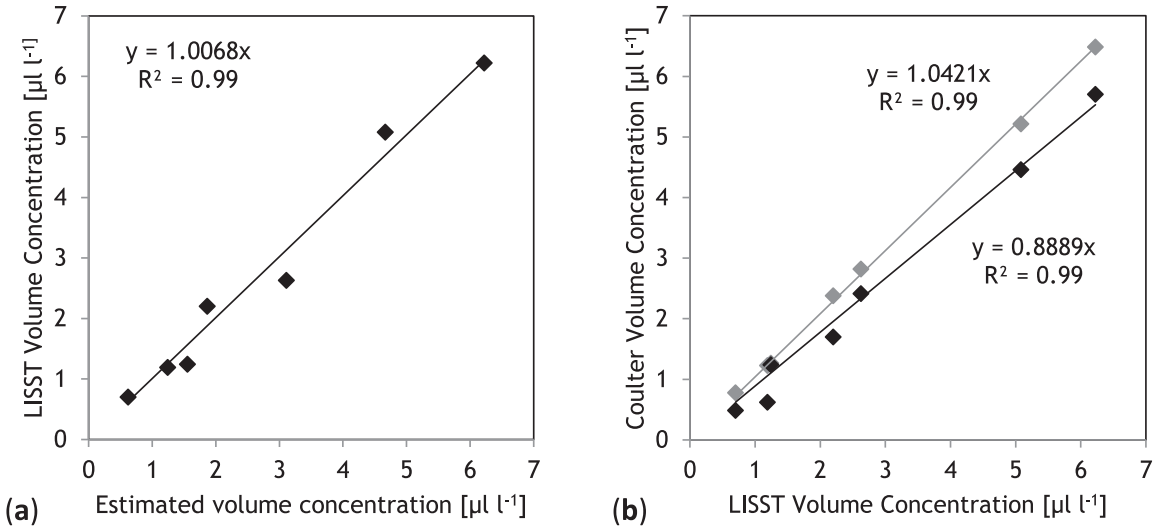

Figure 4 (**a**) Comparison of estimated concentration of pine pollen grains in the solutions and its values determined using by LISST method; (**b**) Relationship between the volume concentration obtained from Coulter-measured particle size distributions and those obtained from the LISST-100X distributions. The real pine pollen grain concentrations obtained using by with both instruments are shown in black, whereas the pollen grain concentrations obtained after the addition of the LISST measurements of pollen grains larger than 60 µm to the Coulter measurements are shown in grey.

We further compared the pollen grain counts using the two aforementioned instruments. It turned out that, despite employing two different measurement techniques, the correlation between the results obtained with both was very high (coefficient of determination r^2=0.99) (Figure 4b – concentrations shown in black). However, the pollen concentrations in all the samples measured with the LISST were somewhat higher than with the Coulter counter. This is because, as mentioned above, the Coulter counter diaphragm is too small and is incapable of measuring pollen grains with ESD > 60 µm. That is why to estimate the total number of pollen grains in the suspension, the data from two size classes > 60 µm obtained with the LISST-100X were added to the Coulter measurements. The results, shown in grey, are illustrated in Figure 4b. This figure shows that after this correction, the measurements obtained with both instruments differ only slightly, the slope of the straight line is close to 1, and the coefficient of determination r^2=0.99. It should be noted that there are always certain differences in the readings given by the two instruments because they employ different measurement techniques and differently interpret ESD (Jennings and Parslow, 1988; Jonasz, 1987; Karp-Boss et al., 2007).

3.3. PSD measurements using LISST in multicomponent sea water

Determining the concentration of one SPM constituent in a mixture containing other such constituents on the basis of PSD spectra poses a considerable challenge. As will be shown below, this is more or less possible if one knows the size distribution parameters of the sought-after SPM constituent. Pine pollen occurs in sea water together with other substances suspended in it in various combinations of concentrations. It is obvious, therefore, that measurements of such multi-constituent SPM are best carried out in situ. However, the sampling technique and the time elapsing between sampling and analysis in the laboratory are just two factors that can lead to errors that are hard to estimate. That is why for this part of our research we tested the possibility of analysing the pollen concentration using only the LISST-100X, an instrument which permits in situ measurements in sea water. The preliminary results of that study, published in Pawlik and Ficek (2016), showed that in situ measurements of pollen concentrations using the LISST-100X are feasible. Later, we tested the accuracy of that method. For this purpose, measurements were made on mixtures of Baltic Sea water with known concentrations of pollen grains. To estimate the numbers of pollen grains suspended in sea water, we applied our knowledge of their size distribution from microscope measurements (Figure 2, Table 1) and the LISST-measurements of pollen suspensions in distilled water (Figure 3). Besides pollen in sea water, there are multifarious other particles that modify the PSD spectrum, so when estimating the pollen grain concentration, we adopted a number of simplifications. We assumed that the concentration of SPM with ESD both below (ESD<24.6 µm) and above (ESD>92.6 µm) the value measured microscopically in pollen grains constituted a background unrelated to the pollen grains and that we should take only values above that background level into consideration when estimating pollen concentrations. We also assumed that the level of the background signal between the limiting values varied linearly (see Figure 5). We included in the pollen signal all those values that were above the line drawn between the concentrations from beyond the pollen ESD intervals (the yellow columns in Figure 5). The choice of the upper limit (92.6 µm) to estimate pine pollen is related to the property of the device LISST-100X, which is used near forward light scattering measurements to obtain information about the size and concentration of suspended particles.

Then we examined how various concentrations of pollen grains affected the volume distributions of marine SPM mea-

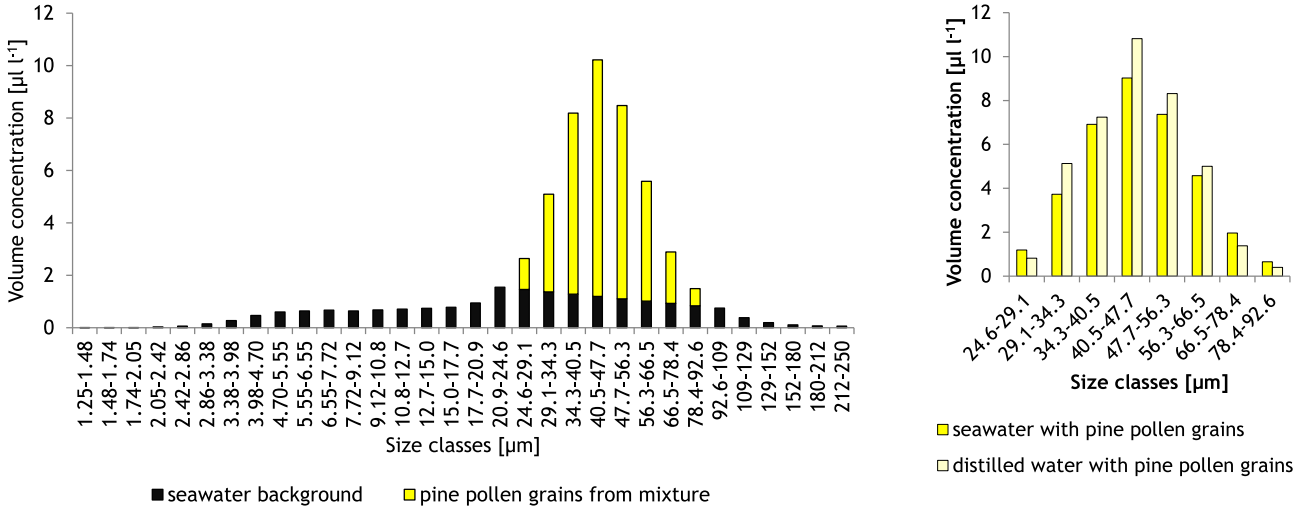

Figure 5 Diagram illustrating the methodology for measuring the concentration of pine pollen grains in any suspension using the LISST instrument.

Table 2 Proportions of pine pollen grains mixed with distilled water and sea water used for measurements in the study experiment.

Number of a sample	Proportion ofpreliminary suspension (pollen mixed with distilled water)		Mixture 1 Distilled water	Mixture 2 Natural sea water
Natural sea water	—		—	100 ml
Preliminary suspension of pine pollen grains	100%	100 ml	—	—
Sample 1	10%	10 ml	90 ml	90 ml
Sample 2	20%	20 ml	80 ml	80 ml
Sample 3	25%	25 ml	75 ml	75 ml
Sample 4	30%	30 ml	70 ml	70 ml
Sample 5	50%	50 ml	50 ml	50 ml
Sample 6	75%	75 ml	25 ml	25 ml

sured using the LISST-100X and its ability to measure the pine pollen concentration. The research material for this experiment consisted of mixtures containing set proportions of pine pollen grains in distilled water and sea water (Table 2).

We then measured the pollen grain concentrations in these suspensions; the results are shown in Figure 6. This figure shows that all the distributions are characterized by distinct peaks, which testify to the presence of particular groups of SPM constituents in the water. The blue line indicates the measurement made in sea water without the addition of pollen grains. The sea water was dominated by SPM with ESD between 2.86 and 40.5 µm, with a distinct peak between 10.8 and 12.7 µm. The species composition of the taxa microphytoplankton present in the sea water samples and its dimensions are listed in Table 3. Microscopic measurements showed that, apart from the pollen, the samples analyzed did not contain any large concentrations of phyto- or zooplankton of dimensions within the range of the dominant maximum shown in Figure 2. The next curves on this figure show the measurements of sea water with pollen grains. We see that the addition of ever larger quantities of the pollen grain — distilled water mixture to the sea water generates a conspicuous bulge in the 24.6—78.4 µm range, with a distinct peak in the pollen grain group of diameter 44 µm. At the same time, we note a gradual decline in the concentration of nanoplankton in the marine suspensions. A gradual decline concentration of nanoplankton depends on the relative size and concentration of the pine pollen grains in the marine suspensions.

In order to test the proposed methods of estimating pollen grain concentrations, this time in sea water containing other SPM as well, we analysed the measurements of the above samples containing different amounts of pollen. Here, we utilized the fact that when mixing a known volume of distilled water containing pollen with a known volume of sea water, we can calculate the relative changes of pollen concentration in the samples with respect to the initial pollen grain concentration. These measurements confirmed the linear dependence between the calculated concentrations and the LISST-measured ones (coefficient of determination r^2=0.99; see Figure 6d). Thus, when sea water concentrations of pollen are high, PSD spectra analysis discriminates the pine pollen fraction from the total SPM, and its concentration can be measured with a satisfactory level of accuracy.

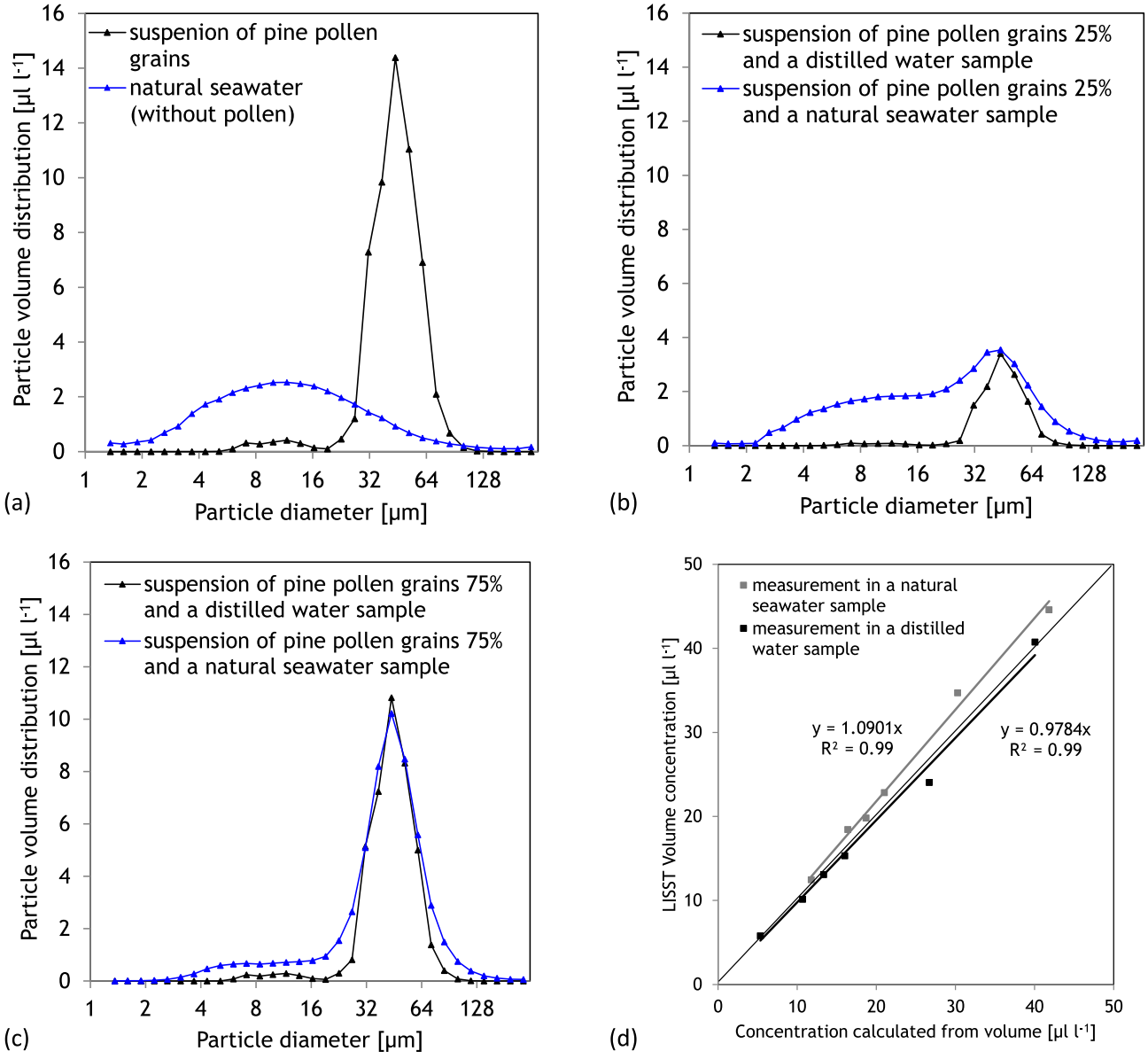

Figure 6 (**a—c**) LISST-measured particle volume distribution for suspensions of pine pollen grains and natural seawater sampled from the Ustka Pier on 6 May 2019. The mixed suspension was produced by combining different concentrations of pine pollen grain suspensions in different concentrations of natural seawater and distilled water; (**d**) Comparison of LISST concentration of pine pollen grains and concentration of the same pine pollen grains calculated from the volume (measurements in a natural seawater samples and a distilled water samples).

Table 3 List and characteristics of microphytoplankton taxa and taxonomic groups identified in the water used for measurements (sampled on 6 May 2019) in the Baltic Sea with mean ESDs; ESD — equivalent spherical diameter.

Taxonomic groups	Species	Calculated volume [µm^3]	ESDs [µm]
Chlorophyceae	*Pseudopediastrum boryanum*	15896—49749	31.2—45.6
Bacillariophyceae	*Actinocyclus* spp.	110214—371972	59.5—89.2
Dinophyceae	*Gyrodinium* spp.	2685—15656	17.2—31.0
Dinophyceae	*Dinophysis acuminata*	29401—34006	38.3—40.2

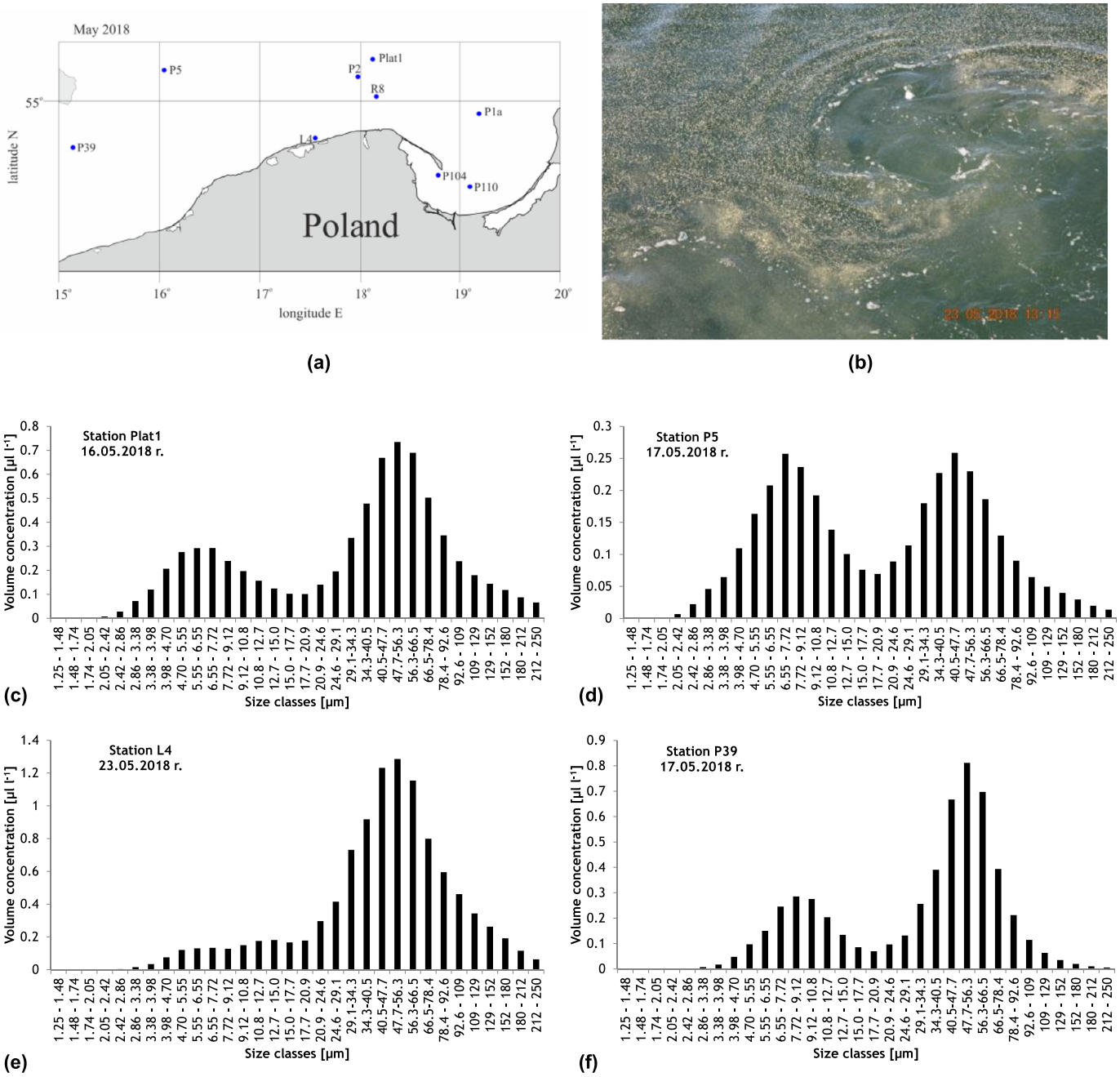

Figure 7 In situ concentrations measured with the LISST at different stations in the Baltic during the pine pollen season. (**a**) Locations of the stations where large concentrations of pollen grains were observed in the southern Baltic Sea. (**b**) Concentration of pine pollen grains in waters of the Baltic Sea (visible with the naked eye). (**c—f**) In situ concentrations of pine pollen at four measurement stations in the Baltic Sea.

The final part of this work presents examples of in situ PSD measured with the LISST at different stations in the Baltic during the pine pollen season (Figure 7). The positions of the stations are shown in Figure 7a. Large concentrations of suspended pollen at these stations were visible with the naked eye — this is illustrated by the photograph in Figure 7b. The presence of large pollen concentrations was also confirmed by the distinct peak in the PSD spectrum between 24.6 and 78.4 μm, with maxima at ca 44 and 52 μm (Figure 7c—f). As shown earlier by the laboratory measurements, this range coincides with the size range in which pollen grains are observed. Application of the above method to calculate the pollen concentration at the various stations showed that the pollen grain concentrations and the proportions of suspended pollen in the total SPM in the 1.25—250 μm size range were: 2.4 μl l^{-1} (34.2%) at station Plat1, 0.8 μl l^{-1} (23.5%) at P5, 4.1 μl l^{-1} (39.6%) at L4 and 2.7 μl l^{-1} (49.2%) at P39. These measurements demonstrate that pollen suspensions in the Baltic Sea can locally reach very high concentrations, sometimes even being the dominant constituent of the SPM.

4. Conclusions

This paper is the first to describe and validate a method of counting pine pollen grains in an aquatic environment. Numerical and volume distributions of this important constituent of marine SPM were calculated using a LISST-100X and a Coulter counter and the results compared. Even though these two instruments employ different techniques for detecting particles, a high correlation was achieved between the concentrations of pine pollen grains in water. The experiment described shows that if we know the PSD of the pollen grains, we can use both the LISST-100X and the Coulter counter to identify and detect this suspension. When used for laboratory measurements, both instruments yielded similar size distributions and concentrations. The LISST-100X is superior for the detection of pine pollen grains, because it is capable of measuring the in situ volume concentration of this pollen in Baltic Sea water relatively quickly and simply. However, the correct interpretation of LISST data requires that the pollen concentrations in the suspensions be large enough for the signal (peak) due to it at 40.5—47.7 μm to be readily visible against the background PSD of other SPM.

Research into SPM in surface waters nowadays is especially important, when remote monitoring techniques are in the ascendancy. Ongoing global and local environmental changes demand the intensification of studies of the Baltic Sea, a sensitive ecosystem endangered by eutrophication. There is no doubt that if the correctly interpreted SPM composition signal reaching the satellite is incorporated in satellite algorithms, it will significantly improve the quality of remotely-sensed data.

Declaration of competing interest

The authors of the manuscript declare that they have no known competing financial interests or personal relationships that could have appeared to influence the work reported in this paper.

Acknowledgments

We are indebted to PhD Katarzyna Bradtke from Institute of Oceanography, University of Gdańsk, for performing Coulter counter laboratory analyses of pine pollen grains.

This research was funded by the project awarded to M. M. Pawlik by National Science Centre, Poland, entitled "Optical Characteristics of Pine Pollen Grains and their affect the quality of remote sensing measurements in the Baltic Sea" (contract No. 2017/25/N/ST10/02578).

References

Agrawal, Y.C., Pottsmith, H.C., 2000. Instruments for particle size and settling velocity observations in sediment transport. Mar. Geol. 168, 89—114. https://doi.org/10.1016/S0025-3227(00)00044-X

Ahn, J.H., Grant, S.B., 2007. Size distribution, sources, and seasonality of suspended particles in southern California marine bathing waters. Environ. Sci. Technol. 41, 695—702. https://doi.org/10.1021/es061960+

Anglès, S., Jordi, A., Garcés, E., Masó, M., Basterretxea, G., 2008. High-resolution spatio-temporal distribution of a coastal phytoplankton bloom using laser in situ scattering and transmissometry (LISST). Harmful Algae. 7, 808—816. https://doi.org/10.1016/j.hal.2008.04.004

Bradtke, K., Latała, A., Czabański, P., 1997. Temporal and spatial variations in particle concentrations and size distributions in the Gulf of Gdańsk. Oceanol. Stud. XXVI (2—3), 39—59.

Bureau for Forest Management and Geodesy, 2020. National Forest Inventory (2015—2019). Sękocin Stary, 5—95.

Cho, Y.-J., Kim, I.S., Kim, P.-G., Lee, E.J., 2003. Deposition of airborne pine pollen in a temperate pine forest. Grana 42 (3), 178—182. https://doi.org/10.1080/00173130310016158

Dyakowska, J., 1959. Textbook of palynology. Methods and problems. Geological Publ., Warsaw, Poland.

Eisma, D., P., Bernard, G.C., Cadeé, V., Ittekkot, J., Kalf, R., Laane, J.M., Martin, W.G., Mook, van Put A., Schumacher, T., 1991. Suspended-matter particle size in some West-European estuaries, part I: particle size distribution. Neth. J. Sea Res. 28 (3), 193—214. https://doi.org/10.1016/0077-7579(91)90017-U

Emelyanov, E.M. (Ed.), 2002. Geology of the Gdańsk Basin, Baltic Sea. Yantarny Skaz, Kaliningrad, 494 pp.

Erdtman, G., 1954. Pollen morphology and plant taxonomy. Bot. Notis. H. 2

Ficek, D., Zapadka, T., Dera, J., 2011. Remote sensing reflectance of Pomeranian lakes and the Baltic. Oceanologia 53 (4), 959—970. https://doi.org/10.5697/oc.53-4.959.

Gartner, J.W., Cheng, R.T., Wang, P.F., Richter, K., 2001. Laboratory and field evaluations of the LISST-100 instrument for suspended particle size determinations. Mar. Geol. 175, 199—219. https://doi.org/10.1016/S0025-3227(01)00137-2

Jennings, B.R., Parslow, K., 1988. Particle size measurement: the equivalent spherical diameter. Proc. Roy. Soc. London A419, 137—149. https://doi.org/10.1098/rspa.1988.0100

Jonasz, M., 1987. Nonspherical sediment particles: Comparison of size and volume distributions obtained with an optical and resistive particle counter. Mar. Geol. 78, 137—142. https://doi.org/10.1016/0025-3227(87)90072-7

Kahru, M., Savchuk, O., Elmgren, R., 2007. Satellite measurements of cyanobacterial bloom frequency in the Baltic Sea: interannual

and spatial variability. Mar. Ecol. Prog. Ser. 343, 15—23. https://doi.org/10.3354/meps06943

Karp-Boss, L., Azevedo, L., Boss, E., 2007. LISST-100 measurements of phytoplankton size distribution: Evaluation of the effects of cell shape. Limnol. Oceanogr. 5, 396—406. https://doi.org/10.4319/lom.2007.5.396

Keller, M.D., Matrai, P.A., 1998. Optical Characteristics of Pollen Grains in Coastal Waters of the Gulf of Marine. West Boothbay Harbor, Bigelow Laboratory for Ocean Sciences 6.

Krężel, A., Cyberski, J., 1993. Influence of the Vistula River on suspended matter content in the Gulf of Gdańsk waters. Stud. Mat. Oceanol. 64, 27—39.

Menden-Deuer, S., Lessard, E.J., Satterberg, J., 2001. Effect of preservation on dinoflagellate and diatom cell volume and consequences for carbon biomass predictions. Mar. Ecol. Prog. Ser. 222, 41—50. https://doi.org/10.3354/meps222041

Pawlik, M., Ficek, D., 2016. Pine pollen grains in coastal waters of the Baltic Sea. Oceanol. Hydrobiol. Stud. 45 (1), 35—41. https://doi.org/10.1515/ohs-2016-0004

Pempkowiak, J., Bełdowski, J., Pazdro, K., Staniszewski, A., Leipe, T., Emeis, K., 2002. The contribution of fine sediment fraction to the fluffy layer suspended matter (FLSM). Oceanologia 44 (4), 513—527.

Pohl, Fr., 1937. Die Pollenerzeugung der Windblütler. Beih. Bot. Zbl. Abt. A, und Fruchtknotenbau. I. Beih. Bot. Cbl., Bd. 46.

Reinart, A., Kutser, T., 2006. Comparison of different satellite sensors in detecting cyanobacterial bloom events in the Baltic Sea. Remote Sens. Environ. 102, 74—85. https://doi.org/10.1016/j.rse.2006.02.013

Reynolds, R.A., Stramski, D., Wright, V.M., Woźniak, S.B., 2010. Measurements and characterization of particle size distributions in coastal waters. J. Geophys. Res. 115, C08024. https://doi.org/10.1029/2009JC005930

Rienecker, E., Ryan, J., Blum, M., Dietz, C., Coletti, L., Marin, R., Bissett, W.P., 2008. Mapping phytoplankton in situ using a laser scattering sensor. Limnol. Oceanogr. - Methods 6, 153—161. https://doi.org/10.4319/lom.2008.6.153

Rzadkowolski, C.E., Thornton, D.C.O., 2012. Using laser scattering to identify diatoms and conduct aggregation experiments. European J. Phycol. 47 (1), 30—41. https://doi.org/10.1080/09670262.2011.646314

Schiewer, U., 2008. Ecology of Baltic coastal water. Springer Verlag.

Serra, T., Colomer, J., Cristina, X.P., Vila, X., Arellano, J.B., Casamitjana, X., 2001. Evaluation of laser in situ scattering instrument for measuring concentration of phytoplankton, purple sulfur bacteria, and suspended inorganic sediments in lakes. J. Environ. Eng. 127 (11), 1023—1030. https://doi.org/10.1061/(ASCE)0733-9372(2001)127:11(1023)

Serra, T., Colomer, J., Baserba, C., Soler, M., Casamitjana, X., 2002. Quantified distribution of diatoms during the stratified period of Boadella reservoir. Hydrobiologia 489, 235—244.

Szefer, P., 2002. Metals, metalloids and radionuclides in the Baltic Sea ecosystem. Elsevier, Amsterdam—London—New York—Oxford—Paris—Shannon—Tokyo.

Turner, A., Millward, G.E., 2002. Suspended particles: their role in estuarine biogeochemical cycles. Estuar. Coast. Shelf Sci. 55, 857—883. https://doi.org/10.1006/ecss.2002.1033

Woźniak, B., Bradtke, K., Darecki, M., Dera, J., Dudzińska-Nowak, J., Dzierzbicka-Głowacka, L., Ficek, D., Furmańczyk, K., Kowalewski, M., Krężel, A., Majchrowski, R., Ostrowska, M., Paszkuta, M., Stoń-Egiert, M., Stramska, M., Zapadka, T., 2011. SatBaltic — A Baltic environmental satellite remote sensing system — an ongoing project in Poland part 2: practical applicability and preliminary results. Oceanologia 53 (4), 925—958. https://doi.org/10.5697/oc.53-4.925

Wodehouse, R., 1935. Pollen grains. Their structure, identification and significance in science and medicine. McGraw-Hill Book Company, Inc., New York and London, 574 pp.

Zarauz, L., Irigoien, X., 2008. Effects of Lugol's fixation on the size structure of natural nano-microplankton samples, analyzed by means of an automatic counting method. J. Plankton Res. 30, 1297—1303. https://doi.org/10.1093/plankt/fbn084

Oceanologia 64 (2022) 244—266

Available online at www.sciencedirect.com

ScienceDirect

journal homepage: www.journals.elsevier.com/oceanologia

ORIGINAL RESEARCH ARTICLE

Size-fractionated primary production in the south-eastern Black Sea

Ertugrul Agirbas*, **Mustafa Bakirci**

Dept. of Marine Biology, Faculty of Fisheries, Recep Tayyip Erdogan University, Rize, Turkey

Received 18 August 2021; accepted 17 November 2021
Available online 10 December 2021

KEYWORDS
C-14;
Phytoplankton;
Primary production;
Size-fractionated;
South-Eastern Black Sea

Abstract Size-fractionated primary production (PP) and chlorophyll-*a* (Chl-*a*) with phytoplankton abundance and nutrients were investigated in the south-eastern Black Sea from November 2014 to August 2015. A 14C radio-tracing technique was used to estimate phytoplankton primary production. C-14 experiments revealed that total PP ranged from 295 mgC m^{-2} d^{-1} to 5931 mgC m^{-2} d^{-1} along the study area. Size-fractionated PP varied from 84 to 1848 mgC m^{-2} d^{-1}, from 96 to 3156 mgC m^{-2} d^{-1} and from 56 to 3363 mgC m^{-2} d^{-1} for pico-, nano- and microphytoplankton, respectively. Overall, winter (4163 mgC m^{-2} d^{-1}) and spring (5931 mgC m^{-2} d^{-1}) were the most productive seasons, which coincided with high phytoplankton abundance. Contributions of microphytoplankton and nanophytoplankton were prominent in spring with maximum PP values. Winter was the second productive season with high contributions of nano- and microphytoplankton PP. Summer and autumn were less productive seasons, which were characterised by a high contribution of pico- and nanophytoplankton PP. Dinoflagellates were represented with the highest species richness (68 species, 53.54%) and diatoms were the second group along the area. Diatoms and other phytoplankton species (mainly *Emiliania huxleyi*) were the most abundant groups in terms of quantitative contribution. The results show that microphytoplankton along the study area are responsible for the majority of PP. However, the measured high Chl-*a* against low size-fractionated PP clearly indicates that smaller groups (i.e., pico- and nanophytoplankton) were dominant during these periods. Hence, the quantification of size-fractionated PP rates together with ecological indicators will allow for a more comprehensive assessment of the Black Sea ecosystem.

* Corresponding author at: Dept. of Marine Biology, Faculty of Fisheries, Recep Tayyip Erdogan University, Rize, Turkey.
E-mail address: ertugrul.agirbas@erdogan.edu.tr (E. Agirbas).
Peer review under the responsibility of the Institute of Oceanology of the Polish Academy of Sciences.

Production and hosting by Elsevier

https://doi.org/10.1016/j.oceano.2021.11.002

1. Introduction

Phytoplankton community composition and size classes (i.e., pico-, nano- and micro-phytoplankton) affect biogeochemical processes, carbon fixation and transferring of organic matter to upper trophic levels via photosynthesis mechanism (Guidi et al., 2010; Kiørboe, 1993; Margalef, 1965; Uitz et al., 2010). This mechanism builds the base of the marine food web, and regulates trophic interactions, nutrient dynamics, and energy transfer to upper trophic levels (Paerl et al., 2003; Platt and Sathyendranath, 2008). Since phytoplankton physiologically quickly respond to environmental changes, this makes them sensitive indicators of environmental degradation in the aquatic ecosystems (Hays et al., 2005; McQuatters-Gollop et al., 2007).

Photosynthetic capacity, trophic role and physiology of the phytoplankton are closely related to their size structure (Song et al., 2019). Size structure of phytoplankton influences food web efficiency and carbon export in the pelagic ecosystem (Tilstone et al., 2017). For example, microphytoplankton (>20 μm in size) are responsible for new production and contribute significantly (nearly 20% of annual primary production) to carbon fixation (Eppley and Peterson, 1979; Goldman, 1993; Michaels and Silver, 1988; Nelson et al., 1995; Tilstone et al., 2017). Nanophytoplankton (2—20 μm in size) are responsible for most of the primary production (PP) in many shelf seas (Joint et al., 1986). Picophytoplankton are dominant in the low Chl-*a* areas of oligotrophic subtropical and tropical seas (Aiken et al., 2009; Veldhuis et al., 2005), and their contributions to annual PP are generally low when compared with other size groups (Curran et al., 2018). Moreover, phytoplankton size classes can be associated with different biogeochemical regions and trophic status for a given area. Oligotrophic waters are generally dominated by picophytoplankton with low Chl-*a* and PP rates (Curran et al., 2018; Platt et al., 1983; Viviani et al., 2011). Differently, nanophytoplankton have moderate Chl-*a* and PP rates in the mesotrophic regions. By contrast, the microphytoplankton inhabit eutrophic areas (i.e., nutrient replete waters) with high Chl-*a* and PP capacity (Cho and Azam, 1988; Eppley and Peterson, 1979; Falkowski et al., 1998, Tilstone et al., 2017). Moreover, microphytoplankton plays a major role in global carbon cycle (Tilstone et al., 2017). Hence, measuring of size-fractionated primary production and monitoring of changes in phytoplankton size structure have vital role in understanding biogeochemical carbon cycle, biological pump, ecosystem management strategies and sustainable ecosystem policies (Aumont et al., 2003; Le Quéré et al., 2005; Tilstone et al., 2017; Uitz et al., 2010).

The Black Sea is a biologically productive and the largest anoxic marine environment (Yilmaz et al., 2006; Yunev et al., 2002). However, due to ecological deteriorations, shifts in the ratio of major phytoplankton groups, qualitative and quantitative changes in community structure, phenological changes in bloom pattern and decline in PP rates have been observed over the decades (Agirbas et al., 2014; Bat et al., 2011; Feyzioglu and Seyhan, 2007; Kideys, 1994, 2002; Kopelevich et al., 2002). The Black Sea is characterized with two phytoplankton blooms throughout the year. The major bloom (mainly diatoms) occurs in early spring, while a secondary bloom of coccolithophores appears in autumn (Sorokin, 1983; Vedernikov and Demidov, 1997). However, additional summer blooms of dinoflagellates and coccolithophores have frequently been reported from the Black Sea (Hay et al., 1990; Sur et al., 1996; Yayla et al., 2001; Yilmaz et al., 1998).

Production rates were generally high in the northwestern Black Sea, they ranged from 570 to 1200 mgC m^{-2} d^{-1}, whereas values varied from 320 to 500 mgC m^{-2} d^{-1} in the regions of continental slope, 100 to 370 mgC m^{-2} d^{-1} in the central deep-sea regions during 1960—1991 (Bologa et al., 1986; Demidov, 2008; Vedernikov and Demidov, 1997). On the contrary, PP rates along the southern Black Sea were reported as 247—1925 mgC m^{-2} d^{-1} for spring, and 405—687 mgC m^{-2} d^{-1} for summer-autumn period during 1995—1996 (Yilmaz et al., 2006). Recently, monthly production rates for the south-eastern coasts of the Black Sea were reported as 285—565 mgC m^{-2} d^{-1} for coastal stations, and as 126—530 mgC m^{-2} d^{-1} for offshore stations (Agirbas et al., 2014). Majority of studies have focused on the simultaneous analysis of size-fractionated PP in the oceans (Cermeño et al., 2005; Han and Furuya, 2000; Jochem and Zeitzschel, 1989; Tamigneaux et al., 1999), however, no studies that include size-fractionated PP rates were reported from the Black Sea, and therefore, it is essential to understand which size classes of phytoplankton are seasonally active and make a major contribution to primary production.

In this study, we consider the spatial and temporal variations in seasonal size-fractionated PP and Chl-*a* with phytoplankton abundance and nutrient data in the south-eastern Black Sea during the 2014—2015 sampling period. The present study also provides the first measurement of size-fractionated PP rates for the study area, and specifically focuses on determining the contribution of phytoplankton size classes to total PP rates in the study area throughout a seasonal cycle.

2. Material and methods

2.1. Study area and sampling regime

Samplings were performed seasonally at the 12 stations from November 2014 to August 2015 along the south-eastern Black Sea (Figure 1). The station coordinates and sampling details are given in Supplementary Material Table 1. Seawater samples were obtained from the particular depths (surface, 10 m, 20 m, 30 m and 40 m) by using a SBE 32 Carousel rosette sampler. A SBE 25 plus CTD probe was deployed (from surface to 100 m) to reveal the vertical profile of temperature, salinity and Chl-*a* during samplings. Similarly, photosynthetically active radiation (PAR) was measured seasonally by using a Li-Cor (LI-193 SA) sensor mounted to CTD (conductivity, temperature, depth) probe. The 1% light penetration depth was also calculated from PAR values in order to determine the base of euphotic zone along the study area. Variations of the parameters measured for the study area are summarized in Table 1.

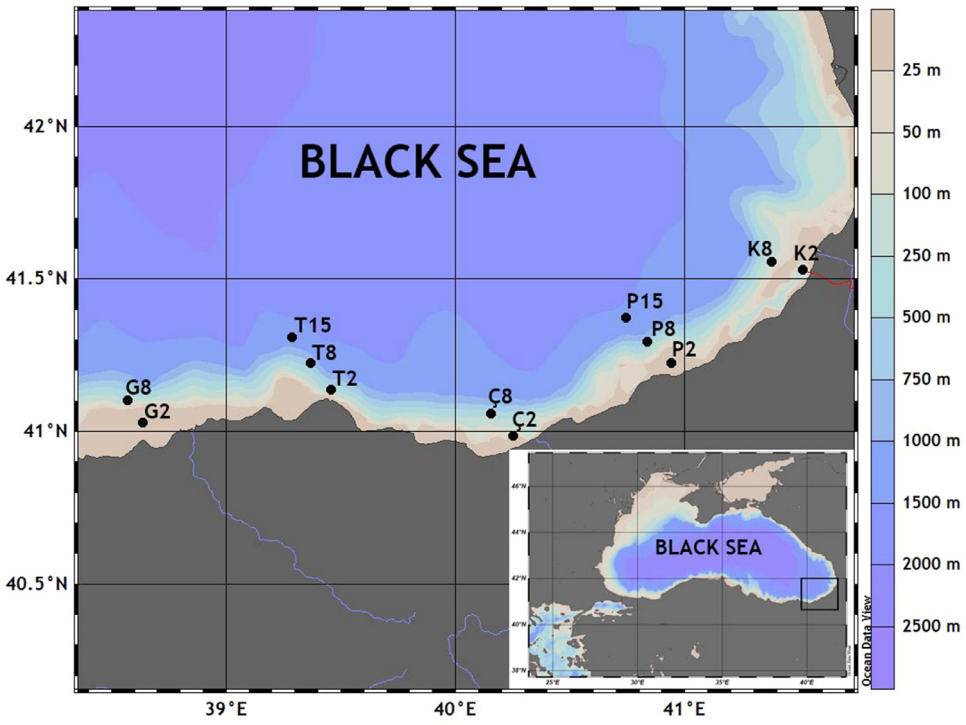

Figure 1 Map of study area and station locations (K2: Kemalpasa 2 nm, K8: Kemalpasa 8 nm, P2: Pazar 2 nm, P8: Pazar 8 nm, P15: Pazar 15 nm, Ç2: Camburnu 2 nm, Ç8: Camburnu 8 nm, T2: Trabzon 2 nm, T8: Trabzon 8 nm, T15: Trabzon 15 nm, G2: Giresun 2 nm, G8: Giresun 8 nm).

Table 1 Seasonal ranges of the parameters (mean, minimum and maximum values) obtained for the study area.

Parameters	Autumn	Winter	Spring	Summer	Overall
Temperature (°C)	12.27 (8.35-18.20)	8.67 (8.123-10.52)	10.37 (8.14-19.79)	13.06 (8.379-28.41)	11.08 (8.12-28.41)
Salinity (‰)	18.38 (17.43-19.98)	18.23 (17.354-18.88)	18.30 (16.13-19.54)	18.39 (17.63-19.71)	18.33 (16.13-19.98)
Chl-*a* ($\mu g\ l^{-1}$)	1.25 (0.35-4.57)	1.60 (0.27-4.96)	0.68 (0.21-2.50)	0.60 (0.161-2.75)	1.03 (0.16-4.96)
Euphotic zone (m)	22.33 (19-26)	28.67 (18-36)	29.83 (23-45)	35.25 (31-40)	29.02 (18-45)
NO_{2+3}-N (μM)	0.59 (0.001-2.12)	0.60 (0.014-1.55)	0.0449 (0.001-0.61)	0.23 (0.001-0.88)	0.37 (0.001-2.12)
PO_4-P (μM)	0.060 (0.001-0.28)	0.059 (0.001-0.11)	0.030 (0.001-0.14)	0.029 (0.001-0.14)	0.04 (0.001-0.28)
SiO_2-Si (μM)	4.24 (1.58-13.63)	2.04 (0.01-6.30)	1.94 (0.60-4.75)	1.55 (0.28-5.19)	2.444 (0.01-13.63)
Pico_PP (mgC m^{-2} d^{-1})	347.67 (84-582)	433.50 (120-1143)	817.50 (275-1848)	486.33 (119-1335)	521.25 (84-1848)
Nano_PP (mgC m^{-2} d^{-1})	409.25 (188-637)	947.42 (97-2095)	1318.17 (263-3156)	414.08 (96-1168)	772.23 (96-3156)
Micro_PP (mgC m^{-2} d^{-1})	217.92 (86-529)	702.83 (56-1710)	1301.33 (169-3363)	444.42 (73-1204)	666.63 (56-3363)
Total_PP (mgC m^{-2} d^{-1})	974.67 (521-1444)	2084.08 (323-4163)	3437.17 (951-5931)	1344.83 (295-2555)	1960.19 (295-5931)

2.2. Phytoplankton analysis

Samples (1 litre) for the phytoplankton analysis were preserved with 4% formalin, and later the samples were concentrated to 10 ml by sedimentation method after keeping the samples immobile for 2 weeks in a dark and cool place until microscopic analysis (Utermöhl, 1958). The excess seawater after settling was gently removed with a pipette. A subsample of 1 ml from the concentrated sample (10 ml) was counted by using a Sedgewick-Rafter cell under a phase-contrast binocular microscope (Leica DM4000). The phytoplankton groups (diatoms, dinoflagellates, other phytoplankton groups) were identified according to Balech (1988), Tomas (1996) and Rampi and Bernard (1978).

2.3. Nutrient analysis

Samples for nutrient (NO_{2+3}-N, SiO_2-Si and PO_4-P) analyses were filtered through 0.45 μm cellulose acetate membrane filters. The filtrate was collected in 100 ml acid-washed high-density polyethylene bottles, and then was kept frozen (−20°C) until the analysis. An auto-analyser (SEAL) was used to measure nutrient concentrations. Nitrite and Nitrate (NO_{2+3}-N) were analysed according to cadmium coil reduction method followed by sulfanilamide reaction in the presence of N-(1-naphthylethylenediamine) dihydrochloride (Std. Methods 4500-NO_3^-F, APHA, 1998). Ortho-phosphate (PO_4-P) was detected according to OrthoAcidic molybdate/antimony with ascorbic acid reduction (phosphomolybdenum blue) method (Std. Methods 4500-P F, APHA, 1998). Reactive silicate (SiO_2-Si) was measured by using acidic molybdate with ANSA reduction (silicomolybdenum blue) method (Std. Methods 4500-SiO_2 D, APHA, 1998).

2.4. Size-fractionated primary production experiments

A 14C radio-tracing technique was deployed in order to estimate phytoplankton primary production (Steemann-Nielsen, 1952; Richardson, 1991). For this purpose, sea water samples from each depth were sub-sampled into 50 ml clear polycarbonate bottles. All bottles were pre-cleaned following JGOFS protocols to reduce trace metal contamination. Each bottle (50 ml) was inoculated with 50 μL $NaH^{14}CO_3^-$ (1 μCi; 2220000 dpm). After inoculations, the polycarbonate bottles were transferred to an on-deck incubation system (ICES Incubator HYDROBIOS) with simulated subsurface irradiance over depth to 97%, 55%, 33%, 20%, 14%, 7%, 3%, 1% or 0.1% of the surface value and incubated for two hours (between 10.00 and 12.00 pm).

After the incubation, each sample was filtered through 0.2, 2 and 10 μm polycarbonate filters to measure the pico-, nano- and microphytoplankton primary production, respectively. The filters were exposed to concentrated hydrochloric acid (HCl) fumes for 12 hours. Then, the filters were transferred to scintillation vials and 4 ml of scintillation cocktail was added. The carbon activities (as disintegration time per minute, DPM) of each sample were measured with a liquid scintillation counter (LSC, PerkinElmer TriCarb 1550). Dark-bottle values were subtracted from the counts obtained from different light depths to calculate net production. Hourly rates of production were calculated from the measurements, and then these rates were converted to depth-integrated PP rates (mgC m^{-2} d^{-1}) using the trapezoidal method (O'reilly and Zetlin, 1998). Hourly production rates were converted to daily rates depending on PAR measurements.

Following equation was used to calculate the rates of PP:

$$Pt = \frac{dpm(a).total\ CO2(c).12(d).1.05(e).1.06(f).k1.k2.k3}{dpm(b)}$$

where Pt = carbon uptake, mgC m^{-3} h^{-1} and:

(a) = sample dpm − background dpm = net dpm/sample
(b) = the activity of the added ^{14}C solution dpm
(c) = concentration of total CO_2 in experimental water, μMdm^{-3}
(d) = 12: the atomic weight of carbon, converts μMdm^{-3}'to mgdm^{-3}
(e) = a correction for the effect of 14C discrimination
(f) = a correction for the respiration of organic matter produced during the experiment

$k1$ = a correction factor for sub-sampling
$k2$ = a time correction factor
$k3$ = a unit conversion factor

2.5. Evaluation of data

Kolmogorov-Smirnov test was applied to check whether the distribution of data was normal. One-way analysis of variance (ANOVA) test was used to test for significant differences between data sets (e.g., size-fractionated PP, Chl-*a*, phytoplankton abundance, inorganic nutrients and hydrography).

3. Results

3.1. Temperature and salinity profiles

Sea surface temperature (SST) ranged from 8.58°C (winter 2015) to 28.41°C (summer 2015) with a statistically significant difference (ANOVA, $p<0.001$) during the study period (Figure 2). The water column was uniform in winter due to the strong convectional mixing, whereas thermal stratification was observed in summer and continued until autumn. The seasonal thermocline was detected between 20 and 50 m depths in summer and autumn. Surface salinity values revealed a typical Black Sea pattern and varied from 16.13‰ (spring 2015) to 18.18‰ (summer 2015) with seasonal differences (ANOVA, $p<0.001$). Depending on the depth, salinity increased to 20‰ which indicates the presence of Mediterranean origin waters at deeper depths (Figure 3). Surface salinity values clearly show that the upper layer of the study area is influenced by the river inflow, particularly during spring. Euphotic zone depth derived from PAR values ranged from 18 m (winter 2014) to 45 m (spring 2015) along the area. In general, the thickness of euphotic zone in summer and spring was greater than in other seasons (Table 1).

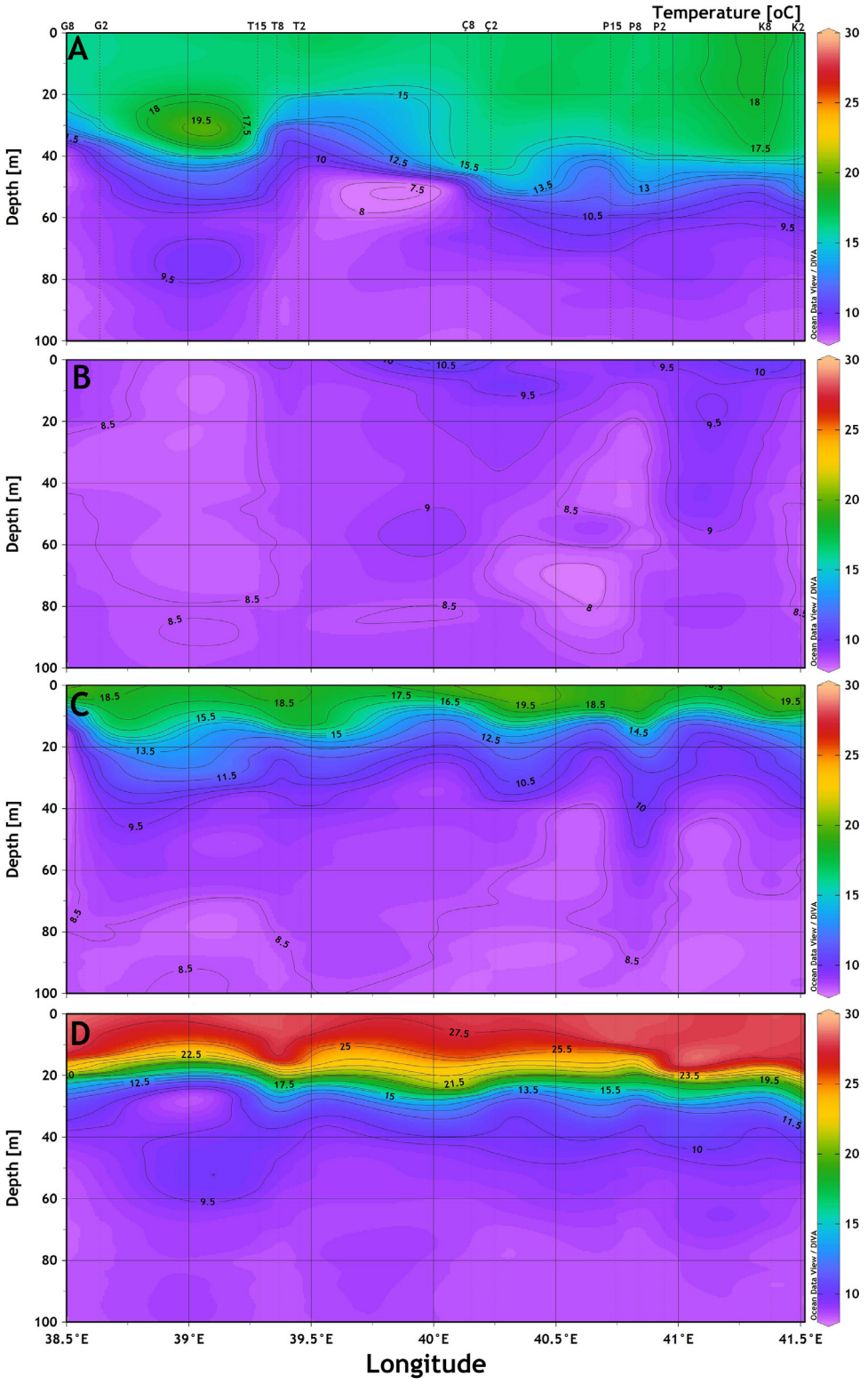

Figure 2 Spatio-temporal variations in temperature (A: autumn, B: winter, C: spring, D: summer).

3.2. Nutrient dynamics

Seasonal dynamics of nutrients (i.e., nitrite plus nitrate, phosphate and silicate) were given in Figures 4—6. Over the study period, nutrient concentrations substantially varied, and revealed statistically significant seasonal differences (ANOVA, $p<0.001$). Extensive vertical mixing during autumn and winter seasons resulted in high nutrient concentrations

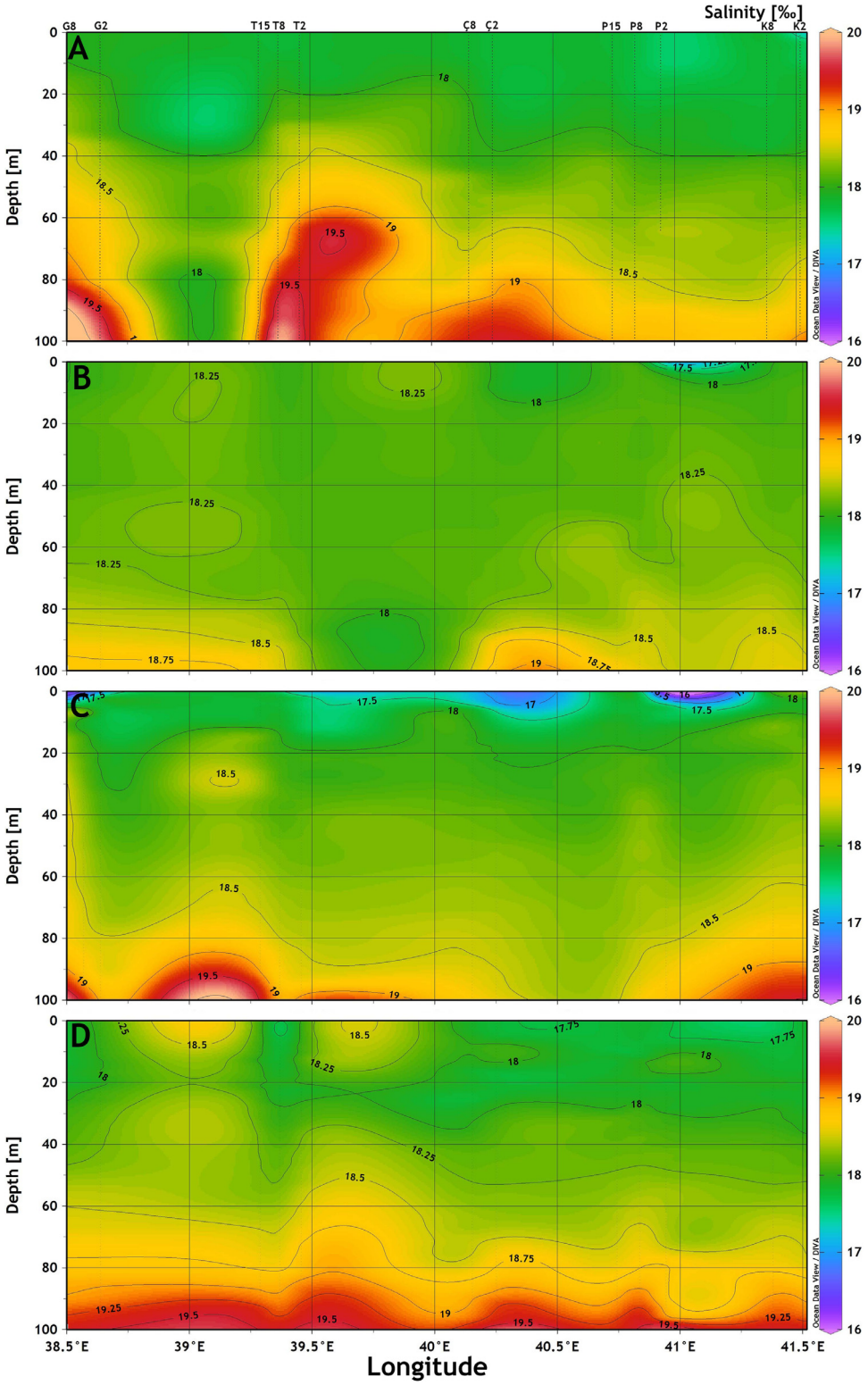

Figure 3 Spatio-temporal variations in salinity (A: autumn, B: winter, C: spring, D: summer).

in the euphotic zone. On the other hand, the concentrations were relatively low and showed a more uniform pattern during spring and summer along the study area. In general, the nutrient concentrations were high in the autumn and winter, and depending on phytoplanktonic activity, the concentrations decreased in the spring and summer. Overall, phosphate concentrations (0.001—0.28 ±0.04 μM) were very low, however, concentrations of NO_{2+3} (0.001—2.12 ±0.39 μM) and silicate (0.01—13.63 ±1.93 μM) were significantly high along the stations (Table 1).

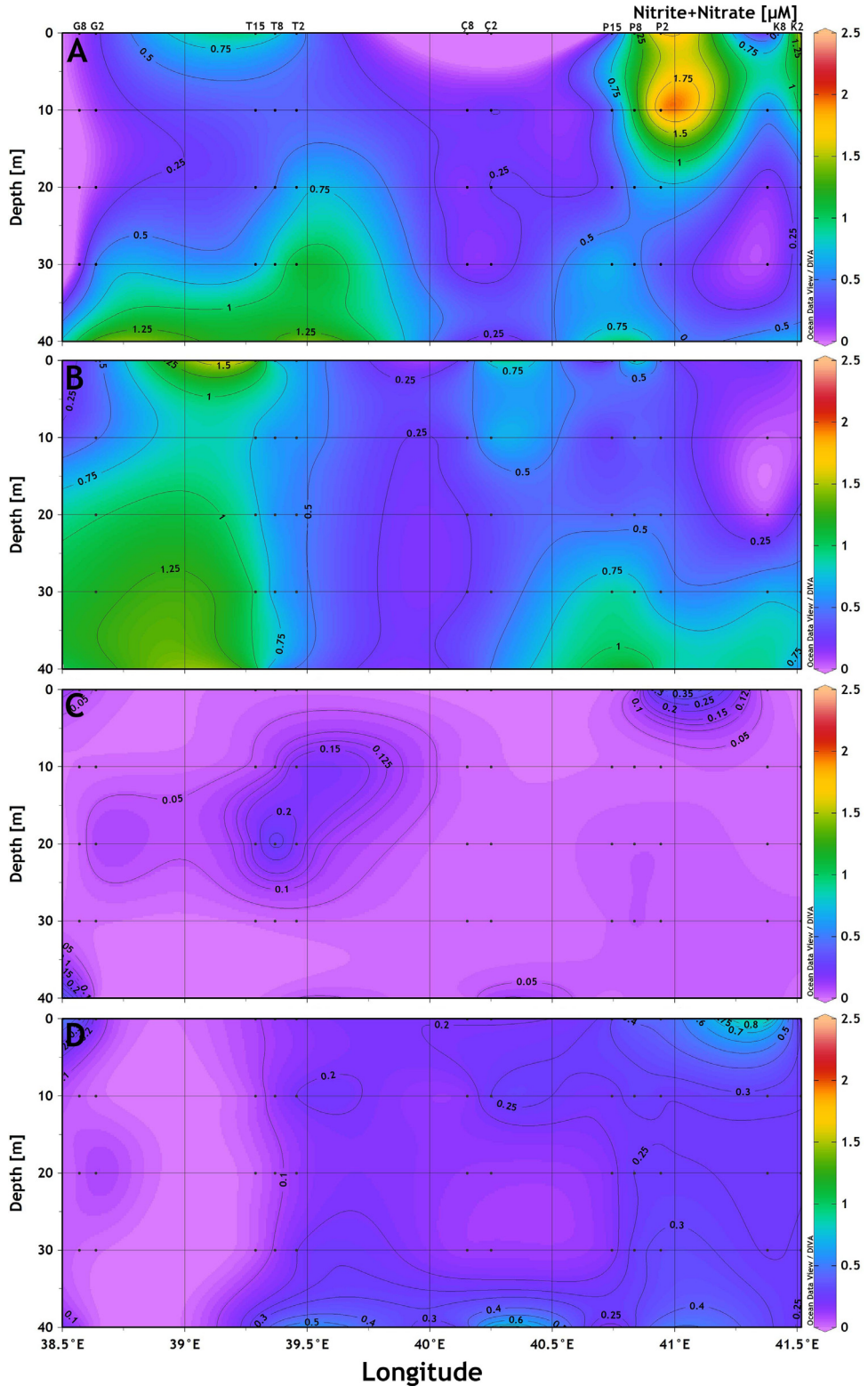

Figure 4 Spatio-temporal variations in nitrite and nitrate concentrations (A: autumn, B: winter, C: spring, D: summer).

NO_{2+3}-N concentrations were generally high in autumn (0.001—2.12 µM) and winter periods (0.014—1.55 µM) when mixing process took place and phytoplanktonic activity were low, differently, the concentrations were low in spring (0.001—0.61 µM) and summer (0.001—0.88) periods (Figure 4). Depending on the depth, high concentrations were recorded between 10 m and 20 m, except for the summer (Ç2 station, 40 m).

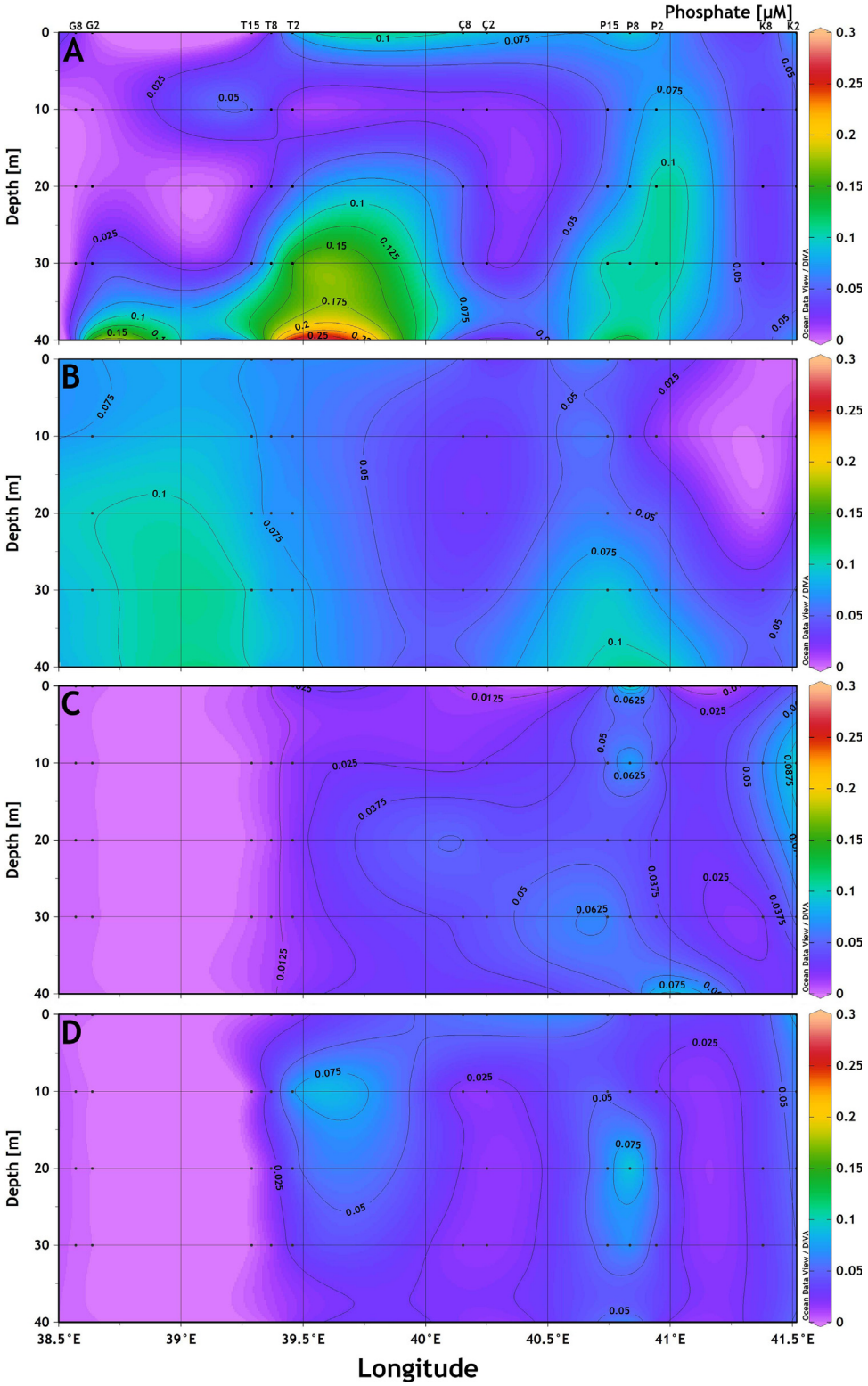

Figure 5 Spatio-temporal variations in phosphate concentrations (A: autumn, B: winter, C: spring, D: summer).

PO_4-P concentrations were generally low (generally less than 0.5 µM) with statistically significant differences (ANOVA, $p<0.05$) in the study area (Figure 5). The highest concentrations were measured in the autumn (0.001—0.28 µM), while the lowest values were measured in spring and summer (0.001—0.14 µM). During the study period, deeper waters were characterized by high phosphate concentration in autumn (T2 station, 40 m) and winter (P8

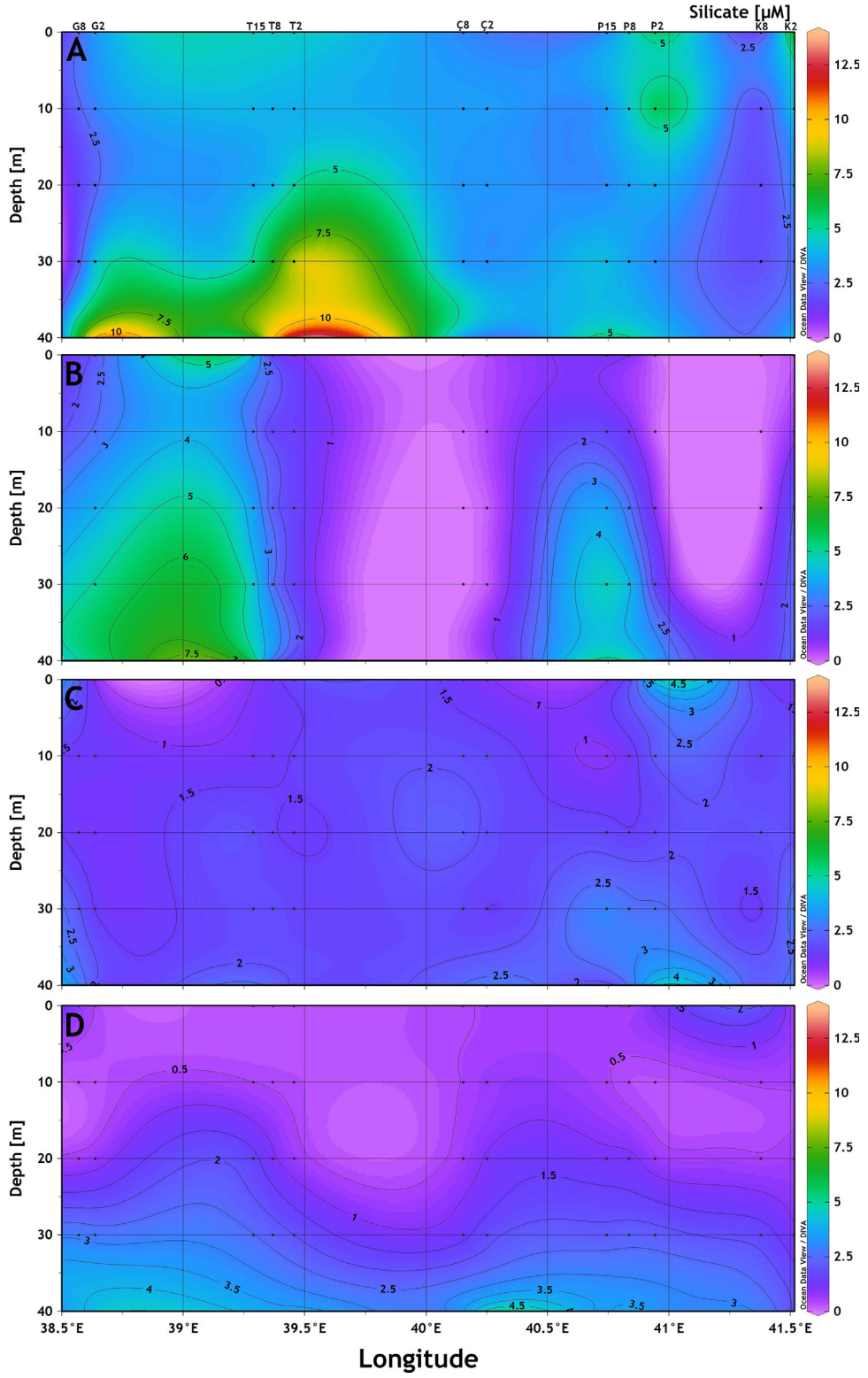

Figure 6 Spatio-temporal variations in silicate concentrations (A: autumn, B: winter, C: spring, D: summer).

station, 40 m), while the surface waters had much phosphate in spring (P8 station surface) and summer (P8 station, 20 m).

In general, SiO_2-Si concentrations revealed an increasing pattern with depth (Figure 6), and varied significantly (ANOVA, $p<0.05$) along the study area. The highest concentrations were generally recorded in autumn (1.58—13.63 µM) and winter (0.01—6.30 µM). On the other hand, the concentrations decreased in spring (0.60—4.75 µM) and summer (0.28—5.19 µM).

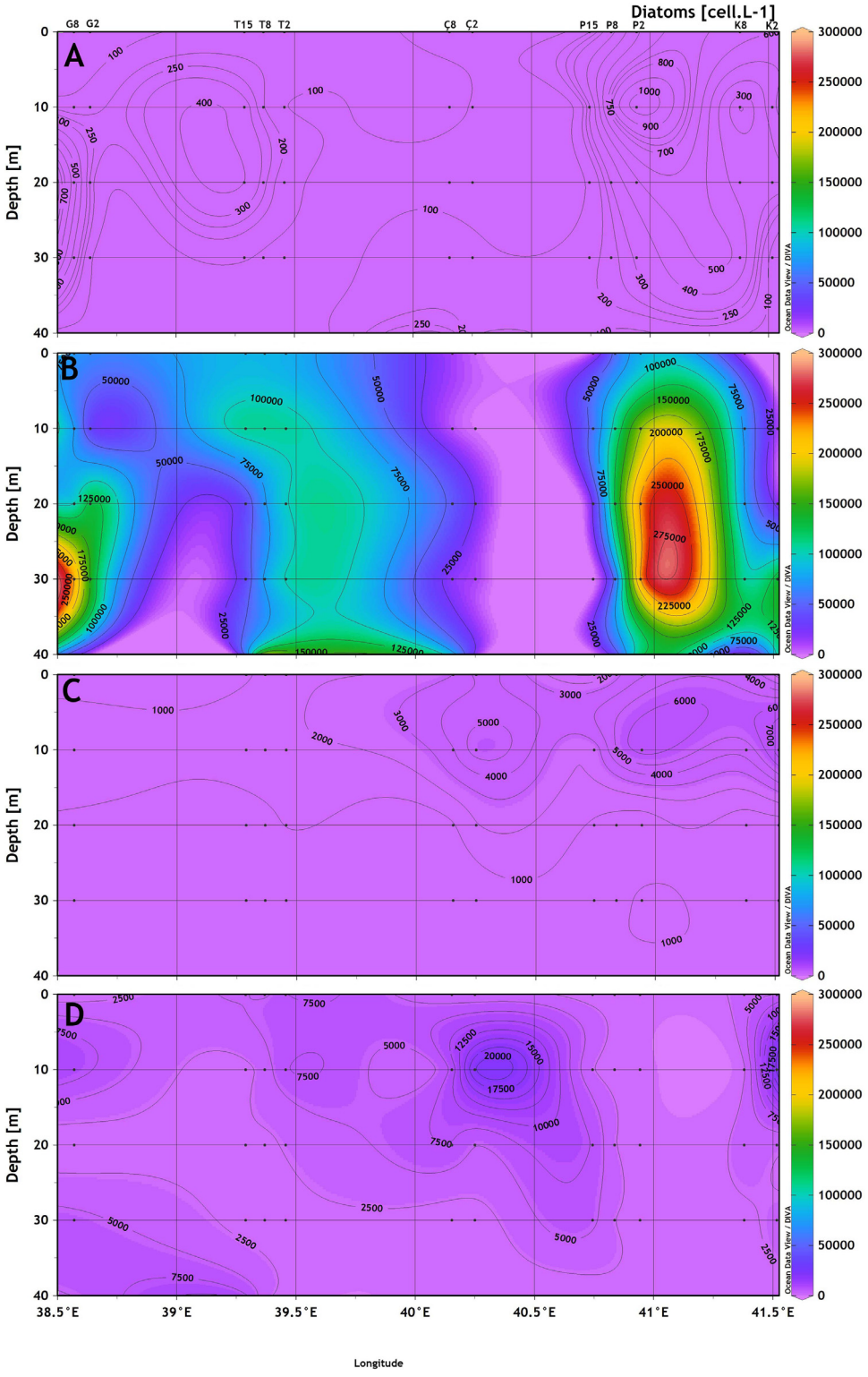

Figure 7 Spatio-temporal variations in diatom abundance (A: autumn, B: winter, C: spring and D: summer).

3.3. Phytoplankton composition and abundance

A total of 127 species were identified along the study area. 53.54% of these were dinoflagellate species (68 species), 40.94% were diatom species (52 species) and 5.51% consisted of other species (7 species), mainly coccolithophores (*Emiliania huxleyi*). The most dominant and common species were *Chaetoceros decipiens*, *Coscinodiscus granii*, *Coscinodiscus radiatus*, *Pseudo-nitzschia delicatissima*, *Rhizosolenia calcar-avis*, *Rhizosolenia setig-*

era, Thalassionema nitzschioides, Thalassiosira angustelineata, Alexandrium minutum, Ceratium furca, Ceratium fusus, Ceratium tripos, Dinophysis acuminata, Dinophysis acuta, Dinophysis ovata, Gymnodinium sp., *Noctiluca scintillans, Prorocentrum compressum, Prorocentrum micans, Prorocentrum minimum, Protoperidinium depressum, Protoperidinium steinii, Scrippsiella triquedium* and *Emiliania huxleyi* along the study area.

Quantitative phytoplankton distribution along the study area varied seasonally. Dinoflagellates (up to 5×10^3 cells l^{-1}) and other taxonomic groups (up to 1.5×10^5 cells l^{-1}) were in notable abundance during the autumn. On the other hand, diatoms (up to 3×10^5 cells l^{-1}) abundance remarkably increased in winter (Figures 7–9). In spring, dinoflagellates abundance (up to 10×10^3 cells l^{-1}) and other taxonomic groups (maximum 4×10^4 cells l^{-1}) were remarkably high, however, a decrease in diatom abundance was detected when compared to the previous sampling period. Quantitative phytoplankton density significantly decreased in the summer, and the abundance remained below 3×10^3 cells l^{-1} when compared to other seasons (Figures 7, 8 and 9)

In terms of total cell number, winter was the most prominent period with a maximum of 4.1×10^5 cells l^{-1}, followed by autumn (up to 1.5×10^5 cells l^{-1}) and spring (up to 5×10^4 cells l^{-1}), respectively (Figure 10). Over the study period, the abundance of diatoms revealed statistically significant differences among all seasons, while dinoflagellates were statistically different in spring and summer, other taxonomic groups were only statistically different in the autumn and summer (ANOVA, $p<0.05$). Similarly, total cell numbers also showed statistically significant differences between all seasons except for the autumn and spring seasons (ANOVA, $p<0.05$).

3.4. In-situ Chlorophyll-*a*

In-situ Chl-*a* concentrations (0.16-4.96 $\pm$ 0.87 $\mu g\ l^{-1}$) significantly varied (ANOVA, $p<0.01$) over the study period. In the autumn (0.35–4.57 $\mu g\ l^{-1}$), the first 20 m of the water column was rich in terms of Chl-*a*, and its concentrations reached up to 4.57 $\mu g\ l^{-1}$ (Figure 11A). After these depths, Chl-*a* profile showed a more uniform pattern. In the winter (0.27–4.96 $\mu g\ l^{-1}$), Chl-*a* was much patchy due to the intensive vertical mixing process (Figure 11B). In this period, Chl-*a* concentration reached up to 5 $\mu g\ l^{-1}$. In the spring (0.21–2.50 $\mu g\ l^{-1}$), the first 20–40 m of the water column was much richer in terms of Chl-*a* concentration. However, Chl-*a* concentration did not exceed 2.50 $\mu g\ l^{-1}$ during this period when the river runoff was intense, and the nutrient concentration was high (Figure 11C). In the summer (0.16–2.75 $\mu g\ l^{-1}$), Chl-*a* concentrations were lower than other seasons, and the highest concentrations (2.75 $\mu g\ l^{-1}$) were generally detected at 20–25 m (Figure 11D).

3.5. Total and size-fractionated primary production

During the study period, total PP revealed significant seasonal variations (Figure 12, Table 1). Total and group-specific depth-integrated Primary Production rates for the stations are given in Supplementary Material Table 2. Spring was the most productive season with the highest total PP rates (5931 mgC m^{-2} d^{-1}) over the study period. Winter was the second productive period, and total PP rates reached up to 4163 mgC m^{-2} d^{-1}. Summer and autumn had relatively low total PP levels when compared to other seasons, and their PP rates were 2555 mgC m^{-2} d^{-1} and 1444 mgC m^{-2} d^{-1}, respectively. Among the stations, Kemalpasa and Pazar stations, which are under the effect of river runoff, were the most productive stations, whereas Camburnu station had the lowest production rates in terms of total primary production rates.

The rates of size-fractionated PP varied remarkably throughout the study period (Figure 13, Table 1). In general, the rates of PP varied from 84 to 1848 mgC m^{-2} d^{-1}, 96 to 3156 mgC m^{-2} d^{-1} and 56 to 3363 mgC m^{-2} d^{-1} for pico-, nano- and microphytoplankton, respectively. The autumn period was characterised with high nanophytoplankton PP (637 mgC m^{-2} d^{-1}) and followed by picophytoplankton PP (582 mgC m^{-2} d^{-1}) along the study area (Figure 13A, Table 1). A substantial increase in PP rates of nano- (2095 mgC m^{-2} d^{-1}) and microphytoplankton PP (1710 mgC m^{-2} d^{-1}) were recorded in the winter (Figure 13B). In this period, PP rates increased by almost 2–3 folds compared to the autumn period. In the spring, the highest size-fractionated production rates were detected, and reached up to 3000–3500 mgC m^{-2} d^{-1} along the stations (Figure 13C). In this period, the most significant contribution was made by microphytoplankton (3363 mgC m^{-2} d^{-1}). The second group was nanophytoplankton with the rates of 3156 mgC m^{-2} d^{-1} levels. Picophytoplankton was the last group with the maximum rate of 1848 mgC m^{-2} d^{-1} in spring (Table 1). Summer period was characterized by picophytoplankton, and the production rates reached up to 1335 mgC m^{-2} d^{-1} (Figure 13D). In terms of spatial variation, microphytoplankton was generally dominant along the coastal stations, however their production rates (1200 mgC m^{-2} d^{-1}) was less than picophytoplankton. Nanophytoplankton were high in offshore stations with the rates of 1168 mgC m^{-2} d^{-1} during summer (Table 1).

4. Discussion

The present study facilitates to examine the spatio-temporal changes in size-fractionated PP, total PP, and *in-situ* Chl-*a* with phytoplankton abundance and nutrient data along the south-eastern Black Sea. More importantly, this work is also the first study that revealed size-fractionated primary production rates with a seasonal basis for the Black Sea.

4.1. Spatio-temporal variations in nutrients

The surface waters of the southern coasts of the Black Sea are characterised with low nutrient concentrations especially during stratified periods (Basturk et al., 1994; Bingel et al., 1993; Codispoti et al., 1991). The concentrations are mostly affected by sub-surface nutricline and vertical mixing processes (Yayla et al., 2001). Besides, regional rivers are also the primary resources of nutrients, especially in coastal areas. Nutrient concentrations in the

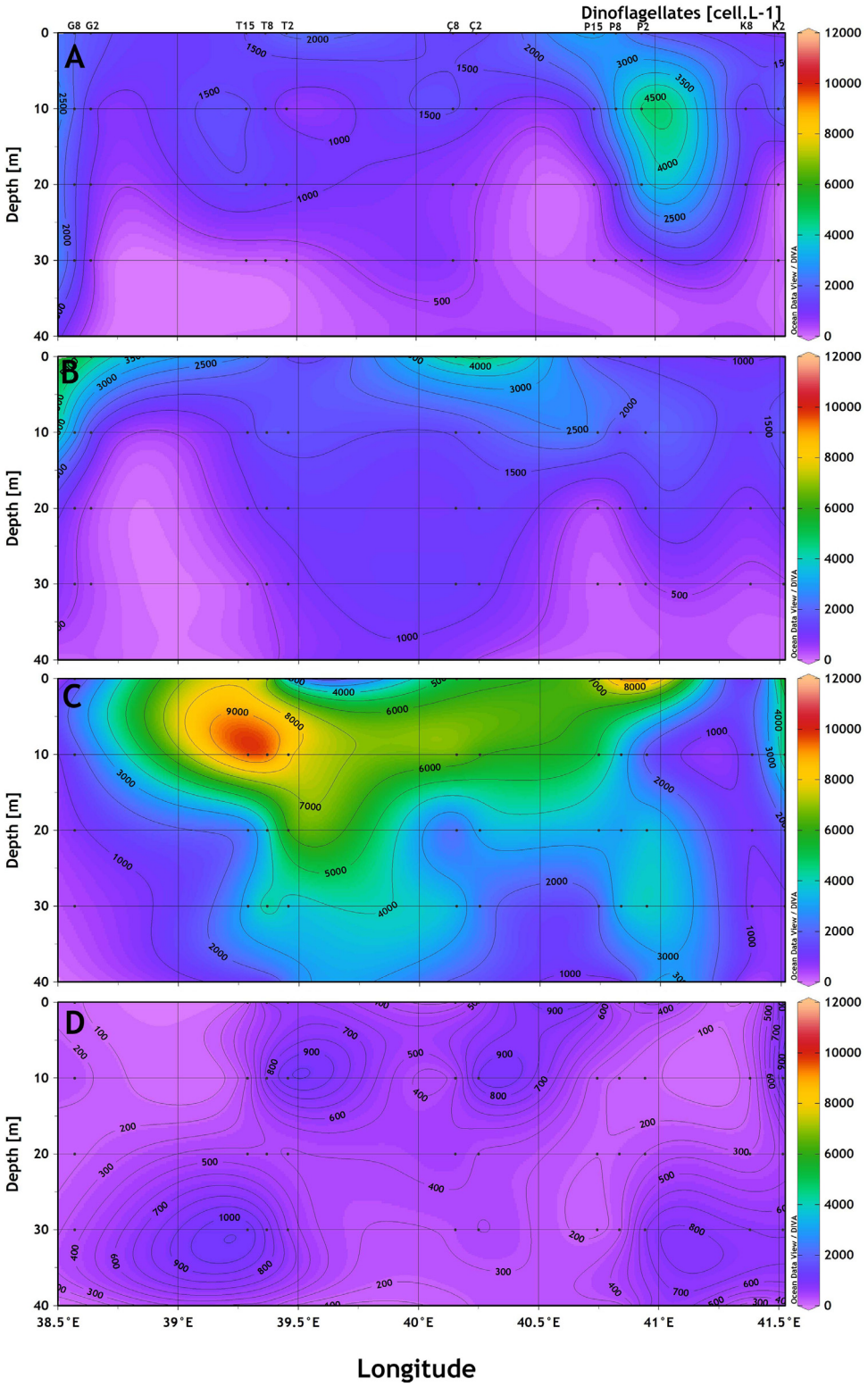

Figure 8 Spatio-temporal variations in dinoflagellates abundance (A: autumn, B: winter, C: spring and D: summer).

euphotic zone varied seasonally from 0.16 to 1.5 μM for TNOx, and from 0.03 to 0.35 μM for phosphate in the spring-autumn period of 1995—1996 (Yilmaz et al., 1998). During July 1997—September 1998 period, concentrations in the euphotic zone were detected as <0.35 μM for PO_4, <0.5 μM for NO_{2+3} and 5 μM for silicate along the southern Black Sea (Yayla et al., 2001). In the present study, nutrient concentrations varied seasonally, and detected as 0.001—2.12 μM; 0.001—0.28 μM and 1.58—13.63 μM for NO_{2+3}-N, PO_4-P and SiO_2-Si, respectively. Throughout the seasons, au-

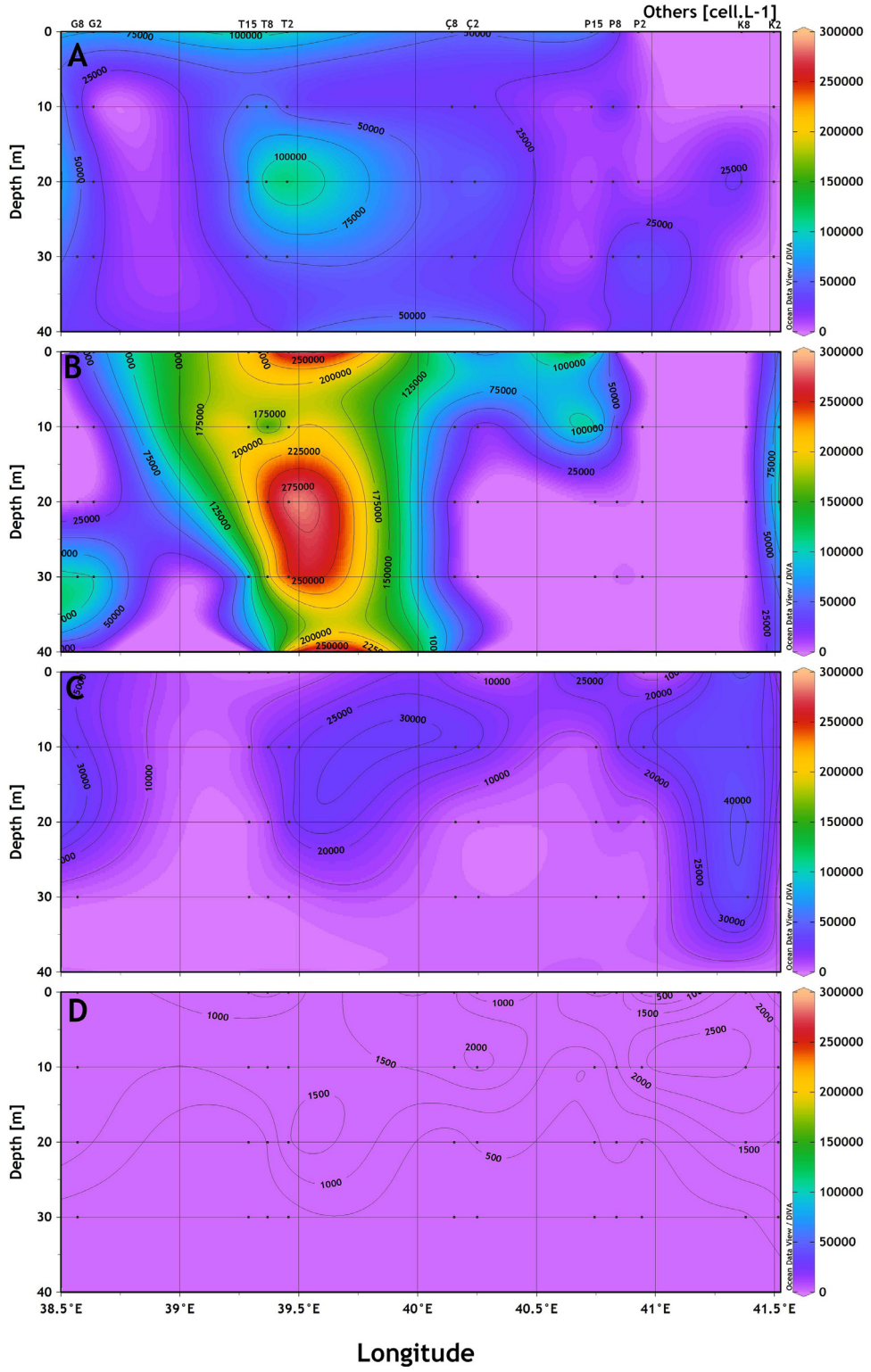

Figure 9 Spatio-temporal variations in other phytoplankton groups abundance (A: autumn, B: winter, C: spring and D: summer).

tumn was detected as the richest period in terms of nutrient concentrations along the study area. In the study area, coastal stations were richer in terms of nutrient concentrations than offshore stations. In particular, some stations (e.g., T2 and P2) are under influence of major river runoffs (e.g., Değirmendere and Fırtına Rivers) which lead to detect high nutrient concentrations even at the base of the euphotic zone.

Total NO_{2+3}-N concentrations for the southern Black Sea were reported as 0.11—0.59 μM (Eker-Develi et al., 2003). In another study, total NO_{2+3}-N concentrations were reported as 0.02—4.14 μM for the Anatolian coast of the Black Sea

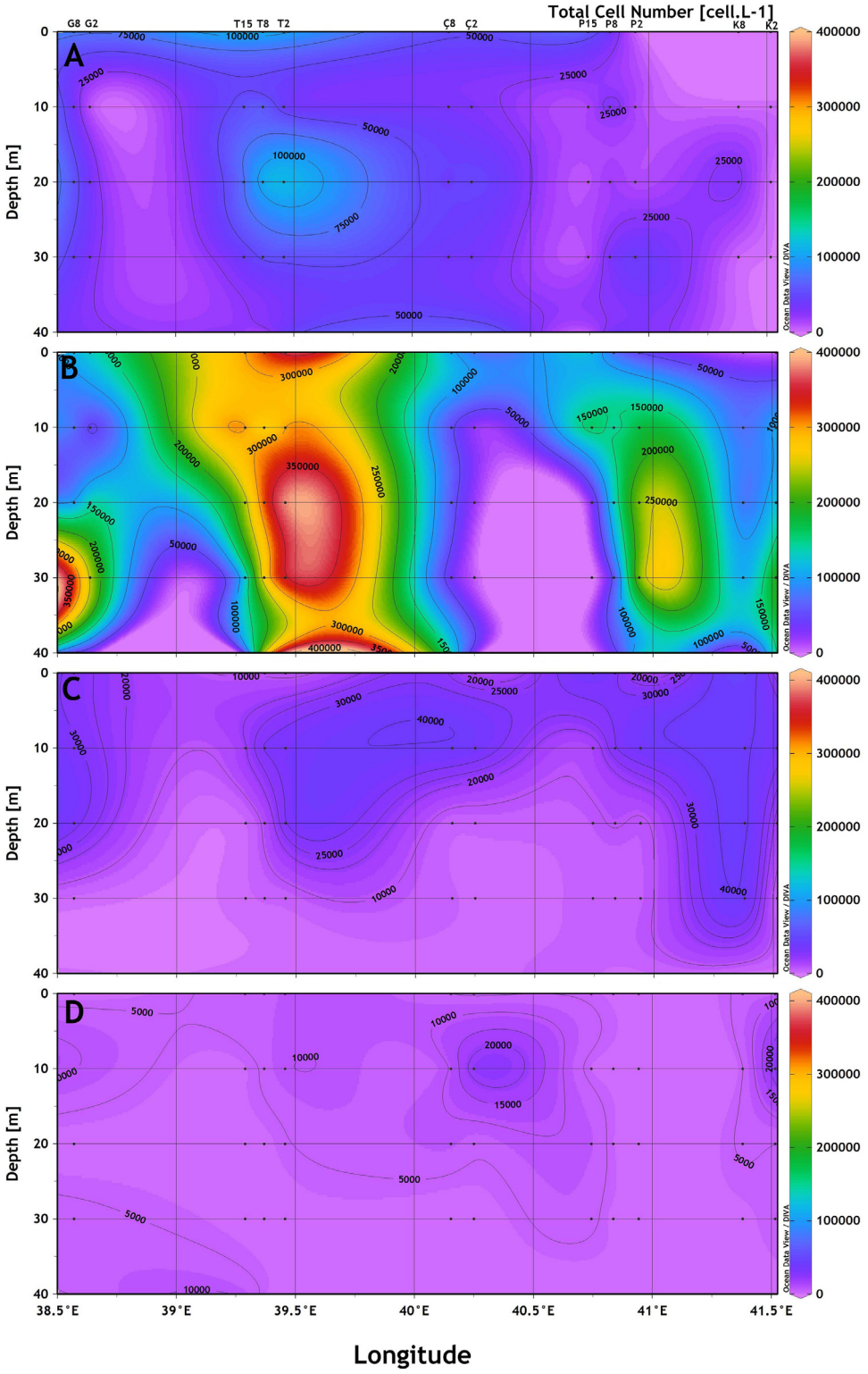

Figure 10 Spatio-temporal variations in total phytoplankton cell numbers (A: autumn, B: winter, C: spring and D: summer).

(Coban-Yildiz et al., 2000). Along the south-eastern Black Sea coasts, the total NO_{2+3}-N concentrations varied between 0.37 and 4.71 μM in coastal waters and ranged from 0.31 to 4.46 μM in open waters (Agirbas, 2010). In a study conducted by Koca (2014), NO_{2+3}-N concentrations were detected between 0.52 and 9.88 μM along the south-eastern Black Sea (Rize) (Koca, 2014). In the present study, the total NO_{2+3}-N concentration varied between 0.001 and 2.12 μM with significant seasonal variations. Compared to previous studies, NO_{2+3}-N concentrations were found to be lower

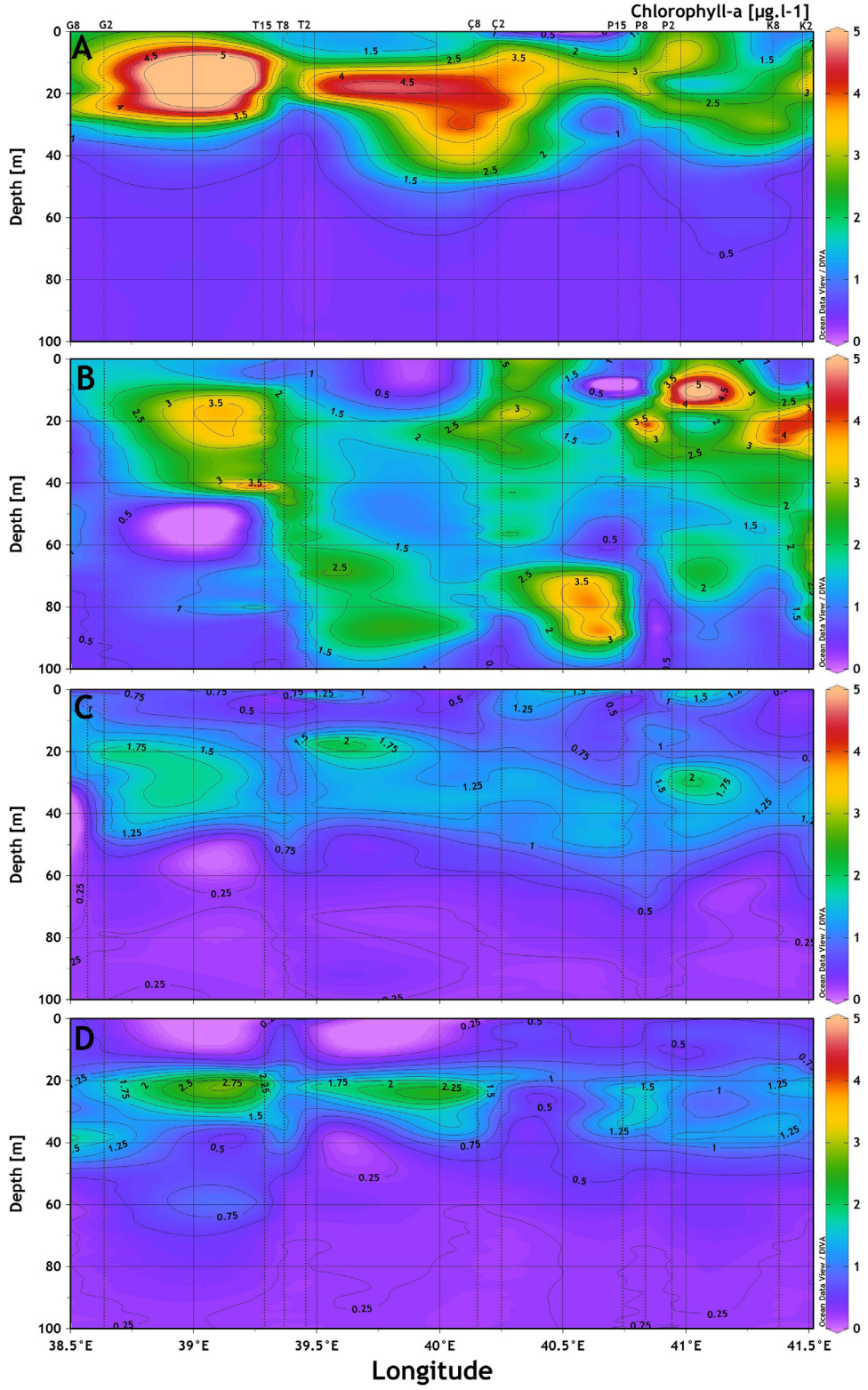

Figure 11 Spatio-temporal variations in *in-situ* Chl-*a* concentrations (A: autumn, B: winter, C: spring and D: summer).

than those of studies conducted along southern coasts of the Black Sea.

Average PO_4-P concentration in surface waters was reported as 0.419 μM in the Black Sea (Sorokin, 1983). In a time-series study conducted along the Romanian coasts, average PO_4-P concentrations were measured as 0.26 μM for the period of 1959—1965, 6.54 μM for the period of 1983—1990 period, 1.86 μM for the period of 1991—2000 and 0.49 for the period of 2001—2005 (Oguz et al., 2008). The average PO_4-P concentration was reported as 0.002 μM (Novem-

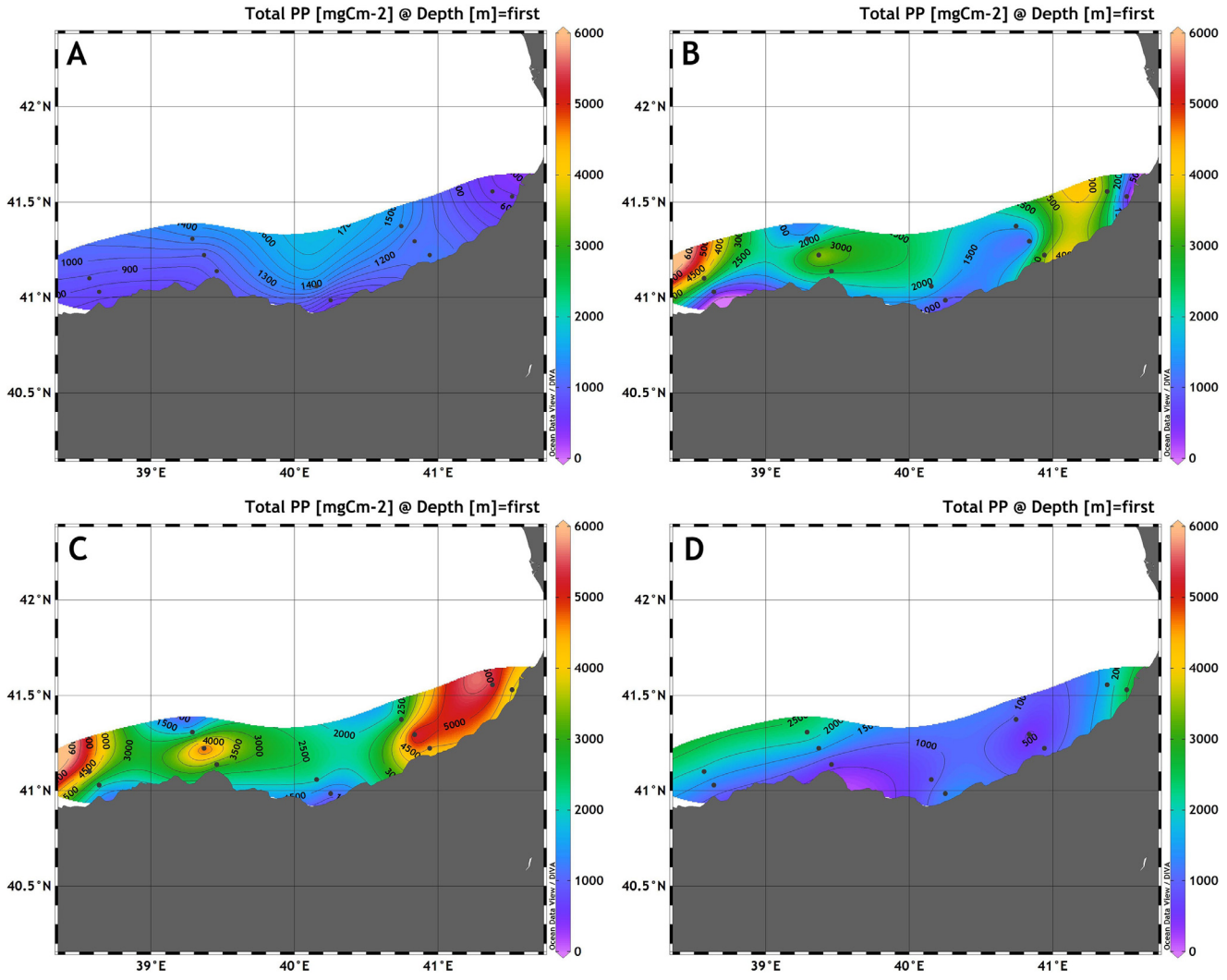

Figure 12 Spatio-temporal variations in integrated size-fractionated primary production rates (A: autumn, B: winter, C: spring and D: summer).

ber 2009) to 0.052 μM (June 2009) at the coastal stations in the south-eastern Black Sea (Agirbas, 2010). In the open waters, concentrations varied between 0.002 μM (November 2009) and 0.068 μM (June 2009). Similarly, the phosphate concentration for the south-eastern Black Sea varied between 0.01—0.06 μM (Kopuz, 2012). Along the south-eastern coasts (Rize), PO_4-P concentration varied between 0.03 and 0.90 μM (Koca, 2014). In this study, PO_4-P concentrations ranged from 0.001 to 0.28 μM. The highest PO_4-P concentrations were observed in autumn while, the lowest values were measured in winter. Overall, a significant decrease was observed in PO_4-P concentrations over the years when compared to the previous decades along the study area.

As a general trend, SiO_2-Si concentration of seawater varies between 7—15 μM in surface waters during the winter period, concentrations may decrease down to 0.35 μM in the summer period (Tait, 1988). Depending on phytoplankton activity, SiO_2-Si concentrations decrease especially after intense diatom blooms in the Black Sea, and its concentration increases again with river inputs and precipitation (Bologa, 1986). The average annual surface water SiO_2-Si concentrations were reported as 40.5 μM for the period of 1959—65; 11.0 μM for the period of 1983—1990; 12.6 μM for the period of 1991—2000 and 13.7 μM for the period 2001 of 2005 along the Romanian coasts (Oguz et al., 2008). Particularly, after the 70's, reactive silicate concentration in surface waters of Black Sea decreased by 60% due to dam constructions on river Danube, and this decline led to dramatic changes in phytoplankton compositions especially in diatoms in the early 1990s (Kideys et al., 2000). It was reported that SiO_2-Si concentrations varied between 1.20 and 14.08 μM in the south-eastern Black Sea coast (Agirbas, 2010). In another study conducted in the same region, SiO_2-Si concentrations ranged from 0.37 to 16.63 μM (Kopuz, 2012). Similarly, silicate concentrations were reported between 1.92 and 16.25 μM along the south-eastern Black Sea (Koca, 2014). In the present study, SiO_2-Si concentrations varied between 1.58 and 13.63 μM. The highest concentrations were detected in the autumn due to vertical mixing and low phytoplanktonic activity.

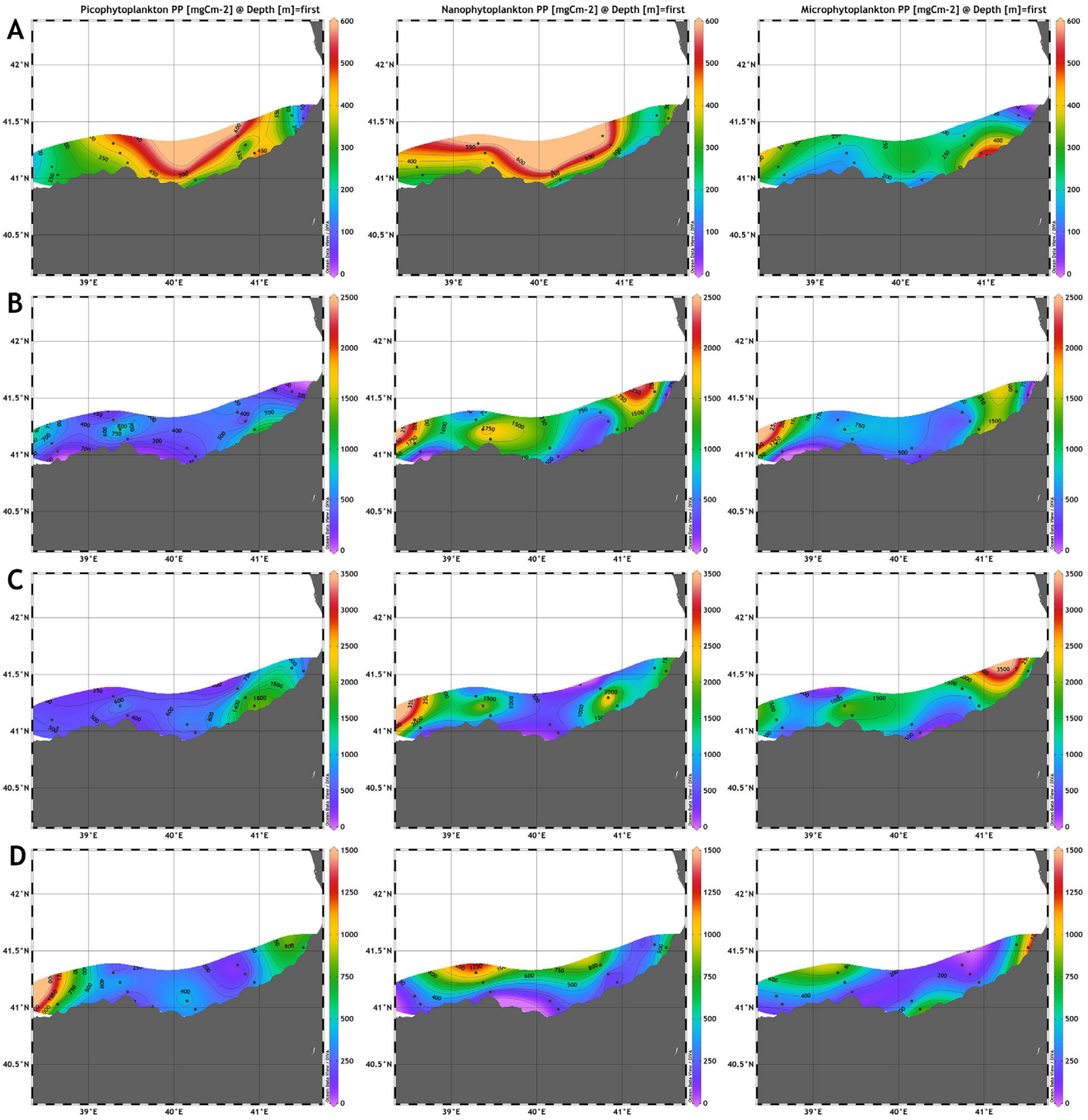

Figure 13 Spatio-temporal variations in total integrated primary production rates (A: autumn, B: winter, C: spring and D: summer).

4.2. Spatio-temporal variations in phytoplankton

The seasonal dynamics of the Black Sea phytoplankton exhibit a typical spring bloom of which diatom are main responsible groups, whereas in the autumn bloom is stimulated by the coccolithophore *Emiliania huxleyi* (Honjo et al., 1987; Oguz and Ediger, 2006; Sorokin, 1983; Vedernikov et al., 1993). However, ecological changes occurred in the ecosystem after the 80′s have led to unusual summer phytoplankton blooms (Hay et al., 1990; Sur et al., 1996; Yayla et al., 2001; Yilmaz et al., 1998). Moreover, these changes have also caused significant shifts in phytoplankton composition and bloom patterns along the Black Sea. In general, diatoms were considered as the main group (46%) contributing to the total phytoplankton biomass, followed by dinoflagellates with a rate of 27% (Zaitsev and Alexandrov, 1997). However, after eutrophication and the retention of inorganic nutrients (mainly silicate) caused shifts in phytoplankton group ratios in favour of coccolithophores and dinoflagellates rather than diatoms (Bodeanu et al., 1998; Bologa et al., 1995; Cociasu et al., 1996; Humborg et al., 1997; Moncheva and

Krastev, 1997). Qualitative changes were also reported in the phytoplankton composition during the eutrophication period, in which the diatom ratio decreased from 67% (209 species) to 46% (172 species) between 1960—1970 and 1972—1977 (Bologa, 1986). In addition, the gradual increases in number of dinoflagellates species in recent years, especially during summer, have made them the dominant group along the Black Sea (Mikaelyan et al., 2013; Moncheva et al., 2001; Uysal and Sur, 1995; Uysal et al., 1998; Zaitsev and Alexandrov, 1997). Similarly, a high dinoflagellate species number (81% of total species number) were reported from south-western Black Sea (Ediger et al., 2006). Agirbas et al. (2015) also reported a high dinoflagellate dominance (71%) from the south-eastern Black Sea for the period of February—December 2009. In the present study, a high dinoflagellate dominancy (53.54%) was also observed throughout the study period. Overall, the results are consistent with recent trends reported from previous studies thus suggesting the dinoflagellate species have become the dominant group in terms of species richness in the study area.

During the study period, two distinct phytoplankton bloom were identified in terms of phytoplankton abundance. These periods were autumn (1.5×10^5 cells l^{-1}) and winter (4.1×10^5 cells l^{-1}). Especially in winter, diatoms were represented with the high cell abundance, followed by *E. huxleyi*. In the autumn, major contributions were made by *E. huxleyi* and dinoflagellates. Throughout the study period, diatoms reached the highest abundance (3×10^5 cells l^{-1}) in the winter, whereas dinoflagellates reached the highest abundance (1×10^4 cells l^{-1}) in the spring. *E. huxleyi* was the most abundant species represented in the other groups and reached the highest abundance (1.5×10^5 cells l^{-1}) in winter.

The north-western shelf of the Black Sea was characterized with higher phytoplankton abundance than other parts of the region. However, the abundance of phytoplankton along the south-eastern Black Sea is quite low when compared with north-western coasts. Phytoplankton abundance, ranged from 3×10^4 to 4.1×10^5 cells l^{-1}, obtained from the present study were found to be similar to those of previous studies conducted on the Anatolian coasts of the Black Sea (Bat et al., 2007; Eker, 1999; Feyzioglu, 1996), however, values were lower than the studies carried out on the north-western continental shelf.

4.3. Spatio-temporal variations in Chl-*a*

Chl-*a* concentrations vary spatially and temporally along the Black Sea. The concentrations in the Black Sea were reported as 0.15 ± 0.04 μg/l for the period of 1964—1986 (Kideys, 1994; McQuatters-Gollop et al., 2008; Mikaelyan et al., 2013; Vinogradov et al., 1999; Yunev et al., 2002). However, the seasonal variations in Chl-*a* are not spatially uniform in the Black Sea (McQuatters-Gollop et al., 2008). The average Chl-*a* concentrations for the entire Black Sea varied between 0.59 and 0.69 μg l^{-1} (Kopelevich et al., 2004). In the shelf region, winters were generally characterised with low Chl-*a* concentrations (McQuatters-Gollop et al., 2008). On the other hand, maximum concentrations in Chl-*a* are generally observed during autumn and winter in the open areas of the Black Sea, while reaches to minimum concentrations in summer (Vinogradov et al., 1999).

For the Anatolian coasts of the Black Sea, Chl-*a* concentrations ranged from 0.1 to 1.5 μg/l during 1995—1996 (Yilmaz et al., 1998). In another study, the surface Chl-*a* values along the coast of Turkey for the period of 1996—1998 ranged from 0.34 to 0.42 μg l^{-1} (Eker-Develi et al., 2003). Ediger et al. (2006) reported that the mean Chl-*a* concentration for the south-western Black Sea varied between 0.15 and 1.23 μg l^{-1}. In the SE Black Sea, surface water of Chl-*a* values was reported as 1.97 μg l^{-1} and 1.84 μg l^{-1} for coastal (2 miles) and offshore (8 miles) stations, respectively (Agirbas, 2010). In another study, Chl-*a* concentrations along the SE Black Sea changed between 0.34 and 2.71 μg l^{-1} (Koca, 2014). Along the south-eastern Black Sea ecosystem, the average surface Chl-*a* concentrations for the period of November 2014—August 2015 were reported as 0.37—2.68 μg l^{-1}; 0.16—2.04 μg l^{-1} and 0.32—1.79 μg l^{-1} for 2, 8, and 15 miles, respectively (Turkmen, 2016). In another study, monthly surface Chl-*a* concentrations varied between 0.51 and 3.97 μg l^{-1} for river mouth, between 0.16 and 2.47 μg l^{-1} for coastal and 0.18 and 3.04 μg l^{-1} for offshore stations (Genc, 2018). Karadeniz (2019) reported that mean surface water *in-situ* Chl-*a* concentrations varied between 2.61 μg l^{-1}, 2.56 μg l^{-1} and 2.23 μg l^{-1} for 2, 8 and 15 miles, respectively. Overall, the Chl-*a* concentrations obtained from the present study exhibited a distinct seasonal pattern, autumn and winter were characterized with high Chl-*a* concentrations (0.35—4.57 and 0.27—4.96 for autumn and winter, respectively), however, the lowest values were detected during spring and summer when the stratification started in spring and strengthened in summer along the study area. The differences in Chl-*a* values observed between the present study and previous studies emphasise that regional differences, study period, sampling regime and frequency as well as changes in phytoplankton communities under changing ecosystem conditions are the main factors.

4.4. Spatio-temporal variations in total and size-fractionated primary production

The Black Sea is commonly reported one of the largest eutrophic (greater than 500 gC m^{-2} y^{-1}) marine environment in the world (Arai, 2001). Over the decades, considerable changes in nutrient input (especially silicate) and other ecological factors altered trophic food web structure of the Black Sea. These changes affected the succession, intensity, frequency, and extension of phytoplankton besides the rates of PP throughout the Black Sea (Oguz, 2005). Previous studies in the Black Sea on the PP reported that the values for the north-western shelf as 570—1200 mgC m^{-2} d^{-1}, for the continental slope as 320—500 mgC m^{-2} d^{-1} and for deep-sea regions as 100—370 mgC m^{-2} d^{-1} for the period of 1960—1991 (Bologa, 1986; Demidov, 2008; Vedernikov and Demidov, 1993). PP values were reported for the nearshore as 785 mgC m^{-2} d^{-1} in July 1997 in the western Black Sea, and the rates of PP for the deep regions of the Black Sea were reported as 62—461 mgC m^{-2} d^{-1} during the spring 1998 period (Yayla et al., 2001). For the southern coasts of the Black Sea, PP rates were measured as 247—1925 mgC m^{-2} d^{-1} for

spring period, and 405—687 mgC m^{-2} d^{-1} for summer and autumn periods from 1995 to 1996 (Yilmaz et al., 2006). In another study, monthly PP rates for the south-eastern coasts of the Black Sea were calculated as 285—565 mgC m^{-2} d^{-1} for the coastal station, and as 126—530 mgC m^{-2} d^{-1} for the offshore station (Agirbas et al., 2014). Recently, a time-series study obtained from the Wavelength Resolving Model (WRM) for the period of 1998—2011 using SeaWiFS data revealed spatial and temporal variations in mean annual PP values for the open Black Sea. PP rates were significantly higher in the western Gyre (110—2196 mgC m^{-2} d^{-1}) than the eastern Gyre (111—1806 mgC m^{-2} d^{-1}) (Agirbas et al., 2017). In the present study, total PP production rates were significantly varied, and values ranged from 1444 mgC m^{-2} d^{-1} (autumn) to 5931 mgC m^{-2} d^{-1} (spring) along the study area. The differences observed in PP values along the different parts of the Black Sea are thought to be due to nutrient concentrations (Cociasu et al., 1997). In addition, variability in the rim current and the physics of the gyres also play a significant role in regional differences of PP (Enriquez et al., 2005; Zatsepin et al., 2003). The cyclonic boundary of rim current which constitutes a biogeochemical barrier between coastal and offshore areas, and frontal jet instabilities between the rim current and the interior eddy fields affect the spatial variability in PP around the Black Sea (Oguz et al., 1994; Yilmaz et al., 1998). Moreover, Batumi anticyclone along the eastern Gyre, which appears as warm core rings during summer, may also led to decrease in PP (Oguz et al., 1993). Similarly, low PP rates detected in the summer period coincided with low nutrient concentrations and phytoplankton abundance along the stations. Changes in PP rates could be also related to community structure than abiotic factors (Richardson and Schoeman, 2004). In the study area, rates of PP closely coupled with phytoplankton abundance in some seasons. Spring was the most productive period which coincided with high dinoflagellates number. The second productive period was winter, which concur with high diatom abundance along the study area.

The main contribution of this study, which sets the current study apart from those of previous ones is the no studies on the size-fractionated PP have been conducted in the Black Sea so far. In this respect, this study includes comprehensive data on spatio-temporal variations in size-fractionated PP measurements in the Black Sea for the first time. In general, the rates varied from 84 to 1848 mgC m^{-2} d^{-1}, 96 to 3156 mgC m^{-2} d^{-1} and 56 to 3363 mgC m^{-2} d^{-1} for pico-, nano- and microphytoplankton fractions, respectively. During the study period, the contribution of each size class to total PP changed seasonally along the study area. Overall, microphytoplankton was the major group contributing to total PP in the study area. The PP values for the microphytoplankton were high in spring (3363 mgC m^{-2} d^{-1}) and in winter (1710 mgC m^{-2} d^{-1}). The second important group was nanophytoplankton, and their contribution was generally high in winter (2095 mgC m^{-2} d^{-1}) and spring (3156 mgC m^{-2} d^{-1}). The production rates for the picophytoplankton were generally low along the study area, however, their contribution was substantial in summer, and occasionally detected in spring.

In terms of spatial variability, coastal stations were generally dominated by microphytoplankton. On the other hand, offshore stations were characterised by nano- and picophytoplankton during the study period (Figure 13). Earlier studies reported that picophytoplankton biomass and PP rates are lower than larger size classes, however, high in oligotrophic gyres. On the other hand, nanophytoplankton significantly contribute to total PP in coastal upwelling areas due to ability of light utilisation (Hirata et al., 2009; Moreno-Ostos et al., 2011; Maranon et al., 2001; Tilstone et al., 1999; Uitz et al., 2010). The differences in size-fractionated PP values between coastal and offshore areas evidently emphasize that physical factors are the major drivers in PP rates along the study area. Coastal ecosystems of the Black Sea are principally governed by freshwater inflow and climatic factors (Bodeanu, 2002, 2004), however, the open sea areas are controlled by stratification, mixing and circulation processes (Sorokin, 2002). Moreover, spatial and temporal variation in PP of different size classes vary greatly in the oceans with respect to hydrography, irradiance, nutrient availability and biogeochemistry (Bricaud et al., 2004; Poulton et al., 2006).

Water column stratification decreases nutrients input from below the thermocline to the euphotic zone, thus possibly limiting PP especially in the micro- and nanophytoplankton in the oligotrophic areas of Atlantic Ocean (Aldridge et al., 2014; Maranon et al., 2003). Especially, diatoms due to their nitrogen metabolism can respond rapidly to nitrate enrichment (Fogg, 1991), any deficiencies in nutrient affect the PP rates of diatoms and microphytoplankton. Similarly, due to high nutrient concentrations in spring, the highest PP rates were recorded with dominance of microphytoplankton along the study area. A significant relationship between abiotic factors and spring PP rates, were detected, particularly in silicate and nitrate concentrations with high PP rates in Western English Channel (WEC). Besides, high nutrient concentrations are generally thought to promote larger cells such as diatoms (Barnes et al., 2015; McAndrew et al., 2007; Poulton et al., 2006). Moreover, nanophytoplankton may have a moderate PP capacity in low Chl-*a* areas because of their mixotrophic characteristic (Riemann et al., 1995).

5. Conclusions

The data presented here contribute to our understanding of spatio-temporal variations in total PP, size-fractionated PP and Chl-*a* with phytoplankton abundance and nutrient data along the south-eastern Black Sea. More importantly, the study mainly focuses on the revealing the PP rates of size-classes in the study area throughout a seasonal cycle. We observed that microphytoplankton had the highest PP rates (3363 mgC m^{-2} d^{-1}), followed by nanophytoplankton (3156 mgC m^{-2} d^{-1}) and picophytoplankton (1848 mgC m^{-2} d^{-1}) along the study area. Overall, winter (4163 mgC m^{-2} d^{-1}) and spring (5931 mgC m^{-2} d^{-1}) were the most productive seasons in terms of total PP which coincided with high phytoplankton abundance. Earlier studies on PP reported two distinct periods in early spring and autumn, however, summer blooms have been also detected along the Black Sea (Hay et al., 1990; Sur et al., 1996; Yilmaz et al., 1998). Similarly, two distinct periods in PP rates were also detected in the present study, however, seasonality of bloom timing was

different from previous studies. Mikaelyan et al. (2017) have reported similar phenological changes in phytoplankton bloom pattern along the Black Sea.

Chl-*a* concentrations were high in autumn (4.57 $\mu g\ l^{-1}$) and winter (4.96 $\mu g\ l^{-1}$); however, its values were relatively low in spring and summer. Along the study area, dinoflagellates were the dominant group in terms of species richness (68 species, 53.54%), and diatoms was the second most abundant group. On the other hand, diatoms and other phytoplankton species (mainly *E. huxleyi*) were the most abundant groups in terms of quantitative contribution. SST varied seasonally between 8.58 and 28.41°C is an important factor which affects the hydrography. Along the study area, depending on the seasonal thermocline and phytoplankton activity, nutrient concentrations were low in spring and summer when compared with autumn and winter. On the other hand, high nutrient concentrations (especially NO_{2+3}-N and SiO_2-Si) provoke productivity of microphytoplankton in coastal waters. The coastal stations of the southern Black Sea have different characteristics (e.g., river inflow, hydrography, light conditions and current properties etc.) and were separated statistically from the offshore stations with high production rates, phytoplankton abundance and nutrient concentrations. The results suggest that microphytoplankton along the study area are responsible for the majority of PP. However, the measured high Chl-*a* against low size-fractionated PP clearly indicates that smaller phytoplankton size classes (i.e., pico- and nanophytoplankton) were dominant during these periods. Hence, the quantification of size-fractionated PP rates with ecological drivers (hydrography, nutrient availability, irradiance etc.) will give a more comprehensive picture for the Black Sea ecosystem.

Declaration of competing interest

The authors declare that they have no known competing financial interests or personal relationships that could have appeared to influence the work reported in this paper.

Acknowledgements

We are grateful to the project team and the crew of r/v *Surat Arastirma I* for their assistance during samplings. This research was supported by The Scientific and Technological Research Council of Turkey (TUBITAK) in the framework of the 113Y189 project (Determination of effects of phytoplankton size class on the seasonal primary productivity).

Supplementary materials

Supplementary material associated with this article can be found, in the online version, at https://doi.org/10.1016/j.oceano.2021.11.002.

References

Agirbas, E., 2010. Interaction of pigment concentration and primary production with environmental condition in the Southeastern Black Sea. PhD Thesis, Karadeniz Technical University.

Agirbas, E., Feyzioglu, A.M., Kopuz, U., 2014. Seasonal changes of phytoplankton chlorophyll a, primary production and their relation in the Continental Shelf Area of the South-Eastern Black Sea. Turk. J. Fish. Aquat. Sc. 14, 713—726. https://doi.org/10.4194/1303-2712-v14_3_14

Agirbas, E., Feyzioglu, A.M., Kopuz, U., Llewellyn, C.A., 2015. Phytoplankton community composition in the south-eastern Black Sea determined with pigments measured by HPLC-CHEMTAX analyses and microscopy cell counts. J. Mar. Biol. Assoc. UK. 95 (1), 35—52. https://doi.org/10.1017/S0025315414001040

Agirbas, E., Tilstone, G., Feyzioglu, A.M., 2017. Contrasting wind regimes cause differences in primary Production in the Black Sea Eastern and Western Gyres. Turk. J. Fish. Aquat. Sc. 17, 981—994. https://doi.org/10.4194/1303-2712-v17_5_13

Aiken, J., Pradhan, Y., Barlow, R., Lavender, S., Poulton, A., Holligan, P., Hardman-Mountford, N., 2009. Phytoplankton pigments and functional types in the Atlantic Ocean: A decadal assessment, 1995-2005. Deep Sea Res. Pt. II 56 (15), 899—917. https://doi.org/10.1016/j.dsr2.2008.09.017

Aldridge, D., Purdie, D.A., Zubkov, M.V., 2014. Growth and survival of *Neoceratium hexacanthum* and *Neoceratium candelabrum* under simulated nutrient-depleted conditions. J. Plankton Res. 36, 439—449. https://doi.org/10.1093/plankt/fbt098

APHA, 1998. Standard Methods for the examination of water and waste water, 20th Edn. American Public Health Association, Washington, D.C., 874 pp.

Arai, M.N., 2001. Pelagic coelenterates and eutrophication: a review. Hydrobiologia 451, 69—87. https://doi.org/10.1023/A:1011883905394

Aumont, O., Maier-Reimer, E., Blain, S., Monfray, P., 2003. An ecosystem model of the global ocean including Fe, Si, P colimitations. Global Biogeochem. Cy. 17. https://doi.org/10.1029/2001GB001745

Balech, E., 1988. Los Dinoflagelados del Atlántico Sudoccidental. Publ. Espec. Inst. Esp. Oceanography, Madrid, 310 pp.

Barnes, M.K., Tilstone, G.H., Suggett, D.J., Widdicombe, C.E., Bruun, J., Martinez-Vicente, V., Smyth, T.J., 2015. Temporal variability in total, micro- and nano-phytoplankton primary production at a coastal site in the Western English Channel. Prog. Oceanogr. 137, 470—483. https://doi.org/10.1016/j.pocean.2015.04.017

Basturk, O., Saydam, C., Salihoglu, I., Eremeva, L.V., Konovalov, SK., Stoyanov, A., Dimitrov, A., Cociasu, A., Dorogan, L., Altabet, M., 1994. Vertical variation in the principle chemical properties of Black Sea in the autumn of 1991. Mar. Chem. 45, 149—165. https://doi.org/10.1016/0304-4203(94)90099-X

Bat, L., Sahin, F., Satilmis, H.H., Ustun, F., Ozdemir, Z.B., Kideys, A.E., Shulman, G.E., 2007. The changed ecosystem of the Black Sea and its impact on anchovy fisheries. J. Fisher. Sci. 1 (4), 191—227, (in Turkish). https://doi.org/10.3153/jfscom.2007024

Bat, L., Sezgin, M., Satilmis, H.H., Sahin, F, Ustun, F., Birinci-Ozdemir, Z., Baki, O.G., 2011. Biological diversity of the Turkish Black Sea coast. Turk. J. Fish. Aquat. Sci. 11, 683—692. https://doi.org/10.4194/1303-2712-v11_4_04

Bingel, F., Kideys, A.E., Ozsoy, E., Tugrul, S., Basturk, O., Oguz, T., 1993. Stock assessment studies for the Turkish Black Sea coast. NATO-TU Fisheries, Final Report. METU, Institute of Marine Sciences.

Bodeanu, N., 2002. Algal blooms in Romanian Black Sea waters in the last two decades of the 20th century. Cercatari Mar. 34, 7—22.

Bodeanu, N., Andrei, C., Boicenco, L., Popa, L., Sburlea, A., 2004. A new trend of the phytoplankton structure and dynamics in the Romanian marine waters. Cercetari Mar. 35, 77—86.

Bodeanu, N., Moncheva, S., Ruta, G., Popa, L., 1998. Long-term evolution of the algal blooms in Romanian and Bulgarian Black Sea waters. Cercetari Mar. 31, 37—55.

Bologa, A.S., 1986. Planktonic Primary Productivity of the Black Sea: A Review. Thalassia Jugoslavica 21—22, 1—22.

Bologa, A.S., Bodeanu, N., Petran, A., Tiganus, V., Zaitsev, Yu. P., 1995. Major modifications of the Black Sea benthic and planktonic biota in the last three decades. Bulletin de L'Institute Oceanographique 15, CIESM Science Series, Monaco, 85—110.

Bricaud, A., Claustre, H., Ras, J., Oubelkheir, K., 2004. Natural variability of phytoplanktonic absorption in oceanic waters: Influence of the size structure of algal populations. J. Geophys. Res. 109. https://doi.org/10.1029/2004JC002419

Cermeno, P., Maranon, E., Rodriguez, J., Fernandez, E., 2005. Large-sized phytoplankton sustain higher carbon specific photosynthesis than smaller cells in a coastal eutrophic ecosystem. Mar. Ecol. Progr. Ser. 297, 51—60. https://doi.org/10.3354/meps297051

Cho, B.C., Azam, F., 1988. Major role of bacteria in biogeochemical fluxes in the ocean's interior. Nature 332, 441—443. https://doi.org/10.1038/332441a0

Coban-Yildiz, Y., Tugrul, S., Ediger, D., Yilmaz, A., Polat, S.C., 2000. A comparative study on the abundance and elemental composition of POM in three interconnected basins: the Black, the Marmara and the Mediterranean Seas. Mediterr. Mar. Sci. 1, 51—63. https://doi.org/10.12681/mms.5

Cociasu, A., Diaconu, V., Teren, L., Nae, I., Popa, L., Dorogan, L., Malciu, V., et al., 1997. Nutrient stocks on the Western shelf of the Black Sea in the last three decades. In: Özsoy, E., Mikaelyan, A. (Eds.), Sensitivity to change: Black Sea, Baltic and North Sea, NATO ASI Series. Kluwer Academic Publishers.

Cociasu, A., Dorogan, L., Humborg, C., Popa, L., 1996. Long-term ecological changes in Romanian coastal waters of the Black Sea. Mar. Pollut. Bull. 32 (1), 32—38. https://doi.org/10.1016/0025-326X(95)00106-W

Codispoti, L.A., Friederich, G.E., Murray, J.W., Sakamato, C.M., 1991. Chemical variability in the Black Sea: Implications of continuous vertical profiles that penetrated the oxic/anoxic interface. Deep-Sea Res 38, 691—710. https://doi.org/10.1016/S0198-0149(10)80004-4

Curran, K., Brewin, R.J.W., Tilstone, G.H., Bouman, H.A., Hickman, A., 2018. Estimation of size-fractionated primary production from Satellite Ocean Colour in UK Shelf Seas. Remote Sens. 10, 1389. https://doi.org/10.3390/rs10091389

Demidov, A.B., 2008. Seasonal dynamics and estimation of the annual primary production of phytoplankton in the Black Sea. Oceanology 5 (48), 664—678. https://doi.org/10.1134/S0001437008050068

Ediger, D., Soydemir, N., Kideys, A.E., 2006. Estimation of phytoplankton biomass using HPLC pigment analysis in the Southwestern Black Sea. Deep-Sea Res Pt. I. 53, 1911—1922. https://doi.org/10.1016/j.dsr2.2006.04.018

Eker-Develi, E., Kideys, A.E., 2003. Distribution of phytoplankton in the Southern Black Sea in summer 1996, spring and autumn 1998. J. Marine Syst. 39, 203—211. https://doi.org/10.1016/S0924-7963(03)00031-9

Eker, E., 1999. Abundance and biomass of micro and nanophytoplankton in the northwestern and southern Black Sea in 1995. Middle East Technical University, IMS, Erdemli, Icel, Turkey, 212 pp.

Enriquez, C.E., Shapiro, G.I., Souza, A.J., Zatsepin, A.G., 2005. Hydrodynamic modelling of mesoscale eddies in the Black Sea. Ocean Dynam. 55 (5—6), 476—489. https://doi.org/10.1007/s10236-005-0031-4

Eppley, R.W., Peterson, B.J., 1979. Particulate organic-matter flux and planktonic new production in the Deep Ocean. Nature 282, 677—680. https://doi.org/10.1038/282677a0

Falkowski, P.G., Barber, R.T., Smetacek, V., 1998. Biogeochemical controls and feedbacks on ocean primary production. Science 281, 200—206. https://doi.org/10.1126/science.281.5374.200

Feyzioglu, A.M., 1996. Seasonal changes on phytoplankton dynamics in eastern Black Sea Ecosystem. Karadeniz Technical University, Trabzon, 120 pp.

Feyzioglu, A.M., Seyhan, K., 2007. Phytoplankton Composition of South East Black Sea Coast. J. Black Sea/Mediterr. Environ. 13, 61—71.

Fogg, G.E., 1991. The phytoplanktonic ways of life. New Phytol 118, 191—232. https://doi.org/10.1111/j.1469-8137.1991.tb00974.x

Genc, N., 2018. Photic zone dynamics of phytoplankton size classes derived from pigments in the south-eastern Black Sea. Master Thesis. Recep Tayyip Erdogan University.

Goldman, J.C., 1993. Potential role of large oceanic diatoms in new primary production. Deep-Sea Res. Pt. I 40, 159—168. https://doi.org/10.1016/0967-0637(93)90059-C

Guidi, L., Stemmann, L., Jackson, G.A., Ibanez, F., Claustre, H., Legendre, L., Picheral, M., Gorsky, G., 2010. Effects of phytoplankton community on production, size, and export of large aggregates: A World-Ocean analysis. Limnol. Oceanogr. 54 (6), 1951—1963. https://doi.org/10.1364/OE.20.011882

Han, M.S., Furuya, K., 2000. Size and species-specific primary productivity and community structure of phytoplankton in Tokyo Bay. J. Plankton Res. 22, 1221—1235. https://doi.org/10.1093/plankt/22.7.1221

Hay, B.J., Honjo, S., Kempe, S., Itekkot, V.A., Degens, E.T., Konuk, T., Izdar, E., 1990. Interannual variability in particle flux in the southwestern Black Sea. Deep-Sea Res. 37, 911—928. https://doi.org/10.1016/0198-0149(90)90103-3

Hays, G.C., Richardson, A.J., Robinson, C., 2005. Climate change and marine plankton. Trends Ecol. Evol. 20, 337—344. https://doi.org/10.1016/j.tree.2005.03.004

Hirata, T., Hardman-Mountford, N.J., Barlow, R., Lamont, T., Brewin, R.J.W., Smyth, T., Aiken, J., 2009. An inherent optical property approach to the estimation of size specific photosynthetic rates in eastern boundary upwelling zones from satellite ocean colour: an initial assessment. Prog. Oceanogr. 83, 393—397. https://doi.org/10.1016/j.pocean.2009.07.019

Honjo, S., Hay, B., Manganini, S.J., Degens, E.T., Kempe, S., Ittekkot, V.A., Izdar, E., Konuk, T., Benli, H.A., 1987. Seasonal cyclicity of lithogenic particle fluxes at a Southern Black Sea Sediment Trap Station. Mitt. Geol. Palaont. Inst., University of Hamburg, F.R.G. 19—39.

Humborg, C., Ittekkot, V., Cociasu, A., Von Bodungen, B., 1997. Effect of Danube River dam on Black Sea biogeochemistry and ecosystem structure. Nature 386, 385—388. https://doi.org/10.1038/386385a0

Jochem, F., Zeitzschel, B., 1989. Productivity regime and phytoplankton size structure in the tropical and subtropical North Atlantic in spring. Deep-Sea Res. Pt. II. 40, 495—519. https://doi.org/10.1016/0967-0645(93)90029-M

Joint, I., Owens, N., Pomroy, A., Pomeroy, A., 1986. Seasonal production of photosynthetic picoplankton and nanoplankton in the Celtic Sea. Mar. Ecol. Prog. Ser. 28 (3), 251—258.

Karadeniz, M.N., 2019. Phytoplankton pigment profiles and phytoplankton size classes along the South-Eastern Black Sea Ms. Thesis. Recep Tayyip Erdogan University.

Kideys, A.E., 1994. Recent dramatic changes in the Black Sea ecosystem: The reason for the sharp decline in Turkish anchovy fisheries. J. Marine Syst. 5, 171—181. https://doi.org/10.1016/0924-7963(94)90030-2

Kideys, A.E., 2002. Fall and Rise of the Black Sea Ecosystem. Science 297 (5586), 1482—1484. https://doi.org/10.1126/science.1073002

Kideys, A.E., Kovalev, A.V., Shulman, G., Gordina, A., Bingel, F., 2000. A review of zooplankton investigations of the Black Sea over the last decade. J. Marine Syst. 24, 355—371. https://doi.org/10.1016/S0924-7963(99)00095-0

Kiorboe, T., 1993. Turbulence, phytoplankton cell-size, and the structure of pelagic food webs. Adv. Mar. Biol. 29 (29), 1—72. https://doi.org/10.1016/S0065-2881(08)60129-7

Koca, L., 2014. Temporal variation of Diatom/Dinoflagellate ratios and pigment composition along the South-Eastern coasts (Rize) of the Black Sea, Ms. Thesis. Recep Tayyip Erdogan University.

Kopelevich, O.V., Burenkov, V.I., Ershova, S.V., Sheberstov, S.V., ve Evdoshenko, M.A., et al., 2004. Application of SeaWiFS data for Studying Variability of Bio-Optical Characteristics in the Barents, Black and Caspian Seas. Deep Sea Research Pt. II 51, 1063—1091.

Kopelevich, O.V., Sheberstov, S.V., Yunev, O., Basturk, O., Finenko, Z.Z., Nikonov, S., Vedernikov, V.I., 2002. Surface chlorophyll-a in the Black Sea over 1978—1986 derived from satellite and in situ data. J. Marine Syst. 3, 145—160. https://doi.org/10.1016/S0924-7963(02)00184-7

Kopuz, U., 2012. Dynamics of picoplankton in microbial loop and their Impotence at pelagic food web in the South-Eastern Black Sea, PhD Thesis. Karadeniz Technical University.

Le Quéré, C., Harrison, S.P., Prentice, I.C., Buitenhuis, E.T., Aumont, O., Bopp, L., 2005. Ecosystem dynamics based on plankton functional types for global ocean biogeochemistry models. Global Change Biol. 11, 2016—2040. https://doi.org/10.1111/j.1365-2486.2005.1004.x

Maranon, E., Behrenfeld, M.J., Gonzalez, N., Mourino, B., Zubkov, M.V., 2003. High variability of primary production in oligotrophic waters of the Atlantic Ocean: uncoupling from phytoplankton biomass and size structure. Mar. Ecol. Progr. Ser. 257, 1—11. https://doi.org/10.3354/meps257001

Maranon, E., Holligan, P.M., Barciela, R., Gonzalez, N., Mourino, B., Pazo, M.J., Varela, M., 2001. Patterns of phytoplankton size structure and productivity in contrasting open-ocean environments. Mar. Ecol. Progr. Ser. 216, 43—56. https://doi.org/10.3354/meps216043

Margalef, R., 1965. Ecological correlation and relationship between primary producing and plankton structure. Mem. Ist. Ital. Idrobiol. 18, 355—364.

McAndrew, P.M., Bjorkman, K.M., Church, M.J., Morris, P.J., Jachowski, N., Williams, P.J.L.B., Karl, D.M., 2007. Metabolic response of oligotrophic plankton communities to deep water nutrient enrichment. Mar. Ecol. Progr. Ser. 332, 63—75. https://doi.org/10.3354/meps332063

McQuatters-Gollop, A., Mee, L.D., Raitsos, D.E., Shapiro, G.I., 2008. Non-linearities, regime shifts and recovery: The recent influence of climate on Black Sea chlorophyll. J. Marine Syst. 74, 649—658. https://doi.org/10.1016/j.jmarsys.2008.06.002

McQuatters-Gollop, A., Raitsos, D.E., Edwards, M., Pradhan, Y.Mee, Lavender, L.D., Attrill, S.J., M, J., 2007. A long-term chlorophyll dataset reveals regime shift in North Sea phytoplankton biomass unconnected to nutrient levels. Limnol. Oceanogr. 52, 635—648. https://doi.org/10.4319/lo.2007.52.2.0635

Michaels, A.F., Silver, M.W., 1988. Primary production, sinking fluxes and the microbial food web. Deep-Sea Res. Pt. I 35, 473—490. https://doi.org/10.1016/0198-0149(88)90126-4

Mikaelyan, A.S., Chasovnikov, V.K., Kubryakov, A.A., Stanichny, S.V., 2017. Phenology and drivers of the winter—spring phytoplankton bloom in the open Black Sea: The application of Sverdrup's hypothesis and its refinements. Prog. Oceanogr. 151, 163—176. https://doi.org/10.1016/j.pocean.2016.12.006

Mikaelyan, A.S., Zatsepin, A.G., Chasovnikov, V.K., 2013. Long-term changes in nutrient supply of phytoplankton growth in the Black Sea. J. Marine Syst. 117—118, 53—64. https://doi.org/10.1016/j.jmarsys.2013.02.012

Moncheva, S., Gotsis-Skretas, O., Pagou, K., Krastev, A., 2001. Phytoplankton blooms in Black Sea and Mediterranean coastal ecosystems subjected to anthropogenic eutrophication: similarities and differences. Estuar. Coast. Shelf Sci. 53 (3), 281—295. https://doi.org/10.1006/ecss.2001.0767

Moncheva, S., Krastev, A., 1997. Some aspects of phytoplankton long-term alterations off Bulgarian Black Sea shelf. In: Ozsoy, E., Mikhaelian, A. (Eds.), Sensitivity to Change: Black Sea, Baltic Sea and North Sea. NATO ASI Series, Kluwer Acad. Publ., 79—94.

Moreno-Ostos, E., Fernandez, A., Huete-Ortega, M., Mourino-Carballido, B., Calvo-Diaz, A., Moran, X.A.G., Maranon, E., 2011. Size-fractionated phytoplankton biomass and production in the tropical Atlantic. Sci. Mar. 75, 379—389. https://doi.org/10.3989/scimar.2011.75n2379

Nelson, D.M., Treguer, P., Brzezinski, M.A., Leynaert, A., Queguiner, B., 1995. Production and dissolution of biogenic silica in the ocean: Revised global estimates, comparison with regional data and relationships to biogenic sedimentation. Global Biogeochem. Cy. 9, 359—372. https://doi.org/10.1029/95GB01070

Oguz, T., Aubrey, D.G., Latun, V.S., Demirov, E., Koveshnikov, L., Sur, H.I., Diaconu, V., Besiktepe, S., Duman, M., Limeburner, L., Eremeev, V., 1994. Mesoscale circulation and thermohaline structure of the Black Sea observed during HydroBlack'91. Deep-Sea Res. Pt. I 41 (4), 603—628. https://doi.org/10.1016/0967-0637(94)90045-0

Oguz, T., Ediger, D., 2006. Comparison of in-situ and satellite-derived chlorophyll pigment concentrations and impact of phytoplankton bloom on the sub-oxic layer structure in the western Black Sea during May-June 2001. Deep-Sea Res. Pt. II 53 (17—19), 1923—1933. https://doi.org/10.1016/j.dsr2.2006.07.001

Oguz, T., Latun, V.S., Latif, M.A., Vladimirov, V.V., Sur, H.I., Markov, A.A., Ozsoy, E., Kotovshchikov, V.V., Eremeev, V.V., Unluata, U., 1993. Circulation in the surface and intermediate layers of the Black Sea. Deep-Sea Res. 40 (8), 1597—1612. https://doi.org/10.1016/0967-0637(93)90018-X

Oguz, T., Velikova, V., Cociasu, A., Korchenko, A., 2008. State of the Environment Report 2001-2006/7, the State of Eutrophication, 83—112.

Oguz, T., 2005. Black Sea Ecosystem response to climatic teleconnections. Oceanography 18 (2), 122—133. https://doi.org/10.5670/oceanog.2005.47-v18_2_133

O'reilly, E.J., Zetlin, C., 1998. Seasonal, horizontal and vertical distribution of phytoplankton chlorophyll Northeast US continental shelf ecosystems. Report NMFS 139. A Tech. Rep. the Fishery Bulletin. U.S. Department of Commerce, Seattle, WA, 126 pp.

Paerl, H.W., Valdes, L.M., Pinckney, J.L., Piehler, M.F., Dyble, J., Moisander, P.H., 2003. Phytoplankton photopigments as indicators of estuarine and coastal eutrophication. BioScience 53, 953—964. https://doi.org/10.1641/0006-3568(2003)053[0953:PPAIOE]2.0.CO;2

Platt, T., Rao, D.S., Irwin, B., 1983. Photosynthesis of picoplankton in the oligotrophic ocean. Nature 301, 702—704. https://doi.org/10.1038/301702a0

Platt, T., Sathyendranath, S., 2008. Ecological indicators for the pelagic zone of the ocean from remote sensing. Remote Sens. Environ. 112, 3426—3436. https://doi.org/10.1016/j.rse.2007.10.016

Poulton, A.J., Holligan, P.M., Hickman, A., Kim, Y.N., Adey, T.R., Stinchcombe, M.C., Holeton, C., Root, S., Woodward, E.M.S., 2006. Phytoplankton carbon fixation, chlorophyll biomass and diagnostic pigments in the Atlantic Ocean. Deep-Sea Res. Pt. II. 53, 1593—1610. https://doi.org/10.1016/j.dsr2.2006.05.007

Rampi, L., Bernard, M., 1978. Key for the determination of Mediterranean pelagic diatoms. Comit. Naz. Energia Nucleare, Roma 71.

Richardson, 1991. Comparison of 14C primary production determinations made by different laboratories. Mar. Ecol. Progr. Ser. 72, 189—201. https://doi.org/10.3354/MEPS072189

Richardson, A.J., Schoeman, D.S., 2004. Climate impact on plankton ecosystems in the Northeast Atlantic. Science 305, 1609—1612. https://doi.org/10.1126/science.1100958

Riemann, B., Havskum, H., Thingstad, F., Bernard, C., 1995. The role of mixotrophy in pelagic environments. In: Joint, I. (Ed.), Molecular Ecology of Aquatic Microbes, NATO AS1 Series, Vol.

38. Springer-Verlag, Berlin, 87—114. https://doi.org/10.1007/978-3-642-79923-5_6

Song, L., Wu, J., Du, J., Li, N., Wang, K., Wang, P., 2019. Comparison of two methods to assess the size structure of phytoplankton community assemblages, in Liaodong Bay. China. J. Ocean Univ. China (Oceanic and Coastal Sea Research) 18 (5), 1207—1215. https://doi.org/10.1007/s11802-019-3960-0

Sorokin, Yu.I., 1983. The Black Sea. In: Ketchum, P.H. (Ed.), Estuaries and enclosed seas. Elsevier, Amsterdam, 253—291.

Sorokin, Y.U., 1983. The Black Sea, In: Ecosystem of the World 26. In: Estuaries and Enclosed Seas, Edited by, Ketchum, B.H. Elsevier Scientific Publishing Company, New York, 253—292.

Sorokin, Y.A., 2002. The Black Sea: ecology and oceanography. Biology of Inland Waters. Backhuys, Leiden, The Netherlands, 875 pp.

Steemann-Nielsen, E., 1952. The use of radioactive carbon (14C) for measuring organic production in the sea. J. Cons. Perm. Int. Explor. Mer. 18, 117—140.

Sur, H.I., Ozsoy, E., Ilyin, Y.P., Unluata, U., 1996. Coastal/deep ocean interactions in the Black Sea and their ecological environmental impacts. J. Marine Syst. 7, 293—320. https://doi.org/10.1016/0924-7963(95)00030-5

Tait, R.V., 1988. Elements of Marine Ecology, 3rd Edn. University Press, Cambridge, 356 pp.

Tamigneaux, E., Legendre, L., Klein, B., Mingelbier, M., 1999. Seasonal dynamics and potential fate of size-fractionated phytoplankton in a temperate nearshore environment (western Gulf of St Lawrence, Canada). Estuar. Coast. Shelf Sci. 48 (2), 253—269. https://doi.org/10.1006/ecss.1999.0416

Tilstone, G.H., Figueiras, F.G., Fermin, E.G., Arbones, B., 1999. Significance of nanophytoplankton photosynthesis and primary production in a coastal upwelling system (Ria de Vigo, NW Spain). Mar. Ecol. Progr. Ser. 183, 13—27.

Tilstone, G.H., Lange, P.K., Misra, A., Brewin, R.J.W., Cain, T., 2017. Micro-phytoplankton photosynthesis, primary production and potential export production in the Atlantic Ocean. Prog. Oceanogr. 158, 109—129. https://doi.org/10.1016/j.pocean.2017.01.006

Tomas, C.R., 1996. Identification marine diatoms and dinoflagellates. Acad. Press, San Diego, 598 pp.

Turkmen, P., 2016. Seasonal Changes of Pigment Composition along South-Eastern Coasts (Artvin-Giresun) of the Black Sea Master Thesis. Recep Tayyip Erdogan University.

Uitz, J., Claustre, H., Gentili, B., Stramski, D., 2010. Phytoplankton class-specific primary production in the world's oceans: Seasonal and interannual variability from satellite observations. Global Biogeochem. Cy. 24. https://doi.org/10.1029/2009GB003680

Utermöhl, H., 1958. Zur Vervollkommnung der quantitativen phytoplankton. Methodik Mitteilung Internationale Vereinigung Theoretische und Angewandte Limnologie 9, 1—8.

Uysal, Z., Kideys, A.E., Senichkina, L., Georgieva, L., Altukhov, D., Kuzmenko, L., Manjos, L., Mutlu, E., Eker, E., 1998. Phytoplankton patches formed along the southern Black Sea coast in spring and summer 1996. In: Ivanov, L., Oguz, T. (Eds.), Ecosystem modelling as a management tool for the Black Sea. Vol. 1, Kluwer Acad. Publ., Dordrecht, 151—162.

Uysal, Z., Sur, H.I., 1995. Net phytoplankton discriminating patches along the Southern Black Sea Coast in winter 1990. Oceanolog. Acta 18 (6), 639—647.

Vedernikov, V.I., Demidov, A.B., 1993. Primary production and chlorophyll in the deep regions of the Black Sea. Oceanology 33, 229—235.

Vedernikov, V.I., Demidov, A.B., 1997. Vertical distribution of primary production and chlorophyll during different seasons in deep regions of the Black Sea. Oceanology 37, 376—384.

Veldhuis, M.J.W., Timmermans, K.R., Croot, P., van der Wagt, B., 2005. Picophytoplankton; a comparative study of their biochemical composition and photosynthetic properties. J. Sea Res. 53 (1—2), 7—24. https://doi.org/10.1016/j.seares.2004.01.006

Vinogradov, M., Shushkina, E., Mikaelyan, A., Nezlin, N.P., 1999. Temporal (seasonal and interannual) changes of ecosystem of the open waters of the Black Sea. In: Beşiktepe, S.T., Ünlüata, Ü., Bologa, A.S. (Eds.), Environmental Degradation of the Black Sea: Challenges and Remedies. Kluwer Acad. Publ., Dordrecht, 109—129.

Viviani, D.A., Björkman, K.M., Karl, D.M., Church, M.J., 2011. Plankton metabolism in surface waters of the tropical and subtropical Pacific Ocean. Aquat. Microb. Ecol. 62 (1), 1—12. https://doi.org/10.3354/ame01451

Yayla, M., Yilmaz, A., Morkoc, E., 2001. The Dynamics of nutrient enrichment and primary production related to recent changes in the ecosystem of the Black Sea. Aquat. Ecosyst. Health and Manage. 4, 33—49. https://doi.org/10.1080/146349801753569261

Yilmaz, A., Coban-Yildiz, Y., Tugrul, S., 2006. Biogeochemical cycling and multilayer production in the Black Sea. Geophys. Res. Abst. 8, 00541.

Yilmaz, A., Tugrul, S., Polat, C., Ediger, D., Coban, Y., Morkoc, E., 1998. On the production, elemental composition (C, N, P) and distribution of photosynthetic organic matter in the Southern Black Sea. Hydrobiologia 363, 141—156. https://doi.org/10.1023/A:1003150512182

Yunev, O., Vladimir, A., Basturk, O., Yilmaz, A., Kideys, A.E., Moncheva, S., Konovalov, S.K., 2002. Long-term variation of surface chlorophyll-a and primary production in the open Black Sea. Mar. Ecol. Progr. Ser. 230, 11—28. https://doi.org/10.3354/meps230011

Zaitsev, Yu.P., Alexandrov, B.G., 1997. Recent man-made changes in the Black Sea Ecosystem. In: Ozsoy, E., Mikaelyan, A. (Eds.), Sensitivity to Change: Black Sea, Baltic Sea and North Sea. Kluwer Acad. Publ., Dordrecht, the Netherlands, 25—31.

Zatsepin, A.G., Ginzburg, A.I., Kostianoy, A.G., Kremenetskiy, V.V., Krivosheya, V.G., Stanichny, S.V., Poulain, P-M., 2003. Observations of Black Sea mesoscale eddies and associated horizontal mixing. J. Geophys. Res. 108 (C8). https://doi.org/10.1029/2002JC001390

Oceanologia 64 (2022) 267—275

Available online at www.sciencedirect.com

ScienceDirect

journal homepage: www.journals.elsevier.com/oceanologia

ORIGINAL RESEARCH ARTICLE

Multivariate approach to evaluate the factors controlling the phytoplankton abundance and diversity along the coastal waters of Diu, northeastern Arabian Sea

P. Sathish Kumar[a,b,*], S. Venkatnarayanan[a], Vikas Pandey[a], Krupa Ratnam[a], Dilip Kumar Jha[a], S. Rajaguru[a], G. Dharani[a,*], R. Arthur James[b,*], M.A. Atmanand[a]

[a] *National Institute of Ocean Technology (NIOT), Ministry of Earth Sciences (Govt. of India), Chennai, Tamil Nadu, India*
[b] *Department of Marine Science, Bharathidasan University, Tiruchirappalli, Tamil Nadu, India*

Received 30 June 2021; accepted 24 November 2021
Available online 9 December 2021

KEYWORDS
TSS;
Phytoplankton;
Dinoflagellate;
Chlorophyll *a*;
Nutrient;
Monsoon

Abstract The present study investigated the phytoplankton assemblage and diversity with physicochemical parameters of Diu coastal waters in different seasons during 2018—19. During the study period, 61 phytoplankton species comprising diatoms (50 sp.), dinoflagellates (8 sp.), and cyanophyceae (3 sp.) were recorded. Diatom was found to be a major community and contributed 79 to 99% of total phytoplankton abundance. Reduction in dinoflagellate and dominance of pennate-diatoms were observed during the monsoon. Chlorophyll-*a* concentration also showed a similar trend and decreased during the monsoon. However, the phytoplankton abundance was low particularly during the monsoon which might be due to the elevated total suspended solids (TSS) load. Canonical correspondence analysis revealed that diatoms were able to survive in high TSS with the support of high nutrients; while dinoflagellates were limited due to those conditions. Overall, the reduction in phytoplankton abundance, diversity, and biomass was recorded due to the elevated TSS input along the coastal waters of Diu.

* Corresponding authors at: National Institute of Ocean Technology (NIOT), Ministry of Earth Sciences, Govt. of India, Pallikaranai, Chennai, India; Department of Marine Science, Bharathidasan University, Tiruchirappalli, Tamilnadu, India.
E-mail addresses: marinesathis@gmail.com (P.S. Kumar), dhara@niot.res.in (G. Dharani), james.msbdu@gmail.com (R.A. James).

Peer review under the responsibility of the Institute of Oceanology of the Polish Academy of Sciences.

ELSEVIER Production and hosting by Elsevier

https://doi.org/10.1016/j.oceano.2021.11.005

1. Introduction

Phytoplankton dynamics are mainly controlled by a wide range of environmental variables like nutrients, temperature, salinity, light availability, current circulation, water turbidity, and grazing pressure by other trophic level organisms (Gao and Wang, 2008; Levy et al., 2007; Margalef, 1978; Verlencar and Parulekar, 2006; Zarauz et al., 2008). Studies related to the controlling factors of phytoplankton community composition and its fate in the northern Arabian Sea are limited (Geeta and Kondalarao, 2004; Nair et al., 2005; Naqvi et al., 2006). Identification of the main factors controlling phytoplankton in a particular water body is crucial for choosing an appropriate management strategy for the maintenance of the desired state of ecosystem (Peretyatko et al., 2007). Phytoplankton species have different traits and based on their size, shape, growth rate, and motility are together determine their ecological niche and favorable environmental conditions (Litchman and Klausmeier, 2008; Spilling et al., 2018). In recent decades, rapid growth in industrialization, urbanization in coastal zones, tourism, and harbor activities have exerted enormous anthropogenic pressure on nearshore ecology (Bhavya et al., 2016; Seitzinger et al., 2010). The aquatic environment like estuaries and coastal waters is affected by both riverine nutrient input and water properties like turbidity (Wang et al., 2019).

The total suspended solids (TSS) is one of the important environmental factors which reflect the turbidity characteristic of eroding coastline or the entry of the suspended materials into the coastal seawater through land runoff and determines the plankton composition and abundance (Wu et al., 2011). TSS is a significant variable that impacts the spatio-temporal patterns of phytoplankton and regulates the biogeochemical processes of aquatic ecosystems (Weyhenmeyer et al., 1997). The increase in TSS strongly affects the light attenuation which further influences the chlorophyll-*a* concentration in seawater and consequently affects the zooplankton and higher tropical organisms (Dunton, 1990). The natural process of particular coastal regions has unique characteristics that are controlled by water exchange with nearby areas, the topology of the coastline, rainfall, and river discharge (Ilyash et al., 2015). A combination of these processes with anthropogenic activities results in the formation of a gradient in biotic and abiotic factors which impacts phytoplankton species composition, succession, and abundance (Biswas et al., 2015; Hardikar et al., 2017). Diu Island (20.71°N, and 70.98°E) is located along the northeastern Arabian Sea, Gujarat. The geographical area of Diu is about 40 km^2. The climate is particularly warm and humid, the average annual rainfall ranges between 2300 and 4800 mm, the annual atmospheric temperature ranged from 15°C to 42°C (Jha et al., 2021). In Diu, the TSS load is always high throughout the year which originates from the erosion of farmlands and forests which are discharged through rivers and increases mainly during the monsoon. Disturbance of shore sediments and resuspension in shallow parts of estuarine and coastal regions due to tidal currents also play a major role in higher TSS load in the coastal region (NCCR, 2018; NIO, 2015). Phytoplankton distribution patterns are strongly correlated with environmental factors such as TSS (Lepisto et al., 2004). Studies related to phytoplankton community dynamics concerning environmental drivers are deficient in Diu and the surrounding coast.

In view of this above, the present study was conducted in the coastal waters of Diu, the northeastern Arabian Sea, 1) to investigate the distribution patterns of phytoplankton community composition and diversity during different seasons, 2) to examine the relationship between the phytoplankton groups, and the environmental variables, and 3) addressing the physicochemical factors controlling the abundance of diatoms and dinoflagellates.

2. Material and methods

In the present study, seven sampling locations (Station-1,2,3,4,5,6, and 7) with the depth of 2 to 18 m were selected for the seawater collection and analysis of physicochemical and biological parameters (Figure 1). The seasonal samples were collected in Pre-monsoon (PRM) (February), Monsoon (MON) (September), and Post-monsoon (POM) (November) from the study region during the period 2018 to 2019. Rainfall data were collected from the Indian Meteorological Department (IMD). Sea surface temperature (SST), salinity, and pH were measured using a calibrated portable multi-parameter water quality instrument (HANA-HI 9829). Surface water samples were collected using a Niskin sampler for the estimation of dissolved oxygen (DO), total suspended solids (TSS), nutrients, and chlorophyll-*a* (Chl-*a*). DO was measured using the modified Winkler's method (Carrit and Carpenter, 1966). The TSS was determined by filtering known quality of well-mixed sample through a preweighed standard glass-fiber filter (0.45 μm Millipore GF/C), and the residue retained on the filter was dried at 103—105°C to a constant weight. The increase in the weight of the filter represents the total suspended solids (APHA, 2012). All the nutrients (ammonia, nitrite, nitrate, phosphate, and silicate) were analyzed following standard spectrophotometric procedures (Grasshoff et al., 1999). For chl-*a* analysis, 1 L of seawater sample was filtered by GF/F filter and was wrapped with an aluminum foil and frozen at −20°C until analysis. Chl-*a* was analyzed spectrofluorometrically by following the standard protocol (Parson et al., 1984). For phytoplankton analysis, 5 L of the surface water sample was collected and preserved with Lugol's iodine solution. In the laboratory, samples were kept for 48 h for settling. For the enumeration of phytoplankton, the concentrated sample was examined under the microscope (ZEISS J-902984) and identified to the lowest possible taxonomic level using the identification keys (Subrahmanyan, 1946, 1959; Taylor, 1976; Tomas, 1997).

Diversity indices (viz., Shannon Weiner diversity index (H') and Margalef's species richness (d) and Pielou's evenness (J')) were calculated for all the seasons by using the statistical software package PRIMER 6.0. One-way analysis of variance (ANOVA) was performed on XLSTAT software to evaluate the statistical significance of diversity indices. Pearson correlation and multivariate regression analyses were performed to find out the linear relationship between the biotic and abiotic factors. Canonical Correspondence Analysis (CCA) was performed to examine the rela-

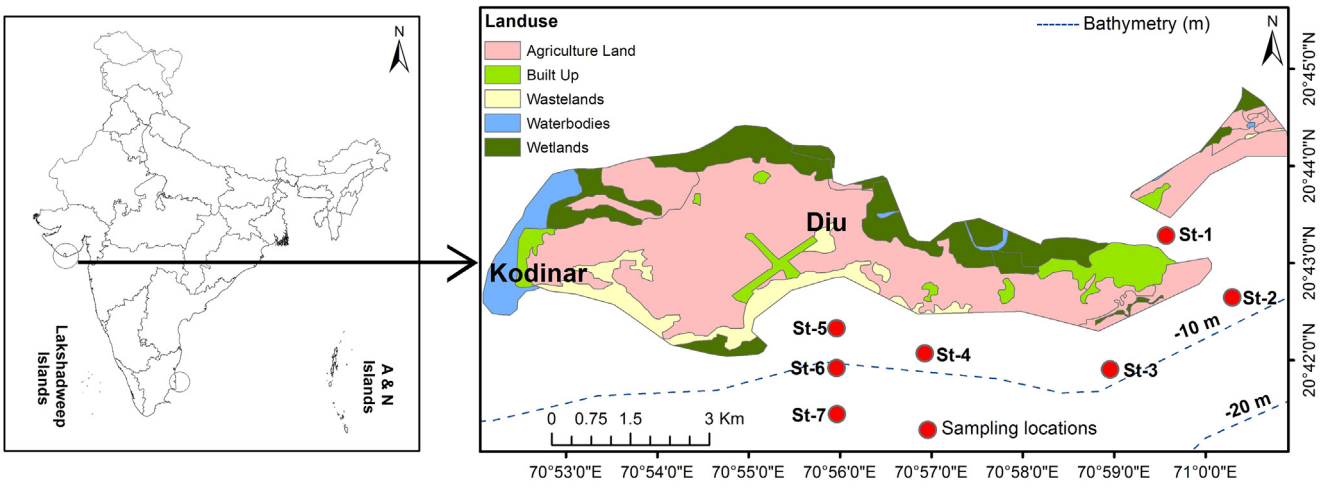

Figure 1 Map showing the study locations along the coastal waters of Diu, northeastern Arabian Sea.

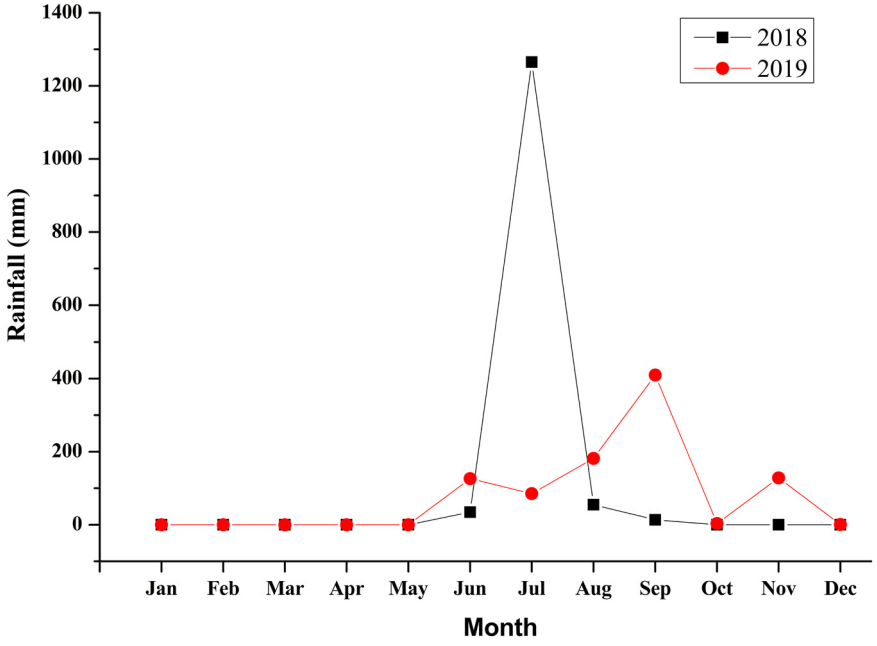

Figure 2 Temporal variation of Rainfall in the coastal region of Diu, northeastern Arabian Sea during 2018—2019.

tionships between the phytoplankton community and environmental variables by using CANOCO statistical software. Prior to statistical analysis, the heterogeneity in the phytoplankton data was removed by converting all the data to log (x+1) transformation.

3. Results and discussion

3.1. Seasonal variation of environmental parameters

During the study period, the monthly total rainfall was higher during July 2018 (Figure 2). In the last six years, the maximum rainfall in Diu was recorded in July 2018 (1265.4 mm). Spatio-temporal variations of physio-chemical parameters are presented in Figure 3. The TSS load in the coastal waters of Diu is moderately high throughout the year which may be due to the erosion of coastal land, farmlands, and forests which are discharged through rivers and increase mainly during heavy rainfall. During the study period, the TSS level ranged from 17.7 to 202.2 mg L^{-1}, the mean concentration was lower during the PRM and 2 to 3 times higher during the MON (Figure 3). Erosion of soil from farmlands and forests may be the major source for TSS load which was brought through the runoff and river discharge mainly during the high rainfall (NCCR, 2018). High TSS level (202.2 mg L^{-1}) at the river mouth station (St-1) during the MON confirmed that the main source for the elevated TSS was through land runoff caused by the high rainfall. Previous studies also reported that siltation caused by the large river run-off was the main reason for the high concentration of TSS along the Gulf of Khambhat (Raghunathan et al., 2004). Disturbance of shore sediments and resuspension in shallow

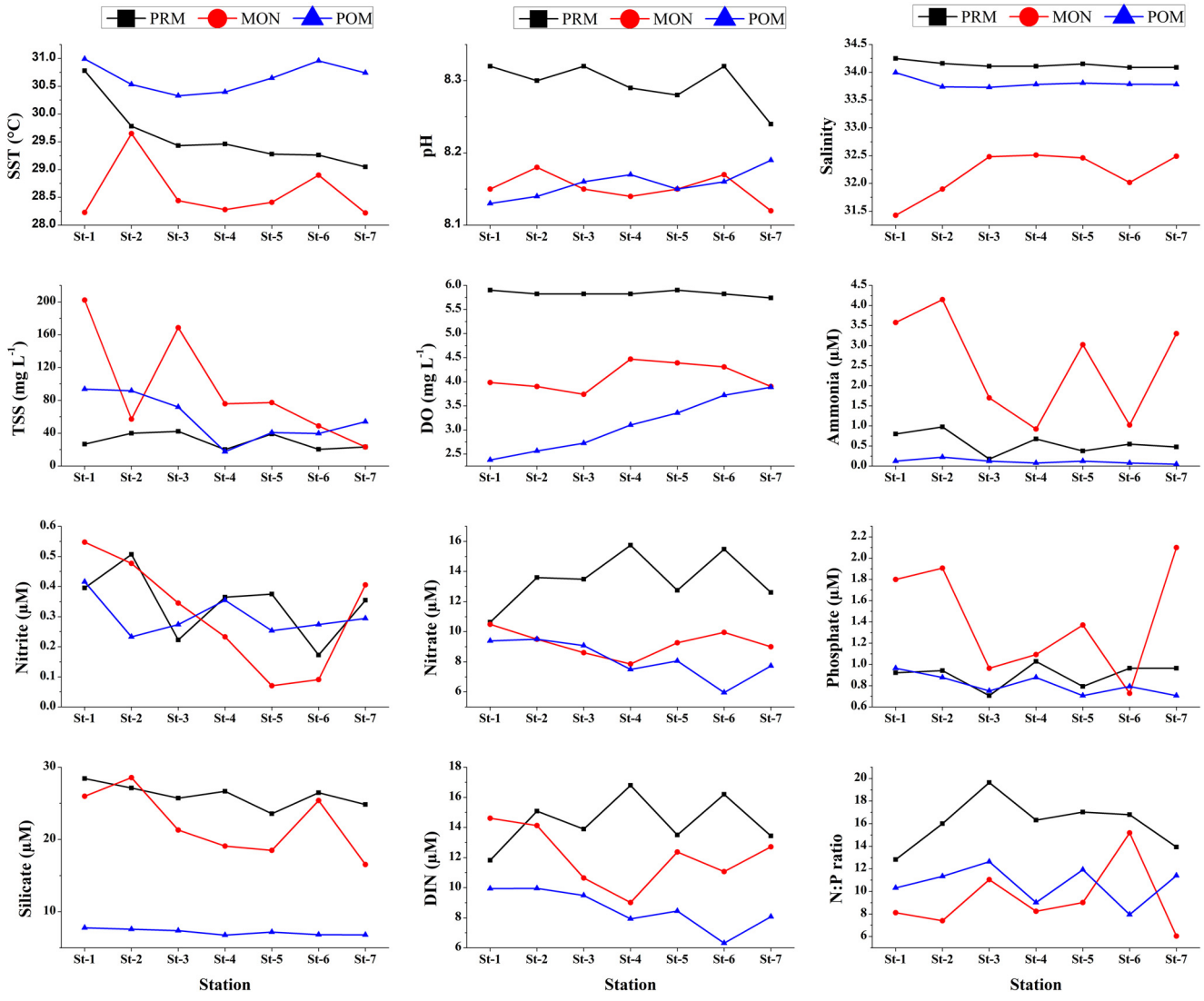

Figure 3 Spatio-temporal variation of physico-chemical variables along the coastal waters of Diu, northeastern Arabian Sea for the different seasons like pre-monsoon (PRM), monsoon (MON), and post-monsoon (POM).

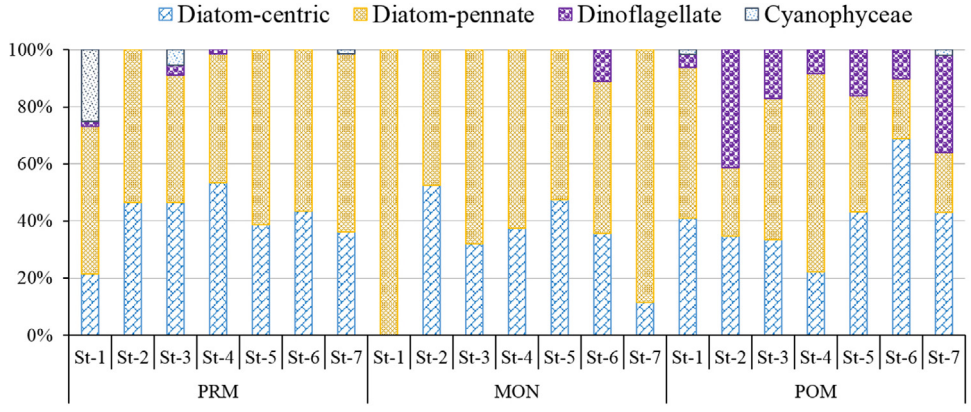

Figure 4 Seasonal changes in the taxonomical composition of phytoplankton abundance in the coastal waters of Diu, northeastern Arabian Sea for the different seasons like pre-monsoon (PRM), monsoon (MON), and post-monsoon (POM).

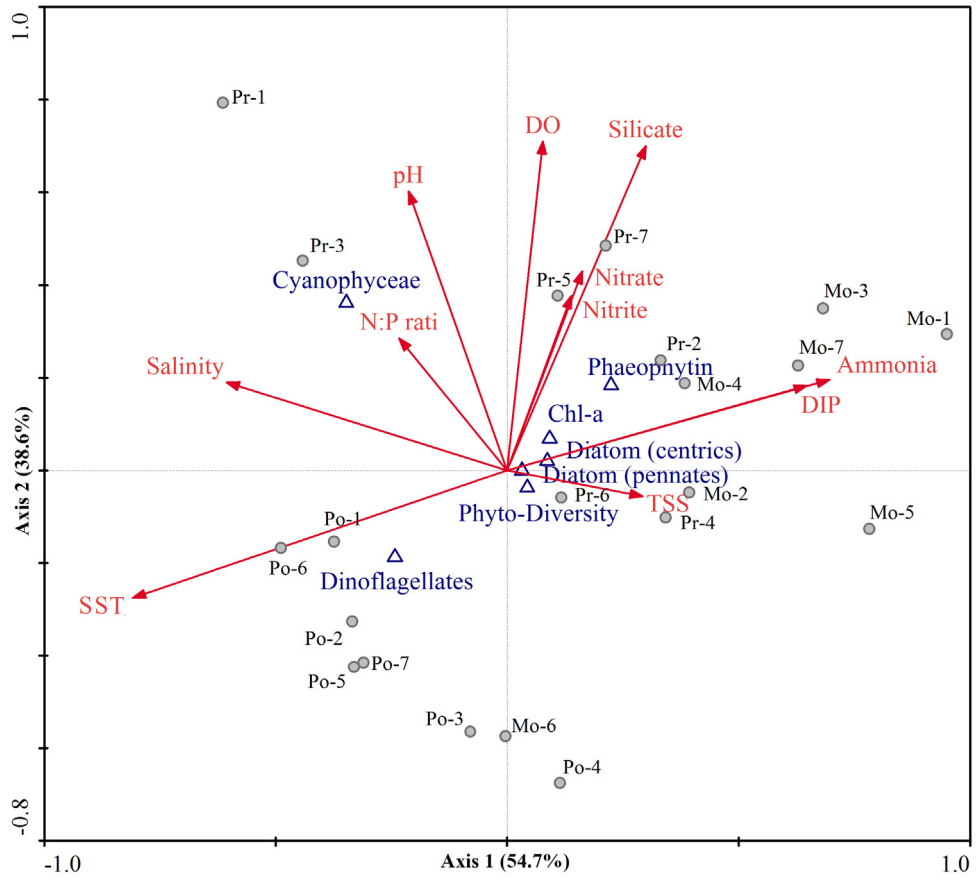

Figure 5 Canonical correspondence analysis (CCA) triplots for phytoplankton abundance, biomass (Chl-*a*), and diversity with associated environmental variables in the coastal waters of Diu, northeastern Arabian Sea. Environmental variables (SST — sea surface temperature, salinity, DO — dissolved oxygen, TSS — total suspended solids, pH, DIP — dissolved inorganic phosphorus, nitrite, nitrate, ammonia, silicate, and N:P ratio) are represented by arrows. Stations represented as Pr-1 to Pr-7 (pre-monsoon stations 1—7), Mo-1 to Mo-7 (monsoon stations 1—7), and Po-1 to Po-7 (post-monsoon stations 1—7).

parts of estuarine and coastal regions due to tidal currents also plays a major contribution to TSS load in the coastal region (NIO, 2015). The SST varied from 28.22 to 30.99°C, the higher and lower SST was found during the POM and MON, respectively. Salinity fluctuated highly among the seasons, higher salinity was recorded during the PRM (34.25) and lower during the MON (31.43). Drop in the SST and salinity might be due to the intense rainfall recorded during the MON. The pH was higher during the PRM and lower during the MON and POM. However, the salinity ($r = 0.81$, $p < 0.01$) and pH ($r = 0.88$, $p < 0.01$) showed strong positive correlation with the phytoplankton abundance, whereas the TSS ($r = -0.60$, $p < 0.01$) was correlated negatively. The DO ranged from 2.38 to 5.9 mg L^{-1}, the higher mean concentration of DO was found during the PRM which might be due to the higher primary production (Kumar et al., 2018).

Inorganic nutrients showed significant variation (n=21, $p<0.01$) between the stations (Figure 3). The dissolved inorganic nitrogen (DIN) ($NH_4^+ + NO_2^- + NO_3^-$) was high during the PRM and MON, which might be due to the increased concentration of nitrate and ammonia. The increased nitrate concentration could be due to anthropogenic input (Kumar et al., 2018; Zhou et al., 2008). JiyalalRam et al. (2011) also reported that the significant positive correlation between TSS and DIN indicates the erosion of soil and nutrient flux which is carried through river discharge. The mean concentration of ammonia was high during the MON. The phosphate and silicate concentrations were also higher during the MON and lower during the POM. Ammonia and phosphate formed a strong positive correlation (r=0.90, $p < 0.01$), the similar result from the previous study suggested that it could be the indication of sewage disposal and sediment release leading to higher phosphate concentration (Hardikar et al., 2019; Howarth et al., 2011). The mean N:P ratio was higher during the PRM (~16) and lower during the MON (~9) and POM (~10), the optimal N:P ratio during the PRM resulted in higher phytoplankton abundance and biomass.

3.2. Seasonal variation of phytoplankton biomass, abundance, and diversity — relationship with environmental variables

The phytoplankton biomass (chlorophyll-*a*) varied from 0.09 to 0.31 mg m^{-3}, the mean concentration of chl-*a* was higher during the PRM and lower in the MON and POM, respectively (Table 1). Depletion in phytoplankton biomass during the MON might be due to the elevated level of TSS ($r = -0.72$, $p < 0.01$). The phaeophytin concentration varied from 0.01

Table 1 Seasonal variations of phytoplankton abundance, biomass, and species diversity indices in the coastal waters of Diu, northeastern Arabian Sea. Values in the open and parentheses represent the minimum-maximum and mean values ± standard error respectively. PRM — Pre-monsoon; MON — Monsoon; POM — Post-monsoon.

	PRM	MON	POM
Phytoplankton abundance (x 10^3 cells L^{-1})	13.5—42.0 (23.6±3.5)	1.2—2.8 (1.8±0.2)	2.6—5.3 (4.0±0.4)
Chlorophyll *a* (mg m^{-3})	0.20—0.31 (0.26±0.01)	0.09—0.23 (0.15±0.02)	0.09—0.24 (0.15±0.02)
Phaeophytin (mg m^{-3})	0.29—0.44 (0.36±0.02)	0.18—0.45 (0.29±0.04)	0.01—0.25 (0.07±0.03)
Species diversity (*H'*)	2.06—2.56 (2.30±0.07)	1.10—2.18 (1.71±0.17)	2.14—2.71 (2.40±0.09)
Species richness (*d*)	1.26—1.70 (1.51±0.07)	0.28—1.03 (0.68±0.12)	1.09—1.88 (1.45±0.11)
Species evenness (*J'*)	0.72—0.89 (0.83±0.02)	0.97—1.00 (0.99±0.004)	0.91—0.97 (0.94±0.01)

to 0.45 mg m^{-3}, the higher and lower concentration was observed during the MON and POM, respectively. Phytoplankton diversity indices showed a significant variation (n=21, $p < 0.01$) between the seasons (Table 1). The mean phytoplankton diversity (H') was higher during the POM (2.40 ± 0.24) followed by the PRM (2.30 ± 0.18) and low during the MON (1.71 ± 0.45). The maximum and minimum species richness (*d*) was recorded during the PRM and MON, respectively. The species evenness (J') did not show much variation between the seasons, however, the higher evenness was found during the MON (0.99) despite low diversity and richness, which could be due to the lower abundance of phytoplankton species at all the locations.

The phytoplankton taxa identified during the study period are shown in Table S1 (supplemental material). A total of 61 phytoplankton species (23-centric diatoms, 27-pennate diatoms, 8 dinoflagellates, and 3 cyanophyceae) were recorded along the coastal waters of Diu. Diatoms were the most dominant phytoplankton group during all the seasons, whereas dinoflagellate and cyanophyceae were low. The higher number of phytoplankton taxa was recorded during the POM (38) followed by the PRM (27) and MON (17). The phytoplankton abundance varied from 1.2 to 41.9 × 10^3 cells L^{-1}, the higher abundance was observed during the PRM which could be attributed to a higher N:P ratio. The mean phytoplankton abundance was higher during the PRM (23581 cells L^{-1}) and lower during the MON (1780 cells L^{-1}) followed by the POM (4046 cells L^{-1}). A similar trend was also observed in phytoplankton biomass (chl-*a*) during the present study. During the PRM phytoplankton abundance was high at St-1 and decreased towards St-7. Whereas during the MON and POM the abundance was low at St-1 and increased towards St-7, which might be due to the higher TSS release from the riverside. Many studies along the west coast of India encountered higher phytoplankton abundance and biomass during the MON (Hardikar et al., 2019; Kumar et al., 2018; NIO, 2015). However, the present phytoplankton abundance and biomass were low compare to the previous reports of Diu and surrounding regions (Hardikar et al., 2019; NIO, 2015). Though, very few studies reported low phytoplankton abundance in the Diu coast, the reason was not documented (Raghunathan et al., 2004). However, the present study explored the limiting factors for phytoplankton growth. During the study period, 79 to 99% of the phytoplankton density was contributed by diatoms, the detailed contribution of phytoplankton groups during all the seasons are presented in Figure 4. Diatoms were dominant during the MON (99%) followed by PRM (92%) and POM (79%). Total phytoplankton abundance during the MON was very low and varied from 1189 to 2788 cells L^{-1} and the maximum abundance was contributed by diatoms (pennate diatoms — 68% and centric diatoms — 31%). Dinoflagellate's contribution was higher during the POM (21%) and dropped during the MON (1%) and PRM (1%). Particularly during the MON, only one species of dinoflagellate (*Protoperidinium pallidum*) was observed and contributed 1% to the total phytoplankton community. The drop in the dinoflagellate abundance and diversity during the MON and PRM might be due to the higher TSS ($r = -0.23$). During the MON, resulting 100% pennate diatoms at the riverine station (St-1, Figure 4) indicate that mixing of bottom waters due to the high rainfall and runoff could be the reason for the higher TSS and dominance of pennate diatoms.

Canonical correspondence analysis (CCA) was performed to determine the environmental factors controlling the phytoplankton groups (Figure 5). Eigenvalues of axes 1 (λ_1=0.104) and 2 (λ_2=0.074) explained 93.3% of the relationship between the phytoplankton community and environmental variables. The axis-1 was associated with the MON and PRM stations, where the diatoms (pennate and centric) and phytoplankton biomass (Chl-*a*) were positively correlated with TSS, nutrients, and negatively correlated with SST and salinity (Figure 5). Whereas, for dinoflagellates, the reverse trend was observed and associated with the POM stations. CCA result suggests that diatoms could survive in high TSS and favored to low SST, salinity, and high nutrients; while the dinoflagellates were restricted due to those elevated TSS, nutrients and favored to high SST and salinity. Ke et al. (2012) also observed a similar trend that diatoms favor the high silicate, phosphorus with low temperature, and the dinoflagellate favors the low silicate, phosphorus

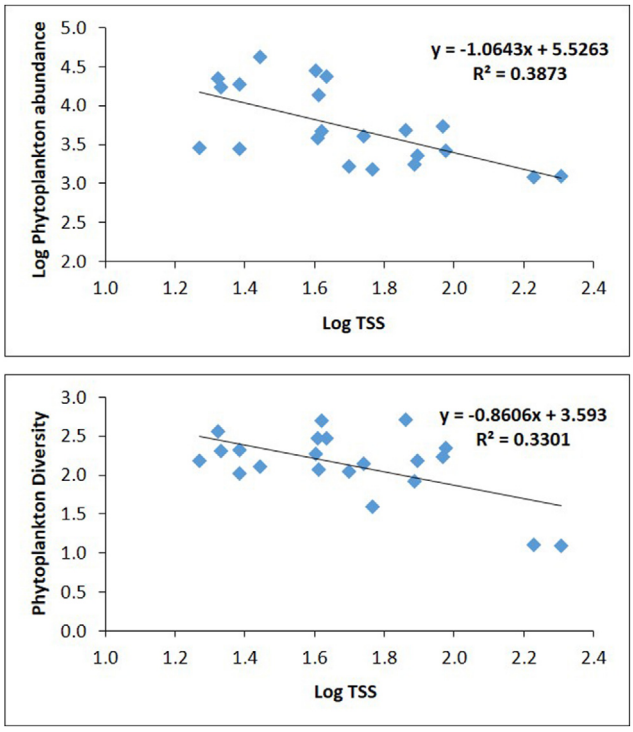

Figure 6 Relationship between TSS with phytoplankton abundance, and diversity in the coastal waters of Diu, northeastern Arabian Sea.

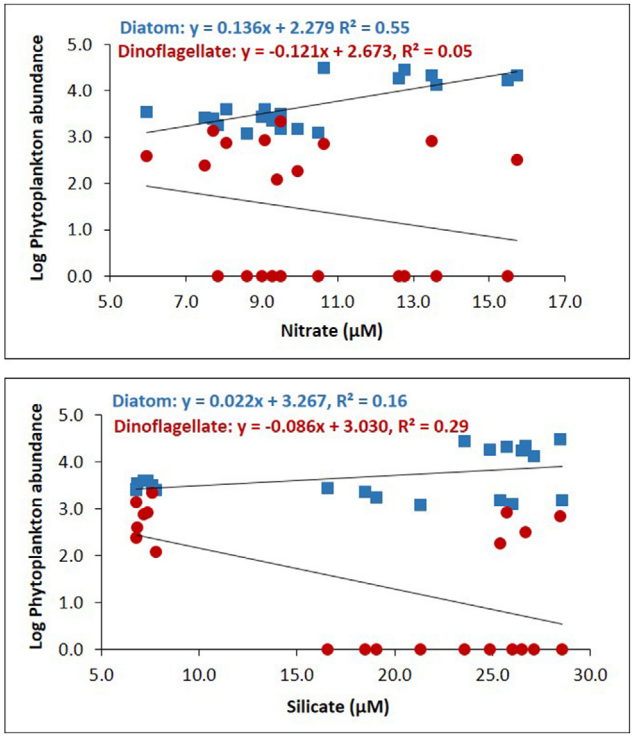

Figure 7 Relationship between diatom and dinoflagellate abundance with nitrate, and silicate, respectively, in the coastal waters of Diu, northeastern Arabian Sea.

with high SST. In addition to that, the regression analysis conformed that, overall the decline in phytoplankton abundance, and diversity due to the elevated level of TSS (Figure 6). The previous study at Veraval also encountered a reduction in phytoplankton growth due to the elevated level of turbidity (Hardikar et al., 2019). The regression analysis illustrated that the nitrate and silicate were the main factors influencing the abundance of diatoms, whereas the dinoflagellates were reducing with those factors (Figure 7). Further studies need to be carried out for the better understaning about the fluctuation among the phytoplankton groups with varying nutrients.

Several studies have reported the increased phytoplankton abundance or harmful algal blooms due to the elevated nutrients in the coastal environmment by land runoff and upwelling phenomenon (Hardikar et al., 2019; Kumar et al., 2020; Levy et al., 2007). In the present study, the reduction in phytoplankton abundance was observed due to the elevated level of TSS which could be attributed to natural erosion patterns as well as anthropogenic activities. Continuous reduction in phytoplankton abundance could also affect the zooplankton and higher tropical levels which may impact the fish stock in the future. Further studies need to be carried out in the future for a better understanding of the TSS, nutrients load, and their effect on plankton and higher tropical level. Thus, the present study suggests that to control erosion through plantation and shore protection measures and managing the anthropogenic discharge in the coastal waters of Diu. Though the TSS load is due to natural erosion, there is a need for shore protection measures which will ultimately conserve the coastal environment and enhance biological productivity.

4. Conclusion

Though light is the primary limiting factor for the phytoplankton growth, the high TSS recorded in the present study could have reduced the light and result in the lower phytoplankton abundance. Hence, the TSS played a key role in affecting the phytoplankton abundance, diversity, and biomass in the coastal waters of Diu. Possibly the coastal erosion and land runoff could be attributed to higher TSS load which might affect the growth of phytoplankton and higher trophic level. Thus, the present study suggests to develop the plantation in the coast and nutrient management strategy for the coastal waters of Diu. Reduction in phytoplankton abundance and biomass could reflect in fish stock, hence, more attention and continuous monitoring are required for developing better conservation and management plan in the coastal regions.

Declaration of competing interest

The authors declare that they have no known competing financial interests or personal relationships that could have appeared to influence the work reported in this paper.

Acknowledgments

The authors are grateful to the Ministry of Earth Sciences, Govt. of India, for providing financial support to carry out the present study. We also thank the scientific and supporting staffs of NIOT, Chennai, India, for their support in the field and the laboratory during this study.

Supplementary materials

Supplementary material associated with this article can be found, in the online version, at https://doi.org/10.1016/j.oceano.2021.11.005.

References

APHA, 2012. Standard Methods for the Examination of Water and Wastewater, 22nd edition 2540 D. Total Suspended Solids Dried at 103—105°C, 2—56.

Bhavya, P.S., Kumar, S., Gupta, G.V.M., Sudheesh, V., Sudharma, K.V., Varrier, D.S., Dhanya, K.R., Saravanane, N., 2016. Nitrogen uptake dynamics in a tropical eutrophic estuary (Cochin, India) andadjacent coastal waters. Estuar. Coasts. 39, 54—67.

Biswas, H., Reddy, N.P.C., Rao, V.S., Bharathi, M.D., Subbaiah, C.V., 2015. Time series monitoring of water quality and microalgal diversity in a tropical bay under intense anthropogenic interference (SW coast of the bay of Bengal, India). Environ. Impact Assess. Rev. 55, 169—181.

Carrit, D.E., Carpenter, J.H., 1966. Recommendation procedure for Winkler analyses of sea water for dissolved oxygen. J. Plankton Res. 24, 313—318.

Dunton, K.H., 1990. Growth and production of *Laminaria Solidungida*: relation to continuous underwater light levels in the Alaskan High Artie. Mar. Biol. 106, 297—304.

Gao, S., Wang, H., 2008. Seasonal and spatial distributions of phytoplankton biomass associated with monsoon and oceanic environments in the South China Sea. Acta Oceanol. Sin. 27 (2), 17—32.

Geeta, V.M., Kondalarao, B., 2004. Distribution of phytoplankton in the coastal waters of India. Indian J. Mar. Sci. 33, 262—268.

Grasshoff, Klaus, Kremling, Klaus, Ehrhardt, M., 1999. Methods of seawater analysis -chapter 10- nutrients. Methods Seawater Anal. 159—228.

Hardikar, R., Haridevi, C.K., Chowdhury, M., Shinde, N., Ram, A., Rokade, M.A., Rakesh, P.S., et al., 2017. Seasonal distribution of phytoplankton and its association with physico-chemical parameters in coastal waters of Malvan, west coast of India. Environ. Monit. Assess. 189 (4), 151.

Hardikar, R., Haridevi, C.K., Ram, A., Khandeparker, R., Amberkar, U., Chauhan, M., et al., 2019. Inter-annual variability of phytoplankton assemblage and Tetraspora gelatinosa bloom from anthropogenically affected harbour, Veraval, India. Environ. Monit. Assess. 191 (2), 87.

Howarth, R., Chan, F., Conley, D.J., Garnier, J., Doney, S.C., Marino, R., Billen, G., et al., 2011. Coupled biogeochemical cycles: eutrophication and hypoxia in temperate estuaries and coastal marine ecosystems. Front. Ecol. Environ. 9, 18—26.

Ilyash, L.V., Belevich, T.A., Stupnikova, A.N., Drits, A.V., Flint, M.V., 2015. Effects of local hydrophysical conditions on the spatial variability of phytoplankton in the White Sea. Oceanology 55 (2), 216—225.

Jha, D.K., Dharani, G., Verma, Pankaj, Ratnam, Krupa, Sendhil Kumar, R., Rajaguru, S., 2021. Evaluation of factors influencing the trace metals in Puducherry and Diu coasts of India through multivariate techniques. Mar. Pollut. Bull. 167, 112342.

JiyalalRam, M., Mandalia, A.V., Narvekar, S.M., Karangutkar, S.H., 2011. Nutrient fluxes and adaptation to environmental dynamics by phytoplankton in the Gulf of Khambhat. Int. J. Curr. Res. 3, 5—13.

Ke, Zhixin, Tan, Yehui, Huang, Liangmin, Zhang, Jianlin, Lian, Shumin, 2012. Relationship between phytoplankton composition and environmental factors in the surface waters of southern South China Sea in early summer of 2009. Acta. Oceanol. Sin. 31 (3), 109—119.

Kumar, P.S., Kumaraswami, M., Rao, G.D., Ezhilarasan, P., Sivasankar, R., Rao, V.R., Ramu, K., 2018. Influence of nutrient fluxes on phytoplankton community and harmful algal blooms along the coastal waters of southeastern Arabian Sea. Cont. Shelf Res. 161, 20—28.

Kumar, P.S., Kumaraswami, M., Ezhilarasan, P., Rao, G.D., Sivasankar, R., Rao, V.R., Ramu, K., 2020. Blooming of *Gonyaulax polygramma* along the southeastern Arabian Sea: Influence of upwelling dynamics and anthropogenic activities. Mar. Pollut. Bull. 151, 110817.

Lepisto, L., Holopainen, A.L., Vuoristo, H., 2004. Type-specific and indicator taxa of phytoplankton as a quality criterion for assessing the ecological status of Finnish boreal lakes. Limnologica 34, 236—248.

Levy, M., Shankar, D.J., Andre, M., Shenoi, S.S.C., Durand, F., De Boyer, C.M., 2007. Basin-wide seasonal evolution of the Indian ocean's phytoplankton blooms. Geophys. Res. 112.

Litchman, E., Klausmeier, C.A., 2008. Trait-based community ecology of phytoplankton. Annu. Rev. Ecol. Evol. Syst. 39, 615—639.

Margalef, R., 1978. Life-forms of phytoplankton as survival alternatives in an unstable environment. Oceanologica Acta 1, 493—509.

Nair, V.R., Gajbhiye, S.N., Jaiswar, J.M., 2005. Biogeography of plankton of Gulf of Kachchh, Northwest Coast of India, Dynamic Planets, Cairns Australia.

Naqvi, S.W.A., Narvekar, P.V., Desa, E., 2006. Coastal biogeochemical processes in the North Indian Ocean, The Sea, Vol. 14, A. Robinson and K. Brink, Harvard Univ. Press, Cambridge, 723—780.

NCCR, 2018. National Assessment of Shoreline Changes along Indian Coast: Status Report for 26 years 1990—2016.

NIO, 2015. Marine EIA Associated with Proposed Dredging Carried out in the Vanakbara and Diu-Ghoghla Creeks and Construction of Jetties at Diu-Ghoghla and Vanakbara by. UT Administration of Daman and Diu.

Parson, T.R., Maita, Y., Lalli, C.M., 1984. A Manual of chemical and biological methods for seawater. Analysis. https://doi.org/10.1016/B978-0-08-030287-4.50002-5

Peretyatko, A., Teissier, S., Symoens, J.J., Triest, L., 2007. Phytoplankton biomass and environmental factors over a gradient of clear to turbid peri-urban ponds. Aquat. Conserv. Mar. Freshwater Ecosyst. 17, 584—601.

Raghunathan, C., Gupta, R.S., Wangikar, U., Lakhmapurkar, J., 2004. A record of live corals along the Saurashtra coast of Gujarat, Arabian Sea. Curr. Sci. 1131—1138.

Seitzinger, S.P., Mayorga, E., Bouwman, A.F., Kroeze, C., Beusen, A.H.W., Billen, G., Harrison, J.A., 2010. Global river nutrient export: A scenario analysis of past and future trends. Global Biogeochem. Cy. 2.

Spilling, K., Olli, K., Lehtoranta, J., Kremp, A., Tedesco, L., Tamelander, T., Klais, R., Peltonen, H., Tamminen, T., 2018. Shifting diatom—dinoflagellate dominance during spring bloom in the Baltic Sea and its potential effects on biogeochemical cycling. Front. Mar. Sci. 5, 327.

Subrahmanyan, R., 1946. A systematic account of the marine plankton diatoms of the Madras coast. Proc. Indian Acad. Sci. 24, 85—197.

Subrahmanyan, R., 1959. Studies on the phytoplankton of the west coast of India. parts I and II. Proc. Indian Acad. Sci. 50B, 113—187.

Taylor, F.J.R., 1976. Dinoflagellates from the international Indian Ocean expedition. A report on material collected by R.V Anton Bruun 1963—64. In: Plates, 1—46.

Tomas, C.R., 1997. Identifying Marine Phytoplankton: San Diego. Academic Press, California.

Verlencar, X.N., Parulekar, A.H., 2006. In: Nutrients and phytoplankton production in the Southern Ocean in a section 10° to 52° E in the Indian Ocean. Fourth Indian Scientific Expedition to Antarctica. 4th Sci. Rep., Dept. of Ocean Development, Tech. Publ., New Delhi, 159—167.

Wang, Y., Wu, H., Lin, J., Zhu, J., Zhang, W., Li, C., 2019. Phytoplankton blooms off a high turbidity estuary: a case study in the Changjiang River Estuary. J. Geophys. Res. Oceans. 124 (11), 8036—8059.

Weyhenmeyer, G.A., Hakanson, L., Meili, M., 1997. A validated model for daily variations in the flux, origin, and distribution of settling particles within lakes. Limnol. Oceanogr. 42, 1517—1529.

Wu, N., Schmalz, B., Fohrer, N., 2011. Distribution of phytoplankton in a German lowland river in relation to environmental factors. J. Plankton Res. 33 (5), 807—820.

Zarauz, L., Irigoien, X., Fernandes, J.A., 2008. Modelling the influence of abiotic and biotic factors on plankton distribution in the Bay of Biscay, during three consecutive years (2004-06). J. Plankton Res. 30 857—572.

Zhou, M.-J., Shen, Z.-L., Liang, Yu, R.-Ch., 2008. Responses of a coastal phytoplankton community to increased nutrient input from the Changjiang (Yangtze) River. Cont. Shelf Res. 28, 1483—1489.

Oceanologia 64 (2022) 276—286

Available online at www.sciencedirect.com

ScienceDirect

journal homepage: www.journals.elsevier.com/oceanologia

ORIGINAL RESEARCH ARTICLE

Ecological assessment of heavy metals accumulation in sediments and leaves of *Avicennia marina* along the Diu coast of the northeast Arabian Sea

Varsha Patale, Jigna G. Tank*

Department of Biosciences, Saurashtra University, Gujarat, India

Received 6 May 2021; accepted 3 December 2021
Available online 17 December 2021

KEYWORDS
Ecological assessment;
Heavy metals;
Sediments;
Avicennia marina;
Diu coast

Abstract The Coastal region of Diu is the natural habitat dominated by *Avicennia marina* mangrove species at the southeast coast of Saurashtra in Gujarat state of India. However, Diu being a famous industrial and tourism place survival of these mangrove species is threatened due to anthropogenic activities. In present studies, sediment and leaf samples of *A. marina* were collected from the Diu coast to evaluate the ecological threat of heavy metals accumulation in the marine habitat. There was remarkable presence of heavy metals such as copper, nickel, cadmium, chromium and lead in sediments and leaf samples of *A. marina*. The values of Biological concentration factors (BCFs) of heavy metals in leaf samples were high for cadmium, chromium and lead which suggest chelation of these heavy metals with biomolecules. The geo-accumulation index suggested that Site-4 and Site-5 were heavily contaminated with copper and nickel. The ecological risk index suggested that there is no significant effect of heavy metals on growth of plants in the mangrove ecosystem. Principal component analysis revealed that the samples collected from the natural habitats (Site-4 and Site-5) near the fishing and industrial areas were the main sources of heavy metal contamination. Hence, it was concluded that the concentration of heavy metals in the studied ecosystem had limited impact on growth of plants at Site-1, Site-2 and Site-3. However, growth of plants at Site-4 and Site-5 were threatened due to the toxic effect of copper and nickel present in its sediments.

* Corresponding author at: Department of Biosciences, Saurashtra University, Rajkot, 360005, Gujarat, India.
E-mail address: jignagtank@gmail.com (J.G. Tank).
Peer review under the responsibility of the Institute of Oceanology of the Polish Academy of Sciences.

Production and hosting by Elsevier

https://doi.org/10.1016/j.oceano.2021.12.002

1. Introduction

The coastal region of the Diu with vast tidal flats is one of the richest zones for mangroves along the west coast of India. It is the natural habitat of *Avicennia marina* in the Gulf of Khambhat. Conservation of this natural habitat of *A. marina* is important as it is the only island dominated by these plants. *A. marina* species are distributed sparsely in these regions in the form of patches and survival of these mangrove patches is significantly threatened due to anthropogenic human activities in subtidal and intertidal zone of coastal region. As it is a famous tourism place and industrial zone of Gujarat, it is continuously influenced by urbanization activities. This strong anthropogenic forcing has a highly negative impact on subtidal and intertidal habitats within the region. Major industries present in the Diu region are polyester, cotton yarn, plasticizers, paper petroleum byproducts, pharmaceuticals, plastics, electrical conductors and marble tiles. These industries are known to induce high concentrations of heavy metals in water and sediments of the marine ecosystem through pollutants from urban runoff and industrial waste disposal (Bodin et al., 2013; Marchand et al., 2006).

Various studies have depicted that mangroves have ability to survive in changing environmental conditions such as alternating floods, low oxygen level in sediments, changing osmotic potential, organic, inorganic or metal pollution (Buajan and Pumijumnong, 2010; Li et al., 2016). Even, they have ability to accumulate heavy metals in aerial roots and translocate them to other organs of the plant (Fernández-Cadena et al., 2014; Li et al., 2016; Usman et al., 2013). The concentrations of heavy metals were found high in aerial roots of mangrove species such as *Avicennia, Rhizophora* and *Kandelia* as compared to shoots (Chiu et al., 1995; MacFarlane and Burchett, 2002; Peters et al., 1997; Tam and Wong, 2000; Thomas and Fernandez, 1997). Heavy metals are hazardous to mangrove plants if its concentration increases above 5 gm/cm^3. They threaten survival of mangroves by affecting on their metabolic processes which in turn reduces growth and reproduction in plants (Wright and Welbourn, 2002). These in turn reduces density and diversity of plant species in the ecosystem (Järup, 2003; Yan et al., 2017). Therefore, the ecological assessment and subsequent protection measures framework for preserving the only natural habitat of *A. marina* are a necessity needed promptly.

2. Material and methods

2.1. Geographical locations of the study area

Present research was conducted on five locations where *A. marina* inhabits the coastal region of Diu. These five locations were selected for this research on the basis of the geographical dominance of *A. marina* species, the anthropogenic activities, aggregation of fishing community and sewage pollution in the area. The sites were located at the following geographical locations: 1) Site-1 (Near Goghala bridge: GPS 20°43′46.66″N 70°59′17.52″E); 2) Site-2 (Opposite Jethibai Bus Station: GPS 20°43′7.31″N 70°58′52.16″E); 3) Site-3 (Airport road, Diu: GPS 20°42′51.90″N 70°57′28.26″E); 4) Site-4 (Behind Goa Industrial Development Corporation area: GPS 20°42′57.40″N 70°56′59.87″E); 5) Site-5 (Taad village bridge: GPS 20°44′7.35″N 70°55′48.07″E) (Figure 1).

2.2. Sediments samples collection and heavy metals analysis

Heavy metals analysis from sediments and leaves samples was done by following the method prescribed by Enders and Lehmann (2012) with some modifications. Sediments and leaves samples were collected from five different places (Site-1 to Site-5) in plastic collection vessels. Sediments and leaf samples were dried in an oven at 70°C and then grinded using mechanical grinder. The powder of samples was passed through 0.3 mm size sieves. Further dry ash oxidation method was used to digest the powder samples of soil and leaves. The well grinded dry powder of each sample was filled in cruscible of muffle furnish. In Muffle furnesh ash of each sample powder was prepared by incubating the cruscible for 5 hrs. at 550°C. Then after cooling ash was dissolve in 5 ml of 25% HCl. The mixture was filtered using acid wash filter paper and final volume of 50 ml was prepared using distilled water. Concentration of all microelements (Mg, S, B, Fe, Zn, Cu, Mn, Ni) and heavy metals (As, Cd, Cr, Pd, Hg, Se) were determined from this digested sample solution using ICP-MS (ICAP Q Thermo Fisher Scientific, Waltham, MA, USA). Samples were analyzed in triplicate using the following operation conditions of instrument: Power=1550W, cool gas flow=14.1 L/min, nebulizer gas flow = 0.94 L/min, auxillary gas flow = 0.79 L/min, dwell time =0.01 s, perostatic pump speed = 40 rpm, total time for each sample measurement= 3 min.

2.2.1. Comparison of heavy metal estimation data with sediment quality guidelines (SQGs)

The data obtained in present studies was compared with sediment quality guidelines (SQGs) as described by Bakan and Özkoc (2007), Luo et al. (2010) and MacDonald et al. (2000). These guidelines consists of the data on probable effect level (PEL), threshold effect level (TEL), lowest effect level (LEL), effect range low (ERL), toxic effect threshold (TET), effect range median (ERM), and severe effect level (SEL) of heavy metals in coastal regions.

2.2.2. Determination of the biological concentration factor (BCF) in leaves samples

The biological concentration factor (BCF) of leaves was calculated to evaluate the accumulation level of heavy metals in plant tissues from sediments. BCF values for leaves were expressed as original data averages for the heavy metals such as Cu, Ni, Cd, Cr, and Pb. The BCF values were calculated based on the equation described by Cui et al. (2007) and Yoon et al. (2006):

$$BCF_{leaf}=C_{leaf}/C_{sediment}$$

where C_{leaf} are the heavy metal concentrations in the leaf and $C_{sediment}$ is the heavy metal concentration in the sediment.

Figure 1 Topography of study area which shows the five natural habitats of *Avicennia marina* at Diu coast.

2.2.3. Determination of geo-accumulation index (I_{geo})

Geo-accumulation index (I_{geo}) of heavy metals was determined to assess the changes of concentration of heavy metals by associating it with the heavy metal concentrations in aquatic sediments with the geochemical background. It was calculated by following the equation described by Müller (1969)

$$I_{geo} = \log_2 C_n/(1.5)B_n$$

where, C_n is the concentration of metal measured in mangrove sediments, B_n is the geochemical background value of the earth's crust (Taylor and McLennan, 1985).

1.5 is a constant applied to account for the potential variability in the reference value due to the influence of lithogenic processes.

I_{geo} values can be categorized in the following manner: uncontaminated sediment when $I_{geo} = 0$; uncontaminated to moderately contaminated sediment when $0 < I_{geo} < 1$; moderately contaminated sediment when $1 < I_{geo} < 2$; moderately to heavily contaminated sediment when $2 < I_{geo} < 3$; heavily contaminated sediment when $3 < I_{geo} < 4$; heavily to extremely contaminated sediment when $4 < I_{geo} < 5$; and extremely contaminated sediment when $5 < I_{geo}$.

2.2.4. Determination of the probable ecological risk coefficient (E^i_r)

The probable ecological risk coefficient (E^i_r) was determined by following the formula given by Hakanson (1980)

$$E^i_r = T^i_r * C^i_r = T^i_r * C^i_r / C^i_n$$

where, T^i_r values for measured heavy metals are Cr = 2, Cu = 5, Ni = 5, Pb = 5 and Cd = 30; C^i_r is the contamination factor, C^i_s is the concentration of heavy metals in the sediment, C^i_n — a background value for heavy metals and T^i_r is the metal toxic response factor.

E^i_r values can be categorized in the following manner:

$E^i_r < 40$ then low risk, $40 < E^i_r < 80$ then moderate risk, $80 < E^i_r < 160$ then considerable risk, $160 < E^i_r < 320$ then high-risk and $E^i_r > 320$ then very high risk

2.2.5. Statistical analysis

Multivariate cluster analysis was performed to construct a dendrogram based on the similarity matrix data using the paired group (UPGMA) method with arithmetic averages and Euclidean similarity index. All the measured parameters were also subjected to Principle component analysis to determine significant relationship of one component with another. Comparisons and similarity groupings of all measured parameters were done by using two-way ANOVA to determine significant variation between means. All the analysis was performed using Past: Palaeontological Statistics software package.

3. Results

3.1. Sediments quality assessment at natural habitats of *Avicennia marina*

From present studies, it was observed that the mean concentration of heavy metals in sediments varied in range from 1.34 to 2.64 μg/g for copper, 0.028 to 2.093 μg/g for nickel, 0.023 to 0.09 μg/g for cadmium, 0.012 to 0.099 μg/g for chromium, and 0.024 to 0.098 μg/g for lead. The con-

Table 1 Variation in mean concentration of heavy metals accumulation in leaves samples due to season changes.

ANOVA *Source of Variation*	*SS*	*df*	*MS*	*F*	*P-value*	*F crit*
Sites	0.000105	4	2.63E-05	6.701746	**0.000176**	3.674045
Seasons	0.032951	14	0.002354	600.3941	**1.24E-55**	2.417951
Error	0.00022	56	3.92E-06			
Total	0.033276	74				

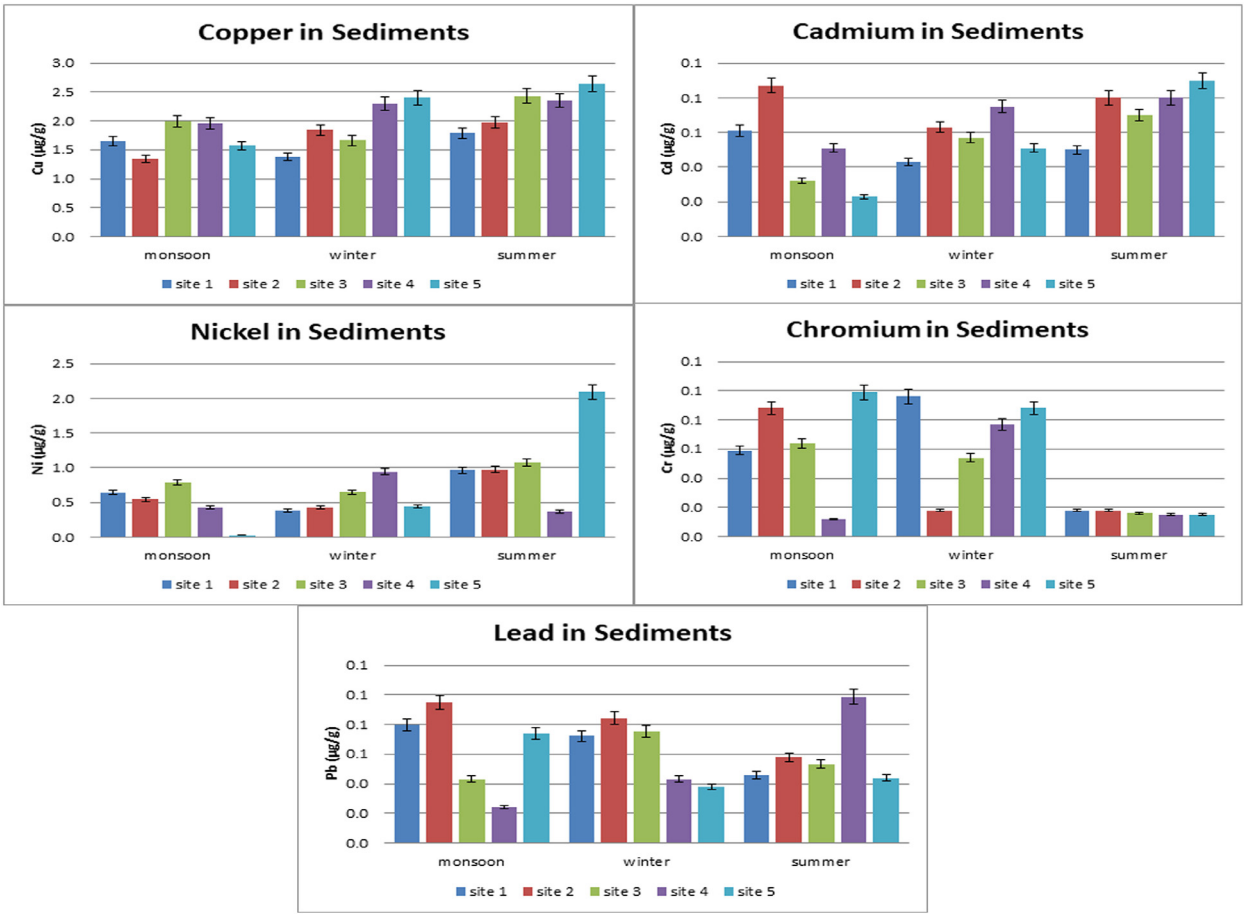

Figure 2 Changes in the mean concentration of heavy metals in sediments at all the five natural habitats of *Avicennia marina* during different seasons.

centrations of heavy metals in sediments were in following order Cu>Ni>Cd>Cr>Pd. There was remarkable significant variation ($p<0.01$) of mean heavy metals concentration at all the five natural habitats of *A. marina* at Diu coast (Table 1). There was also significant ($p<0.01$) influence of seasonal changes on concentration of heavy metals in sediments of all the five natural habitats of *A. marina* at Diu coast. The concentration of copper was high during summer season as compared to winter and monsoon season at all the five habitats. The copper concentration remained high at Site-4 and Site-5 as compared to other sites (Figure 2). The concentration of nickel was high during summer season as compared to monsoon and winter season at all the five habitats (Figure 2). The concentration of cadmium was high during summer and winter season as compared to monsoon. The cadmium concentration remained high at Site-4 and Site-5 as compared to other sites (Figure 2). The concentration of chromium was high during monsoon and winter season as compared to summer. The chromium concentration remained high at site-1 and Site-5 as compared to other sites (Figure 2). The concentration of lead was high during winter and monsoon season as compared to summer. The concentration of lead remained high at Site-2 and Site-4 as compared to other sites (Figure 2).

Table 2 Variation in the mean concentration of heavy metals in sediments at all the five natural habitats due to seasonal changes.

ANOVA *Source of Variation*	*SS*	*df*	*MS*	*F*	*P-value*	*F crit*
Sites	0.255424	4	0.063856	1.053742	**0.387995**	3.674045
Seasons	42.59691	14	3.042636	50.20916	**1.74E-26**	2.417951
Error	3.393557	56	0.060599			
Total	46.24589	74				

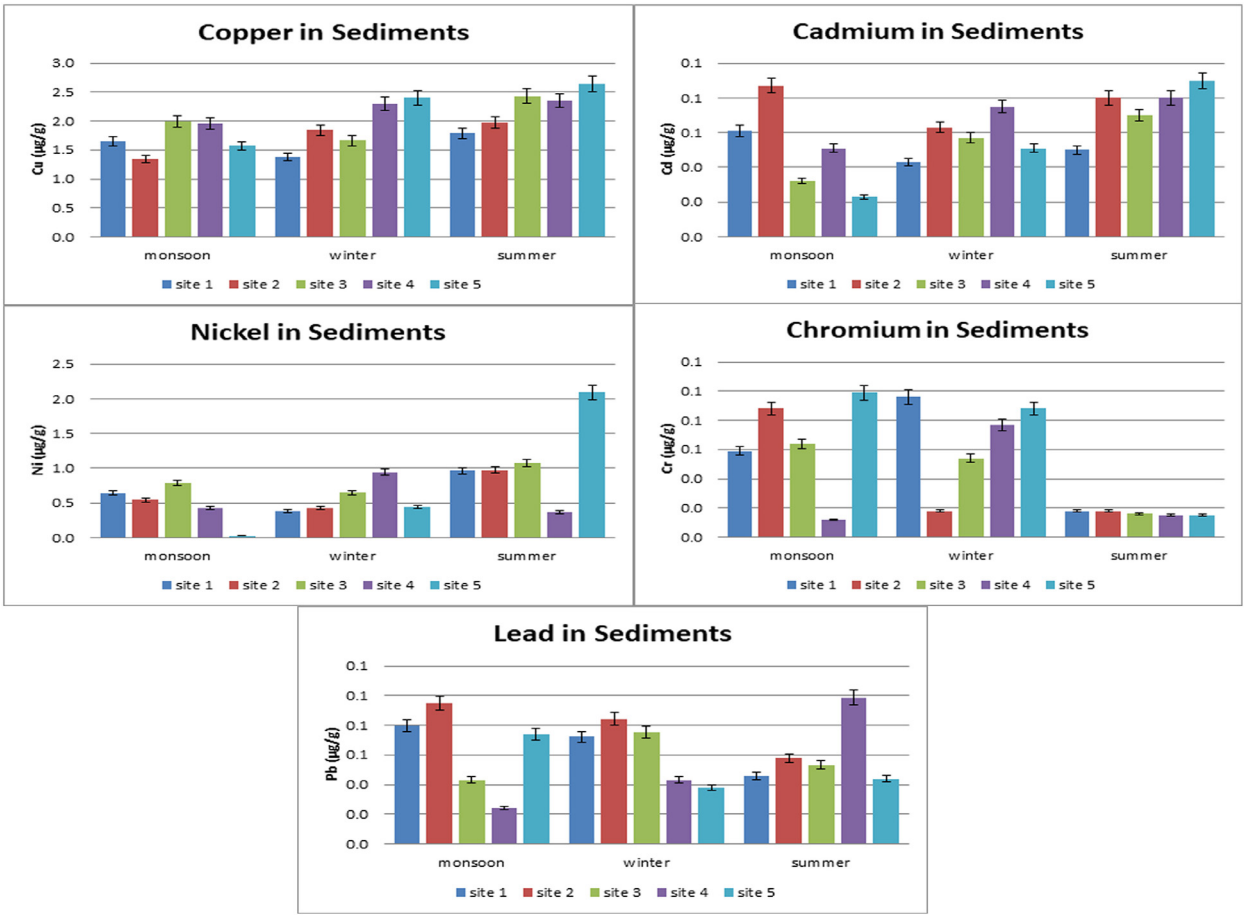

Figure 3 Changes in accumulation of heavy metals in leaves of *Avicennia marina* during different seasons.

3.2. Accumulation of heavy metals in leaves of *Avicennia marina*

From present studies, it was observed that the mean concentration of heavy metals in leaves varied in range from 0.049 to 0.067 µg/g for copper, 0.009 to 0.028 µg/g for nickle, 0.003 to 0.009 µg/g for cadmium, 0.021 to 0.052 µg/g for chromium and 0.001 to 0.0039 µg/g for lead. The concentrations of heavy metals in leaves were in following order Cu>Cr>Pd>Ni>Cd. There was no significant ($p>0.01$) difference in the accumulation of heavy metals in leaves of *A. marina* at all the five natural habitats. However, there was remarkable high influence of seasonal change on accumulation of heavy metals in leaves (Table 2). There was slightly higher accumulation of copper in leaves of *A. marina* during monsoon as compared to summer and winter (Figure 3). There was high accumulation of nickle in leaves of *A. marina* during summer season as compared to monsoon and winter (Figure 3). There was high accumulation of cadmium during winter and summer season as compared to monsoon (Figure 3). There was high accumulation of chromium during summer season as compared to winter and monsoon (Figure 3). There was high accumulation of lead during summer season as compared to monsoon and winter (Figure 3).

3.3. Biological concentration factors

The mean values of biological concentration factors obtained from leaves samples were in range 0.023—0.044 µg/g for copper, 0.01—0.39 µg/g nickel, 0.033—0.26 µg/g for cadmium, 0.0029—0.36 µg/g for chromium and 0.015—

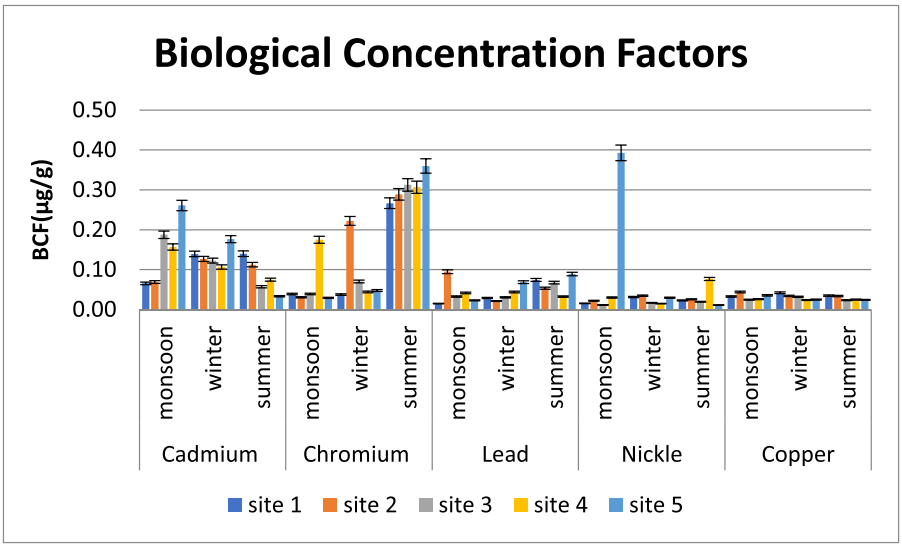

Figure 4 Biological concentration factors of heavy metals in leaves of *Avicennia marina* during different seasons.

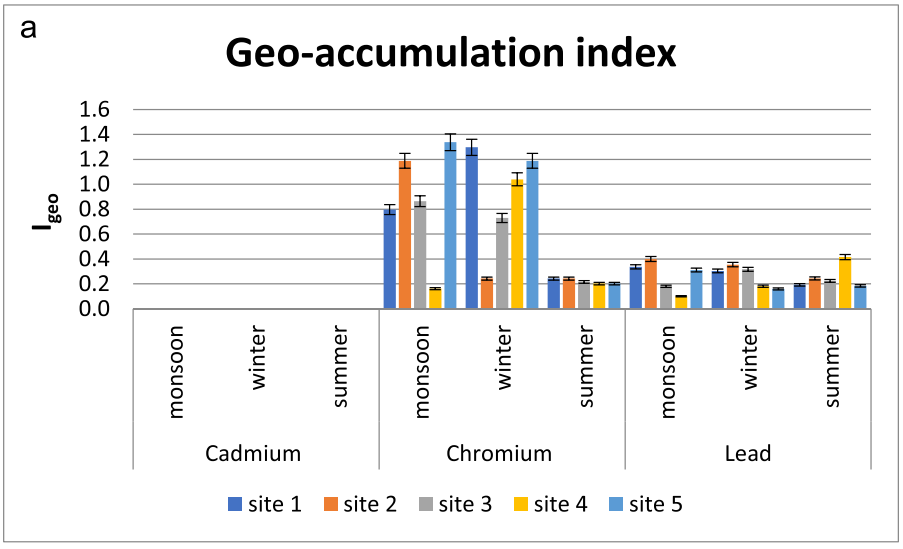

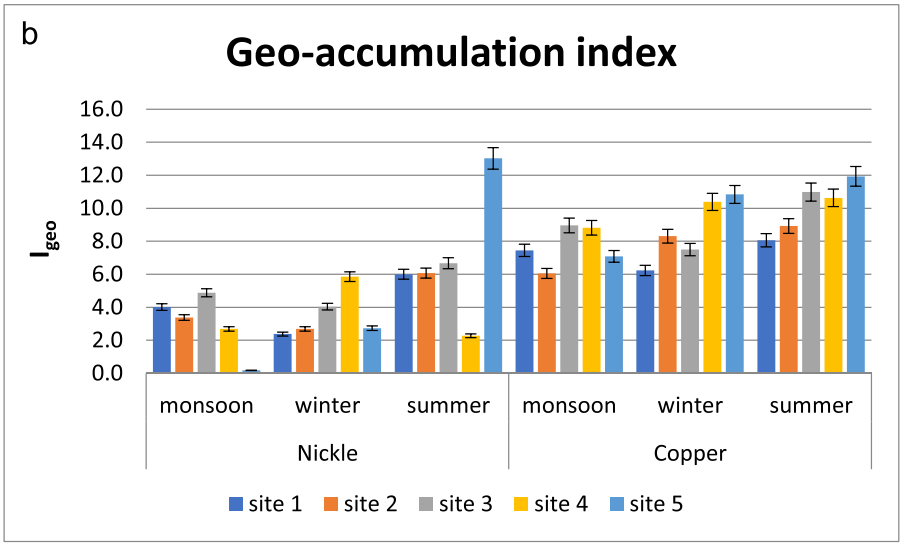

Figure 5 Geo-accumulation index of heavy metals (Cd, Cr, Pb) in sediments of *Avicennia marina* during different seasons (a). Geo-accumulation index of heavy metals (Ni, Cu) in sediments of *A. marina* during different seasons (b).

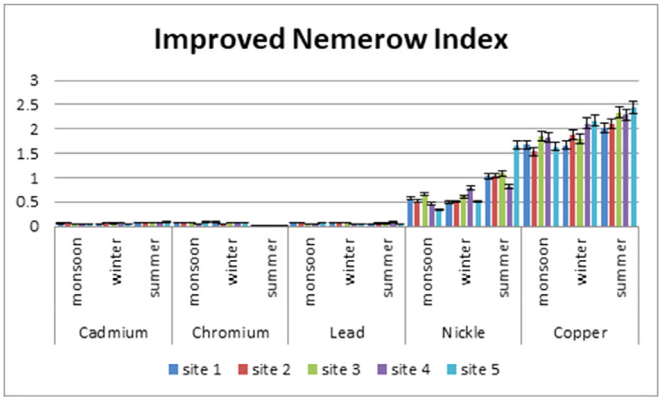

Figure 6 Improved Nemerow index of heavy metals in sediments of *Avicennia marina* during different seasons.

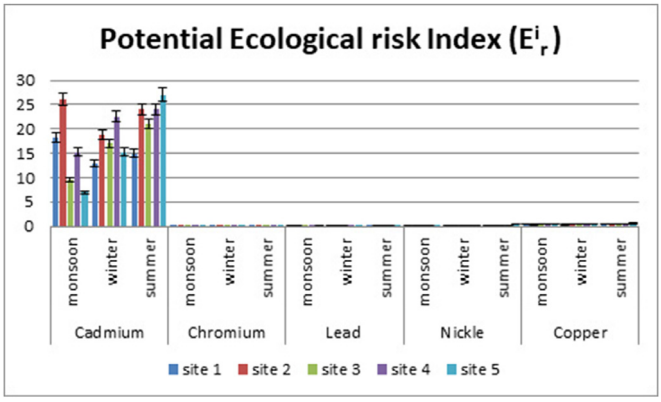

Figure 7 Potential Ecological Risk index (E^i_r) of heavy metals in sediments during different seasons.

0.094 μg/g for lead. The highest biological concentration factors among all the five habitats during three seasons were obtained for cadmium and chromium in leaves samples (Figure 4).

3.4. Geo-accumulation index and ecological risk coefficient

The geo-accumulation index (I_{geo}) suggested that cadmium and lead demonstrated uncontaminated sediments with I_{geo} greater than equal to 0 at all the five habitats during all seasons. The chromiun demonstrated moderately contaminated sediments with I_{geo} value greater than 1 at Site-2 and Site-5 during monsoon season and at Site-4 and Site-5 during winter season. However, during summer season chromium showed uncontaminated sediments with I_{geo} value greater than 0. The copper and nickel demonstrated moderately to heavily contaminated sediments with I_{geo} value greater than 2 in all the five habitats during all seasons (Figures 5a and 5b). The improved Nemerow index (Figure 6) and potential ecological risk index showed the same pattern as that of the geo-accumulation index. However, the copper, nickel, cadmium, chromium, and lead demonstrated uncontaminated sediments with E^i_r values less than 40 (Figure 7).

3.5. Multivariate cluster analysis

Multivariate cluster analysis was used to detect the similarity between the five habitats during three seasons. Cluster analysis grouped the five habitats in to two groups on the basis of its mean heavy metal concentrations in sediments during three seasons. Group A included Site-1, Site-2 and Site-3 and Group B included Site-4 and Site-5. Group B corresponds to high concentration of Cu, Ni, Cr, Pd and Cd during summer and winter season as compared to group A which suggests high pollution in group B as compared to group A. Similar clusters were also formed by non-metric multidimentional scaling (MDS) (Figure 8) which supported the results of multivariate Cluster analysis. From the Prin-

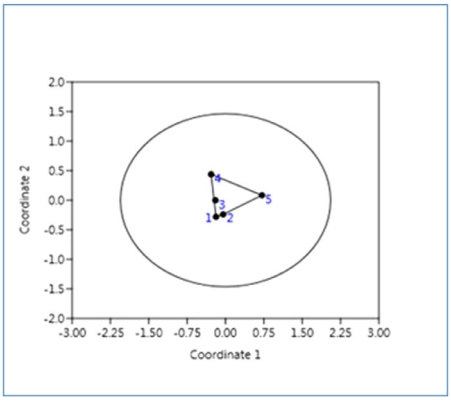

Figure 8 Non-metric multidimensional scaling of five natural habitats of *Avicennia marina* on the basis of heavy metals concentrations in sediments.

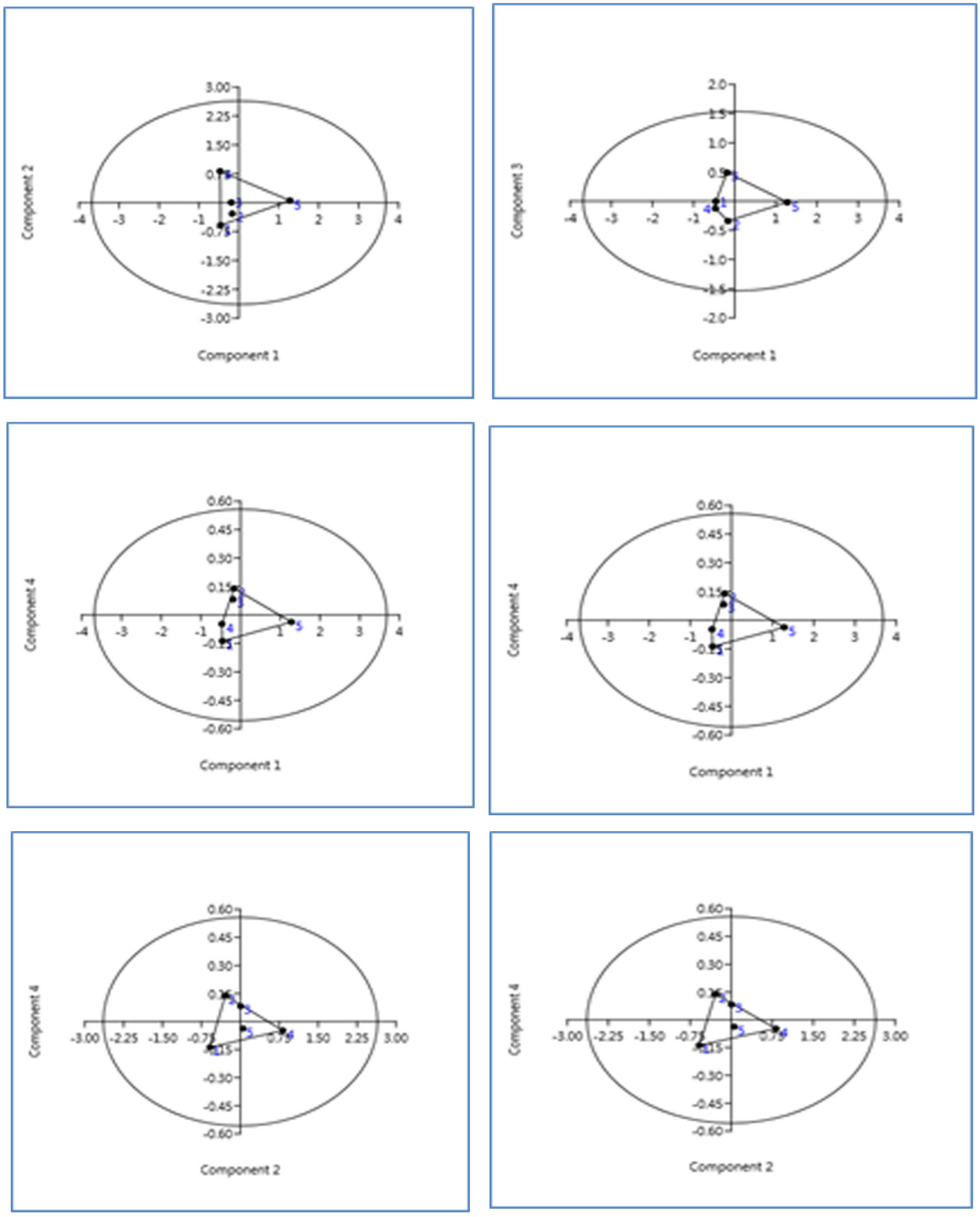

Figure 9 Principal component analysis of heavy metals in sediments of five natural habitats *Avicennia marina* during different seasons (summer, winter and monsoon).

ciple component analysis, it was observed that there was 99.9% total variations were retained on the basis of the eigenvalue. The first and second principle components explained 58.435% and 30.059% of variance in the heavy metals, respectively. However, third and fourth priniciple component explained only 10.167% and 1.338 % of the variance, respectively. This suggests that cluster B which includes Site-4 and Site-5 has more pollution of heavy metals than cluster A which includes Site-1, Site-2 and Site-3 (Figure 9).

4. Discussion

In present studies, there was significant ($p<0.01$) influence of seasonal changes on concentration of heavy metals in sediments of all the five natural habitats of *A. marina* at Diu coast. The concentration of copper was high during summer season as compared to winter and monsoon at all the five habitats. The concentration of cadmium was high during summer and winter season as compared to monsoon. The concentration of chromium was high during monsoon and winter season as compared to summer. The concentration of lead was high during winter and monsoon season as compared to summer. It was assumed that the presence of higher concentration of copper in sediments is due to the presence of many fishing boats that use antifouling paints that contains $CuSO_4$ as a major ingredient which is being also suggested by Usman et al. (2013). The presence of other heavy metals in the natural habitats of mangroves is due to several anthropogenic activities such as fishing, sewage and industrial pollution which are the major causes for the accumulation of heavy metals in the sediments. Major industries present in the Diu region are polyester, paper, cotton yarn, petroleum by products, plasticizers, pharmaceuticals, electrical conductors, marble tiles, and plastics which are the key sources of heavy metal pollution in mangrove sediments. Previous studies have also recorded

Table 3 Comparison of total heavy metals [μg/g] in mangrove sediments at different sites along the coastal region of Diu and standard quality guidelines.

Heavy metals	Cu	Ni	Cd	Cr	Pd	
Threshold effect concentration (TEC) SQGs						
Threshold effect level (TEL)	16	16	0.596	26	31	
Lowest (2000) effect level (LEL)	35.7	18	0.6	37.3	35	MacDonald et al. (2000)
Effect range low (ERL)	70	30	5	80	35	
Canadian sediment quality guidelines (TEL)	18.7	—	0.7	—	30.2	Canadian Council of Ministers of Environment (2002)
Probable effect concentration (PEC) SQGs						
Probable effect level (PEL)	149	36	3.53	90	91.3	
Severe effect level (SEL)	110	75	10	110	250	
Toxic effect threshold (TET)	86	61	3	100	170	
Effective range median (ERM)	390	50	9	145	110	
Canadian sediment quality guidelines (PEL)	108	—	112	—	112	Canadian Council of Ministers of Environment (2002)
Present studies						
Monsoon Season						
Site-1	1.65	0.645	0.061	0.059	0.08	
Site-2	1.34	0.543	0.087	0.088	0.095	
Site-3	1.984	0.784	0.032	0.064	0.043	
Site-4	1.953	0.432	0.051	0.012	0.024	
Site-5	1.569	0.028	0.023	0.099	0.074	
Summer Season						
Site-1	1.785	0.965	0.05	0.018	0.0458	
Site-2	1.976	0.976	0.08	0.018	0.0579	
Site-3	2.432	1.072	0.07	0.016	0.0533	
Site-4	2.355	0.365	0.08	0.015	0.0986	
Site-5	2.643	2.093	0.09	0.015	0.0438	
Winter Season						
Site-1	1.38	0.382	0.043	0.096	0.0723	
Site-2	1.84	0.432	0.063	0.018	0.0843	
Site-3	1.66	0.649	0.057	0.054	0.0753	
Site-4	2.3	0.941	0.075	0.077	0.0432	
Site-5	2.4	0.439	0.051	0.088	0.0379	

high concentrations of heavy metals in mangrove sediments and have suggested that anthropogenic activities are the main source of heavy metal pollution in mangrove habitats (Defew et al., 2005; Tam and Wong, 2000).

The results obtained in the present studies were compared with the standard quality guidelines (SQGs) of heavy metals given by Bakan and Özkoc (2007), Luo et al. (2010) and MacDonald et al. (2000). The threshold effect concentrations of copper, nickel cadmium, chromium and lead were lower than the values of TEL, LEL, ERL, PEL, SEC TET and ERM (Tables 3). This suggest that the season changes has maximum influence on accumulation of heavy metals in sediments of mangroves habitat which can cause infrequent threat to the marine organisms (MacDonald et al., 2000).

In present studies, the highest biological concentration factors among all the five habitats during three seasons were obtained for cadmium and chromium in leaves samples. This clearly suggests the bioavailability of cadmium and chromium in sediments of all the five natural habitats of *A. marina*. The low values of biological concentration factors for copper, nickel, and lead suggests low bioavailability of these metals in the sediments. This reflects the chelation of heavy metals with organic molecules which results in formation of immovable compounds (Li et al., 2016; Nath et al., 2014).

The geo-accumulation index (I_{geo}) was introduced by Müller (1969) to assess metal pollution in sediments. It has been applied in present studies to facilitate the qualitative assessment of heavy metal contamination in sediments of five natural habitats (Shi et al. 2014; Srinivasa et al. 2010). The improved Nemerow index and potential ecological risk index showed the same pattern as that of the Geo-accumulation index. These results suggests that the sediments are influenced by anthropogenic sources such as industrial wastes, untreated sewage effluents and antifouling paints from fishing boats (Usman et al., 2013). The ecological risk index suggested that there is no significant effect of heavy metals on growth of plants in the mangrove ecosystem. Multivariate cluster analysis, non-multidimentinal scaling and Principal component analysis revealed that the samples collected from the natural habitats (Site-4 and Site-5) near the fishing and industrial areas were the main sources of heavy metal contamination.

5. Conclusions

From the present studies, it was concluded that the levels of heavy metals were lower than the toxic effect threshold level and probable effect level which indicates a very limited biological impact on the marine environment. The higher concentrations of heavy metals in the leaves samples of mangroves indicated that *A. marina* accumulates heavy metals. The values of biological concentration factors (BCFs) suggested that the bioavailability of cadmium, chromium and lead were high as compared to copper and nickel. According to I_{geo} index, Site-4 and Site-5 were heavily contaminated with copper and nickel. However, Site-1, Site-2 and Site-3 were moderately affected by heavy metals. The ecological risk index suggested that there is no significant effect of heavy metals on growth of plants in the mangrove ecosystem. Principal component analysis revealed that the samples collected from the natural habitats (Site-4 and Site-5) near the fishing and industrial areas were the main sources of heavy metal contamination.

Conflict of interest declaration

Authors declare that there is no conflict of interest regarding publication of present research work in journal.

Acknowledgements

Authors are highly thankful to Department of Biosciences, Saurashtra University, Rajkot for providing necessary facilities to carry out this research work.

References

Bakan, G., Özkoc, H.B., 2007. An ecological risk assessment of the impact of heavy metals in surface sediments on biota from the mid-Black Sea coast of Turkey. Int. J. Environ. Stud. 64 (1), 45—57. https://doi.org/10.1080/00207230601125069

Bodin, N., N'Gom-Kâ, R., Kâ, S., Thiaw, O.T., De Morais, L.T., Le Loc'h, F., Rozuel-Chartier, E., Auger, D., Chiffoleau, J.F., 2013. Assessment of trace metal contamination in mangrove ecosystems from Senegal, West Africa. Chemosphere 90 (2), 150—157. https://doi.org/10.1016/j.chemosphere.2012.06.019

Buajan, S., Pumijumnong, N., 2010. Distribution of heavy metals in mangrove sediment at the Tha China estuary, Samut Sakhon province. Thailand. Appl. Environ. Res. 32 (2), 61—77.

Canadian Council of Ministers of the Environment (CCME), 2002. Canadian sediment quality guidelines for the protection of aquat-ic life: summary tables. In: Canadian Environmental Quality Guidelines, 1999, Winnipeg. Canadian Council of Ministers of Environment, 1—5.

Chiu, C.Y., Hsiu, F.S., Chen, S.S., Chou, C.H., 1995. Reduced toxicity of Cu and Zn to mangrove seedlings (Kandelia candel (L.) Druce.) in saline environments. Bot. Bull. Acad. Sin. 36 (1), 19—24.

Cui, S., Zhou, Q., Chao, L., 2007. Potential hyperaccumulation of Pb, Zn, Cu and Cd in endurant plants distributed in an old smeltery, northeast China. Environ. Geol. 51 (6), 1043—1048. https://doi.org/10.1007/s00254-006-0373-3

Defew H, L, Mair M, J, Guzman M, H, 2005. An assessment of metal contamination in mangrove sediments and leaves from Punta Mala Bay, Pacific Panama. Marine Poll. Bull. 50 (5), 547—552. https://doi.org/10.1016/j.marpolbul.2004.11.047

Enders, A., Lehmann, J., 2012. Comparison of wet-digestion and dry-ashing methods for total elemental analysis of biochar. Commun. Soil. Sci. Plan. 43 (7), 1042—1052.

Fernández-Cadena, J.C., Andrade, S., Silva-Coello, C.L., De la Iglesia, R., 2014. Heavy metal concentration in mangrove surface sediments from the north-west coast of South America. Mar. Pollut. Bull. 82 (1), 221—226. https://doi.org/10.1016/j.marpolbul.2014.03.016

Hakanson, L., 1980. Ecological risk index for aquatic pollution control. A sedimentological approach. Water Res. 14 (8), 975—1001. https://doi.org/10.1016/0043-1354(80)90143-8

Järup, L., 2003. Hazards of heavy metal contamination. Br. Med. Bull. 68 (1), 167—182. https://doi.org/10.1093/bmb/ldg032

Li, R., Chai, M., Qiu, G.Y., 2016. Distribution, fraction, and ecological assessment of heavy metals in sediment-plant system in

Man-grove Forest, South China Sea. PLOS ONE 11 (1), e0147308. https://doi.org/10.1371/journal.pone.0147308

Luo, W., Lu, Y., Wang, T., Hu, W., Jiao, W., Naile, J.E., Khim, J.S., Giesy, J.P., 2010. Ecological risk assessment of arsenic and metals in sediments of coastal areas of northern Bohai and Yellow Seas. China. AMBIO 39 (5—6), 367—375. https://doi.org/10.1007/s13280-010-0077-5

MacDonald, D.D., Ingersoll, C.G., Berger, T.A., 2000. Development and evaluation of consensus-based sediment quality guidelines for freshwater ecosystems. Arch. Environ. Contam. Toxicol. 39 (1), 20—31. https://doi.org/10.1002/etc.5620190524

MacFarlane, G.R., Burchett, M.D., 2002. Toxicity, growth and accumulation relationships of copper, lead and zinc in the grey mangrove *Avicennia marina* (Forsk.) Vierh. Mar. Environ. Res. 54 (1), 65—84. https://doi.org/10.1016/S0141-1136(02)00095-8

Marchand, C., Lallier-Verges, E., Baltzer, F., Albéric, P., Cossa, D., Baillif, P., 2006. Heavy metals distribution in mangrove sediments along the mobile coastline of French Guiana. Mar. Chem. 98 (1), 1—17. https://doi.org/10.1016/j.marchem.2005.06.001

Müller, G., 1969. Index of geoaccumulation in sediments of the Rhine River. Geo J. 2 (3), 108—118.

Nath, B., Birch, G., Chaudhuri, P., 2014. Assessment of sediment quality in *Avicennia marina*-dominated embayments of Sydney Estuary: the potential use of pneumatophores (aerial roots) as a bio-indicator of trace metal contamination. Sci. Total Environ. 472, 1010—1022. https://doi.org/10.1016/j.scitotenv.2013.11.096

Peters, E.C., Gassman, N.J., Firman, J.C., Richmond, R.H., Power, E.A., 1997. Ecotoxicology of tropical marine ecosystems. Environ. Toxicol. Chem. 16 (1), 12—40. https://doi.org/10.1002/etc.5620160103

Shi, P., Xiao, J., Wang, Y., Chen, L., 2014. Assessment of ecological and human health risks of heavy metal contamination in agriculture soils disturbed by pipeline construction. Int. J. Environ. Res. Public. Health. 11, 2504—2520.

Srinivasa, G.S., Ramakrishna, R.M., Govil, P.K., 2010. Assessment of heavy metal contamination in soils at Jajmau (Kanpur) and Unnao industrial areas of the Ganga plain, Uttar Pradesh, India. J. Hazard. Mater. 174, 113—121.

Tam, N.F.Y., Wong, Y.S., 2000. Spatial variation of heavy metals in surface sediments of Hong Kong mangrove swamps. Environ. Pollut. 110 (2), 195—205. https://doi.org/10.1016/S0269-7491(99)00310-3

Taylor, S.R., McLennan, S.M., 1985. The Continental Crust: Its Composition and Evolution. Blackwell Scientific Publ., Carlton, 312 pp.

Thomas, G., Fernandez, T.V., 1997. Incidence of heavy metals in the mangrove flora and sediments in Kerala, India. In: Wong, Y.S., Tam, N.F.Y. (Eds.), Asia-Pacific Conference on Science and Management of Coastal Environment, Developments in Hydrobiology, vol. 123. Springer, Dordrecht, 77—87. https://doi.org/10.1007/978-94-011-5234-1_9

Usman, A.R., Alkredaa, R.S., Al-Wabel, M.I., 2013. Heavy metal contamination in sediments and mangroves from the coast of Red Sea: *Avicennia marina* as potential metal bioaccumulator. Ecotoxicol. Environ. Saf. 97, 263—270. https://doi.org/10.1016/j.ecoenv.2013.08.009

Wright, D.A., Welbourn, P., 2002. Environmental Toxicology. Vol. 11. Cambridge Univ. Press, 656 pp.

Yan, Z., Sun, X., Xu, Y., Zhang, Q., Li, X., 2017. Accumulation and tolerance of mangroves to heavy metals: a review. Curr. Pollut. Rep. 3 (4), 302—317. https://doi.org/10.1007/s40726-017-0066-4

Yoon, J., Cao, X.D., Zhou, Q.X., Ma, L.Q., 2006. Accumulation of Pb, Cu, and Zn in native plants growing on a contaminated Florida site. Sci. Total Environ. 368 (2—3), 456—464. https://doi.org/10.1016/j.scitotenv.2006.01.016

Oceanologia 64 (2022) 287—298

Available online at www.sciencedirect.com

ScienceDirect

journal homepage: www.journals.elsevier.com/oceanologia

ORIGINAL RESEARCH ARTICLE

Distribution and ecological risk evaluation of bioavailable phosphorus in sediments of El Temsah Lake, Suez Canal

Alaa M. Younis[a], **Naglaa F. Soliman**[b,c,*], **Eman M. Elkady**[d], **Lamiaa I. Mohamedein**[d]

[a] *Department of Aquatic Environment, Faculty of Fish Resources, Suez University, Suez, Egypt*
[b] *Department of Environmental Studies, Institute of Graduate Studies & Research — Alexandria University, Egypt*
[c] *Basic and Applied Science Institute, Egypt-Japan University of Science and Technology (E-JUST), Alexandria, Egypt*
[d] *National Institute of Oceanography & Fisheries (NIOF), Suez, Egypt*

Received 23 March 2021; accepted 3 December 2021
Available online 17 December 2021

KEYWORDS
Sediments;
Bioavailable phosphorus;
Chemical extraction methods;
Phosphorus ecological risk;
El Temsah Lake;
Egypt

Abstract Phosphorus reactivity and bioavailability in lake sediments is determined by diverse fractions of phosphorus (P) and their distribution. To gain deeper insights into P dynamics in Lakes, sediments from El Temsah Lake were investigated for water soluble P (WSP), readily desorbable P (RDP), algal available P (AAP) and Olsen-P using different chemical extraction methods. Total P (TP), organic P (OP), inorganic P (IP) contents, were also investigated. The TP, OP and IP concentrations in the sediments were 598.39 μg/g, 199.76 μg/g and 398.63 μg/g, correspondingly. Concentrations of the bioavailable P in the sediments followed the order AAP (48.42 μg/g)>WSP (14.60 μg/g)>RDP (1.82 μg/g)>Olsen-P (1.50 μg/g). Pearson correlation analysis exposed that there were significant correlations among the bioavailable P fractions concentrations and the TP concentrations ($r=0.83$; $p>0.01$, $r=0.94$; $p>0.01$, $r=0.62$; $p>0.05$); for WSP, AAP, and Olsen-P respectively. Moreover, there were no obvious associations amongst total P and N, Al, Ca, Fe, Mg, Mn, and OM in the sediments. The outcomes of phosphorus ecological risk assessment in sediments by single pollution standard index method revealed that the standard index of TP varied from 0.19 to 1.85. It demonstrated that the ecological pollution risks of phosphorus in El Temsah Lake sediments was comparatively low.

* Corresponding author at: Basic and Applied Science Institute, Egypt-Japan University of Science and Technology (E-JUST) campus, P.O. Box 179, New Borg El-Arab City, Postal Code 21934, Alexandria, Egypt. Telephone: +201004830165; fax: +2034251038.
E-mail address: naglaa_farag2007@yahoo.com (N.F. Soliman).

Peer review under the responsibility of the Institute of Oceanology of the Polish Academy of Sciences.

Production and hosting by Elsevier

https://doi.org/10.1016/j.oceano.2021.12.001

1. Introduction

Phosphorus (P) has a crucial role in defining the function and productivity of the ecosystems. Sediments and soils embrace considerable amounts of inorganic, organic and microbial P. Therefore, phosphorus dynamics are managed by chemical and biological properties and processes (Reddy et al., 2005). Phosphorus is existing in the sediment matrix in the formulas of aluminum, calcium, iron complex salts and organic species, or adsorbed on the surface minerals (Pettersson et al., 1988). The quantity of mobile or bioavailable P in the sediments is a significant sign for supposing impending internal loading and the discharge to the water column (Rydin, 2000). In this context, it is requisite to identify not only the total P level in the sediments but also the levels of diverse P forms (Aydin et al., 2009).

A valuable way to appraise the stock of possibly available fractions is to fractionate P depending on the extractability by leaching chemicals of accumulative aggressiveness (Perkins and Underwood, 2001; Tiyapongpattana et al., 2004). Chemical sequential extractions have been projected to designate the several fractions in which phosphorus presents in the sediment (Psenner and Pucsko, 1988; Ruban et al., 1999; Ruttenberg, 1992). The chemical sequential extraction methods for P fractions in sediment are complicated and inefficient. The bioavailable P levels in lake sediments may be simply considered by quantifying the levels of readily desorbable P (RDP), water soluble P (WSP), algal available P (AAP), or $NaHCO_3$ extractable P (Olsen-P) (Zhou et al., 2001) than by P fractions as labile P, reductant P, metal bound P, occluded P and organic P (Soliman et al., 2017; Wang et al., 2010). These fractions of P in lake sediments were extensively considered by several investigators (Bo et al., 2014; Dapeng et al., 2011; Okbah, 2006; Soliman et al., 2017; Wang et al., 2010; Zhou et al., 2001; Zhu et al., 2013) and can be, easily analyzed by diverse chemical extraction methods (Zhou et al. 2001).

To the best of our knowledge, this corresponds to the first study to relate phosphorus fractionation to scrutinize its probable bioavailability in El Temsah Lake sediments. So, the leading objectives of the present study is to (1) appraise the spatial variability in total and bioavailable phosphorus levels in El Temsah Lake sediment, (2) evaluate the ecological risk of P, (3) recognize the relationship between P and various sedimentary parameters. Phosphorus fractions were also appraised in relative to the levels of the most important P binding elements Al, Ca, Fe, Mg, and Mn, along with other sediment physicochemical characteristics.

2. Material and methods

2.1. Sampling and study area

El Temsah Lake is the backbone of the tourism and fishing industries in the Suez Canal area (Kiser et al., 2009). However, the Lake suffers from accumulative pollution levels which are affected by untreated domestic and industrial wastewater (Donia, 2011) in addition to agricultural wastes consequences from land-based activities of Ismailia City, and fresh water from some drains: El-Mahsama, El-Bahtini and El-Forsan (Abdel Sabour et al., 1998) (Figure 1). The deterioration of the lake has prolonged to a severe level where urgent action is mandatory to restore the lake ecosystem (Donia, 2011).

Twelve surface sediment samples were collected in summer 2017 using Peterson grab sampler. Sampling sites were selected to cover different sorts of pollution to the Lake; domestic, agricultural, and industrial (Figure 1).

2.2. Geochemical characteristics of the sediments and elemental composition

Organic matter was assessed by the wet oxidation method following the method of (Loring and Rantala, 1992). Total carbonate was determined as designated by Black (1965). Grain size analysis was analyzed using the standard sieving technique (Folk, 1974). Total levels of Al, Ca, Fe, Mg and Mn in the sediment were measured after wet digestion (Oregioni and Aston, 1984) using an atomic absorption spectrometer (AAS, Model AA-6800 Shimadzu) operating in the flame mode. The total nitrogen (TN) was analyzed by Kjeldahl procedure (Bremner, 1960). Total phosphorus (TP) was analyzed by treating at 550°C (2.5 h), succeeded by 1 M HCl extraction for 16 h. Inorganic phosphorus (IP) was directly extracted with 1 M HCl for 16 h. Organic phosphorus (OP) was measured as the difference between TP and IP (Aspila et al., 1976).

2.3. Bioavailable phosphorus

Extractable P that is correlated to P bioavailability in the sediments incorporates algal available P (AAP), readily desorbable P (RDP), sodium bicarbonate ($NaHCO_3$) extractable P (Olsen-P), and water soluble P (WSP). These fractions of phosphorus were measured in line with Zhou et al. (2001) (Table 1).

2.4. Ecological risk assessment

The extensively used evaluation method for ecological risk of phosphorus is the single pollution index that was established based on the guidelines for environmental quality assessment expressed by the Department of Environment and Energy of Ontario, Canada (1992). This index was calculated using the subsequent formula:

$$S_{TP} = \frac{C_{TP}}{C_s}$$

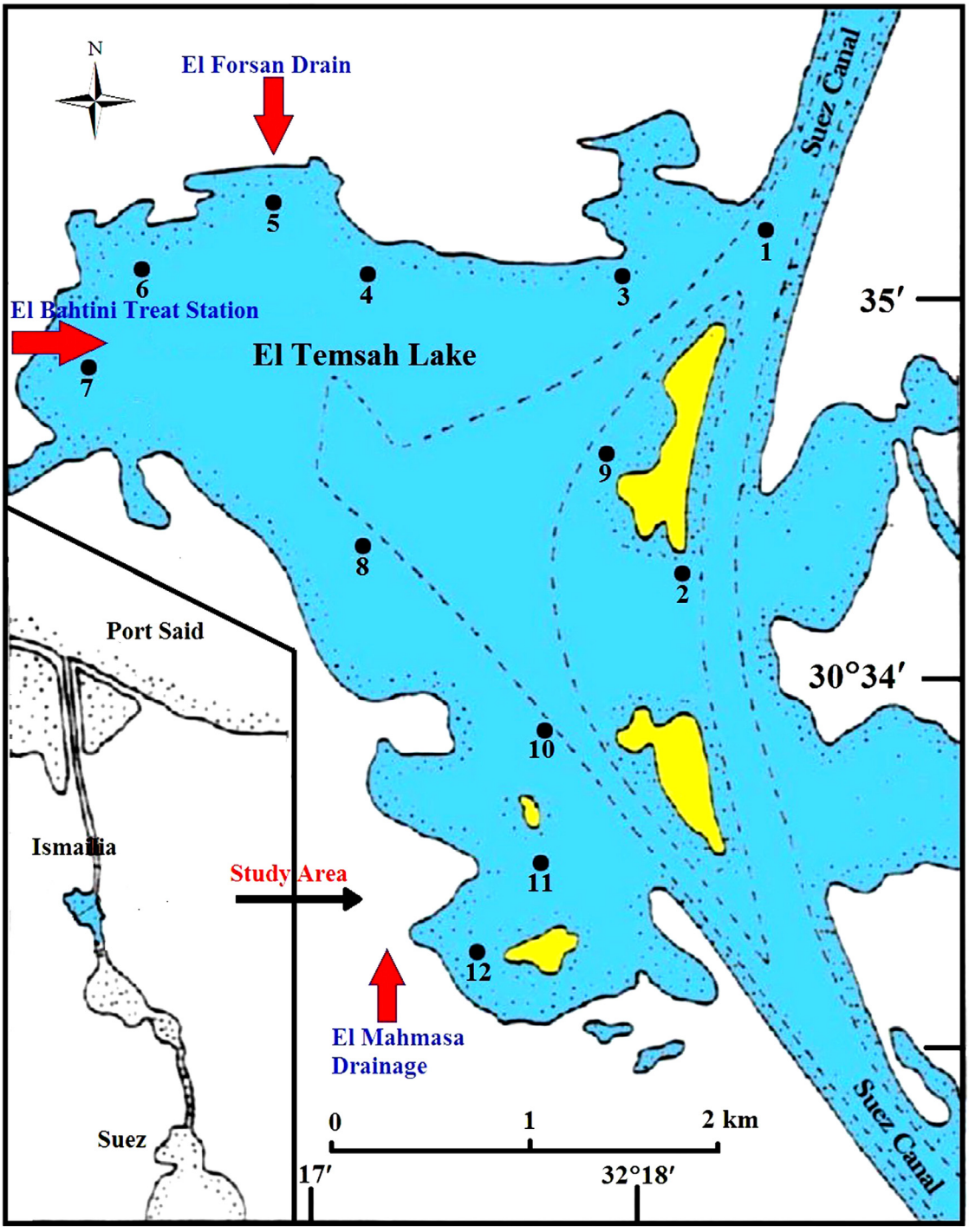

Figure 1 Study area of El Temsah Lake.

where S_{TP} is the single pollution index, C_{TP} is the determined concentration of *TP* and C_s is the standard concentration of *P*.

Relative to the regulations of the safe concentration limits for nutrients in the Sediment Quality Guidelines (SQGs) (Alvarez-Guerra et al., 2010), the standard concentrations of TP should be 600 μg/g. Consistent with the value of S_{TP} index, the risks are categorized into four grades, as indicated in Table 2.

2.5. Data analysis

Graphically depicting groups of numerical data through their quartiles were prepared using Minitab version 17. The correlation analyses and means appraisal analyses were accomplished by Pearson Correlation in SPSS 13.0 (Statistical Program for Social Sciences). Significance levels were labelled as non-significant (no signs, $p \geq 0.05$), significant (*, $0.05 > p \geq 0.01$) or highly significant (**, $p < 0.01$).

Table 1 Chemical extraction methods protocol (Zhou et al., 2001).

Bioavailable P form	Method
Algal available phosphorus (AAP)	0.2 g of sediment sample was shaken with 0.1 M NaOH (pH 13.1) for 4 h.
$NaHCO_3$ extractable phosphorus (Olsen-P)	2.5 g of sediment sample was shaken in 50 ml of 0.52 M $BaHCO_3$ (pH 8.5) for 0.5 h.
Readily desorbable phosphorus (RDP)	2 g of sediment sample was shaken in 50 ml of 0.01 M $CaCl_2$ for 1 h.
Water soluble phosphorus (WSP)	1 g of sediment sample was shaken with 100 ml of deionized water for 2 h at 25 °C.

Note: The P extracts in the four steps were filtered through0.45 mm pore size membrane filters.

Table 2 Evaluation criteria and values for ecological risk of phosphorus in sediments of El Temsah Lake.

Risk level	Value	Pollution assessment	Results for El Temsah Lake
Level I	$S_{TP} < 0.5$	Clean	Sites: 1, 2, 3, 9, 10
Level II	$0.5 \leq S_{TP} < 1$	Slightly polluted	Sites: 8, 11, 12
Level III	$1 \leq S_{TP} < 1.5$	Moderately polluted	Sites: 4, 5
Level IV	$1.5 \leq S_{TP}$	Seriously polluted	Sites: 6, 7

3. Results and discussion

3.1. Physicochemical characteristics of the sediments

Physical and chemical characters of sediments are essential for appraising the P exchange procedures between sediments and overlying waters (Gonsiorezyk et al., 1998). Outcomes of physicochemical characteristics of the sediments are demonstrated in Figure 2 in box and whisker plots.

Carbonate concentrations are considerably low, designating the influx of terrigenous materials (Soliman et al., 2018). Organic matter is needed in the fractionation of P under definite hydrolyzing circumstances. It may formulate complexes with elements, such as Al, Ca, Fe, Mg, and Mn, which possibly govern P fate in the aquatic ecosystems (Fu et al., 2000; Pardo et al., 2003). In this study, OM display concentrations ranging from 0.19 to 10.25%. The dispersal of grain size reveals the domination of the sand fraction (3.26—90.01%) followed by the clay fraction (3.03—89.88%).

Descriptive statistics of elemental composition in sediments of El Temsah Lake are presented in Table 3 and their distribution is illustrated in Figure 2. Calcium levels range from 5.62 to 22.63%, Mg from 1.9 to 10.85%, Al from 2280 to 3860 μg/g dw, while Fe from 4100 to 5778 μg/g dw, and Mn from 123.56 to 642.37 35 μg/g dw. The coefficients of variation (CV) for Mn in sediments are as high as 46.93%, followed by Mg (CV: 43.88%) and Ca (CV: 38.26%) (Table 3). This entitles the relatively great alterations in total Mn, Mg, and Ca levels in the sediments, which may be owing to manmade intrusions of metals (Huang et al., 2019), and the prevalent physicochemical conditions and complex reactions such as adsorption, flocculation and redox condition happening in the sediments (Sekhar et al., 2003). While the lowest metal

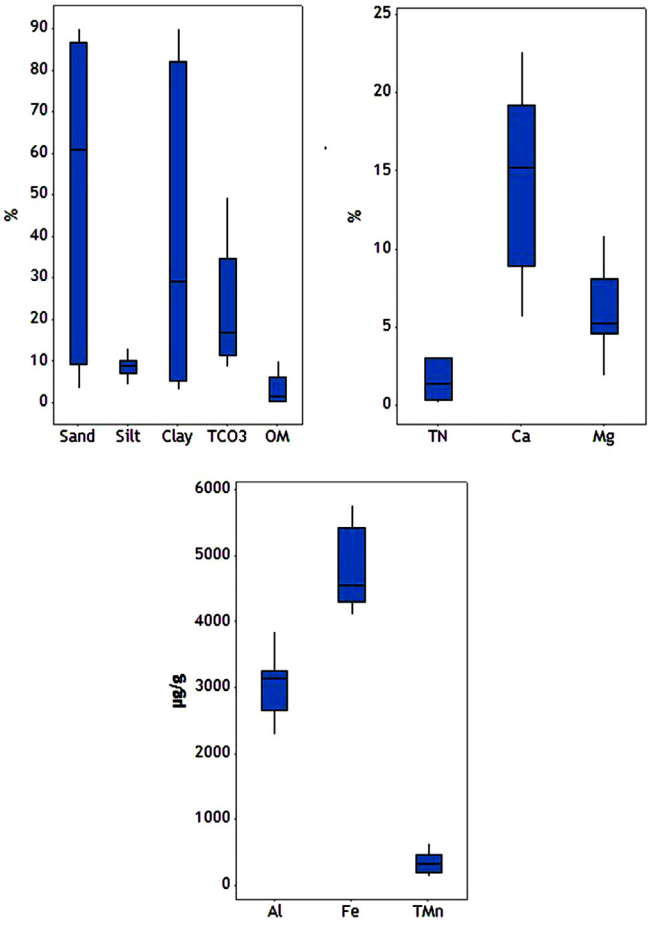

Figure 2 Box and whisker plots of $CaCO_3$, OM, Sand, Silt, Clay (%), and N, Ca, Mg (%), and Al, Fe, Mn (μg/g).

Table 3 Descriptive statistics of elemental composition in sediments of El Temsah Lake.

	Al (μg/g)	TP (μg/g)	Fe (μg/g)	Mn (μg/g)	Ca (%)	Mg (%)	IP (μg/g)	OP (μg/g)	TN (μg/g)	OC (%)
Min	2280	131.84	4100	123.56	5.64	1.9	73.44	32.91	1200	0.17
Max	3860	2028.76	5778	642.37	22.63	10.85	1365.74	663.02	31300	5.31
Average	3024	598.39	4783.7	335.43	14.52	5.98	398.63	199.76	15450	2.11
SD	462	563.78	588.6	157.41	5.55	2.625	384.5	183.04	12823	2.09
CV (%)	15.3	106.13	12.30	46.93	38.26	43.88	96.45	91.63	82.99	99.22

CV — coefficient of variance.
TP — total phosphorus.
IP — inorganic phosphorus.
OP — organic phosphorus.
TN — total nitrogen.
OC — organic carbon.

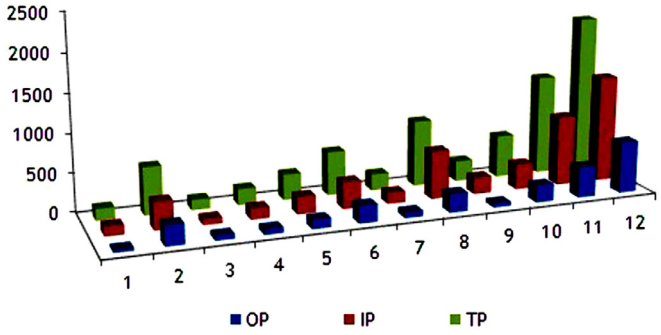

Figure 3 Distribution of organic, inorganic and total phosphorus (μg/g) in El Temsah Lake sediments.

deviations are perceived for Fe (CV: 12.30%) and Al (CV: 15.30%), proving an identical distribution of these elements in the considered sites (Bastami et al., 2016).

Total nitrogen (TN) fluctuates from 1200 to 31300 μg/g dw (CV: 82.99%). This proposes that the TN levels of the sediments varied significantly. Sites 4, 5, 6, 7, 11, and 12 display intensely greater levels than the other sites. All results exceed 1000 μg/g which is the Chinese environmental protection and EPA standard (US EPA, 2002; Wang et al., 2010). The standard is a level where the sediments must be dredged to protect the environment (US EPA, 2002; Wang et al., 2010).

The total phosphorus (TP) contents at different sites of the sediments are demonstrated in Figure 3. Total P contents are in general high, alternating from 131.84 to 2028.76 μg/g dw (CV: 106.13%), attaining the maximum concentrations in the sediments from sites (2, 6, 8, 10, 11, and 12). This entitles that the lake sediments may have a high prospective to provide P to the overlying water (Gao et al., 2005). There is no obvious homogeneousness recognized in the spatial distribution of TP levels in the sediments. The areas of the maximum TP accumulation in the sediments for the most part covered the areas of maximum TN levels in the sediments. This may be explained by the effluents of agriculture, domestic wastes, and shipping activities resulting from the governorate of Ismailia (Said and El Agroudy, 2006).

3.2. Phosphorus fractions and bioavailability

3.2.1. Inorganic, and organic fractions of phosphorus

Outcomes for the levels of inorganic phosphorus (IP) and organic phosphorus (OP) in El Temsah Lake sediments are depicted in Figure 3. It can be seen in Figure 3 that inorganic phosphorus is the most important form (around 66% of the TP). Inorganic phosphorus level range from 73.44 μg/g dw to 1365.74 μg/g dw. IP has been shown to be an essential source of bioavailable P in eutrophic sediments. NaOH-P, which mostly comprises P bound to Al and Fe oxides and hydroxides (Ruban et al., 2001), may be leached from sediment and bring about the growing of phytoplankton under the anoxic circumstances that succeed at the sediment—water interface (Bo et al., 2014). The level range of the organic phosphorus is 23.91—663.02 μg/g dw (about 33.56% of the TP). The concentrations of OP in sediments are in generally low. OP is leached only when organic matter in the lake is mineralized (Pedro et al., 2013). This is a significant character distinguishing sediments from soils, in which organic forms prevail (Gunduz et al., 2011). In general, OP may release bioavailable fractions of P which may possibly be utilized directly or indirectly by algae (Liu et al., 2012). The content of bioavailable P reveals the amount of contamination and the endogenous release capacity. Bioavailable P may be converted into active P by chemical and biological reactions and consecutively affect the water quality (Bridgeman et al., 2012). Numerous investigations have exposed that elevated quantities of bioavailable P in the sediments lead to superior release of P (Liu et al., 2012). According to Rydin (2000), around 50—60% of OP in sediments may be degraded or hydrolyzed to bioavailable P.

3.2.2. Bioavailable phosphorus

The levels of diverse bioavailable P fractions considered in this work are presented in Figure 4. The comparative involvement of each form to the TP is depicted in Figure 5. The rank order owing to the average levels of P fractions in El Temsah Lake is AAP>WSP>RDP>Olsen-P. A detached discussion of each bioavailable P form is given below.

3.2.2.1. Water soluble phosphorus (WSP). WSP is deliberated as the best evaluation of directly available P the sediments (Zhou et al., 2001). Levels of WSP are considerably

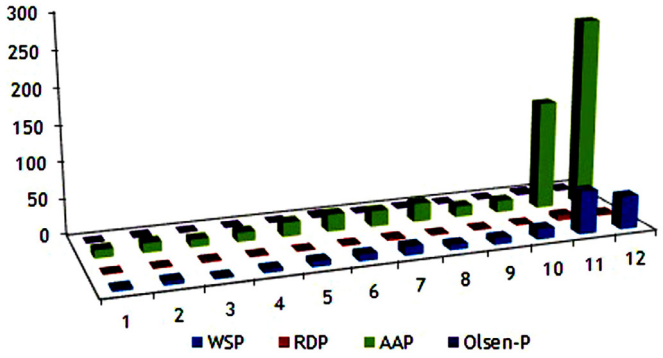

Figure 4 Distribution of bioavailable phosphorus fractions (μg/g) in El Temsah Lake sediments.

Table 4 Literature data concerning bioavailable phosphorus worldwide.

Location	Bioavailable Phosphorus fractions (μg/g)				Reference
	WSP	RDP	AAP	Olsen-P	
El Temsah Lake	14.60	1.84	48.42	1.50	This study
Lake Mariut, Egypt	40.81	9.08	107.12	89.27	Soliman et al. (2017)
Lake Edku, Egypt	9.77	1.70	59.70	42.40	Okbah (2006)
Taihu Lake, China	1.8	0.3	340	38.7	Bo et al. (2014)
West Lake, China	77.1	44.8	354.1	238.9	Zhou et al. (2001)
Lough Erne, Ireland	188.4	67.2	1293.9	512.2	Zhou et al. (2001)

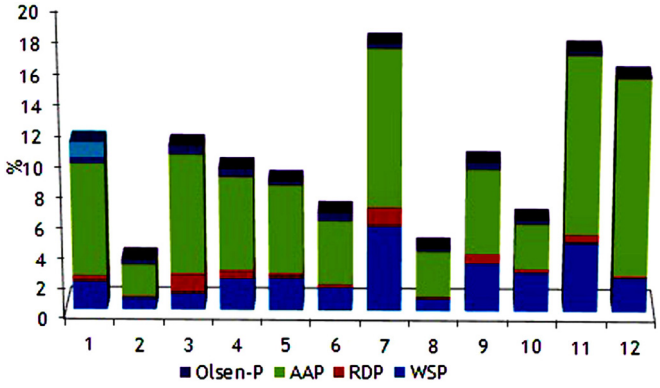

Figure 5 Percentage of bioavailable P fractions in El Temsah Lake sediments.

interrelated with P bound to clays (Hu et al., 2007). In El Temsah Lake the levels of WSP in the considered sediments range from 1.49 μg/g dw to 58.99 μg/g dw, and average 14.60 μg/g dw. The highest WSP concentration is demonstrated in sediment from site 11. This faction of phosphorus accounts for 2.39% of sedimentary TP in El Temsah Lake. These values are to some extent low in consideration to the values (40.81, 77.1 and 188.4 μg/g dw) described for Lake Mariut in Egypt, West Lake, China, and Lough Erne, Ireland, correspondingly, and higher than Lake Taihu, China (1.8 μg/g dw) and Lake Edku, Egypt (9.77 μg/g dw) (Table 4).

3.2.2.2. Readily desorbable phosphorus (RDP). Readily desorbable phosphorus signifies the simply desorbed and released P reflected as algal available P (Zhou et al., 2001). The RDP levels in El Temsah Lake display high variations ranging from 0.55 μg/g dw in site 1 to 6.85 μg/g dw in site 11 (Figure 4). The RDP concentration is nearly 12 times greater in sediment from site 11 than in sediment from site 1. By discharge of industrial wastes this site is contaminated with: 1) Liquid wastes such as oil and grease, paints, in addition to wastes from ships and discarding of domestic wastewater. 2) Solid wastes as metals, sand including metals debris and fouling (Abdel Sabour et al., 1998; Soliman et al., 2019). The proportional contribution of RDP to the available phosphorus ranges from 0.1% to 1.27%, and the average is lower than 1% (0.47%) (Figure 5). This designates that most of the phosphorus is bound in such a fraction that isn't exchangeable, and therefore, not available for direct uptake by plants (Branom and Sarkar, 2004). These levels are fairly small in accordance with the levels described for Mariut Lake, West Lake, China and Lough Erne, Ireland, and higher than Lake Taihu, China and Lake Edku, Egypt (Table 4).

3.2.2.3. Algal available phosphorus (AAP). This faction of sedimentary phosphorus denotes phosphorus combined with metal (hydr) oxides, mostly of Al, and Fe, which is exchangeable again with OH^-, anion of organic ligands and inorganic phosphorus complexes dissolved in alkali (Rydin, 2000). NaOH extractable P may be released for the growing of phytoplankton once anoxic circumstances dominate at the sediment-water interface (Ting, 1996). The AAP levels in the studied sediment samples range from 10.37 μg/g dw in sediment from site 3 to 262.47 μg/g dw in sediments from site 12 (Figure 4). The comparative contribution of AAP to the available phosphorus is between 2.13% (in site 2) to 12.94% (in site 12) (Figure 5). The outcomes acquired in this work were lesser than the outcomes described for other lakes (Table 4). This may be related to the sediment tex-

ture (high clay and silt amounts in the lake. Furthermore, these results were comparable to the outcomes in earlier researches that the comparative involvement of NaOH—P to TP ranged from 5 to 70% with elevated values in eutrophic lakes, and NaOH—P was an essential origin for bioavailable P in eutrophic sediments (Penn et al. 1995; Wang et al., 2010).

3.2.2.4. $NaHCO_3$ extractable phosphorus (Olsen-P). Olsen-P is an appropriate measure for demonstrating the situation of nutrients in soils. In agreement with Zhou et al. (2001), Olsen-P levels in soils that are >46 μg/g dw specify a high nutrient rank. Consequently, Olsen-P may be moreover deliberated as a measurable indicator of the availability of P for algae. Commonly, Olsen-P is represented as the active HCl—P since a possibly mobile percentage is shown to be involved in the HCl—P fraction (Kisand and Noges, 2003). The levels of this fraction of P in El Temsah Lake sediment range from 0.53 μg/g dw in site 1 to 3.3 μg/g dw in site 11, and accounts for from 0.1% in site 12 to 0.58% in site 3 of total phosphorus (Figures 4 and 5). The attained data reveals that agreeing to the standards of agricultural soils, all the locations of the study area have low Olsen-P.

Table 4 displays that the results attained in this work are lesser than the results of 89.72, 42.40, 238.9, 512.2, 38.7 μg/g dw designated for Lake Mariut, Lake Edku, West Lake, and Lough Erne, Lake Taihu, respectively.

3.2.2.5. Ecological risk of phosphorus in the sediments. The considered samples may be distributed into two categories based on the Chinese environmental dredging common standard (Liu et al. 1999). Samples that their TP levels were higher than 500 μg/g dw (sites 2, 6, 8, 10, 11, and 12) are deliberated as heavily polluted with certain ecological risk effects and would be dredged. The others (sites 1, 3, 4, 5, 7, and 9) are slightly polluted (mesotrophic or oligotrophic), in which TP levels were lesser than 500 μg/g dw.

Based on the Canadian Sediment Quality Guidelines (SQGs) (Mudroch and Azcue, 1995), the TP levels at 42% of the investigated sites surpassed the lower SQGs value (550 μg/g), and the TP concentrations at site 12 reached the upper SQGs value (2,000 μg/g) (Figure 4), demonstrating that there will be elevated levels of toxicity to sediment-dwelling organisms from phosphorus at site 12. Phosphorus gets into El Temsah Lake from greater amounts of wastes, comprising raw liquid and solid municipal wastewater, industrial wastewater and agricultural runoff that dumped into the lake (Abdel Sabour et al., 1998).

The single pollution index of phosphorus in El Temsah Lake sediment samples varies from 0.19 to 1.85, and the risk grade ranges from Grade I to III. Noticeably, 41% of the samples in El Temsah Lake are clean (grade I). On the other hand, other sites of the sediment samples are slightly (25%) or moderately (17%), or seriously (17%) polluted. Consequently, the average risk of total phosphorus contamination in El Temsah Lake is relatively low.

3.2.2.6. Relationships between bioavailable phosphorus fractions and geochemical components of the sediments. Phosphorus dynamics is associated with its collaboration with the diverse sediment matrix components, so the understanding of the diverse forms in which phosphorus exists in the sediments is required (Pardo et al., 2003). The correlation of Fe, Mn, and P in lake sediments is not obviously assumed, though there is an overall agreement from the deliberation of solubility product interactions that chemical interaction of phosphate would happen with Al, Ca, and Fe complexes. Phosphate anions may be taken up from the water by alumina, kaolinites, and montmorillonites (Chen et al., 1973) and similarly by precipitated ferric and aluminum hydroxides (Carritt and Goodall, 1954; Hsu, 1965).

Fe:P proportion is deliberated as a degree of available sorption places for phosphate ions on iron oxyhydroxide surfaces. The proportion of Fe:P beyond 15 is adequate for iron to adjust the benthic fluctuation of phosphorus from sediment to oxic water (Jensen et al., 1992). Rydin and Brunberg (1998) also designated the development of an active oxic barrier with the overhead Fe:P proportion. In El Temsah Lake sediments, the Fe:P proportion is lower than 15 excluding site 1 and, leading to lower levels of Fe:P. This can prove that the perceived phosphorus is associated with the geochemistry of the lake sediment. Consequently, there is no sufficient iron in the sediments to combine with phosphorus at the majority of the sampling locations, representing that iron can't manage the phosphorus release and the influence of NaOH-P on the water column phosphorus is great (Soliman et al., 2017). Additionally, a substantial negative relationship (−0.76; $p>0.01$) is established between the Fe:P atom proportion in surface sediments and mean values of TP in the lake sediments. These results propose, but do not ascertain, that the internal phosphorus loadings in this lake are not associated with the Fe:P atom proportion.

In this study, a high significant positive correlation coefficient (r= 0.79; $p>0.01$) between Fe-Mn is exhibited (Table 5). The close chemical resemblance between Fe and Mn is revealed geologically in their corporate association in rocks of all types. Hydrous oxides of iron and manganese are approximately plentiful in clays, soils, and sediments (Bortleson and Lee, 1974). However, there is no obvious relationship between TP-Fe and TP-Mn in El Temsah Lake. Agreeing with Mackereth (1966) P deposition is not affected by differences in the iron and manganese cycle, but the precipitation of P can be basically biological and constant. Fe is appearing to be associated with clay minerals (r= 0.94; $p>0.01$) which will afford slight prospects for P precipitation with Fe complexes (Bortleson, 1971). Additionally, there is no relationship between Ca and any of the bioavailable phosphorus fractions. This is similar with the results of others (Jensen et al., 1992) and confirms that the extent of calcium existing in the sediment has no effect on the dispersal of the different P pools (De Groot, 1991).

Results exhibit that, no association may be recognized between the IP/OP and the organic matter level in the sediment samples (Table 5). Consequently, the dispersal of phosphorus between the inorganic and organic fractions seemed not to be associated with the organic matter concentration in apparent way. This is possibly owing to the composite properties of organic matter and to the intricate relations amongst the diverse sediment characteristics (Pardo et al., 2003).

A significant relationship exists between organic matter (OM) and total nitrogen (TN) in the sediments of El Temsah Lake ($r = 0.92$, $P < 0.01$) which proposes that the content of TN can be regulated by organic source (Hakanson and Jansson, 1983) while total phosphorus associates nega-

Table 5 Correlation matrix for the different studied components in sediments of El Temsah Lake.

	Al	Ca	Fe	Mg	Mn	TN	TP	IP	OP	$CaCO_3$	OM	WSP	RDP	AAP	Olsen-P	Sand	Silt	Clay
Al	1																	
Ca	0.74**	1																
Fe	-0.76**	-0.95**	1															
Mg	-0.09	-0.51	0.59*	1														
Mn	-0.07**	-0.89**	0.79**	0.23	1													
TN	-0.73**	-0.83**	0.81**	0.53	0.59*	1												
TP	-0.48	-0.29	0.18	-0.59*	0.51	0.1	1											
IP	-0.47	-0.28	0.16	-0.61*	0.50	0.1	0.99**	1										
OP	-0.51	-0.31	0.21	-0.54	0.51	0.11	0.99**	0.97**	1									
$CaCO_3$	-0.54	-0.68**	0.62*	0.39	0.54	0.89**	0.14	0.14	0.152	1								
OM	-0.51	-0.61*	0.58*	0.51	0.35	0.92**	-0.11	-0.11	-0.09	0.94**	1							
WSP	-0.63*	-0.33	0.21	-0.61*	0.41	0.2	0.83**	0.84**	0.79**	0.11	-0.03	1						
RDP	-0.61*	-0.25	0.15	-0.49	0.24	0.18	0.50	0.53	0.44	0.002	0.001	0.87**	1					
AAP	-0.52	-0.38	0.25	-0.57*	0.59*	0.18	0.94**	0.94**	0.91**	0.27	0.003	0.88**	0.58*	1				
Olsen-P	-0.54	-0.26	0.17	0.34	0.16	0.20	0.62*	0.60*	0.64*	0.07	0.02	0.69**	0.63*	0.51	1			
Sand	0.73**	0.98**	-0.95**	-0.48	-0.88**	-0.82**	-0.33	-0.31	-0.35	-0.71**	-0.63*	-0.32	-0.19	-0.43	-0.24	1		
Silt	0.14	-0.21	0.13	0.34	-0.12	0.16	-0.43	-0.39	-0.49	0.09	0.2	-0.17	0.14	-0.28	-0.12	-0.12	1	
Clay	-0.75**	-0.98**	0.94**	0.46	0.89**	0.81**	0.36	0.34	0.38	0.71**	0.59*	0.33	0.19	0.46	0.25	-0.99**	0.06	1

Correlation is significant at * $P < 0.05$, ** $P < 0.01$; $n = 12$

Table 6 Total organic carbon/total nitrogen (TOC/TN), total organic carbon/total phosphorus (TOC/TP) and total nitrogen/total phosphorus (TN/TP) organic carbon/organic phosphorus (OC/OP), Iron/phosphorus, manganese/phosphorus ratios in El Temsah Lake sediments.

Station	TOC/TN	TOC/TP	TN/TP	OC/OP	Fe:P	Mn:P
1	1.50	14.75	9.84	54.70	15.20	0.72
2	1.00	15.32	15.32	6.60	4.09	0.16
3	1.46	17.65	12.11	87.33	19.31	1.74
4	1.74	74.37	42.86	774.57	12.12	0.59
5	1.47	53.09	36.12	377.74	9.67	0.79
6	1.30	36.60	28.15	182.90	5.40	0.43
7	1.63	49.56	30.34	715.30	14.82	1.33
8	0.68	14.32	20.99	24.20	2.82	0.22
9	0.78	10.14	13.04	39.47	8.82	0.26
10	0.33	10.67	32.02	8.64	4.35	0.22
11	0.99	50.68	51.22	47.39	2.08	0.15
12	1.36	47.28	34.69	41.93	1.42	0.18
Min	0.33	10.14	9.84	6.60	1.42	0.15
Max	1.74	74.37	51.22	774.57	19.31	1.74
Average	1.19	32.87	27.22	196.73	8.34	0.57
SD	0.43	21.68	13.15	276.37	5.92	0.51
CV	36.10	65.95	48.29	140.48	70.99	90.42

tively with OM (Table 5). This entails that sediment TP is influenced by parameters other than organic matter (Knosche, 2006). If N and P in the sediments are originated from the similar origin, they must have a good relationship. Though, it is designated that the relationship between TN and TP is insignificant in El Temsah Lake sediments, displaying dissimilar sources (Table 5).

Earlier investigations have revealed that the ratios of nutrient elements in sediments may reveal the geochemical reactions of elements, the environment and the origins of internal and external contaminations (Gu et al., 2017). Particularly, the TOC/TN ratio is extensively utilized to categorize the probable origins of organic matters and the differences among species. The TOC/TP ratio reveals the decomposition rate of OC and P fractions in sediments to a definite range (Peng, 2016). The TN/TP ratio reveals the dynamic progressions of the accumulation, deposition and release of N and P in water (Peng, 2016). If TOC/TN $>$ 10, the OM is principally from land sources; if TOC/TN $=$ 10, the internal and external OM is essentially in equilibrium; if TOC/TN $<$ 10, the OM is mostly from water bodies (Peng, 2016).

From Table 6, the TOC/TN in El Temsah Lake sediments differs from 0.3 to 1.7. Consequently, the TOC accumulation and TOC/TN in sediments in El Temsah Lake are positively interrelated to the organic components from the water body. The TOC/TP in sediments in El Temsah Lake alters from 10.1 to 74.4. The average value of the TOC/TP ratios is 32.9. Furthermore, the spatial dissimilarities of TOC/TP in the sediments have comparatively high coefficient of variance (CV) of 65.95% $>$ 50%. Great TOC contents in sites (4, 5, 6, 7, 11, and 12) have a substantial influence on the spatial differences of nutrient element ratios, compared with the other sites. These sites have greater amounts of TOC, which may be introduced into the sediments by untreated municipal and urban wastes (Abdel Sabour et al., 1998). Consequently, the accumulation of TOC dominates the TOC/TP ratio. Data of the ratio between OC and OP (OC/OP) may support the understanding of the provenance, decomposition and preservation of sedimentary organic matter (Sardans et al., 2012), in addition to the transformation of phosphorus in sediments. In general, approximately all of the sediment OM types in aquatic ecosystems are originated from biological photosynthetic activity in the aquatic and/or terrestrial environments. The OC/OP ratio of marine plankton is closer to the Redfield C/P ratio of 106:1 (Anderson and Sarmiento, 1994; Redfield et al., 1963), and differ from ~50:1 to 150:1 (Li and Peng, 2002), with an average of about 117:1 (Anderson and Sarmiento, 1994). In this work, the OC/OP ratios range from 6.6 to 774.6, with an average of 196.7± 276.37 (Table 6), which exceed the Redfield ratio, representing that El Temsah Lake sediments receive substantial quantity of OC from land-based origins.

Nitrogen and phosphorus are key parameters for the categorization of trophic status as they are nutrients most probable to limit aquatic primary producers in lakes and rivers. The total N to total P (TN:TP) ratio is usually utilized as a guide that signifies the nutrient limitation for algal growth. Elser et al. (2009) indicate that phosphorus is limiting when TN: TP by weight is $>$16, nitrogen is limiting when TN: TP is $<$14, and either nitrogen or phosphorus or both are limiting when TN:TP is between 14 and 16. Results display that the TN:TP in El Temsah Lake is fluctuated from 9.8 to 51.2 (average: 27.2), signifying that the limiting nutrient for the algal growth in El Temsah Lake is P.

The ratio of N: P in sediment is greater than the Redfield value, displaying that P in the considered lake sediment is primarily autogenic.

Table 5 exhibits that there is a significant relationship between WSP and TP in El Temsah Lake sediments (r=0.83; p>0.01). More or less P may be simply desorbed and released, predominantly when the level of P in the water column is decreased (Zhou et al., 2001). Additionally, outcomes of Pearson correlation analysis display a poor positive relationship concerning RDP and TP or IP (Table 5).

The Olsen-P fraction was the smallest of the extracted P fractions. In particular, RDP in sediments of El Temsah Lake only accounted for 0.34% of TP (Figure 5). The correlation between Olsen-P and TP was poorer than in any other analysis, but still highly significant ($P < 0.05$).

It is perceived that the AAP fraction displayed an enhanced sign of P bioavailability. The AAP fraction extracted greater quantities of P compared to WSP, RDP and Olsen-P, ranging between 2.13 and 12.94% (average: 6.67%) (Figure 5). The relationships between P extracted in the AAP fraction and TP or IP are somewhat much better than the other extracted fractions and are significant at a <0.01 level (Table 5), proposing that the elevation in TP and coinciding leaching of P from sediment improved the bioavailability and increase risk of P (Wang and Liang, 2015).

The comparatively larger quantity of extracted P and the significant relationship between extracted and sedimental TP designates that a substantial part of P in El Temsah Lake sediments is combined with Fe/Al oxides (Anjos et al., 2000), and a comparatively substantial fraction of Fe/Al-bound P is bioavailable. These fractions of P are easily dissolved under alkaline conditions and converted into dissolved P when the redox environment changes (Han et al., 2014). Dissolved P may then enter the overlying water, and finally deteriorates the water quality (Wang and Liang, 2015).

AAP discloses the impact of sediment texture, while a high clay percentage improves the level of AAP. This end result is sustained by Pearson correlation analysis where a positive correlation between AAP and clay ($r=0.46$) (Table 5) is designated.

4. Conclusion

This paper presents the results of P fractions (TP, OP, IP, and bioavailable P) in the surface sediment and from El Temsah Lake. Total phosphorus concentration is on average 598.39 μg/g. The IP level was higher than OP for the studied area and its average % contents were 66.50% of TP. Where the average level of the OP was 33.50% of TP. Relative abundances of the bioavailable P fractions in the sediment follow the rank: AAP>WSP>RDP>Olsen-P. The AAP method extracted the most P and the RDP and Olsen-P methods extracted the least P. Clearly, as the levels of WSP, RDP, and Olsen-P were low, accounting for lower than 4% of TP, these fractions were as insignificant as available P sources for algal growth. In contrast, AAP accounted for more than 7% of TP. WSP, AAP, and Olsen-P forms gave bioavailable P levels that were correlated to the IP, TP, and OP levels. Correlation coefficients showed that there were significant correlations among the bioavailable P fractions concentrations and the TP concentrations. Moreover, there were no apparent relationships between TP and N, Al, Ca, Fe, Mg, Mn, and OM in the sediments. This study exhibited that the TN:TP ratio in the water column fluctuated from 9.8 to 51.2, proposing that P was the limiting nutrient for the algal growth in El Temsah Lake. Moreover, Fe:P ratio was lower than 15 supposing that there wasn't adequate iron in the sediment to combine with phosphorus at most of the investigated samples. Consistent with the single pollution index method, the risk level of P contamination in the sediments was comparatively low. Results from this study establish a background of bioavailable phosphorus fractions in sediments from El Temsah Lake and can be utilized as a reference for forthcoming investigations on the fluctuations of phosphorus bioavailability over time.

Declaration of competing interest

This research did not receive any specific grant from funding agencies in the public, commercial, or not-for-profit sectors. The authors declare that they have no conflict of interest.

Authors' contributions

Naglaa F. Soliman and Alaa M. Younis developed the concept and designed the experiments. Lamiaa I. Mohamedein carried out the sediments collection. Naglaa F. Soliman and Eman M. Elkady carried out sediment pollution analysis and risk assessment. Naglaa F. Soliman and Alaa M. Younis participated in the sequence alignment and drafted the manuscript. Alaa M. Younis, Eman M. Elkady and Lamiaa I. Mohamedein participated in the final version of manuscript and statistical analysis. All authors listed have made a significant, fundamental and direct contribution to the work, and approved it for publication.

Data availability

The dataset used and/or analyzed during the current study are available from the corresponding author on reasonable request.

References

Abdel Sabour, M.F., Ali, R.O., Khalil, M.T., Attwa, A.H.A., 1998. Indicators of Lake Temsah potential pollution by some heavy. Metals ii) heavy metals in sediment. International conference on hazardous waste sources, effects and management.

Alvarez-Guerra, M., Viguri, J.R., Casado-Martínez, M.C., Del-Valls, T.A., 2010. Sediment quality assessment and dredged material management in Spain: Part I, application of sediment quality guidelines in the Bay of Santande. Integr. Environ. Assess. Manag. 3, 529—538. https://doi.org/10.1897/IEAM_2006-055.1

Anderson, L.A., Sarmiento, J.L., 1994. Redfield ratios of remineralization determined by nutrient data analysis. Global Biogeochem. Cy. 8, 65—80. https://doi.org/10.1029/93GB03318

Anjos, S.M., De Ros, L.F., De Souza, R.S., De Assis Silva, C.M., Sombra, C.L., et al., 2000. Depositional and diagenetic controls on the reservoir quality of Lower Cretaceous Pendencia sandstones, Potiguar rift basin, Brazil. AAPG Bulletin 84 (11), 1719—1742. https://doi.org/10.1306/8626C375-173B-11D7-8645000102C1865D

Aspila, K.I., Agemian, H., Chau, A.S.Y., 1976. Semi-automated method for the determination of inorganic, organic and total phosphate in sediments. Analyst 101, 187—197. https://doi.org/10.1039/an9760100187

Aydina, I., Aydin, F., Saydut, A., Hamamci, C., 2009. A sequential extraction to determine the distribution of phosphorus in the

seawater and marine surface sediment. J. Hazard. Mater. 168, 664—669. https://doi.org/10.1016/j.jhazmat.2009.02.095

Bastami, K.D., Neyestani, M.R., Zadeh, M.E., Haghparast, S., Alavi, C., Fathi, S., Nourbakhsh, S., Shirzadi, E.A., Parhizgar, R., 2016. Geochemical speciation, bioavailability and source identification of selected metals in surface sediments of the Southern Caspian Sea. Marine Pollut. Bull. 114 (2), 1014—1023. https://doi.org/10.1016/j.marpolbul.2016.11.025

Black, C.A., 1965. Methods of Soil Analysis, Part 2: Chemical and Microbiological Properties. American Society of Agronomy, Inc., Madison, WI.

Bo, L., Wang, D., Zhang, G., Wang, C., 2014. Evaluating the relationship between phosphorus bioavailability and speciation in sediments from rural rivers in the Tahiu Lake area, China. Pol. J. Environ. Stud. 23, 1933—1940. https://doi.org/10.15244/pjoes/24924

Bortleson, 1971. The chemical investigation of recent lake sediments from Wisconsin lakc and their interpretation. U.S. Environ. Prot. Agency, 1601OEIIRO 3/71 Water Pollut. Contr. Res. Ser. Washington, D.C.

Bortleson, G.C., Lee, F., 1974. Phosphorus, iron, and manganese distribution in sediment cores of six Wisconsin lakes. Limnol. Oceanogr. 19 (5), 794—801. https://doi.org/10.4319/lo.1974.19.5.0794

Branom, J.R., Sarkar, D., 2004. Phosphorus bioavailability in sediments of a sludge disposal lake. Environ. Geosc. 11, 42—52. https://doi.org/10.1306/eg.08220303021

Bremner, J.M., 1960. Determination of nitrogen in soil by the Kjeldahl method. J. Agric. Sci. 55, 11—33. https://doi.org/10.1017/S0021859600021572

Bridgeman, T.B., Chaffin, J.D., Kane, D.D., Conroy, J.D., Panek, S.E., Armenio, P.M., 2012. From River to Lake: Phosphorus partitioning and algal community compositional changes in Western Lake Erie. J. Great Lakes Res. 38 (1), 90—97. https://doi.org/10.1016/j.jglr.2011.09.010

Carritt, D.E., Goodall, S., 1954. Sorption reactions and some ecological implications. Deep-Sea Res. 1, 224—243.

Chen, Y.S.R., Bulter, J.N., Stumm, W., 1973. Kinetic study of phosphate reaction with aluminum oxide and kaolinit. Environ. Sci. Technol. 7, 327—332. https://doi.org/10.1021/es60076a007

Dapeng, L., Yong, H., Chengxin, F., Yan, Y., 2011. Contributions of phosphorus on sedimentary phosphorus bioavailability under sediment resuspension conditions. Chem. Eng. J. 168, 1049—1054. https://doi.org/10.1016/j.cej.2011.01.082

De Groot, C., 1991. The influence of FeS on the inorganic phosphorus retention in lakes determined from ass balance and sediment core calculations. Wat. Res. 27, 659—668.

Donia, N., 2011. Water quality management of lake Temsah, Egypt using geographical information system (GIS). IJESE 2, 1—8. http://www.pvamu.edu/texged

Elser, J.J., Andersen, T., Baron, J.S., Bergström, A., Jansson, M., Kyle, M., Nydick, K.R., Steger, L., Hessene, D.O., 2009. Shifts in lake N: P stoichiometry and nutrient limitation driven by atmospheric nitrogen deposition. Science 326 (5954), 835—837. https://doi.org/10.1126/science.1176199

Folk, R.L., 1974. Petrology of sedimentary rocks. Austin: Hemphill Pub. Co.

Fu, Y., Zhoh, Y., Li, J., 2000. Sequential fractionation of reactive phosphorus in the sediment of a shallow eutrophic lake Donghu Lake. China, Int. J. Environ. Sci. 12, 57—62.

Gao, L., Zhou, J.M., Yang, H., Chen, J., 2005. Phosphorus fractions in sediment profiles and their potiential contributions to eutrophication in Dianchi Lake. Environ. Geol. 48, 835—844. https://doi.org/10.1007/s00254-005-0005-3

Gonsiorezyk, T., Casper, P., Koschel, R., 1998. Phosphorus binding forms in the sediment of an oligotrophic and an eutrophic hardwater lake of the Baltic Lake District (Germany). Water Sci. Technol. 37 (3), 51—58. https://doi.org/10.2166/wst.1998.0173

Gunduz, B., Aydın, F., Aydin, I., Hamamci, C., 2011. Study of phosphorus distribution in coastal surface sediment by sequential extraction procedure (NE Mediterranean Sea, Antalya-Turkey). Microchem. J. 98, 72—76. https://doi.org/10.1016/j.microc.2010.11.006

Gu, Y.G., Ouyang, J., Ning, J.J., Wang, Z.H., 2017. Distribution and sources of organic carbon, nitrogen and their isotopes in surface sediments from the largest mariculture zone of the eastern Guangdong coast, South China. Mar. Pollut. Bull. 120, 286—291. https://doi.org/10.1016/j.marpolbul.2017.05.013

Hakanson, L., Jansson, M., 1983. Principles of Lake Sedimentology. Springer-Verlag, Berlin.

Han, H., Lu, X., Burger, D.F., Joshi, U.M., Zhang, L., 2014. Nitrogen dynamics at the sediment-water interface in a tropical reservoir. Ecol. Eng. 73, 146—153. https://doi.org/10.1016/j.ecoleng.2014.09.016

Hu, J., Shen, Q., Liu, Y.D., 2007. Mobility of different phosphorus pools in the sediment of Lake Dianchi during cyanobacterial blooms. Environ. Monit. Assess. 132, 141—153. https://doi.org/10.1007/s10661-006-9509-x

Huang, B., Guo, Z., Xiao, X., Zeng, P., Peng, C., 2019. Changes in chemical fractions and ecological risk prediction of heavy metals in estuarine sediments of Chunfeng Lake estuary. China. Mar. Pollut. Bull. 138, 575—583. https://doi.org/10.1016/j.marpolbul.2018.12.015

Hsu, P.H., 1965. Fixation of phosphate by aluminum and iron in acidic soils. Soil Sci. 99, 398—402.

Jensen, H., Kristensen, P., Jeppesen, E., Skytthe, A., 1992. Iron: phosphorus ratio in surface sediment as an indicator of phosphate release from aerobic sediments in shallow lakes. Hydrobiologia 235/236, 731—743. https://doi.org/10.1007/BF00026261

Kaiser, M.F., Amin, A.S., Aboulela, H.A., 2009. Environmental Hazards in the El-Temsah Lake, Suez Canal District, Egypt. Adv. Geosci. Remote Sens. 57—70. https://doi.org/10.5772/8335

Knosche, R., 2006. Organic sediment nutrient concentrations and their relationship with the hydrological connectivity of floodplain waters (River Havel, NE Germany). Hydrobiologia 560, 63—76. https://doi.org/10.1007/s10750-005-0983-x

Kisand, A., Noges, P., 2003. Sediment phosphorus release in phytoplankton dominated versus macrophyte dominated shallow lakes: importance of oxygen conditions. Hydrobiologia 506—509, 129—133. https://doi.org/10.1023/B:HYDR.0000008620.87704.3b

Li, Y., Peng, T., 2002. Latitudinal change of remineralization ratios in the oceans and its implication for nutrient cycles. Global Biogeochem. Cy. 16 (4). https://doi.org/10.1029/2001GB001828Yuan-Hui

Liu, H.L., Jin, X.C., Jing, Y.F., 1999. Environmental dredging technology of lake sediment. Chinese Eng. Sci. 1, 81—84.

Liu, L., Zhang, Y., Efting, A., Barrow, T., Qian, B., Fang, Z., 2012. Modeling bioavailable phosphorus via other phosphorus fractions in sediment cores from Jiulongkou Lake, China. Environ. Earth Sci. 65 (3), 945—956. https://doi.org/10.1007/s12665-011-1295-2

Loring, D.H., Rantala, R.T.T., 1992. Manual for the geochemical analyses of marine sediments and suspended particulate matter. Earth Sci. Revi. 32, 235—283. https://doi.org/10.1016/0012-8252(92)90001-A

Mackereth, F.J.H., 1966. Some chemical observations on post-glacial lake sediments. Philos. T. Roy. Soc. B 250, 165—213

Mudroch, A., Azcue, O.M., 1995. Manual of Aquatic Sediment Sampling. Lewis Publisher, Ann. Arbor, Michigan, USA.

Okbah, M.A., 2006. Bioavailablility of phosphorus in Abu Qir and Lake Edku sediments, Mediterranean Sea. Egypt. Chem. Ecol. 6, 451—462. https://doi.org/10.1080/02757540601025006

Oregioni, B., Aston, S.R., 1984. The determination of selected trace metals in marine sediments by flame atomic absorption spec-

trophotometry. IAEA Monaco Laboratory Internal Report. UNEP, reference methods for marine pollution studies No 38.
Pardo, P., Lopez-Sanchez, J.F., Rauret, G., 2003. Relationships between phosphorus fractionation and major components in sediments using the SMT harmonized extraction procedure. Anal. Bioanal. Chem. 376, 248—254.
Pedro, T., Kimberley, S., Fernando, P., 2013. Dynamics of phosphorus in sediments of a naturally acidic lake. Int. J. Sediment Res. 28 (1), 90—102. https://doi.org/10.1007/s00216-003-1897-y
Peng, R., 2016. Spatiotemporal distribution and stoichiometry characteristics of carbon, nitrogen and phosphorus in surface soils of freshwater and brackish marshes in the Min River estuary. China Environ. Sci. 36, 917—926 (in Chinese).
Penn, M.R., Auer, M.T., Van Orman, E.L., Korienek, J.J., 1995. Phosphorus Diagenesis in Lake Sediments: Investigations using Fractionation Techniques. Mar. Freshwater Res. 46, 89—99. https://doi.org/10.1071/MF9950089
Perkins, R.G., Underwood, G.J.C., 2001. The potential for phosphorus release across the sediment—water interface in a eutrophic reservoir dosed with ferric sulphate. Water Res. 35, 1399—1406. https://doi.org/10.1016/S0043-1354(00)00413-9
Pettersson, K., Bostrom, B., Jacobsen, O.S., 1988. Phosphorus in sediments — speciation and analysis. Hydrobiologia 170, 91—101. https://doi.org/10.1007/BF00024900
Psenner, R., Pucsko, R., 1988. Phosphorus fractionation: advantages and limits of the method for the study of sediment P origins and interactions. Arch. Hydrobiol. Beih. 30, 43—59.
Reddy, K.R., Wetzel, R.G., Kadlec, R.H., 2005. Biogeochemistry of phosphorus in wetlands. In: Sims, J.T., Sharpley, A.N. (Eds.), Phosphorus: agriculture and the environment. Soil Science Society of America, Madison, 263—316.
Redfield, A.C., Ketchum, B.H., Richards, F.A., et al., 1963. The Influence of Organisms on the Composition of the Sea Water. In: In: Hill, M.N., Ed., The Sea, 2. Interscience Publishers, New York, 26—77.
Ruban, V., López-Sánchez, J.F., Pardo, P., Rauret, G., Muntau, H., Quevauviller, Ph., 1999. Selection and evaluation of sequential extraction procedures for the determination of phosphorus forms in lake sediment. J. Environ. Monitor. 1, 51—56. https://doi.org/10.1039/A807778I
Ruban, V., Lopez-Sanchez, J.F, Pardo, P., Rauret, G., Muntau, H., Quevauviller, P., 2001. Harmonized protocol and certified reference material for the determination of extractable contents of phosphorus in freshwater sediments — A synthesis of recent works. Fresenius. J. Anal. Chem. 370 (2—3), 224. https://doi.org/10.1007/s002160100753
Ruttenberg, K.C., 1992. Development of sequential extraction method for different forms of phosphorus in marine sediments. Limnol. Oceanogr. 37, 1460—1482. https://doi.org/10.4319/lo.1992.37.7.1460
Rydin, E., Brunberg, A.K., 1998. Seasonal dynamics of phosphorus in Lake Erken surface sediments. Archiv für Hydrobiologie 51, 157—167. https://doi.org/10.1023/A:1004050204587
Rydin, E., 2000. Potentially mobile phosphorus in Lake Erken sediment. Water Res. 34, 2037—2042. https://doi.org/10.1016/S0043-1354(99)00375-9
Said, T.O., El Agroudy, N.A., 2006. Assessment of PAHs in water and fish tissues from Great Bitter and El Temsah lakes, Suez Canal, as chemical markers of pollution sources. Chem. Ecol. 22, 159—173. https://doi.org/10.1080/02757540500526476
Sardans, J., Rivas-Ubach, A., Penuelas, J., et al., 2012. The elemental stoichiometry of aquatic and terrestrial ecosystems and its relationships with organismic lifestyle and ecosystem structure and function: A review and perspectives. Biogeochemistry 111 (1—3), 1—39. https://doi.org/10.1007/s10533-011-9640-9
Sekhara, K.C., Charya, N.S., Kamalaa, C.T., Suman, D.S., Rajb, A., Raoc, S., 2003. Fractionation studies and bioaccumulation of sediment-bound heavy metals in Kolleru lake by edible fish. Environ. Int. 29, 1001—1008. https://doi.org/10.1016/S0160-4120(03)00094-1
Soliman, N.F., El Zokm, G.M., Okbah, M.A., 2017. Evaluation of phosphorus bioavailability in El Mex Bay and Lake Mariut sediments. Int. J. Sediment Res. 32, 432—441. https://doi.org/10.1016/j.ijsrc.2017.05.006
Soliman, NF., Younis, A.M., Elkady, E.M., Mohamedein, L.I., 2018. Geochemical associations, risk assessment, and source identification of selected metals in sediments from the Suez Gulf, Egypt. Hum. Ecol. Risk Assess. 25 (3), 1—17. https://doi.org/10.1080/10807039.2018.1451301
Soliman, N.F., Younis, A.M., Elkady, E.M., 2019. An insight into fractionation, toxicity, mobility and source apportionment of metals in sediments from El Temsah Lake, Suez Canal. Chemosphere 222, 165—174. http://doi.org/10.1016/j.chemosphere.2019.01.009
Ting, D.S., Appan, A., 1996. General characteristics and fractions of phosphorus in aquatic sediments of two tropical reservoirs. Water Sci. Technol. 34, 53—59. https://doi.org/10.1016/S0273-1223(96)00724-X
Tiyapongpattana, W., Pongsakul, P., Shiowatana, J., Nacapricha, D., 2004. Sequential extraction of phosphorus in soil and sediment using a continuous-flow system. Talanta 62, 765—771. https://doi.org/10.1016/j.talanta.2003.09.018
US EPA (2002). National Recommended Water Quality Criteria: 2002. Office of Water, EPA-822-R-02047, U.S. Environmental Protection Agency, Washington DC. http://www.epa.gov/waterscience/standards/wqcriteria.html
Wang, S., Jin, X., Bu, Q., Liao, H., Wu, F., 2010. Evaluation of phosphorus bioavailability in sediments of the shallow lakes in the middle and lower reaches of the Yangtze River region, China. Environ. Earth Sci. 60, 1491—1498. https://doi.org/10.1007/S12665-009-0284-1
Wang, L., Liang, T., 2015. Distribution Characteristics of Phosphorus in the Sediments and Overlying Water of Poyang Lake. PLoS ONE 10 (5), e0125859. https://doi.org/10.1371/journal.pone.0125859
Zhou, Q., Gibson, C.E., Zhu, Y., 2001. Evaluation of phosphorus bioavailability in sediments of three contrasting lakes in China and the UK. Chemosphere 42, 221—225. https://doi.org/10.1016/s0045-6535(00)00129-6
Zhu, M., Zhu, G., Li, W., Zhang, Y., Zhao, L., Gu, Z., 2013. Estimation of the algal-available phosphorus pool in sediments of a large, shallow eutrophic lake (Taihu, China) using profiled SMT fractional analysis. Environ. Pollut. 173, 21. https://doi.org/10.1016/j.envpol.2012.10.016

Oceanologia 64 (2022) 299—311

Available online at www.sciencedirect.com

ScienceDirect

journal homepage: www.journals.elsevier.com/oceanologia

ORIGINAL RESEARCH ARTICLE

Diurnal variation of cloud cover over the Baltic Sea

Marcin Paszkuta[a,*], **Tomasz Zapadka**[b], **Adam Krężel**[a]

[a] *Institute of Oceanography, University of Gdańsk, Gdynia, Poland*
[b] *Institute of Physics, Pomeranian University in Słupsk, Poland*

Received 3 January 2021; accepted 13 December 2021
Available online 29 December 2021

KEYWORDS
Clouds;
Baltic Sea;
Environmental assessment

Abstract Instantaneous cloud cover over the Baltic Sea, estimated from satellite information, may differ by as much as several dozen percent between the day and night. This difference may result from both weather conditions and different algorithms used for the day and night. The diurnal differences in cloudiness measured by proprietary and operational systems were analysed as part of research on marine environmental assessment and monitoring. An optimised algorithm for 2017 was presented and supplemented with information from radiation modelling. The study showed that, in general, the average values of daily changes in cloud cover over the sea depend on the season, which generally corresponds to the length of the day and contrasts with the amount of cloudiness. The results were compared with available online data that met the night and day detection criteria, the climate model, and the climate index. The averaged analysis of seasonal changes showed that similar values of the satellite estimates are higher than those obtained from the climate model and the lidar estimation. The satellite estimates from SatBaltic showed the lowest uncertainty. The diurnal cycle was confirmed by all analysed systems. These results may indicate common physical mechanisms and a methodological reason for the uncertainty of satellite-based data. The results clearly showed the existing diurnal difference in the amount of cloud cover over the Baltic Sea and indicated that this difference is not always explained by the physical properties of the atmosphere. The probable causes for these uncertainties were identified and diagnosed.

1. Introduction

The study of cloudiness above the sea surface based on observations from satellites is a very complex problem. The complexity involves results of measurements in both the shortwave and longwave ranges, i.e. the visible (VIS) and infrared (IR) radiation. The literature includes numerous studies (Anthis et al., 1999; Bennouna et al., 2010; Finkensieper et al., 2018; Saunders et al., 1988) on remote cloud cover detection systems which are applicable to aver-

* Corresponding author at: Institute of Oceanography, University of Gdańsk, al. Marszałka Piłsudskiego 46, 81—378, Gdynia, Poland.
E-mail address: marcin.paszkuta@ug.edu.pl (M. Paszkuta).
Peer review under the responsibility of the Institute of Oceanology of the Polish Academy of Sciences.

Production and hosting by Elsevier

https://doi.org/10.1016/j.oceano.2021.12.005

Figure 1 An example of cloudiness estimation and the resultant statistical error (Baltic Sea, 18 May 2017, 5:30 UTC) (LW, left-hand side; SW, right-hand side) [source: www.satbaltic.pl].

aged global-scale situations, but their actual regional-scale utility is frequently debated. Due to the nature of radiation, measuring it involves a lot of uncertainties. Cloud detection systems based on satellite data mostly use physical parameters calculated from the radiation spectrum, i.e. colour, shape, thickness, gradient, height, and inter-band relationships or interactions between the detected objects themselves (Mahajan et al., 2020). Different detection techniques as well as different classification methods are used, e.g. binary classification and measurement of cloud cover opacity based on pixel values. For the Baltic Sea region, a review of cloudiness in reference to climate change was carried out by Post et al. (2020). The study analysed the regional mean time series and regional maps of trends in the Baltic Sea area. The cloud parameters studied were total fractional cloud cover and cloud-top height. In the study carried out by Reuter et al. (2014), a SEVIRI-based cloud detection algorithm was developed for the Baltic Sea catchment area. The total cloudiness obtained from the satellite data was 0.65 compared to 0.63 for the model. Large discrepancies were observed in the 24-hour cloud-cycle phase. There was no significant trend in the total cloud amount, either from the model or from the satellite data. Li et at. (2020) proposed a cloud detection method based on genetic reinforcement learning in order to improve cloud detection at a regional scale. Banks et al. (2015) showed that the standard cloud mask used routinely in processing global ocean colour data from National Aeronautics and Space Administration (NASA) can mask optical phenomena such as intense algal blooms in the Baltic Sea. These blooms have a significant impact on the environment and require appropriate monitoring. Their findings show that replacing the standard cloud mask can increase the data accuracy by 22% during the seasonal cycle in the Baltic Sea. On the other hand, Kowalewska-Kalkowska et al. (2019) showed the difficulties and limitations of poor cloud masking over the Baltic Sea in identifying and modelling coastal upwelling. It was also demonstrated that the usefulness of this factor for predicting threats associated with extreme conditions is still limited as a consequence of the regional estimation of hazardous weather events (Latos et al., 2021). Jakobson et al. (2014) showed that the diurnal variability of precipitable water over the Baltic Sea is the inverse of water vapour variability over land. Finally, Mahajan et al. (2020) discussed the current trends and direction of development for modern regional cloud detection systems based on satellite data. A hybrid approach using machine learning, physical parameter acquisition and ground-based validation was recommended for model improvement. The cited publications mostly concern issues of improving the quality and daily variability of the data at the regional scale, which suggests that the actual usefulness of cloud algorithms is questionable. This study discusses the possibility of using a simple algorithm to assess cloudiness in regions with similar geographical conditions as the Baltic Sea. Paszkuta et al. (2019) explained those methods in more detailed recommendations. They show new results on the extent and size of cloud cover during the day and night time. Detection methods have been identified as the main source of uncertainty. First, to minimise errors, efforts were made to limit the research area to a more homogenous region. The proximity of the northern part of the Baltic Sea to

Table 1 Spectral characteristics of the SEVIRI radiometer channels.

Waveband		Spectral range (μm)			Remarks
		λ_{cen}	λ_{min}	λ_{max}	
1	VIS0.6	0.64	0.56	0.71	Atmospheric visible window
2	VIS0.8	0.81	0.74	0.88	Atmospheric visible window
3	NIR1.6	1.64	1.50	1.78	Near infrared atmospheric window
4	IR3.9	3.90	3.48	4.36	Atmospheric thermal window
5	WV6.2	6.25	5.35	7.15	Water vapour absorption
6	WV7.3	7.35	6.85	7.85	Water vapour absorption
7	IR8.7	8.70	8.30	9.10	Atmospheric thermal window
8	IR9.7	9.66	9.38	9.94	Ozone absorption
9	IR10.8	10.80	9.80	11.80	Atmospheric thermal window
10	IR12.0	12.00	11.00	13.00	Atmospheric thermal window
11	IR13.4	13.40	12.40	14.40	Carbon dioxide absorption
12	HRV	0.75	0.40	1.10	Atmospheric visible window + water vapour absorption

the northern polar circle rules out, for a considerable period of time, the possibility of using the entire bandwidth range, particularly the bandwidths in the short-wave part, and poses a serious challenge for geostationary satellites, e.g. the Meteosat Second Generation (MSG) (Bennouna et al., 2010). It is, therefore, interesting to begin with cloudiness detection broken down into shortwave and longwave band ranges, the division being important not only for the transition from daytime to night-time, but also for the measurement site. The changes will then depend primarily on the available information; for obvious reasons (including the high solar angle limitation), only data from the longwave band can be used during the night (Table 1). Differences between night-time and daytime cloud cover estimates are quite natural and are visible when comparing information from shortwave and longwave band daytime routines. The differences are explained by the physical parameters of cloudiness because high-reflectance warm formations are usually the only reference for brightness temperature studies, and cold fog does not always affect the visible radiation range (Jakobson et al., 2014; Jedlovec, 2009; Krężel and Paszkuta, 2011; Paszkuta et al., 2019). As the problem is the regional scale, different methodologies, which are a fairly important source of uncertainty, introduce artefacts emerging along the shoreline or at the edge of low clouds. The artefacts result from an incorrect estimation, e.g. with the use of the textural image analysis techniques. At the same time, they are difficult to eliminate due to convections forming in the area and the presence of near-shore effects such as upwellings. There are numerous examples of instantaneous, regional over- and underestimation of cloudiness in the atmosphere. Figure 1 shows examples of differences in cloudiness estimation done by operational detection systems during the day and night. The date and time (Figure 1) was chosen due to the apparent variability of data and the availability of a wide range of different types of cloud cover. Generally, methods adapted to the global scales (Figure 2), show the daytime cloudiness to be lower when compared to regional scales (Figure 1), with the night-time cloudiness being comparably higher. For this reason, the averaged characteristics show relatively small differences which increase with the change of the Solar Zenith Angle (SZA): the higher north, the larger the difference due to a change in the proportions between the daytime vs. night-time routines. In many comparisons, it is difficult to unequivocally state whether and which physical process is responsible for the differences between the routines. It is certain, however, that the presence of a large body of water substantially affects the detection results, and physical analyses should be conducted separately for the daytime and night-time routines. The paper is an extension of the study conducted by Paszkuta et al. (2019), but it is the first study to show the optimisation of the algorithm in the process of generalizing Planck's law based on satellite results and published materials. To reveal the variability in the detection of diurnal Baltic Sea cloudiness, the results are compared with alternative sources and the North Atlantic Oscillation (NAO) index. The goal is to increase the quality of oceanographic data. An overestimation of cloudiness can often deprive us of information about important sea surface phenomena that can last several hours, such as coastal upwelling. An underestimation can have a negative impact, e.g. on the balance of radiation reaching the sea surface. The aim is to identify and estimate the source of uncertainty arising from the satellite measurement process. Clearly, considering the availability, scope and amount of information, satellite measurements have an undeniable value. The article consists of five sections. In Section 1 the problem is described using the example of the briefly summarised SatBaltic project, the state of knowledge on cloud detection using satellite data is presented, and daily analyses taking into account some outside factors on the Baltic are performed, followed by a literature review. Section 2 focuses on the description of data used in the analyses and suitable for comparing the differences between day and night values. The methods used in the paper are based on the technique published and presented in detail for the first time by the authors, which consists in linearising Planck's law. It has been proposed to improve the method further. In Section 3, we clearly describe the modifications to that method and the changes in cloud cover detection. In Section 4, we present

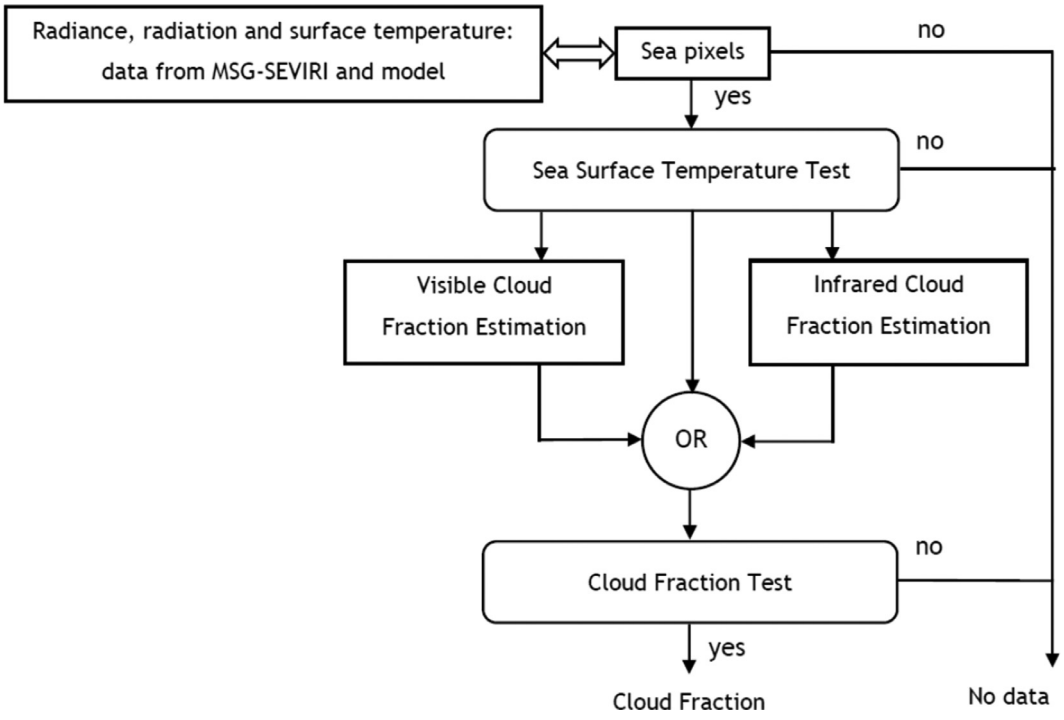

Figure 2 Block diagram of the cloud detection data flow (Paszkuta et al., 2019).

the significance of our findings. In the last section, we discuss the results and list the probable reasons for the differences.

2. Material and methods

A flagship product of satellite cloudiness data developed within the SatBaltic project (Woźniak et al., 2011a,b), consists of a series of tests using the split-windows technique and model estimations for cloudless atmosphere (Figure 2). The detection technique is, in principle, based on a difference between the Spinning Enhanced Visible and Infrared Imager (SEVIRI) ranges (Table 1) and compares the outcomes with values modelled for cloudless conditions. It generalises radiation transmission equations using relationships between two neighbouring spectral bands, and is, in fact, based on the magnitude of the difference between them (Kriebel et al., 2003; Kryvobok et al., 2005). The technique of split windows and model estimation for the cloudless atmosphere at the Baltic Sea was used both in the short and long range of waves. In this way, the SatBaltic system uses two values of the cloud fraction: one referring to shortwave radiation and the other to longwave band. The difference between the magnitude of radiation at full cloudiness and in the absence of clouds under identical thermal conditions over the Baltic Sea may be as high as 120 W m^{-2}. The semi-empirical formulae reported in the literature are frequently based on the general cloudiness function as the main factor determining the bottom-up flux of longwave-band radiation. This is, however, a far-flung approximation which may be subject to a statistical error of as much as even 30% (Zapadka et al., 2015). The characteristic feature of the method proposed is that it is region-specific and based on radiation models developed by the authors to avoid relying on external sources. Similarly to most of the studies referred to, the division into daytime and nighttime is included, with the incident radiation angle of 67° being used as a criterion (Paszkuta et al., 2019). The differences in the diurnal cycle of cloud cover, and hence in the radiative cycle, can lead to significant changes in the energy balance. Clouds generally attenuate the solar radiative energy flux. The problem of absorption or transmission by different types of clouds has been explained in the literature (Kaczmarek and Dera, 1998; Rozwadowska, 2004). The Baltic Sea has thermodynamic properties that are different from those of the land and the oceans, and some of those properties have a significant influence on the atmosphere. Seawater is subject to constant phase changes that absorb large amounts of energy. The energy required for these processes comes mainly from the atmosphere. Therefore, changes in the water can cause significant changes in the atmosphere, which occur in a continuous diurnal cycle, different (on a different scale) than in the open oceans. The air temperature varies by a few to a dozen degrees per day, with little change in water temperature. Therefore, it happens that the water in the Baltic Sea has a higher temperature than the air as a consequence of air temperature fluctuations. If the sea is cooler than the air, the water will draw heat from its surroundings in an attempt to compensate for this difference. Conversely, when the water in the sea contains more energy, the air temperature changes. These mechanisms can partly explain the diurnal differences in cloud cover. At night, when the air warms up, it rises higher. When the rising air reaches the height where condensation occurs, the conditions for the formation of clouds occur. During the day, the situation can reverse and a cloud-free atmosphere can form. If the water is warmer

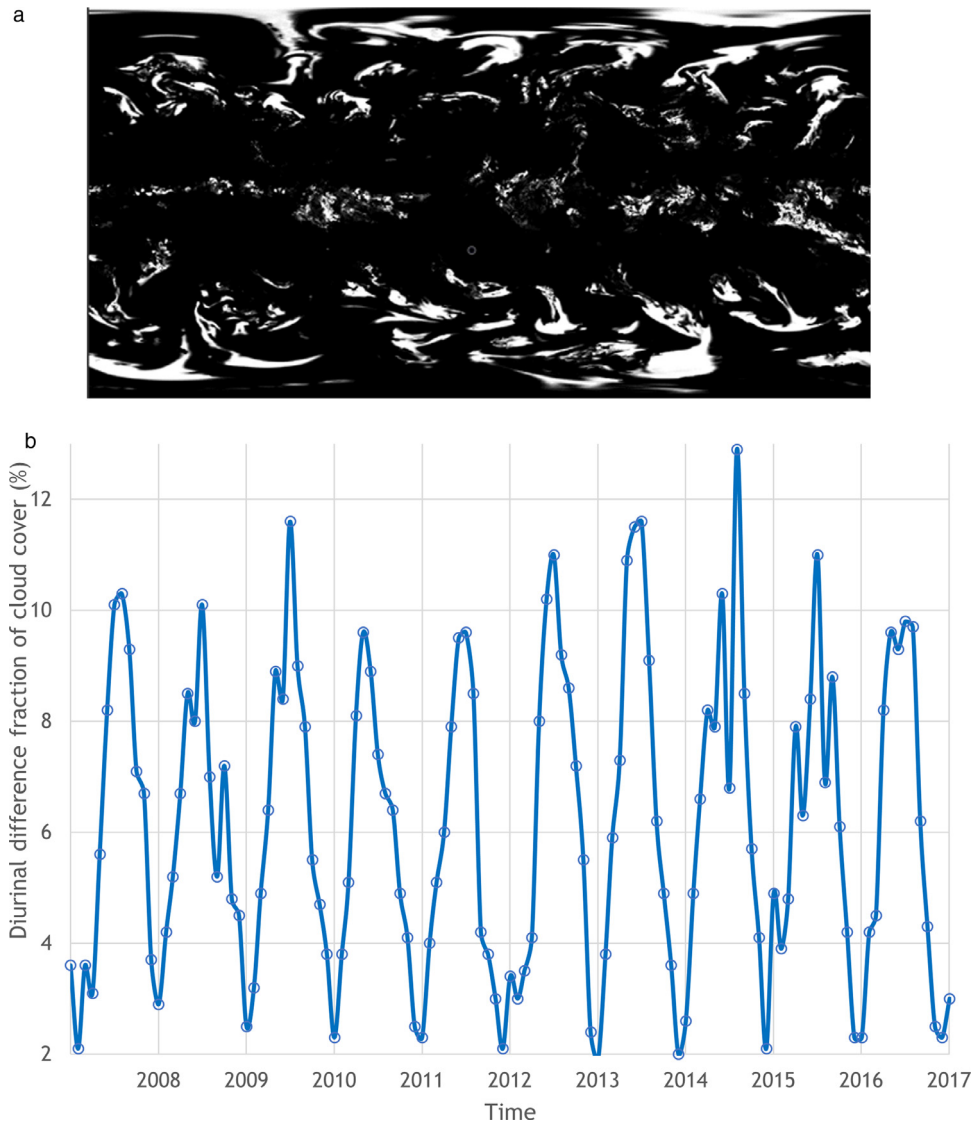

Figure 3 Example of global fraction of cloud cover on 5 May 2017 at 12:00 UTC (a), and (b) Monthly average diurnal variation fraction of cloud cover for the Baltic Sea, data obtained from ECMWF—ERA5 (https://cds.climate.copernicus.eu).

than the environment, clouds may even form around the clock. Based on the European Centre for Medium-Range Weather Forecasts climate reanalysis data[1] (ECMWF—ERA5) shown in (Figure 3), the average daily difference in the percentage of cloud cover on the Baltic Sea (between 2008 and 2017) was up to a few percent, depending on the location and season: a maximum of 13% was recorded which is lower than the value obtained in the study using satellite data. This confirms the results obtained by the authors; however, the question remains whether these phenomena have natural causes. The daily changes in cloud cover over the Baltic Sea shown in the study could even modify the atmospheric circulation, if they have a natural basis. In the rest of the paper, we will identify other causes that are not indicative of natural physical processes. It is interesting to look for trends and long-term changes in the climate related to the cloud cover parameter; however, at the moment, this is not the subject of this analysis, although the arbitrary period of 30 years of climate changes already covers the period of data collected by satellite instruments. The satellite-based cloudiness data calculated by the Advanced Very High Resolution Radiometer (AVHRR) (mounted on the Tiros N satellite series operated by the National Oceanic and Atmospheric Administration, NOAA) is based on the AVHRR Processing Over Land cLoud and Ocean (APOLLO) algorithm (Saunders and Kriebel, 1988). The algorithm involves five independent tests. It analyses a sequence of threshold, textural, and inter-waveband relations. Significantly, one of the routines is dedicated to marine areas and simultaneously analyses the relationship between short and longwave channels while using separate series of daytime and nighttime data (Cracknell, 1997). Results of the algorithm have been repeatedly compared with alternative solutions and in situ measurements (Kriebel et al., 1989). The AVHRR data, owing to the regional measurement system, does not have an inferior spatial structure to the data generated by SE-

[1] https://cds.climate.copernicus.eu

VIRI. From the standpoint of instantaneous regional observations, the MSG is more advantageous for the measurement of rapidly changing cloud cover (particularly at the estimated range). Average differences between the data generated by AVHRR and SEVIRI are up to several per cent, the values being higher for the night-time data. The cloud products offered on-line from MODIS data combine the IR and VIS ranges, similarly to the algorithm proposed in this study. The cloud fractional cover product developed in 2004 by the Satellite Application Facility on Climate Monitoring (CM SAF) consortium within the CLoud property dAtAset (CLAAS-2) using SEVIRI (Edition 2) (today the Interim Climate Data Record [ICDR]) is based on NWC SAF cloudiness detection and classification algorithms. The Cloud-Aerosol Lidar and Infrared Pathfinder (CALIPSO) was designed to investigate the effects of clouds on the radiation budget (Chepfer et al., 2013). Equipped with the Cloud-Aerosol Lidar with Orthogonal Polarization (CALIOP), the device offers information based on active detection.

3. Results

3.1. New approaches

In line with the goal of this study, we estimated the averages for daytime and night-time events separately. According to this important classification, the data sets relate to physical processes taking place during the day and at night. Although marked differences in cloudiness between the day and the night, such as those discussed in the previous section, are likely not to have physical underpinnings, certain differences in the emission of the sea will always happen. They emerge, for example, due to the cyclical course of solar radiation and its consequences during the daytime, whereas at night they occur because of, e.g., the formation of a humid zone just above the sea surface, which affects the long waveband emission. For the IR range, the method is based on the three-dimensional numerical hydrodynamic M3D model (Kowalewski, 1997), which allows us to calculate the emission temperature of the sea both during the daytime and at night. As the T_9 (9.80—11.80 μm) and T_{10} (11.00—13.00 μm) frequency bands are close on the spectrum (Table 1), the first approximation disregarded the non-linear nature of Planck's law, and brightness temperatures in the SEVIRI channels were estimated from the modelled sea-surface temperature (*SST*). This simplification (approach 1) has some advantages, as it produces more general results, but involves unavoidable errors which, owing to the structure of the algorithm (the difference between the two wavebands is estimated with comparable uncertainty) may only be acceptable on account of the broad objectives of the detection model. The relationships can be illustrated as:

$$T^M = SST_{M3D} \cdot A, \tag{1}$$

where T^M equals estimated brightness temperature; SST_{M3D} equals sea surface temperature determined by M3D; A equals calibration constant from Table 2.

This approximation assumes the coefficient which in fact causes the ratio between the black body and true emission in the SEVIRI channels 9 and 10 to approach one. The coefficient should be understood as an effect of averaging the daytime and night-time values calculated according to the split-window formula and simultaneously taking into account the differences between the surface temperature and the *SST*. More detailed estimations based on the IR range for the day and the night should result from different emissive characteristics of the spectral bands used. The problem seems to be well-explored for the sea surface; unfortunately, the emissivity of inhomogeneous cloud layers at poor radiation is difficult to measure. This is one of the reasons why noticeable differences, resulting from the nature of the radiation itself, occur when the cloudiness coefficient is calculated from VIS and IR. Should the emissivity values (a coefficient showing the difference between the properties of the true body and the black body) be switched, the radiation in the channel would — depending on the temperature — be higher or lower at the same values of the emitting body temperature. In the first approximation (approximation 1 in Figure 7), the relationship was a priori assumed to be linear, which influences the difference between the daytime and night-time cloud cover detection. To solve the problem of the non-linearity of Planck's law, the subsequent approximations 2 and 3 use two different radiation transmission equations, one for the night and the other for the day for the same thermal channels. The function of fitting the spectral radiation to the black body radiation is non-linear (Figure 4) and makes it possible to, e.g. measure *SST* using satellite techniques (Wang et al., 2019). Radiation emitted by the sea surface in the range of IR wavelengths recorded by SEVIRI can be approximated by a function correlating

Table 2 Estimation constants for the SEVIRI thermal channels.

Channel	*k*	*A*	*B*	*C*
$T^M{}_9$	9.3066	0.992	0.627	0.9983
$T^M{}_{10}$	8.3966	0.998	0.397	0.9988

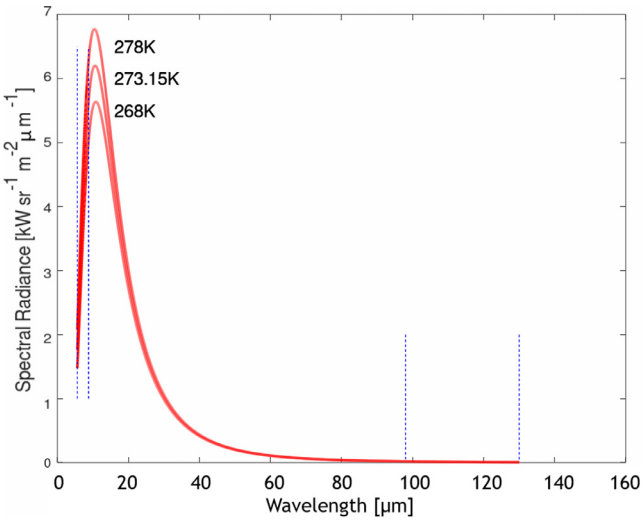

Figure 4 Planck's law for the temperatures analysed, with spectral ranges.

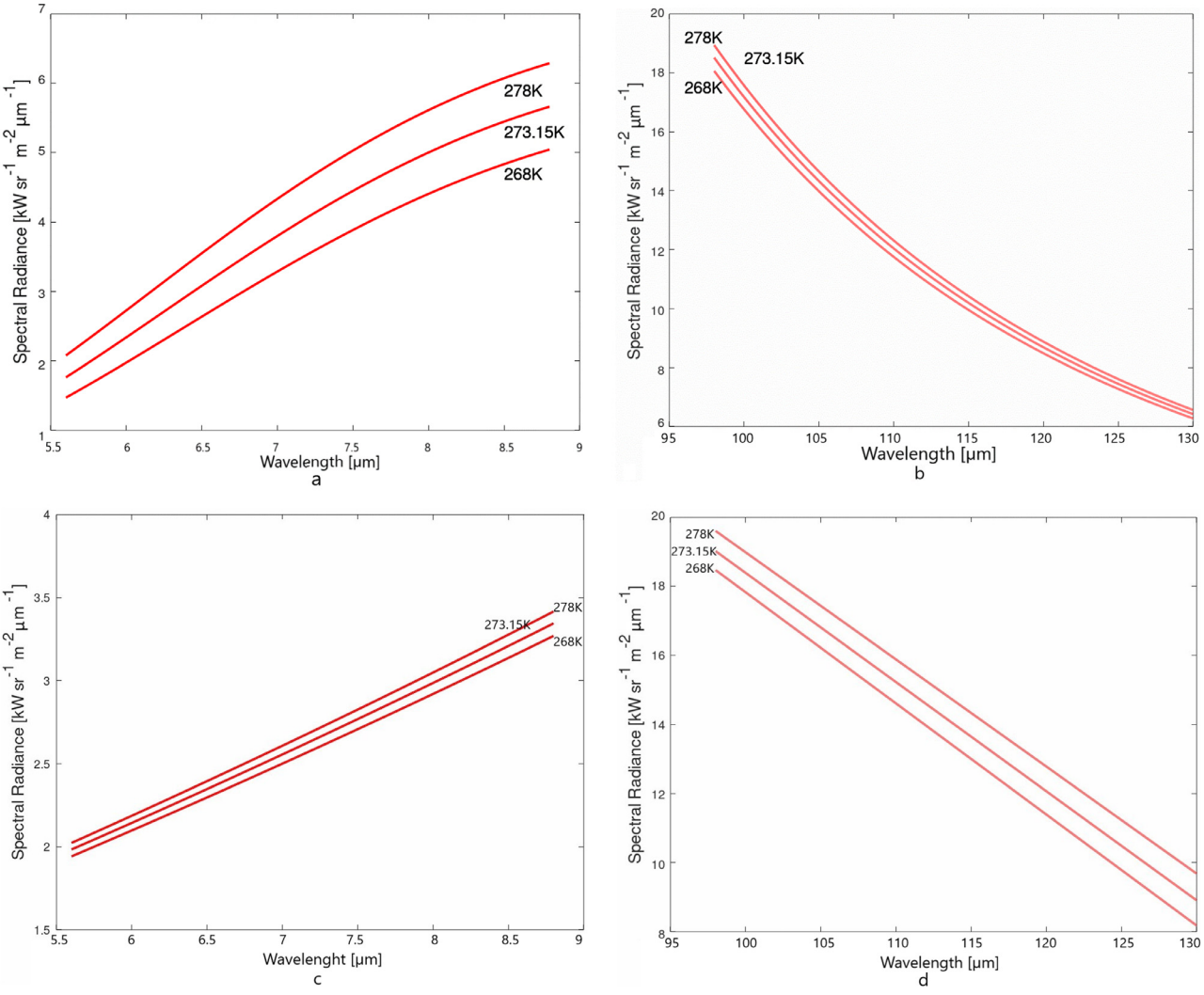

Figure 5 Examples of linear approximation of Planck's laws to: a,c) Short; b,d) Long; wave-areas analysed in the study.

with the Planck function:

$$I(\lambda) = \varepsilon F \frac{2hc^2}{\lambda^5} \frac{1}{e^{hc/\lambda k_B T}}; \qquad \left(\frac{hc}{\lambda k_B T} \gg 1\right), \tag{2}$$

where: ε equals ambient emissivity; F equals device-specific coefficient involving geometric and radiometric factors; T equals black body temperature; λ equals wavelength; h equals the Planck constant; c equals light speed; and k_B equals the Boltzmann constant.

Eq. (2) is valid provided that $hc/\lambda kT >> 1$, i.e. the wavelength is below the function maximum. Figure 4 and Figure 5 show blackbody radiation in the detection temperature range for semi-transparent objects, i.e. objects with radiation emission similar to that at sea. Spectral ranges corresponding to the channels analysed in this work are marked. As the temperature increases, the function maximum (the near-IR) shifts towards shorter wavelengths. This behaviour is described by the Wien's law, $\lambda = b/T$, where b equals 2.8978 $\times$ 10^6 nm-K. As seen in Figure 4 and Figure 5, the spectral ranges marked are below the function maximum. This presents a challenge for satellite-aided remote sensing, because it means that the intensity of the signal analysed will be correspondingly lower. In such cases, when the brightness temperature of the atmosphere is close to that of the sea surface, certain linearisation of Planck's law is observable (Figure 5). An appropriate transformation of the function simplifies it to $1/\lambda$:

$$\ln(\lambda^5 I) = \ln\left(2hc^2 \varepsilon F\right) - \frac{hc}{k_B T} \frac{1}{\lambda}. \tag{3}$$

This makes it possible to carry out linear fitting to the linearised radiation spectra. In addition to advantages related to usability, this operation ensures an ideal representation of deviations by the blackbody curves. Therefore, the fitting can be carried out in a more universal form, excluding naturally non-analysed parts of the non-linear spectrum. This is particularly useful at temperatures corresponding to shorter wavelengths where uncertainties are crucial and the blackbody radiation is relatively low. Non-linear procedures call for the fitting of the Planck formula parameters (ε, F, T, and λ) which are less sensitive than those of the linear equation and, if they are different from true values, the fitting will not converge (Wang et al., 2019). The brightness temperature computed on the basis of satellite sources is based

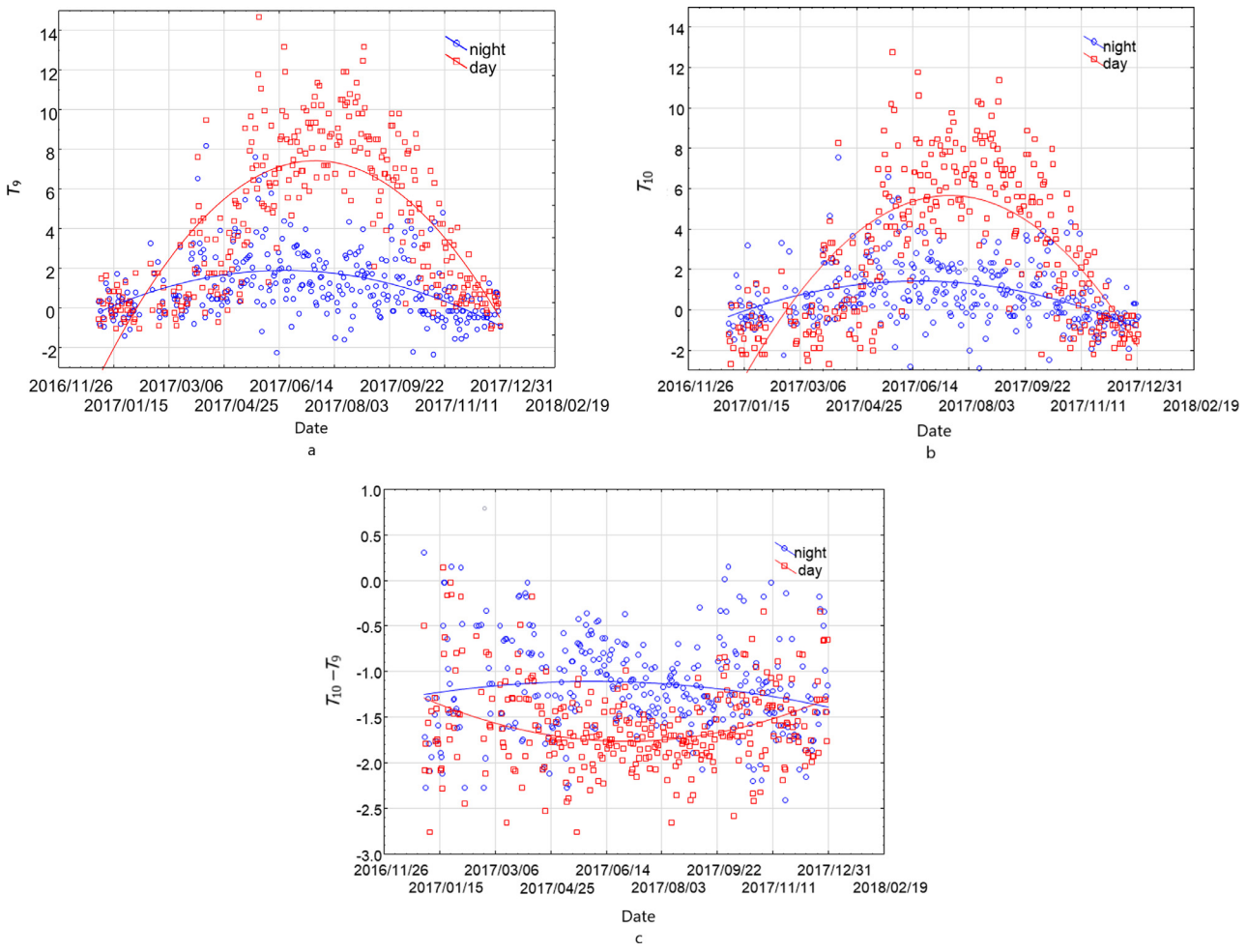

Figure 6 A comparison of daytime and night-time MSG data series cloudless sea in 2017: a) Radiation temperatures in channel 9; b) Radiation temperatures in channel 10; c) Difference between the (10—9) radiation temperatures for the BalticBeta station. Filled shapes for May 17.

on Planck's law, but *SST* (determined by the M3D), used to calculate the brightness temperature under cloudless conditions, not necessarily does. The temperature ratio proposed in this study includes the *SST* with an identical value within channels 9 and 10, multiplied by the linear factor. Unfortunately, in reality, brightness temperatures differ across different spectral ranges, although the difference may be small. Generally, the source of temperature may be of no importance if multiplied by the fourth root of the emissivity coefficient. In an appropriate channel, the result is the emission temperature in this spectral channel. According to the Stefan—Boltzmann law, the amount of thermal radiation estimated for a satellite channel from brightness temperature is:

$$\begin{aligned} L &= \varepsilon\sigma SST_{M3D}^4 \\ L &= T^4 \\ L &= (\varepsilon)^{\frac{1}{4}}\ SST_{M3D}. \end{aligned} \tag{4}$$

According to Masuda et al. (1988), at the wavelength of 10.8 μm (SEVIRI channel 9) and at the latitude of the Baltic Sea (SZA of about 60°), emissivity is about 0.967. Obviously, the emissivity determined this way will additionally depend on the SZA and wind speed; including these factors will produce the constant A as shown in Table 2. The coefficients calculated are the fourth roots of the emissivity coefficient. Figure 7 provides a comparison between results obtained with the algorithm proposed earlier, broken down into successive approach 1 with Eq. (1), approach 2 with Eq. (3) and approach 3 with Eq. (4). With such approaches, however, the daytime and night-time data are difficult to compare because the situations are completely different. This will be important for the identification of the common parameter which affects, e.g. the value of transmission or emission. Within 24 hours, the temperature of both the clouds and the atmosphere can vary significantly. In the algorithm, *SST* is of only auxiliary importance. It will never be ideal, because it stems from theoretical estimation. Therefore, emissivity was determined empirically, that is, cloudless events were selected — in a controlled manner — for pixels T_9 and T_{10}. Figure 6 shows the relationships (for 2017) between brightness temperatures measured at 12:00 and 00:00 UTC in channels 9 and 10 and the differences between them. Calculations were made for areas identified as cloudless, conditionally and simultaneously at 12:00 and 00:00 UTC.

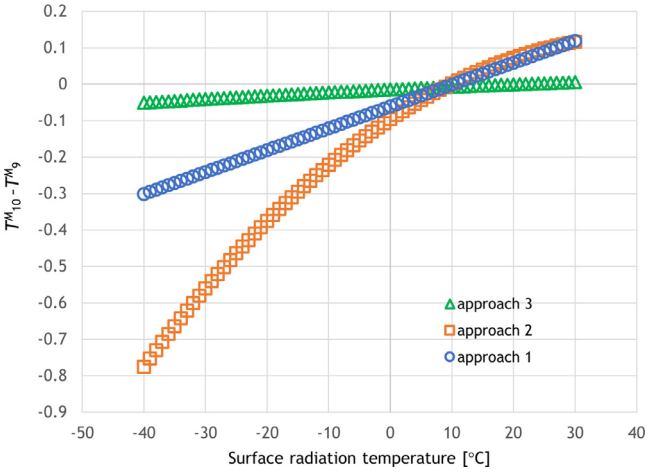

Figure 7 Evolution of the IR cloudiness algorithm: a modelled difference between satellite channels as a function of the surface radiation temperature.

Figure 6 allows us to conclude that during the day the sea warms up in synchrony with the solar zenith angle (in summer and spring the most) and tends to cool down during the night. The previously mentioned example of May 17 (Figure 1) was marked with filled shapes. It is not the cooling-down itself that is interesting, but its extent. Statistically, the cooling-down effect is included in radiation budgets; unfortunately, however, it cannot be observed in radiation models, e.g. in the M3D. To demonstrate the changes in the physical properties of the water during the night, an additional analysis of the $T_{10}-T_9$ difference was included in Figure 6c. This way, we learned that physical properties of the water do undergo diel changes. This confirms the hypothesis that, if cloudiness is derived from IR channels, different methods ought to be used for the night and for the day. Interpretation of the effect during the daytime in the VIS range is undoubtedly related to absorption and to evaporation at night. The general formulae showed in the functional diagram (approximation 1, Figure 7) should be modified to better fit the regional conditions by means of non-linear combination of the Planck function and the spectral wave length (approach 2 and approach 3, Figure 7). It is assumed that the relationship between radiation in two neighbouring spectral bands is non-linear, whereby the diel period should be divided into at least two zones: the daily and nightly zone:

$$T^M = \frac{c_1 k}{\left(\ln\left(\frac{c_2 k^3}{SST_{M3D}} + 1\right) - \mathrm{B}\right)\mathrm{C}}, \tag{5}$$

where T^M equals brightness temperature [K], k equals wave number [m^{-1}]; c_1=0.014388 K m, and c_2=119.10659 mW sr^{-1} m^{-7} are empirical constants; while the remaining values are the same as defined in Table 2 (EUMETSAT, 2007; EUMETSAT, 2012). In the last approximation, for a more effective illustration of the difference between the day and the night, we applied Planck's radiation law directly. This time, we used the calibration values of the satellite radiometer as measured prior to launching. The brightness temperature can be estimated as:

$$T^M = a_0 + a_1 T_S + a_2 T_S^2, \tag{6}$$

where:

$$T_s = \frac{ch}{\kappa\lambda(ln(\frac{2c^2h}{\lambda^5 SST_{M3D}} + 1) - B)C},$$

a_0, a_1 and a_2 are constants fitted to every SEVIRI band, available from the European Space Agency catalogue.

Like earlier, the SST_{M3D} is calculated for each pixel by the M3D. The remaining constants are defined in Table 2. The development of the cloudiness algorithm from long wavelength channels in Table 1 generally involved a technical fitting of the formula to the constraints of the satellite device. This should restrict the uncertainties generated by the first approximation. The solutions proposed treat the cloudiness data (for brightness temperatures >-3°C) and clear sea in a characteristic manner. The second Eq. (3) and third Eq. (4) approximations involve the non-linear Planck's law (Figure 7). The difference between the channels is most pronounced in the second approximation: while considering channels with the ability of remarkable cloud detection, the differences are in agreement with the first approximation Eq. (1), and the differences for temperatures corresponding to cloudy pixels are considerable. The general underestimation and overestimation of satellite cloud detection was analysed taking into account the full available channel range. In the analysis, they were taken into account according to the detection algorithm. However, there is a high risk for cloud cover to be overestimated and for clear pixels to be classified as cloudy. Approximation 3, Eq. (4), produced a completely different pattern. While retaining non-linearity, it poorly reflected the difference. Results of comparing the approximations shown in Figure 7 along with estimations from short wavelength channels proposed below are discussed in the next section. As the cloudiness (extent and type of clouds) changes, the magnitude of the satellite signal recorded alters as well. As demonstrated above, this also affects the change in the VIS radiation difference between the neighbouring satellite channels. Under cloudless conditions, the difference remains more or less stable. The values can be estimated from a radiation model, e.g. the Solrad model (Krężel and Paszkuta, 2011; Krężel et al., 2008). Such operations require estimation of the radiation from the Earth surface to the satellite radiometer.

3.2. Comparison of calculated and estimated equivalents of cloud cover

The methods described above were used to determine the unitless equivalent of cloudiness, an equivalent of the 'cloud fraction' calculated from external sources due to different terminology used in the literature to define the same cloudiness variable for the marine environment. The validation involved both qualitative and quantitative aspects. Estimations were performed for instantaneous and temporary averaged situations. The qualitative analysis of the cloudiness product involved a comparison between irradiance data series recorded in 2017 by stationary instruments at Lotos Baltic Beta stations (55°28′50.67″N, 18°10′54.03″E) (data from the SatBaltic portal). Information on the empirical data used is detailed in the publication by Zapadka et al. (2020). The comparison of in situ data with cloudiness val-

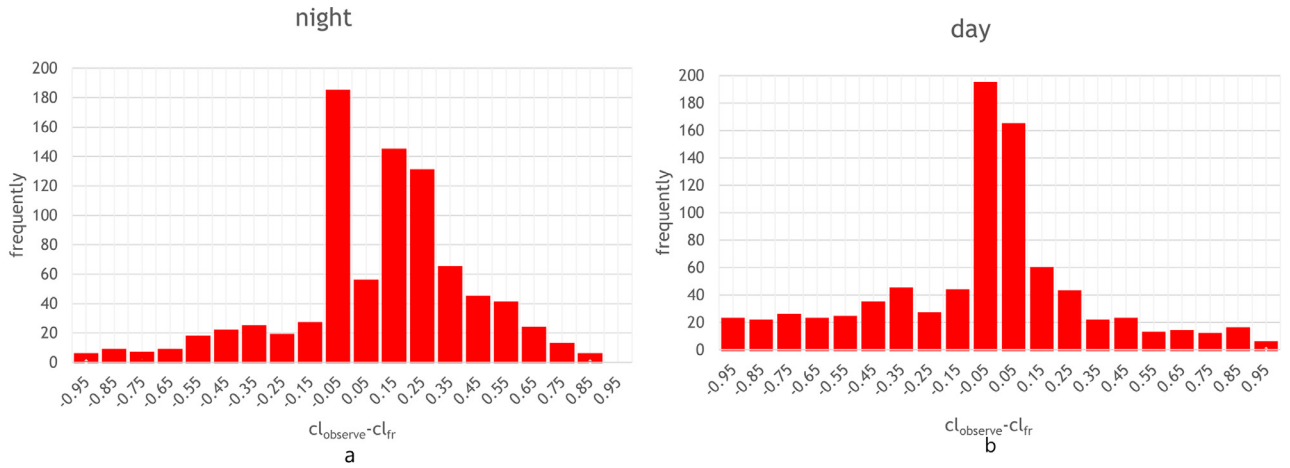

Figure 8 Distribution of the differences between the cloudiness estimated in situ and calculated from satellite data: a) at night (data collected during the day was applied to the night-time algorithm); b) during the day; the data was collected on 26 April 2019 on board of the r/v *Oceanograf*.

ues estimated from the satellite-derived data requires generalisation of reference points assigned not only to the place, but also to the time of the nearest available projection. This pertains to both VIS and IR routines. Therefore, most of similar analyses show fairly large uncertainties associated primarily with the methodology of the measurement itself, and use radiation information collected during the day. At this stage, estimation showed about 80% of the cases to be estimated correctly, which means that in 20% of the cases the algorithm may be 100% wrong: cloudless areas may be interpreted as completely clouded (in IR situations) and vice versa.

Figure 8 shows the distribution of differences between the cloudiness equivalent estimated on land ($cl_{observe}$) and calculated from satellite data for the night (clfrIR, Figure 8a) and the day (clfrVIS, Figure 8b). The largest discrepancies occur when the value of a pixel is estimated by averaging a totally cloudless and clouded area. The former situation may be rectified by appropriately testing the channels, while the latter may be corrected by applying appropriate validation techniques and procedures. The remaining differences are most likely caused by the detection methodology. Figure 8 shows exclusively the daytime data series, i.e. for SZA less than 67°, the cloudiness was estimated with the night-time algorithm for measurements taken during the day (in the long waveband channels only). Calculations for the night-time scenario in Figure 8b, conducted with an algorithm published by Paszkuta et al. (2019) showed the mean of 0.06, standard deviation of 0.34, and the correlation coefficient of 0.66. Figure 8a illustrates the distribution of the differences between the cloud cover estimated with the daytime routine (in the shortwave-band channels); while deviations that appear due to the precision of waveband range were calculated from the solar constant and the Solrad results for cloudless atmosphere. The difference between the estimated cloudiness for the daytime routine showed the mean error of 0.12, standard deviation of 0.26, and the correlation coefficient of 0.77. In order to restrict the error of measurement, our further analysis involved routines that show the best characteristics, with the methodological error reduced to the minimum under the current conditions. The quantitative characteristics were applied for the entire 2017 for data acquired with different detection systems and satellite devices.

4. Discussion

The cloud factor (Paszkuta et al., 2019) was averaged temporally and compared with the unitless cloudiness parameter (tentatively termed the 'cloudiness equivalent' because of the need to standardise the results within 0—100%) produced by various satellite systems available on line: APOLLO (The Cloud Physical Properties Royal Netherlands Meteorological Institute) (Kriebel et al., 2003), CM SAF (The Satellite Application Facility on Climate Monitoring) (Finkensieper et al., 2018), MODISCP (The Moderate Resolution Imaging Spectroradiometer Cloud Product) (Platnick et al., 2017) and CALIPSO—CALIOP (Cloud-Aerosol Lidar Pathfinder Satellite Observations—Cloud-Aerosol Lidar with Orthogonal Polarization) (Chepfer et al., 2008; Winker et al., 2009). It should be mentioned that these systems compute data separately for the shortwave and longwave bands, using different satellite sources, thus rendering the analysis still more valuable. Figure 9 illustrates the relationship between cloudiness (termed differently and variously standardised in different systems, hence the general term 'equivalent') that has been normalised for the needs of this study to the common conversion factor in the range of 0—100%. Despite substantial differences in instantaneous estimations, the routines show the mean annual cloudiness over the Baltic Sea to be at a similar level of about 64%. As could be expected, the highest and the lowest cloudiness was recorded during winter (November—January) and summer (May—August), respectively. This trend was repeated by all the systems. At the monthly averaging level, substantial differences in the amount of cloudiness, of up to several per cent, can be seen. The increase in the difference between the systems in cloudiness estimations may be associated with the true magnitude of cloudiness which is at its lowest in summer (3—4%) and may be as high as several per cent in winter. Because data from all seasons was used, the

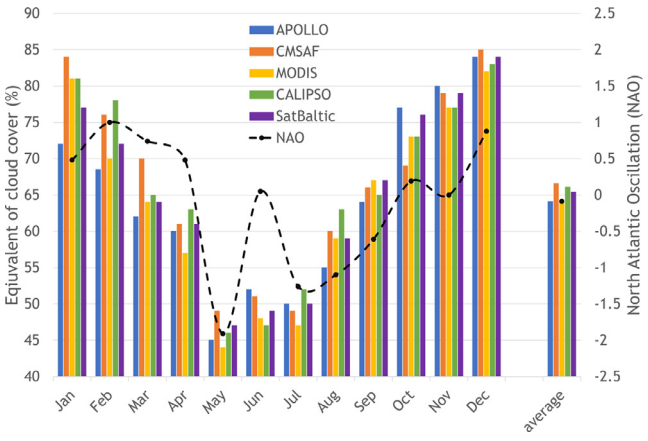

Figure 9 Different estimates of average monthly equivalent of cloud cover (colour-coded), and the NAO index (dashed line) for the Baltic Sea basin in 2017.

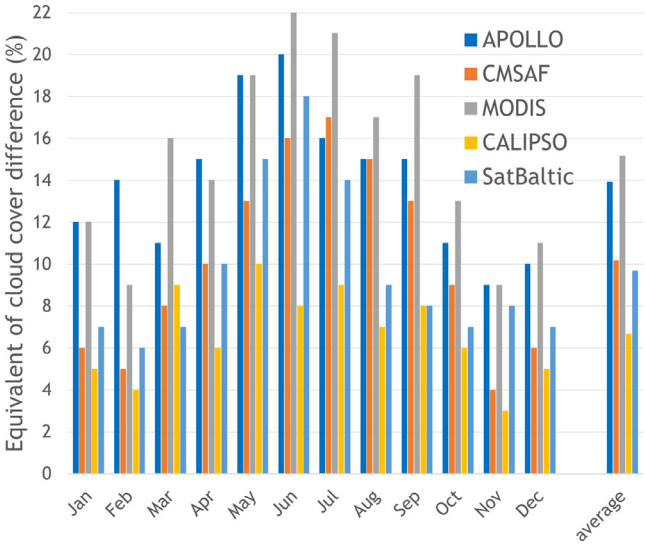

Figure 10 The absolute difference between the cloudiness equivalent determined during the day and at night (%).

impact of meteorological parameters may be significant. In Figure 9, the general weather property is represented by the NAO (North Atlantic Oscillation) index (Jędrasik and Kowalewski, 2019) as a function of cloudiness. The quantitative dependence of variables is represented by the dashed line. The NAO oscillates in the positive (NAO $>$ 0) and negative (NAO $<$ 0) directions. The positive phase represents the period of the strong Azores and deep Icelandic Atmospheric Lows, which move large air masses containing heat and moisture to the area of Northern Europe (including the Baltic Sea). As a result of low movement (from the west to the east), there is an increase in cloud cover/reduction of direct upwelling radiation, the number of storms and an increase in wind speed (Jędrasik and Kowalewski, 2019). There are thaws in winter, and frequent rainfall and temperature drops in summer. During the negative phase, there are opposing conditions, as humid air masses are moved by baric systems (weaker by the Azores High and shallower by the Icelandic Lows) towards the Mediterranean Sea. Continental masses from the east and north-east flow to the area of Northern Europe, which consequently generates sunny and cloudless summers and severe winters with reduced cloudiness. In Figure 9, the monthly trend of cloudiness in 2017 shows a decrease from January (about 80%) to May (20%), a slight increase in June and July (a little over 30%), and a regular increase from August to December (40% to 90%, respectively). Almost simultaneously, the fluctuations of the NAO index rise from the positive phase (NAO = 1.6 in January) and fall to −2.0 in May, then alternately rise and fall to the negative phase in June and July. In the subsequent period that year, from August to December (fall–winter), the index value rose to 0.95, thus indicating a transition to the positive phase. The correlation seems to be obvious, as the decrease of cloud cover at the beginning of the year follows the decrease of the NAO index, which, during the winter, represented the conditions of intense Atlantic circulation over the Baltic Sea. Light cloudiness causes the solar radiation to increase. Slight variations (increase in June and decrease in July) in cloudiness are accompanied by an increase in the values of the (negative) NAO index. From August to December, there is a steady increase in cloudiness and a shift of the NAO index from the negative to the positive phase, characterised by a return to the Atlantic circulation.

The dominance of the positive phase in the autumn–winter period in the Baltic Sea area confirms the crucial role of the winter circulation in the NAO/North Atlantic Oscillation (Hurrel, 1995). More discussion on the conditions of the NAO index in relation to cloudiness in the Baltic Sea is presented by Gomis et al. (2008), Jędrasik (2019), Lehmann et al. (2002), Ruiz et al. (2008). Generally, data averaging increases the similarity between the methods: the longer the data series averaged, the more convergent the results. For the needs of this research, due to the nature of the measurements, it may be assumed that the lowest cloudiness deviations were obtained with measurements conducted with the active CALIPSO methods. Using this data series as a reference, the methods producing higher and lower values can be treated as over- and underestimating the measurements, respectively. Figure 10 shows the relationship between the absolute differences in cloudiness estimated during the day and at night. The differences between the methods used are fairly distinct and range from a few to several per cent. Should the differences be more or less consistent, an effect of the physical parameters of cloudiness could be suspected, but the differences suggest a methodological issue with most of the data sources, which can be rectified technically. The difference increases in summer, i.e. when the estimated cloud cover is at its lowest. The absolute difference between day and night is not mainly a function of the cloudiness: it is mainly the result of the measurement method. One may try to relate it to the day-to-night length ratio, particularly in winter for the northern areas of the Baltic Sea when darkness prevails over much of the diel cycle. As could be expected, the lowest difference was shown by the CALIPSO data series. The value of 8% is closest to the absolute day vs. night difference. Disregarding the averaging effects and lidar data modelling, it may be assumed that the differences between various systems result from the methodology of cloudiness assessment. Chepfer et al. (2019) combine satellite observations of cloud profiles and relative humidity profiles to document

diurnal variations in water vapour and vertical cloud distribution. While the average daily water vapour and cloud profiles are different over the land and the ocean, their day-to-day changes from their daily averages have similar characteristics. The relative humidity and optically thin cloud fraction profiles change together, reaching the maximum values in the troposphere at night and the minimum values during the day. It has been shown that when atmosphere over terrestrial regions shows a diurnal positive anomaly for low thin clouds, there are positive anomalies of opaque clouds in the lower atmosphere over oceanic regions in the second half of the night, which continue to grow until sunrise. According to Bergman et al. (1996), most of the diurnal variation in cloudiness is explained by regressions of only three variables: the daily solar position, the surface temperature, and the cloud level. The diurnal variability of cloudiness does not show a strong correlation with any climatological variable, as the variations are geographically independent and thus highly consistent spatially. Bergman et al. (1997), studied the diurnal variation of cloudiness over time and found that the effect of clouds on radiative fluxes is due to the diurnal variation of their properties. Time-averaged energies are obtained from radial transfer calculations in which cloud cover, temperature, and humidity are estimated from satellite observations.

5. Conclusions

Results obtained with the algorithm proposed showed the average cloudiness at night to be higher by a few per cent than during the day, the results being similar to those produced by standard routines. This difference may stem from natural or procedural causes. Therefore, regional algorithms should not rule out the natural character of the marine environment. However, results of similar satellite-based estimations should be treated with utmost caution because detection methods remain the primary source of uncertainty, which is usually explained by technical problems associated with low quality of the data. Unfortunately, there is no reliable information which would confirm that the changes over the Baltic Sea are significant enough to modify atmospheric circulation and increase/decrease the cloud amount by several per cent, which would suggest a natural cause of the changes. As the location and even the time of the uncertainty are known, it is possible to develop a targeted correction method. For this reason, application of the algorithm results to environmental studies on a regional scale should consider the factors that have a potential to improve the reliability of data. The obtained results can be successfully used to determine the average cloud cover metrics over the Baltic Sea because the analysis is inter-seasonal and climate comparisons do not show much correlation. Finally, the procedural factors responsible may be associated with radiation transmission through the atmosphere and, obviously, with the conditions of the solar radiation flux.

References

Anthis, A.I., Cracknell, A.P., 1999. Use of satellite images for fog detection (AVHRR) and forecast of fog dissipation (METEOSAT) over lowland Thessalia, Hellas. Int. J. Remote Sens. 20, 1107—1124. https://doi.org/10.1080/014311699212876

Banks, A., Melin, F., 2015. An Assessment of Cloud Masking Schemes for Satellite Ocean Colour Data of Marine Optical Extremes. Int. J. Remote Sens. 36, 797—821. https://doi.org/10.1080/01431161.2014.1001085

Bennouna, Y.S., Curier, L., de Leeuw, G., Piazzola, J., Roebeling, R., de Valk, P., 2010. An automated day-time cloud detection technique applied to MSG-SEVIRI data over Western Europe. Int. J. Remote Sens. 31, 6073—6093. https://doi.org/10.1080/01431160903376399

Bergman, J.W., Salby, M.L., 1996. Diurnal variations of cloud cover and their relationship to climatological conditions. J. Climate 9 (11), 2802—2820. https://doi.org/10.1175/1520-0442(1996)009⟨2802:DVOCCA⟩2.0.CO;2

Bergman, J.W., Salby, M.L., 1997. The role of cloud diurnal variations in the time-mean energy budget. J. Climate 10 (5), 1114—1124. https://doi.org/10.1175/1520-0442(1997)010⟨1114:TROCDV⟩2.0.CO;2

Chepfer, H., Brogniez, H., Noel, V., 2019. Diurnal variations of cloud and relative humidity profiles across the tropics. Sci. Rep-UK 9, 16045. https://doi.org/10.1038/s41598-019-52437-6

Chepfer, H., Cesana, G., Winker, D., Getzewich, B., Vaughan, M., Liu, Z., 2013. Comparison of two different cloud climatologies derived from CALIOP attenuated backscattered measurements (Level 1): the CALIPSO-ST and the CALIPSO-GOCCP. J. Atmos. Ocean. Tech. 30, 725—744. https://doi.org/10.1175/JTECH-D-12-00057.1

Chepfer, H., Bony, S., Winker, D.M., Chiriaco, M., Dufresne, J.-L., Seze, G., 2008. Use of CALIPSO lidar observations to evaluate the cloudiness simulated by a climate model. Geophys. Res. Lett. 35, 1—6. https://doi.org/10.1029/2008GL034207

Cracknell, A.P., 1997. The Advanced Very High Resolution Radiometer AVHRR. Taylor & Francis, London, 1—556.

EUMETSAT, 01 17, 2007. Radiometric Calibration of MSG SEVIRI Level 1.5 Image Data in Equivalent Spectral Blackbody Radiance, Doc. No.: EUM/OPS-MSG/TEN/03/0064, 26. https://www.eumetsat.int

EUMETSAT, 10 25, 2012. Conversion from radiances to reflectances for SEVIRI warm channels. Description of the conversion from radiance to reflectance for the SEVIRI reflective bands (VIS06, VIS08, NIR16 and HRV), 6. http://www.eumetsat.int

Finkensieper, S., Stengel, M., Selbach, N., Hollmann, R., Werscheck, M., Meirink, F., 2018. J. ICDR SEVIRI Clouds — based on CLAAS-2 methods, Satellite Application Facility on Climate Monitoring. https://wui.cmsaf.eu

Gomis, D., Ruiz, S., Sotillo, M.G., Álvarez-Fanjul, E., Terradas, J., 2008. Low frequency Mediterranean sea level variability: The contribution of atmospheric pressure and wind, Global Planet. Change 63, 215—229. https://doi.org/10.1016/j.gloplacha.2008.06.005

Hurrell, J.W., 1995. Decadal Trends in the North Atlantic Oscillation. Science 269, 676—679. https://doi.org/10.1126/science.269.5224.676

Jakobson, E., Keernik, H., Luhamaa, A., Ohvril, H., 2014. Diurnal variability of water vapour in the Baltic Sea region according to NCEP-CFSR and BaltAn65+ reanalyses. Oceanologia 56 (2), 191—204. https://doi.org/10.5697/oc.56-2.191

Jedlovec, G., 2009. Automated detection of clouds in satellite imagery. Adv. Geosci. Remote Sens. 303—316. https://doi.org/10.5772/8326

Jędrasik, J., 2019. Modelowanie retrospektywne i prognozowanie hydrodynamiki Morza Bałtyckiego, Gdańsk, UG, 190 pp.

Jędrasik, J., Kowalewski, M., 2019. Mean annual and seasonal circulation patterns and long-term variability of currents in the Baltic Sea. J. Marine Syst. 193, 1—26. https://doi.org/10.1016/j.jmarsys.2018.12.011

Kaczmarek, S., Dera, J., 1998. Radiation flux balance of the sea-atmosphere system over the southern Baltic Sea. Oceanologia 40, 277—306.

Kowalewska-Kalkowska, H., Kowalewski, M., 2019. Combining Satellite Imagery and Numerical Modelling to Study the Occurrence of Warm Upwellings in the Southern Baltic Sea in Winter. Remote Sens.-Basel. 11 (24), 2982. https://doi.org/10.3390/rs11242982

Kowalewski, M., 1997. A three-dimensional, hydrodynamic model of the Gulf of Gdańsk. Oceanol. Stud. 26 (4), 77—98.

Krężel, A., Kozłowski, Ł., Paszkuta, M., 2008. A simple model of light transmission through the atmosphere over the Baltic Sea utilising satellite data. Oceanologia 50 (2), 125—146.

Krężel, A., Paszkuta, M., 2011. Automatic Detection of Cloud Cover over the Baltic Sea. J. Atmos. Ocean. Tech. 28, 1117—1128. https://doi.org/10.1175/JTECH-D-10-05017.1

Kriebel, K.T., Gesell, G., Kästner, M., Mannstein, H., 2003. The cloud analysis tool APOLLO: improvements and validations. Int. J. Remote Sens. 24 (12), 2389—2408. https://doi.org/10.1080/01431160210163065

Kriebel, K.T., Saunders, R.W., Gesell, G., 1989. Optical properties of clouds derived from fully cloudy AVHRR pixels. Beiträge zur Physik der Atmosphäre 62, 165—171.

Kryvobok, O., Senesi, S., Morel, C., 2005. Using Meteosat second generation high resolution visible data for the improvement of the rapid developping thunderstorm product. World Weather Research, Programme Symposium on Nowcasting and Very Short Range Forecas. Toulouse, France.

Latos, B., Lefort, T., Flatau, M.K., Flatau, P.J., Permana, D.S., Baranowski, D.B., Paski, J.A.I., Makmur, E., Sulystyo, E., Peyrillé, P., Feng, Z., Matthews, A.J., Schmidt, J.M., 2021. Equatorial Waves Triggering Extreme Rainfall and Floods in Southwest Sulawesi, Indonesia. Mon. Weather Rev. 149 (5), 1381—1401. https://doi.org/10.1175/MWR-D-20-0262.1

Lehmann, A., Krauss, W., Hinrichsen, H.-H., 2002. Effects of remote and local atmospheric forcing on circulation and upwelling in the Baltic Sea. Tellus A 54 (3), 299—316. https://doi.org/10.3402/tellusa.v54i3.12138

Li, X., Zheng, H., Han, C., Wang, H., Dong, K., Jing, Y., Zheng, W., 2020. Cloud Detection of SuperView-1 Remote Sensing Images Based on Genetic Reinforcement Learning. Remote Sens.-Basel. 12 (19), 3190. https://doi.org/10.3390/rs12193190

Mahajan, S., Fataniya, B., 2020. Cloud detection methodologies: variants and development—a review. Complex & Intelligent Systems 6, 251—261. https://doi.org/10.1007/s40747-019-00128-0

Masuda, K., Takashima, T., Takayama, Y., 1988. Emissivity of pure and sea waters for the model sea surface in the infrared window regions. Remote Sens. Environ. 24 (2), 313—329. https://doi.org/10.1016/0034-4257(88)90032-6

Paszkuta, M., Zapadka, T., Krężel, A., 2019. Assessment of cloudiness for use in environmental marine research. Int. J. Remote Sens. 40 (24), 9439—9459. https://doi.org/10.1080/01431161.2019.1633697

Platnick, S., Meyer, K., King, M.D., Wind, G., Amarasinghe, N., Marchant, B., Arnold, G.T., Zhang, Z., Hubanks, P.A., Holz, R.E., Yang, P., Ridgway, W.L., Riedi, J., 2017. The MODIS cloud optical and microphysical products: Collection 6 updates and examples from Terra and Aqua. IEEE T. Geosci. Remote 55, 502—525. https://doi.org/10.1109/TGRS.2016.2610522

Post, P., Aun, M., 2020. Changes in satellite-based cloud parameters in the Baltic Sea region during spring and summer (1982—2015). Adv. Sci. Res. 17, 219—225. https://doi.org/10.5194/asr-17-219-2020

Reuter, M., Fischer, J., 2014. A comparison of satellite-retrieved and simulated cloud coverage in the Baltic Sea area as part of the BALTIMOS project. Theor. Appl. Climatol. 118, 695—706. https://doi.org/10.1007/s00704-009-0208-8

Rozwadowska, A., 2004. Optical thickness of stratiform clouds over the Baltic inferred from on-board irradiance measurements. Atmos. Res. 72, 129—147. https://doi.org/10.1016/j.atmosres.2004.03.012

Ruiz, S.D., Gomis, M.S., Josey, S., 2008. Characterization of surface heat fluxes in the Mediterranean Sea from a 44-year high-resolution atmospheric data set, Global Planet. Change 63 (2—3), 258—274. https://doi.org/10.1016/j.gloplacha.2007.12.002

Saunders, R.W., Kriebel, K.T., 1988. An improved method for detecting clear sky and cloudy radiances from AVHRR data. Int. J. Remote Sens. 9, 123—150. https://doi.org/10.1080/01431168808954841

Wang, M., He, G., Zhang, Z., Wang, G., Wang, Z., Yin, R., Cui, S., Wu, Z., Cao, Xi., 2019. A radiance-based split-window algorithm for land surface temperature retrieval: Theory and application to MODIS data. Int. J. Appl. Earth Obs. 76, 204—217. https://doi.org/10.1016/j.jag.2018.11.015

Winker, D.M., Vaughan, M.A., Omar, A., Hu, Y., Powell, K.A., 2009. Overview of the CALIPSO mission and CALIOP dataprocessing algorithms. J. Atmos. Ocean. Tech. 26, 2310—2323. https://doi.org/10.1175/2009JTECHA1281.1

Woźniak, B., Bradtke, K., Darecki, M., Dera, J., Dudzińska-Nowak, J., Dzierzbicka-Głowacka, L., Ficek, D., Furmańczyk, K., Kowalewski, M., Krężel, A., Majchrowski, R., Ostrowska, M., Paszkuta, M., Stoń-Egiert, J., Stramska, M., Zapadka, T., 2011a. SatBaltic — a Baltic environmental satellite remote sensing system- an ongoing project in Poland. Part 1: Assumptions, scope and operating range. Oceanologia 53 (4), 897—924. https://doi.org/10.5697/oc.53-4.897

Woźniak, B., Bradtke, K., Darecki, M., Dera, J., Dudzińska-Nowak, J., Dzierzbicka-Głowacka, L., Ficek, D., Furmańczyk, K., Kowalewski, M., Krężel, A., Majchrowski, R., Ostrowska, M., Paszkuta, M., Stoń-Egiert, J., Stramska, M., Zapadka, T., 2011b. SatBaltic — a Baltic environmental satellite remote sensing system — an ongoing project in Poland. Part 2: Practical applicability and preliminary results. Oceanologia 53 (4), 925—958. https://doi.org/10.5697/oc.53-4.925

Zapadka, T., Krężel, A., Paszkuta, M., Darecki, M., 2015. Daily radiation budget of the Baltic sea surface from satellite data. Pol. Marit. Res. 22 (3), 50—56. https://doi.org/10.1515/pomr-2015-0056

Zapadka, T., Ostrowska, M., Stoltmann, D., Krężel, A., 2020. A satellite system for monitoring the radiation budget at the Baltic Sea surface. Remote Sens. Environ. 240, 11683. https://doi.org/10.1016/j.rse.2020.111683

Oceanologia 64 (2022) 312—326

Available online at www.sciencedirect.com

ScienceDirect

journal homepage: www.journals.elsevier.com/oceanologia

ORIGINAL RESEARCH ARTICLE

Regime shift in sea-ice characteristics and impact on the spring bloom in the Baltic Sea

Ove Pärn[a,*], **René Friedland**[b], **Jevgeni Rjazin**[c], **Adolf Stips**[a]

[a] *European Commission, Joint Research Centre, Ispra, Varese, Italy*
[b] *Leibniz-Institute for Baltic Sea Research Warnemünde, Rostock, Germany*
[c] *Hereditas, Tartu, Estonia*

Received 31 May 2021; accepted 14 December 2021
Available online 29 December 2021

KEYWORDS
Climate change;
Ecosystem;
Biogeochemical model;
Sea surface temperature;
Chlorophyll-a concentration

Abstract We evaluated the temporal and spatial trends of the hydrological (temperature and sea ice) and biochemical (chlorophyll-a concentration) characteristics in springtime in the Baltic Sea. Both are strongly affected by climate change, resulting in a decrease in the duration of sea-ice melting in the previous decade. A new regime of sea ice began in 2008 and in all basins of the Baltic Sea, a rapid warming during spring could be detected. Using satellite data, the temporal and spatial variations in spring bloom were analysed during severe and warmer winters. Using a coupled hydrodynamic-biogeochemical model, we tested the response of spring bloom to the changing ice conditions. The results of the modelling indicated that the presence of ice significantly influences the predicted chlorophyll-a concentration values in the Baltic Sea. Therefore, it is necessary that any coupled model system has a realistic ice model to ensure the best simulation results for the lower trophic food web as well.

1. Introduction

The Baltic Sea is a semi-enclosed, brackish regional sea with a unique large-scale gradient from temperate marine to subarctic climate. Located in Northern Europe, the Baltic Sea is seasonally covered with ice (Leppäranta and Myrberg, 2009). Its ecosystem is dominated by a strong salinity gradient (Zettler et al., 2014) and is simultaneously threatened by eutrophication (Norbäck Ivarsson et al., 2019), pollution from hazardous substances and marine litter (Abalansa et al., 2020; HELCOM 2018; Selin and Van-Deveer 2004), and climate changes (Murray et al., 2019), which make the sea extremely vulnerable.

* Correspondening author at: European Commission, Joint Research Centre, Ispra, Varese, Italy.
E-mail address: ove.parn@ext.ec.europa.eu (O. Pärn).
Peer review under the responsibility of the Institute of Oceanology of the Polish Academy of Sciences.

Production and hosting by Elsevier

https://doi.org/10.1016/j.oceano.2021.12.004

This study aimed to (i) describe the melting season of the Baltic Sea and its spatial and temporal variability, (ii) understand the trends of sea ice melting and variability of the sea surface temperature, (iii) analyse the phytoplankton (chlorophyll-a concentration values) during the melting season, and (iv) test the response of spring blooms (concentration peak values) to changes in the sea ice by using a biogeochemical model.

The ice season lasts up to seven months (Vihma and Haapala, 2009) with the typical maximum ice extent in late February and early March (BACC II Author Team, 2015). The melting season starts in March, but the sea ice is observed in the northernmost Bothnian Bay until June (Leppäranta and Myrberg, 2009). The maximum ice extent observed during the mildest winter (2019/20) was only 37 000 km^2 (∼9%), and that in the harshest winter (1986/87) was 407 000 km^2 (97%). Hence, both the ice extent and level of sea ice thickness vary largely (BACC II Author Team, 2015). The sea ice is up to 1.8-m thick (Haas, 2004), and due to the ice drift, ice ridges are typically 5—15 m thick (Leppäranta and Myrberg, 2009), with the maximum drift measured in the Gulf of Finland with 1 m s^{-1} (Lilover, 2018).

Sea ice severely affects turbulent fluxes at the water surface and beyond, influencing the thermodynamics of the ocean and water-mixing. The sea ice and snow cover, which prevent the exchange of heat, CO_2, and other gases among the air, sea and water vaporisation, are good insulators between the ocean and the atmosphere. Furthermore, the sea ice is often covered with snow, which severely influences light attenuation. The albedo of a new snow cover can be up to 0.9, and that of melting bare ice is only 0.4, which is considerably larger than that of the open sea (<0.1) (Vihma and Haapala, 2009). Therefore, a small decrease in the ice or snow cover leads to a large increase in net solar radiations under water.

In early March, the phytoplankton spring bloom starts in the southern parts of the Baltic Sea and extends to the melting sea ice edge of the Gulf of Finland in April (Spilling et al., 2018). Several physical processes drive the spring bloom. First, light availability exhibits a strong impact as the necessary force of primary production (Wasmund et al., 1998). Second, water temperature controls the intensity of most biological and chemical processes (Brierley and Kingsford, 2009). For most fish species, the initial signal of spawning is the crossing of a certain threshold of water temperature. For instance, herring spawning peaks at 5.6°C in the middle Baltic Proper (Jørgensen, 2005). The process rate increases by approximately a factor of 2 per 10°C (Jørgensen, 1994), and climbs up to 2.3 times for zooplankton metabolism (Ivanova, 1985). Thus, changing sea ice conditions not only indicate changing water temperatures but also affect spring bloom timings and phytoplankton species compositions (Klais et al., 2017a, Klais et al., 2017b; Pärn et al., 2021), with further implications on nutrient cycles and ecosystem dynamics (Klais et al., 2013). The presence of sea ice leads to calm conditions under water; thus, most of the heavy plankton (e.g., diatoms) sink below the euphotic zone (∼10 m) with velocities, at times, reaching as high as 15 to 30 m d^{-1} (Passow, 1991); while dinoflagellates stay in the euphotic zone and reproduce (Gemmell et al., 2016; Pärn et al., 2021).

Various climate features including temperature, ice phenomena and ecosystem characteristics can be found in relatively stable regimes, which can last for several decades. However, these states can abruptly change to another regime due to several reasons. The shift of the regime in these features in the Baltic Sea was studied by Hagen and Feistel (2005), Keevallik (2011), Neumann et al. (2011), Stips and Lilover (2010). According to Kahru et al. (2016), the water transparency has decreased since 2007 in the central Baltic Sea. Rjazin et al. (2020) analysed the severity characteristics of the ice season, maximum ice extent and ice cover duration of the winter seasons from 1982—2016. They showed that in the winter of 2007, a shift occurred in the ice severity characteristics. Global warming is a driver of this shift and can severely influence the sea ice season and extent. Friedland et al. (2013) estimated that the sea ice extent may decrease by 20% to 40% by the end of the 21st century, depending on the assumed climate change scenario. In the Baltic Sea, the phytoplankton spring bloom accounts for a large part of annual biomass production (Macias et al., 2020) and bloom timing affects carbon recycling, ∼50% annual carbon fixation is during spring bloom (Lipsewers, 2020). Spring indicates the beginning of the growth season, and spring bloom is the key to pelagic and benthic (secondary) production (Chiswell, 2015; Griffiths, 2017; Spilling et al., 2018). Climate variations in the Baltic Sea affect plankton communities mostly in the beginning of the production season (Käse and Geuer, 2018; Winder and Sommer, 2012). Global warming affects the timing, composition and magnitude of the phytoplankton spring bloom in the Baltic Sea (Hjerne et al., 2019; Meier et al., 2018). This phenomenon has dramatic implications on the food web dynamics and carbon recycling (Winder and Sommer, 2012). The temporal match with zooplankton consumption is disturbed (Winder, 2004).

Biogeochemical models are one key to understanding potential implications (Eilola et al., 2013; Neumann et al., 2012), if these models are able to reproduce the key features of spring bloom. Therefore, realistic ice models are necessary to be able to simulate the timing, composition and magnitude of the phytoplankton spring bloom. During the melting season, in the Baltic Sea, air temperature exceeds water freezing temperature, even when the water body is covered with ice. Marine ecosystem models, using simplified ice calculations, usually ignore the ice cover during the melting period. Because of the ice cover, the effect of wind on water circulation is eliminated, the sunlight is largely reflected back into the atmosphere, and the warm air does not come in direct contact with the water surface. If these processes are ignored, inaccurate model results are obtained for the timing, composition, and magnitude of spring bloom dynamics. Although few biogeochemical models incorporate ice sub-models (Tedesco et al., 2016), only NEMO Nordic and MOM-ERGOM provide an ice model validated against Baltic Sea observation data (Pemberton et al., 2017; Rjazin, 2019, Neumann et al., 2020). Eilola et al. (2013) investigated the impact of sea ice on Baltic Sea biogeochemistry by using an ice model validated by (Meier, 1999). Neumann (2010) applied MOM-ERGOM to estimate that the sea ice extent may decrease by two-thirds due to climate change by the end of

the 21st century, which can lead to an earlier offset of spring bloom up to one month in the Bothnian Sea and Bay.

Climate impact research is important because politicians, decision makers and the society require guidance regarding the environmental effects of global warming. Therefore, sea ice modelling must be corrected to predict spring bloom dynamics to improve biogeochemical models of the Baltic Sea.

2. Material and methods

2.1. Observational data

2.1.1. Sea ice data

The daily ice fractions of the Baltic Sea were provided by the Copernicus Marine Environment Monitoring Service (Von Schuckmann et al., 2018). Ice concentration data was acquired from the Swedish Meteorological and Hydrological Institute (SMHI) at 5.5 km horizontal resolution. Secondly, the ice product (daily ice concentration) of ERA5 was used, which is the latest reanalysis product from the European Centre for Medium-range Weather forecast (ECMWF), covering the 1979–2020 period (Hersbach, 2020). The mean ice extent was determined daily.

This data was used to calculate the ice melting period of the Baltic Sea for the ice seasons of 1982–2020. The ice extent reaches its maximum near the end of February or beginning of March. Therefore, the days before 1st March were not counted to focus purely on the melting period. The average melting time (MT) was computed as follows: 1) calculate the number of days when ice concentration is at least 30% for each grid cell for each year; 2) calculate the spatial average of the number of ice-covered days on the Baltic Sea or sub-basins.

$$MT = \frac{1}{i_{max}} \sum_{1}^{i_{max}} \sum_{d_0}^{n} C_{it} \quad (1)$$

where $C_{it} = 1$; if the ice concentration on the day d in the grid cell i is >30% and 0 otherwise, t_0 is 01 March, and n is the maximal melting season length (days) in the grid cell (110 days), i_{max} is the number of cells in the Baltic Sea or the sub-basin.

Rjazin (2017) defined the characteristic difference of the ice season, which is the difference between the maximum ice extent (Emax) and the ice extent sum (IES). IES describes the ice cover extent from the starting of ice appearance to its end. In normalised form, the IES can be interpreted as the number of ice days, which, daily, considers the ice-covered area.

$$IES = \sum_{t_0}^{t_n} A_t \quad (2)$$

where A_t is the ice cover extent on the day t, t_0 is the ice appearance date, and t_n is the last day of the ice cover. In the reference winter of 1986/87, the maximum ice extent was 97% of the entire Baltic Sea.

We defined ice season characteristics *dch* as the ratio of both values:

$$dch = IES / Emax \quad (3)$$

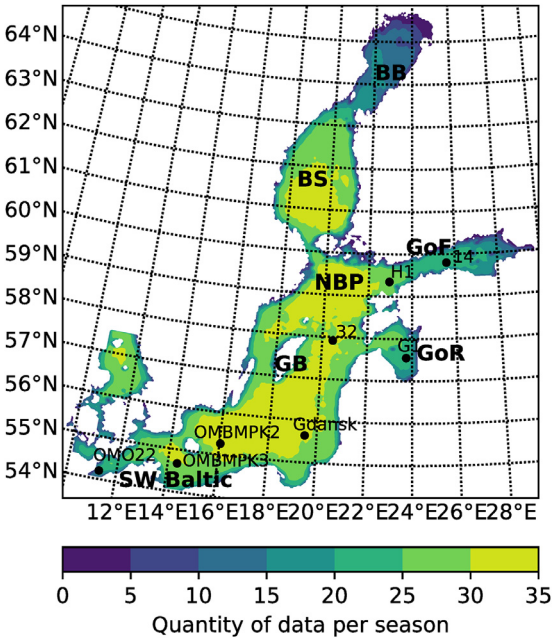

Figure 1 Quantity of chlorophyll data collected during the March, April, and May of 1998–2020 for the stations included in this study.

Emax is the value of the maximal ice extent in a particular season.The regime shift detection method was used to identify regime shifts in the MT time series and dch.

2.1.2. Sea surface temperature (SST) and meteorological data

The Danish Meteorological Institute (DMI) reanalysed the daily sea surface temperature (SST) data on a grid of 0.03° × 0.03° by combining Pathfinder AVHRR satellite data records, along-track scanning radiometer (ATSR) reprocessing for a climate (ARC) dataset, and in situ observations. Validation against an independent set of in situ observations showed a highly stable performance of the reanalysed dataset with the mean deviation and standard deviation (SD) of −0.06 and 0.46°C, respectively, with respect to data from the moored buoys (Von Schuckmann et al., 2018). The meteorological forcing data of the ERA5 reanalysis obtained from the ECMWF for every 6 hours was applied to the model and used for SST.

2.1.3. Chlorophyll-a data

To investigate the annual, monthly, and daily variations in surface chlorophyll-a concentrations, data was used which was provided by the Global Ocean Satellite monitoring and marine ecosystem study group (GOS) of the Italian National Research Council (CNR) with a spatial resolution of 1 km, which was estimated using the BalAlg algorithm (Pitarch et al., 2016). The spring data from March to May for 1998–2020 was extracted. Daily data was unevenly available, especially for the northern part of the Baltic Sea, and only a few observations were available (Figure 1). For 2008 and 2015–2018, we acquired the data of up to 26 days for May for some regions of the Baltic Sea (Figure 2). In March and April 1999, the data of only 8 and 9 days, respectively, were available, and in 2013, the data of 22 days

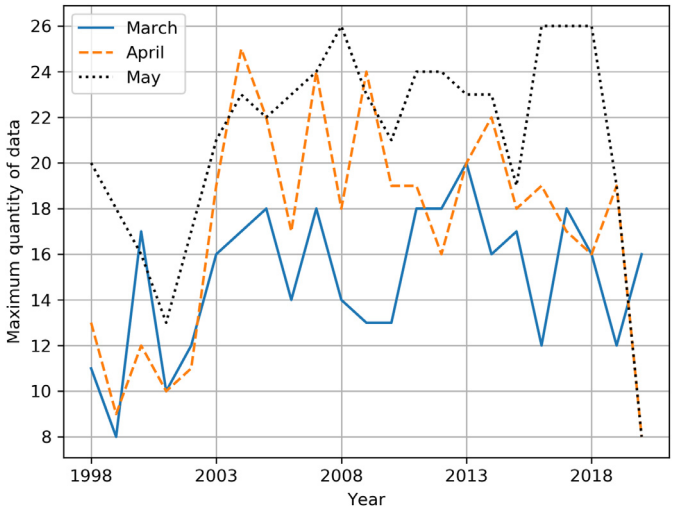

Figure 2 Maximum quantity of satellite data for a single-grid cell during March (solid), April (dashed), and May (dotted).

was available. The rate at which data were recorded fluctuated throughout the study with an increasing trend towards May. There is no day for which satellite data is available for all the 23 years; however, for a minimum of 8 years, data is available for each grid point. On 4 days (16, 22, 23, and 29 May), data was collected for 18 years.

Chlorophyll-a concentration data revealed speckle errors such as large or negative values. Although satellite data was not as accurate as in situ measurement data, this was the only data available for daily measurements covering large parts of the Baltic Sea. The raw satellite data was corrected as follows: (1) only values between 0 and 20 mg m^{-3} were used; (2) the time series was smoothed out with a 5-day moving average to prevent the occurrence of individual high-concentration values; and (3) horizontal smoothing was conducted at each grid point through a weighted average of the grid point and the nearest eight surrounding points. The center point received a weighting of 1, the points on either side and those above and below received a weighting of 0.5, and the corner points received a weighting of 0.3.

2.2. Model description

2.2.1. Setup

Simulations were performed using a coupled three-dimensional model system, comprising a hydrodynamic model GETM (https://getm.eu/; Burchard, 1999; Burchard and Bolding, 2002; Stips, 2004) and a biogeochemical model (ERGOM; www.ergom.net), based on the model described by Neumann (2000). A general ocean turbulence model (GOTM; www.gotm.net) was coupled with the GETM to resolve vertical mixing (Umlauf and Burchard, 2005) and ice existence problems. The default diatom sinking velocity is 0.5 m d^{-1}. Our implementation of the model for the Baltic Sea had a horizontal resolution of 2 × 2 nm and included 25 vertical σ layers with an open boundary in northern Kattegat. Hourly sea level data was interpolated from gauge measurements at Kattegat. The model considers the land-based runoff and nutrient loads that had incorporated into 20 major rivers (Neumann and Schernewski, 2008).

Pärn (2020) provided the main validation for the coupled model. Hydrodynamic features such as salinity, temperature, and surface elevation were well reproduced. The comparison of the modelled SST with satellite data revealed a bias of approximately 0.7°C. The root-mean-square errors (RMSEs) of the sea surface and bottom salinity were 0.3—1.7 PSU. All the modelled eutrophication indicators, chlorophyll-a, oxygen, nitrate, and phosphate followed the dominant seasonal cycles. The simulated chlorophyll-a model was highly suitable to the southern Baltic Sea (RMSE = 0.9), but it was improvable in the ice-covered parts such as the Gulf of Finland.

2.2.2. Model scenarios

The model was applied to study the effects of physical processes on the spring bloom affected by the sea ice. The results of runs A and B were compared and the difference between the two scenarios with respect to the chl-a concentrations was analysed. Six melting seasons, 1986—1987, 1995—1996, 2002—2003, 2009—2010, 2010—2011 and 2012—2013 were modelled, and the biogeochemical model variables had the same initial distributions on 1st March (at the beginning of melting time). Two scenarios were modelled to estimate the ice effect.

In Run (A), we used the ice data obtained from SMHI (section 2.1.1. sea ice data). If the model grid cell was assumed to be ice covered, the water surface temperature was set equal to the freezing point temperature and the wind stress was set to 0. The underwater light conditions were limited due to sea ice. In the case of sea ice, PARi = 0.7*PAR, where PAR is photosynthetically active radiation and PARi is PAR under ice (Lei et al., 2011).

For Run (B), a simple approach was implemented to model ice conditions assuming a minimal thermodynamic ice approximation. When the sea surface temperature (SST) was equal to the freezing temperature, the model grid cell is assumed to be "ice covered", PARi = 0.7*PAR, and the wind stress was set to 0. When the sea surface temperature (SST) was above freezing temperature, the model grid cell is assumed to be open water. The key difference of this approach compared to Run (A) is that the simple "ice" model in Run (B) did not consider ice during spring even though ice

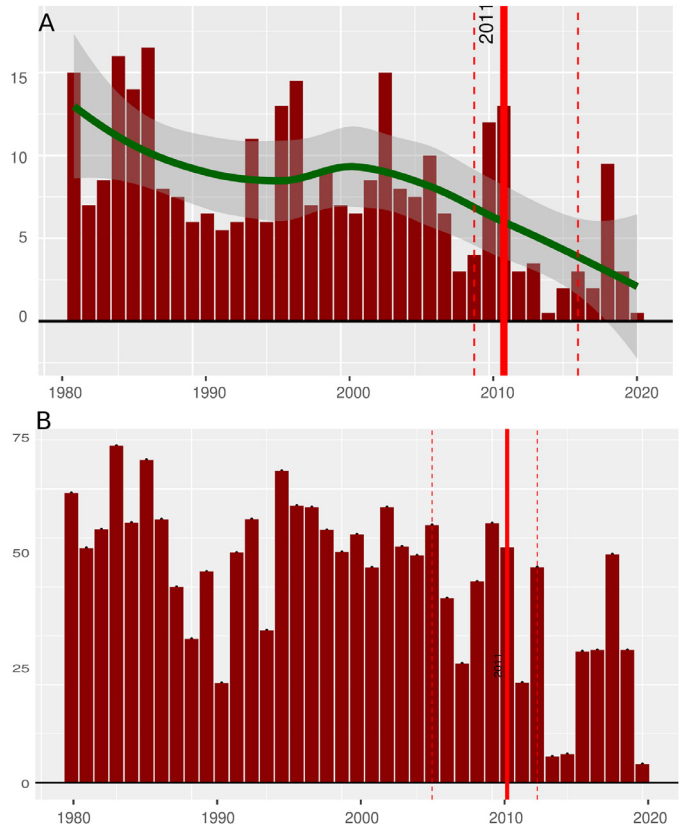

Figure 3 Average ice melting duration (MT) for the Baltic Sea and Bothnian Bay for the years 1982—2020.

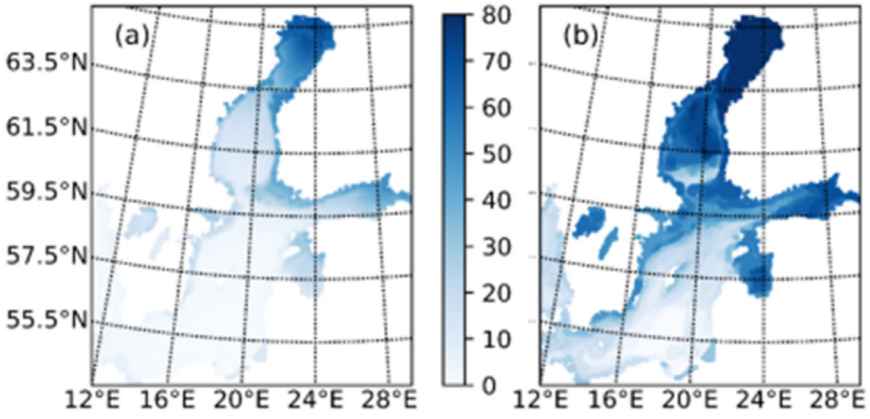

Figure 4 (a) Average number of ice-melting days in the Baltic Sea for 1982—2020 and (b) number of ice-melting days for 1987. SMHI dataset.

cover existed on the sea as seen by satellite data. From this point of view, during the spring bloom, this period is the key issue.

2.3. Regime shift detection methodology

The detection of regime shifts in time series data can be applied to identify points in time when abrupt changes in the data structure occurred. This specific point in time is hereafter referred to as the changepoint.

Several well-documented methods are available for changepoint detection (e.g., (Zeileis, 2003)). These methods are based on solid statistics and can reproducibly identify regime shifts as a significant change in the time series mean. First, Bai (1994, 1997) developed a method that can be used to test the occurrence of a single changepoint in a time series. Bai and Perron (1998) then extended this method to determine multiple changepoints. Rodionov (2004) developed a principally similar method, and other methods are provided in the review by Mantua (2004). We used the method developed by Bai and Perron (2003) and described by (Zeileis, 2003). This method is a widely used technique for the detection of structural changepoints in time series regression models. Their method was implemented in the *strucchange* package of the statistical software **R**, which is freely available on the Comprehensive R Archive Network (CRAN, http://cran.r-project.org/).

The method of Zeileis (2003) is based on a test used to assess deviations from the classical linear regression model. A time series is assumed to have b changepoints, at which the coefficients shift from one stable regression relationship to another. Consequently, b + 1 segments with constant regression coefficients must exist. These optimal segments may be determined through a dynamic programming approach, thereby minimising the residual sum of squares for certain observation intervals. The selected interval search length influences the results. The default value of 0.15 allows a maximum of 5 changepoints to be found in the time series. Therefore, optimising the search interval and maximum number of changepoints searched by using the investigated data is important. The F statistics were used to estimate the optimal number of changepoints, including confidence interval determination. To detect changepoints on an annual time scale, high-frequency contributions (such as seasonal cycles) must be eliminated by applying appropriate filtering or averaging methods before the analysis. Low-frequency oscillations with a period exceeding the selected segment length can lead to changepoint detection. This is especially relevant for the time series with considerable autocorrelations and/or linear trends, which require prewhitening or even trend removal. All the significance tests were used with respect to a 5% error probability threshold. Corresponding confidence intervals are presented in the figures by using a time range indicated with the dashed vertical lines.

3. Results for the melting period

The ice melting time and characteristics of ice seasons analysed for the Baltic Sea used the SMHI and ERA5 database. As the data correlates well with each other (cross correlation 0.9) and refers to the same trends, we used only SMHI data to describe the results. The following sub-basins were used in the analysis: Bothnian Bay (BB), Bothnian Sea (BS), Northern Baltic Proper (NBP), Gulf of Finland (GoF), Gulf of Riga (GoR), Gotland Basin (GB), Southwest Baltic (SWB) (Figure 1).

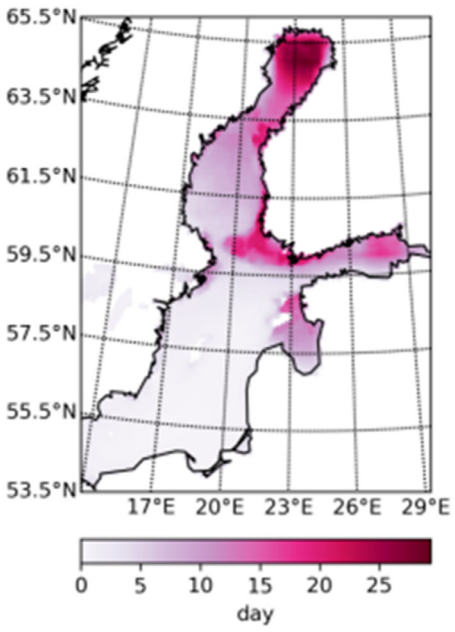

Figure 5 Duration of periods with strong winds (speed > 6 m s^{-1}) in ice-covered areas during the sea-ice melting period. ERA5 wind data of 1982—2020 has been used.

3.1. Duration of the melting time

The sea ice is a prominent feature of the Baltic Sea. The overall Baltic Sea melting time (MT) was acquired for an average of 10.8 days through SMHI data for the studied period (Figure 3). The study period was divided into three parts, 1979—1994, 1995—2007, 2008—2020, the average ice melting time of the period was 14.6 days, 11.6 days and 4.4 days, respectively. Spatial differences were quite large, and thus, the range was from 0 days in the southern and central Baltic

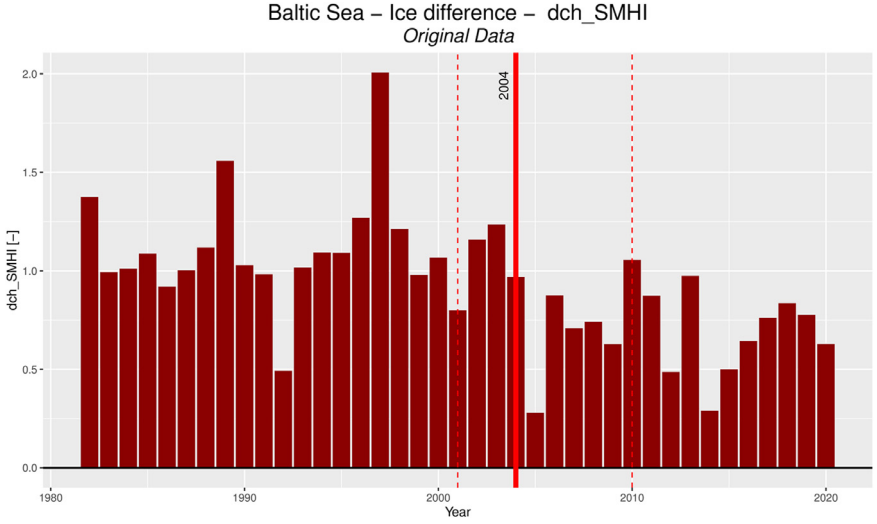

Figure 6 Time series of ice season severity characteristic dch in winter 1982—2020, a statistically significant changepoint (red line) in 2004 in the Baltic Sea.

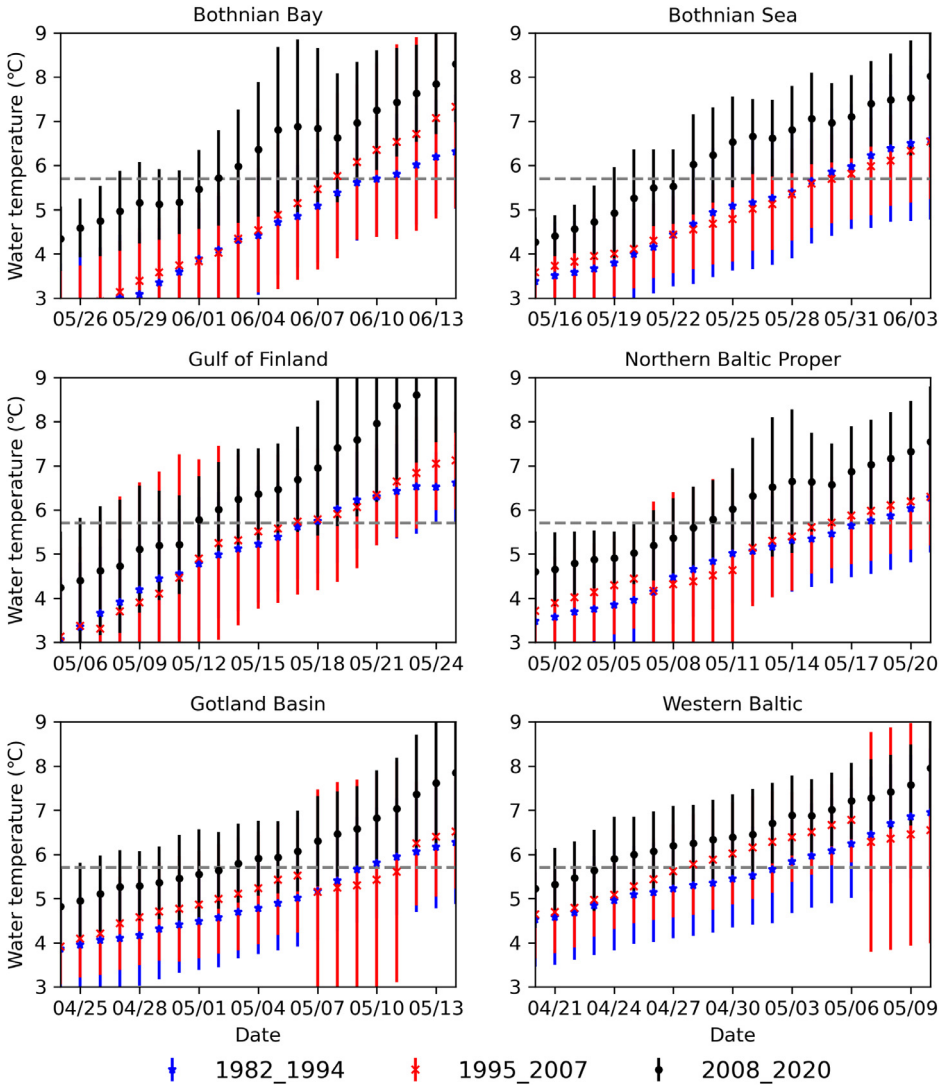

Figure 7 Time series of multiannual daily mean SST over the Baltic Sea basins.

Sea to 70 days in Bothnian Bay (Figure 4a). The most severe winter in the study period occurred in 1987, which resulted in ice formation almost everywhere, except in the southern central Baltic, and melting times of >90 days (Figure 4b). Thus, spatial gradients were relatively less strong because the high ice concentrations led to less mobile ice.

The average ice melting duration for the Baltic Sea showed a statistically significant changepoint in 2013 (Figure 3a). After 2013, the ice melting duration decreased considerably to <4 days (except in 2018). The MT time series data was analysed to determine the occurrence of breakpoints in the different basins of the Baltic Sea (Table 4). For the entire Baltic Sea, GoF and the BB (Figure 3b), statistically significant changepoints were identified.

Because the spring period is characterised by high-speed wind, the existence of ice plays an important role in wind stress hampering. We estimated how long the sea ice led to the elimination of the effects of strong winds (Figure 5). For the area with the longest melting period (Bothnian Bay), it was up to 20 days, and it was lesser in the other basins. On average it was 12 days in the Gulf of Bothnia, 10 days in the Gulf of Finland, 8 days in the Gulf of Riga, 2 days in the North and mid Baltic Proper, and 0.2 days in the southern part of the Baltic Proper.

The ice season severity of the Baltic was classified into three classes: mild (>135 000 km^2), average (135 000 to 180 000 km^2) and severe (<180 000 km^2). Classification is done according to the maximum ice extent. Types of winters in our study: Mild winters occurred during 1988/1989, 1989/1990, 1990/1991, 1991/1992, 1992/1993, 1993/1994, 1999/2000, 2001/2002, 2007/2008, 2008/2009, 2013/2014, 2014/ 2015, 2015/2016, 2016/2017 and 2019/2020; average winters occurred during 1982/1983, 1987/1988, 1997/1998, 1998/1999, 2000/2001, 2003/2004, 2004/2005, 2006/2007, 2011/2012 and 2017/2018; and severe winters occurred during 1981/1982, 1983/1984, 1984/1985, 1985/1986, 1986/1987,1993/1994, 1995/1996, 2002/2003, 2005/2006, 2009/2010, 20010/2011 and 2012/2013.

3.2. Characteristics of ice seasons (dch)

The dch time mean over the Baltic Sea is 0.9. If the value of dch for the respective season is higher than the average,

Table 1 Comparison of the dates when the surface temperature of the water reached 5.6°C.

Basin	a) 1982—1994	b) 1995—2007	c) 2008—2020	a—b(days)	b—c(days)
Bothnian Bay	12 Jun	9 Jun	3 Jun	3	6
Bothnian Sea	31 May	31 May	23 May	0	8
Northern Baltic Proper	19 May	17 May	11 May	2	6
Gulf of Finland	19 May	20 May	13 May	—1	7
Gulf of Riga	9 May	9 May	5 May	0	4
Gotland Basin	11 May	12 MAY	5 May	—1	6
Western Baltic	4 May	31 April	24 April	—4	7

then the ice cover lasts for a relatively long time compared to the maximum ice extent of the same winter. The ice seasons' characteristic dch mainly exhibited higher than average values for 1982—2003 and lower than average values for 2004—2020, except for 2010 (Figure 6). The lower values of dch indicated the seasons (winters) when the ice cover was extensive for some time, but it did not last for a long duration. Before 2004, the ice cover duration was longer than that of the maximum ice extent. The duration of the ice cover of the previous decade decreased compared to the maximum ice extent of the same winter. The time series of 1982—2020 had a statistically significant changepoint in 2004 in the Baltic Sea.

3.3. Shift of Sea Surface Temperature (SST) in spring

We observed that the dates of the water threshold temperature, i.e., 5.6°C, changed during 1982—2020. To find out if the surface temperature of the sea had changed over time (Figure 7), the study period was divided into three periods: 1982—1994, 1995—2007 and 2008—2020. The threshold temperature was observed in the last period, 4 to 8 days earlier compared to the middle interval (Table 1). Between the first and second period, there was not such a clear trend, and only for some basins the threshold temperature was reached earlier.

BB and GoF differed from other basins. The April average SST over BB and GoF had a statistically significant changepoint in 2006 (Table 4). In other basins (BS, NBP, GoR, GB, SWB) the surface temperature was strongly in accordance with the average surface temperature over the Baltic Sea, and the correlation was >0.92. Also, the correlation coefficient between all the sub-basins (except BB) was >0.88, but the mean SST between BB and Baltic was 0.68. The correlation coefficient between MT and mean SST over the Baltic Sea was —0.9.

3.4. Analysis of chlorophyll-a concentrations

Satellite-based chlorophyll-a average (1998—2020) concentrations for the Baltic Proper were 0.6, 0.9, 1.4, 2.3 and 1.6 mg m^{-3} for January, February, March, April and May, respectively. The chlorophyll-a time average concentrations (Figure 8) showed the highest gradient and values of the chlorophyll-a concentration in the Gulf of Finland (up to 8 mg m^{-3}) and the Gulf of Riga (up to 7 mg m^{-3}). However, the northernmost data for the Baltic Sea and easternmost data for the Gulf of Finland must be viewed with some caution

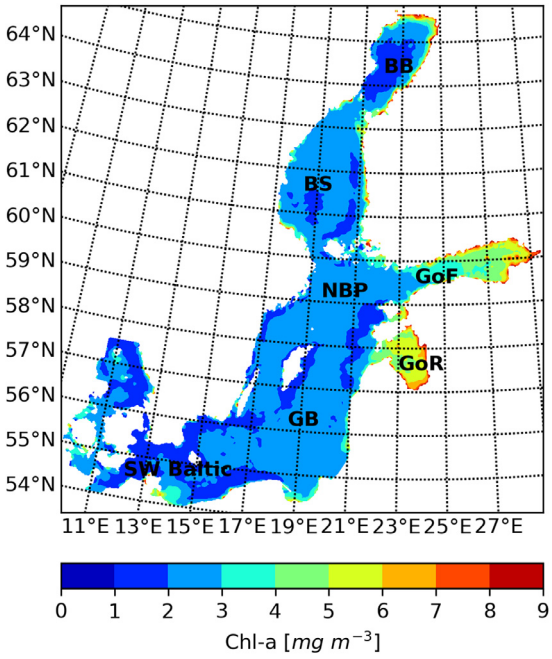

Figure 8 March—May average chlorophyll-a concentration (mg m^{-3}) for 1998—2020 over the Baltic Sea. Satellite-based Chl-a data from Copernicus product.

because the ice cover lasts longer in these areas. We investigated the pattern of spring bloom according to winter severity (Section 3.1). Figure 9 shows the multiannual daily mean of chlorophyll-a concentration for spring in Baltic Sea basins. The Bothnian Bay and Gulf of Riga were excluded because when they are covered with sea ice from March—May, satellites provide unreliable data or there is a lack of satellite data for these areas. In the SW Baltic, the spring bloom begins on average on March 10—15, and average chlorophyll-a concentration values decrease (<2 mg m^{-3}) in mid-April. In the beginning of spring, chlorophyll-a concentration values are low (up to 2 mg m^{-3}) in all basins except the Gulf of Finland. In other basins, concentrations started to increase in early April, and the peak was reached in late April.

The peak of chlorophyll-a multiannual daily mean concentration lasted for a shorter duration after severe winters than after average and mild winters (Table 2). In severe winters, peak of concentration only lasts a few days, except in the Gulf of Finland. In all the basins, chlorophyll-a concentration values were lower in severe winters than in average and mild ones, mainly during the whole season (Figure 9). We compared the chlorophyll-a multiannual daily mean con-

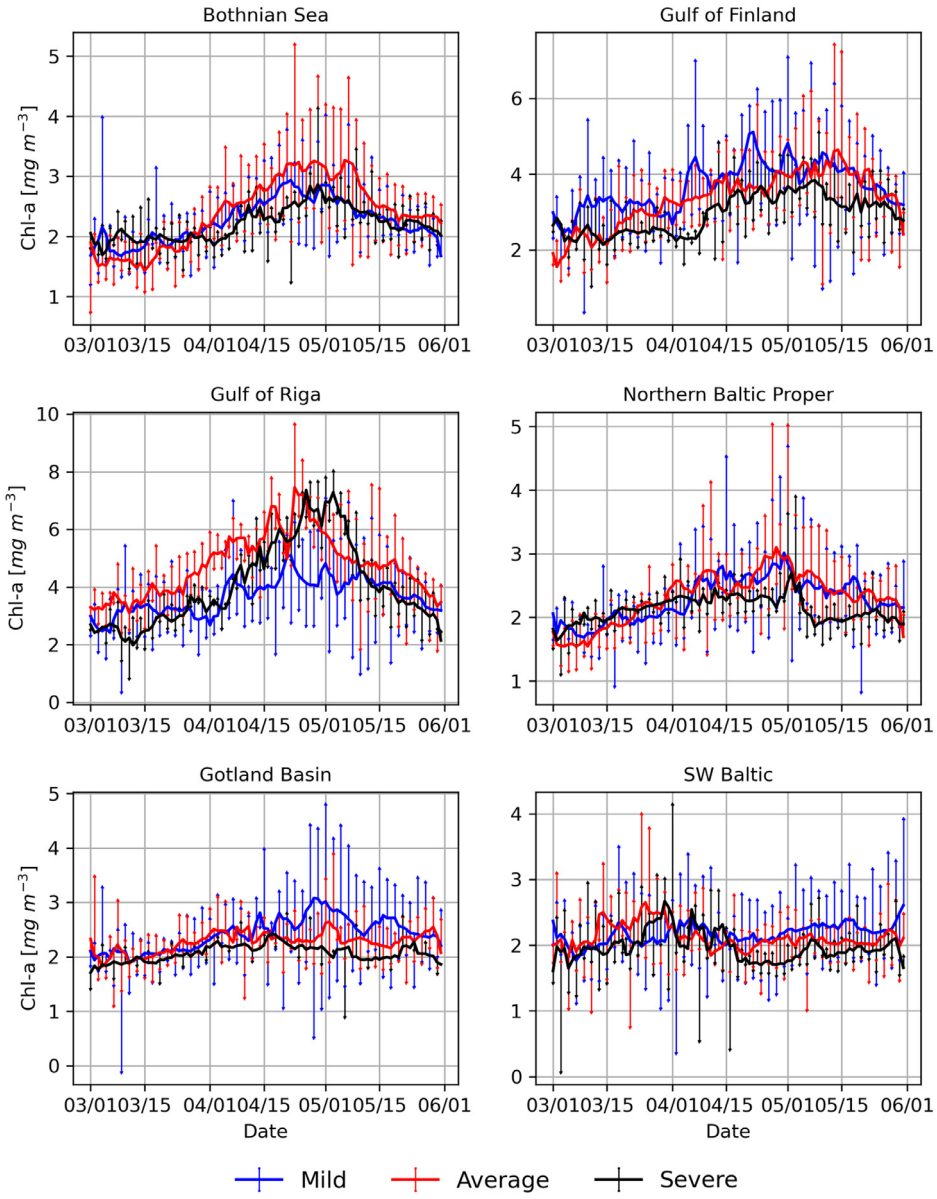

Figure 9 Chlorophyll-a multiannual daily mean concentration over the Baltic Sea basins from March to May for severe, average, and mild winters.

Table 2 Number of days when the daily chlorophyll-a concentration values were higher than the mean.

Basin	Severe (Day)	Average (Day)	Mild (Day)	Before shift (Day)	After shift (Day)
Bothnian Sea	31	56	42	50	22
Northern Baltic Proper	31	58	46	59	31
Gulf of Finland	25	54	56	54	25
Gotland Basin	7	56	57	58	8
SWS Baltic	18	41	60	41	18

centration (1998—2020) in each basin with the daily values of severe, average, and mild winters. We summed up the number of days when the daily values were higher than the mean concentration (Table 2).

The chlorophyll-a data does not correlate with the MT and SST data shown in the previous sections (3.1 and 3.3). The GoF and GoR chlorophyll-a data did not correlate with each other (r=—0.068) or with other basins (Figure 10). The April mean chlorophyll-a concentration from the period 1998—2020 was analysed for the selected sub-basins. The chlorophyll data series is shorter than the ice data, however, the statistically significant changepoint was in 2002 and 2011 in the April mean chlorophyll-a time series in NBP and, in 2011, in the whole Baltic Sea. Statistically significant changepoints were identified for the other basins as shown in Table 4.

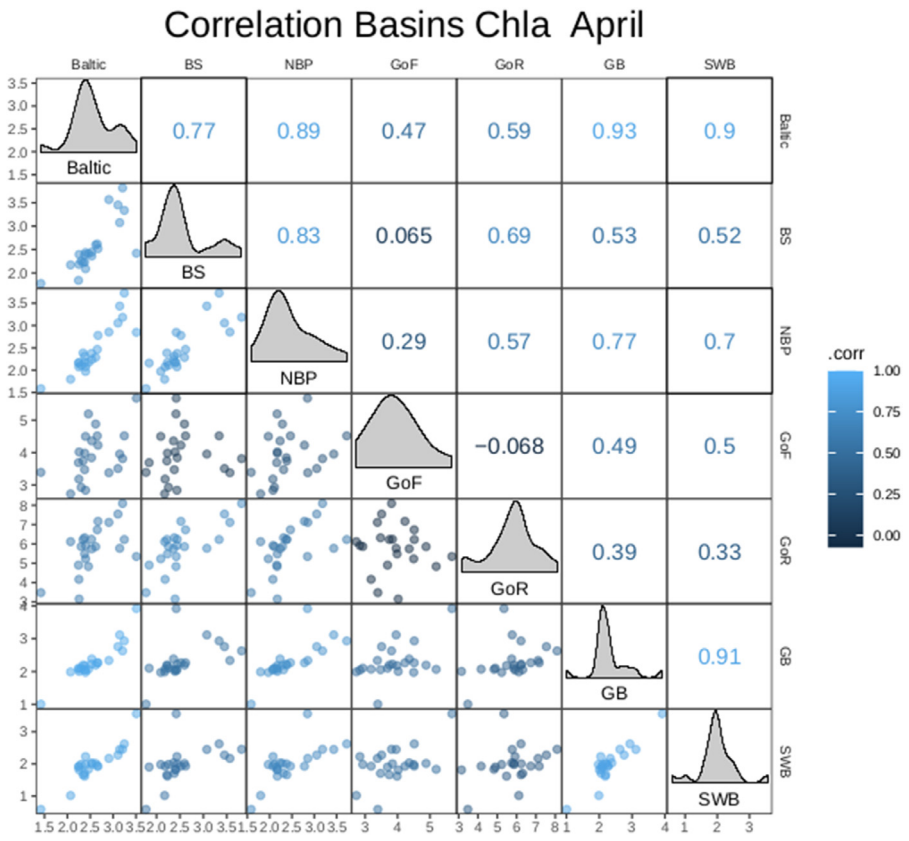

Figure 10 Correlation between April mean chlorophyll-a concentration between the subbasin.

Phytoplankton and chlorophyll-a concentration profiles were rarely measured in the areas covered with the sea ice. No such data are available for the GoF and GoR. An exception is the Bay of Mecklenburg (St. OMO22), for which the measurement data is available for March 2009—2019 in the ICES database. The Bay of Mecklenburg is covered with ice in cold winters (Schmelzer et al., 2014). The number of ice days in Rostock (the nearest port to the station) were: 0, 67, 77, 23, 54, 4, 2, 22, 11, 39, 2, 0 days according to 2009—2020. In severe winters, the chlorophyll-a concentration on the surface (Figure 11) is lower than that for deep underwater (10 m). In mild winters, concentration values are the same, or the surface concentration is high. An exception is 2015, when the surface, a deep layer of 5 m, and a deep layer of 10 m exhibited chlorophyll-a concentrations of 8, 7, and 11 mg m^{-3}, respectively. The day before the measurements, March 17, 2015, the average wind speed was low <5 m s^{-1} (ERA5 data) and the diatom sinking velocity during the spring bloom in the central Baltic Sea is 15 to 30 m d^{-1} (Passow, 1991).

3.5. Impact of the sea ice on the spring bloom in the ecosystem model

A coupled hydrodynamic—biogeochemical model was implemented to analyse the difference between the two scenarios with respect to the chl-a concentrations at stations.

We examined the frequency of the predictions coinciding with the timing of the spring phytoplankton bloom for the two different runs. If both the run results were in the range of ± 3 days, we counted the results as coinciding. The dates predicted by the two runs for the spring phytoplankton bloom peak slightly coincided with each other. Stations OMBMPK2 and OMBMPK3 coincided 4 times, station Gdańsk 2 times while stations H1, 14, and G1 did not coincide with any of the considered cases. The prediction difference for the timing of the spring phytoplankton bloom peaks for each station are presented in Table 3. If the bloom peaks of run (A) and run (B) coincided by (± 3 days), then we consider the blooming difference to be 0 days. The interval in the southern part of the Baltic Sea (OMBMPK2 and OMBMPK3) was 4 days, and in the Gdańsk Bay, it was 6 days. The correlation of the diatom concentration between runs (A) and (B) was 0.2—0.9 (Figure 11, Table 3). The correlation coefficient is sensitive to the selected time interval. The same period (25.03—5.05) was considered for all the stations. The critical value of the Pearson correlation coefficient is 0.44 ($p = 0.05$). The correlation of the diatom concentration between runs (A) and (B) is not significant at stations H1 and G1. Differences existed in the bloom timing, with the four stations having a timing of >10 days. This shows that the presence of ice significantly influences the values predicted while using the model.

3.6. Influence of sea ice on the dynamics of chlorophyll-a sinking

Sea ice reduces wind-induced turbulence in the euphotic layer even if it is temporary. The effect of the mechanism on chlorophyll-a concentration was tested with the model. The

Table 3 Correlation of the concentration between runs (A) and (B). Correlation of the concentration between runs (A) and (B).

Stations	Correlation (1.03—31.05)	Correlation during bloom (25.03—5.05)	Interval of the spring bloom timing peak (days)
14	0.6	0.4	10.2
32	0.8	0.45	13.7
G1	0.5	0.2	17.8
Gdańsk	0.8	0.75	6
H1	0.57	0.4	13.8
OMBMPK2	0.9	0.8	3.8
OMBMPK3	0.85	0>.7	3.7

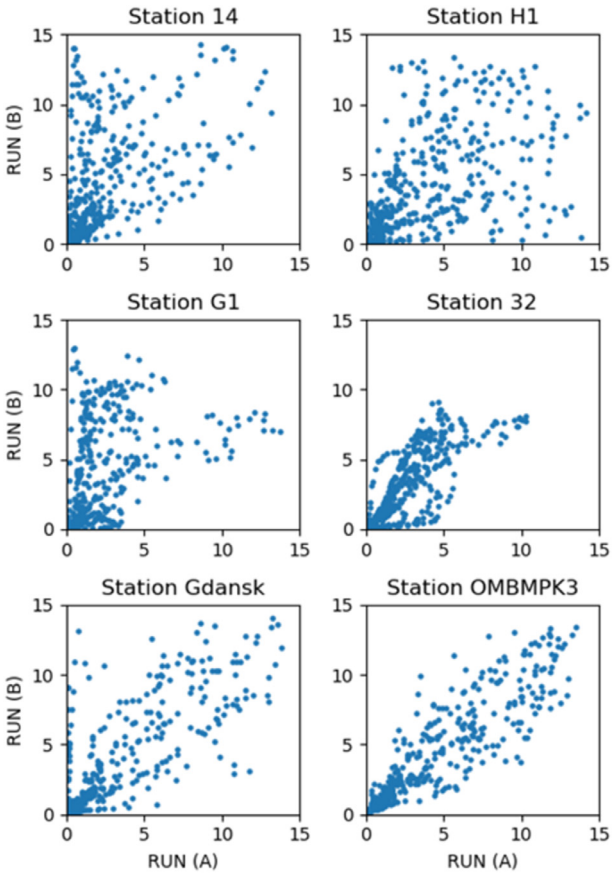

Figure 11 Scatter diagram of the chlorophyll-a concentrations from the two different model simulations, evaluated for stations indicated in Figure 1.

conditions for the sinking of chlorophyll-a varied considerably depending on the presence of open water or sea ice. Figure 12 depicts the multiannual daily mean chlorophyll-a concentration in run (A) and run (B) for six modelled spring seasons. The chlorophyll-a concentration started to increase in the middle of March in both the simulations. The chlorophyll-a concentration values were higher at a depth of 10—15 m for run A (Figure 12) which is caused by the diatoms sinking. Therefore, the spring bloom of dinoflagellates appeared only in the sea area with thin ice (or low wind conditions), and thus, the chlorophyll-a concentration values were lower in the upper 5 m layer. For run B, the diatoms dominated in the ice-free water and in the upper 5 m.

Table 4 Changepoint of the MT, SST and average April clorophyll-a concentration for the Baltic Sea and its parts.

Basin	MT (SMHI)	SST	Chl-April	Chl-May
BB	2013	1992+2006	No data	No data
BS	1987	1988	2002	2002
NBP	No	No	2002+2011	2002+2010
GB	1987	No	2011	No
GoF	2013	2006	No	No
GoR	No	No	2011	2013
SWB	No data	1987	No	No
Baltic	1987+2011	No	2011	2008

4. Discussion

The Baltic Sea is seasonally ice covered with biological activity being the lowest during winter. The average chlorophyll-a concentrations over the Baltic Proper as seen using satellite data were <1 mg m^{-3} before March. The activity of biota during spring depends strongly on the ice cover duration. Climate changes have affected the living environment of the Baltic Sea. The average ice melting time (MT) of the Baltic Sea showed a statistically significant changepoint in 2011.

The average MT in spring decreased over the last decade. Before 2011, the average MT for the Baltic Sea was ~13 days. Since 2012, the MT was ~4 days.

Our study showed a larger change in the northern part of the Baltic Sea, however, Rjazin et al. (2017) reported a larger change in the mean air temperatures over the southwest (compared to the north) of the Baltic Sea. In the southern Baltic region, the average skewness of air temperature distribution shifted from 0.39 to 0.8 (Rjazin et al., 2017).

The generation of sea ice has been episodic after regime shift, and ice has not been able to grow to a large thickness. The ice season characteristic dch shifted from 1.1 to 0.7 in 2004 (Figure 6). Compared to the maximum ice extent of the season, the ice cover lasted longer before 2004. After 2004, the lower values of dch indicated the winters

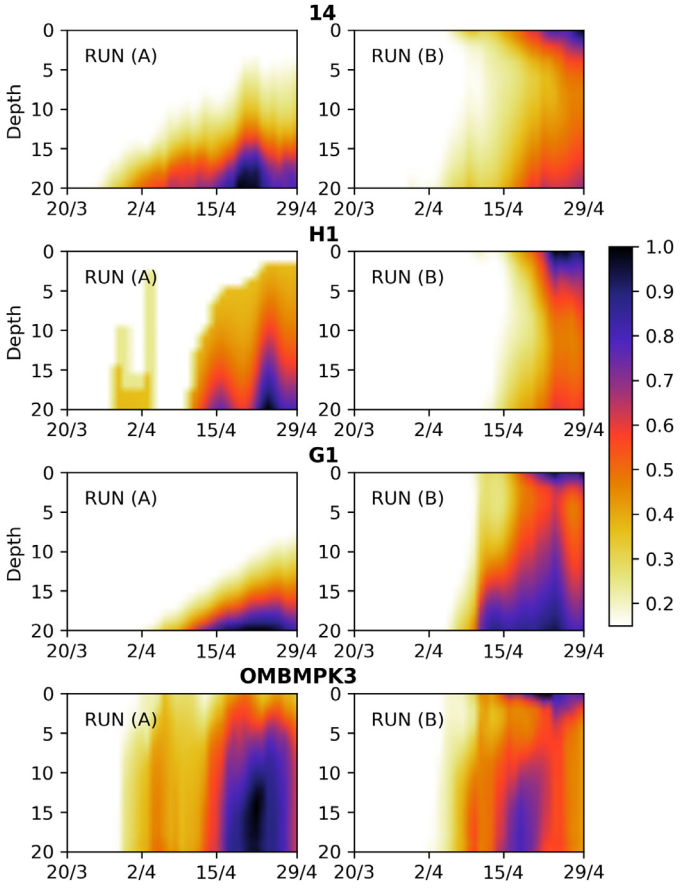

Figure 12 Daily average chlorophyll-a concentration values (normalise scale, values start at 0.2) at the four selected stations (Figure 1) averaged for the severe winters of 1987, 1996, 2003, 2010, 2011, and 2013.

in which the ice cover was extensive for some time but did not last for a long duration. However, considerable strong winds occur during the MT. Wind speeds higher than 6 m s^{-1} occur in some areas for 20 days (Figure 5) during the spring period. This creates conditions for changes in the species composition of phytoplankton.

Changes in the productivity regimes in spring were observed. The April average SST of the Bothnian Bay and the Gulf of Finland showed a statistically significant changepoint in 2006. The water temperature triggered many life processes which have threshold values. It can be concluded that the date of the water threshold temperature of 5.6°C changed during 1982—2020. The threshold temperature dates changed after the changepoint and were on average achieved on 11 May in 1982—2007, and 6 days earlier (05 May) in 2008—20 in the Baltic Proper (Figure 7). The interval 4—8 days between the dates was detected in all the basins in the Baltic Sea (Table 1).

Sub-arctic ecosystems are strongly dependent on environmental factors such as water temperature and changes in it will influence the ecosystem. The spawning temperature of herring is just one example that we took as the threshold value. Phytoplankton cannot compensate for the temporal shift, as the spring bloom is also limited by the available light, shown for the southern Baltic Sea by Friedland et al. (2012). Climate change effects are very quickly identified as a high-risk for herring spawning (Gröger et al. 2014).

The most active period in the sea, the spring bloom, occurs at the end of April (Figure 9), when chlorophyll concentrations were highest in the Baltic Sea, according to satellite data. In the southern parts of the Baltic Sea, the spring bloom starts in early March. The beginning of the spring boom (according to satellite data) did not occur progressively from the south to the north. Chlorophyll-a concentration values in the Gotland Basin, North Baltic Proper and Bothnian Sea started to increase when the spring bloom in the Southwest Baltic was over, i.e., in mid-April, reaching its peak by the end of April (Figure 9). In the Gulf of Finland, chlorophyll-a concentrations started to increase in early April. They were lower in severe winters throughout most of the spring season in all Baltic Sea basins (Figure 9). The Gulf of Finland and the Gulf of Riga are biologically independent basins, chlorophyll-a concentration during spring bloom did not correlate with each other or with the rest of the Baltic Sea sub-basins. The correlation coefficient between GoF and GoR is —0.068, with other sub-basins it is in the range of 0.068—0.69 (Figure 10).

The modelling experiment compared the results of a reference run (A) with observed sea ice with those of a run (B) with underestimated sea ice (imitating a mild and ice-free winter), which confirmed that ecological conditions dif-

fered significantly for both the scenarios. It has been found that there are low chlorophyll-a concentrations in the upper 5 m layer in run (A) and the concentration values increased at the surface in run (B). The results of the expeditions in the Bay of Mecklenburg gave a similar result in March 2009—2019. In mild winters, the measured values of chlorophyll-a concentration are the same in the euphotic zone, or the surface concentration is higher (with the exception of 2015); however, in severe winters, the concentration of chlorophyll-a on the surface is lower than in the deeper layer (10 m).

It can be seen from the observations and the model experiment that it is not enough to present the surface values alone to describe spring bloom. The deeper layers of the water column should also be considered. It can therefore be assumed that even in severe winters (shown by satellite data), the concentrations are lower throughout the season (Figure 9) than in mild winters. The presence of ice eliminates the effect of wind, thus creating calm conditions when the heavier particles (diatoms) sink below the euphotic zone (~10 m). The ice conditions during spring are one of the key factors affecting the magnitude, timing and composition of the spring bloom. The correlation of the chlorophyll-a concentration between simulations with sea ice (A) and simulations with the simple ice model (B) was 0.2—0.9. The southern parts of the sea are less affected by sea ice (correlation is higher), and the regions of the central Baltic Sea are more affected.

During ice free conditions in the spring bloom, the diatoms with a higher growth rate were predominant and quickly consumed nutrients. This indicated a faster end of the spring bloom leading to a rapid decrease in the chlorophyll-a concentration. During moderate ice cover and windless springs, the physical conditions were suitable for dinoflagellates. Their nutrient intake was lower than the diatoms allowing the nutrients to be available for longer in the euphotic zone. Diatoms lost their competitive advantage under sea ice and calm wind as these conditions led the diatoms to sink into the deeper layers of water where light was not available. The changes in dominance of these two phytoplankton classes strongly affected the marine food web and showed that they have a role in the net transfer of CO2 to the oceans and then to the sediments.

Extrapolating our results to a future with higher water temperatures and less ice, we can expect an increase in the diatom bloom magnitudes, although this event could potentially not occur in calm winds. This is according to our study, but blooming is the product of complex processes, which need to be investigated more widely to understand the mechanisms behind the underlying change in phytoplankton dynamics. The focus of our study was on the southern and central Baltic Sea. In conditions such as those in the northern part, where ice is thicker and closer along with the presence of snow, there is less light in the sea during spring. This part was not described in our work.

Declaration of competing interest

The authors declare that they have no known competing financial interests or personal relationships that could have appeared to influence the work reported in this paper.

Acknowledgements

Many thanks to Jürgen Holfort for the data from the German Ice Service. Many thanks to Anisha Bhosa for assistance in drafting the text and editing the language.

References

Abalansa, S., El Mahrad, B., Vondolia, G.K., Icely, J., Newton, A., 2020. The marine plastic litter issue: a social-economic analysis. Sustainability 12 (20), 8677. https://doi.org/10.3390/su12208677

BACC II Author Team, 2015. Second Assessment of Climate Change for the Baltic Sea Basin. Springer International Publ., 146 pp.

Bai, J., 1994. Least squares estimation of a shift in linear processes. J. Time Ser. Anal. 15 (5), 453—472. https://doi.org/10.1111/j.1467-9892.1994.tb00204.x

Bai, J., 1997. Estimation of a change point in multiple regression models. Rev. Econ. Stat. 79 (4), 551—563.

Bai, J., Perron, P., 1998. Estimating and testing linear models with multiple structural changes. Econometrica 66 (1), 47—78. https://doi.org/10.2307/2998540

Bai, J., Perron, P., 2003. Computation and analysis of multiple structural change models. J. Appl. Econ. 18 (1), 1—22. https://doi.org/10.1002/jae.659

Brierley, A.S., Kingsford, M.J., 2009. Impacts of climate change on marine organisms and ecosystems. Curr. Biol. 19 (14), R602—R614. https://doi.org/10.1016/j.cub.2009.05.046

Burchard, H., 1999. Burchard, Hans. Recalculation of surface slopes as forcing for numerical water column models of tidal flow. Applied Mathematical Modelling 23 (10), 737—755.

Burchard, H., Bolding, K., 2002. GETM, a general estuarine transport model. Technical report, European Commsission.

Chiswell, S.M., Calil, P.H., Boyd, P.W., 2015. Spring blooms and annual cycles of phytoplankton: a unified perspective. J. Plankton Res. 37 (3). https://doi.org/10.1093/plankt/fbv021

Eilola, K., Mårtensson, S., Meier, H.E.M., 2013. Modeling the impact of reduced sea ice cover in future climate on the Baltic Sea biogeochemistry. Geophys. Res. Lett. 40 (1), 149—154. https://doi.org/10.1029/2012GL054375

Friedland, R., Hiller, A., Janßen, H., 2013. Melting Sea Ice in the Baltic Sea — changes and possible effects. Coast. Mar. 22 (1), 9.

Friedland, R., Neumann, T., Schernewski, G., 2012. Climate change and the Baltic Sea action plan: model simulations on the future of the western Baltic Sea. J. Mar. Syst. 105, 175—186. https://doi.org/10.1016/j.jmarsys.2012.08.002

Gemmell, B.J., Oh, G., Buskey, E.J., Villareal, T.A., 2016. Dynamic sinking behaviour in marine phytoplankton: rapid changes in buoyancy may aid in nutrient uptake. Proc. Royal Soc. B Biol. Sci. 283 (1840). https://doi.org/10.1098/rspb.2016.1126

Griffiths, J. R.Griffiths, J. R., Kadin, M., Nascimento, F. J. A., Tamelander, T., Törnroos, A., Bonaglia, S., et al., 2017. The importance of benthic—pelagic coupling for marine ecosystem functioning in a changing world. Glob. Change Biol. 23, 2179—2196. https://doi.org/10.1111/gcb.13642

Gröger, J.P., Hinrichsen, H.H., Polte, P., 2014. Broad-scale climate influences on spring-spawning herring (Clupea harengus, L.) recruitment in the Western Baltic Sea. PLoS One 9 (2), e87525. https://doi.org/10.1371/journal.pone.0087525

Hagen, E., Feistel, R., 2005. Climatic turning points and regime shifts in the Baltic Sea region: the Baltic winter index (WIBIX) 1659—2002. Boreal Environ. Res. 10 (3), 211—224.

Haas C, Christian, 2004. Late-summer sea ice thickness variability in the Arctic Transpolar Drift 1991—2001 derived from ground-based electromagnetic sounding. Geophys. Res. Lett. 31 (9). https://doi.org/10.1029/2003GL019394

HELCOM, 2018. Inputs of hazardous substances to the Baltic Sea. In: Baltic Sea Environment Proceedings No. 162.

Hersbach, H., et al., 2020. The ERA5 global reanalysis. Q. J. Roy. Meteor. Soc. 146, 1999—2049. https://doi.org/10.1002/qj.3803

Hjerne, O., Hajdu, S., Larsson, U., Downing, A., Winder, M., 2019. Climate driven changes in timing, composition and size of the Baltic Sea phytoplankton spring bloom. Front. Mar. Sci. 6, 482. https://doi.org/10.3389/fmars.2019.00482

Ivanova, M.B., 1985. Productivity of Planktonic Crustaceans in Freshwater Water Bodies. Nauka 220.

Jørgensen, S.E., 1994. Models as instruments for combination of ecological theory and environmental practice. Ecol. Modell. 75—76, 5—20. https://doi.org/10.1016/0304-3800(94)90003-5

Jørgensen H, Hanne B. Hede, et al.Michael Møller Hansen, Volker Loeschcke, 2005. Spring-spawning herring (Clupea harengus L.) in the southwestern Baltic Sea: do they form genetically distinct spawning waves? ICES J. Mar. Sci. 62 (6). https://doi.org/10.1016/j.icesjms.2005.04.007

Kahru, M., Elmgren, R., Savchuk, O.P., 2016. Changing seasonality of the Baltic Sea. Biogeosci. Discuss. 13 (4), 1009—1018. https://doi.org/10.5194/bg-13-1009-2016

Käse, L., Geuer, J.K., 2018. Phytoplankton responses to marine climate change—an introduction. In: Jungblut, S., Liebich, V., Bode, M. (Eds.), YOUMARES 8—Oceans Across Boundaries: Learning from Each Other. Springer, Cham, 55—71. https://doi.org/10.1007/978-3-319-93284-2_5

Keevallik, S., 2011. Shifts in meteorological regime of the late winter and early spring in Estonia during recent decades. Theor. Appl. Climatol. 105 (1—2), 209—215. https://doi.org/10.1007/s00704-010-0356-x

Klais, R., Norros, V., Lehtinen, S., Tamminen, T., Olli, K., 2017a. Community assembly and drivers of phytoplankton functional structure. Funct. Ecol. 31 (3), 760—767. https://doi.org/10.1111/1365-2435.12784

Klais, R., Otto, S.A., Teder, M., Simm, M., Ojaveer, H., 2017b. Winter—spring climate effects on small-sized copepods in the coastal Baltic Sea. ICES J. Mar. Sci. 74 (7), 1855—1864. https://doi.org/10.1093/icesjms/fsx036

Klais, R., Tamminen, T., Kremp, A., Spilling, K., An, B.W., Hajdu, S., Olli, K., 2013. Spring phytoplankton communities shaped by interannual weather variability and dispersal limitation: mechanisms of climate change effects on key coastal primary producers. Limnol. Oceanogr. 58 (2), 753—762. https://doi.org/10.4319/lo.2013.58.2.0753

Lei, R., Leppäranta, M., Erm, A., Jaatinen, E., Pärn, O., 2011. Field investigations of apparent optical properties of ice cover in Finnish and Estonian lakes in winter 2009. Est. J. Earth Sci. 60 (50). https://doi.org/10.3176/earth.2011.1.05

Leppäranta, M., Myrberg, K., 2009. Physical Oceanography of the Baltic Sea. Springer Science & Business Media.

Lilover, M.-J., Pavelson, J., Kõuts, T., Lepparanta, M., 2018. Characteristics of high-resolution sea ice dynamics in the Gulf of Finland, Baltic Sea. Boreal Env. Res. 23, 175—191.

Lipsewers, T., 2020. Spring bloom dynamics in the Baltic Sea: from the environment to macro-elements and microbial interactions. Dissertationes Schola Doctoralis Scientiae Circumiectalis, Alimentariae, Biologicae. Universitatis Helsinkiensis.

Macias Moy, D., Friedland, R., Stips, A., Miladinova, S., Parn, O., Garcia-Gorriz, E., Melin, F., 2020. Applying the Marine Modelling Framework to Estimate Primary Production in EU Marine Waters, EUR 30546EN. Publications Office of the European Union, Luxembourg.

Mantua, N.J., 2004. Methods for detecting regime shifts in large marine ecosystems: a review with approaches applied to North Pacific data. Progr. Oceanogr. 60 (2—4), 165—182. https://doi.org/10.1016/j.pocean.2004.02.016

Meier, H.E.M., Döscher, R., Coward AC., Nycander J., Döös K., 1999. RCO—Rossby Centre regional Ocean climate model: modeldescription (version 1.0) and first results from the hindcast period1992/93. Reports Oceanography 26, 102.

Meier, H.E.M., Edman, M.K., Eilola, K.J., Placke, M., Neumann, T., Andersson, H.C., Brunnabend, S.E., Dieterich, C., Frauen, C., Friedland, R., Gröger, M., Gustafsson, B.G., Gustafsson, E., Isaev, A., Kniebusch, M., Kuznetsov, I., Müller-Karulis, B., Omstedt, A., Ryabchenko, V., Saraiva, S., Savchuk, O.P., 2018. Assessment of eutrophication abatement scenarios for the Baltic Sea by multi-model ensemble simulations. Front. Mar. Sci. 5, 440. https://doi.org/10.3389/fmars.2018.00440

Murray, C.J., Müller-Karulis, B., Carstensen, J., Conley, D.J., Gustafsson, B.G., Andersen, J.H., 2019. Past, present and future eutrophication status of the Baltic Sea. Front. Mar. Sci. 6, 2. https://doi.org/10.3389/fmars.2019.00002

Neumann, T., 2000. Towards a 3D-ecosystem model of the Baltic Sea. Journal of Marine Systems 25, 405—419. https://doi.org/10.1016/S0924-7963(00)00030-0

Neumann, T., 2010. Climate-change effects on the Baltic Sea ecosystem: a model study. J. Mar. Syst. 81 (3), 213—224. https://doi.org/10.1016/j.jmarsys.2009.12.001

Neumann, T., Eilola, K., Gustafsson, B., Müller-Karulis, B., Kuznetsov, I., Markus Meier, H.E., Savchuk, O.P., 2012. Extremes of temperature, oxygen and blooms in the Baltic Sea in a changing climate. Ambio 41 (6), 574—585.

Neumann, T., Friedland, R., 2011. Climate change impacts on the Baltic Sea. In: Schernewski, G., Hofstede, J., Neumann, T. (Eds.), Global Change and Baltic Coastal Zones. Springer Science Business Media (Coastal Research Library), Dordrecht, 23—32.

Neumann, T., Schernewski, G., 2008. Eutrophication in the Baltic Sea and shifts in nitrogen fixation analysed with a 3D ecosystem model. J. Mar. Syst. 74 (1—2), 592—602.

Neumann, T., Siegel, H., Moros, M., Gerth, M., Kniebusch, M., Heydebreck, D., 2020. Ventilation of the northern Baltic Sea. Ocean Sci. 16, 767—780. https://doi.org/10.5194/os-16-767-2020

Norbäck Ivarsson, L., Andrén, T., Moros, M., Andersen, T.J., Lönn, M., Andrén, E., 2019. Baltic sea coastal eutrophication in a thousand-year perspective. Front. Environ. Sci. 7, 88. https://doi.org/10.3389/fenvs.2019.00088

Passow, U., 1991. Species-specific sedimentation and sinking velocities of diatoms. Mar. Biol. 108 (3), 449—455.

Pärn, O., Friedland, R., Garcia Gorriz, E., Stips, A., 2020. Report on the biogeochemical model setup for the Baltic Sea and its applications. *Luxembourg: EUR, 30252*. Luxembourg: EUR, 30252 https://doi.org/10.2760/672255

Pärn, O., Lessin, G., Stips, A., 2021. Effects of sea ice and wind speed on Phytoplankton spring bloom in Central and Southern Baltic Sea. PLoS ONE 16 (3), e0242637. https://doi.org/10.1371/journal.pone.0242637

Pemberton, P., Löptien, U., Hordoir, R., Höglund, A., Schimanke, S., Axell, L., Haapala, J., 2017. Sea-ice evaluation of NEMO-Nordic 1.0: a NEMO-LIM3. 6-based ocean-sea-ice model setup for the North Sea and Baltic Sea. Geosci. Model Dev. 10 (8), 3105—3123. https://doi.org/10.5194/gmd-10-3105-2017

Pitarch, J., Volpe, G., Colella, S., Krasemann, H., Santoleri, R., 2016. Remote sensing of chlorophyll in the Baltic Sea at basin scale from 1997 to 2012 using merged multi-sensor data. Ocean Sci. 12 (2), 379—389. https://doi.org/10.5194/os-12-379-2016

Rjazin, J., Alari, V., Pärn, O., 2017. Classifying the ice seasons 1982-2016 using the weighted ice days number as a new winter severity characteristic. EUREKA: Phys. Eng. 5, 49—56.

Rjazin, J.,Hordoir, R., Pärn, O.„ 2019. Evaluation of the nemo-nordic model by comparing the sea-ice concentration values in the Baltic Sea. J. Ocean Tech. 14 (2).

Rjazin, J., Parn, O., 2020. Determining the regime shift of the Baltic Sea ice seasons during 1982—2016. NAŠE MORE: znanstveni časopis za more i pomorstvo 67 (1), 53—59. https://doi.org/10.17818/NM/2020/1.8

Rodionov, S.N., 2004. A sequential algorithm for testing climate regime shifts. Geophys. Res. Lett. 31 (9), L09204. https://doi.org/10.1029/2004GL019448

Schmelzer, N., Holfort, J., Tegtmeier, J., Düskau, T., 2014. Ice Winters 2009/2010 to 2013/2014 on the German North and Baltic Sea Coasts. Bundesamtes für Seeschifffahrt und Hydrographie Nr. 53/2014.

Selin, H., VanDeveer, S.D., 2004. Baltic Sea hazardous substances management: results and challenges. Ambio 33 (3), 153—160.

Spilling, K., Olli, K., Lehtoranta, J., Kremp, A., Tedesco, L., Tamelander, T., Klais, R., Peltonen, H., Tamminen, T., 2018. Shifting diatom-dinoflagellate dominance during spring bloom in the Baltic Sea and its potential effects on biogeochemical cycling. Front. Mar. Sci. 5, 327. https://doi.org/10.3389/fmars.2018.00327

Stips, A., Bolding, K., Pohlmann, T., Burchard, H., 2004. Simulating the temporal and spatial dynamics of the North Sea using the new model GETM (general estuarine transport model). Ocean Dynam. 54, 266—283. https://doi.org/10.1007/s10236-003-0077-0.

Stips, A., Lilover, M., 2010. Yet another assessment of climate change in the Baltic Sea area: Breakpoints in climate time series. 2010 IEEE/OES Baltic International Symposium (BALTIC), 1—9.

Tedesco, L., Piroddi, C., Kämäri, M., Lynam, C., 2016. Capabilities of Baltic Sea models to assess environmental status for marine biodiversity. Marine Policy 70, 1—12. https://doi.org/10.1016/j.marpol.2016.04.021

Umlauf, L., Burchard, H., 2005. Second-order turbulence closure models for geophysical boundary layers: a review of recent work. Cont. Shelf Res. 25 (7—8), 795—827. https://doi.org/10.1016/j.csr.2004.08.004

Vihma, T., Haapala, J., Matthäus, W., 2009. Geophysics of sea ice in the Baltic Sea: a review. Progr. Oceanogr. 80 (34), 129—148. https://doi.org/10.1016/j.pocean.2009.02.002

Von Schuckmann, K., Le Traon, P.-Y., Smith, N., et al., 2018. Copernicus Marine Service Ocean State Report. J. Operational Oceanogr. 11 (Sup. 1), S1—S142. https://doi.org/10.1080/1755876X.2018.1489208

Wasmund, N., Nausch, G., Matthäus, W., 1998. Phytoplankton spring blooms in the southern Baltic Sea — spatio-temporal development and long-term trends. J. Plankt. Res. 20 (6), 1099—1117. https://doi.org/10.1093/plankt/20.6.1099

Winder, M., Schindler, D., 2004. Climate change uncouples trophic interactions in an aquatic ecosystem. Ecology 85, 2100—2106. https://doi.org/10.1890/04-0151

Winder, M., Sommer, U., 2012. Phytoplankton response to a changing climate. Hydrobiologia 698 (1), 5—16.

Zeileis, A., Kleiber, C., Krämer, W., Hornik, K., 2003. Testing and dating of structural changes in practice. Comput. Stat. Data An. 44 (1—2), 109—123. https://doi.org/10.1016/S0167-9473(03)00030-6

Zettler, M.L., Karlsson, A., Kontula, T., Gruszka, P., Laine, A.O., Herkül, K., Schiele, K.S., Maximov, A., Haldin, J., 2014. Biodiversity gradient in the Baltic Sea: a comprehensive inventory of macrozoobenthos data. Helgol. Mar. Res. 68, 49—57. https://doi.org/10.1007/s10152-013-0368-x

Oceanologia 64 (2022) 327—345

Available online at www.sciencedirect.com

ScienceDirect

journal homepage: www.journals.elsevier.com/oceanologia

ORIGINAL RESEARCH ARTICLE

Numerical simulation of tidal hydrodynamics in the Arabian Gulf

Fawaz Madah[a,*], **Sameer H. Gharbi**[a,b]

[a] *Department of Marine Physics, Faculty of Marine Sciences, King Abdul-Aziz University, Jeddah, Saudi Arabia*
[b] *Department of Physical Oceanography, Faculty of Marine Sciences and Environment, Hodeidah University, Hodeidah, Yemen*

Received 28 August 2021; accepted 13 January 2022
Available online 31 January 2022

KEYWORDS
Arabian Gulf;
Delft3D;
Strait of Hormuz;
Amphidromic point;
Co-tidal charts

Abstract A vertically 2-D numerical model based on the *Delft3D* modelling system is set up, calibrated, and validated to simulate the tidal hydrodynamics in the Arabian Gulf. The model is a barotropic solution, controlled by 13 tidal components at open boundaries. The performance of the numerical model was evaluated using the hourly water level observations and the TOPEX/Poseidon altimetry data. Statistical analysis showed a good agreement between the simulated and observed water levels. *RMS* error was found to be ranged from 0.07 to 0.23 m, with maximum discrepancies observed at Ras Tanura and Mina Sulman stations. However, the *IOA* between the simulated and observed water levels was significant (0.95—0.99). On average, the errors for the tidal constituents considered in the analysis are in the order of <0.02 m (4%). The M_2, S_2, K_1 and O_1 tidal waves represent the largest among other constituents, where the amplitude of S_2 represents almost 30% of the M_2, and the O_1 tidal wave represents about 50% of the K_1 tide. The co-tidal charts of the semidiurnal tides show the existence of two anticlockwise amphidromic systems in the north and south ends (centred around 28.25° and 24.5°N respectively) close to the western side, while the diurnal constituents form only a single amphidromic point in the central part, centred around 26.8°N (North Bahrain). On the other hand, the velocity amplitudes of the *U* and *V* components of the numerical model were compared with a previous observational study and found to be agreed well.

* Corresponding author at: Department of Marine Physics, Faculty of Marine Sciences, King Abdulaziz University, Jeddah, Saudi Arabia.
E-mail address: fmaddah@kau.edu.sa (F. Madah).
Peer review under the responsibility of the Institute of Oceanology of the Polish Academy of Sciences.

Production and hosting by Elsevier

https://doi.org/10.1016/j.oceano.2022.01.002

1. Introduction

On the global level, the Arabian Gulf (AG) (known also as the Persian Gulf) is an important region environmentally, economically, and politically due to the oil-related activities and gas resources. The physical border of the AG is surrounded by the shoreline of Saudi Arabia, Bahrain, and Qatar on the western edge, the coastline of Iran on the eastern side, Kuwait in the north-western part, Iraq on the northern part, and the United Arab Emirates (UAE) on the southwestern coastline (Figure 1). Generally, the AG experiences a sub-tropical climate due to its location in the north of the tropic of cancer. A common weather event in the region is known as the "Shamal", which is a north-westerly wind predominant throughout the year (Perrone, 1979). However, the weather condition experiences seasonal variations connected with the amplitudes of the Arabian and Indian thermal lows (Emery, 1956; Perrone, 1979). The AG region is characterized by high evaporation rates ($\sim$ 2 m yr^{-1}) (Ahmad and Sultan, 1991; Privett, 1959) which exceed the net freshwater either by precipitation or rivers flow (Al-Subhi, 2010; Pous et al., 2012). As a result, the AG acts as a large inverse-estuarine system, where the Strait of Hormuz is the only mechanism that controls the exchange between the AG and the northern Indian Ocean. The physical and hydrographic conditions of the AG including water temperature, salinity, wind conditions, heat flux, flow exchange regime, etc, can be found in the previous investigations (e.g., Ahmad and Sultan, 1991; Al-Subhi, 2010; Brewer et al., 1978; Brewer and Dyrssen, 1985; Chao et al., 1992; Emery, 1956; Johns et al., 2003; Kämpf and Sadrinasab, 2006; Pous et al., 2004; Reynolds, 1993; Yao, 2008).

Tides in the AG are an important driving force (Elshorbagy et al., 2006). The tidal wave in the AG is to be oscillating at a period of 22.6 or 21.7 hours where the main tidal motion in the AG is due to Kelvin waves (Defant, 1961). Several studies were carried out in the AG to study the tidal conditions using tide gauge data (Akbari et al., 2016; Al-Mahdi et al., 2009; Al-Subhi, 2010; Khalilabadi, 2016; Sharaf El-Din, 1988; Siddig et al., 2019; Sultan et al., 1995). On the other hand, a number of modelling studies were applied to study the tidal components considering only the four principal tidal components (M_2, S_2, O_1, K_1), which considered for producing the amplitude and phase charts (Bashir, 1993; Lardner et al., 1982,1988; Poul et al., 2016; Najafi and Noye, 1997; Pous et al., 2012; Thompson et al., 1994; Trepka, 1968). The conclusion drawn from these studies suggests that the tidal system is complex and changes from being primarily semi-diurnal to diurnal throughout the basin. Interaction between semidiurnal (M_2, S_2) and diurnal (O_1, K_1) tidal constituents yield resonance, where the former results in two amphidromic systems (one in the north-

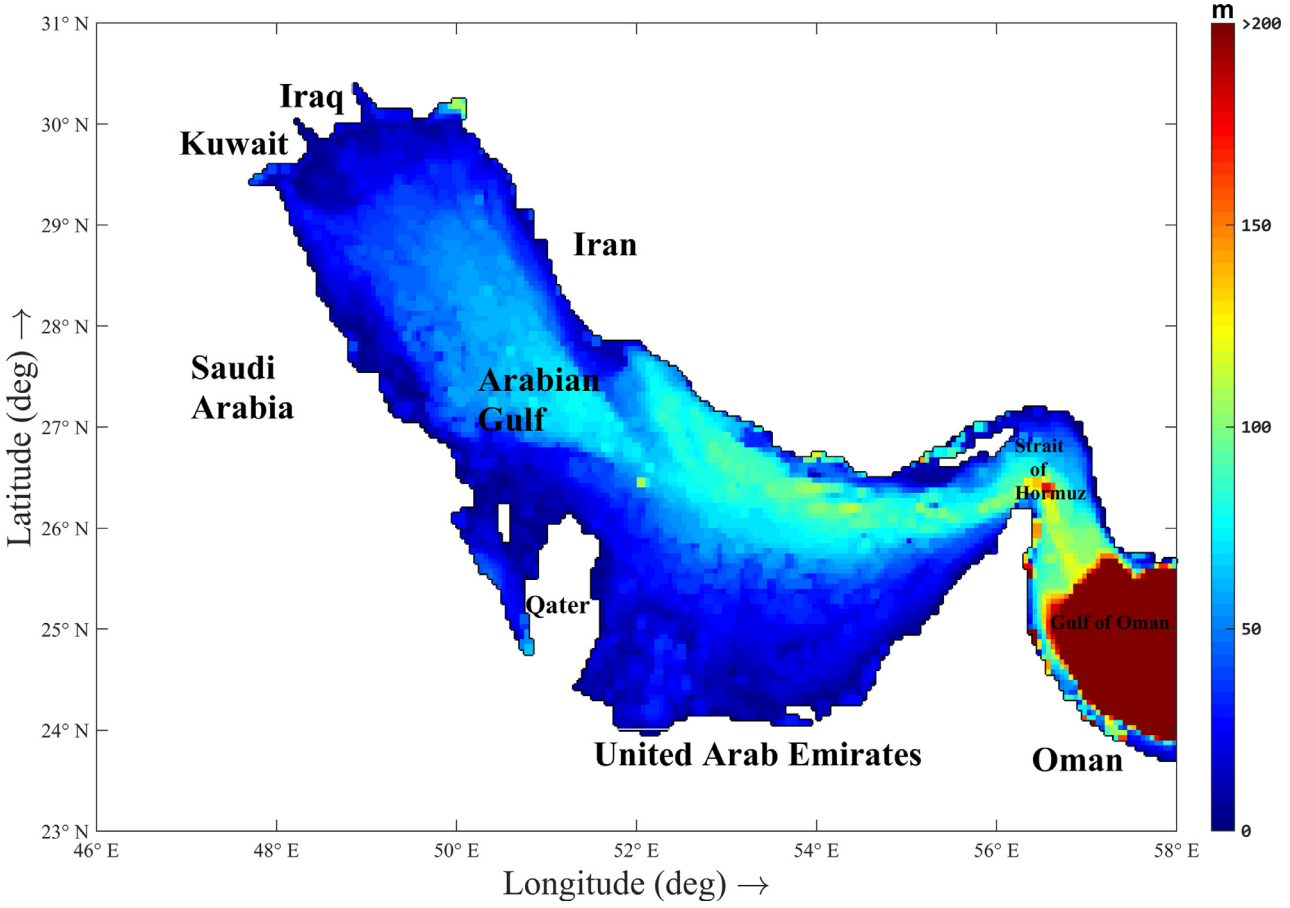

Figure 1 Map of the Arabian Gulf including numerical model bathymetry based on 'GEBCO_2021' global bathymetry datasets for the world ocean.

ern and one in the southern parts), and the latter forms only a single amphidromic point in the central part, near Bahrain. However, the earlier modelling studies showed that amplitudes and phases of the tidal components were not accurately produced by the used models, mainly due to using coarse mesh-resolution, as well as low resolution of bathymetry along the coastlines. Trepka (1968) used nonlinear Cartesian coordinate of Hansen Scheme to predict M_2 in the Gulf considering a coarse resolution grid (14 km). His model predictions of amplitude and phase were good in general, but large discrepancies of about 20% were found along the coastal areas. Later, he conducted an experiment considering 7 tidal constituents and compared the results with predictions of low and high water presented in the German and English Tide Tables. Their model discrepancies were in the range of 0.1 m in high and 0.36 m in low waters, with maximum deviation of about 60 min. Lardner et al. (1982) simulated the tides in the Gulf using the finite difference scheme considering a coarse grid (20 km) to generate the co-charts of the M_2 and K_1 constituents. They concluded that the computed amplitudes and phases are under-overestimated in several regions in the Gulf, due to the method of computation used, where the amplitudes are calculated as the average of all the maximum tidal elevations and the phases are calculated from the time of the last maximum of elevation. Later, Lardner et al. (1988) used the method of characteristics to predict M_2 and K_1 tidal constituents and compared their model results with co-tidal charts. They found that the phase contours are in good agreement while the amplitude contours include large discrepancies. They attributed the discrepancies to the low grid resolution along the coastline. Bashir (1993) modeled the tides using a $\sim$ 9 km grid model resolution and four tidal constituents (M_2, S_2, O_1, K_1) to drive the model. He validated his model using data from Admiralty chart, where his model tended to underestimate the amplitudes and overestimate the phases. Najafi and Noye (1997) modelled the AG tides using a Cartesian depth-averaged model and a spherical coordinate model (8.7 km x 9.7 km) forced by 10 tidal constituents mainly the major semidiurnal and diurnal and (L_2, μ_2). They found that the predicted phases for M_2 and O_1 are not consistent with the Admiralty charts in the strait of Hormuz. They attributed the discrepancies to the boundary effect. Pous et al. (2012) used a 9 km grid resolution model forced by 7 tidal constituents to generate only the co-charts for M_2 and K_1. They concluded that their model error ratio is in the order of 0.05 m (10%) on average with maximum discrepancies observed for P_1, O_1 and K_2. Recently, a modelling study by Poul et al. (2016) have considered 13 tidal constituents to describe the tides and focusing on effect of Qeshm canal in the Gulf, but only qualitative comparisons were provided in this study, thus, nothing can be stated about the discrepancies assessment.

As seen above that all previous modelling efforts used coarse-resolution models forced by a limited number of tidal constituents (depending on the study interest) along the open boundaries. In this study, we setup, calibrate and validate a vertically 2-D barotropic tidal model, considering a spatial horizontal mesh size of 5 km, bathymetry data at a resolution of 15 arc-seconds, and 13 tidal components along the open boundary. For this purpose, the *Delft3D* model, which was developed in the Netherlands by D*elft* Hydraulics is used. To select optimal parameters in the numerical model, sensitivity tests of the numerical and physical parameters were conducted. The simulation results were evaluated using water level measurements at 7 tide gauge stations and TOPEX/Poseidon (T/P) altimetry data. Moreover, one ADCP mooring station was used to validate the model in terms of U and V components. Once, the model has been validated, tidal conditions are described for the AG region. The rest of the manuscript is arranged as follows. Section 2 introduces the materials and methods, including a brief description of the modelling system and the AG Model configuration. The results and discussion of the numerical simulations are given in section 3. Section 4 sheds light on the summary and conclusion of this study.

2. Material and methods

2.1. Study area

The selected domain for the current study covers the entire AG basin including the Strait of Hormuz and part of the Gulf of Oman. The AG is located between 30°, 24°N latitude, and 48°, 57°E longitude, oriented in the NW and SE direction. It is a marginal, semi-enclosed hypersaline sea, with a maximum width of 370 km to a minimum of about 60 km found in the Strait of Hormuz. The length of the AG is about 1000 km along its main axis. The surface area of the water basin is about 239,000 km^2 (Emery, 1956). The bottom topography of the Gulf is relatively shallow, with a maximum depth of 90—100 m in the Strait of Hormuz, and a mean depth of about 35 m (Pous et al., 2004; Roos and Schuttelaars, 2011; Siddig et al., 2019). The deeper topographic features ($>$ 50 m) in the region are found along the Iranian coast while the shallower areas ($<$ 20 m) are found along the southwestern coasts. The AG is connected through the southern boundary with the Gulf of Oman (where the typical depth is $\sim$900 m), and the northern Indian Ocean via the Strait of Hormuz.

2.2. Data source

In this study, hourly time-series of tidal data at seven stations, namely Arabiyah Island, Jubail, Marjan Island, Qurayyah Pier, Ras Tanura, Mina Sulman, and Jask Harbour (see Figure 2 for their locations) were made available. These data were obtained from ARAMCO Oil Company except for Mina Sulman and Jask Harbour stations, they were downloaded from the Sea Level Centre at University of Hawaii (UHSLC) from the following link (http://uhslc.soest.hawaii.edu/data/?rq#uh182a). The hourly recorded time series from ARAMCO Oil Company covers the year 1999 while the sea level data for Mina Sulman and Jask Harbour includes the years 1997 and 2012 respectively. The main purpose of using the hourly tidal data is to carry out harmonic analysis and validate the numerical tidal model. Moreover, tidal constituents at 20 points selected within the model domain extracted from TOPEX/Poseidon (T/P) altimetry data (http://volkov.oce.orst.edu/tides/global) were considered to validate the numerical model. On the other hand, barotropic tidal currents in terms of U and V components

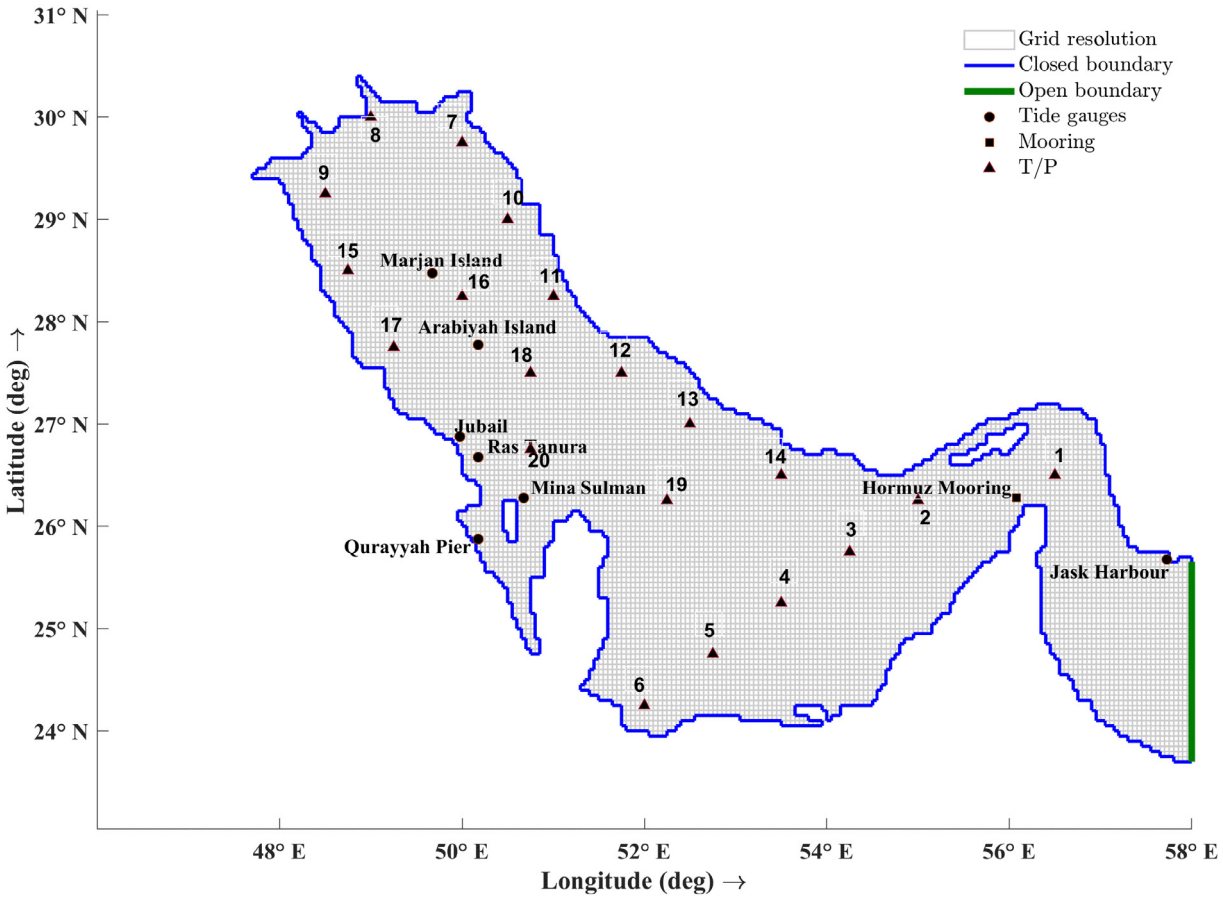

Figure 2 Computational grid distribution of the AG-Model, blue line represents the closed boundaries, green line represents the open boundary, (●) denotes tide gauge stations, and (■) denotes ADCP mooring, (▲) denotes T/P data locations.

(based on ADCP data) were taken from a published study (Johns et al., 2003) for the year 1997 at one station located in the Strait of Hormuz (26.2678°N, 56.0867°E) to validate the numerical model. The bathymetry data used is derived from the new release of the global bathymetry dataset "GEBCO_2021 Grid" at a 15 arc-second interval grid (~ 450 m), (https://www.gebco.net/data_and_products/gridded_bathymetry_data/gebco_2021/). To drive the tidal hydrodynamic model, 13 harmonic constituents, mainly semidiurnal tides (M_2, N_2, S_2, K_2) and diurnal tides (k_1, P_1, O_1, Q_1) including (M_f, M_m, M_4, MS_4, and MN_4) in the form of amplitudes and phases were extracted from the global ocean tidal model TPXO8 (Egbert and Erofeeva, 2002) (https://www.tpxo.net/global/tpxo8-atlas).

2.3. Statistical analysis

In the present study, several statistical parameters were considered to evaluate the performance of the numerical model. These are determined by calculating the *BIAS* (Eq. (1)), the index of agreement (*IOA*) (Eq. (2)), and the root mean square difference (*RMSD*) (Eq. (3)) based on the following formula:

$$BIAS = \frac{1}{n}\sum_{1}^{n} abs\,(Simulated - Observed) \tag{1}$$

$$IOA = \frac{\sum_{i=1}^{n}(O_i - S_i)^2}{\sum_{i=1}^{n}\left(|S_i - \bar{o}| + |O_i - \bar{o}|\right)^2},\ 0 \le IOA \le 1 \tag{2}$$

where o_i is the observation and s_i is the simulation and $\bar{o}$ is the average observation value (Willmott, 1981).

$$RMSD = \sqrt{\frac{1}{n}\sum_{1}^{n}(Simulated - Observed)^2} \tag{3}$$

On the other hand, the *Delft3D-TRIANA* program of the *Delft3D* modelling system has been employed to perform the tidal analysis and derive the main semidiurnal (N_2, M_2, S_2, K_2) and diurnals (Q_1, O_1, P_1, K_1) tidal constituents for both predictions and observations. The program also provides a statistical assessment of the discrepancies between observations and simulation results. The statistical assessment includes the standard deviation of the tidal analysis (SD), the Upper Extreme of the Residual (UER) and Lower Extreme of the Residual (LER), and the Summed Vector Difference (SVD) (Eq. (4)), which is calculated as:

$$\sum_{Obs}\sqrt{[H_C\cos(G_C) - H_O\cos(G_O)]^2 + [H_C\sin(G_C) - H_O\sin(G_O)]^2} \tag{4}$$

in which $\sum_{Obs}$ refers to a summation over the stations with observed amplitude and phase.

2.4. Model description

In the current research, the numerical hydrodynamic model was developed with the *Delft3D* modelling system. The modelling system was developed in the Netherlands by WL | D*elf*t Hydraulics (Deltares, 2011), The *Delft3D-Flow* model (the main module) is capable to solve two- (2D) or three-dimensional (3D) non-steady flow and transport processes produced from tidal and meteorological elements including the temperature and salinity differences effects. The *Delft3D* modelling system is based on the primitive Navier-Stokes equations for incompressible free surface flow, under the Boussinesq approximation (Roelvink and Banning, 1995). The system solves the momentum (Eq. (5)—(6), and continuity equations (Eq. (7)) for velocities and water levels. The equations include the horizontal equations of motion and the transport equations for conservative constituents.

The governing equations of the model are as follows:

$$\frac{\partial u}{\partial t}+u\frac{\partial u}{\partial x}+v\frac{\partial u}{\partial y}+g\frac{\partial \eta}{\partial x}-fv+\frac{gu|U|}{C^2\,(d+\eta)}-v_w\left(\frac{\partial^2 u}{\partial x^2}+\frac{\partial^2 v}{\partial y^2}\right)=0 \tag{5}$$

$$\frac{\partial v}{\partial t}+u\frac{\partial u}{\partial x}+v\frac{\partial v}{\partial y}+g\frac{\partial \eta}{\partial y}-fu+\frac{gv|U|}{C^2(d+\eta)}-v_w\left(\frac{\partial^2 u}{\partial x^2}+\frac{\partial^2 v}{\partial y^2}\right)=0 \tag{6}$$

$$\frac{\partial \eta}{\partial t}+\frac{\partial (d+\eta)u}{\partial x}+\frac{\partial (d+\eta)v}{\partial y}=0 \tag{7}$$

In which η is the water level elevation (m), d is the still water depth (m), f is the Coriolis parameter (1 s^{-1}), t is the time (s), U is the magnitude of the total velocity (m s^{-1}), C is the Chézy's friction coefficient ($m^{1/2}$ s^{-1}), u and v are the depth-averaged velocities in the x- and y-directions (m s^{-1}), v_w is the diffusion coefficient (m^2 s^{-1}), g is the acceleration due to gravity (m^2 s^{-1})

The numerical solution of the equations is discretized using the centred second-order finite differences method in a staggered Arakawa C-grid (Arakawa and Lamb, 1977). To solve the shallow water equations, the Alternating Differential Implicit (ADI) technique is used, which separates one integration time step into two stages. Therefore, the solution is implicit, and each stage is comprised of half a time step (Stelling and Leendertse, 1992). Since the solution is implicit, the consistency of the model is not limited by the time step. The wave propagation is primarily related to the Courant number (Eq. (8)), and to ensure accurate wave propagation in the grid, and accurate solution by Equation (8), the C_r is less than $4\sqrt{2}$ (Roelvink and Banning, 1995; Stelling and Leendertse, 1992).

$$C_r=2\Delta t\sqrt{gH\left(\frac{1}{\Delta x^2}+\frac{1}{\Delta y^2}\right)}<4\sqrt{2} \tag{8}$$

where C_r is the Courant number, Δt is the time step (s), g is the acceleration due to gravity (m s^{-2}), H is the local water depth (m), and Δx, Δy are the grid mesh sizes in the x- and y-directions (m).

2.5. Model configuration

The computational mesh of the AG model (hereafter AG-Model) covers the entire AG and extended to the Gulf of Oman at 58°E. The model area was structured using a rectangular grid with a uniform horizontal grid resolution of Δx and Δy =5 km (Figure 2). The figure also shows the positions of the water level observations considered in calibrating and validating the hydrodynamic model. The bathymetry of the AG-Model was based on the "GEBCO_2021 Grid" at a 15 arc-second interval grid ($\sim$ 450 m). The resulting bathymetric map based on this data is shown in Figure 1. In terms of open boundary, the modelling system (*Delft3D*) permits the use of the Riemann-invariant boundary condition to reduce error reflections in the open boundary (Verboom and Slob, 1984). When there is no incoming wave, then a zero Riemann invariant is imposed to ensure that all waves can leave the domain freely. The open boundary of the AG-Model was set at the Gulf of Oman (58°E). Along the open boundary, 13 harmonic constituents, mainly semidiurnal tides (M_2, N_2, S_2, K_2) and diurnal tides (K_1, P_1, O_1, Q_1) including (M_f, M_m, M_4, MS_4, and MN_4) in the form of amplitudes and phases were prescribed and linearly interpolated. The coordinates system of the AG-Model is spherical, which means that the variation of the Coriolis force is specified in the latitude direction. At the closed boundaries, a free slip condition was applied (U and V=0). In terms of initial conditions of water levels, they were set to zero. A time step of Δt = 60 seconds was set to carry out the simulations. The water density and gravitational acceleration values were set respectively 1028 kg m^{-3} and 9.81 m s^{-2}. The model was initialized for different periods, (1 January 1997, 1 January 1999, and 1 January 2012) and the simulations were carried out for 12 consecutive months. However, due to warming up processes, the equilibrium state was attained after ten days; thus, the first ten days of the simulation were removed before the analyses.

2.6. Tuning model parameters

Owing to the simplification, approximation, and assumptions employed in the numerical model, assessment of the model inputs is required (Palacio et al., 2005). To assess the general performance of the numerical model, sensitivity tests were carried out to adopt optimal numerical and physical parameters to the AG-Model. These parameters involved the boundary condition, time step, bottom roughness, and horizontal eddy viscosity (HEV). In terms of open boundary forcing, the model at eastern (U-direction) boundary was driven by the major eight semidiurnal and diurnal tidal components including (M_f, M_m, M_4, MS_4, and MN_4). The initial run showed that the AG-Model produces similar tidal elevations to the observed ones, therefore, the amplitudes and phases of the tidal components were adopted to carry out all simulations. On the other hand, changing the value of the time step did not influence the numerical model results; however, the smaller the time step, the higher the accuracy of the computations. As mentioned above that the wave propagation is related to the Courant number (Eq. (8)), accordingly, a time step of 1 minute was used in all runs to meet the stability criteria and accuracy requirements. The

Table 1 Sensitivity analysis of Chézy coefficient parameter.

Station ID	Water depth (m)	Chézy ($m^{1/2}$ s^{-1})	BIAS (m)	*RMSE* (m)	*IOA*
Arabiyah Island	56	45	0.06	0.19	0.97
		65	0.07	0.15	0.97
		85	0.07	0.13	0.97
Jubail	10	45	0.07	0.26	0.98
		65	0.07	0.19	0.98
		85	0.08	0.14	0.98
Marjan Island	46	45	0.07	0.17	0.94
		65	0.08	0.14	0.94
		85	0.08	0.12	0.95
Qurayyah Pier	25	45	0.08	0.10	0.75
		65	0.06	0.08	0.85
		85	0.03	0.04	0.95
Ras Tanura	8	45	0.10	0.29	0.98
		65	0.10	0.23	0.98
		85	0.10	0.22	0.98
Mina Sulman	11	45	0.01	0.32	0.99
		65	0.01	0.25	0.99
		85	0.01	0.23	0.99
Jask Harbour	10	45	0.01	0.07	0.99
		65	0.01	0.07	0.99
		85	0.01	0.07	0.99

Note: The P-value related to all comparisons is very low ($P > 0.0001$), indicating that the results from correlation are significant. *IOA* represents Index of agreement; *RMSD* represents Root mean square difference and BIAS.

Delft3D model applies Chézy coefficient formulation ($c = \frac{H^{1/6}}{n}$) which is based mainly on the bottom roughness and the water depth height. The bottom roughness is an important parameter that plays a crucial role in the hydrodynamic flow models. To investigate its influence on the model results, three different Chézy coefficient values of 45, 65, and 85 $m^{1/2}$ s^{-1} as uniform over the entire domain were examined (Table 1). The analysis revealed that using higher or lower values from 65 $m^{1/2}$ s^{-1} (a default value of the *Delft3D* system) causes slight influences on the model results. However, the simulations carried out with bottom roughness (Chézy) of 85 $m^{1/2}$ s^{-1} led to provide better results based on the values of *RMS* error. Therefore, a constant Chézy bottom-roughness coefficient of 85 $m^{1/2}$ s^{-1} was applied temporally and spatially throughout the model domain. Owing to its essential role in defining turbulence mixing, the influence of the HEV was also tested by comparing different cases with the original simulation. It was found that the EHV coefficient has insignificant influence on the outcome of the simulation. The optimal settings chosen for the final simulations of the AG tidal hydrodynamics are summarized in Table 2.

Table 2 Numerical and physical parameters adopted for the AG-Model.

Parameters	Value	Unit
Grid Resolution	5	(km)
Time Step	60	(s)
Chezy Coefficient	85	($m^{1/2}$ s^{-1})
Horizontal Eddy Viscosity (HEV)	1	(m^2 s^{-1})
Water Density	1028	(kg m^{-3})
Gravitational Acceleration	9.81	(m s^{-2})

3. Results and discussion

A 2-D hydrodynamic tidal model (5 km) has been setup for the entire AG system environment to study the tidal characteristics. To test the performance and quality of the AG-Model settings, two approaches were considered. Firstly, the model performance was assessed by comparing the model results in terms of water level with available hourly observed time series and tidal constituents based on T/P data. The model performance was also assessed by comparing the model results in terms of current velocities (U and V components) with the previous observational study of (Johns et al., 2003) for the year 1997. Both qualitative and statistical comparisons were carried out. In the second approach, discrepancies in terms of amplitudes and phases for the major semidiurnal and diurnal astronomical components were quantified statistically. In the following, the model evaluation, co-charts analysis, and simulated tidal currents are discussed.

3.1. Tidal elevation

In this section, comparisons of tidal elevations and statistical assessments of discrepancies between the model simulations and observations are presented. Figure 3a–g shows examples of the qualitative comparison for all stations, while Table 3 lists the statistical assessment. In general, the figure shows a good match between the simulated and observed

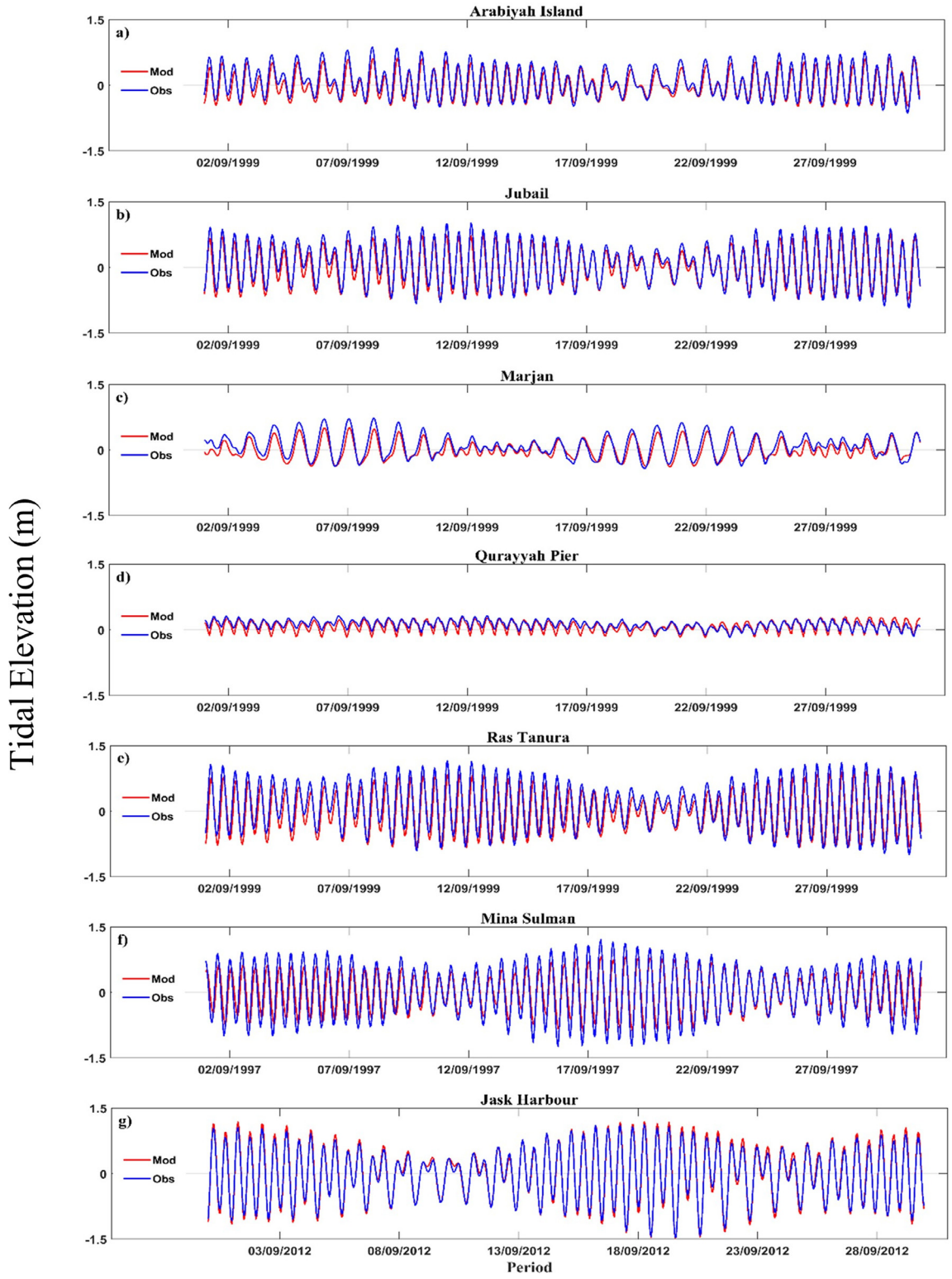

Figure 3 Comparisons between tidal predictions and observations at (a) Arabiyah Island, (b) Jubail, (c) Marjan, (d) Qurayyah Pier, (e) Ras Tanura, (f) Mina Sulman, (g) Jask Harbour.

tidal elevations. This is confirmed by predicting low and high water during neap and spring tidal cycles (Figure 3) and by reproducing the different tidal regimes in the Gulf region. However, there is an underestimation of high/low water at all stations, except for Jask Harbour. It is pronounced largely at Ras Tanura and Mina Sulman stations. These discrepancies may arise from several aspects, the most important is the bathymetry of the model, especially the

Table 3 Statistical analysis of all stations considered in the model validation.

Station No.	Station ID	*BIAS* (m)	*RMSD* (m)	*IOA*
1	*Arabiyah Island*	0.07	0.13	0.98
2	*Jubail*	0.08	0.14	0.99
3	*Marjan Island*	0.08	0.12	0.95
4	*Qurayyah Pier*	0.03	0.04	0.96
5	*Ras Tanura*	0.10	0.22	0.98
6	*Mina Salman*	0.01	0.23	0.99
7	*Jask Harbour*	0.01	0.07	0.99

Note: The P-value related to all comparisons is very low ($P > 0.0001$), indicating that the results from correlation are significant. *IOA* represents Index of agreement; *RMSD* represents root mean square difference and BIAS.

shallow coastal bathymetry. Previous studies indicated that the performance and accuracy of tidal regional models depend highly on correct seabed data, where these models are often restricted by seabed data, especially in shallow regions (Madah et al., 2015; Quaresma and Pichon, 2013). Moreover, the locations of the tide gauge stations of Ras Tanura and Mina Sulman are mainly at port constructions or marine platforms, which have topographic influences. Such influences may be difficult to be resolved by the present numerical model because of the mesh resolution and bathymetry along these locations. This suggests that using high-resolution bathymetry data in shallow regions is indispensable for tidal simulation in the AG. For phase conditions, there is a very slight phase lag between the model simulations and observations, pronounced mainly at the Marjan station (Figure 3).

To further quantify the discrepancies between the water level observations and the AG-Model predictions, calculation of the respective discrepancies at the high/low water level was conducted (Table 3). Statistical parameters have been determined for each observation point considered in the visual interpretation for Figure 3. In general, Table 3 shows a very good agreement between the water level observations and simulated time series. It was found that *RMS* error ranges from 0.07 to 0.23 m while the *BIAS* value varies from 0.01 to 0.1 m with maximum discrepancies observed at Ras Tanura and Mina Sulman stations. However, the *IOA* between the simulated and observed water levels was significant with p-values less than 0.0001. The *IOA* values are found to be varied between 0.95—0.99 for all stations. These statistical values reflect that the AG-Model is able to reproduce the tidal levels in the Arabian Gulf region to a very good degree.

Further validation of the AG-Model was carried out considering T/P altimetry data at 20 points selected within the Gulf domain (see Figure 2 for their locations). In general, the predicted amplitudes and phases of semidiurnal and diurnal tidal constituents are in very good agreement with the values of T/P data (Figure 4a, b).

In the second approach, harmonic analysis of the simulated and observed tidal data was performed to evaluate the discrepancies in terms of amplitude and phase of the major semidiurnal and diurnal astronomical components. An overview of the discrepancies at the stations of Jask Harbour, Qurayyah, Ras Tanura, and Marjan Island is presented in Table 4. The last column in the table lists the signal-to-noise ratio (*SNR*). The results of the other stations are shown in Appendix A. Statistical assessment of the discrepancies which includes *SD*, *UER*, *LER*, and *SVD* of the residuals based on the *Delft3D-TRIANA* tool is presented in Table 5.

From Table 4, the simulated and observed amplitudes errors ($H_C - H_O$) of all components are found to be in the range of a few centimetres, varying between -0.065 to 0.02 m in all stations. Maximum discrepancies are found for the M_2 tidal wave in the Marjan and Ras Tanura stations (0.020 and -0.055) respectively and K_1 tidal wave (-0.065) in the Marjan station only. However, the Mina Sulman station having slightly the largest discrepancies as shown in Appendix A. Excluding this station, the results indicate that the tidal model (AG-Model) in terms of amplitudes of the major semidiurnal and diurnal tides is performing well. On the other hand, the amplitude ratio (H_c / H_o) for semidiurnal tidal constituents is found to be 1 in all stations except the Marjan station, which is showing a slightly larger value, while for diurnal constituents is ranged between 0.5 to 1. The phase errors ($G_c - G_o$) between the computed and observed tidal constituents are observed to be satisfactorily in all stations, with maximum phase errors observed at Ras Tanura station for S_2. Statistical assessment in Table 5 shows that the *SD* of the tidal analysis is close to zero. In terms of *LER* and *UER*, they range from -0.13 to -0.09, and from 0.03 to 0.16, respectively. The *SVD*, (which is a ratio for the total discrepancies of all constituents) is found to be 0.074, 0.269, 1.397, and 0.741 for Jask Harbour, Qurayyah, Ras Tanura, and Marjan Island stations, respectively. These results indicate that the tidal model (AG-Model) in terms of amplitude and phase is performing well.

3.2. Co-amplitude and co-phase charts analysis

To generate co-tidal charts, the tidal components obtained from the harmonic analysis of the AG-Model outcomes were used. Three dominant tidal regimes have been identified in the AG, mainly the mixed, semidiurnal, and diurnal tides (e.g., Akbari et al., 2016; Siddig et al., 2019). As mentioned in the introduction that previous modelling studies considered only the four tidal components (M_2, S_2, P_1, O_1) to show co-amplitude and co-phase charts. In this study, the four major tidal constituents of each tidal regime (M_2, N_2, S_2, K_2, K_1, P_1, O_1, Q_1) dominate the region were considered in the analysis to enhance our understanding and knowledge of the tidal hydrodynamics in the AG. The resulting co-amplitudes and co-phases were analysed and compared with the previous modelling studies as well as the British

Table 4 Comparison between amplitudes and phases of computed and observed tidal components for Jask Harbour, Qurayyah Pier, Ras Tanura, and Marjan stations.

Components	*Jask Habour*								*Qurayyah Pier*							
	H_o	H_c	G_o	G_c	$H_c - H_o$	$G_c - G_o$	H_c / H_o	*SNR*	H_o	H_c	G_o	G_c	$H_c - H_o$	$G_c - G_o$	H_c / H_o	*SNR*
M_2	0.681	0.666	155.7	156.9	0.015	1.2	1.02	6E+04	0.08	0.095	252.5	195.0	0.011	-57.7	1.10	4E+04
S_2	0.265	0.259	185.0	187.9	0.006	3.0	1.02	8E+03	0.02	0.024	309.9	238.0	0.002	-71.7	1.10	2E+03
N_2	0.166	0.166	140.9	139.7	0.000	-1.2	1.00	3E+03	0.02	0.018	219.5	161.0	0.003	-58.4	1.20	1E+03
K_2	0.076	0.069	180.6	182.3	0.007	1.7	1.10	5E+02	0.01	0.007	289.0	229.0	0.000	-60.4	1.00	2E+02
K_1	0.395	0.397	338.4	339.8	-0.002	1.4	1.00	9E+03	0.03	0.017	110.3	48.5	-0.008	-61.8	0.70	2E+03
O_1	0.205	0.205	339.6	341.8	0.000	2.2	1.00	3E+03	0.02	0.014	24.5	348.0	-0.003	-36.9	0.80	1E+03
P_1	0.117	0.122	335.2	338.5	-0.005	3.3	0.96	1E+03	0.01	0.003	83.5	13.6	-0.003	-69.9	0.50	8E+01
Q_1	0.044	0.045	345.4	344.5	-0.001	-0.9	0.97	1E+02	0.00	0.002	6.6	309.0	0.000	-57.6	1.00	2E+01
Components	*Ras Tanura*								*Marjan*							
	H_o	H_c	G_o	G_c	$H_c - H_o$	$G_c - G_o$	H_c / H_o	*SNR*	H_o	H_c	G_o	G_c	$H_c - H_o$	$G_c - G_o$	H_c / H_o	*SNR*
M_2	0.613	0.558	128.9	63.0	-0.055	-65.9	0.91	6E+04	0.056	0.076	262.8	204.0	0.020	-59.0	1.36	4E+03
S_2	0.216	0.179	185.2	111.8	-0.037	-73.4	0.82	8E+03	0.031	0.035	216.8	165.0	0.004	-51.7	1.14	1E+03
N_2	0.125	0.118	98.8	30.1	-0.007	-68.7	0.94	3E+03	0.015	0.018	155.7	92.0	0.004	-64.2	1.25	3E+02
K_2	0.080	0.075	177.2	104.4	-0.005	-72.9	0.90	5E+02	0.008	0.010	17.5	324.0	0.003	-53.5	1.25	6E+01
K_1	0.147	0.120	339.1	298.2	-0.027	-40.9	0.81	9E+03	0.312	0.248	97.2	67.0	-0.065	-29.9	0.80	3E+03
O_1	0.116	0.104	281.2	254.4	-0.012	-26.8	0.90	3E+03	0.193	0.169	137.1	119.0	-0.024	-18.3	0.90	1E+03
P_1	0.045	0.032	328.4	283.0	-0.013	-45.4	0.70	1E+03	0.097	0.072	101.8	70.0	-0.025	-31.6	0.74	3E+02
Q_1	0.020	0.020	269.8	230.1	0.000	-39.7	0.98	1E+02	0.033	0.030	23.3	0.3	-0.003	-23.0	0.91	3E+01

H_o: amplitude of observed tide, ***G_o***: phase of the observed tide, ***H_c***: amplitude of simulated tide, ***G_c***: phase of the simulated tide, ***H_c - H_o***: amplitude difference, ***G_c - G_o***: Phase difference, ***H_c / H_o***: Amplitude ratio, ***SNR***: signal-to-noise ratio.

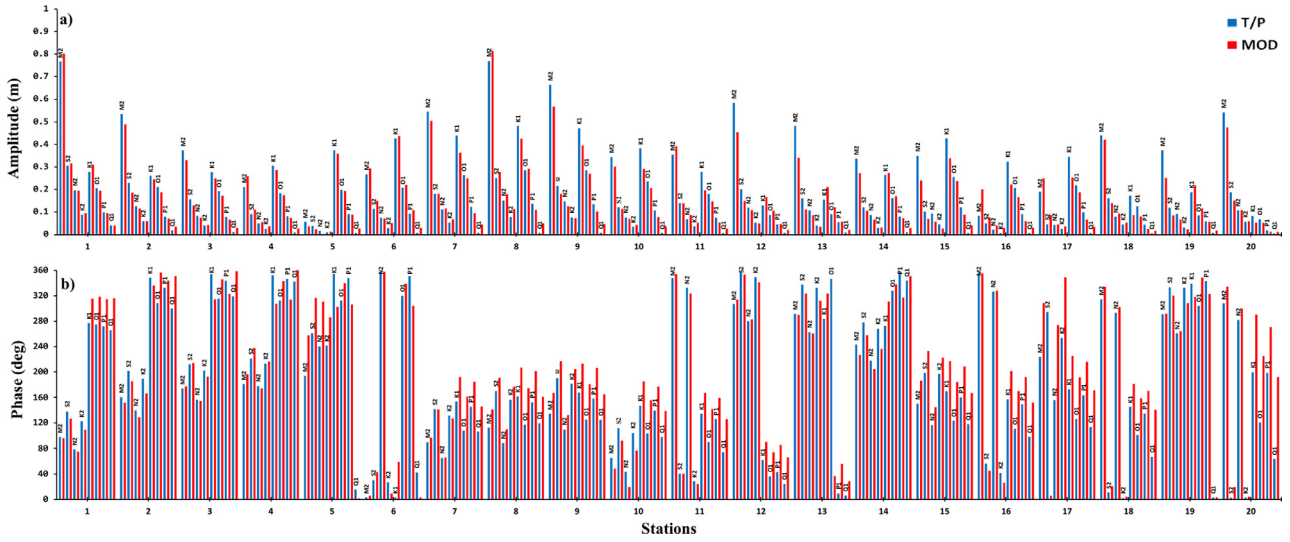

Figure 4 Comparisons of tidal (a) amplitudes and (b) phases between the AG-Model and T/P data.

Table 5 Statistical Assessment obtained from *Delft3D-TRIANA*.

Parameters	Station ID			
	Jask Harbour	*Qurayyah Pier*	*Ras Tanura*	*Marjan Island*
SD	0.008	0.029	0.047	0.030
LER	-0.027	-0.090	-0.130	-0.103
UER	0.032	0.092	0.165	0.091
SVD	0.074	0.269	1.397	0.741

SD: Standard deviation of tidal Analysis; **LER:** Lower extreme for residuals; **UER:** Upper extreme for residuals; **SVD:** Summed vector differences.

Admiralty (Admiralty, 2012) co-charts especially, the M_2, S_2, K_1, and O_1 tidal constituents.

3.2.1. Semidiurnal constituents

Co-amplitudes and co-phases of the major semidiurnal constituents (M_2, S_2, N_2, K_2) are displayed in Figure 5a–d, respectively. In general, the amplitudes of M_2, S_2, N_2, and K_2 tidal waves have the same performance in the AG basin. The dominant pattern of these tidal waves is the generation of two anticlockwise amphidromic points, one is in the northwestern part, and one is in the southern end of the basin centred around 28.25° and 24.5°N, respectively.

The M_2 tidal wave represents the largest among other constituents with a maximum amplitude of 0.9 m. The amplitude of S_2 tidal wave is low and represents almost 30% of the M_2, while N_2 and K_2 tides are relatively smaller in amplitudes compared to the S_2 tide. As can be seen from the figure that the semidiurnal M_2, S_2, N_2, and K_2 tidal waves have amplification in tidal height at several locations inside the AG basin (Figure 5). These locations are, the northern end of the Gulf (near Kuwait, Iraqi coast, and the northern coast of Iran), the middle part of the basin, mainly on the eastern coast (Iran) and on the Saudi coast, the northern Bahrain, the southwestern end of the basin and the Strait of Hormuz. On the other hand, the co-amplitude chart shows low amplitudes at the southeast coast of Iran, the UAE coast, the eastern coast of Qatar, the south of Bahrain, the Saudi coast, mainly in the vicinity of the Ras Tanura, Qurayyah Pier, and Mina Sulman stations. Figure 5 also shows the calculated phases for the major semidiurnal tidal constituents in the AG. In general, the tidal amplitudes and phases are in good agreement with the co-amplitude and co-phase lines of the British Admiralty charts (Admiralty, 2012).

3.2.2. Diurnal constituents

co-amplitudes and co-phases of the major diurnal constituents (K_1, P_1, O_1, Q_1) are shown respectively in Figure 6a–d, respectively. The major feature of these tidal waves is the generation of a single amphidromic point in the central portion of the AG centred around 26.8°N (North Bahrain). In general, the diurnal constituents show amplification in tidal amplitude at several different locations, with a minimum value in the central part where a virtual amphidromic system is developed.

The diurnal component K_1 represents the largest among other constituents with a maximum amplitude of 0.42 m. The amplitude of O_1 tidal wave is about 50% lower than the K_1 tide, while P_1 and Q_1 tides are smaller in amplitudes compared to the O_1 tide. Maximum computed amplitudes for P_1 and Q_1 are respectively 0.1 and 0.04 m (Figure 6 c, d). The K_1, P_1, O_1, and Q_1 tidal waves have amplification in tidal height toward the head of the Gulf (Kuwait, Iraqi coasts, and northern coast of Iran), and the southeastern coast of Qatar, the southern Emirate coast, and

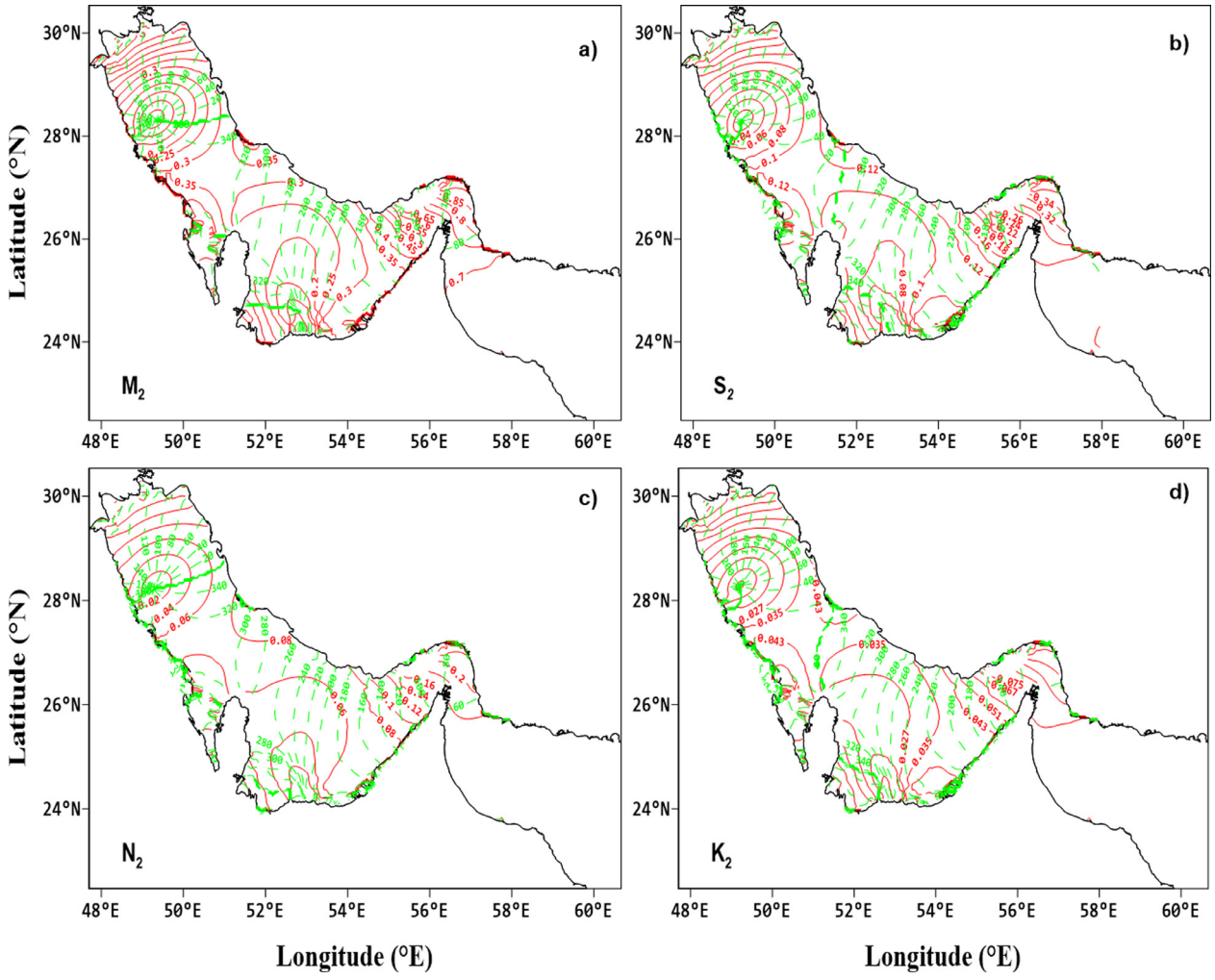

Figure 5 Co-amplitudes (red solid-lines) and co-phases (green dashed-lines) of major semidiurnal components (M_2, S_2, N_2, K_2).

the Gulf of Oman including the strait of Hormuz (Figure 6). The patterns observed along the southern Emirate coast are consistent with the tidal values reported in the coastal studies by Balaji (2012) and Mohamed and El-Dahshan (2002), however, they were not shown in the previous modelling studies. On the other hand, low amplitudes were observed at the south of Bahrain, the Saudi coast (mainly in the vicinity of Qurayyah Pier and Mina Sulman stations), the UAE coast, the south-western coast of Qatar. The computed amplitudes and phases are in good agreement with the British Admiralty Charts (Admiralty, 2012).

The above basic tidal patterns, in general, are consistent with all previous modelling studies and the British Admiralty charts (Admiralty, 2012); however, the position of the amphidromic points especially for semidiurnal constituents as well as locations of high/low amplitudes are slightly different when comparing with some previous modelling studies but comparable to the latter. The Admiralty (2012) charts, Lardner et al. (1988, 1982), Trepka (1968), Najafi and Noye (1997), and our model results show that the position of the amphidromic systems produced by (M_2, S_2) tidal waves is close to the western coast, unlike few studies that showed positions that are mostly near the centre of the basin. However, Lardner et al. (1982) produced the co-chart for M_2 with under- overestimation in some areas and later produced the amplitudes and phases of M_2 and K_1 tidal waves with also underestimations of amplitudes due to the coarse grid model used along the coastline (20 km) (Lardner et al., 1988). Moreover, Trepka (1968) found that the amplitude error of S_2, K_1, and O_1 tidal constituents was large. He recommended using a finer grid resolution and more than 7 tidal constituents along the open boundary to get the prediction of the minor tides. Najafi and Noye (1997) also modelled the AG tides using Cartesian coordinates to produce the M_2, S_2, K_1, and O_1 tidal charts and found that the predicted phases were not well reproduced by the model.

3.3. Sensitivity analysis for the number of tidal constituents at the open boundary

To test the accuracy of the numerical model in representation of the tidal conditions in the Gulf region, three different scenarios were carried out considering different number of tidal constituents along the open boundary. In the first scenario (SN-1), the model was run using only the four tidal constituents (M_2, S_2, K_1, O_1) at the open sea boundary. In the second scenario (SN-2), the model was driven

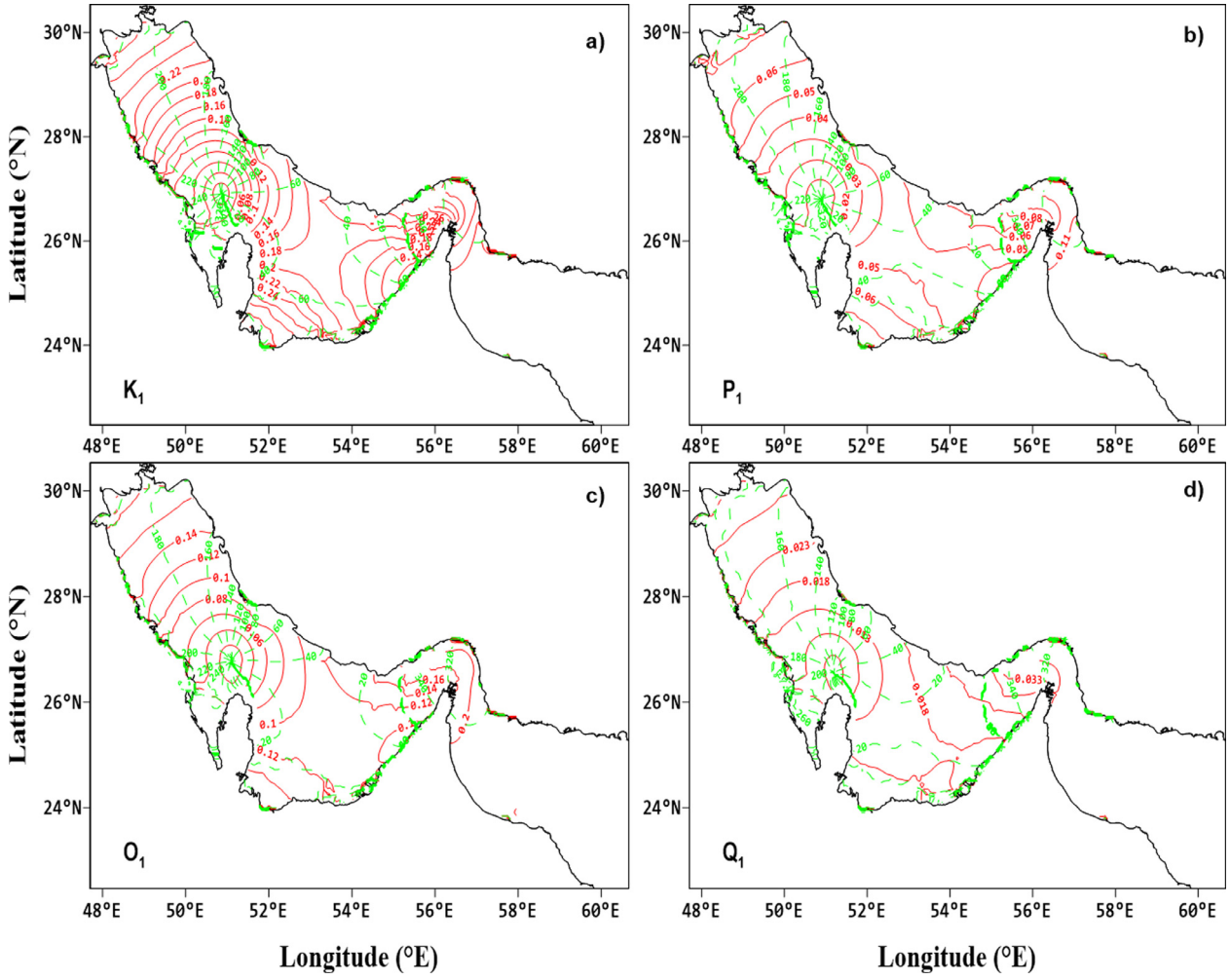

Figure 6 Co-Amplitudes (red solid-lines) and co-phases (green dashed-lines) of major diurnal components (K_1, P_1, O_1, Q_1).

by the major eight semidiurnal (M_2, N_2, S_2, K_2) and diurnal tidal components (K_1, O_1, P_1, Q_1). In the third scenario (SN-3), the same as the second one but with additional five tidal constituents (M_f, M_m, M_4, MS_4, MN_4). Figure 7 shows an example of the model predictions of the three scenarios against the observations at two coastal stations (Ras Tanura and Mina Sulman), while Table 6 lists the statistical assessment for all stations considered in the analysis. The initial simulation (SN-1) shows that the AG-Model produces similar tidal elevations to the observed ones, however the discrepancies are large at the coastal areas, where the *RMSE* varies between 0.12 to 0.28 m. The simulation of the SN-2 shows slight improvements in tidal amplitudes compared with the SN-1. The *RMS* error ranges from 0.07 to 0.25 m with maximum discrepancies found at the coastal stations (Ras Tanura and Mina Sulman). The tidal predictions of the last scenario (SN-3) confirms that the AG-Model produces better results compared to the two previous scenarios (SN-1 and SN-2), especially at the coastal stations, where the discrepancies are less than 0.24 m (Figure 7 and Table 6).

The statistical assessment in Tables 3 and 5 also confirms the model ability to reproduce the tidal regimes in the Gulf accurately. This indicates that using 13 tidal constituents along the open boundary is very important in simulating the tidal conditions in the AG region. Such tidal constituents are necessary to be incorporated to reproduce the regional propagation of tidal waves (Quaresma and Pichon, 2013), thus, they can interact nonlinearly. The AG-Model predictions based on using 13 tidal constituents along the open boundary conditions showed a very good agreement with the water level time series observations in the Gulf region (Figure 3). Maximum discrepancies in amplitudes are found in the range of 0.065 m at Marjan station only for K_1, while on average, the errors for all tidal constituents considered in the analysis are in the order of less than 0.02 m (4%) (Table 4 and Appendix A). This error value is reflecting a very good performance of the AG-Model compared with the previous modelling studies carried out in the Gulf, where minimum discrepancies (on average 0.05 m, 10%) were found in the study by Pous et al. (2012) who used only 7 tidal constituents along the open boundary. On the other hand, the comparison of the tidal constituents between the AG-Model and T/P altimetry data showed a very good agreement (Figure 4), indicating the effectiveness of the tidal constituents prescribed along the open boundary in explaining the tidal conditions in the Gulf region.

Although the AG-Model underestimates slightly the amplitudes of the tidal constituents, especially at Ras Tanura,

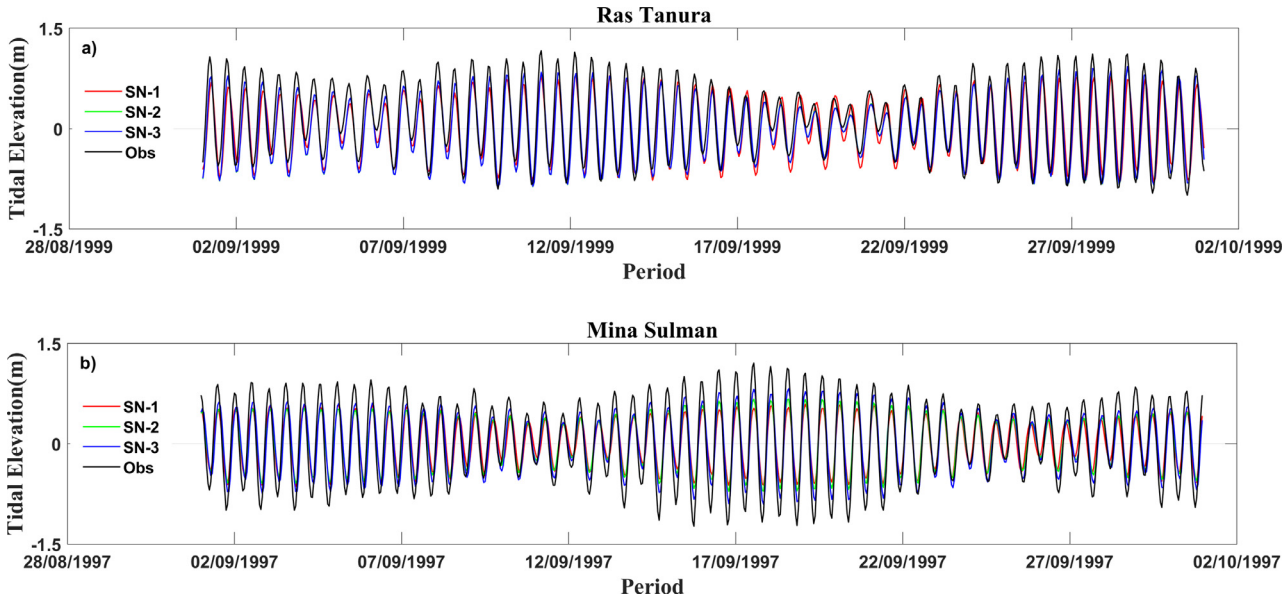

Figure 7 Comparisons between tidal predictions and observations at (a) Ras Tanura and (b) Mina Sulman stations considering a different number of tidal constituents at the open boundary.

Table 6 Statistical analysis for the number of tidal constituents at the open boundary.

Station ID	*Scenarios*	*RMSE (m)*
Arabiyah	SN-1: 4TC	0.15
Island	SN-2: 8TC	0.14
	SN-3: 13TC	0.13
Jubail	SN-1: 4TC	0.16
	SN-2: 8TC	0.15
	SN-3: 13TC	0.14
Marjan	SN-1: 4TC	0.12
Island	SN-2: 8TC	0.13
	SN-3: 13TC	0.12
Qurayyah	SN-1: 4TC	0.08
Pier	SN-2: 8TC	0.07
	SN-3: 13TC	0.04
Ras	SN-1: 4TC	0.26
Tanura	SN-2: 8TC	0.23
	SN-3: 13TC	0.22
Mina	SN-1: 4TC	0.28
Sulman	SN-2: 8TC	0.25
	SN-3: 13TC	0.23
Jask	SN-1: 4TC	0.17
Harbour	SN-2: 8TC	0.08
	SN-3: 13TC	0.07

Note: The **TC** represents tidal constituents, ***RMSE*** represents Root mean square difference. SN-1: [M_2, S_2, K_1, O_1]; SN-2: [M_2, S_2, N_2, K_2, K_1, O_1, P_1, Q_1]; SN-3: [M_2, S_2, N_2, K_2, K_1, O_1, P_1, Q_1, M_f, M_m, M_4, MS_4, MN_4]

Mina Sulman stations (the western coast) as shown from the statistical analysis (Section 2.3), the model captures all regions of high and low amplitudes accurately (Figure 5, 6) identical to the British Admiralty Charts (Admiralty, 2012). However, the coastal areas of Ras Tanura and Mina Sulman stations are shallow and complex due to coastal constructures, indicating that the grid resolution along these stations is inadequate to resolve the tidal amplitudes accurately. These results may be improved by applying a nesting approach as explained by Spall and Holland (1991), considering parent and child grids with changing grid spacings, in which the child grid has a finer resolution in areas of question. In this approach, the data is exchanged between the coarse parent grid and the finer child grid, allowing the child model to resolve better the tidal hydrodynamic patterns in such complex regions, as applied in several regional ocean modelling (e.g., Barth et al., 2005; Debreu et al., 2012; Mason et al., 2010). In this frame, the numerical model reliability would be enhanced, thus, the AG-Model can be applied as a regional model.

3.3. Form factor analysis

To find out the relative importance of the semidiurnal and diurnal tidal components in the AG, the form factor (*FF*) is calculated based on (Pugh, 2004):

$$FF = \frac{O_1 + K_1}{M_2 + S_2}$$

where O_1, K_1, M_2, and S_2 are the elevation amplitudes of the indicated components. To classify, if $FF < 0.25$ the tide is semidiurnal; if *FF* is between 0.25 and 1.5, the tide is mixed semidiurnal; if *FF* is between 1.5 and 3, the tide is mixed diurnal, and when $FF > 3$, the tide is diurnal. Figure 8 shows the spatial distribution of the *FF* in the AG basin. As can be observed that the AG-Model reproduces the tidal types observed in the region accurately, where the tidal type varies according to the location. The relative importance is clear in the northern and southern portions of the AG where anticlockwise amphidromic points are developed, and it is not constant in the whole AG. Thus, the diurnal tide is greater in the northern and southern parts of the AG, showing mixed

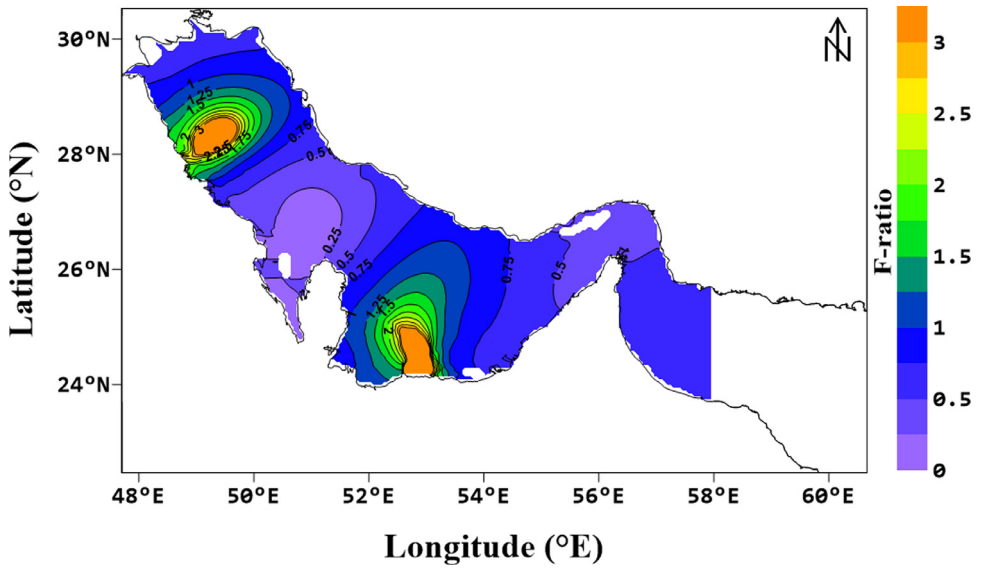

Figure 8 Distribution of form factor based on the model results.

Table 7 Comparison between amplitudes and phases of computed and observed tidal components of East velocities (m s^{-1}) at the Strait of Hormuz for the year 1997.

Components	H_o	H_c	G_o	G_c	$H_c - H_o$	$G_c - G_o$	H_c / H_o
M_2	0.208	0.249	35.4	42.0	0.041	6.7	1.1
S_2	0.085	0.096	69.3	74.1	0.011	4.8	1.1
N_2	0.053	0.059	18.2	24.6	0.006	6.4	1.1
K_1	0.236	0.228	204.6	213.8	-0.008	9.1	0.9
O_1	0.091	0.107	177.5	202.0	0.016	24.6	1.1
P_1	0.072	0.063	185.9	210.5	-0.009	24.6	0.9

H_o: amplitude of observed tide, G_o: phase of the observed tide, H_c: amplitude of simulated tide, G_c: phase of the simulated tide, H_c - H_o: amplitude difference, G_c - G_o: Phase difference, H_c / H_o: Amplitude ratio.

nature dominant with semidiurnal and diurnal components on the eastern coast and the western coast respectively. The figure reveals that the diurnal nature (orange) dominates in the northern part of the AG, at around 28°N; while the surrounding is dominated by the mixed tides, mainly diurnal (green) and semidiurnal (blue). Similar characteristics are observed in the southwestern part of the basin, at approximately 24.5°N, while the central part of the AG and the strait of Hormuz are dominated by semidiurnal components (purple). These results agree with the previous studies in the region (e.g., Akbari et al., 2016; Siddig et al., 2019).

3.4. Tidal currents

To evaluate the simulation results in terms of U and V components, barotropic tidal currents based on ADCP observations reported in Johns et al. (2003) for the year 1997 at one station located in the Strait of Hormuz were considered. Table 7,8 list the comparisons between amplitudes and phases of observed and simulated tidal constituents of east and north velocities, while Table 9 shows the statistical assessment. The comparison indicates that the simulated and observed amplitude errors ($H_C - H_O$) of M_2, N_2, S_2, K_1, P_1, and O_1 are found to be in the range of a few m s^{-1}, varying between -0.01 to 0.041 m s^{-1} for east and north velocity components. The maximum discrepancies are found for M_2 tidal velocity with 0.041 and 0.024 m s^{-1} for U and V respectively, while minimum errors are observed for P_1. On the other hand, the phase errors ($G_c - G_o$) between the computed and observed *U* and *V* components are found to be reasonable, with maximum phase errors of 32.9 and 32.3 degrees for the north velocity of O_1 and P_1 respectively. To obtain an evaluation of the model performance regarding horizontal and/or vertical tide, the deviations in terms of amplitude ratio and phase errors were considered. The typical value of phase error is 0 and the amplitude ratio is 1 (Deltares, 2011). It was observed that the amplitude ratio (H_c / H_o) is approximately close to 1 for all components of *U* and *V* tide, and the phase errors ($G_c - G_o$) are found to be less than 33 degrees. Statistical assessment in Table 9 shows that the *SD* of the tidal analysis is 0.01, while the *SVD* is less than 0.2. These results indicate that the tidal model (AG-Model) in terms of east and north velocities is performing well.

To study the tidal currents in the AG, the simulated tide-induced currents from the numerical model are analysed. The simulation results are analysed under flood and ebb conditions during the spring tide. The simulated tide-induced current patterns during flood and ebb are shown in Figure 9a,b. The tidal currents in general are changing

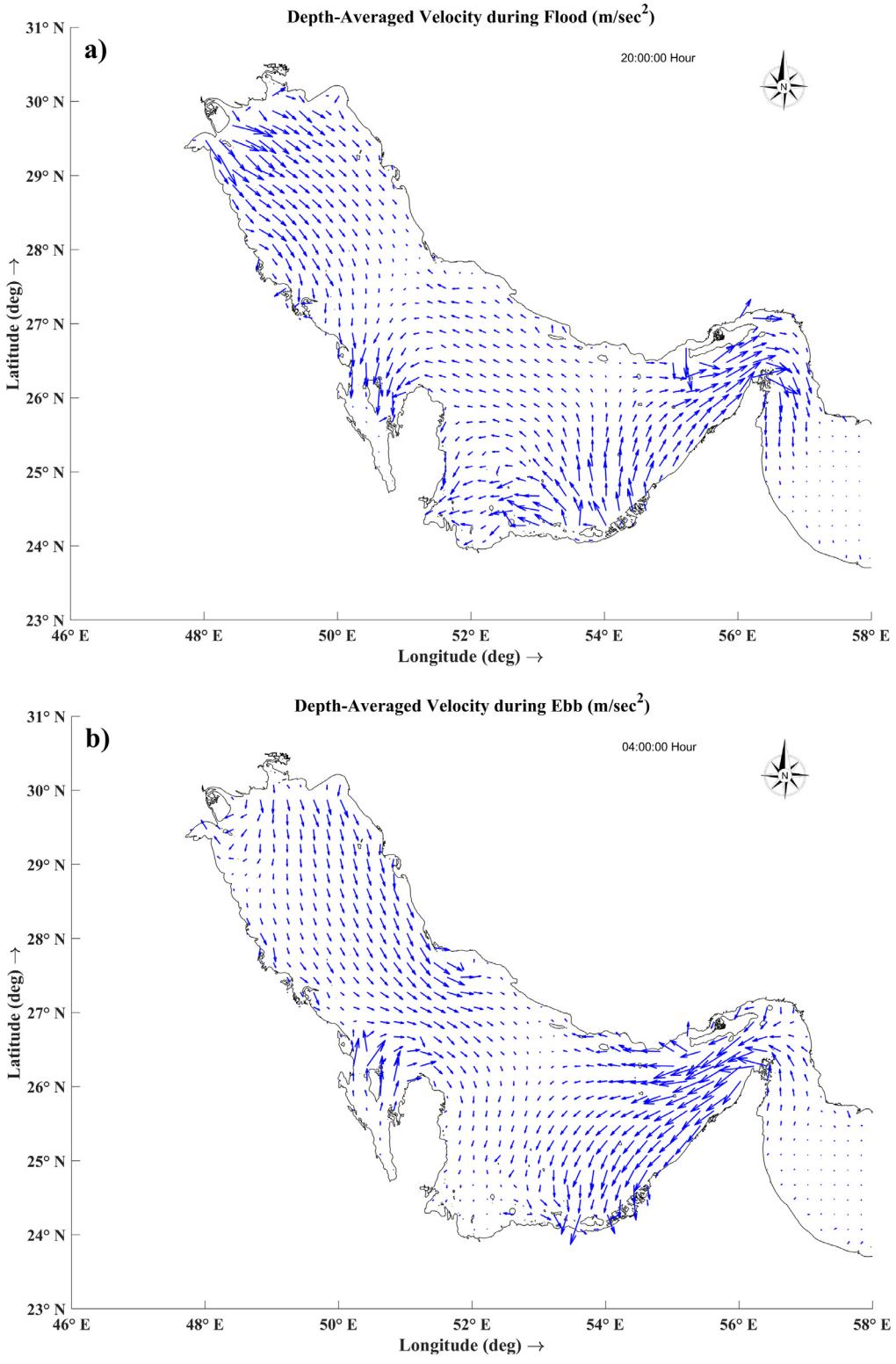

Figure 9 Depth averaged velocity during (a) flood (20:00:00 hr) and (b) ebb (04:00:00 hr) conditions.

based on the basin geometry and ocean currents of flood and ebb tides. The simulation results reveal that the current magnitude of 0.25—0.5 m s^{-1} is dominated in the AG. The highest velocities during flood tide were observed in the Strait of Hormuz, in the vicinity of the northern part, in the vicinity of Bahrain and western coast of Qatar, and in the shallow coastal areas along UAE. The maximum current velocities extend up to 0.86 m s^{-1} in the vicinity of the Strait of Hormuz and the head of the Gulf. The simulation results are comparable with the tidal simulations of Najafi and Noye, (1997) and the more recent modelling study of Mehri et al. (2021).

The simulation results suggest an intensification of currents along the north-western coast (Saudi coast) directed

Table 8 Comparison between amplitudes and phases of computed and observed tidal components of North velocities (m s^{-1}) at the Strait of Hormuz for the year 1997.

Components	H_o	H_c	G_o	G_c	$H_c - H_o$	$G_c - G_o$	H_c / H_o
M_2	0.152	0.176	34.9	49.7	0.024	14.8	1.1
S_2	0.062	0.068	69.7	81.1	0.007	11.4	1.1
N_2	0.038	0.042	18.2	32.2	0.004	14.0	1.0
K_1	0.171	0.163	204.6	221.9	-0.008	17.3	0.9
O_1	0.062	0.075	177.5	210.4	0.013	32.9	1.2
P_1	0.055	0.045	185.8	218.1	-0.010	32.3	0.8

H_o: amplitude of observed tide, G_o: phase of the observed tide, H_c: amplitude of simulated tide, G_c: phase of the simulated tide, H_c - H_o: amplitude difference, G_c - G_o: Phase difference, H_c / H_o: Amplitude ratio.

Table 9 Statistical assessment obtained from *Delft3D-TRIANA*.

Parameters	East velocities at Strait of Hormuz	North velocities at Strait of Hormuz
SD	0.01	0.01
LER	-0.04	-0.03
UER	0.04	0.03
SVD	0.18	0.19

SD: Standard deviation of tidal Analysis; **LER:** Lower extreme for residuals; **UER:** Upper extreme for residuals; **SVD:** Summed vector differences.

southward, and along the UAE shallow areas directed northward and eastward. On the other hand, maximum currents magnitude during ebb tide (0.25 m s^{-1}) is also detected in the Strait of Hormuz, and along the UAE shallow coastal waters (0.4 m s^{-1}). The simulation results reveal that the direction of tidal currents contains some variability. In the northern and central part, the tidal currents are directed southward, however, in the Strait of Hormuz and the southern part, it is opposite, causing a deviation to the tidal currents towards the south-western coast.

4. Conclusion

The current study is concerned with the simulation of tidal hydrodynamics in the AG using a vertically 2-D hydrodynamic model based on the *Delft3D* modelling system. The model is a barotropic solution forced by 13 tidal components at the open boundaries in the eastern Gulf of Oman (58°E). The model results were validated against the available water level observations at 7 locations, and data from T/P, where statistical analyses in terms of *BIAS*, *RMSD*, *IOA*, *SD*, and *SVD* parameters were considered to evaluate the numerical model. Using 13 tidal constituents along the open boundary indeed provided very good results (error 4%) compared with the previous modelling studies carried out in the Gulf, which considered only a limited number of tidal constituents to drive the models, indicating that nonlinear interactions cannot be ignored. Sensitivity analysis also showed that the model prediction based on 13 tidal constituents produces much better results than the model prediction using 4/8 tidal components at the open sea boundary. The analysis showed that the *BIAS* value varies from 0.01 to 0.1 m while, *RMS* error was found to be ranged from 0.07 to 0.23 m, with maximum discrepancies observed at Ras Tanura and Mina Sulman stations. These two stations are mainly located at marine platforms/constructions, and characterised by complex bathymetry, therefore, a small-scale high-resolution 'child' model coupled with a coarse-scale 'parent' model applying the nesting approach would improve the accuracy of predictions in such areas, as shown in different studies (e.g., Barth et al., 2005; Debreu et al., 2012). However, the *IOA* was found to be significant with p-values less than 0.0001. The *IOA* values are found to be over 0.95 for all stations, except the Qurayyah Pier station, with a value of 0.83 (Table 3). The *SD* of the tidal analysis is found close to zero, while the *SVD* is found to be 0.074, 0.269, 1.397, and 0.741 for Jask Harbour, Qurayyah, Ras Tanura, and Marjan Island stations respectively (Table 5). On the other hand, the amplitude ratio (H_c /H_o) for semidiurnal tidal constituents and diurnal constituents is found close to 1, while the phase error ($G_c - G_o$) is observed to be satisfactorily in all stations. Based on the statistical evaluation, the simulation results were analysed to generate co-tidal charts. The results showed that the semidiurnal tides generate two amphidromic points located in the northern and southern parts, around 28.25° and 24.5°N respectively, while diurnal tides generate a single amphidromic system located in the central part around 26.8°N.

The hydrodynamic model was also validated in terms of *U* and *V* velocity components in the Strait of Hormuz with a previous study by Johns et al. (2003). The amplitude ratio (H_c / H_o) is found to be close to 1 for all components of *U* and *V* tide, and the phase error ($G_c - G_o$) is found to be less than 33 degrees. The simulation showed that the highest velocities occur in the Strait of Hormuz, in the vicinity of the northern part, in the vicinity of Bahrain and western coast of Qatar, and in the shallow coastal areas along UAE. The simulation also suggests an intensification of tidal currents along the north-western coast (Saudi coast) during flood condition

and the eastern coast of Iran during ebb condition directed southward. In summary, although the AG-Model underestimates slightly high/low waters, the analysis indicates that the model can reproduce the tidal surface elevations in the AG region with very good accuracy. In the next step, the 2-D tidal model will be extended into a 3-D approach to investigate the relevant forcing mechanisms that play a major role in the circulation of the AG, including wind conditions and thermohaline fluxes.

Acknowledgment

The simulations in this work were performed at King Abdul-Aziz University's High-performance Computing Centre (Aziz super-computer) (http://hpc.kau.edu.sa). This project was funded by the Deanship of Scientific Research (DSR), King Abdulaziz University, Jeddah, under grant No. (D-086—150-1441). The authors, therefore, gratefully acknowledge DSR technical and financial support. The authors are also highly thankful to the ARAMCO Oil Company and Sea Level Centre at University of Hawaii for providing the Sea Level data.

Appendix

Table 1a, 2a, 3a and 4a.

Table 1a Comparison between amplitudes and phases of computed and observed tidal components at Jubail station.

Components	H_o	H_c	G_o	G_c	$H_c - H_o$	$G_c - G_o$	H_c / H_o	*SNR*
M_2	0.544	0.502	137.6	231.1	-0.042	93.5	0.9	1E+03
S_2	0.246	0.206	90.4	153.4	-0.040	63.1	0.8	1.9E+02
N_2	0.093	0.098	105.7	19.1	0.004	-86.6	1.0	2.8E+01
K_2	0.025	0.064	160.9	99.1	0.039	-61.8	2.6	7.2E-03
K_1	0.144	0.102	84.5	64.3	-0.042	-20.2	0.7	1.9E+02
O_1	0.144	0.119	293.1	292.4	-0.024	-0.7	0.8	2.1E+02
P_1	0.043	0.036	100.8	98.2	-0.006	-2.6	0.9	3.8E+00
Q_1	0.020	0.022	264.8	221.2	0.002	-43.6	1.1	2.3E+00

H_o: amplitude of observed tide, G_o : phase of the observed tide, H_c: amplitude of simulated tide, G_c: phase of the simulated tide, H_c - H_o: amplitude difference, G_c - G_o: Phase difference, H_c / H_o: Amplitude ratio, *SNR*: signal-to-noise ratio.

Table 2a Comparison between amplitudes and phases of computed and observed tidal components at Arabiyah Island station.

Components	H_o	H_c	G_o	G_c	$H_c - H_o$	$G_c - G_o$	H_c / H_o	*SNR*
M_2	0.365	0.336	191.2	147.8	-0.029	-43.4	0.9	2.5E+03
S_2	0.132	0.111	162.1	115.0	-0.020	-47.2	0.8	2.6E+02
N_2	0.069	0.069	61.9	15.2	-0.001	-46.7	1.0	8.4E+01
K_2	0.038	0.037	327.7	278.6	-0.001	-49.1	1.0	3.2E+01
K_1	0.189	0.150	95.8	66.3	-0.039	-29.5	0.8	1.8E+03
O_1	0.129	0.113	136.3	118.7	-0.016	-17.6	0.9	6.5E+02
P_1	0.061	0.044	98.0	67.0	-0.017	-31.0	0.7	1.8E+02
Q_1	0.022	0.021	25.3	357.8	-0.001	-27.4	1.0	2.1E+01

H_o: amplitude of observed tide, G_o: phase of the observed tide, H_c: amplitude of simulated tide, G_c: phase of the simulated tide, H_c - H_o: amplitude difference, G_c - G_o: Phase difference, H_c / H_o: Amplitude ratio, *SNR*: signal-to-noise ratio.

Table 3a Comparison between amplitudes and phases of computed and observed tidal components at Mina Sulman station.

Components	H_o	H_c	G_o	G_c	$H_c - H_o$	$G_c - G_o$	H_c / H_o	*SNR*
M_2	0.710	0.550	319.3	330.7	-0.160	11.4	0.8	5.4E+03
S_2	0.208	0.165	97.0	92.9	-0.042	-4.1	0.8	3.7E+02
N_2	0.156	0.125	6.5	17.4	-0.031	10.8	0.8	2.7E+02
K_2	0.081	0.050	252.7	249.2	-0.031	-3.5	0.6	9.5E+01
K_1	0.098	0.082	156.6	152.2	-0.016	-4.4	0.8	3.2E+02
O_1	0.065	0.056	16.4	32.2	-0.008	15.8	0.9	1.3E+02
P_1	0.036	0.022	166.1	155.2	-0.014	-10.8	0.6	4.3E+01
Q_1	0.009	0.010	60.4	79.9	0.001	19.5	1.0	2.9E+00

H_o: amplitude of observed tide, G_o: phase of the observed tide, H_c: amplitude of simulated tide, G_c: phase of the simulated tide, H_c - H_o: amplitude difference, G_c - G_o: Phase difference, H_c / H_o: Amplitude ratio, ***SNR***: signal-to-noise ratio.

Table 4a Statistical assessment obtained from *Delft3D-TRIANA*.

Parameters	Station ID		
	Jubail	*Mina Sulman*	*Arabiyah Island*
SD	0.040	0.049	0.028
LER	-0.143	-0.208	-0.099
UER	0.119	0.127	0.085
SVD	1.092	1.563	1.078

SD: Standard deviation of tidal Analysis; **LER**: Lower extreme for residuals; **UER**: Upper extreme for residuals; **SVD**: Summed vector differences.

References

Admiralty, 2012. Co-tidal atlas Persian Gulf. NP 214.

Ahmad, F., Sultan, S.A.R., 1991. Annual mean surface heat fluxes in the Arabian Gulf and the net heat transport through the Strait of Hormuz. Atmos. Ocean 29 (1), 54—61. https://doi.org/10.1080/07055900.1991.9649392

Akbari, P., Sadrinasab, M., Chegini, V., Siadatmousavi, M., 2016. Tidal constituents in the Persian Gulf, Gulf of Oman and Arabian Sea: a numerical study. Indian J. Geo-Mar. Sci. 45 (8), 1010—1016.

Al-Mahdi, A.A., Abdullah, S.S., Husain, N.A., 2009. Some features of the physical oceanography in Iraqi marine waters. Mesopotamian J. Mar. Sci. 24, 13—24.

Al-Subhi, A.M., 2010. Tide and sea level characteristics at Juaymah, west coast of the Arabian Gulf. J. King Abdulaziz Univ. Mar. Sci. 21, 133—149. https://doi.org/10.4197/Mar.21-1.8

Arakawa, A., Lamb, V.R., 1977. Computational Design of the Basic Dynamical Processes of the UCLA General Circulation Model. Methods Comput. Phys. 173—265. https://doi.org/10.1016/B978-0-12-460817-7.50009-4

Balaji, R., 2012. A case study on curtailed tidal hydrodynamic modeling along UAE coast. Int. J. Ocean Clim. Syst. 3, 45—56.

Barth, A., Alvera-Azcárate, A., Rixen, M., Beckers, J.-M., 2005. Two-way nested model of mesoscale circulation features in the Ligurian Sea. Prog. Oceanogr. 66, 171—189.

Bashir, M., 1993. Numerical modelling of tidal flows in the Arabian gulf. Brunel University, School of Information Systems, Computing and Mathematics.

Brewer, P.G., Dyrssen, D., 1985. Chemical oceanography of the Persian Gulf. Prog. Oceanogr. 14, 41—55.

Brewer, P.G., Fleer, A.P., Kadar, S., Shafer, D.K., Smith, C.L., 1978. Chemical oceanographic data from the Persian Gulf and Gulf of Oman. WHO Rep. 78, 37.

Chao, S.-Y., Kao, T.W., Al-Hajri, K.R., 1992. A numerical investigation of circulation in the Arabian Gulf. J. Geophys. Res. Ocean. 97, 11219—11236.

Debreu, L., Marchesiello, P., Penven, P., Cambon, G., 2012. Two-way nesting in split explicit ocean models: Algorithms, implementation and validation. Ocean Model. 49, 1—21.

Defant, A., 1961. In: Physical Oceanography, 1. Pergamon Press, London, 729 pp. https://doi.org/10.1017/S0025315400070089

Deltares, 2011. Delft3D-FLOW User Manual Simulation of Multi-dimensional Hydrodynamic Flows and Transport Phenomena, Including Sediments, User Manual, Hydro Morphodynamics, Version: 3.15

Egbert, G.D., Erofeeva, S.Y., 2002. Efficient Inverse Modeling of Barotropic Ocean Tides. J. Atmos. Ocean. Technol. 19, 183—204. https://doi.org/10.1175/1520-0426(2002)019⟨0183:EIMOBO⟩2.0.CO;2

Elshorbagy, W., Azam, M.H., Taguchi, K., 2006. Hydrodynamic characterization and modeling of the Arabian Gulf. J. Waterw. port, coastal, Ocean Eng. 132, 47—56.

Emery, K.O., 1956. Sediments and water of Persian Gulf. Am. Assoc. Pet. Geol. Bull. 40, 2354—2383.

Johns, W.E., Yao, F., Olson, D.B., Josey, S.A., Grist, J.P., Smeed, D.A., 2003. Observations of seasonal exchange through the Straits of Hormuz and the inferred heat and freshwater budgets of the Persian Gulf. J. Geophys. Res. 108 (12), 12—21. https://doi.org/10.1029/2003JC001881

Kämpf, J., Sadrinasab, M., 2006. The circulation of the Persian Gulf: a numerical study. Ocean Sci. 2 (1), 27—41. https://doi.org/10.5194/os-2-27-2006

Khalilabadi, M.R., 2016. Tide—surge interaction in the Persian Gulf, Strait of Hormuz and the Gulf of Oman. J. Weather 71 (10), 256—261. https://doi.org/10.1002/wea.2773

Lardner, R.W., Belen, M.S., Cekirge, H.M., 1982. Finite difference model for tidal flows in the Arabian Gulf. Comput. Math. Appl. 8 (6), 425—444. https://doi.org/10.1016/0898-1221(82)90018-9

Lardner, R.W., Lehr, W.J., Fraga, R.J., Sarhan, M.A., 1988. A model of residual currents and pollutant transport in the Arabian Gulf. Appl. Math. Model. 12, 379—390.

Madah, F., Mayerle, R., Bruss, G., Bento, J., 2015. Characteristics of tides in the Red Sea region, a numerical model study. Open J. Mar. Sci. 5, 193—209. https://doi.org/10.4236/ojms.2015.52016

Mason, E., Molemaker, J., Shchepetkin, A.F., Colas, F., McWilliams, J.C., Sangrà, P., 2010. Procedures for offline grid nesting in regional ocean models. Ocean Model 35, 1—15.

Mehri, F., Torabi Azad, M., Mansoury, D., 2021. A Hydrodynamic Model of Tidal Current in the Strait of Hormuz. Int. J. Coast. Offshore Eng. 37—45.

Mohamed, K.A., El-Dahshan, M.E., 2002. Tidal analysis and prediction of the flow characteristics around. Abu dhabi Island. WIT Trans. Eng. Sci. 36.

Najafi, H.S., 1997. Modelling tides in the Persian Gulf using dynamic nesting. Univ. Adelaide, South Australia, 145 PP.

Palacio, C., Mayerle, R., Toro, M., Jimenez, N., 2005. Modelling of flow in a tidal flat area in the south-eastern German bight. Die Küste, 69 PROMORPH, 141—174.

Perrone, T.J., 1979. Winter shamal in the Persian Gulf. Tech. Rep., Naval Environ. Predict. Res. Facil., Monterey, Calif. 79—106.

Poul, H.M., Backhaus, J., Huebner, U., 2016. A description of the tides and effect of Qeshm canal on that in the Persian Gulf using two-dimensional numerical model. Arab. J. Geosci. 9, 148.

Pous, S., Carton, X., Lazure, P., 2012. A process study of the tidal circulation in the Persian Gulf. Open J. Mar. Sci. 2, 131—140.

Pous, S.P., Carton, X., Lazure, P., 2004. Hydrology and circulation in the Strait of Hormuz and the Gulf of Oman—Results from the GOGP99 Experiment: 2. Gulf of Oman. J. Geophys. Res. Ocean. 109.

Privett, D.W., 1959. Monthly charts of evaporation from the N. Indian Ocean (including the Red Sea and the Persian Gulf). Q. J. R. Meteorol. Soc. 85, 424—428.

Pugh, D.T., 2004. Changing Sea Levels: Effects of Tides, Weather and Climate. Eos, Trans. Am. Geophys. Union 85, 468. https://doi.org/10.1029/2004EO450010

Quaresma, L.S., Pichon, A., 2013. Modelling the barotropic tide along the West-Iberian margin. J. Mar. Syst. 109, S3—S25.

Reynolds, R.M., 1993. Physical oceanography of the Gulf, Strait of Hormuz, and the Gulf of Oman—Results from the Mt Mitchell expedition. Mar. Pollut. Bull. 27, 35—59.

Roelvink, J.A., Banning, V.G., 1995. Design and development of DELFT3D and application to coastal morphodynamics. Oceanogr. Lit. Rev. 11, 925.

Roos, P.C., Schuttelaars, H.M., 2011. Influence of topography on tide propagation and amplification in semi-enclosed basins. Ocean Dyn. 61, 21—38.

Sharaf El-Din, S.H., 1988. Sea Level Variation along the Saudi Coast of the Arabian Gulf and their Relation to Meteorological Parameters. Spec. Rep. 1409.

Siddig, N.A., Al-Subhi, A.M., Alsaafani, M.A., 2019. Tide and mean sea level trend in the west coast of the Arabian Gulf from tide gauges and multi-missions satellite altimeter. Oceanologia 61 (4), 401—411. https://doi.org/10.1016/j.oceano.2019.05.003

Spall, M.A., Holland, W.R., 1991. A nested primitive equation model for oceanic applications. J. Phys. Oceanogr. 21, 205—220.

Stelling, G.S., Leendertse, J.J., 1992. Approximation of convective processes by cyclic AOI methods. Estuar. Coastal Model. 771—782.

Sultan, S.A.R., Ahmad, F., Elghribi, N.M., Al-Subhi, A.M., 1995. An analysis of Arabian Gulf monthly mean sea level. Cont. Shelf Res. 15, 1471—1482.

Thompson, E.F., Demirbilek, Z., Hadley, L.L., Rivers, P., Huff, K.E., 1994. Water Level and Current Simulation for LOTS Operations-Persian Gulf and Gulf of Oman.

Trepka, V.L., 1968. Investigation of the tides in the Persian Gulf by means of ahydrodynamic numerical model. In: Proceeding of Symposium on Mathematical Hydrological Investigations of Physical Process in the Sea, 59—63.

Verboom, G.K., Slob, A., 1984. Weakly reflective boundary conditions for two-dimensional water flow problems. 5th Int. Conf. on Finite Elements in Water Resources, June 1984, Vermont. Also Adv. Water Resour., 7.

Willmott, C.J., 1981. On the validation of models. Phys. Geogr. 2, 184—194.

Yao, F., 2008. Water mass formation and circulation in the Persian Gulf and water exchange with the Indian Ocean Ph.D. thesis. Univ. of Miami.

Oceanologia 64 (2022) 346—362

Available online at www.sciencedirect.com

ScienceDirect

journal homepage: www.journals.elsevier.com/oceanologia

ORIGINAL RESEARCH ARTICLE

Seasonal carbonate system *vis-à-vis* pH and Salinity in selected tropical estuaries: Implications on polychaete diversity and composition towards predicting ecological health

Palanivel Partha Sarathy[a,*], **Veeraiyan Bharathidasan**[a], **Perumal Murugesan**[a], **Palanichamy Selvaraj**[b], **Rengasamy Punniyamoorthy**[a]

[a] *Centre of Advanced Study in Marine Biology, Faculty of Marine Sciences, Annamalai University, Tamil Nadu, India*
[b] *Department of Biotechnology, Sri Kaliswari College (Autonomous), Sivakasi -626130*

Received 5 December 2020; accepted 13 January 2022
Available online 31 January 2022

KEYWORDS
Salinity;
pH;
Estuaries;
Polychaetes;
Ecological status

Abstract Salinity and pH play a fundamental role in structuring spatial patterns of physical properties, biota, and biogeochemical processes in the estuarine ecosystem. In this study, the influence of salinity-pH gradient and carbonate system on polychaete diversity in Ennore, Uppanar, Vellar, and Kaduvaiyar estuaries was investigated. Water and sediment samples were collected from September 2017 to August 2018. Univariate and multivariate statistical analyses were employed to define ecological status. Temperature, salinity, pH, and partial pressure of carbon-di-oxide varied between 21 and 30°C; 29 and 39 ppt; 7.4 and 8.3; and 89.216 and 1702.558 μatm, respectively. PCA and CCA results revealed that DO, chlorophyll, carbonate species, and sediment TOC have a higher influence on polychaete community structure. Forty-two species such as *Ancistrosyllis parva*, *Cossura coasta*, *Eunice pennata*, *Euclymene annandalei*, *Lumbrineris albidentata*, *Capitella capitata*, *Prionospio cirrifera*, *P. pinnata*, *P. cirrobranchiata*, and *Notomastus* sp. were found dominantly in all estuaries. Shannon index values ranged between 1.619 (UE-1) and 3.376 (VE-2). Based on these findings, high levels of carbonate species and low pH have a greater impact on polychaete diversity and richness val-

* Corresponding author at: Centre of Advanced Study in Marine Biology, Faculty of Marine Sciences, Annamalai University, Parangipettai, 608 502, Tamil Nadu, India.
E-mail address: partha7915@gmail.com (P.P. Sarathy).
Peer review under the responsibility of the Institute of Oceanology of the Polish Academy of Sciences.

Production and hosting by Elsevier

https://doi.org/10.1016/j.oceano.2022.01.001

ues. The results of the AMBI Index revealed that stations UE-1, UE-2, UE-3 in Uppanar, EC-1, EC-2 in Ennore indicate “moderately disturbed”, while other stations are under the “slightly disturbed” category. This trend was quite evident in M-AMBI as well.

1. Introduction

Estuaries are dynamic ecosystems that host one of the highest biodiversity and biological production in the world (Bianchi, 2007). They have been increasingly vulnerable to anthropogenic inputs in recent decades, undergoing complex biogeochemical and hydrological processes. They are vulnerable aquatic ecosystems due to the constant influx of contaminants, mostly from land runoff, agricultural and industrial discharges (Fiorino et al., 2018; Plhalova et al., 2018). Among the environmental parameters prevailing in estuaries, salinity is known to be one of the most important key environmental parameters that control the biological components of the estuarine and marine ecosystems. Equally, changes in water pH mainly depend on CO_2 fluxes through photosynthesis, bicarbonate decomposition, freshwater influx, salinity, and temperature, as well as organic matter degradation (Rajasegar et al., 2002). pH fluctuation may also have negative impacts on the metabolism and growth rate of marine organisms (Guinotte and Fabry, 2008). Furthermore, temperature, salinity, and pH in tandem are known to affect seawater chemistry directly, as well as buffering capacity and elevated CO_2 in estuarine systems (Dickinson et al., 2012; Lannig et al., 2010; Nikinmaa, 2013). It is also reported that the uncharacteristic changes in temperature, pH, and salinity exacerbate adverse effects on biota distribution, mostly on benthic organisms (Bochert et al., 1996; Dean, 2008).

Understandably, estuaries play a key role in the global carbon (C) cycle and carbon dioxide (CO_2) budget (Le Quéré et al., 2016; Regnier et al., 2013). They are characterized by a dynamic range of carbon dioxide (pCO_2) fluxes, which are sequestered in the terrestrial system by photosynthesis and weathering reactions and transported to the ocean through rivers and estuaries. The high fluctuation of pCO_2 in estuaries reflects similar trends of organic carbon stocks and degradation compared to other coastal environments as exemplified in the levels of dissolved organic carbon (DOC), oxygen saturation level ($\%O_2$), and chlorophyll-*a* (Chl *a*). Furthermore, an increase in pCO_2 concentration in the aquatic environment also reduces the availability of carbonate ions, affecting biological and physicochemical processes significantly (Doney et al., 2009; Frankignoulle et al., 1998). Earlier studies have also reported the negative responses to increased pCO_2 exposure on a variety of endpoints in marine organisms at various physicochemical (acid-base) and biological parameters namely survival, growth rate, and reproduction (Freitas et al., 2016; Rodriguez-Romero et al., 2014a,b).

On the other hand, benthic organisms also play a pivotal role in the functioning of estuaries and coastal environments, through re-mineralization and nutrients churning between sediment and the overlying water column (Ingole et al., 2009; Jayaraj et al., 2007). Polychaetes constitute the most dominant component with high species richness and abundance in the invertebrate communities in aquatic environments besides possessing varying levels of tolerance to environmental stress as they have been known as bio-indicators of environmental quality assessment studies worldwide (Jayaraj et al., 2007; Khan et al., 2014; Papageorgiou et al., 2006; Sigamani et al., 2019). Conversely, anthropogenic disturbances, especially pollutants from industrial clusters and urban discharges located along the coast, may result in deleterious effects on the biotic and abiotic variables of an ecosystem leading to dwindling biodiversity in estuarine and marine environments. Earlier studies have done elsewhere also reported that the estuaries act as a sink for pollutants and become impacted by a wide variety of contaminants (Khan et al., 2014; Natesan et al., 2017; Senthilnathan and Balasubramanian, 1994).

The present study aims to investigate the status of ecosystem variability in relation to salinity-pH and carbonate systems influence on the distribution of polychaetes in four select estuaries viz., (i) Ennore, (ii) Uppanar, (iii) Vellar, and (iv) Kaduvaiyar, Southeast coast of India. Ennore estuary is known for the dumping of fly ash slurry from the nearby Ennore thermal plant, and the disposal of municipal domestic wastes. Similarly, on the northern bank of Uppanar, where clusters of industries are located, discharges including coolant water are finding their way into this ecosystem. Quite on the contrary, Vellar and Kaduvaiyar estuaries are known to receive wastes from anthropogenic activities, sewage disposal, and agricultural run-off.

2. Material and methods

2.1. Study area

Ennore estuary is a backwater that drains the Koratalliyar River. It is located in the north-eastern part of Chennai city, Tamilnadu, India, and is spread over an area of 4 km along the coast of the Bay of Bengal. The southern arm of the creek, fringing the northern areas of the city of Chennai, has well-developed industries, utilities, suburban residential areas, and fishing hamlets. The northern section of the creek or Kosastalaiyar backwater is connected to Lake Pulicate and has two major developments: the north Chennai Thermal Power Plant and Ennore port. Development in the northern area is likely to intensify with a major industrial park being proposed at present, including power utilities, petrochemical industries, and chemical storage units.

The confluence of Gadilam and Paravanar rivers forms the Uppanar estuary at Cuddalore’s old town area and opens

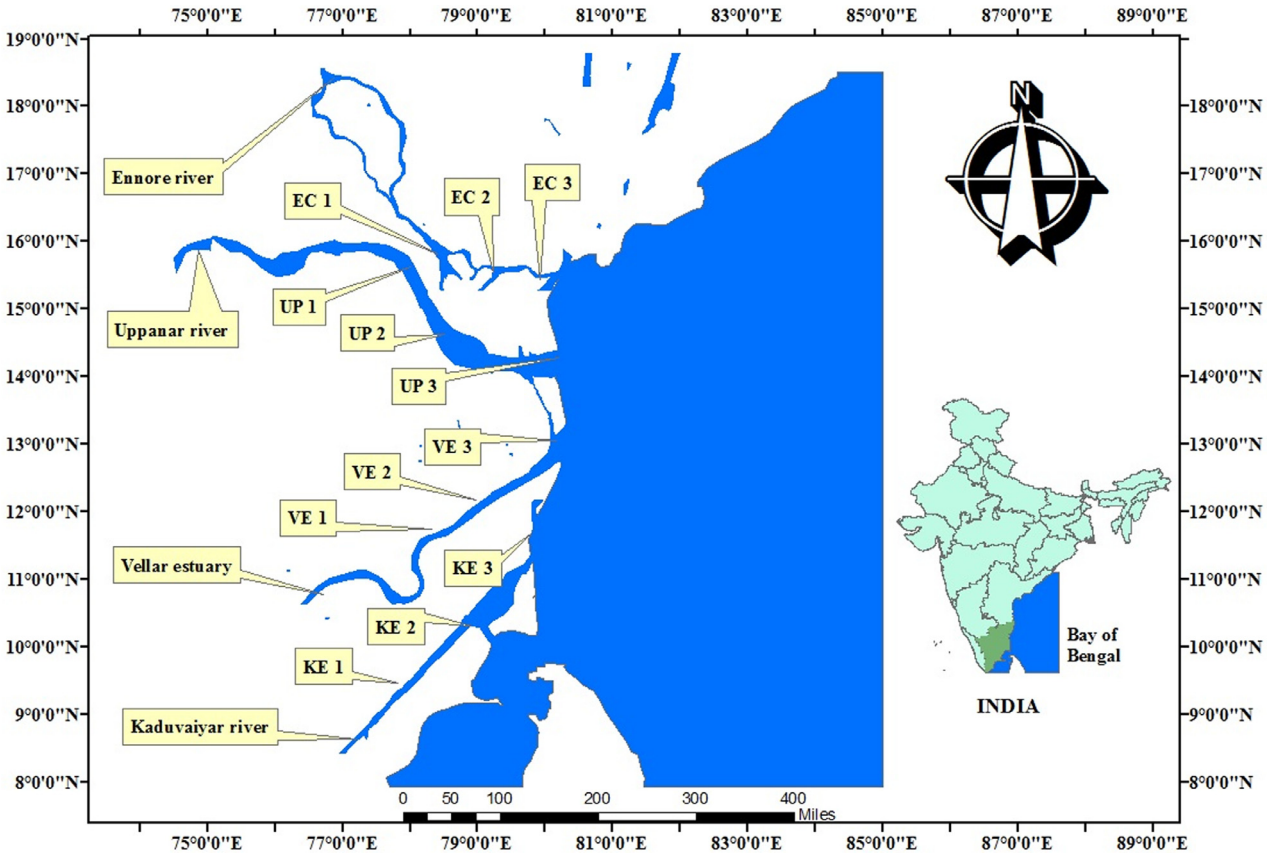

Figure 1 Map showing the sampling stations.

into the Bay of Bengal. The Uppanar estuary is the open type of estuary with the tidal action extending up to a distance of approximately 6 km. The width of the estuary ranges from 20 to 30 m, with an average depth of 2.5 m. It acts as a sink since the large quantity of effluents/discharges accumulated from these industries located on the northern bank of the Uppanar estuary are finding their way into the river.

Contrarily, the Vellar estuary, situated along the southeast coast of India is relatively undisturbed. It presents a semi-diurnal tidal action range from 10—15 km towards the upstream region. The average width and depth of this estuary are 100 m and 2.5 m, respectively, and it receives terrestrial runoff from the river and different channels. The intrusion of neritic water from the sea and freshwater from the land source forms the brackish nature of the Vellar estuary.

The river Kaduviyar is situated near the town Nagapattinam on the east (Coromandel) coast of India. The Kaduviyar estuary has its source in another major river, Cauvery of Tamil Nadu. The Kaduviyar estuary has a year-round connection with the sea and is subjected to semi-diurnal tides with a maximum tidal amplitude of approximately 1.0 m. It flows for a distance of 380 km through an area of red, sandy, leached and laterised black soil in loamy red soil, and finally joins with the Bay of Bengal. A selection of estuaries was made based on their nature and the accrual of discharges from nearby industries and other anthropogenic sources, as well as salinity intrusion; sampling was made accordingly in three stations/locations in each of the following estuaries:

Ennore estuary: EC-1, EC-2, EC-3 (Lat. 13°13′59.19"N, Long. 80°19′1.44"E);
Uppanar estuary: UE-1, UE-2, UE-3 (Lat. 11°42′14.24"N, Long. 79°45′23.89"E);
Vellar estuary: VE-1, VE-2, VE-3 (Lat. 11°29′43.36"N, Long. 79°45′21.42"E) and
Kaduvaiyar estuary: KE-1, KE-2, KE-3 (Lat. 10°45′52.16"N, Long. 79°50′56.95"E) of Southeast coast of India (Figure 1).

2.2. Collection of water and sediment samples

The estuaries are exposed to a microtidal regime, with a tidal range varying between 0.22 m to 1.5 m. The tidal regime is mostly composed of semi-diurnal components. The tidal phase at estuaries is semidiurnal having two peaks and two lows every day. Samples were collected during high tide periods. Water samples were collected using clean plastic 1 L poly-propylene bottles. Parameters such as temperature, pH (Eutech Instrument, Singapore), and salinity (Hand refractometer, Atago co. Ltd., Japan) were recorded in-situ. Dissolved oxygen (DO) and Biological Oxygen Demand (BOD) were measured by following Winkler's titration method (Strickland and Parsons, 1972). To estimate the other physicochemical parameters, water samples were preserved immediately in an icebox and brought to the laboratory in a controlled condition. Total Alkalinity (TA) was quantified in the laboratory by a titrimetric method using methyl orange and phenolphthalein indica-

tors (Gran, 1952); Chlorophyll-*a* concentration was analyzed using Strickland and Parson's method (1972); Dissolved Organic Carbon (DOC) was analyzed using a Shimadzu TOC analyzer (Shimadzu TOC-VCPH); Particulate Organic Carbon (POC) was obtained with GF/F filters (0.45 μm), dried at 65°C and analyzed using an elemental analyzer (Perkin Elmer, 2400), carbonate ion (CO_3), bicarbonate ion (HCO_3), Dissolved Inorganic Carbon (DIC) and carbon-dioxide partial pressure of (pCO_2) were calculated from pH, temperature, salinity and measured using 'Seacarb' package available in 'R' software (Gattuso et al., 2019). The Venice System method was used for the classification of salinity zones (with slight modifications for the requirements of the present study) (Anonymous, 1959). Accordingly, the salinity zones viz., polyhaline (25—30), and euhaline (30—40) were classified. Based on this, stations in various estuaries were categorized.

Sediment samples were collected using a stainless grab sampler. After collection, the sediment samples were shade dried and then homogenized using a mortar and pestle. A known quantity of homogenized samples was subjected to sediment texture using the pipette method of Krumbein and Pettijohn (1938) and Total Organic Carbon (TOC) was calculated with the chromic acid oxidation method (El Wakeel and Riley, 1957).

2.3. Benthic samples

For faunal analysis, sediment samples were collected using a long-armed Peterson Grab, which covered an area of 0.1 m^2. In each station, three replicate samples were collected and then passed through sieves of 0.5 mm. Retained organisms were stored in a clean plastic container and were fixed immediately with 5% formalin to which Rose Bengal (0.1 g/100 ml distilled water) dye was added for easy spotting at the time of sorting. After sorting, the polychaetes were counted and identified to species level by consulting standard references (Day, 1967; Fauvel, 1953).

2.4. Diversity indices and benthic ecological assessment tools

Polychaete data were subjected to the following diversity descriptors i) Shannon index (H') (Shannon and Weaver, 1949), Margalef richness (Margalef, 1958), and Pielou's evenness (Pielou, 1966) using PRIMER software (version 7.0). In addition to diversity indices, ecological health indices namely AMBI (AZTI Marine Biotic Index) and M-AMBI (Multivariate-AZTI Marine Biotic Index) were also adopted by following the method proposed by Borja et al. (2000, 2008); Muxika et al. (2007); AZTI Laboratory (http://ambi.azti.es). To perform AMBI indices, benthic species were assigned to the following five ecological groups based on their sensitivity to the pollutants:

i Ecological Group I (EG-1) — very sensitive to organic enrichment,
ii Ecological Group II (EG-II) — indifferent to organic enrichment,
iii Ecological Group III (EG-III) — tolerant to excess organic enrichment,
iv Ecological Group IV (EG-IV) — second-order opportunistic species and
v Ecological Group V (EG-V) — first-order opportunistic species.

Borja et al. (2000) further categorized the following classifications with their scale ranges based on the above-mentioned ecological groups as unpolluted (0.0—1.0); slightly polluted (1.1—2.0); moderately polluted (2.1—4.0); heavily polluted (4.1—6.0) and extremely polluted (6.1—7.0). Accordingly, the distribution of these ecological groups were further analyzed according to their sensitivity to pollution stress using BI (Biotic Index) with eight levels (0—7) (Hily et al., 1986; Majeed, 1987). To confirm the trend of AMBI, the M-AMBI index was also calculated which expresses the relationship between observed values and reference condition values. At high quality status, the M-AMBI approaches 1 and at bad quality status, it approaches 0. The threshold values are as follows: high quality > 0.80, good quality 0.57—0.80, moderate quality 0.38—0.57, and bad quality < 0.20 (Muxika et al. 2007). These reference values were accomplished with the WFD requirements.

2.5. Statistical treatment for environmental parameters

Variations in physicochemical parameters are shown in a scatterplot. One-way ANOVA was performed using Tukey's test to observe the variation among the stations. To ascertain the relationship among the environmental parameters, a PCA biplot was drawn using physicochemical parameters *vs* seasons. Canonical Correspondence Analysis (CCA) was drawn to determine the relationship between environmental parameters and polychaetes. All the above-stated graphical and various multivariate analyses were performed using the statistical language R version 3.5 (R Development Core Team, 2018). Scatterplot and PCA biplot was plotted using "ggplot2" of 'R' software (Wickham et al., 2018). The CCA was used to run "Vegan 2.4.4" of 'R' software (Oksanen et al., 2017).

3. Results

3.1. Physico-chemical characteristics

The mean with SD values of physicochemical parameters recorded at each sampling location is summarized in Supplementary Table 1. The surface water was characterized by a salinity gradient from 26.0 to 39.0 ppt (mean 32.0±3.5, $F = 1.181$, $p < 0.1$) with a maximum during summer (VE-3) and a minimum during monsoon season (KE-1); pH varied between 7.4 (UE-1) and 8.3 (EC-1 & VE-3) (mean 7.9±0.2, $F = 1.691$, $p < 0.1$) showing significant variations and water temperature reaching 30.0°C (EC-2) during summer and a trough of 21.0°C (VE-1) during pre-monsoon, with statistically significant variations (mean 25.4±1.9, $F = 4.058$, $p < 0.05$).

A positive linear relationship was inferred between water temperature versus salinity and pH (Figure 2a). Dissolved oxygen ranged between 3.1 (EC-2, summer) and 4.8 mg/l (UE-1, pre-monsoon), (mean 3.9±0.4, $F = 2.189$,

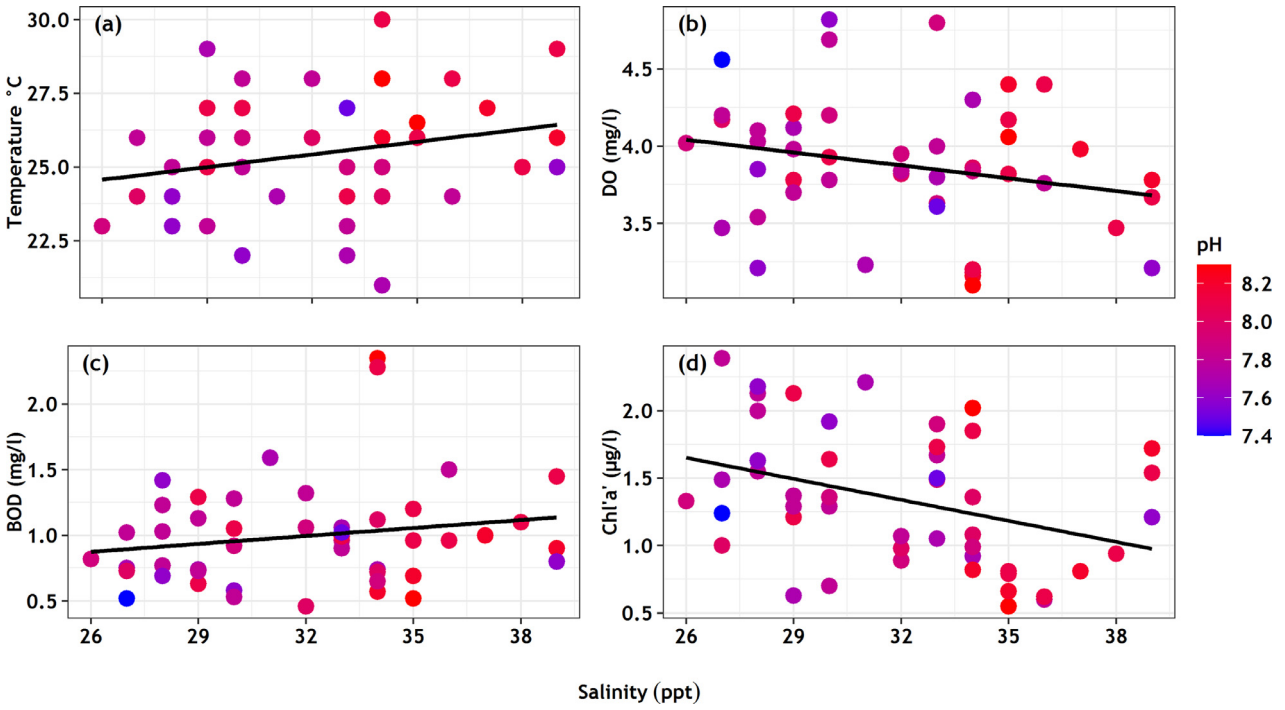

Figure 2 Variation of physico-chemical parameters during the study period; (a) temperature versus salinity-pH, (b) dissolved oxygen (DO) versus salinity-pH, (c) biological oxygen demand (BOD) versus salinity-pH, and (d) chlorophyll versus salinity-pH.

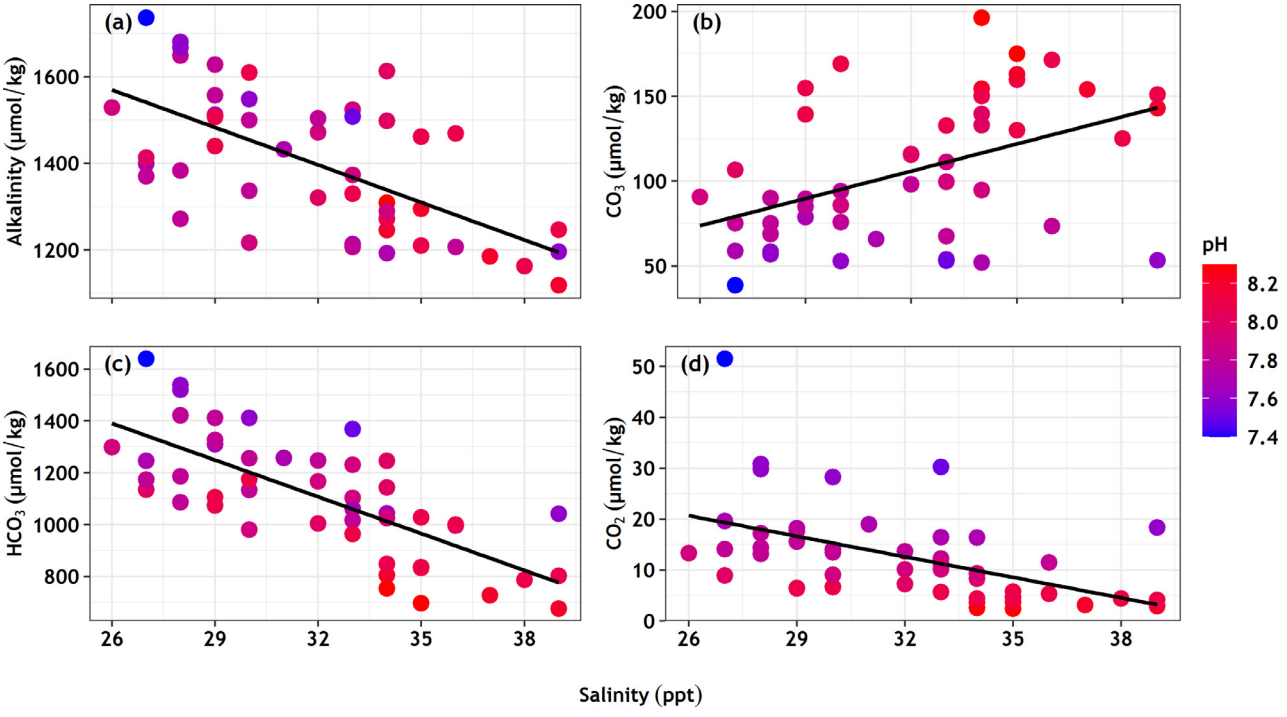

Figure 3 Variation of physico-chemical parameters during the study period; (a) alkalinity versus salinity-pH, (b) carbonate ion versus salinity-pH, (c) bicarbonate ion versus salinity-pH, and (d) carbon dioxide versus salinity-pH.

$p < 0.05$). Unlike temperature, a negative linear relationship was found between DO versus salinity-pH (Figure 2b). The range of BOD was found to vary between 0.5 (UE-1) and 2.4 mg/l (EC-2) with lower values during the monsoon season and high values during the summer season (mean 1.0±0.4, $F = 3.515$, $p < 0.05$). Biological oxygen demand versus salinity and pH showed a positive linear relationship (Figure 2c). Chlorophyll-*a* concentration exhibited high values (2.4 µg/l) at VE-1 during the monsoon season and lower values (0.6 µg/l) at KE-3 during summer season. A negative linear relationship was found between chlorophyll-*a* and salinity-pH (Figure 2d).

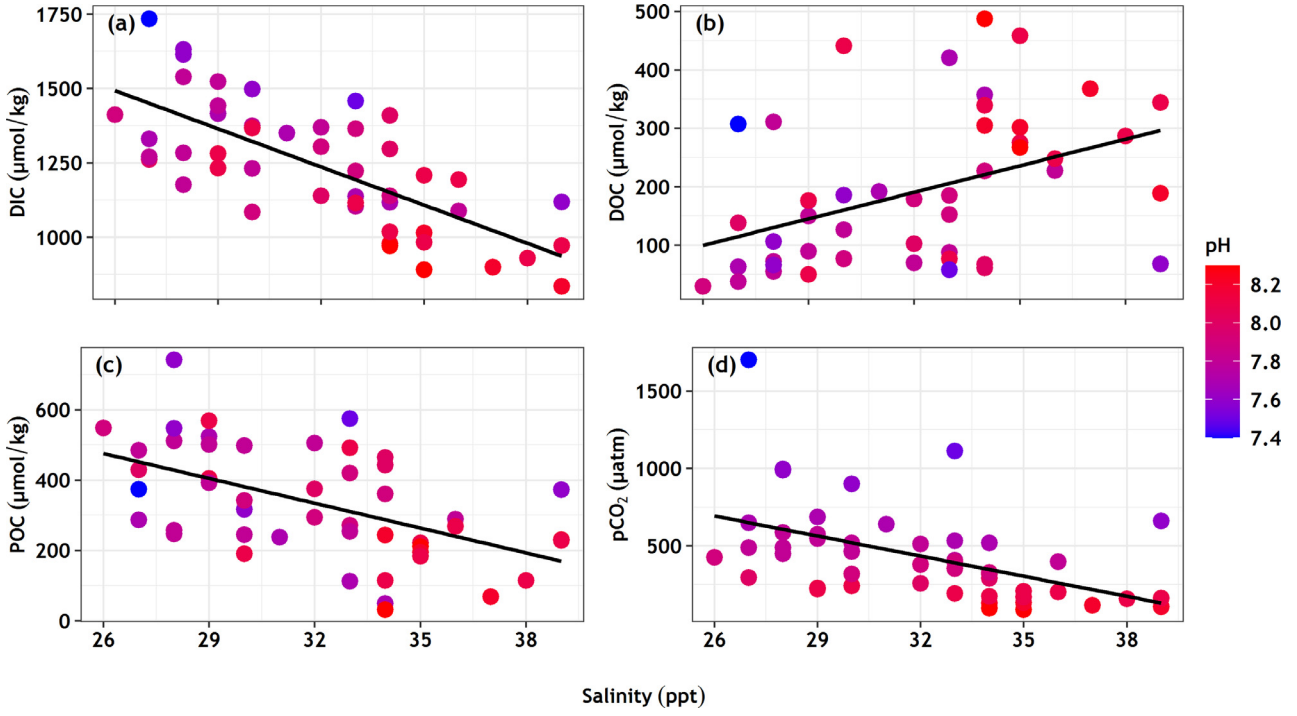

Figure 4 Variation of physico-chemical parameters during the study period; (a) dissolved inorganic carbon (DIC) versus salinity-pH, (b) dissolved organic carbon (DOC) versus salinity-pH, (c) particulate organic carbon (POC) versus salinity-pH, and (d) partial pressure of CO_2 (pCO_2) versus salinity-pH.

Further, total alkalinity varied from 1118.9 (VE-3) to 1736.4 µmol/kg (UE-1) with significant variations among stations (mean 1396.4±160.6, $F = 7.747$, $p < 0.001$). For total alkalinity, salinity and pH, a negative linear relationship was observed (Figure 3a). Carbonate ion and bicarbonate ion values exhibited a maximum of 196.3 µmol/kg (EC-1) during summer and a minimum of 38.7 µmol/kg (UE-1) during monsoon season (mean 105.8±41.4, $F = 1.769$, $p < 0.1$) and from 676.2 µmol/kg (VE-3, summer) to 1640.4 µmol/kg (UE-1, monsoon), respectively (mean 1107.2±227.7, $F = 3.031$, $p < 0.05$). For carbonate ions versus salinity — pH gradient, a positive correlation was observed (Figure 3b) while HCO_3 showed a negative correlation with salinity and pH (Figure 3c). Similarly, pCO_2 showed a wide variation from 2.4 (KE-3) to 51.5 µmol/kg (UE-1) (mean 12.6±9.3, $F = 3.202$, $p < 0.05$) with a negative linear relationship against salinity-pH gradient (Figure 3d).

Dissolved inorganic carbon (DIC) concentrations ranged between 835.8 (VE-3) and 1734.3 µmol/kg (UE-1) with a non-conservative decreasing trend along the salinity-pH gradient (Figure 4a) during the summer season whereas increasing trend during the monsoon season (mean 1236.2±207.9, $F = 3.965$, $p < 0.001$). Dissolved organic carbon concentration ranged from 30.1 (KE-1) to 487.5 µmol/kg (EC-1) (mean 190.4±125.8, $F = 0.864$, $p < 0.1$) with a maximum during summer and a minimum during the monsoon season showing a positive linear relationship along the salinity-pH gradient (Figure 4b). Particulate organic carbon varied greatly between 32.0 (VE-3) and 742.5 µmol/kg (EC-1), with a maximum value recorded during the monsoon season and minimum during summer season (mean 334.3±175.5, $F = 0.936$, $p < 0.1$) and thus a negative linear

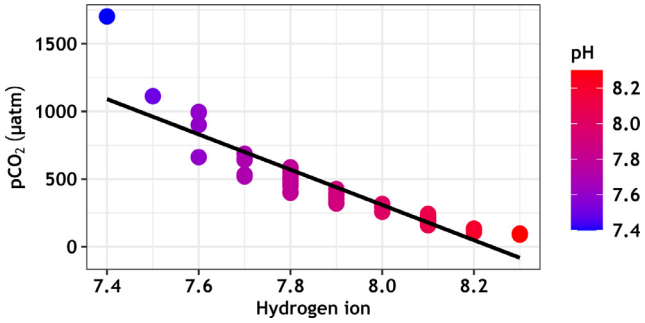

Figure 5 Partial pressure of carbon dioxide versus pH during the study period.

relationship was observed between POC versus salinity — pH gradient (Figure 4c). pCO_2 also varied significantly from 89.2 (KE-3) to 1702.6 µatm (UE-1), with significant variations (mean 434.0±307.1, $F = 3.084$, $p < 0.01$), coupled with a non-conservative decreasing trend along with the salinity — pH gradient (Figure 4d). Similarly, linking pCO_2 versus pH, a negative linear relationship emerged (Figure 5). Similarly, an increasing trend was observed with DIC (Figure 6a), POC (Figure 6c), and pCO_2 (Figure 6d) along the pH gradient barring DOC wherein a negative linear relationship was found (Figure 6b).

3.2. Sediment characteristics

TOC content ranged between 3.7 (VE-2) and 9.7 mgC/g (EC-1) with a maximum value during the summer and min-

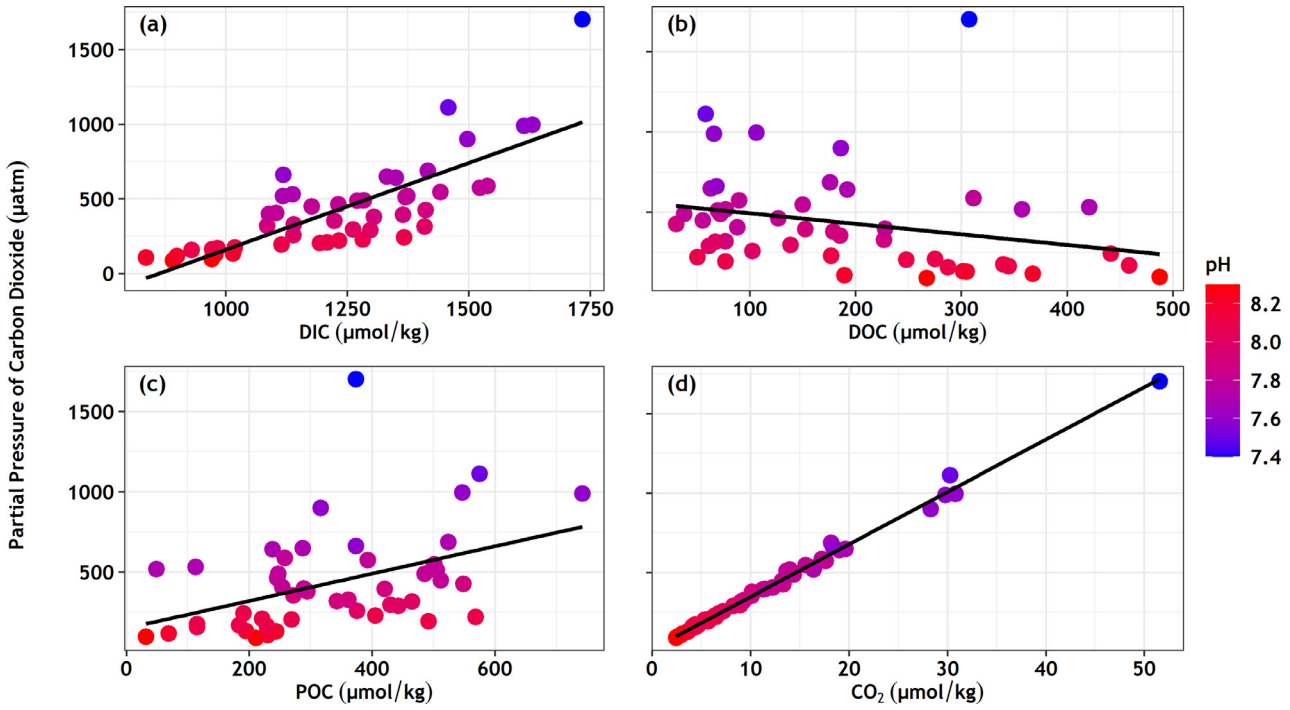

Figure 6 Variation of physico-chemical parameters during the study period; (a) dissolved inorganic carbon (DIC) versus partial pressure of CO_2 (pCO_2), (b) dissolved organic carbon (DOC) versus partial pressure of CO_2 (pCO_2), (c) particulate organic carbon (POC) versus partial pressure of CO_2 (pCO_2), and (d) carbon dioxide versus partial pressure of CO_2 (pCO_2).

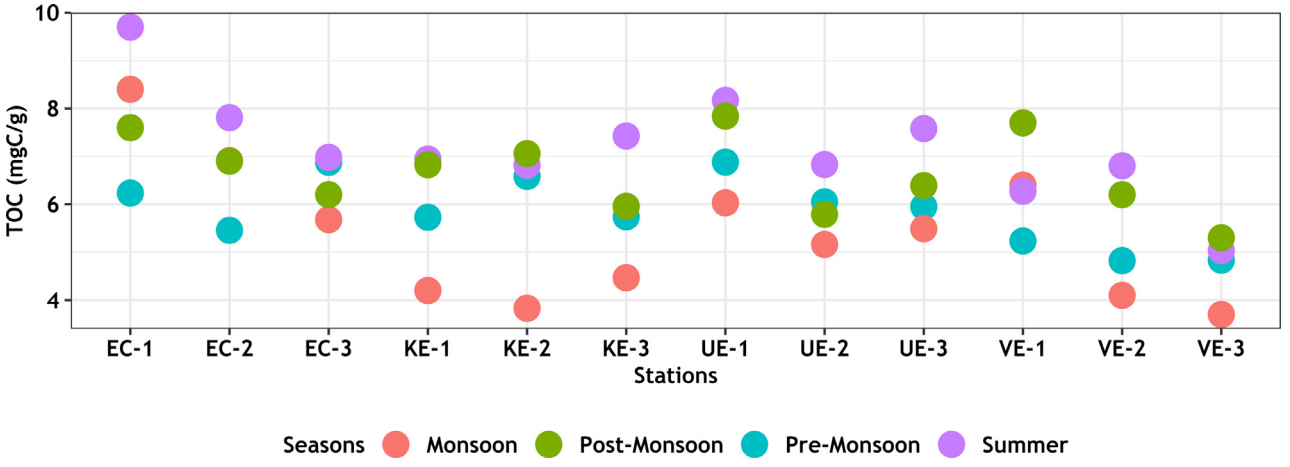

Figure 7 Seasonal variations of sedimentary total organic carbon (TOC) recorded in various stations of the study area.

imum value during the monsoon season (mean 6.3±1.2, $F = 2.301$, $p < 0.05$) (Figure 7). Sediment texture indicated that clay content is relatively high compared to sand and silt. Clay ranged between 4.25 (VE-1, monsoon) and 87.47% (KE-1, summer) followed by sand with a range from 2.37 (UE-1, monsoon) to 56.45% (VE-1, premonsoon) and silt from 5.35 to 49.34% with a peak in VE-3 (monsoon) and a trough in KE-1 (summer) (Figure 8).

3.3. Principal Component Analysis (PCA)

The principal component analysis plot revealed four large groups (Figure 9). Two components explained 55.69% of total variance with 41.54% and 14.15% of components 1 and 2, respectively. The component representing DO, chlorophyll, HCO_3, alkalinity, DIC, POC, pCO_2, CO_2, sediment TOC, and clays point towards pre-monsoon, monsoon, and postmonsoon, while those representing temperature, salinity, pH, BOD, CO_3, DOC, sand, and silt point towards the summer season. PCA plots drawn for individual estuaries are illustrated in Supplementary Figure 1.

3.4. Canonical Correspondence Analysis (CCA)

The canonical correspondence analysis describes the principal tendencies in the relationship between the environmental variables and polychaete assemblage. Components 1 and 2 explained 42.24% of the total variability

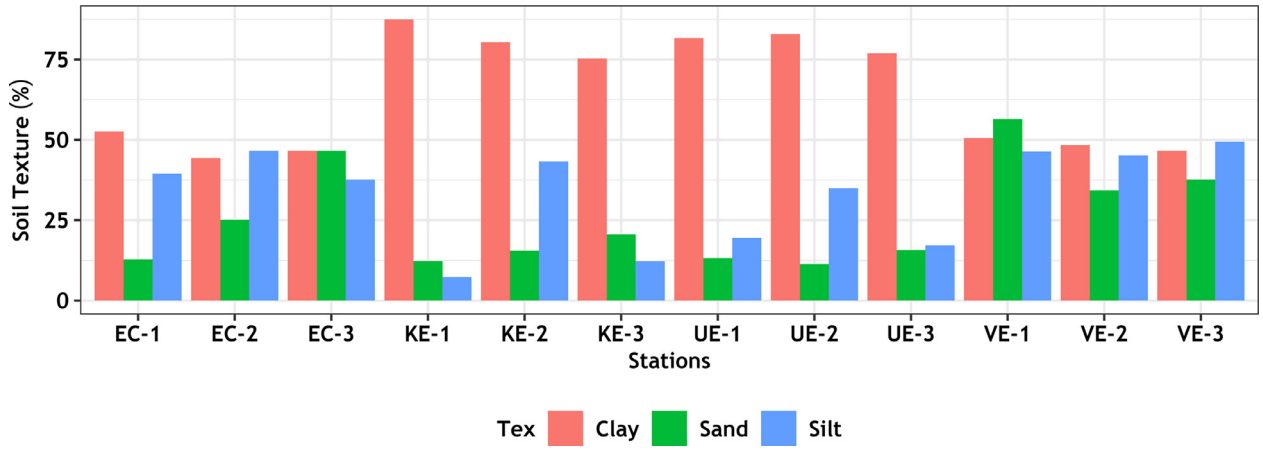

Figure 8 Variations in the sediment texture recorded in various stations of the study area.

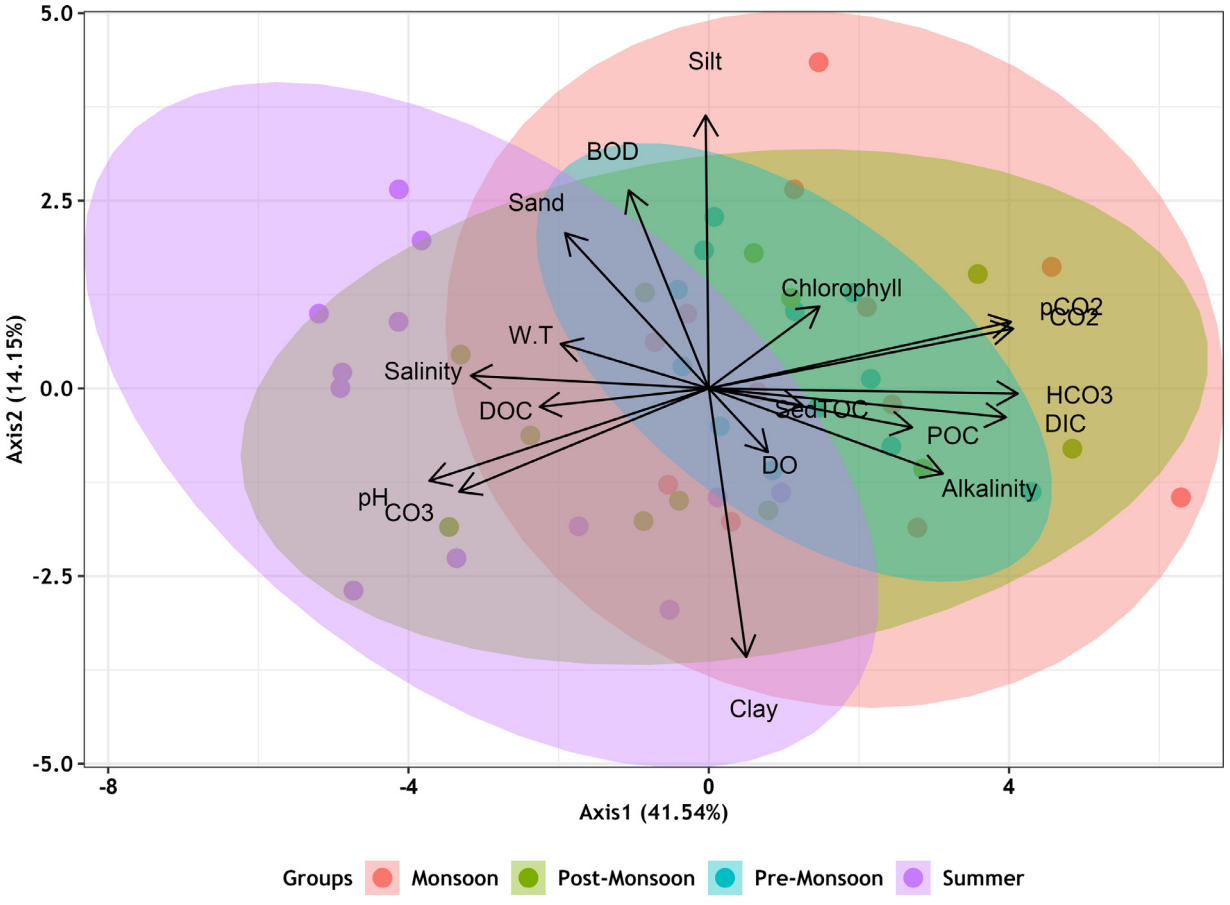

Figure 9 Principal component analysis drawn for the interrelation among environmental parameters and seasons.

of species-environment biplot and accordingly the following environmental parameters such as pH, salinity, DO, CO_3, sand, clay, DOC had a positive correlation in component 1 and polychaetes namely *Cirratulus cirratus*, *Cossura coasta*, *Diopatra cuprea*, *Diopatra neapolitana*, *Dorvillea* sp., *Glycera benguellana*, *Maldane sarsi*, *Marphysa* sp., *Nephtys dibranchis*, *Notomastus aberans*, *Phylo capensis*, *Pista cristata*, *Pygospio elegans*, *Sabella* sp., *Syllis anops*, *Thelepus* sp., emerged as highly correlated species with maximum canonical values (0.5376, 0.4554, 0.2993, 0.2990, 0.2879, 0.2040, 0.1967 and 0.1929) (Figure 10). Contrarily in component 2, temperature, BOD, chlorophyll, alkalinity, HCO_3, DIC, POC, pCO_2, CO_2, Sed.TOC, and silt exhibited a negative correlation with *Ancistrosyllis parva*, *Ancistrosyllis* sp., *Capitella capitata*, *Cirratulus filiformis*, *Euclymene annandalei*, *Eunice pennata*, *Eunice* sp., *Glycera unicornis*, *Goniada emerita*, *Goniada* sp., *Lumbrineris aberrans*, *Lumbrineris albidentata*, *Nereis diversicolor*, *Nereis* sp., *Notomastus* sp., *Ophelia* sp., *Pectinaria* sp., *Pista quadrilobata*, *Platynereis dumerilii*, *Platynereis* sp., *Poly-*

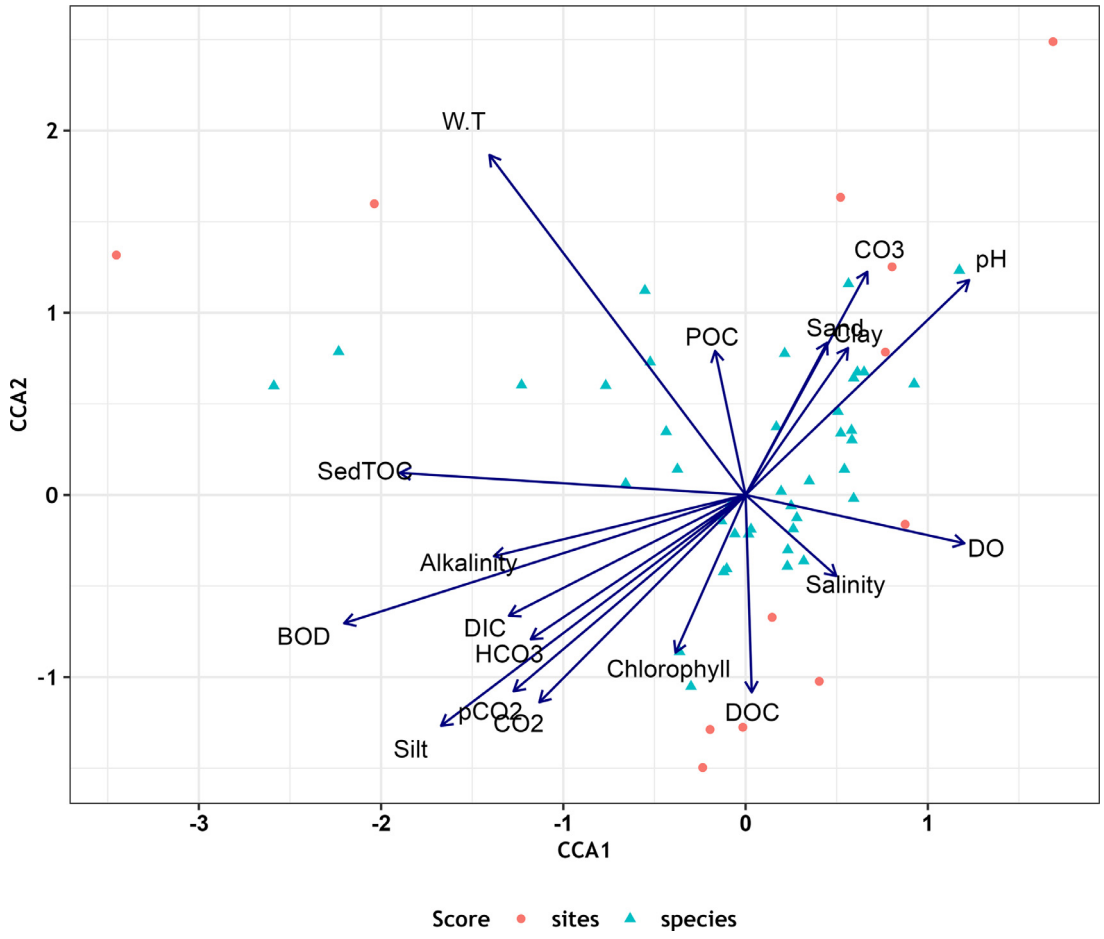

Figure 10 Ordination of polychaete species against environmental variables recorded during the study.

dora capensis, Prionospio cirriferra, P. cirrobranchiata, P. pinnata, Serpula sp. as highly associated polychaete species.

3.5. Biological entities

Polychaete density was found to vary from 518 to 4723 in d m^{-2} with a maximum observed during summer and minimum during monsoon season. Together 42 species of benthic polychaetes were recorded during the study with a maximum species in Vellar estuary (41 species) followed by Kaduvaiyar estuary (31 species), Ennore creek (30 species), and Uppanar estuary (25 species). The most abundant species were *Capitella capitata, Prionospio cirrifera, P. pinnata, P. cirrobranchiata*, and *Notomastus* sp. in Ennore and Uppanar estuaries; *Ancistrosyllis parva, Cossura coasta, Eunice pennata, Euclymene annandalei, Lumbrineris albidentata, Nephtys dibranchis*, and *Pectinaria* sp. in Vellar and Kaduvaiyar.

Similarly, the species *Cirratulus cirratus, Cirratulus filiformis, Cossura coasta, Diopatra cuprea, Diopatra neapolitana, Prionospio cirrifera, Notomastus aberans*, and *Notomastus* sp. was found to be more common in Vellar, Kaduvaiyar, Ennore, and Uppanar; followed by *Ancistrosyllis parva, Euclymene annandalei, Eunice* sp., *Glycera* sp., *Goniada* sp., *Lumbrineris albidentata, Marphysa* sp., *Nephtys dibranchis, Nereis* sp., *Notomastus* sp., *Pista cristata, Platynereis* sp., *Polydora capensis*, and *Pygospio elegans*.

With respect to the salinity gradient zone, as many as 42 polychaete species were observed, with a maximum number of polychaetes recorded in the polyhaline zone (salinity range from 25 to 30 ppt) and minimum number in the Euhaline zone (salinity range from 30 to 40 ppt). Among the polychaete families, representatives from Capitellidae, Eunicidae, Lumbrineridae, Nephtyidae, Nereididae, Spionidae were found to be dominant in the euhaline zone, and those of Cirratulidae, Cossuridae, Dorvilleidae, Glyceridae, Goniadidae, Maldanidae, Onuphidae, Opheliidae, Orbiniidae, Pectinariidae, Pilargidae, Sabellidae, Syllidae, and Terebellidae in the polyhaline zone. Table 2 lists the number of polychaetes recorded in the salinity zones of various estuaries.

3.6. Diversity indices

Species diversity (H') varied from 1.6 (UE-1, monsoon) to 3.4 (VE-2, summer), species richness (d) fluctuated between 3.0 and 6.9 with a maximum in UE-1(summer) and minimum in VE-2 (monsoon). Regarding Pielou's species evenness (J), it ranged between 0.6 and 0.9 with a peak in VE-2 (summer) and a trough in UE-1 (monsoon).

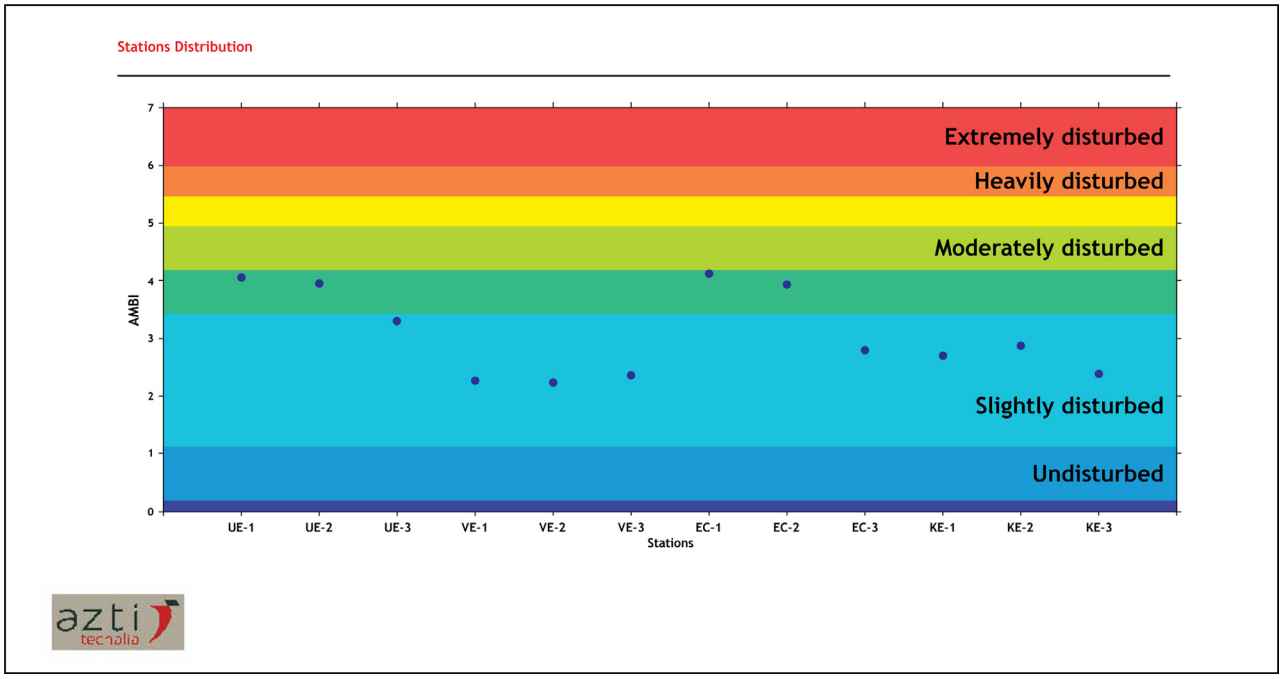

Figure 11 AZTI Marine Biotic Index (AMBI) disturbance classification values in stations of various estuaries during the study.

3.7. Ecological health assessment using biotic indices

The AMBI values calculated for benthic polychaetes fluctuated from 2.23 to 4.12, with a peak at EC-1 and a trough in VE-2 indicated stations UE-1, UE-2, UE-3 in Uppanar; EC-1 and EC-2 in Ennore belong to the category of moderately disturbed; while stations namely VE-1, VE-2, and VE-3 in Vellar, KE-1, KE-2, and KE-3 in Kaduvaiyar and EC-3 in Ennore belonged to the slightly disturbed category (Figure 11). Similarly, M-AMBI values ranged between 0.49 and 0.99 indicating that stations UE-1, UE-2, and EC-1 fell into moderate ecological health status, while other stations into good and high ecological health status (Figure 12, Table 1).

4. Discussion

Estuarine environments are subjected to changes in physicochemical properties due to continuous mixing of freshwater with brackish waters as well as discharges from urban and other sources (Bianchi, 2007). The estimation of water quality is fundamental in determining the health of an ecosystem (Chang, 2008). In the present study, salinity-pH coincided with their variation throughout the study and followed the same pattern with a gradual rise and fall. Among the seasons, a typical upstream-downstream salinity gradient was observed with a minimum of 26.0 ppt (KE-1, monsoon) and a maximum of 39.0 ppt (VE-3, summer). Similarly, water pH showed seasonal variation from 7.4 (UE-1, monsoon) to 8.3 (EC-1 and KE-3, summer). Temperature showed wide variations between 21.0 (VE-1, pre-monsoon) and 30.0°C (EC-2, summer), indicating a positive linear relationship with salinity and pH. High values during summer could be attributed to faster evaporation and low values during the monsoon season due to the dilution of brackish water and freshwater influx in the respective area. The findings of the present study are in close agreement with the trends observed in other studies made elsewhere (Bharathi et al., 2018; Bouillon et al., 2003; Vajravelu et al., 2018).

Dissolved oxygen concentrations ranged between 3.1 (EC-1) and 4.8 mg/l (UE-1) and accordingly a negative linear relationship was observed with salinity and pH. The highest values registered in the pre-monsoon season were attributed to the influx of freshwater. On the contrary, regarding BOD, a maximum value was observed during summer and a minimum level was observed during the monsoon season with a positive correlation to salinity and pH. A similar distribution of DO content with a maximum during the monsoon and minimum during the summer season was reported earlier by Morgan et al. (2006) in Upper Kaskaskia rivers and Sigamani et al. (2015) in Vellar—Coleroon estuarine complex, southeast coast of India.

Conversely, the chlorophyll value exhibited a maximum during the monsoon at VE-1 and a minimum during the summer season at KE-3. The higher value could be due to wind-induced upwelling and river runoff, which would have increased the chlorophyll level. A negative correlation was found between chlorophyll-*a* versus salinity and pH. Chlorophyll concentrations recorded are comparable to those reported in earlier studies (Cloern et al. (2017) in San Francisco Bay and Shanthi et al. (2015) in Bengal Bay).

Total alkalinity is an important factor in determining the estuary's ability to neutralize acidification from rainfall or wastewater. Alkaline compounds such as CO_3, HCO_3, and hydroxides, remove hydrogen ions and thus lower the acidity of the water (Toma, 2013). In the present investigation, the maximum alkalinity was recorded during the monsoon (UE-1) and the minimum (VE-3) during the summer season. There was a negative link between the salinity-pH gradient

Table 1 AMBI, ecological groups, BI-disturbance classification, and M-AMBI status of the stations during the study.

Stations	EG I (%)	EG II (%)	EG III (%)	EG IV (%)	EG V (%)	AMBI	BI from mean AMBI	Disturbance classification	M-AMBI	Status
EC-1	3.093	6.186	11.34	71.649	7.732	4.12	3	Moderately disturbed	0.50	Moderate
EC-2	4.167	8.333	14.583	66.667	6.25	3.94	3	Moderately disturbed	0.59	Good
EC-3	11.864	23.729	42.373	10.169	11.864	2.80	2	Slightly disturbed	0.75	Good
UE-1	1.282	8.333	10.897	77.564	1.923	4.06	3	Moderately disturbed	0.49	Moderate
UE-2	1.961	11.111	13.072	69.281	4.575	3.95	3	Moderately disturbed	0.56	Moderate
UE-3	2.041	14.286	55.102	18.367	10.204	3.31	3	Moderately disturbed	0.64	Good
VE-1	22.581	33.871	19.355	17.742	6.452	2.27	2	Slightly disturbed	0.93	High
VE-2	30.488	20.732	21.951	23.171	3.659	2.23	2	Slightly disturbed	0.98	High
VE-3	20	31.429	25.714	17.143	5.714	2.36	2	Slightly disturbed	0.88	High
KE-1	27.778	8.333	33.333	16.667	13.889	2.71	2	Slightly disturbed	0.70	Good
KE-2	11.111	30.556	19.444	33.333	5.556	2.88	2	Slightly disturbed	0.76	Good
KE-3	26.471	32.353	11.765	14.706	14.706	2.38	2	Slightly disturbed	0.76	Good

AMBI: AZTI marine biotic index; BI: biotic index; M-AMBI: Multivariate-AMBI.

Table 2 Polychaete species recorded in the polyhaline and euhaline zones of the select estuaries (September 2017–August 2018).

Family	Polychaete species	UE (pH 7.4–8.1)		VE (pH 7.6–8.1)		EC (pH 7.5–8.3)		KE (pH 7.7–8.3)	
		Polyhaline Sal (25–30)	Euhaline Sal (30–40)	Polyhaline Sal (25–30)	Euhaline Sal (30–40)	Polyhaline Sal (25–30)	Euhaline Sal (30–40)	Polyhaline Sal (25–30)	Euhaline Sal (30–40)
Capitellidae	*Capitella capitata*	+	-	+	+	+	+	+	+
	Notomastus aberans	+	-	+	-	+	-	+	-
	Notomastus sp.	+	+	+	+	+	+	+	+
Cirratulidae	*Cirratulus cirratus*	+	+	+	+	+	+	+	+
	C. filiformis	-	-	+	-	-	-	+	+
Cossuridae	*Cossura coasta*	-	-	+	+	-	-	-	-
Dorvilleidae	*Dorvillea* sp.	-	-	+	+	+	-	-	-
Eunicidae	*Eunice pennata*	+	+	+	+	+	+	+	+
	Eunice sp.	-	-	+	+	+	+	+	+
	Marphysa sp.	+	+	+	+	+	+	+	-
Glyceridae	*Glycera benguellana*	-	-	+	+	-	-	+	+
	G. unicornis	+	+	+	-	+	+	-	-
Goniadidae	*Goniada emeriti*	+	-	-	-	+	-	-	-
	Goniada sp.	+	+	+	+	+	+	-	-
Lumbrineridae	*Lumbrineris aberrans*	-	-	+	+	-	-	+	-
	L. albidentata	+	+	+	+	+	+	+	+
Maldanidae	*Euclymene annandalei*	-	-	+	+	+	+	+	+
	Maldane sarsi	-	-	+	-	+	-	-	-
Nephtyidae	*Nephtys dibranchis*	+	-	+	+	+	+	+	-
	N. hombergi	+	+	+	+	+	+	+	+
Nereididae	*Nereis diversicolor*	+	-	+	+	+	-	-	-
	Nereis sp.	+	+	+	+	+	+	+	+
	Platynereis dumerilii	+	+	+	+	+	-	-	-
	Platynereis sp.	+	+	+	+	+	+	+	+
Onuphidae	*Diopatra cuprea*	-	-	+	-	-	-	-	-
	D. neapolitana	-	-	+	-	+	-	+	-
Opheliidae	*Ophelia* sp.	-	-	+	+	-	-	+	+
Orbiniidae	*Phylo capensis*	+	+	+	+	-	-	+	+
Pectinariidae	*Pectinaria* sp.	+	+	+	+	+	+	+	+
Pilargidae	*Ancistrosyllis parva*	+	-	+	+	-	-	-	-
	Ancistrosyllis sp.	+	+	+	+	+	+	+	+
Sabellidae	*Sabella* sp.	-	-	+	-	+	-	-	-
	Serpula sp.	-	-	+	-	+	-	-	-
Spionidae	*Polydora capensis*	+	-	+	+	-	-	+	-
	Prionospio cirriferra	+	+	+	+	+	-	+	+
	P. pinnata	+	+	+	+	+	-	+	+
	P. cirrobranchiata	+	+	+	+	+	-	+	+
	Pygospio elegans	+	-	+	+	+	+	-	-
Syllidae	*Syllis anops*	-	-	+	+	+	+	+	+
Terebellidae	*Pista quadrilobata*	-	-	+	-	-	-	+	-
	P. cristata	+	-	+	+	+	-	-	-
	Thelepus sp.	-	-	+	+	-	-	-	-

Note: +, present; -, absent.

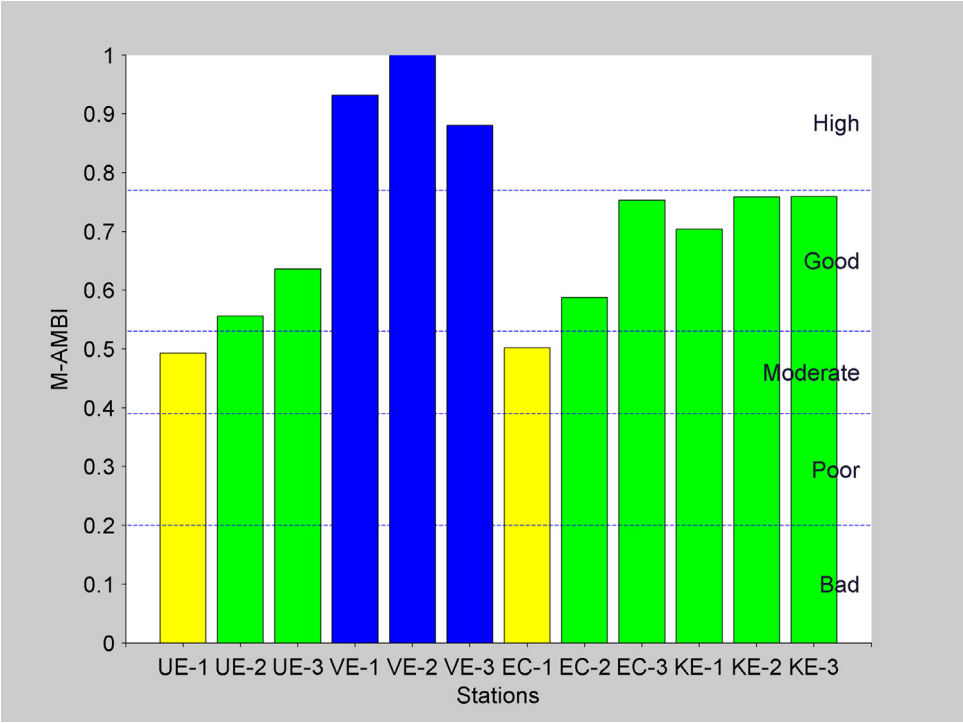

Figure 12 Multivariate-AZTI marine biotic index (M-AMBI) values indicating the ecological status for the stations of various estuaries during the study disturbance classification and M-AMBI status of the stations during the study.

and total alkalinity, HCO_3, and CO_2; and a positive linear association with CO_3. Ray et al. (2018) also reported a similar correlation with parameters combinations. Earlier studies indicated that the range of alkalinity, CO_3, and HCO_3 had increased in areas where heavy anthropogenic activities occur, corroborating the findings of the current study (Bouillon et al., 2003; Oliveira et al., 2018; Thasneem et al., 2018).

Studies conducted elsewhere reported that DIC and DOC are strongly influenced by estuarine processes (Gu et al., 2009). Accordingly, the carbon species namely DIC, DOC, and POC are essential components having an important link in biogeochemical carbon cycling between land and ocean (Wu et al., 2007). The increased concentration of CO_2 and bicarbonate ions reduces the availability of carbonate ions, which affects metabolism, growth rate, and relative abundance of polychaetes (Ho and Carpenter, 2017; Veron, 2011). In the present study, DIC concentration ranged between 835.777 (VE-3, summer) and 1734.268 μmol/kg (UE-1, monsoon) with a non-conservative decreasing trend along the salinity and pH gradient. However, as an oddity, the trend was opposite in DOC, wherein an increasing trend was found along the salinity-pH gradient, with maximum DOC during the summer and a minimum during the monsoon season. POC ranged between 32.0 (EC-1, summer) and 742.5 μmol/kg (EC-1, monsoon), generating a negative linear relationship between POC versus salinity and pH gradient. Likewise, Marescaux et al. (2018) and Ray et al. (2018) reported similar ranges of POC concentrations with a negative linear relationship for the salinity-pH gradient. With respect to pCO_2, values ranged from 89.2 (KE-3) to 1702.6 μatm (UE-1). As that of DIC, pCO_2 also exhibited a non-conservative decreasing trend along the salinity and pH gradient. With respect to pCO_2 with DIC, DOC, POC, and CO_2 concentrations, an increasing trend with a positive linear relationship was found along the pH gradient excluding DOC that showed a negative linear relationship. The study conducted by Hutchins et al. (2019) found a positive linear association versus salinity-pH gradient on large-scale drivers of DIC and POC in the Boreal river. Furthermore, low salinity was found to exacerbate negative effects of elevated CO_2 levels on growth, energy balance, and bio-mineralization of common estuarine invertebrates (Cauwet, 1991; Dickinson et al., 2012; Dutta et al., 2019; Gupta et al., 2008; Hutchins et al., 2019; Marescaux et al., 2018; Palanivel et al., 2019; Ray et al., 2018).

Total organic carbon plays a vital role in the accumulation and release of different micronutrients. It is a well-etched fact that the sediment texture determines the total organic carbon content, which in turn, influences the distribution of benthic organisms. Organic matter in sediments is an essential source of food for benthic fauna (Gray, 1974; Pearson and Rosenberg, 1978; Sanders, 1958; Snelgrove and Butman, 1994). In the present investigation, total organic carbon ranged between 3.7 (VE-2, monsoon) and 9.7 mgC/g (EC-1, summer). Sediment texture revealed clay content to be relatively high compared to sand and silt. Clay ranged between 4.25 (VE-1, monsoon) and 87.47% (KE-1, summer) followed by sand ranging from 2.37 (UE-1. monsoon) to 56.45% (VE-1, premonsoon) and silt between 5.35 and 49.34% with a peak in VE-3 (monsoon) and a trough in KE-1 (summer). Earlier authors reported that during the summer season, a large amount of organic matter settled at the bottom potentially elevating TOC levels in the study area (Khan et al., 2014; Murugesan et al., 2018; Rajasegar et al., 2002).

Multivariate analysis is considered to be an effective method to retrieve information from data sets containing more significant amounts of variance, simultaneously considering the interrelationships of several influential variables. Furthermore, these methods also allow us to analyze the patterns by relating biotic variables with abiotic patterns on spatio-temporal scales (Field, 1987). Accordingly, PCA representing the parameters DO, chlorophyll, HCO_3, alkalinity, DIC, POC, pCO_2, CO_2, sediment TOC, and clay were associated with pre-monsoon, postmonsoon, and monsoon seasons; whereas temperature, salinity, pH, BOD, CO_3, DOC, sand, and silt were associated with summer season (Supplementary Figure 1). Similar seasonal combinations of parameters were also reported by Mukherjee et al. (2014) and Sigamani et al. (2015).

The canonical correspondence analysis describes the principal tendencies in the relationship between the environmental variables and polychaete species assemblages. In component 1, parameters such as pH, salinity, DO, CO_3, sand, clay, and DOC had a positive correlation with *Cirratulus cirratus*, *Cossura coasta*, *Diopatra cuprea*, etc., as highly associated polychaetes; while other parameters such as temperature, BOD, chlorophyll, alkalinity, HCO_3, DIC, POC, pCO_2, CO_2, Sed.TOC and silt exhibited a negative correlation in component 2 with *Ancistrosyllis parva*, *Ancistrosyllis* sp., *Capitella capitata*, and *Cirratulus filiformis* as significantly correlated polychaete species. Similar combinations of environmental variables influencing the benthic faunal distribution were reported by Murugesan et al. (2018), Musale et al. (2015) and Sivaraj et al. (2014).

Moreover, several authors also report that the combinations of pH, salinity, and sediment variables play crucial roles in determining the distribution of the benthic community structure. Sediment-bound organic matter is related to its clay content, which in turn influences the feeding habits of the benthic fauna (Fauchald and Jumars, 1979; Flint, 1981; Gray, 1974), validating the results of the present study.

About polychaete density, the low density recorded during the monsoon season could be attributed to the inflow of copious freshwater from rivers, reducing the salinity level, and leading to unfavorable conditions. Similar trends were reported by Murugesan et al. (2018) and Sivaraj et al. (2014).

Species diversity and richness values were high during the summer and low during the monsoon season, while species evenness largely followed the trend of species diversity. Several researchers stated that terrestrial runoff during monsoon season, industrial wastes, sewage, and anthropogenic activities are known to influence the distribution of benthic organisms, reducing diversity values during the monsoon season (Musale et al., 2015; Natesan et al., 2017). With respect to polychaete diversity and pCO_2, high fluctuation of pCO_2 in estuaries reflects similar trends of organic carbon stocks and degradation in other coastal environments as exemplified by dissolved organic carbon, oxygen saturation level, and chlorophyll-*a*. The increase in partial pressure of carbon-dioxide concentration in the aquatic environment will reduce the availability of carbonate ions, which results in minimal detrimental effects in biological and physicochemical processes (Doney et al., 2009; Frankignoulle et al., 1998). Other researchers elsewhere reported that high pCO_2/low pH reduces polychaete diversity and increases species richness values (Gambi et al., 2016; Molari et al., 2019). Accordingly, high pCO_2/low pH was recorded in stations of Uppanar and Ennore estuaries with minimum polychaete diversity. A similar range of diversity values was recorded earlier by Khan et al. (2014) in Vellar-Uppanar estuary; Sivaleela and Venkataraman (2013) in selected places long the Tamilnadu coast; Natesan et al. (2017) in Ennore coastal waters; Selvaraj et al., (2019) in Vellar and Ennore estuarine ecosystems.

Concerning salinity-zones, the members of the following polychaete families viz., Capitellidae, Eunicidae, Lumbrineridae, Nephtyidae, Nereididae, Spionidae were found to be dominant in the euhaline zone, and those of the Cirratulidae, Cossuridae, Dorvilleidae, Glyceridae, Goniadidae, Maldanidae, Onuphidae, Opheliidae, Orbiniidae, Pectinariidae, Pilargidae, Sabellidae, Syllidae, and Terebellidae families were dominant in the polyhaline zone. Accordingly, it is evident that the polychaete families with the salinity pattern stated above, indicate their ability to regulate hyper and hypo-osmotic environments in different salinity zones as described by earlier researchers (Costa et al., 1980; Freel et al., 1973; Onwuteaka, 2016; Quinn and Bashor, 1982; Richmond and Woodin, 1999; Smith, 1970 and Van Gaest et al., 2007).

AMBI-indices are a widely used tool for assessing the ecological health status of ecosystems (Borja et al., 2000). In the present study, AMBI values calculated for the benthic polychaete species fluctuated from 2.23 to 4.12. According to these values, stations UE-1, UE-2, and UE-3 in Uppanar estuary, EC-1, and EC-2 in Ennore were found to fall in the category of moderately disturbed, while other stations were in the slightly disturbed category. Similarly, M-AMBI values ranged between 0.49 and 0.99 with UE-1, UE-2, and EC-1 falling under the moderate ecological health category, while other stations fell under good and high ecological health categories. In their study, Khan et al. (2014) and Natesan et al. (2017) also reported similar ecological categories since the referred stations of Uppanar-Ennore were located near the discharge points of industrial waste, power-plant discharge of coolant water, indiscriminate discharge of untreated municipal waste, terrestrial river runoff and anthropogenic activities which could have generated variations in the benthic community structure resulting in the dominance of pollution tolerant benthic polychaete groups in the disturbed category.

5. Conclusion

The present study provides benchmark data on the distribution of polychaetes in relation to pH-salinity gradients in the studied estuaries of Tamilnadu. The role of the pH-salinity gradient in conjunction with sediment characteristics on polychaete distribution is intriguing, as there was a decrease in polychaete diversity during monsoonal months, but a few opportunistic polychaete species were found to occur in extremely large numbers in the Uppanar and Ennore estuaries. Although some light has been shed on the role of the salinity-pH gradient on the polychaete commu-

nity in selected estuaries, more research into the interaction modes of biotic/abiotic processes is needed to determine the accuracy of polychaete occurrence along salinity gradients/zones of biological, chemical, and physical processes.

Acknowledgments

The authors are thankful to the Director and Dean, CAS in Marine Biology, Annamalai University, for the encouragement and facilities provided. We gratefully acknowledge the NCCR (National Centre for Coastal Research), Ministry of Earth Sciences, Govt. of India, New Delhi, for the financial support under Project: Grant No: MoES/ICMAM-PD/ME/CAS-MB/53/2017. The authors also thank profusely Dr. Fernando Arenas González, Mexico for language proofreading.

Supplementary materials

Supplementary material associated with this article can be found, in the online version, at https://doi.org/10.1016/j.oceano.2022.01.001.

References

Anonymous, 1959. The Venice system for the classification of marine waters according to salinity: Symposium on the classification of brackish waters, Venice, 8-14th April 1958. Jap. J. Limnol. 20 (3), 119—120. https://doi.org/10.4319/lo.1958.3.3.0346

Bharathi, M.D., Sarma, V.V.S.S., Ramaneswari, K., 2018. Intra-annual variations in phytoplankton biomass and its composition in the tropical estuary: Influence of river discharge. Mar. Pollut. Bull. 129, 14—25.

Bianchi, T.S., 2007. Biogeochemistry of estuaries. Oxford University Press (on demand).

Bochert, R., Fritzsche, D., Burckhardt, R., 1996. Influence of salinity and temperature on growth and survival of the planktonic larvae of *Marenzelleria viridis* (Polychaeta, Spionidae). J. Plankton Res. 18, 1239—1251. https://doi.org/10.1093/plankt/18.7.1239

Borja, A., Dauer, D.M., Diaz, R., Llansó, R.J., Muxika, I., Rodriguez, J.G., Schaffner, L., 2008. Assessing estuarine benthic quality conditions in Chesapeake Bay: a comparison of three indices. Ecol. Indic. 8, 395—403.

Borja, A., Franco, J., Pérez, V., 2000. A marine biotic index to establish the ecological quality of soft-bottom benthos within European estuarine and coastal environments. Mar. Pollut. Bull. 40, 1100—1114.

Bouillon, S., Frankignoulle, M., Dehairs, F., Velimirov, B., Eiler, A., Abril, G., Etcheber, H., Borges, A.V., 2003. Inorganic and organic carbon biogeochemistry in the Gautami Godavari estuary (Andhra Pradesh, India) during pre-monsoon: The local impact of extensive mangrove forests. Global Biogeochem. Cy. 17 (4).

Cauwet, G., 1991. Carbon inputs and biogeochemical processes at the halocline in a stratified estuary: Krka River, Yugoslavia. Mar. Chem. 32, 269—283. https://doi.org/10.1016/0304-4203(91)90043-V

Chang, H., 2008. Spatial analysis of water quality trends in the Han River basin. South Korea. Water. Res. 42, 3285—3304.

Cloern, J.E., Jassby, A.D., Schraga, T.S., Nejad, E., Martin, C., 2017. Ecosystem variability along the estuarine salinity gradient: Examples from long-term study of San Francisco Bay. Limnol. Oceanogr. 62, 272—291. https://doi.org/10.1002/lno.10537

Costa, C.J., Pierce, S.K., Warren, M.K., 1980. The intracellular mechanism of salinity tolerance in polychaetes: volume regulation by isolated *Glycera dibranchiata* red coelomocytes. Biol. Bull. 159 (3), 626—638.

Day, J.H., 1967. A monograph on the Polychaeta of Southern Africa. British Museum of Natural History, Publ. 656, 1—878. https://doi.org/10.5962/bhl.title.8596

Dean, H.K., 2008. The use of polychaetes (Annelida) as indicator species of marine pollution: a review. Rev. Biol. Trop. 56, 11—38. http://www.redalyc.org/articulo.oa?id=44919934004

Dickinson, G.H., Ivanina, A.V., Matoo, O.B., Pörtner, H.O., Lannig, G., Bock, C., Beniash, E., Sokolova, I.M., 2012. Interactive effects of salinity and elevated CO_2 levels on juvenile eastern oysters, *Crassostrea virginica*. J. Exp. Biol. 215, 29—43. https://doi.org/10.1242/jeb.061481

Doney, S.C., Fabry, V.J., Feely, R.A., Kleypas, J.A., 2009. Ocean acidification: the other CO_2 problem. Annu. Rev. Mar. Sci. 1, 169—192. https://doi.org/10.1146/annurev.marine.010908.163834

Dutta, M.K., Kumar, S., Mukherjee, R., Sanyal, P., Mukhopadhyay, S.K., 2019. The post-monsoon carbon biogeochemistry of the Hooghly—Sundarbans estuarine system under different levels of anthropogenic impacts. Biogeosciences 16, 289—307. https://doi.org/10.5194/bg-16-289-2019

El Wakeel, S.K., Riley, J.P., 1957. The determination of organic carbon in marine muds. J. Mar. Sci. 22, 180—183.

Fauchald, K., Jumars, P.A., 1979. The diet of worms: a study of polychaete feeding guilds. Oceanogr. Mar. Biol. Ann. Rev. 17, 193—284.

Fauvel, P., 1953. The Fauna of India including Pakistan, Ceylon, Burma and Malaya. Annelida Polychaeta. Indian Press, Allahabad, 507 pp.

Field, D.J., 1987. Relations between the statistics of natural images and the response properties of cortical cells. J. Opt. Soc. Am. A. 4, 2379—2394. https://doi.org/10.1364/JOSAA.4.002379

Fiorino, E., Sehonova, P., Plhalova, L., Blahova, J., Svobodova, Z., Faggio, C., 2018. Effects of glyphosate on early life stages: comparison between *Cyprinus carpio* and *Danio rerio*. Environ. Sci. Pollut. R. 25, 8542—8549. https://doi.org/10.1007/s11356-017-1141-5

Flint, R.W., 1981. Gulf of Mexico Outer Continental Shelf Benthos: Macroinfaunal-Environmental Relationships. Biol. Oceanogr. 1, 135—155.

Frankignoulle, M., Abril, G., Borges, A.V., Bourge, I., Canon, C., DeLille, B., Libert, E., Théate, J.M., 1998. Carbon dioxide emissions from European estuaries. Science 282, 434—436. https://doi.org/10.1126/science.282.5388.434

Freel, R.W., Medler, S.G., Clark, M.E., 1973. Solute adjustments in the coelomic fluid and muscle fibers of a euryhaline polychaete, *Neanthes succinea*, adapted to various salinities. Biol. Bull. 144 (2), 289—303. https://doi.org/10.2307/1540009

Freitas, R., Pires, A., Moreira, A., Wrona, F.J., Figueira, E., Soares, A.M., 2016. Biochemical alterations induced in *Hediste diversicolor* under seawater acidification conditions. Mar. Environ. Res. 117, 75—84. https://doi.org/10.1016/j.marenvres.2016.04.003

Gambi, M.C., Musco, L., Giangrande, A., Badalamenti, F., Micheli, F., Kroeker, K.J., 2016. Distribution and functional traits of polychaetes in a CO2 vent system: winners and losers among closely related species. Mar. Ecol. Prog. Ser. 550, 121—134.

Gattuso, J.P., Epitalon, J.M., Lavigne, H., Orr, J., Gentili, B., Hagens, M., Hofmann, A., Mueller, J.D., Proye, A., Rae, J., Soetaert, K., 2019. Package 'seacarb'. https://CRAN.R-project.org/package=seacarb

Gran, G., 1952. Determination of the equivalence point in potentiometric titrations. Part II. Analyst. 77, 661. https://doi.org/10.1039/an9527700661

Gray, J.S., 1974. Animal—sediment relationships. Oceanogr. Mar. Biol. Annu. Rev. 12, 223—226.

Gu, D., Zhang, L., Jiang, L., 2009. The effects of estuarine processes on the fluxes of inorganic and organic carbon in the Yellow River estuary. J. Ocean. U. China 8, 352—358. https://doi.org/10.1007/s11802-009-0352-x

Guinotte, J.M., Fabry, V.J., 2008. Ocean acidification and its potential effects on marine ecosystems. Ann. N. Y. Acad. Sci. 1134, 320—342. https://doi.org/10.1196/annals.1439.013

Gupta, G.V., Sarma, V.V., Robin, R.S., Raman, A.V., Kumar, M.J., Rakesh, M., Subramanian, B.R., 2008. Influence of net ecosystem metabolism in transferring riverine organic carbon to atmospheric CO_2 in a tropical coastal lagoon (Chilka Lake, India). Biogeochemistry 87, 265—285. https://doi.org/10.1007/s10533-008-9183-x

Hily, C., Le Bris, H., Glémarec, M., 1986. Impacts biologiques des émissaires urbains sur les écosystèmes benthiques. Oceanis 12, 419—426.

Ho, M., Carpenter, R.C., 2017. Differential growth responses to water flow and reduced pH in tropical marine macroalgae. J. Exp. Mar. Biol. Ecol. 491, 58—65. https://doi.org/10.1016/j.jembe.2017.03.009

Hutchins, R.H.S., Prairie, Y.T., del Giorgio, P.A., 2019. Large-scale landscape drivers of CO_2, CH_4, DOC, and DIC in Boreal River networks. Global Biogeochem. Cy. 33, 125—142. https://doi.org/10.1029/2018GB006106

Ingole, B., Sivadas, S., Nanajkar, M., Sautya, S., Nag, A., 2009. A comparative study of macrobenthic community from harbours along the central west coast of India. Environ. Monit. Assess. 154, 135. https://doi.org/10.1007/s10661-008-0384-5

Jayaraj, K.A., Jayalakshmi, K.V., Saraladevi, K., 2007. Influence of environmental properties on macrobenthos in the northwest Indian shelf. Environ. Monit. Assess. 127, 459—475. https://doi.org/10.1007/s10661-006-9295-5

Khan, S.A., Manokaran, S., Lyla, P.S., 2014. Assessment of ecological quality of Vellar and Uppanar estuaries, southeast coast of India, using Benthos. Indian. J. Mar. Sci. 43, 1989—1995.

Krumbein, W.C., Pettijohn, F.J., 1938. Manual of sedimentary petrography. Appleton-Century Crofts, New York.

Lannig, G., Eilers, S., Pörtner, H.O., Sokolova, I.M., Bock, C., 2010. Impact of ocean acidification on energy metabolism of oyster, *Crassostrea gigas*-changes in metabolic pathways and thermal response. Mar. Drugs 8, 2318—2339. https://doi.org/10.3390/md8082318

Le Quéré, C., Andrew, R., Canadell, J.G., Sitch, S., Korsbakken, J.I., Peters, G.P., Manning, A.C., Boden, T.A., Tans, P.P., Houghton, R.A., Keeling, R.F., 2016. Global carbon budget 2016. Earth. Syst. Sci. 8, 605—649. https://doi.org/10.5194/essd-8-605-2016

Majeed, S.A., 1987. Organic matter and biotic indices on the beaches of North Brittany. Mar. Pollut. Bull. 18, 490—495.

Marescaux, A., Thieu, V., Borges, A.V., Garnier, J., 2018. Seasonal and spatial variability of the partial pressure of carbon dioxide in the human-impacted Seine River in France. Sci. Rep. 8, 13961. https://doi.org/10.1038/s41598-018-32332-2

Margalef, R., 1958. Information theory in ecology. Gen. Syst. 3, 36—71.

Molari, M., Guilini, K., Lins, L., Ramette, A., Vanreusel, A., 2019. CO2 leakage can cause loss of benthic biodiversity in submarine sands. Mar. Environ. Res. 144, 213—229.

Morgan, A.M., Royer, T.V., David, M.B., Gentry, L.E., 2006. Relationships among nutrients, chlorophyll-a, and dissolved oxygen in agricultural streams in Illinois. J. Environ. Qual. 35, 1110—1117. https://doi.org/10.2134/jeq2005.0433

Mukherjee, J., Banerjee, M., Banerjee, A., Roy, M., Ghosh, P.B., Ray, S., 2014. Impact of environmental factors on the carbon dynamics at Hooghly estuarine region. J. Ecosyst. 1—10. https://doi.org/10.1155/2014/607528, 2014

Murugesan, P., Sarathy, P.P., Muthuvelu, S., Mahadevan, G., 2018. Diversity and distribution of polychaetes in mangroves of east coast of India. Mangrove Ecosystem Ecology and Function. 107 pp. https://doi.org/10.5772/Intechopen.78332

Musale, A.S., Desai, D.V., Sawant, S.S., Venkat, K., Anil, A.C., 2015. Distribution and abundance of benthic macro organisms in and around Visakhapatnam Harbour on the east coast of India. J. Mar. Biol. Assoc. UK 95, 215—231. https://doi.org/10.1017/S0025315414001490

Muxika, I., Borja, A., Bald, J., 2007. Using historical data, expert judgement and multivariate analysis in assessing reference conditions and benthic ecological status, according to the European Water Framework Directive. Mar. Pollut. Bull. 55, 16—29.

Natesan, U., Kalaivani, S., Kalpana, G., 2017. Pollution assessment of Ennore (India) creek using macrobenthos. J. Environ. Geol. 1, 9—16. https://doi.org/10.4172/2591-7641.1000004

Nikinmaa, M., 2013. Climate change and ocean acidification-Interactions with aquatic toxicology. Aquat. Toxicol. 126, 365—372. https://doi.org/10.1016/j.aquatox.2012.09.006

Oksanen, J., Blanchet, F.G., Friendly, M., Kindt, R., Legendre, P., McGlinn, D., Minchin, P.R., O'Hara, R.B., Simpson, G.L., Solymos, P., Stevens, M.H.F., 2017. Vegan: Community Ecology Package R package version 2.4-3. https://cran.r-project.org

Oliveira, A., Pilar-Fonseca, T., Cabeçadas, G., Mateus, M., 2018. Local Variability of CO_2 Partial Pressure in a Mid-Latitude Mesotidal Estuarine System (Tagus Estuary, Portugal). Geosci. J. 8, 460. https://doi.org/10.3390/geosciences8120460

Onwuteaka, J., 2016. Salinity induced longitudinal zonation of polychaete fauna on the Bonny River Estuary. Annu. Res. Rev. Biol. 10 (2), 1—14. https://doi.org/10.9734/ARRB/2016/23682

Palanivel, P.S., Veeraiyan, B., Palingam, G., Perumal, M., 2019. Influence of physico-chemical parameters and pCO_2 concentration on mangroves-associated polychaetes at Pichavaram, southeast coast of India. SN Appl. Sci. 1 (12), 1550. https://doi.org/10.1007/s42452-019-1581-2

Papageorgiou, N., Arvanitidis, C., Eleftheriou, A., 2006. Multicausal environmental severity: A flexible framework for microtidal sandy beaches and the role of polychaetes as an indicator taxon. Estuar. Coast. Shelf Sci. 70, 643—653. https://doi.org/10.1016/j.ecss.2005.11.033

Pearson, T.H., Rosenberg, R., 1978. Macrobenthic succession in relation to organic enrichment and pollution of the marine environment. Oceanogr. Mar. Biol. Annu. Rev. 16, 229—311.

Pielou, E.C., 1966. The measurement of diversity in different types of biological collections. J. Theor. Biol. 13, 131—144. https://doi.org/10.1016/0022-5193(66)90013-0

Plhalova, L., Blahova, J., Divisova, L., Enevova, V., Casuscelli di Tocco, F., Faggio, C., Tichy, F., Vecerek, V., Svobodova, Z., 2018. The effects of subchronic exposure to Neem Azal T/S on zebrafish (*Danio rerio*). Chem. Ecol. 34, 199—210. https://doi.org/10.1080/02757540.2017.1420176

Quinn, R.H., Bashor, D.P., 1982. Regulation of coelomic chloride and osmolarity in *Nereis virens* in response to low salinities. Comp. Biochem. Phys. A: Phys. 72 (1), 263—265.

R Core Team (2018). R: A language and environment for statistical computing. R Foundation for Statistical Computing, Vienna, Austria. URL https://www.R-project.org/

Rajasegar, M., Srinivasan, M., Khan, S.A., 2002. Distribution of sediment nutrients of Vellar estuary in relation to shrimp farming. Indian J. Mar. Sci. 31, 153—156.

Ray, R., Baum, A., Rixen, T., Gleixner, G., Jana, T.K., 2018. Exportation of dissolved (inorganic and organic) and particulate carbon from mangroves and its implication to the carbon bud-

get in the Indian Sundarbans. Sci. Total. Environ. 621, 535—547. https://doi.org/10.1016/j.scitotenv.2017.11.225

Regnier, P., Friedlingstein, P., Ciais, P., Mackenzie, F.T., Gruber, N., Janssens, I.A., Laruelle, G.G., Lauerwald, R., Luyssaert, S., Andersson, A.J., Arndt, S., 2013. Anthropogenic perturbation of the carbon fluxes from land to ocean. Nat. Geosci. 6, 597. https://doi.org/10.1038/ngeo1830

Richmond, C.E., Woodin, S.A., 1999. Effect of salinity reduction on oxygen consumption by larval estuarine invertebrates. Mar. Biol. 134 (2), 259—267. https://doi.org/10.1007/s002270050544

Rodriguez-Romero, A., Basallote, M.D., Manoela, R., DelValls, T.Á., Riba, I., Blasco, J., 2014a. Simulation of CO_2 leakages during injection and storage in sub-seabed geological formations: metal mobilization and biota effects. Environ. Int. 68, 105—117. https://doi.org/10.1016/j.envint.2014.03.008

Rodríguez-Romero, A., Jiménez-Tenorio, N., Basallote, M.D., Orte, M.R.D., Blasco, J., Riba, I., 2014b. Predicting the impacts of CO_2 leakage from subseabed storage: effects of metal accumulation and toxicity on the model benthic organism *Ruditapes philippinarum*. Environ. Sci. Technol. 48, 12292—12301. https://doi.org/10.1021/es501939c

Sanders, H.L., 1958. Benthic studies in Buzzards Bay. I. Animal sediment relationships. Limnol. Oceanogr. 3, 245—258. https://doi.org/10.4319/lo.1958.3.3.0245

Selvaraj, P., Murugesan, P., Punniyamoorthy, R., Parthasarathy, P., Marigoudar, S.R., 2019. Assessment of the ecological health of Vellar and Ennore estuarine ecosystems using health indices. Indian J. Mar. Sci. 48 (10), 1580—1592.

Senthilnathan, S., Balasubramanian, T., 1994. Heavy Metals in Plankton of Uppanar, Vellar and Kaduviar Estuaries of Southeast Coast of India. Chem. Ecol. 9, 41—46. https://doi.org/10.1080/02757549408038561

Shannon, C.E., Weaver, W., 1964. The Mathematical Theory of Communication. Univ. Illinois Press, Urbana, 125 pp., https://monoskop.org/images/b/be/Shannon_Claude_E_Weaver_Warren_The_Mathematical_Theory_of_Communication_1963.pdf

Shanthi, R., Poornima, D., Raja, K., Sarangi, R.K., Saravanakumar, A., Thangaradjou, T., 2015. Inter-annual and seasonal variations in hydrological parameters and its implications on chlorophyll a distribution along the southwest coast of Bay of Bengal. Acta Oceanologica Sinica 34, 94—100. https://doi.org/10.1007/s13131-015-0689-5

Sigamani, S., Perumal, M., Arumugam, S., Jose, H.P.M., Veeraiyan, B., 2015. AMBI indices and multivariate approach to assess the ecological health of Vellar—Coleroon estuarine system undergoing various human activities. Mar. Poll. Bull. 100, 334—343.

Sigamani, S., Samikannu, M., Alagiri, T.G., 2019. Assessment of effluent stressed ecosystem of Cuddalore coastal waters—a bioindicator approach. Thalassas: Int. J. Mar. Sci. 35 (2), 437—449. https://doi.org/10.1007/s41208-019-00128-4

Sivaleela, G., Venkataraman, K., 2013. Diversity and Distribution of Benthic Foraminifera from Tamilnadu Coast. India. Rec. Zool. Surv. India 113, 1—12.

Sivaraj, S., Murugesan, P., Muthuvelu, S., Vivekanandan, K.E., Vijayalakshmi, S., 2014. AMBI and M-AMBI indices as a robust tool for assessing the effluent stressed ecosystem in Nandgaon Coastal waters, Maharashtra, India. Estuar. Coast. Shelf. Sci 146, 60—67. https://doi.org/10.1016/j.ecss.2014.05.024

Smith, R.I., 1970. Hypo-osmotic urine in *Nereis diversicolor*. J. Exp. Biol. 53 (1), 101—108.

Snelgrove, P.V.R., Butman, C.A., 1994. Animal—sediment relationships revisited: cause versus effect. Oceanogr. Mar. Biol. Annu. Rev. 32, 111—177.

Strickland, J.D., Parsons, T.R., 1972. A practical handbook of seawater analysis. Bull. Fish Res. Bd. Can. 167, 1—310.

Thasneem, T.A., Nandan, S.B., Geetha, P.N., 2018. Water quality status of Cochin estuary. India. Indian. J. Mar. Sci. 47, 978—989.

Toma, J.J., 2013. Limnological study of Dokan, Derbendikhan and Duhok lakes, Kurdistan region of Iraq. Open. J. Ecol. 3, 23. https://doi.org/10.4236/oje.2013.31003

Vajravelu, M., Martin, Y., Ayyappan, S., Mayakrishnan, M., 2018. Seasonal influence of physico-chemical parameters on phytoplankton diversity, community structure and abundance at Parangipettai coastal waters, Bay of Bengal, South East Coast of India. Oceanologia 60 (2), 114—127.

Van Gaest, A.L., Young, C.M., Young, J.J., Helms, A.R., Arellano, S.M., 2007. Physiological and behavioral responses of *Bathynerita naticoidea* (Gastropoda: Neritidae) and *Methanoaricia dendrobranchiata* (Polychaeta: Orbiniidae) to hypersaline conditions at a brine pool cold seep. Mar. Ecol. 28 (1), 199—207. https://doi.org/10.1111/j.1439-0485.2006.00147.x

Veron, J.E., 2011. Ocean acidification and coral reefs: an emerging big picture. Diversity 3, 262—274. https://doi.org/10.3390/d3020262

Wickham, H., François, R., Henry, L., Müller, K., 2018. dplyr: A Grammar of Data Manipulation. R package version 0.7.5. https://CRAN.R-project.org/package=dplyr

Wu, F., Kothawala, D., Evans, R., Dillon, P., Cai, Y., 2007. Relationships between DOC concentration, molecular size and fluorescence properties of DOM in a stream. Appl. Geochem. 22, 1659—1667. https://doi.org/10.1016/j.apgeochem.2007.03.024

Oceanologia 64 (2022) 363—375

Available online at www.sciencedirect.com

ScienceDirect

journal homepage: www.journals.elsevier.com/oceanologia

ORIGINAL RESEARCH ARTICLE

Coastal upwelling by wind-driven forcing in the Caspian Sea: A numerical analysis

Fatemeh Fallah, Dariush Mansoury*

Faculty of Natural Resources and Marine Sciences, Tarbiat Modares University, Noor, Iran

Received 25 March 2021; accepted 18 January 2022
Available online 31 January 2022

KEYWORDS
Upwelling;
Vertical velocity;
Wind field;
Bottom topography;
Hydrodynamic modelling;
Caspian Sea

Abstract In this study, wind-driven coastal upwelling in the Caspian Sea was investigated using a developed three-dimensional hydrodynamic numerical model based on the Princeton Ocean Model (POM). The model was forced with wind fields and atmospheric fluxes from the ECMWF database and it considers freshwater inflows from the Volga, Kura and Ural Rivers. This model was implemented for 10 years (2008—2018). Findings indicated that the upwelling in the Caspian Sea was due to effects of wind and bottom topography, often occurring from May to September. In June and July, in the eastern part of the middle and sometimes southern basins, up to 3°C water temperature difference occurs between coastal and offshore areas. The vertical temperature gradient in the middle basin was larger than that in the southern basin. Upwelling in August in the eastern coasts of the middle basin within 25 km of coast from the depth of 15 m to the surface was shown, which was due to the effects of wind and bottom topography. In the middle basin, the highest vertical velocities caused by upwelling in June, July and August were 12, 13.82, and 10.36 m/day, respectively.

1. Introduction

Winds in specific areas lead to divergence of water mass in oceans and seas. If surface water is driven by wind action away from the coast, the only way for its replacement is by upwelling from below. Since there is a good chance that the upwelled water has been enriched in nutrients, an upwelling area is likely to be a site of enhanced biological production. Coastal upwelling is mainly influenced by winds and rotational effects of the Earth (Coriolis force), so that its formation is owing to the presence of coast as an impenetrable lateral boundary as well as the relatively shal-

* Corresponding autor at: Faculty of Natural Resources and Marine Sciences, Tarbiat Modares University, Noor, Iran.
E-mail addresses: fa.fallah1374@gmail.com (F. Fallah), mansoury@modares.ac.ir (D. Mansoury).
Peer review under the responsibility of the Institute of Oceanology of the Polish Academy of Sciences.

Production and hosting by Elsevier

https://doi.org/10.1016/j.oceano.2022.01.003

low waters of the continental shelf (Brink, 1983; Kämpf and Chapman, 2016). The denser mass of water rises to sea surface, so that the sea surface temperature drops. The horizontal movement of water masses toward the offshore decreases the sea level in the coastal area, and it creates a horizontal pressure gradient and produces a geostrophic current under Ekman's transfer function (Kämpf and Chapman, 2016). Many studies have related the coastline orientation and the upwelling-favorable winds (Anand et al., 2019; Closset et al., 2021; Li et al., 2018; Nigam et al., 2018; Sun et al., 2017; Wirasatriya et al., 2020). Owing to the prevailing wind regime in the summer, the formation of the upwelling phenomenon in the Caspian Sea is highly important (Ibrayev et al., 2010). The surface waters are often warmer during the summer in the shallow coastal areas of the Caspian Sea, while along the east coast of the middle and southern Caspian basins, due to favorable winds (parallel to the coast), the surface waters move toward the west coast, and create the this phenomenon in the east coast (Ibrayev et al., 2010). Furthermore, they sometimes cause downwelling on the west coast. Several factors, such as wind and bottom topography (length and curvature of the bed), affect the rise of water along the coast (Shanks et al., 2000). The bottom topography plays a key role in the formation of the long upwelling filaments, whose signature extends over the entire water column and influences the upper layer dynamics advecting water parcels offshore (Meunier et al., 2010). The upwelling phenomenon in warm seasons has an almost stable trend as confirmed in atmospheric (Kosarev and Yablonskaya, 1994) and satellite observations (Sur et al., 2000). During the summer, due to the prevailing north wind, a relatively strong current is generated from the eastern part of the sea to the center, creating the Ekman transport along the eastern part (Ibrayev et al., 2010). In July, the prevailing wind in the central Caspian Sea is often from north to south, causing the upwelling phenomenon on the east coast (Knysh et al., 2008), while in the winter, the movement of water mass to the south and north on the western and eastern parts, respectively, in the subsurface layer (up to 30 m depth) of the Caspian Sea creates a seasonal counterclockwise rotation (Gunduz and Özsoy, 2014). Sea surface temperature (SST) satellite data often show relatively colder waters along the coast and filaments penetrating offshore from the upwelling region. The upwelling region extends from 41° to 44°N along the eastern coast with a temperature anomaly of 2–3°C in a region extending 5–20 km from the coast (Gunduz and Özsoy, 2014). The thermohaline structures of the Caspian Sea waters in the areas near the river mouths as well as on the eastern shores of the middle Caspian basin, where upwelling is observed in the summer, have considerable inconsistency in three dimensions, and seasonal changes in the temperature and salinity of sea water are at 100 m and 20 m, respectively (Tuzhilkin and Kosarev, 2005). To investigate the upwelling phenomenon in the eastern coasts of the middle Caspian basin, one study used a three-dimensional COHERENS model whose horizontal model grid was 0.046 × 0.046 degree and, in the vertical direction, it had 30 layers in the sigma coordinates (Shiea and Bidokhti, 2015). The model was implemented for 5 years, and it was investigated by simulation results, studying the horizontal and vertical temperature structure, and velocities of the sea currents in

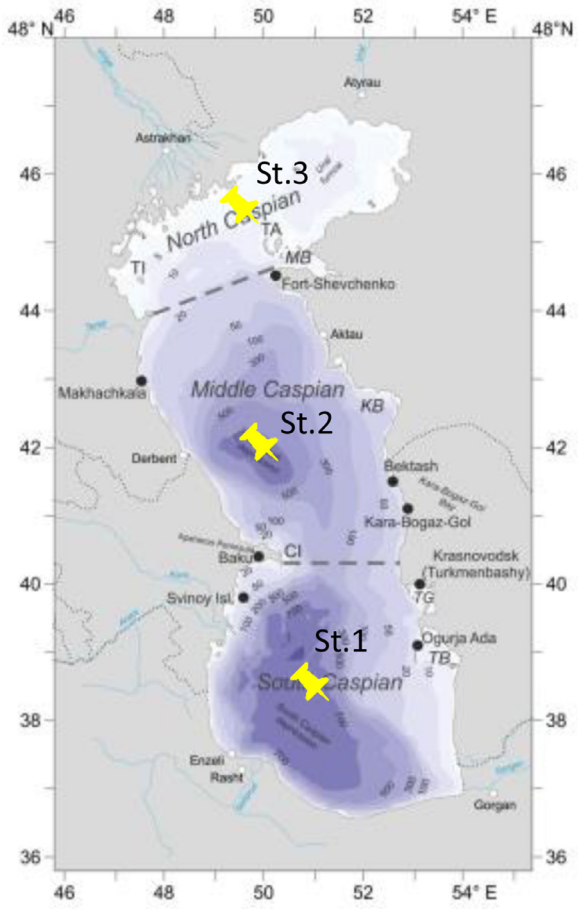

Figure 1 Three basins of the Caspian Sea.

the eastern area of the middle Caspian coast. The maximum vertical velocity was 12 m/day in July and 7 m/day in August (Shiea and Bidokhti, 2015; Shiea et al., 2016). Although previous research focused on studying the circulation of the Caspian Sea, some issues in simulation of the current field remain unresolved. Since currents over the Caspian Sea are primarily wind-driven (Ghaffari et al., 2013), their accurate simulations depend largely upon the wind data resolution (Kitazawa and Yang, 2012). However, to the best of our knowledge, previous studies did not apply well-resolved spatial changes of wind field over the Caspian Sea to predict its current field (e.g. Gunduz and Özsoy, 2014; Ibrayev et al., 2010; Turuncoglu et al., 2013). The major problem using satellite SST images to detect upwelling is that they only provide information about the near sea surface layer (Su and Pohlmann, 2009). In addition to the lack or scarcity of field measurements for the Caspian Sea, a high-resolution hydrodynamic model of the Southern Caspian Sea circulation is also absent in the literature. In this research, upwelling caused by wind and bottom topography during the year and in the whole Caspian Sea by applying more forcing and resolution (compared to previous research), was carried out using Princeton Ocean Model (POM). The purposes of the paper are (1) to implement the 3D hydrodynamic model (POM) for current, salinity and temperature fields modeling of the Caspian Sea by applying a 0.041° resolution; (2) to investigate the frequency of up-

Table 1 Main characteristics of the Caspian Sea (Arpe et al., 2018; Hall, 2002; Kostianoy and Kosarev, 2005).

Surface area (km^2)	North	386,400 in 2017	112,056
	Middle		139,104
	South		135,240
Volume (km^3)	North 1%	78,200	900
	South 66%		27335
	South 33%		49865
Length (km)		1,200	
Width (min-max) (km)		196-435	
Average depth (m)	North	5 (max 20)	
	Middle	190 (max 790)	
	South	330 (max 1025)	
Average surface temperature (°C)	North	Winter: 0°C with ice cover	Summer: 24
	South	Winter: 10	Summer: 27
Average surface salinity (psu)	North	4	
	Middle	12.8	
	South	13	

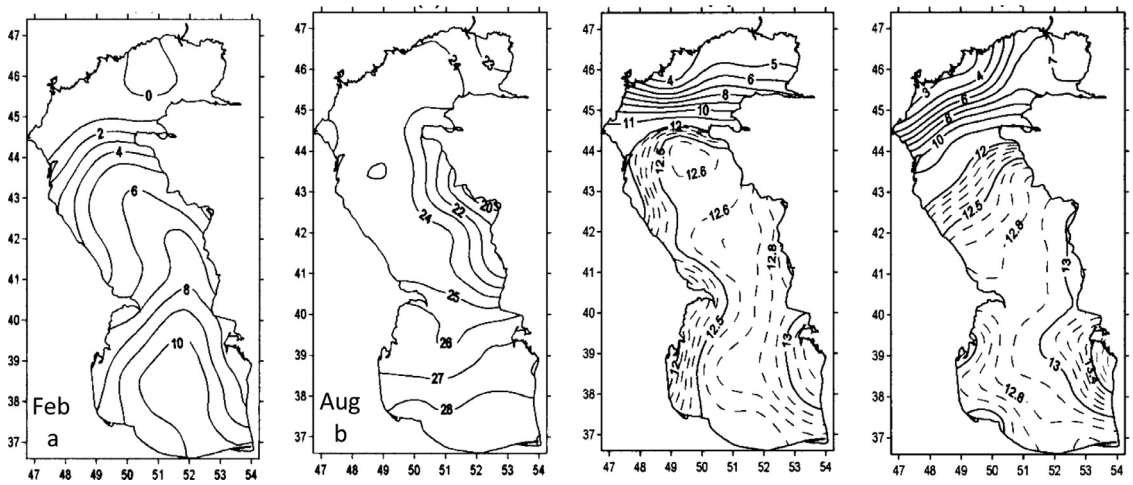

Figure 2 Climatic fields of the water temperature (°C, a, b) and salinity (psu, c, d) in the surface layer of the Caspian Sea in February and August (Tuzhilkin and Kosarev, 2005).

welling (per month) in the Caspian Sea using POM model; (3) In particular, we try to identify the roles of bottom topography and wind field as important upwelling mechanisms in the Caspian Sea.

2. General features of the Caspian Sea

2.1. Study area

The Caspian Sea, a landlocked body of water between Asia and Europe, and the largest enclosed sea basin in the world is located at 36—48°N and 46—55°E, with 40—44% of the total lacustrine waters of the world (Dumont, 1998; Bohluly et al., 2018). According to physical and geographical conditions as well as the bottom topography, the Caspian Sea is divided into three basins (Figure 1, Table 1), North Caspian Basin (NCB), Middle Caspian Basin (MCB) and South Caspian Basin (SCB) (Tuzhilkin and Kosarev, 2005; Zereshkian and Mansoury, 2020).

2.2. The climatic temperature and salinity fields of the Caspian Sea

Based on the results of statistical and physical analyses of ship and coastal measurement data (Tuzhilkin and Kosarev, 2005), the winter surface temperature field is characterized by its significant increase from the north to the south (Figure 2a). Heat losses during the winter in the northern and southern Caspian basins reach approximately 700 MJ m^{-2} and 200 MJ m^{-2}, respectively. Water temperatures are approximately 3°C lower than those in the open sea at the same latitude (Tuzhilkin and Kosarev, 2005). The advection of the waters of the northern and southern Caspian basins affects the surface temperatures of the western and eastern boundaries of the Middle Caspian Sea. The maximum values of the winter surface temperatures in the Middle Caspian result from the advection of warm waters from the south to the north along its eastern boundaries. In the summer, the minimum temperature of the Caspian Sea is observed in part of its eastern coast, which could be due to a summertime upwelling. The high summertime recurrence of upwelling

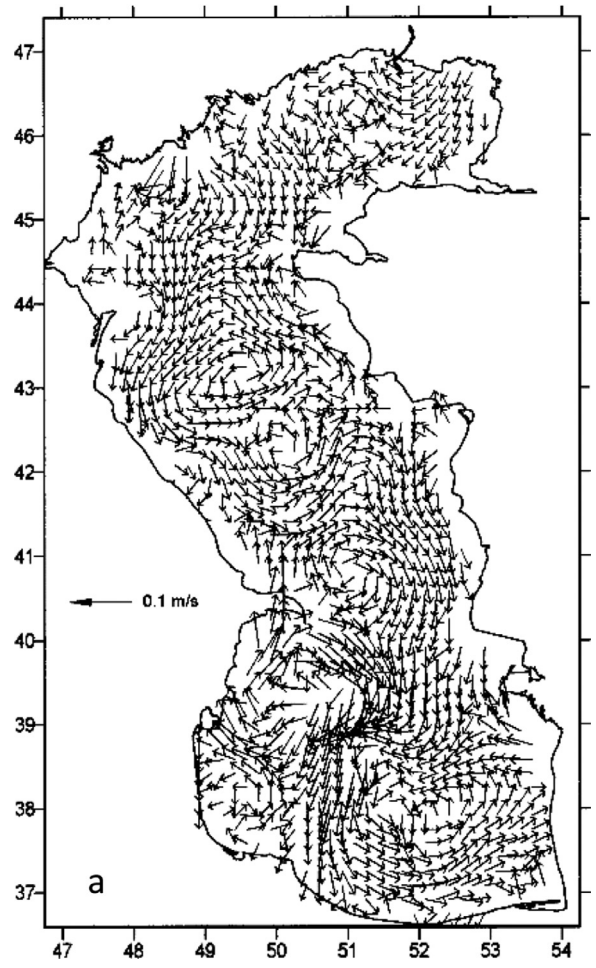

Figure 3 Annual mean climatic field of the current vectors in the surface layer of the Caspian Sea (Tuzhilkin and Kosarev, 2005).

off the eastern coast of the Middle Caspian from May to September makes this phenomenon climatically significant and it is well illustrated in the multiannual mean monthly fields of the water temperature (Figure 2b).

The salinity field in the Caspian Sea is subject to certain seasonal changes owing to its geographical location, river inflow, evaporation (shallow-water zones off arid eastern coasts), and precipitation (Tuzhilkin and Kosarev, 2005). In winter, due to reduced evaporation, surface salinity is low in the central and southern Caspian basins (Figure 2c). The propagation of reduced salinity from the northern basin to the middle is negligible due to high evaporation in the summer (Figure 2d).

2.3. The mean annual field of the current and wind of the Caspian Sea

The mean annual current velocities at the centers of the sub-basin gyres are 0.05—0.10 m s^{-1} and reach 0.20 m s^{-1} at the interfaces of gyres with opposite vorticities (Figure 3). Wind-induced currents play a rather significant role in the sea surface layer (Table 2). The current variability is related to the synoptic variability of the direct wind impact (Medvedev et al., 2020).

3. Data and methods

3.1. POM model

The POM is a simple-to-run yet powerful ocean modeling code to simulate a wide-range of problems, from small-scale coastal processes to global ocean climate change (http://www.ccpo.odu.edu/POMWEB/; Mellor and Blumberg, 1985). Many international researchers have studied numerous applications of this model in the modeling field in oceans and seas in different parts of the world. This model was provided by Princeton University in New Jersey and was developed with the support of the Geophysical Fluid Dynamics Laboratory (GFDL) of the National Oceanic and Atmospheric Administration (NOAA) as well as the Princeton Dynamic Analysis Institute (Blumberg and Mellor, 1987). The message passing interface Princeton Ocean Model (mpiPOM) was developed by Advanced Taiwan Ocean Prediction (ATOP), and it was optimized for the needs and resources of the ATOP system (Oey et al., 2013). This model was developed for the Caspian Sea with modifications and various types of coding as mpiPOM_Caspian Sea (mpiPOM-CS).

3.2. Data preparation to implement the model

Unfortunately, most of the time, there are not sufficient reliable data for the study area due to the lack of field measurements. For the model input, temperature and salinity data of the World Ocean Atlas (Antonov et al., 2006) were used; despite high accuracy (1°), the data do not cover the entire Caspian Sea and an algorithm for extrapolation, in addition to interpolation on the grid, should be used (Mansoury et al., 2015). The General Bathymetric Chart of the Oceans (GEBCO) aims to provide the most authoritative, publicly available bathymetry data sets for the oceans and seas including the Caspian Sea. Atmospheric fluxes data, including wind, precipitation, evaporation, heat fluxes (sensible and latent), and short and long wave solar radiation were received from the ECMWF database with an accuracy of 0.125° and a 6-hour time step. The most important rivers entering the Caspian Sea are Volga (5 branches), Kura and Ural. The monthly average of Naval Research Laboratory (NRL) data was used for the data of the rivers (Table 3; Kara et al., 2010). In this research, the model was implemented for ten years (2008—2018), and the last year outputs of the model implementation were investigated. The model domain is 46.5—55°E and 36.5—47°N with a horizontal resolution of 0.041° (about 4 km) and 35 vertical layers in sigma coordinates. It uses external and internal time steps of 2s and 90s, respectively. To apply the parallel processing, four cores were considered with a computational grid of 135 × 103.

3.3. Stability and validation of the model

In the course of a year, salinity has almost a round cycle, but in the first years of the model, it does not have a clear trend. Its multi-year repetition during model execution indicates that the model is stable (and can also be true for temperature). In this study, salinity changes in the last years of the model implementation show rela-

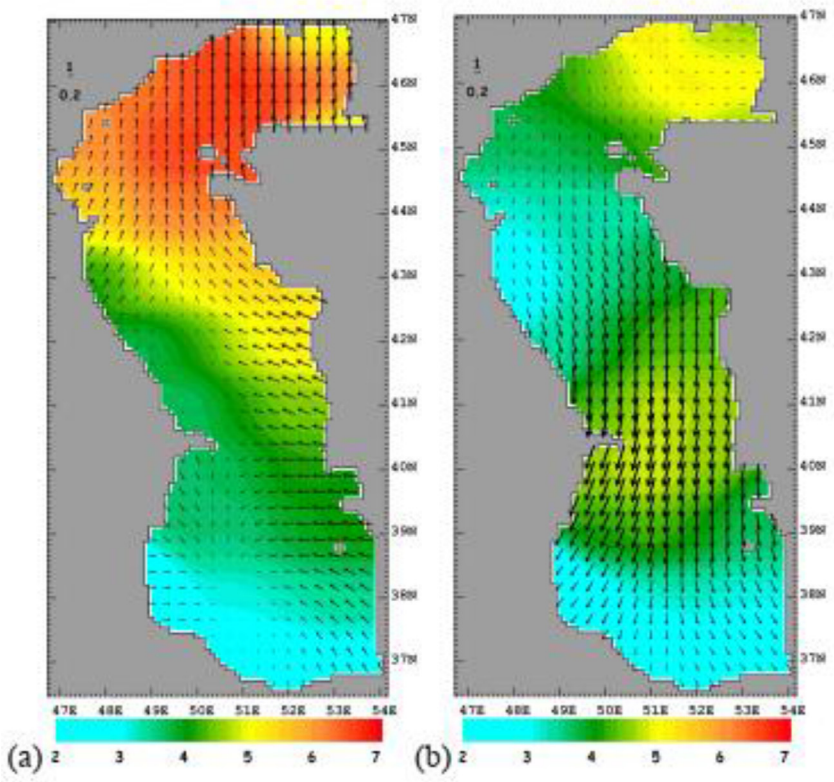

Figure 4 Monthly mean wind velocity vectors in (a) December and (b) July 1982. The units are in m/s (Ibrayev et al., 2010).

Table 2 Some wind features in the Caspian Sea (Ibrayev et al., 2010).

Wind speed (typically)	Summer (approximately 4 m/s) The maximum speed occurs to the east of the Apsheron Winter (approximately 5—6.5 m/s) The maximum speed occurs in the north (Figure 4a)
The classification of the annual cycle of the monthly mean wind	1 — December—January: With the convergence of winds in MCB and SCB due to high land-sea temperature (Figure 4a) 2 — February—July: When large-scale anti-cyclonic winds prevail over the sea (Figure 4b). 3 — August—November: When average wind direction gradually changes from south-, southwestward to westward.

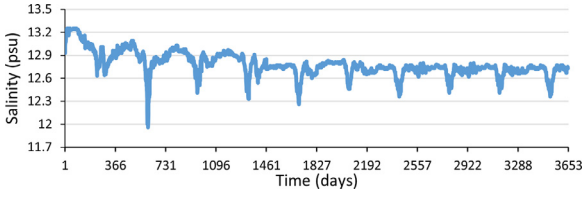

Figure 5 Changes in salinity in the ten-year implementation period of the model.

tively good model stability (Kämpf and Sadrinasab, 2006; Sadrinasab and Kämpf, 2004) (Figure 5).

The data collected during research cruises in the Caspian Sea in August and September (from 30.08.1996 for one week) were used to validate the model results. To validate the model output according to the available measurement data during 1996 (UNESCO-IHP-IOC-IAEA, 1996), the model was re-run for ten years (1988—1997). The results of the model output and measurements were compared to each other (Figure 6) in three positions (Figure 1).

The following comparisons indicate acceptable agreements between the model results and the measurement data and satellite image (https://oceancolor.gsfc.nasa.gov/). Due to the limited availability of the current velocity measurement data in the Caspian Sea, the mean annual current velocities of previous study (Figure 3), SST satellite image (Figure 7a) and this study (Figure 7b) were compared, showing good agreement between them.

3.4. Upwelling detection mechanism

Upwelling occurs due to divergence of currents in the surface layers of the sea caused by wind field, in the presence

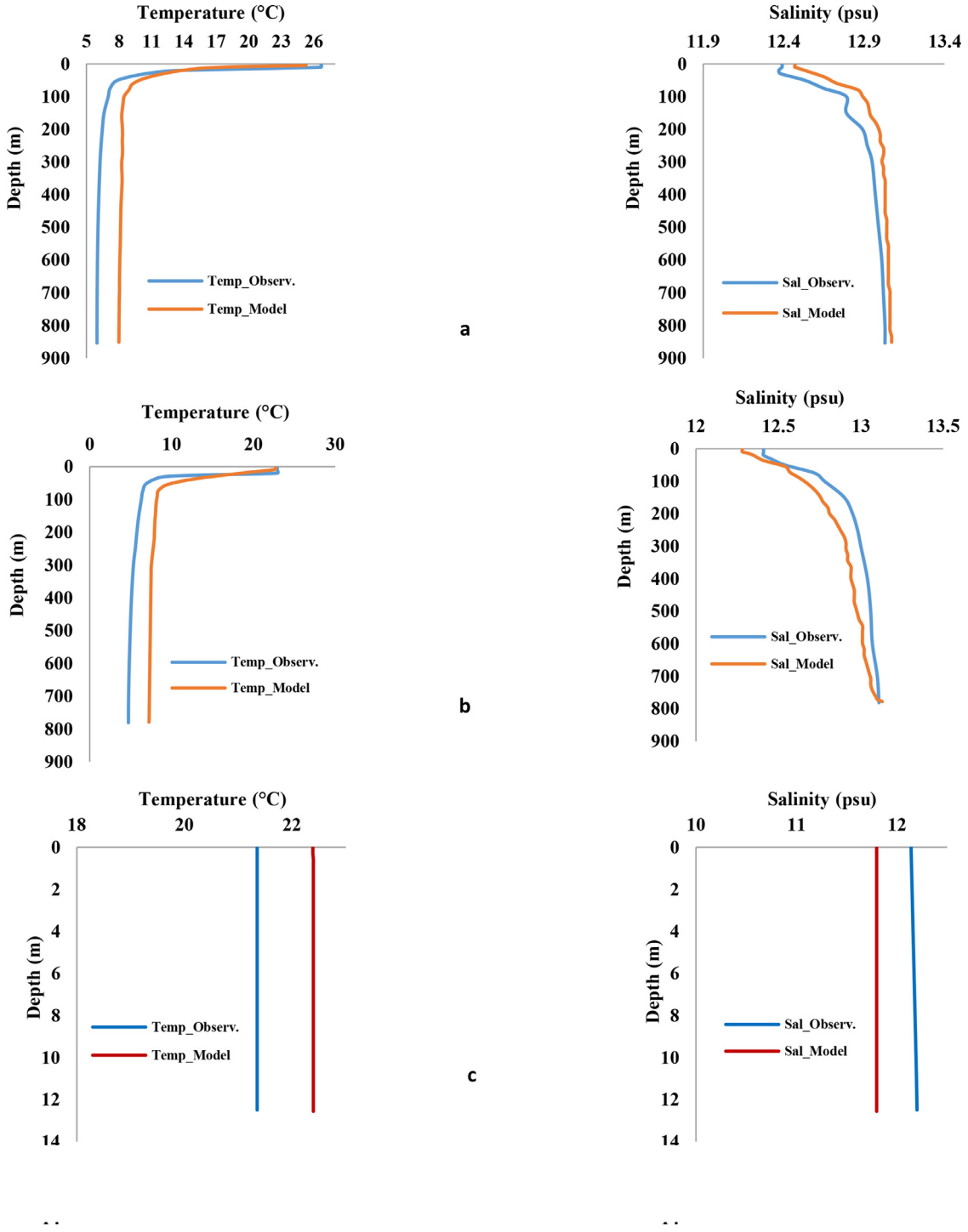

Figure 6 Comparison of modeled and observed temperature—salinity properties: a) St.1, b) St.2 and c) St.3 in 1996.

of the shoreline or other special conditions, after which the water of the lower layer (colder and denser) is transferred to the surface to maintain balance. The lower layers are known as permanent sources of nutrients, so productivity is significant in areas where upwelling occurs. Due to the favorable wind in the sea shores and the resulting ecumenical transfer, there is a difference in water level between the coast and offshore, and the pressure difference caused by them will follow the surface geostrophic flow. Changes in sea water temperature (surface temperature at nearshore and offshore, and the vertical section of seawater temperature) and sea currents (such as vertical velocity) due to a rise in a body of water from depth to surface which can be caused by wind and bottom topographic effects (Meunier et al., 2010), indicate the coastal upwelling (Ghaffari et al., 2013; Olita et al., 2013). In this research, owing to the physical and geographical location of the Caspian Sea, the Coriolis effect in differ-

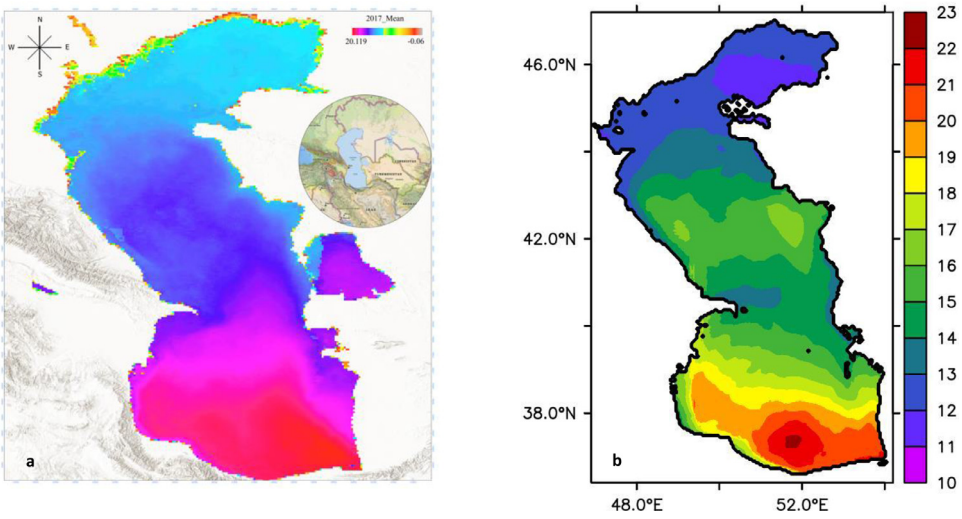

Figure 7 Annual mean climatic field of SST (°C): a) Satellite image (https://oceancolor.gsfc.nasa.gov/); b) Model output in the Caspian Sea.

Table 3 Monthly mean discharge for the major rivers discharged into the Caspian Sea (Kara et al., 2010).

	Volga (m^3/s)	Kura (m^3/s)	Ural (m^3/s)
January	780	490	50
February	790	500	55
March	800	530	60
April	1500	800	900
May	4780	1050	1370
June	4000	800	420
July	1650	450	220
August	1120	310	180
September	1000	315	140
October	1060	400	140
November	1070	420	135
December	780	460	80

Table 4 The maximum vertical velocities of seawater in upwelling events at 43°N in June.

Day	w_{max} (m/day)
11	10.5
12	11
13	10.1
27	10.3
28	11.3
29	12

Table 5 The maximum vertical velocities of seawater in upwelling events at 43°N in July.

Day	w_{max} (m/day)
22	12.09
24	8.64
25	13.82
26	7.77

Table 6 The maximum vertical velocities of seawater in upwelling events at 43°N in August.

Day	w_{max} (m/day)
3	10.36
4	6.04
5	6.9
6	8.64

ent latitudes and a variable wind field, as well as the ice effect were considered with an appropriate accuracy in mpiPOM-CS.

3. Results

3.1. Spatio-temporal variability of sea surface temperature

Figure 8 presents the monthly changes in the Caspian Sea temperature in 2017. In the northern and middle basins, the climate pattern is relatively cold and in the southern basin, the pattern is warm. Sea surface temperature from January to April in the three basins of the Caspian Sea have increased, and this increase in temperature in the northern basin (from January to April) is east-west due to depth changes (Figure 8a—d). These changes are caused by the lower depth of the eastern part compared to the western part of the basin and the lower heat capacity of the seafloor relative to seawater. The mean monthly seawater temperature in some parts of the Caspian Sea, particularly from May to September, undergoes unexpected changes (Figure 8e—i). SST changes in the eastern part of the middle and southern basins, from May to August and into part of September, are colder than offshore ones (blue ovals). From October to December, it resumes its natural trend (Figure 8j—l). In these months, the air temperature rises compared to previous months, and this increase in tem-

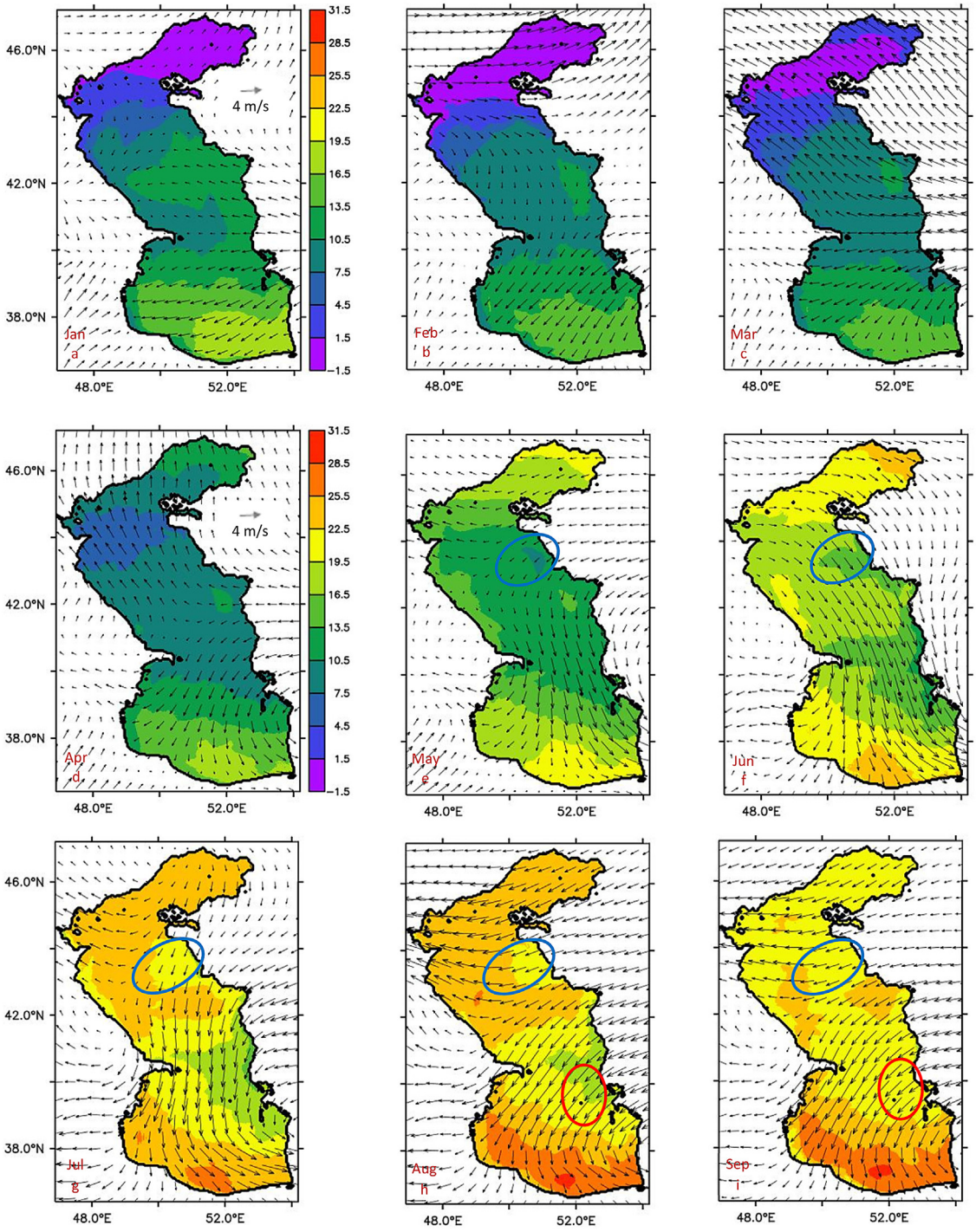

Figure 8 SST (°C) with monthly mean wind overlaid in 2017.

perature is expected to affect the eastern coasts of the Caspian Sea due to the shallow depth and to raise the surface temperature of the water. However, the sea surface water on the eastern shores of the central and southern Caspian basins has been colder compared to the offshore areas, which may be owed to the transfer of cold water from the lower layers to the sea level. The difference between the average sea surface temperature in the eastern part of the middle Caspian Basin (coastal and offshore) indicates the possibility of upwelling in these areas.

Nevertheless, the monthly pattern of the wind field in May, August and September does not show the Ekman transport in favor of upwelling (perpendicular to the coastline) (Figure 8e,h,i). However, the direction of the wind in this part, due to pushing the surface water, causes a difference in the water level between coastal and offshore areas, being consistent with the upwelling event. Since the effect of other factors (other than wind) may play a role in creating upwelling, it is necessary to examine the daily changes for a more detailed study. Northwest and north winds in

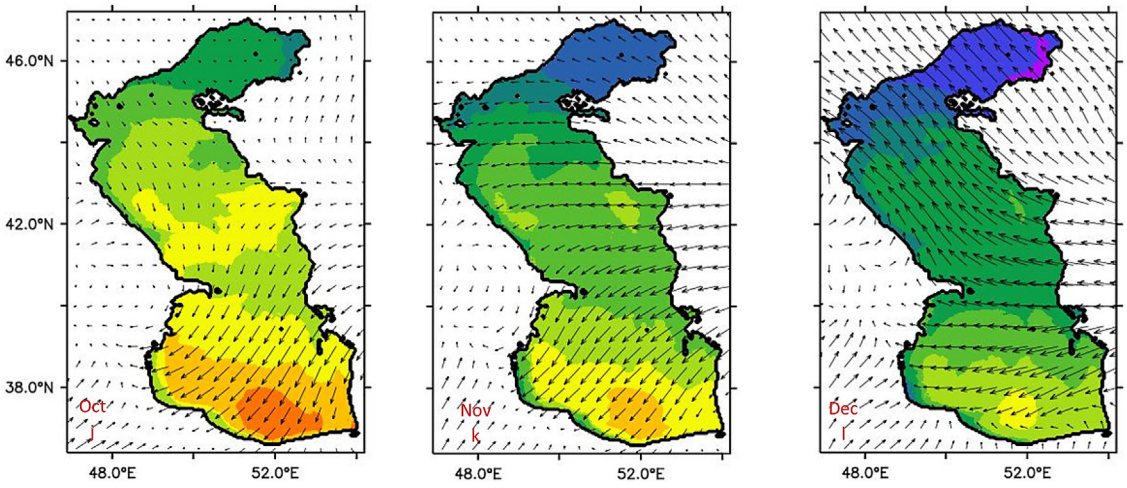

Figure 8 *Continued.*

June and July are the main mechanism of upwelling on the eastern coasts of middle and southern Caspian basins, owing to the Ekman transport perpendicular to the coastline (Figure 8f,g).

3.2. Vertical section of seawater temperature in middle and southern Caspian basins

In May, although the wind direction in the middle Caspian basin (at 43°N) is not parallel to the east coast (Figure 8e), a slight upwelling occurs in lower layers, which may be due to topographic effect (Figure 9a). However, in the southern Caspian basin (at 39°N), it is upwelling-favorable wind. Coastal upwelling is seen in the upper layers, which can be due to wind field effect (Figure 9b). In June, temperature contours show that the water masses of the eastern coasts of the middle and southern Caspian basins are the result of divergence of surface waters and the movement of water from lower layers to upper layers (Figure 9c,d). Wind field is the main factor of upwelling in this month (Figure 8f).The intensity of upwelling due to wind is higher in the middle basin than in the southern basin, so that the topographic effect in this basin is negligible (Figure 9). In July, in the middle basin, the rise of water mass at a depth of 20 m to the surface occurred, and in the southern basin at a depth of 12 m, partially along 52—53°E, according to the north wind (Figure 9e,f). Furthermore, in the middle basin, wind-driven upwelling is predominant.

In August and September, the rise of water mass from lower layers to upper layers in the middle basin (at 43 °N) can be seen in two parts (Figure 9h,i). The first part (blue ovals) indicates weak coastal upwelling considering the east and southeast wind and change at the coastal water level (Less than 10 m depth) (Figure 9g,i). However, the second parts (red ovals) show water rises from a depth of approximately 35 to 10 m (along another longitude), which can be due to sea currents encountering the seafloor (bottom topographic effect). Nevertheless, in the southern basin (at 39°N), rising water is seen only in part, at a depth of 35—10 m (orange ovals), which is similar to the middle basin owing to topographic effects (Figure 9h,j).

3.3. Monthly mean of vertical velocity in June and July

According to Figure 10, the maximum vertical velocity occurs at 51.2°E in June and July considering positive values.

3.4. Daily upwelling in June, July and August

Rising water mass from lower layers to the surface layer on June 27 (Figure 11a) in the longitude 51.2°E occurs considering the northwest wind that is almost parallel to the coastline (Figure 11b). Moreover, according to Table 4, the highest vertical velocity is estimated at 12 m/day in upwelling events this month, where w_{max} is the maximum vertical velocity.

On July 22, the water mass rises vertically in the longitude 51.20°E (Figure 12a,b), and according to Table 5, the highest vertical velocity is 13.82 m/day in upwelling events.

In August, according to the wind direction (southeast), the mechanism of formation of upwelling on the fourth day cannot be the effect of wind (Figure 13a). Although the vector of the wind field in this area is almost parallel to the coastline, its Ekman transport is to the onshore. Therefore, the formation of upwelling in this part of middle basin coasts can be due to topography (Figure 13b). The highest vertical velocity is 10.36 m/day in upwelling events (Figures 13b, 14, Table 6).

4. Conclusion

In this study, upwelling in the Caspian Sea was investigated using a developed three-dimensional hydrodynamic numerical model (mpiPOM-CS). The Validation of the model results based on measurement and observational data (satellite image) showed greater consistency of the simulation results. According to the findings, upwelling often occurs in the Caspian Sea from May to September, which is in good agreement with the results of studies conducted by Lavrova et al. (2011) and Tuzhilkin and Kosarev (2005) in the eastern part of the middle Caspian basin. The difference in SST between

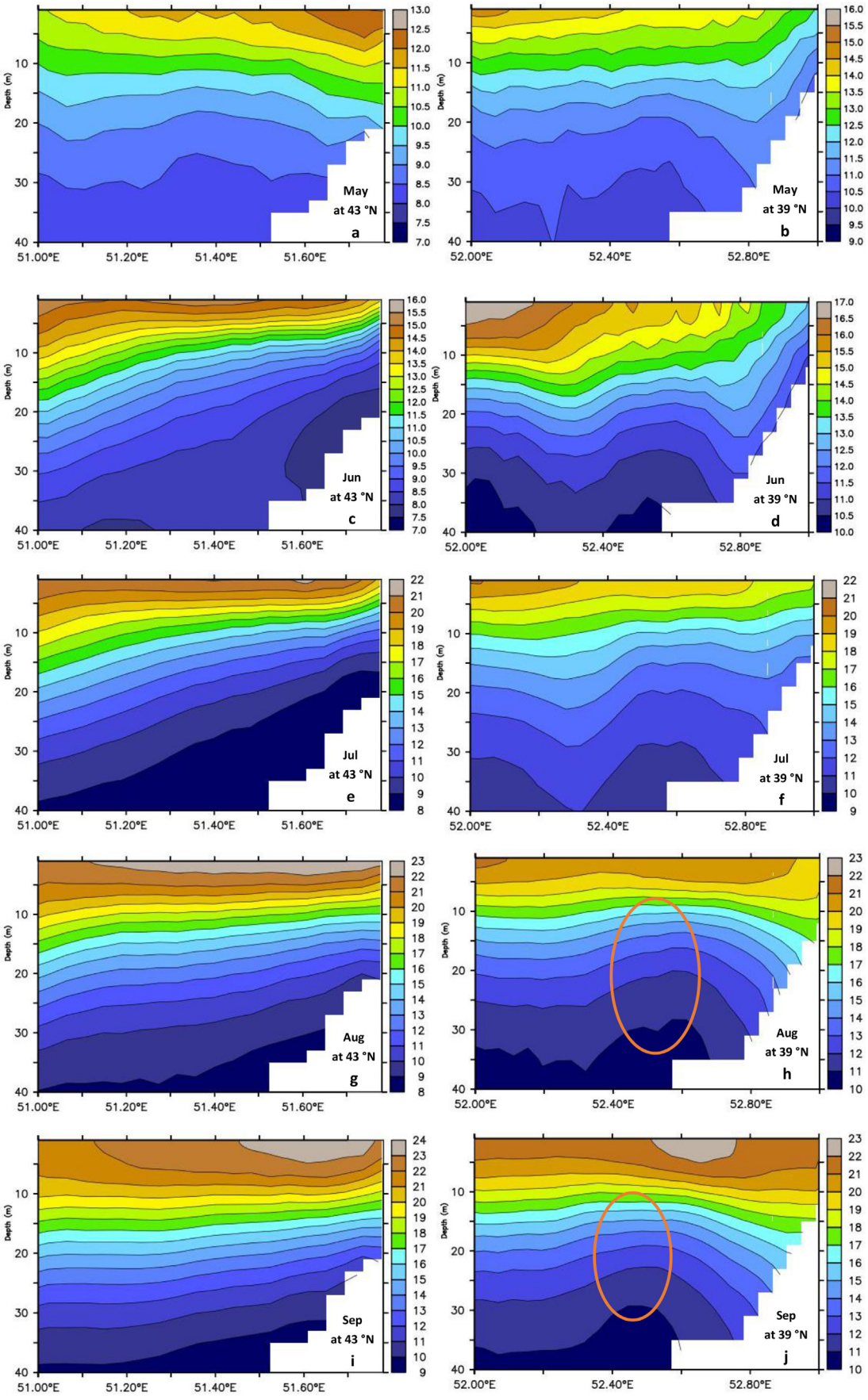

Figure 9 Vertical section of the seawater temperature (°C) in MCB and SCB (May—September).

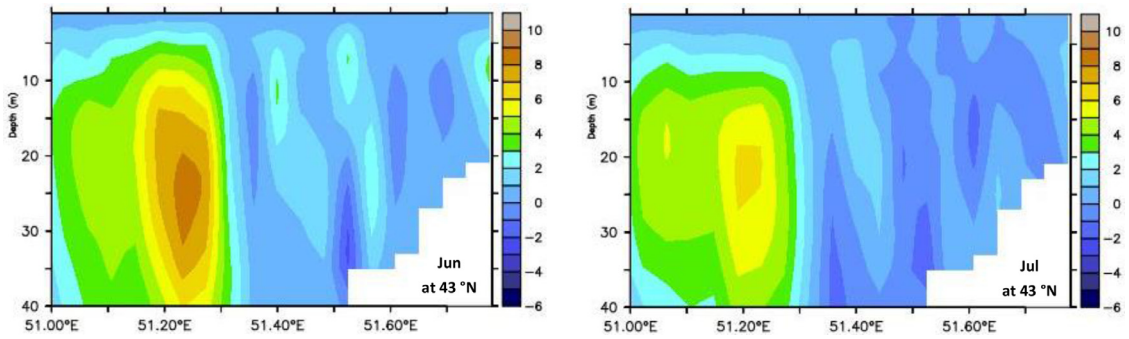

Figure 10 Monthly mean of the vertical velocity (m/day) in MCB.

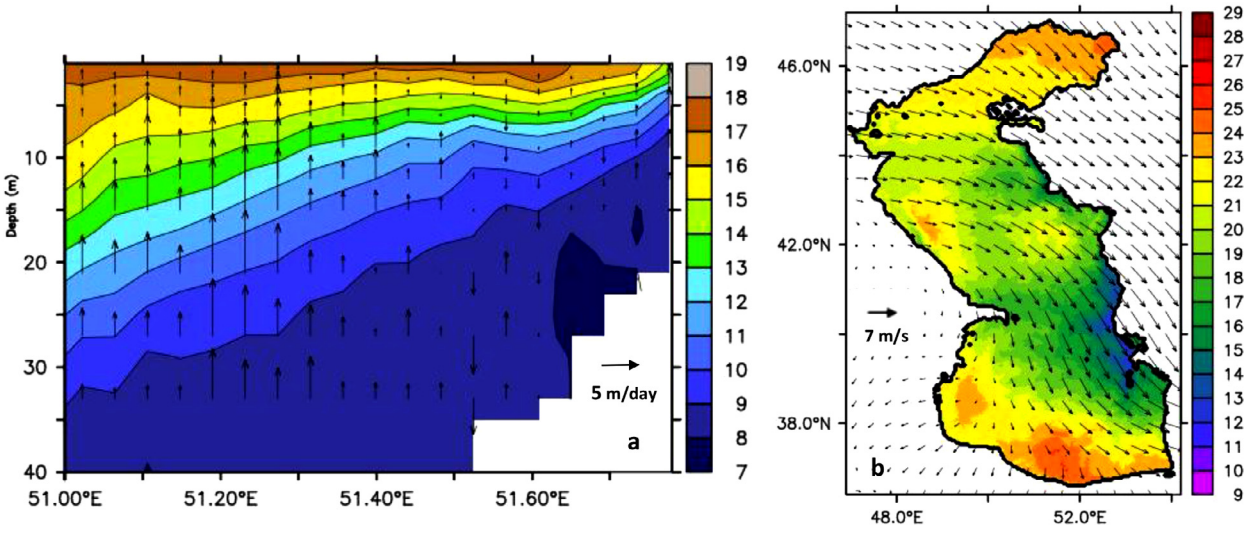

Figure 11 Vertical velocity over the vertical section of seawater temperature (°C) at 43°N (a) and SST (°C) with wind field overlaid (b) in the Caspian Sea on June 27.

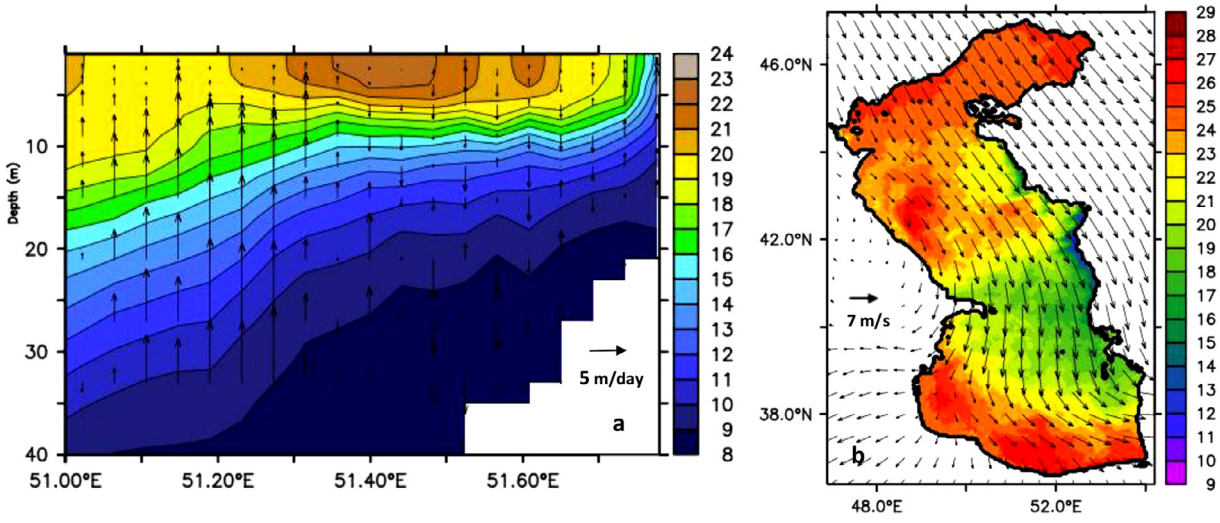

Figure 12 Vertical velocity over the vertical section of seawater temperature (°C) at 43°N (a) and SST (°C) with wind field overlaid (b) in the Caspian Sea on July 22.

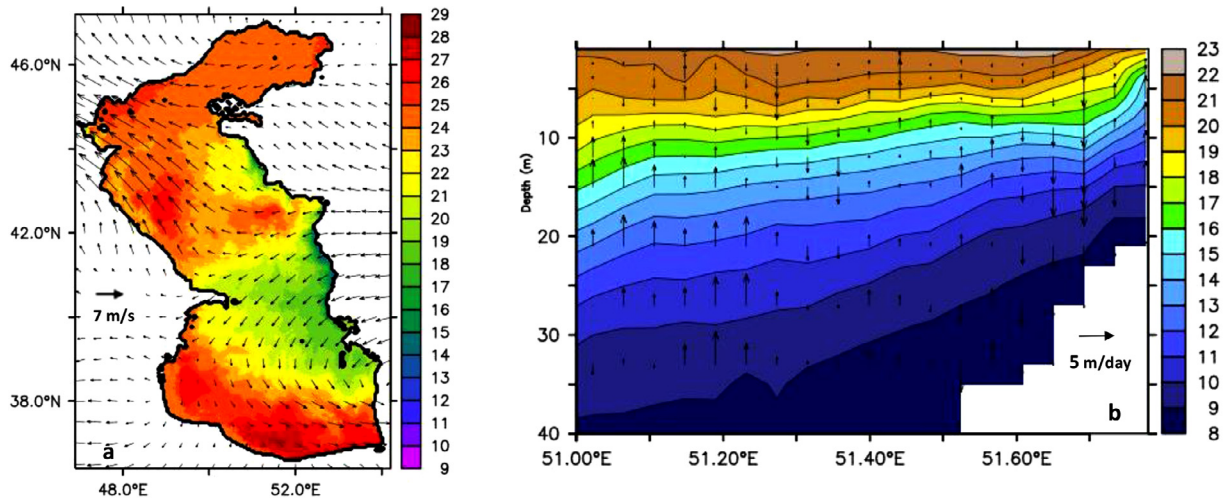

Figure 13 Vertical velocity over the vertical section of seawater temperature (°C) at 43°N (a) and SST (°C) with wind field overlaid (b) in the Caspian Sea on August 4.

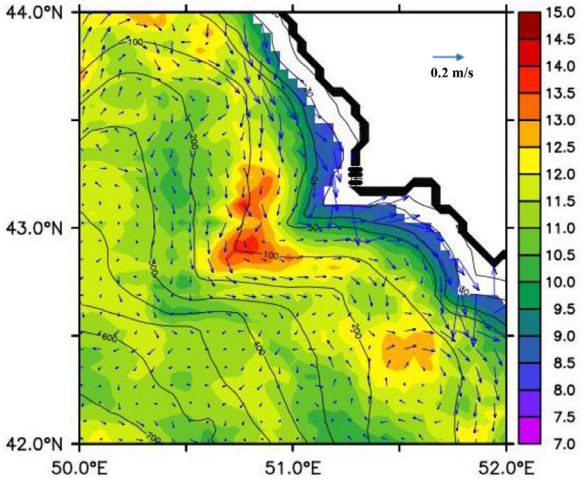

Figure 14 Plan view of the topography and model current vectors at a depth of 27 m and its seawater temperature (°C) in the eastern part of the middle Caspian Basin on August 4.

the eastern coast of the southern basin and the offshore area is noticeable in May. Upwelling occurs in upper layers at the 20 m depth to the surface and 15 km from the coast, which can be due to the wind field effect. However, in the middle Caspian basin, a slight upwelling occurs in lower layers, owing to the topographic effect. In June, in the middle basin, upwelling occurs within 25 km from the coast in upper layers at a depth of 35 m. Although the difference in SST (between coastal and offshore waters) in these two basins is negligible, the vertical temperature gradient is much more intense in the middle basin (43°N) than in the southern basin (39°N). Upwelling in the middle basin occurred 6, 4, and 4 times per month in June, July, and August, respectively, so that its intensity in June and July is much higher than in August. According to the wind field direction, upwelling events in June and July are mainly due to wind field effects and in August due to the bottom topography. In July and August, the mean of the maximum vertical velocities in the middle Caspian basin was estimated 10.58 m/day and 7.98 m/day, respectively, being in good agreement with the results obtained by Shia and Bidokhti (2015) (12 m/day and 7 m/day, respectively). The reason for the slight difference in these values can be explained by the difference in the forcing applied to the model. Wind-driven upwelling in August occurs in the eastern coasts of the middle Caspian basin within 25 km from the coast up to a depth of 15 m. The mechanism of upwelling formation in the middle Caspian basin in June and July is north or northeast wind (parallel to the coastline), being consistent with the results obtained by Knysh et al. (2008) indicating that the reason of upwelling in July is the prevailing wind from north to south in the middle Caspian basin. According to east and southeast winds in August and September in the eastern part of the middle basin, the upwelling in these months can be due to the effect of the bottom topography.

Declaration of competing interest

The authors declare that they have no known competing financial interests or personal relationships that could have appeared to influence the work reported in this paper.

References

Anand, P., Issac, P., Raghunadha Rao, A., 2019. Observed Interannual Variability of upwelling characteristics during 2016—2017: A Study using Princeton Ocean Model. Defence Sci. J. 69 (2), 142—148. https://doi.org/10.14429/dsj.69.14218

Antonov, J.I., Locarnini, R.A., Boyer, T.P., Mishonov, A.V., Garcia, H.E., Levitus, S., 2006. World Ocean Atlas 2005, vol. 2: Salinity. NOAA Atlas NESDIS, 62(2). NOAA: [s.l.], 182 pp.

Arpe, K., Tsuang, B.-J., Tseng, Y.-H., Liu, X.-Y., Leroy, S.A.G., 2018. Quantification of climatic feedbacks on the Caspian Sea level variability and impacts from the Caspian Sea on the large-scale atmospheric circulation. Theor. Appl. Climatol. 136 (1—2), 475—488.

Blumberg, A.F., Mellor, G.L, 1987. A Description of a Three-Dimensional Coastal Ocean Circulation Model. In: Heaps, N.S. (Ed.), Coastal and Estuarine Sciences, Book 4. Am. Geophys. Union, 1—6. https://doi.org/10.1029/CO004p0001

Bohluly, A., Sadat Esfahani, F., Montazeri Namin, M., Chegini, F., 2018. Evaluation of wind induced currents modeling along the Southern Caspian Sea. Cont. Shelf Res. 153, 50—63. https://doi.org/10.1016/j.csr.2017.12.008

Brink, K.H., 1983. The near-surface dynamics of coastal upwelling. Progr. Oceanogr. 12 (3), 223—257. https://doi.org/10.1016/0079-6611(83)90009-5

Closset, I., McNair, H.M., Brzezinski, M.A., Krause, J.W., Thamatrakoln, K., Jones, J., 2021. Diatom response to alterations in upwelling and nutrient dynamics associated with climate forcing in the California current system. Limnol. Oceanogr. 66, 1578—1593. https://doi.org/10.1002/lno.11705

Dumont, H.J., 1998. The Caspian lake: History, biota, structure, and function. Limnol. Oceanogr. 43 (1), 44—52.

Ghaffari, P., Isachsen, P.E., LaCasce, J.H., 2013. Topographic effects on current variabilityin the Caspian Sea. J. Geophys. Res.-Oceans, 118 (12), 7107—7116. https://doi.org/10.1002/2013JC009128

Gunduz, M., Özsoy, E., 2014. Modelling seasonal circulation and thermohaline structure of the Caspian Sea. Ocean Sci. 10 (3), 459—471. https://doi.org/10.5194/os-10-459-2014

Hall, J.K., 2002. Bathymetric compilations of the seas around Israel 1: The Caspian and Black Seas. GSI Current Res. 13, 105—108.

Ibrayev, R.A., Özsoy, E., Schrum, C., Sur, H.I., 2010. Seasonal variability of the Caspian Sea three-dimensional circulation, sea level and air-sea interaction. Ocean Sci. 6 (1), 311—329. https://doi.org/10.5194/os-6-311-2010

Kämpf, J., Chapman, P., 2016. Upwelling systems of the world. Springer Int. Pub., Switzerland, XV, 433 pp. https://doi.org/10.1007/978-3-319-42524-5

Kämpf, J., Sadrinasab, M., 2006. The circulation of the Persian Gulf: a numerical study. Ocean Sci. 2, 27—41. https://doi.org/10.5194/os-2-27-2006

Kara, A.B., Wallcraft, A.J., Metzger, E.J., Gunduz, M., 2010. Impacts of freshwater on the seasonal variations of surface salinity and circulation in the Caspian Sea. Cont. Shelf. Res. 30 (10—11), 1211—1225. https://doi.org/10.1016/j.csr.2010.03.011

Kitazawa, D., Yang, J., 2012. Numerical analysis of water circulation and thermohalinestructures in the Caspian Sea. J. Mar. Sci. Technol. 17 (2), 168—180. https://doi.org/10.1007/s00773-012-0159-0

Knysh, V.V., Ibrayev, R.A., Korotaev, G.K., Inyushina, N.V., 2008. Seasonal variability of climatic currents in the Caspian Sea reconstructed by assimilation of climatic temperature and salinity into the model of water circulation. Izv. Atmos. Ocean Phys. 44 (2), 236—249. https://doi.org/10.1134/S0001433808020114

Kosarev, A.N., Yablonskaya, E.A., 1994. The Caspian Sea. SPB Academic publisher, Russia, 259 pp.

Kostianoy, A., Kosarev, A., 2005. The Caspian Sea environment. Springer, Berlin, XIV, 272 pp. https://doi.org/10.1007/b138238

Lavrova, O.Y., Kostianoy, A.G., Lebedev, S.A., Mityagina, M.I., Ginzburg, A.I., Sheremet, N.A., 2011. Complex satellite monitoring of the Russian seas. Space Research Institute of RAS, Moscow.

Li, Y., Peng, S., Wang, J., Yan, J., Huang, H., 2018. On the mechanism of the generation and interannual variations of the summer upwellings west and southwest off the Hainan Island. J. Grophus. Res.-Oceans, 123, 8247—8263. https://doi.org/10.1029/2018JC014226

Mansoury, M., Sadrinasab, M., Akbarinasab, M., 2015. Modeling of salinity and temperature field structure in the Caspian Sea using POM model. Hydrophysics 1 (1), 1—13.

Medvedev, I.P., Kulikov, E.A., Fine, I.V., 2020. Numerical modelling of the Caspian Sea tides. Ocean Sci. 16, 209—219. https://doi.org/10.5194/os-16-209-2020

Mellor, G.L., Blumberg, A.F., 1985. Modeling vertical and horizontal diffusivities with the sigma coordinate system. Mon. Weather Rev. 113 (8), 1379—1383. https://doi.org/10.1175/1520-0493(1985)113<1379:MVAHDW>2.0.CO;2

Meunier, T., Rossi, V., Morel, Y., Carton, X., 2010. Influence of bottom topography on an upwellingcurrent: Generation of Long Trapped Filaments. Ocean Model. 35 (4), 277—303. https://doi.org/10.1016/j.ocemod.2010.08.004

Nigam, T., Pant, V., Prakash, K.R., 2018. Impact of Indian Ocean dipole on the coastal upwelling features off the southwest coast of India. Ocean Dynam. 68, 663—676. https://doi.org/10.1007/s10236-018-1152-x

Oey, L., Chang, Y.L., Lin, Y.C., Chang, M.C., Xu, F., Lu, H.F., 2013. ATOP-The Advanced Taiwan Ocean Prediction System Based on the mpiPOM. Part 1: Model Descriptions, Analyses and Results. Terr. Atmos. Ocean Sci. 24 (1), 137—158. https://doi.org/10.3319/TAO.2012.09.12.01(Oc)

Olita, A., Ribotti, A., Fazioli, L., Perilli, A., Sorgente, R., 2013. Surface circulation and upwelling in the Sardinia Sea: A numerical study. Cont. Shelf Res. 71, 95—108. https://doi.org/10.1016/j.csr.2013.10.011

Sadrinasab, M., Kämpf, J., 2004. Three dimensional flushing times of the Persian Gulf. Geophys. Res. Lett. 31, L24301. https://doi.org/10.1029/2004GL020425

Shanks, A.L., Largier, J., Brink, L., Brubaker, J., Hooff, R., 2000. Demonstration of the onshore transport of larval invertebrates by the shoreward movement of an upwelling front. Limnol. Oceanogr. 45 (1), 230—236. https://doi.org/10.4319/lo.2000.45.1.0230

Shiea, M., Bidokhti, A.A., 2015. The Study of upwelling phenomenon in the eastern coasts of the Middle Caspian basin using numerical simulation. Earth Space Phys. 41 (3), 535—545. https://doi.org/10.22059/jesphys.2015.55105

Shiea, M., Chegini, V., Bidokhti, A.A., 2016. Impact of wind and thermal forcing on the seasonal variation dimensional circulation in the Caspian Sea. Indian J. Geo-Mar. Sci. 45 (5), 671—686.

Su, J., Pohlmann, T., 2009. Wind and topography influence on an upwelling system at the eastern Hainan coast. J. Geophys. Res. 114, C06017. https://doi.org/10.1029/2008JC005018

Sun, Y.-J., Jalon-Rojas, I., Wang, X.H., Jiang, D., 2017. Coastal upwelling by wind-driven forcing in Jervis Bay, New South Wales: A numerical study for 2011. Estuar. Coast. Shelf. Sci. 206, 101—115. https://doi.org/10.1016/j.ecss.2017.11.022

Sur, H.I., Özsoy, E., Ibrayev, R., 2000. Satellite-derived flow characteristics of the Caspian Sea. In: Elsevier Oceanography Series, Vol. 63, 289—297.

Turuncoglu, U.U., Giuliani, G., Elguindi, N., Giorgi, F., 2013. Modeling the Caspian Seaand its catchment area using a coupled regional atmosphere-ocean model (RegCM4-ROMS): model design and preliminary results. Geosci. Model Dev. 6, 283—299. https://doi.org/10.5194/gmd-6-283-2013

Tuzhilkin, V.S., Kosarev, A.N., 2005. Thermohaline structure and general circulation of the Caspian Sea waters. In: Kostianoy, A.G., Kosarev, A.N. (Eds.), The Caspian Sea Environment, The Handbook of Environmental Chemistry, vol. 5P. Springer, Berlin, Heidelberg, 33—57. https://doi.org/10.1007/698_5_003

UNESCO-IHP-IOC-IAEA, 1996. Workshop on sea level rise and multidisciplinary studies of environmental processes in the Caspian region, IOC workshop No 108. 9—12 May, Paris, France.

Wirasatriya, JA., Setiawan, J.D., Sugianto, D.N., Rosyadi, I.A., Haryadi, H., Winarso, G., Setiawan, R.Y., Susanto, R.D., 2020. Ekman dynamics variability along the southern coast of Java revealed by satellite data. Int. J. Remote Sens. 41 (21), 8475—8496. https://doi.org/10.1080/01431161.2020.1797215

Zereshkian, S., Mansoury, D., 2020. Evaluation of ocean thermal energy for supplying the electric power of offshore oil and gas platforms. J. Earth Space Phys. 46 (2), 331—345. https://doi.org/10.22059/jesphys.2020.289441.1007161

Oceanologia 64 (2022) 376—386

Available online at www.sciencedirect.com

ScienceDirect

journal homepage: www.journals.elsevier.com/oceanologia

ORIGINAL RESEARCH ARTICLE

Investigation of tidal asymmetry in the Shatt Al-Arab river estuary, Northwest of Arabian Gulf

Ali Abdulridha Lafta*

Department of Marine Physics, Marine Science Center, University of Basrah, Iraq

Received 20 July 2021; accepted 21 January 2022
Available online 3 February 2022

KEYWORDS
Tidal asymmetry;
Harmonic analysis;
Tidal skewness;
Arabian Gulf;
Shatt Al-Arab river

Abstract Approximately one-year water level records were utilized for examining the tidal dynamics and tidal asymmetry at the Shatt Al-Arab river estuary. The harmonic and the tidal skewness, two traditional methods in quantifying tidal asymmetry in tidal systems, were used. The water level measurements revealed a presence of a tidal wave attenuation when propagating further towards the inland direction, with notable reductions in the tidal range. The results of the harmonic analysis indicated that the diurnal and semi-diurnal constituents experience considerable damping towards the upstream direction. The largest constituent was M2, followed by K1, O1, and S2. The largest shallow water constituent was MK3, followed by M4, MS4, MN4, and M6. The tidal form number ranged from 0.68 to 0.7 along the estuary; then, mixed, mainly semi-diurnal tidal nature was observed. However, six possible combinations of tidal constituents were used to quantify the tidal asymmetry, involving the interactions between astronomical constituents alone as well as with the higher harmonics. According to the harmonic method, the relative phase difference of M2 and M4 constituents was in the range of 63 to 87.06, suggesting a flood dominance behavior of tidal wave along the estuary. Positive values of the tidal skewness were observed at all stations, with a pronounced increase towards the inland direction. The M2 and M4 interaction was the main contributor to tidal asymmetry, followed by M2-K1-O1, M2-S2-MS4, M2-M4-M6, K1-M2-MK3, and M2-N2-MN4 interactions.

* Corresponding author at: Department of Marine Physics, Marine Science Center, University of Basrah, Iraq.
E-mail address: ali.lafta@uobasrah.edu.iq
Peer review under the responsibility of the Institute of Oceanology of the Polish Academy of Sciences.

Production and hosting by Elsevier

https://doi.org/10.1016/j.oceano.2022.01.005

1. Introduction

The tidal wave generated in the ocean undergoes several changes when propagating towards the coastal regions, which are generally shallow water areas, leading to tidal wave asymmetry (Parker, 2007). The tidal asymmetry refers to the distortion of the tidal wave with an unequal duration of rising and falling tides, as well as the difference in the strength of the flood and ebb velocities (Friedrichs and Aubrey, 1988; Pugh, 1987). Tidal asymmetry plays a major role in sediment transport and water circulation in estuaries and coastal systems. The tide-averaged (residual) sediment movement in tidal environments is mainly related to its tidal asymmetry situation (Gatto et al., 2017; Hoitink et al., 2003). Consequently, the long-term morphological changes of these water systems are mainly associated with their tidal dynamics (Aubery and Speers,1985).

Various factors contribute to tidal asymmetry, resulting from the interaction between the astronomical tide and nonlinearities generated inside the estuary, including bottom friction, river inflow, bathymetric changes, and the morphology of such systems (Dronkers, 1986; Godin, 1991; Oliveira et al., 2006). Bottom frictions play the main role in the dissipation of tidal energy and transformation of the wave energy from the principal tidal constituents to several frequencies. These sets of frequencies are known as shallow water components of the tide (Boon, 2013). The shallow water components of tide are mainly referred to as the multiplying of principle frequencies, such as M4 and M6, representing the constituents generated from the principle semi-diurnal tidal constituent M2 and known as overtides or higher harmonics. Furthermore, the shallow water effects lead to the nonlinear interaction between the principal tidal constituents as well as the overtides, which can generate constituents with various frequencies and are known as compound tides, resulting from two or more constituents such as MN4, MS4, and MK3 (Gallo and Vizon, 2005; Hoitink et al., 2003). River inflow has substantial effects on the tidal dynamics of estuarine systems. However, river discharge can increase the average water level and thus reduce the tidal amplitudes and retards the celerity of tidal propagation, that is, deforming the tidal waves (Godin, 1985; Guo et al., 2015). Moreover, the morphology of the tidal systems can have an impact on their tidal dynamics. The funneling shape estuaries with reducing cross-sections can be damping the tidal wave energy by reflection against boundaries. In contrast, tidal waves can be amplified when the effects of the convergent overcome the effect of frictions. Consequently, tidal wave propagation exhibits a difference between high and low water, and deformation in the tidal wave occurs (Prandle, 2003).

Basically, there are two methods to recognize tidal asymmetry (Guo et al., 2019). The first is the harmonic method, which requires the calculations of amplitudes and phases of the interacted tidal constituents. This method depends on the phase difference between the interacted constituents in order to determine the direction of the tidal asymmetry and the ratio of the amplitudes to quantify the magnitude of the asymmetry (Parker, 2007). The second is the statistical method, which calculates the tidal probability density function and is known as a tidal skewness (Nidzieko, 2010; Song et al., 2011).

Shatt Al-Arab river is formed by the confluence of Euphrates and Tigris rivers at Qurna city in the Basrah province in southern Iraq and discharges to the Arabian Gulf (Figure 1). Shatt Al-Arab river estuary (SARE) represents an international border between Iraq and Iran. SARE has high importance for Basrah province as well as for many cities on the Iranian side. In addition to using its water for various residents' activities, the river is considered to be a navigation channel for shipping, oil transportation, and fishing (Lafta, 2021a). Several ports are located on the two river sides, principally depending on the tidal status in their overall activities (Abdullah et al., 2016; Al-Taei et al., 2014).

Tides of SARE follow the tidal regime of the Arabian Gulf. However, there are limited studies that highlighted the tidal dynamics of SARE. Generally, due to several reasons, the field measurements of physical characteristics in this estuary are scarce (Abdullah et al., 2015). The study of Al-Ramdhan and Pastour (1987) was the first study discussing the water movement in SARE. They indicated that the water dynamics in the estuary is governed by tidal effect and freshwater inflow. The tidal wave in SARE was analyzed by Abdullah (2002). The analysis was based on the data of 29 days of water level taken from the admiralty tide tables at the primary port of Iraq, known as an Outer Bar station. This station is located at the northwest tip of the Arabian Gulf, south of the SARE mouth (Figure 1). He illustrated that M2 constituent was the major tidal component. Moreover, he demonstrated that the tide displays a mixed, predominant semi-diurnal nature with the form number at 0.85. Abdullah (2014), based on the predicted water level acquired from the website (http://easytide), studied the characteristics of tidal phenomena in SARE. He demonstrated that the tidal wave undergoes attenuation as it propagates towards the upper reaches of the river, and the ebb duration was longer than the flood duration. Correspondingly, the aim of the current study is to examine the tidal dynamics and tidal wave deformation based on the continuous field measurements of water level at several locations along the estuary. However, according to our knowledge, there are no studies that explored the tidal dynamics in this estuary through the use of comprehensive field measurements of water level. In particular, to give a picture of tidal dynamics along SARE, evolution of tidal constituents and tidal deformation are discussed.

2. Material and methods

2.1. Study area

SARE is located in southern Iraq and represents the main source of freshwater discharging to the Arabian Gulf (Al-Yamani et al., 2020). The length of the river is about 200 km from Qurna city until it meets the Arabian Gulf at about 12 km south of Faw city (Figure 1). The river width exhibited a funnel shape nature. The width ranges from about 1000 m at its mouth and is reduced to 200 m at the Qurna. The bathymetry of the river is irregular, with the maximum and minimum depths reaching 18 and 6 m, respectively (Lafta, 2021a). Many islands formed along the river course as a result of river depositions, as well as tectonic and anthropogenic activities (Al-Whaely, 2014).

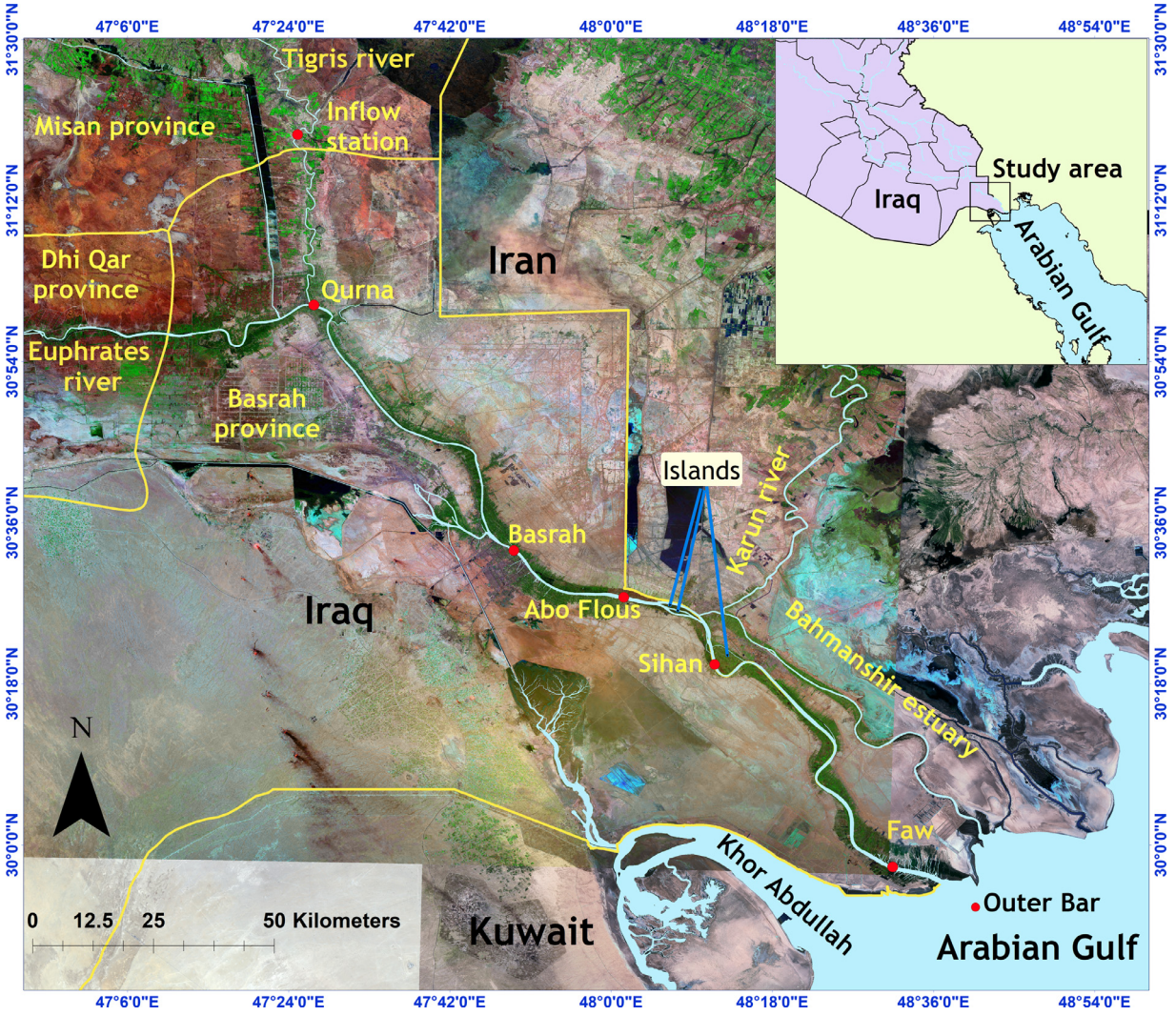

Figure 1 Location map of the study area showing the measurement locations of water level.

The hydrology of SARE is governed by the freshwater discharged from Tigris, Euphrates, and Karun rivers, the tidal force of the gulf, and the climatic conditions (Allafta and Opp, 2020). However, the continuous developments in the upstream countries of the Tigris, Euphrates, and Karun rivers result in very large reductions in the amounts of freshwater arriving at SARE. Additionally, the water resources authorities in Iraq exacerbate the problem after 2009, when the Euphrates river inflow towards SARE is completely segregated by constructing an embankment on its stream, about 35 km west of the Qurna site. Nowadays, due to these developments, SARE receives freshwater mainly from the Tigris river and minorly from the Karun river. These changes result in a pronounced alteration in the river hydrology and consequently affect the tidal propagation along the estuary.

2.2. Data collection

Water level measurements represent the main data required to conduct the study objective. However, the hourly water level records at four sites are conducted by installing water level divers at Faw, Sihan, Abo Flous, and Basrah. The coordinates, distance to the estuary mouth, and length of the data record of these sites are given in Table 1.

The field measurements of water level were accomplished as cooperation between Marine Science Center/University of Basrah and Delft University of Technology during 2014. SARE is a high dynamics, and its navigation channel is always crowded by ships and fishermen's boats. Hence, all water level divers were installed inside steel pipes on the western bank of the estuary to overcome the undesired movement. These pipes contain several holes along their entire course to allow the water to flow through them.

Before installing these instruments, a controlling point on the land was determined by transferring its level relative to the local datum in this region, which is the mean sea level at Faw city (known as Faw 1979 datum). The differential global position system was utilized for transferring the level to the control points. Then, the divers were installed at suitable depths by taking into account that they are submerged during low and high tides.

Table 1 The coordinates, distance to the estuary mouth, and period of the data record at study stations.

Station	Longitude	Latitude	Distance to Estuary Mouth (km)	Period of Record
Faw	48°29.986′E	29°58.104′N	12	1/22/2014 to 1/9/2015
Sihan	48°11.973′E	30°19.423′N	67.7	1/25/2014 to 12/23/2014
Abo Flous	48°1.528′E	30°27.585′N	98.4	1/25/2014 to 12/23/2014
Basrah	47°50.098′E	30°32.041′N	119	3/26/2014 to 12/24/2014

2.3. Methodology

2.3.1. Harmonic analysis of tide

The harmonic method is widely utilized for investigating the tidal dynamics and tidal asymmetry in coastal systems (Iglesias et al., 2019; Lafta et al., 2020, 2021b; Mao et al., 2004; Siddig et al., 2019; Suh et al., 2014). This method is based on calculating the amplitudes and phases of the tidal constituents from the measured tidal data series (Boon, 2013).

The equation for the harmonic model is given as follows (Boon, 2013):

$$h(x,t) = h_{\circ} + \sum_{j=1}^{m} f_j H_j \cos\left(\omega_j t + u_j - k_j^*\right), \tag{1}$$

where t is the time in hours, $h(x,t)$ is the predicted water level, f_j is the lunar node factor for constituent, H_j is the amplitude for constituent, h_0 is the mean water level in that location, u_j is the nodal phase for constituent, $\kappa_j{}^*$ is the phase of constituent, ω_j is the frequency of constituent, and m is the number of constituents. For purely solar constituents, $f_j = 1$ and $u_j = 0$. The Matlab worldtides, a package for tidal analysis, was used in this study. More details on this method, acquiring, and the application of this package can be found on the website (https://www.mathworks.com/matlabcentral/fileexchange/24217-world-tides).

However, tidal asymmetry can be generated when the interacted constituents satisfy $2\omega_1 = \omega_2$ and $\omega_1 + \omega_2 = \omega_3$ (ω is the constituent frequency) (Song et al., 2011). The relative phase relations, likely $2\theta_1 - \theta_2$ and $\theta_1 + \theta_2 - \theta_3$ (θ is the constituent phase in degrees), are mainly utilized for recognizing the nature of tidal deformation. In a semi-diurnal tidal system, for example, the interaction of the principal lunar semi-diurnal constituents M2 with its first harmonic M4 was broadly considered as the main cause that is responsible for tidal asymmetry (Aubrey and Speer, 1985; Friedrichs and Aubrey, 1988). The phase difference ($2\theta_1 = \theta_2$) in the range of 0 to 180 degrees refers to a shorter duration of the rising tide than the falling tide, or a flood dominance, while, in contrast, the phase difference in the range of 180 to 360 degrees refers to an ebb dominance tidal wave. When the phase difference was exactly 0 or 180 degrees, no tidal asymmetry will occur. Similarly, triad constituents interactions can lead to a tidal asymmetry. However, Song et al. (2011) examined the tidal wave deformation in 335 sea-level stations around the world. He reported that, in the mixed, mainly semi-diurnal tidal systems, the most significant triad interactions that can contribute to the total tidal asymmetry are M2-M4, M2-S2-MS4, M2-N2-MN4, M2-K1-O1, M2-K1-MK3, and M2-M4-M6. Similarly, the relative phase difference of these triad interactions in the range of 0 to 180 degrees refers to a longer falling tide than the rising tide, thus flood dominance. Meanwhile, the phase differences in the range of 180 to 360 degrees refer to an ebb dominance tidal system (Song et al., 2011).

2.3.2. Tidal skewness

Tidal skewness is a statistical approach based on the calculation of the probability density function of water level proposed by Nidzieko (2010) and extended by Song et al. (2011). In this method, asymmetry from several constituents combinations taken into account, with only two or three combinations, could contribute to tidal skewness (Zhang et al., 2018). The most remarkable feature of this method is that it can determine the strength and relative contribution of each of such combinations into total tidal asymmetry based on the amplitudes, phases, and frequencies of the tidal constituents. The tidal skewness resulting from the combination of two tidal constituents is given as follows (Song et al., 2011):

$$\gamma_2 = \frac{\frac{3}{4}a_1^2\omega_1^2 a_2\omega_2 \sin(2\varphi_1 - \varphi_2)}{\left[\frac{1}{2}\left(a_1^2\omega_1^2 + a_2^2\omega_2^2\right)\right]^{\frac{3}{2}}}. \tag{2}$$

Meanwhile, the skewness resulting from the combinations of three constituents is given as follows (Song et al., 2011):

$$\gamma_3 = \frac{\frac{3}{2}a_1\omega_1 a_2\omega_2 a_3\omega_3 \sin(\varphi_1 + \varphi_2 - \varphi_3)}{\left[\frac{1}{2}\left(a_1^2\omega_1^2 + a_2^2\omega_2^2 + a_3^2\omega_3^2\right)\right]^{3/2}}, \tag{3}$$

where a_n, φ_n, and ω_n are amplitude, phase, and frequency of the tidal constituent. The contribution of the different combination to the overall tidal asymmetry is obtained as follows: for the combination of two constituents:

$$\beta_2 = \gamma_2\left(\frac{a_1^2\omega_1^2 + a_2^2\omega_2^2}{\sum_{i=1}^{N} a_i^2\omega_i^2}\right)^{3/2} \tag{4}$$

and for the combinations of three constituents:

$$\beta_3 = \gamma_3\left(\frac{a_1^2\omega_1^2 + a_2^2\omega_2^2 + a_3^2\omega_3^2}{\sum_{i=1}^{N} a_i^2\omega_i^2}\right)^{3/2}. \tag{5}$$

Hence, the total skewness can be obtained by the summation of individual β:

$$\gamma_N = \sum \beta_2 + \sum \beta_3. \tag{6}$$

The direction of the tidal asymmetry is determined by the sign of the total skewness γ_N. The positive values of γ_N refer to a short period of rising water and long period of falling water, that is, the flood dominance, while the negative values of γ_N indicate the ebb dominance nature of tidal asymmetry.

2.3.3. Relative Sensitivity Coefficient (RSC)

The sensitivity of tidal asymmetry contributed by different combinations to the evolution of the amplitudes of tidal constituents can be examined by a nondimensional parameter known as a relative sensitivity coefficient (RSC) (Zhang et al. 2018).

The expression of RSC takes the form of two or three combinations (Yu et al. 2020): for the combination of two tidal constituents:

$$S_{a_1} = \frac{2a_2^2\omega_2^2 - a_1^2\omega_1^2}{a_1^2\omega_1^2 + a_2^2\omega_2^2}, \tag{7}$$

$$S_{a_2} = \frac{a_1^2\omega_1^2 - 2a_2^2\omega_2^2}{a_1^2\omega_1^2 + a_2^2\omega_2^2}, \tag{8}$$

and for the combination of three tidal constituents:

$$S_{a_1} = \frac{a_2^2\omega_2^2 + a_3^2\omega_3^2 - 2a_1^2\omega_1^2}{a_1^2\omega_1^2 + a_2^2\omega_2^2 + a_3^2\omega_3^2}, \tag{9}$$

$$S_{a_2} = \frac{a_1^2\omega_1^2 + a_3^2\omega_3^2 - 2a_2^2\omega_2^2}{a_1^2\omega_1^2 + a_2^2\omega_2^2 + a_3^2\omega_3^2}, \tag{10}$$

$$S_{a_3} = \frac{a_1^2\omega_1^2 + a_2^2\omega_2^2 - 2a_3^2\omega_3^2}{a_1^2\omega_1^2 + a_2^2\omega_2^2 + a_3^2\omega_3^2}, \tag{11}$$

where a and ω represents the amplitude and frequency of the tidal constituent, respectively. The RSCs values refer to the correlation between tidal skewness and constituent amplitude. However, the positive RSC implies the positive relationship between the tidal skewness and the amplitude; that is, tidal asymmetry will improve with the increase of the amplitude. In contrast, negative RSC suggests that tidal asymmetry will be reduced as the amplitude increases.

3. Results and discussion

3.1. Tidal harmonics

The time series measurements of water level are shown in Figure 2, which are exhibits the spatial and spring-neap variability of the tidal range. The maximum tidal range was observed in the Faw station, reaching about 3 and 2.5 m in spring and neap tides, respectively. These ranges are nearly similar to the ranges recorded in estuary mouth by Shahidi et al. (2011), which are about 3.2 and 2.65 m in spring and neap tides, respectively. Meanwhile, the tidal range is highly reduced in Basrah station and reaches 0.5 m in spring tide. However, the reduction in the tidal ranges along the SARE reflect the continuous attenuation of the tidal wave when propagating further upstream.

The along-estuary variations in the amplitudes and phases of the tidal constituents (O1, K1, N2, M2, S2, MK3, MN4, M4, MS4, and M6) at the four locations are shown in Table 2. These ten tidal components explain over 92% of the total variance in water level at Faw station. Harmonic analysis results suggested that the tidal form numbers (O1+K1/M2+S2) range between 0.68 and 0.7. Hence, SARE is characterized by mixed, predominantly semi-diurnal tides according to the classification of Defant (Defant, 1960). This result is in accordance with the previous finding of Abdullah (2002). Among the main tidal constituents used in the analysis, the largest was M2 in all stations. The second important constituent was K1, followed by O1, S2, and N2. The maximum amplitudes of the principal tidal constituents (M2, S2, N2, K1, and O1) were observed in the Faw station. However, it is obvious from Table 2 that the amplitudes of the semi-diurnal and diurnal tidal constituents have undergone a large reduction with distance along the longitudinal path of the estuary. The reduction in the constituents' amplitudes could be attributed to local bathymetry, that is, friction effect, which appears to exceed the effect of convergence nature of the estuary. As mentioned before, SARE is characterized by irregular depths along its course as well as the existence of several islands, particularly in the region located north and south of the confluence point of Karun river with SARE, as indicated in Figure 1. These islands can work as barriers that participate in the attenuation and nonlinear transformation of tidal energy and consequently the decay of the tidal harmonics. As illustrated by the results of the harmonic analysis (Table 2), most of the tidal energy is mainly dissipated near these islands, and this is reflected by the sharp decline of the amplitudes of the astronomical tidal constituents at Abo Flous station. However, Wu et al. (2018) demonstrated that the islands have a major effect on tidal hydrodynamics in tidal channels and make the tides more nonlinear. The reduction in the amplitudes of the tidal components towards inland direction was observed in many tidal systems, that is, Murray coastal lagoon (Jewell et al., 2012), Cochin estuary (Vinita et al., 2015), and Yangtze estuary (Lu et al., 2015).

The shallow water tidal constituents are generated when the tidal wave is distorted inside the estuary. The highest amplitudes of these constituents were observed near the estuary mouth (Faw station), except for M6. Unlike the M4 constituent, which is the most significant shallow water component in semi-diurnal tidal systems, MK3 was the largest shallow water constituent in the SARE. This could be because SARE is a mixed, mainly semi-diurnal tidal system, and the dominant astronomical components M2 and K1 control the tidal behavior. Consequently, the nonlinear transfer of energy from these two constituents gives a rise to MK3 among the other shallow water components. The second-largest shallow water constituent was M4, followed by MS4. These two constituents vary almost similarly due to their close frequencies. However, the evolution trend of the shallow water constituents displays a continuous reduction towards the inland direction, generally like the evolution of the principal astronomical components, except for the M6 and MK3. The M6 amplitude reaches its peak value at the Sihan station, about 61% relative to its amplitude at Faw station, and then decreases towards upper stations. In addition, the amplitude of the MK3 constituent showed a little increase between Abo Flous and Basrah stations, in comparison with its continuous reduction from Faw to Abo Flous stations. This inconsistent behavior of the shallow water components reflected the influences of the local geometry of the estuary in such regions.

The phase lags of all tidal constituents exhibited a gradual increase along the SARE. The tidal period in the SARE is close to the period of the M2 constituent, that is, 12.42 hours (Abdullah et al., 2016). Hence, the time of high and low water along the estuary is associated with the time of crest and trough of the M2 wave. However, according to

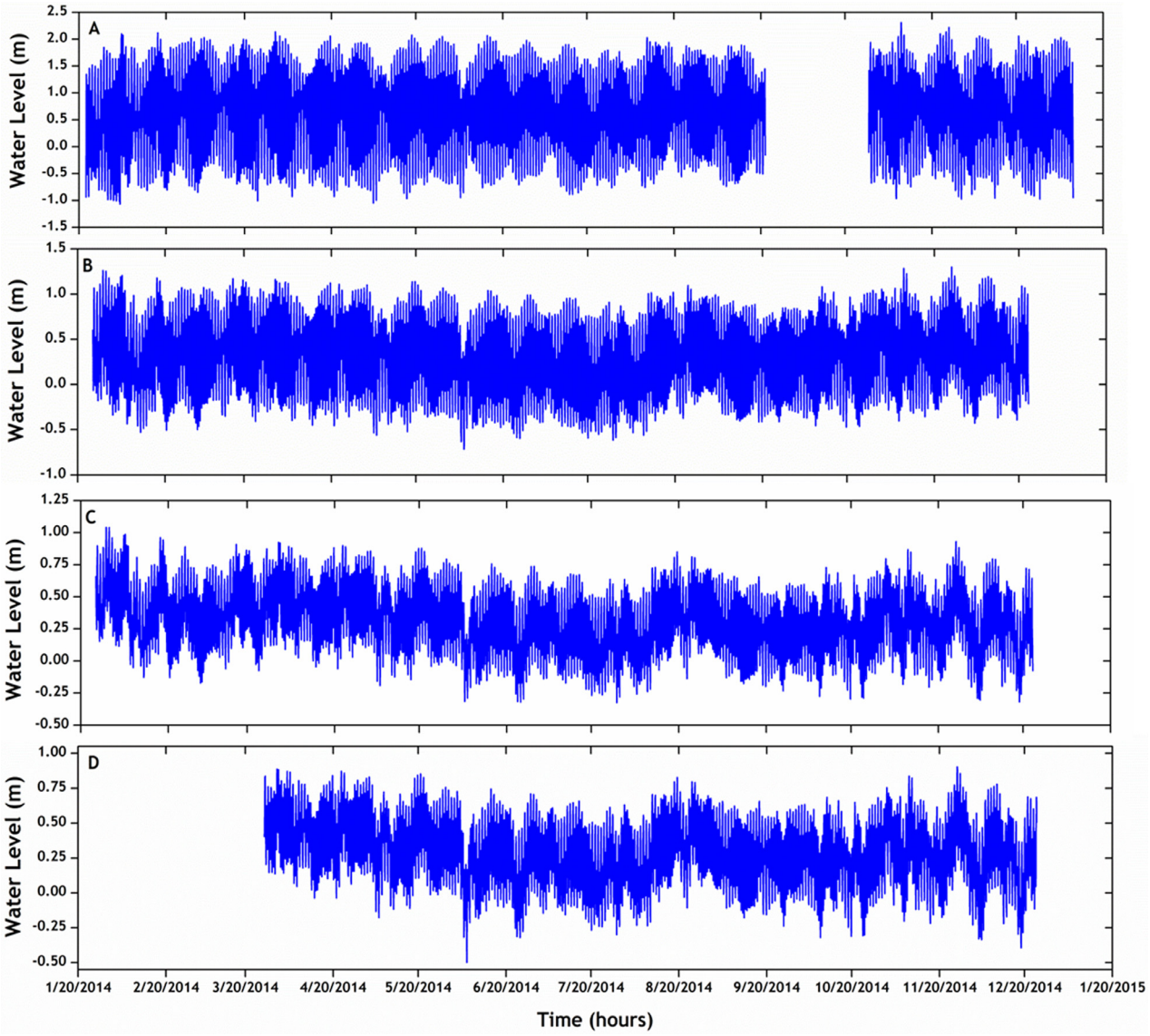

Figure 2 Time series of hourly water level records along the Shatt Al-Arab river estuary at Faw (A), Sihan (B), Abo Flous (c), and Basrah (D) stations during 2014.

Table 2 Amplitudes (m) and phases (degrees) for the tidal constituents used in the analysis.

Tidal Constituent	Faw		Sihan		Abo Flous		Basrah	
	Amp.	Phase	Amp.	Phase	Amp.	Phase	Amp.	Phase
O1	0.261	218.89	0.122	260.66	0.068	297.30	0.059	304.81
K1	0.449	305.53	0.277	346.40	0.133	22.59	0.129	32.58
N2	0.159	166.29	0.081	225.60	0.04	268.27	0.036	298.01
M2	0.799	278.58	0.443	342.32	0.23	28.39	0.221	54.09
S2	0.249	36.59	0.125	101.17	0.06	153.01	0.053	177.94
MK3	0.07	141.26	0.041	239.61	0.027	308.47	0.028	341.25
M4	0.049	110.10	0.03	261.64	0.015	350.85	0.014	30.99
MS4	0.039	236.95	0.022	22.15	0.011	109.57	0.008	154.10
MN4	0.017	2.17	0.009	156.61	0.005	256.09	0.004	299.08
M6	0.005	223.8	0.013	79.98	0.011	202.85	0.008	265.33

Hicks (2006) and Kuang et al. (2017), the time corresponding to the phase lag of the tidal constituent can be estimated by the following:

$$Time = \frac{\Delta G}{360} \times T_{cont.},$$

where ΔG is the phase lag between two locations and $T_{cont.}$ is the period of the tidal constituent. The results revealed that the phase lags of the semi-diurnal constituents increase faster than the phase lags of the diurnal constituents. This is mainly related to the effect of friction, which is proportional to the square of the wave speed (Parker, 2007); that is, wave speeds of semi-diurnal constituents are slower than those diurnal constituents. However, according to Hicks (2006), the speed of the tidal constituents is $360°/T_{cont.}$; hence, semi-diurnal constituents decay faster than the diurnal constituents under the effects of friction. This result is consistent with the theoretical indication of Godin (1999), which illustrated that the decay rate of the tidal constituents is frequency-dependent; that is, constituents with higher frequencies decay faster. The phase lag of M2 ($T_{M2} = 12.42$ *hours*) between Faw and Sihan stations reaches 63.74 degrees; that is, high water, or wave crest, takes about 2.19 hours between these two stations. By taking into account that the distance between Faw and Sihan stations reaches 55 km, hence tidal wave propagates with speed at about 25 km/h. As the tidal wave moves further upstream, a pronounced delay in speed occurs. The phase lag of M2 reaches 46.07 degrees between Sihan and Abo Flous stations, and hence, high water needs about 1.58 hours to cover the distance between these two locations. The distance between Sihan and Abo Flous is about 31 km, and consequently, the tidal wave propagates at a speed that reaches 21 km/hour. The phase lag reaches 135.51 degrees between Faw and Basrah station; that is, about 4.67 hours are required for the tidal wave to move from Faw to Basrah station. The phase lags of the S2 and N2 exhibited a similar evolution trend as M2 but with a few different magnitudes as a result of their different periods. Additionally, the phase lags of the diurnal constituents also showed gradual increases towards upstream. For instance, the phase lag of K1 between Faw and Basrah stations reaches 87.05 degrees. Based on the period of the K1, which equals 23.93 hours, the time required by this wave to move from Faw to Basrah station reaches 5.78 hours. However, since the wave speed of K1 is about half of the speed of M2 (Hicks, 2006), and by comparison of the time required by M2 and K1 to move from Faw to Basrah stations, it is obvious that semi-diurnal constituents experience a large delay along the estuary. Meanwhile, the phase lags for the shallow water constituents are related to their frequencies and increase faster than the astronomical constituents towards upstream under the effect of nonlinear friction.

3.2. Tidal asymmetry

Tidal asymmetry can be created by the combinations of two or more constituents, both astronomical or mixed between astronomical and shallow water constituents (Guo et al., 2019; Provost, 1991; Song et al., 2011).

The results of the harmonic method indicated that the relative phase relation between M2 and M4 ($2\theta_{M_2} - \theta_{M_4}$) at the Faw station is 87.06 degrees and varies along the estuary with 63, 65.93, and 77.19 degrees in Sihan, Abo Flous, and Basrah stations, respectively. Hence, according to Aubrey and Speer (1985), SARE exhibits a flood dominance behavior if only the M2-M4 interaction is taken into account. According to Lu et al. (2015), the M4/M2 amplitude ratio that is greater than 0.01 indicates the significant tidal distortion in the tidal system. In SARE, this ratio ranged between 0.061 and 0.067 and exhibited an inconsistent evolution trend by increasing from Faw towards Sihan, and then, it displayed a little reduction towards the other stations. However, the evolution of this ratio depends on the behavior of both M2 and M4. The spatial distribution of this ratio is highly dependent on the local geometry of the estuary, and when it increases, it refers to the large transfer of energy from M2 to M4.

Tidal asymmetry was investigated further by the tidal skewness metrics. Following Song et al. (2011), the tidal asymmetry in SARE can be induced by several interactions, such as M2-M4, M2-K1-O1, M2-S2-MS4, M2-K1-MK3, M2-N2-MN4, and M2-M4-M6. However, the relative phase relations for all these interactions ranged between 5 and 179 degrees, suggesting a flood dominance tidal asymmetry in the estuary. These results are mainly consistent with the observed longer period of the ebb tide than the flood tide and are in agreement with the previous indications of Abdullah (2014). Figure 3 displays the mean values of the tidal skewness at all stations. Positive values of tidal skewness were observed at all stations, indicating a longer period of the falling tide than the rising tide. The steadily increasing tidal skewness reflected the continuous tidal wave deformation towards the upper reaches of the estuary.

The highest values of tidal skewness were recorded at Basrah and Sihan stations, indicating the nonuniform behavior of tidal wave deformation along the SARE. However, increasing the tidal skewness at the middle reaches of the estuary, that is, at Sihan station, could be mainly attributed to the local characteristics of the estuary as well as to the freshwater inputs from the Karun river, which is sufficient to prolong the ebb duration, and consequently more tidal deformation at this region will occur. Similar behavior of nonuniform tidal wave deformations was observed in several estuaries in the world, that is, the upper St. Lawrence (Godin 1985, 1999), the Amazon estuary (Gallo and Vinzon, 2005), and Changjiang river estuary (Guo et al., 2019). Furthermore, Figure 3 illustrates the contributions of the six combinations to total tidal skewness. The nonlinear interaction between M2 and its first harmonic M4 appears to be the dominant contributor to tidal asymmetry, with a gradual evolution along the estuary. This interaction accounts for 49.17, 51.73, 54.67, and 54.45% of the total skewness at Faw, Sihan, Abo Flous, and Basrah stations, respectively. However, asymmetry generated by this interaction is traditionally increased by the reduction of M2 amplitude and generation of M4, and obviously, this is the case at SARE, which displayed a large reduction of the M2 amplitude towards inland stations. Such behavior was commonly recorded in many estuaries around the world, like the Amazon estuary (Gallo and Vizon, 2005), Yangtze estuary (Lu et al., 2015), and Pearl river delta (Zhang et al., 2018). The interaction of the astronomical M2-K1-O1 triad represents the second main contributor to the tidal asymmetry,

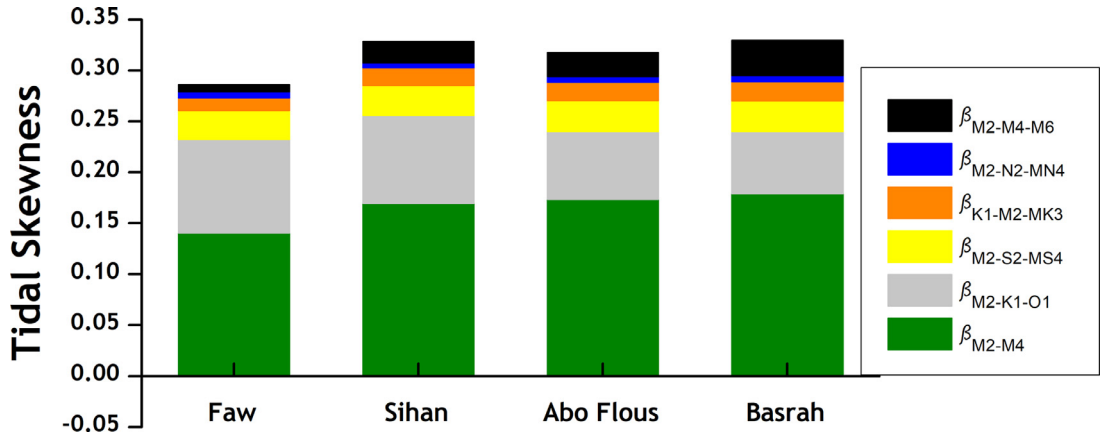

Figure 3 The contributions of the six combinations to total tidal skewness along the Shatt Al-Arab river estuary.

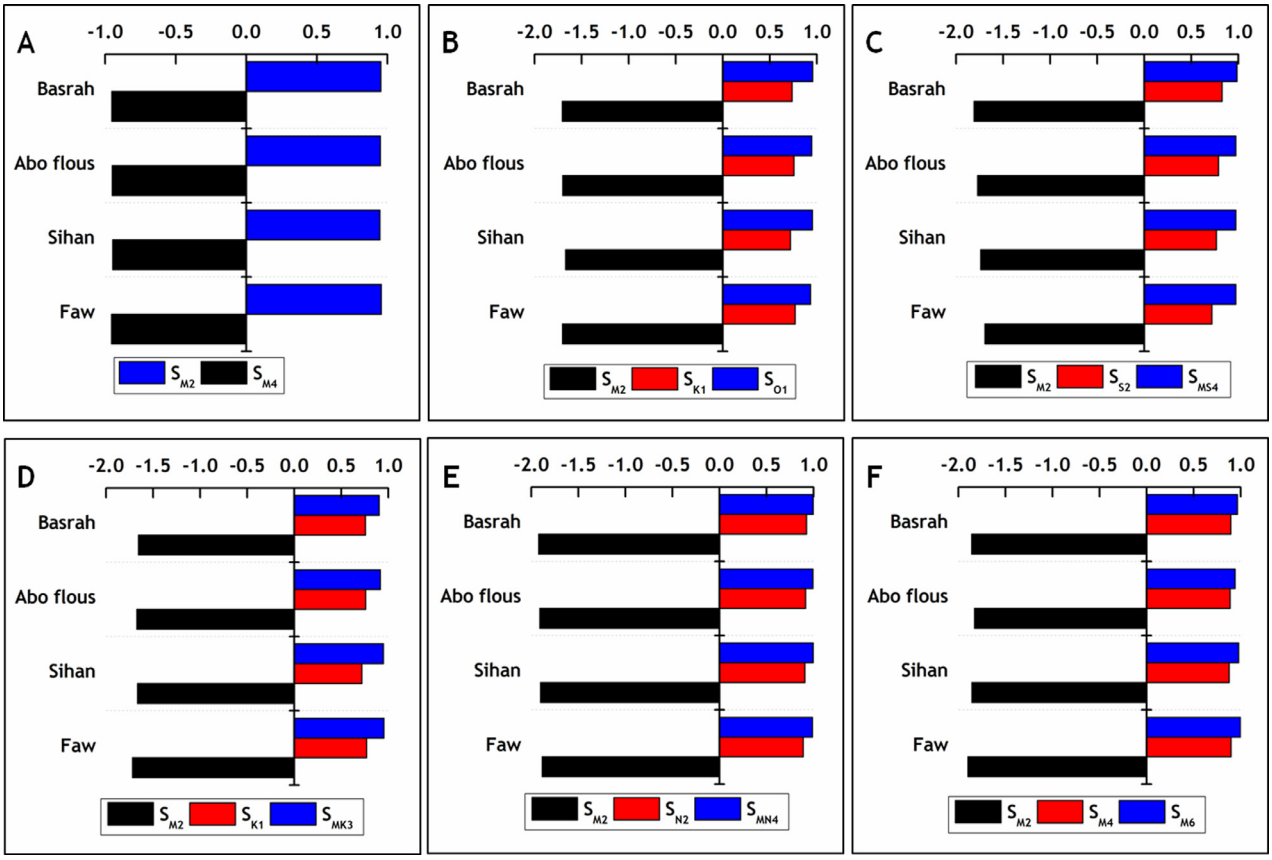

Figure 4 The mean value of relative sensitivity coefficient for different constituents amplitudes contributing to total tidal skewness by M2-M4 (A), M2-K1-O1 (B), M2-S2-MS4 (C), M2-K1-MK3 (D), M2-N2-MN4 (E), and M2-M4-M6 (F) along the Shatt Al-Arab river estuary.

accounting for 32.18, 26.26, 21.03, and 18.42% at four stations, respectively. However, although a substantial decline in the skewness of this interaction occurs towards the inland direction, due to the large reduction of the amplitudes of astronomical constituents, the tidal asymmetry induced by this triad combination is a flood dominant in SARE. This indicates that the tide is mostly a flood dominant in offshore before entering the estuary. It is well known that the northern Arabian Gulf is a shallow water region with maximum depths that do not exceed 20 m (Lafta et al., 2019). Hence, the nonlinear friction in shallow water plays a fundamental role in tidal wave deformation in the northern part of the gulf, resulting in the retard of the tidal wave propagation around low tides to high tides. Similar behaviors of the M2-K1-O1 interaction were observed in some estuarine systems, such as the Cochin estuary (Vinita et al., 2015) and Yangtze estuary (Yu et al., 2020). The M2-S2-MS4 interaction seems to be the third contributor, participating by about

9—10% to the total skewness. The considerable attenuation of both M2 and S2 constituents inside the estuary gave rise to this interaction. However, Song et al. (2011) indicated that, in mixed semi-diurnal tidal systems, M2-S2-MS4 interaction plays a fundamental role in the tidal asymmetry in such systems. The fourth important interaction was M2-M4-M6 with contribution percentage rising from 2% at Faw to 10% at Basrah station. This rise was expected as the M2 constituent experiences more reduction in the upper reaches of the estuary. The interaction of K1-M2-MK3 seems to have a secondary effect on the tidal asymmetry at all stations, with the largest contribution reaching about 5% at Basrah station. While the M2-N2-MN4 interaction has a minor role in the total asymmetry with the contribution not exceeding 2%, this can be attributed to the small amplitudes for both N2 and MN4 constituents.

3.3. Influence of tidal evolution on tidal asymmetry

Sensitivity analysis is conducted to quantify the response of the tidal skewness to the evolution of the tidal constituents along SARE. Figure 4 illustrates the relative sensitivity coefficients for the six combinations contributing to the tidal asymmetry in SARE. The results revealed that RSC for M2 amplitude is negative for all six combinations. This implies that the tidal asymmetry is enhanced by a reduction in the M2 amplitude. The tidal asymmetry induced by the M2-M4 combination is mainly intensified by increasing M4 amplitude and decreasing the M2 amplitude. However, our results showed a relative reduction in the M4 amplitude, which is expected to minimize the tidal skewness of M2-M4 along the estuary. In contrast, a substantial increase in tidal skewness of M2-M4 was observed towards the upper reaches of estuary. This behavior is mainly due to the large reduction in the M2 amplitude in comparison with M4 amplitude along the estuary. Regarding tidal skewness induced by the M2-K1-O1 combination, the relative sensitivity coefficient implies that tidal asymmetry is enhanced by increasing K1 and O1 amplitudes and decreasing the M2 amplitude. The results indicated that tidal skewness that resulted from M2-K1-O1 asymmetry experienced a significant reduction towards the upper reaches of the estuary, despite the substantial attenuation of M2 amplitude. However, both K1 and O1 amplitudes showed a large reduction as they propagate towards the inland direction, leading to an obvious minimizing of the M2-K1-O1 asymmetry. The sensitivity coefficient of M2 for the M2-M4-M6 combination is also negative. The tidal asymmetry induced by this combination undergoes a significant increase towards the inland areas and is associated with a large reduction that occurs in the M2 amplitude, in the same way as the M2-M4 combination. The sensitivity coefficients of M2 for the remaining combinations, including M2-S2-MS4, M2-K1-MK3, and M2-N2-MN4, are also negative. However, all these three combinations illustrated a relative increase along the estuary due to the reduction that occurs in M2 amplitude. Consequently, the reduction of M2 amplitude plays a fundamental role in intensifying the tidal asymmetry in SARE.

4. Conclusions

In this study, the water level measurements indicated that the tidal wave experiences pronounced damping when propagating towards the inland direction. Consequently, the friction effect was overcoming the convergent nature of the estuary. The maximum tidal ranges at the seaside station were 3 and 2.5 m in spring and neap tides, respectively, and decreased in the upper reaches of the estuary. The results of the harmonic analysis indicated that the amplitudes of the principles diurnal K1 and O1 and semi-diurnal M2 and S2 experience considerable reductions towards the inland direction under the effect of friction and the geometry of the estuary. Hence, in this context, higher and compound tides were generated.

Six possible interactions, including the astronomical and nonlinearities to the total asymmetry, were evaluated. The main contributor to the tidal wave deformation coincides with the interaction of M2 and M4 at all stations, followed by other interactions. The results of both the harmonic method and the tidal skewness method demonstrated that SARE exhibited a flood dominance nature of tidal asymmetry. The nonuniform behavior of tidal asymmetry was recognized. The Basrah and Sihan stations presented a more tidal wave deformation due to the local characteristics as well as the effect of the freshwater inflow. The relative sensitivity coefficient of M2 appears to have the largest values in all combinations; hence, the tidal asymmetry of SARE is mainly sensitive to variations in the M2 amplitude.

It is worth mentioning that the results obtained are mainly based on the water level measurements and focused on the tidal duration asymmetry due to the lack of flow velocity data. Hence, it is highly recommended to investigate the velocity asymmetry that is directly correlated with the sediment dynamics and morphological evolution in coastal systems. Additionally, it is highly recommended to study the influence of the river discharge variations on the tidal dynamics. This could be conducted based on the numerical modeling techniques.

Acknowledgments

The author is grateful to the technician team of the Marine Science Center/ University of Basrah for their helping in the field works.

Refrences

Abdullah, S.S., Lafta, A.A., Al-Taei, S.A., Al-Kaabi, A.H., 2016. Flushing Time of Shatt Al-Arab River. South of Iraq. Mesopot. J. Mar. Sci. 31 (1), 61—74.

Abdullah, A.D., Masih, I., van der Zaag, P., Karim, U.F.A., Popescu, I., Al Suhail, Q., 2015. Shatt al Arab River system under escalating pressure: a preliminary exploration of the issues and options for mitigation. Int. J. River Basin Manage. 13 (2), 215—227. https://doi.org/10.1080/15715124.2015.1007870

Abdullah, S.S., 2002. Analysis of Tide Wave in Shatt Al-Arab Estuary, South of Iraq. Mesopot. J. Mar. Sci. 17 (2), 305—315.

Abdullah, S.S., 2014. Tide phenomena in the Shatt Al-Arab River, South of Iraq. Journal of the Arabian Gulf 42 (3), 133—155.

Allafta, H., Opp, C., 2020. Spatio-temporal variability and pollution sources identification of the surface sediments of Shatt Al-Arab River. Southern Iraq. Scient. Rep. 10 (6979), 1—16. https://doi.org/10.1038/s41598-020-63893-w

Al-Ramadhan, B.M., Pastour, M., 1987. Tidal characteristics of Shatt AlArab River. Mesopot. J. Mar. Sci. 2 (1), 15—28.

Al-Taei, S.A., Abdullah, S.S., Lafta, A.A., 2014. Longitudinal intrusion pattern of salinity in Shatt Al Arab estuary and reasons. J. KAU: Mar. Sci. 25 (2), 205—221. https://doi.org/10.4197/Mar.25-2.10

Al-Whaely, U.Q., 2014. Origin and evolution of the Islands of the Shatt Al-Arab River southern Iraq. Ph.D. Thesis, College of Science, Univ. Basrah, 143 pp (in Arabic).

Al-Yamani, F.Y., Polikarpov, I., Saburova, M., 2020. Marine life mortalities and harmful algal blooms in the Northern Arabian Gulf. Aquat. Ecosyst. Health 23, 196—209. https://doi.org/10.1080/14634988.2012.679450

Aubrey, D.G., Speer, P.E., 1985. A study of non-linear tidal propagation in shallow inlet/estuarine systems. Pt. I: Observations. Estuar. Coast. Shelf Sci. 21 (2), 185—205. https://doi.org/10.1016/0272-7714(85)90096-4

Boon, J.D., 2013. Secrets of the Tide: Tide and Tidal Current Analysis and Predictions, Storm Surges and Sea Level Trends. Elsevier, 224.

Defant, A., 1960. Physical oceanography, 2. Peragamon Press, Oxford, 598 pp.

Dronkers, J., 1986. Tidal asymmetry and estuarine morphology. Netherlands J. Sea Res. 20 (2), 107—131. https://doi.org/10.1016/0077-7579(86)90036-0

Friedrichs, C.T., Aubrey, D.G., 1988. Non-linear tidal distortion in shallow well-mixed estuaries: A synthesis. Estuar. Coast. Shelf Sci. 27 (5), 521—545. https://doi.org/10.1016/0272-7714(88)90082-0

Gallo, M.N., Vinzon, S.B., 2005. Generation of overtides and compound tides in the Amazon estuary. Ocean Dynam. 55 (5), 441—448. https://doi.org/10.1007/s10236-005-0003-8

Gatto, V.M., van Prooijen, B.C., Wang, Z.B., 2017. Net sediment transport in tidal basins: quantifying the tidal barotropic mechanisms in a unified framework. Ocean Dynam 67, 1385—1406. https://doi.org/10.1007/s10236-017-1099-3

Godin, G., 1999. The propagation of tides up rivers with special considerations on the upper Saint Lawrence river. Estuar. Coast. Shelf Sci. 48, 307—324. https://doi.org/10.1006/ecss.1998.0422

Godin, G., 1985. Modification of river tides by the discharge. J. Water. Port Coast. Ocean Eng. 111 (2), 257—274. https://doi.org/10.1061/(ASCE)0733-950X(1985)111:2(257)

Godin, G., 1991. Frictional effects in river tides. In: Parker, B.B. (Ed.), Tidal Hydrodynamics. John Wiley, Toronto, 379—402.

Guo, L., Wang, Z.B., Townend, I., He, Q., 2019. Quantification of Tidal Asymmetry and Its Nonstationary Variations. J. Geophys. Res.-Ocean. 124 (1), 773—787. https://doi.org/10.1029/2018JC014372

Guo, L.C., van der Wegen, M., Jay, D.A., Matte, P., Wang, Z.B., Roelvink, J.A., He, Q., 2015. River-tide dynamics: Exploration of nonstationary and nonlinear tidal behavior in the Yangtze River estuary. J. Geophys. Res.-Oceans 120, 3499—3521. https://doi.org/10.1002/2014JC010491

Hicks, S.D., 2006. Understanding Tides. NOAA, National Ocean Service, 83 pp.

Hoitink, A.J., Hoekstra, P., Van Maren, D.S., 2003. Flow asymmetry associated with astronomical tides: implications for the residual transport of sediment. J. Geophys. Res. 108 (C10), 3315. https://doi.org/10.1029/2002JC001539

Iglesias, I., Ailez-Valente, P., Bio, A., Bastos, L., 2019. Modeling the main hydrodynamic pattern in shallow water estuaries: The Minho case study. Water 1 (5), 1040. https://doi.org/10.3390/w11051040

Jewell, S.A., Walker, D.J., Fortunato, A.B., 2012. Tidal asymmetry in a coastal lagoon subject to a mixed tidal regime. Geomorphology 138 (1), 171—180. https://doi.org/10.1016/j.geomorph.2011.08.032

Kuang, C., Liang, H., Mao, X., Karney, B., Gu, J., Huang, H., Chen, W., Song, H., 2017. Influence of potential future sea-level rise on tides in the China sea. J. Coast. Res. 33 (1), 105—117. https://doi.org/10.2112/JCOASTRES-D-16-00057.1

Lafta, A.A., 2021a. Estimation of Tidal excursion Length Along The Shatt Al-Arab Estuary, Southern Iraq. Vietnam J. Sci. Tech. 59 (1). https://doi.org/10.15625/2525-2518/59/1/15433

Lafta, A.A., 2021b. Influence of atmospheric forces on sea surface fluctuations in Iraq marine water, northwest of Arabian Gulf. Arab. J. Geo. 14, 1639. https://doi.org/10.1007/s12517-021-07874-x

Lafta, A.A., Al-Taei, S.A., Al-Hashimi, N.H., 2019. Characteristics of the tidal wave in Khor Abdullah and Khor Al-Zubair Channels, Northwest of the Arabian Gulf. Mesopot. J. Mar. Sci. 34 (2), 112—125.

Lafta, A.A., Altaei, S.A., Al-Hashimi, N.H., 2020. Impacts of potential sea-level rise on tidal dynamics in Khor Abdullah and Khor Al-Zubair, northwest of Arabian Gulf. Earth Syst. Environ. 4, 93—105. https://doi.org/10.1007/s41748-020-00147-9

Lu, S., Tong, C., Lee, D.Y., Zheng, J., Shen, J., Zhang, W., Yan, Y., 2015. Propagation of tidal waves up in Yangtze Estuary during the dry season. J. Geophys. Res.-Oceans 120 (9), 6445—6473. https://doi.org/10.1002/2014JC010414

Mao, Q., Shi, P., Yin, K., Gan, J., Qi, Y., 2004. Tides and tidal currents in the Pearl River Estuary. Continent. Shelf Res. 24, 1797—1808. https://doi.org/10.1016/j.csr.2004.06.008

Nidzieko, N.J., 2010. Tidal asymmetry in estuaries with mixed semidiurnal/diurnal tides. J. Geophys. Res. 115, C08006. https://doi.org/10.1029/2009JC005864

Oliveira, A., Fortunato, A.B., Regob, J.R., 2006. Effect of morphological changes on the hydrodynamics and flushing properties of the Óbidos lagoon (Portugal). Cont. Shelf Res. 26 (8), 917—942. https://doi.org/10.1016/j.csr.2006.02.011

Parker, B.B., 2007. Tidal Analysis and Prediction. National Ocean Service, NOAA Spec. Publ. https://doi.org/10.25607/OBP-191

Prandle, D., 2003. Relationships between tidal dynamics and bathymetry in strongly convergent estuaries. J. Phys. Oceanogr. 33 (12), 2738—2750. https://doi.org/10.1175/1520-0485(2003)033⟨2738:RBTDAB⟩2.0.CO;2

Provost, L.C., 1991. Generation of overtides and compound tides (review). In: Parker, B.B. (Ed.), Tidal Hydrodynamics. John Wiley, Toronto, 269—295.

Pugh, D.T., 1987. Tides, surges and mean sea-level. John Wiley, New York, 486 pp.

Shahidi, A.E., Parsa, J., Hajiani, M., 2011. Salinity intrusion length: comparison of different approaches. Mar. Eng. 164 (1), 33—43. https://doi.org/10.1680/maen.2011.164.1.33

Siddig, N.A., Al-Subhi, A.M., Alsaafani, M.A., 2019. Tide and mean sea level trend in the west coast of the Arabian Gulf from tide gauges and multi-missions satellite altimeter. Oceanologia 61 (4), 401—411. https://doi.org/10.1016/j.oceano.2019.05.003

Song, D., Wang, X.H., Kiss, A.E., Bao, X., 2011. The contribution to tidal asymmetry by different combinations of tidal constituents. J. Geophys. Res. 116, C12007. https://doi.org/10.1029/2011JC007270

Suh, S.W., Lee, H.Y., Kim, H.J., 2014. Spatio-temporal variability of tidal asymmetry due to multiple coastal constructions along the west coast of Korea. Estur. Coast. Shelf Sci. 151, 336—346. https://doi.org/10.1016/j.ecss.2014.09.007

Vinita, J., Shivaprasad, A., Manoj, N.T., Revichandran, C., Naveenkumar, K.R., Jineesh, V.K., 2015. Spatial tidal asymmetry of Cochin estuary, West Coast, India. J. Coast. Conserv. 19, 537—551. https://doi.org/10.1007/s11852-015-0405-9

Wu, R., Jiang, Z., Li, C., 2018. Revisiting the tidal dynamics in the complex Zhoushan Archipelago waters: a numerical experiment. Ocean Model. 132, 139–156. https://doi.org/10.1016/j.ocemod.2018.10.001

Yu, X., Zhang, W., Hoitink, A.J.F., 2020. Impact of river discharge seasonality change on tidal duration asymmetry in the Yangtze river estuary. Sci. Rep. 10, 6304. https://doi.org/10.1038/s41598-020-62432-x

Zhang, W., Cao, Y., Zhu, Y., Zheng, J., Ji, X., Xu, Y., Wu, Y., Hoitink, A.J.F., 2018. Unravelling the causes of tidal asymmetry in deltas. J. Hydrol. 564, 588–604. https://doi.org/10.1016/j.jhydrol.2018.07.023

Oceanologia 64 (2022) 387—395

Available online at www.sciencedirect.com

ScienceDirect

journal homepage: www.journals.elsevier.com/oceanologia

ORIGINAL RESEARCH ARTICLE

Does topography of rocky intertidal habitat affect aggregation of cerithiid gastropods and co-occurring macroinvertebrates?

Soniya Jethva[a], **Kiran Liversage**[b,*], **Rahul Kundu**[a]

[a] *Department of Biosciences, Saurashtra University, Gujarat State, India*
[b] *Estonian Marine Institute, University of Tartu, Tallinn, Estonia*

Received 17 May 2021; accepted 21 January 2022
Available online 3 February 2022

KEYWORDS
Habitat heterogeneity;
Cerithiidae;
Intertidal snails;
Patchiness;
Over-dispersed distribution;
Intertidal ecology

Abstract Species aggregation has important implications for population survivorship and ecological functioning in many habitats, including rocky intertidal shores, which have been valuable to research for understanding ecological patterns and process. Intertidal gastropods of the family Cerithiidae often form extensive aggregations for which the driving mechanism may be positive thigmotaxis, i.e. movement occurring until an obstructing surface is contacted, then cessation of movement. However, it is unknown if thigmotaxis may occur by cerithiids contacting and aggregating around uneven surfaces of the rock topography, or by contacting other conspecific individuals. We quantified aggregation patterns in invertebrate assemblages and topographic complexity at intertidal rock platforms in NW India with extensive cerithiid populations. The cerithiids *Clypeomorus moniliferus* and *Cerithium caeruleum* were the most common species. Distribution analysis confirmed significant over-dispersion indicative of aggregation (densities were often around zero but occasionally reached up to 680 dm^{-2}). Multivariate correlation analyses showed that topographic complexity contributes to overall species assemblage variability, but there was no evidence that topographic complexity correlates with cerithiid abundances or was likely to affect their aggregation. Thus the thigmotaxis producing cerithiid aggregation is probably associated with individuals contacting each other rather

* Corresponding author at: Estonian Marine Institute, University of Tartu, Mäealuse 14, 12618, Tallinn, Estonia.
E-mail address: kiran.liversage@gmail.com (K. Liversage).
Peer review under the responsibility of the Institute of Oceanology of the Polish Academy of Sciences.

Production and hosting by Elsevier

https://doi.org/10.1016/j.oceano.2022.01.006

than any feature of the rock surface such as crevices or raised areas. Overall, while some components of species assemblages were associated with complex topography, regarding the abundant cerithiids, potential population benefits from aggregation (e.g. reduced desiccation and temperature) may be expected on rocky shores with any level of topographic complexity.

1. Introduction

Aggregation or spatial patchiness is one of the most important population features to evaluate for understanding processes controlling species distribution (He et al. 2000) and consequent wider implications (e.g. setting conservation priorities for species of concern or quantifying the fertilization and reproductive capability of broadcast spawners; e.g. Button, 2008; Green and Ostling, 2003). Aggregation may be related to biotic factors such as predation defence (Ray and Stoner, 1994) and food supply (Lauzon-Guay and Scheibling, 2009; Lapointe and Sainte-Marie, 1992; Schmitt,1987) or to environmental factors such as habitat complexity (Stafford and Davies, 2005) and environmental harshness (Chapperon et al., 2013; Rojas et al., 2013). Aggregations can have important ecological implications such as increased population survivorship and altered interactions with co-occurring species (Stafford and Davies, 2005; Stoll and Prati, 2001). There can also be implications related to economic use of species as resources (Hallier and Gaertner, 2008).

Invertebrates on rocky shores including limpets (Aguilera and Navarrete, 2011; Coleman, 2010; Moisez, et al. 2020), gastropods (Chapman and Underwood, 1996; Underwood, 2004) and chitons (Aguilera and Navarrete, 2011; Grayson and Chapman, 2004; Montecinos et al., 2020) are often observed to aggregate or occur in over-dispersed distributions. Past research has shown that habitat complexity is a main driver of aggregation for invertebrates in intertidal rocky habitats. Difficulty of moving through areas of high topographic complexity of the rock substratum may reduce population turn-over (Underwood and Chapman, 1989) and cause higher densities compared to habitat patches of less complex topography (Chapman and Underwood, 1994). Alternatively, a complex rocky intertidal topography may involve crevices and other features where susceptible species aggregate to avoid harsh environmental conditions (Montecinos et al., 2020; Stafford and Davies, 2005) or predation (Garrity and Levings, 1981). Although if predators themselves use crevices, then any prey aggregation may involve higher abundances outside crevices (Fairweather, 1988). More recently there has been interest in increasing the scope of our knowledge about intertidal species aggregation to include other less studied taxa, e.g. research on economically important aggregating gastropods in China (Yu et al., 2020) and on aggregation of poorly studied taxa from cryptic intertidal habitats done by Grayson and Chapman (2004). Stafford et al. (2008) did computer simulations of intertidal gastropod aggregation behaviour in connection with availability of crevices and trail following. Crevice abundance appeared important in determining aggregation patterns. However for broadcast spawning species aggregation behaviour also develops on flat rock. These simulations highlighted the potential complexity of influences from topographic features toward affecting aggregation, which could be followed up with observational or experimental testing.

Rocky intertidal gastropods such as cerithiids and littorinids often have aggregated distributions (Chapman and Underwood, 1996; Denadai et al., 2004; Moulton, 1962; Rohde and Sandland, 1975). Cerithiid aggregations may be formed during movement, involving individuals moving until contact occurs with some obstacle and then cessation of movement (Moulton, 1962). This has been described as positive thigmotaxis, i.e. the tendency for individuals to move into pressure such as from a solid surface. Surfaces causing thigmotaxis and aggregation might be features of the rock associated with uneven topography (Moulton, 1962). Alternatively, it is possible that bodies/shells of other gastropod individuals may be the surfaces most commonly involved in thigmotaxis, in which case aggregation may occur irrespective of topographical features. In addition, aggregation formation appears to vary among cerithiids, an example of apparent lack of aggregation being found for the low density *Cerithium nodulosum* populations (2 individuals per 100 m^2) studied by Yamaguchi (1977); this can be compared to the *Clypeomorus moniliferum* populations studied by Moulton (1962) which had closely positioned clusters containing hundreds to thousands of individuals. Cerithiids are a useful taxon for gaining insight about intertidal aggregation processes because of the wide extent of their distribution globally across temperate (Garilli et al., 2018) and tropical shores (Denadai et al., 2004), and due to the apparent consistency and distinctiveness of the aggregation patterns that have so far been described (e.g. Moulton, 1962). This hints at the possibility of related research programmes on these observations being able to reveal mechanistic ecological understanding with high spatiotemporal consistency (Underwood et al., 2000). Cerithiids can be considered as a model research taxon from which research findings can be applied to other aggregating intertidal species, some of which are economically important (abalone — Button, 2008; whelks — Yu et al., 2020). The potential ecological importance of cerithiids themselves (Nicolaidou and Nott, 1999) also highlights the usefulness of research to understand main processes determining distributions of their populations and functions.

Here we aimed to test hypotheses about patterns of over-dispersion of intertidal macroinvertebrate distributions on the Kathiawar Peninsula of Gujarat State in NW

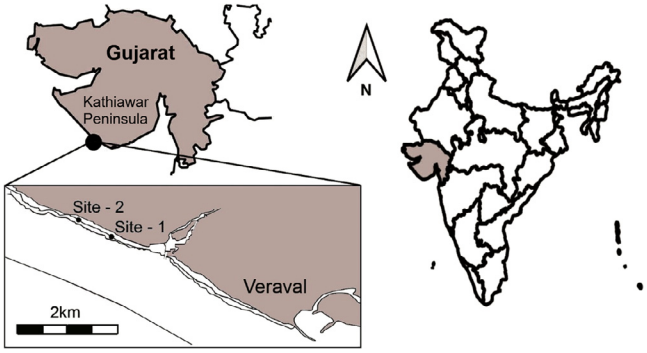

Figure 1 Map showing the coastal sampling sites near the municipality of Veraval in the state of Gujarat in NW India.

India, using an observational study (Underwood et al., 2000). The Kathiawar Peninsula has extensive intertidal rock platforms that harbour diverse plant (Ishakani et al., 2016) and animal (Bhadja et al., 2014) assemblages. The intertidal biota of this region has been quantified in relation to different locations and seasons (Misra and Kundu, 2005) but few studies have revealed specific physical habitat features that may affect species distribution patchiness.

Cerithiid gastropods are particularly widespread on NW Indian rocky shores, often with extremely patchy distributions. This applies to large-scale distributions, with mean densities per m^2 found to vary between 30—279 among different sites and seasons (Thivakaran and Sawale, 2016) and preliminary observations suggested strong patchiness may also be common at smaller scales (here cerithiids were often observed in clusters within areas of about 0.1 m^2 where most individuals were in contact with each other). Our specific aim was to quantify intertidal invertebrate distributions, focusing on cerithiids, as well as features of their habitat. This study tested two main hypotheses: 1) The distribution of cerithiids within rock-platforms is over-dispersed (confirming significant aggregation patterns) and 2) similar to studies on gastropod aggregation as mentioned by Chapman and Underwood (1994) and Meager et al. (2011), cerithiid abundances will positively correlate with rock topographic complexity. In addition to tests focusing on cerithiids, this correlation was also tested of rock topography on the whole invertebrate assemblage structure.

2. Material and methods

Measurements of macroinvertebrate populations and habitat complexity were taken during low tides at two sites near Veraval (i.e. 20°55′01.15″N, 70°20′35.29″E and (20°55′29.36″N, 70°19′46.28″E) on the Kathiawar Peninsula (Figure 1) in January 2020. These were selected as random sites, with biotic and abiotic structure appearing similar between them. The Veraval shore has a gently sloping rock platform at the mid tidal zone below a sand beach at the high zone. A steep drop-off into deep subtidal waters occurs at the seaward end of the low intertidal zone. The nearest settlement is the Veraval municipality approximately 1—2km from the sampling sites. There are extensive algae present, which includes foliose algae but most notably non-geniculate coralline algal mats that had a mean cover of 31% when measured during nearby algal quadrat surveys. The sampling was done during winter, with mean temperature of the intertidal rock surface at low tide being 25.18°C (S.E. = 0.66).

At each site, topographic complexity of the rock substratum was measured along twenty randomly placed 2 m transects at each site (40 transects total). Each transect was separated from other transects by approximately 2—10 metres. The method for measuring topography was using a steel chain draped across the undulating rock surface, which can involve a single measurement taken per quadrat (Aguilera et al., 2014) or multiple measurements (Beck, 1998). The length of each chain link section was 2.6 cm, allowing the chain to provide a topographic profile of features such as crevices and boulders that have previously been shown as important for affecting aggregation of intertidal species of similar body dimension to these cerithiids (Snyder-Conn, 1979). We laid one chain length along each transect which had four 20 × 20 cm quadrats placed along the transect at evenly spaced intervals for sampling densities of all macroinvertebrates, allowing the biotic data to be correlated to the linear topographic measurements that ran through the middle of each quadrat. Complexity of the rock surface did not appear to differ according to any specific spatial axis (e.g. the vertical profile from low to high tide level, compared to the alongshore horizontal profile), so topographic measurement from a single spatial axis was considered sufficient for estimating the general topographic habitat profile within a quadrat.

The first hypothesis was tested using one sample Kolmogorov-Smirnov goodness-of-fit tests, separately for each site. This method was previously used by Grayson and Chapman (2004) for investigating intertidal mollusc aggregation patterns by testing if populations have over-dispersed distributions among discreet patches of rocky habitat, but in our study the over-dispersion was tested among quadrats on a continuous intertidal rock platform. These analyses were done on the most widespread cerithiid species (*Clypeomorus moniliferus* and *Cerithium caeruleum*) and tested if any patterns of over-dispersion in observed distributions among quadrats caused significant differences to the Poisson distributions expected if cerithiids were distributed randomly.

The second hypothesis was tested using permutational analysis of covariance (ANCOVA) to test the correlation between cerithiid density (averaged from the four quadrats included in each transect) and rock surface topography for the transect. Site was included as a categorical random factor. The analysis was done in PRIMER 6 and used the resemblance measure of Euclidean distance and Type III Sums of Squares. Homogeneity of variances was tested with PERMDISP using medians, equivalent to Levene's Test (Anderson et al., 2008). All PRIMER analyses used 9999 permutations.

Lastly, the total invertebrate assemblage (molluscs, arthropods, annelids and cnidarians) was analysed using the Distance Based Linear Modelling (DistLM) function in PRIMER, correlating multivariate assemblage structure (biotic data) with the ratio values characterising topographic complexity (environmental data). Data were combined from both sites. Biotic data were fourth-root transformed to re-

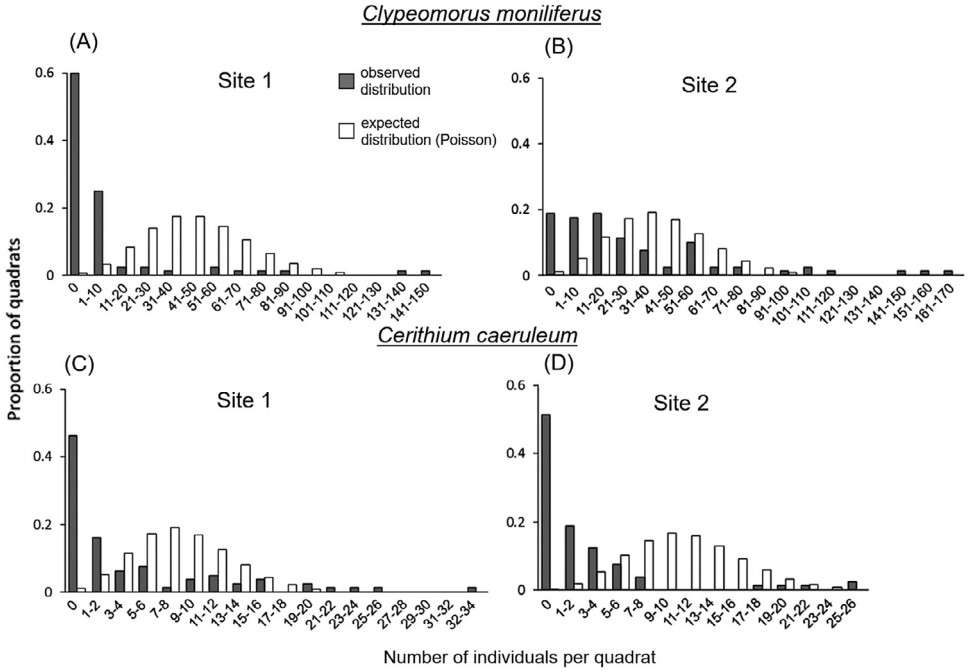

Figure 2 Frequency distributions showing proportions of quadrats (20 × 20 cm) having different abundances of the cerithiid gastropod species *Clypeomorus moniliferus* (A, B) and *Cerithium caeruleum* (C, D) sampled at two sites on the rocky intertidal coast of Veraval. Grey bars show the measured frequency distributions of the actual populations; white bars show the calculated Poisson distributions expected if the populations were distributed randomly. In all cases the actual and Poisson distributions differed significantly (one-sample Kolmogorov-Smirnov goodness-of-fit tests).

duce the influence of abundant taxa. These data were plotted using Principle Coordinates (PCO) with vectors added to visualise which sample groups were associated with which different taxa and values of the topography variable.

3. Results

A total of 24 macroinvertebrate taxa were observed, mostly gastropod molluscs (Table 1). Two species in the family Cerithiidae were observed in large abundances (*Clypeomorus moniliferus* with mean density per quadrat of 21.01 (S.E. = 3.58) and *Cerithium caeruleum* with 3.71 (0.76)) and two others more rarely (*Cerithium zonatum* 0.04 (0.03) and *Rhinoclavis sinensis* 0.01 (0.01)). Analyses were done on the large populations of *C. moniliferus* and *C. caeruleum*. For both species at both sites, observed frequency distributions among transects differed to the distributions expected if cerithiids were distributed randomly (Table 2). They were often sparsely distributed in or absent from the majority of quadrats, while smaller proportions had densities up to 680 dm^{-2} for *C. moniliferus* (Figure 2a,b) and 136 dm^{-2} for *C. caeruleum* (Figure 2c,d), confirming significantly over-dispersed distributions indicative of aggregation. However, in one case (*C. caeruleum* at site 2), the distribution expected with random (Poisson) distribution had similar proportions of samples with large densities compared to the empirical data (Figure 2d), so in this case the significant difference in frequency distributions may be largely attributable to the large proportion of vacant/low-density quadrat samples.

There was highly variable topographic complexity on the sampled rock platforms, indicated by measurements of the ratio of the chain length (that followed the contours of the rock surface) to the linear length of the transect (2 m); values ranged from 0.717 to 0.995. The ANCOVA revealed no correlations between cerithiid abundances and topographic complexity (Table 3). The only significant effect was from the random site factor for *C. moniliferus* (Table 3).

The multivariate assemblage structure was significantly correlated with measures of topographic complexity (DistLM — Pseudo-F = 3.128, P = 0.015). However, there was an R^2 value of only 0.076 so topographic complexity explained relatively minor amounts of the total variation. The vectors on the PCO plot (Figure 3) showed that hermit crabs and *Siphonaria* spp. limpets were most strongly associated with the samples from rock surfaces with more complex/uneven topography.

4. Discussion

Aggregated distributions on the scale of metres are common for invertebrates on rocky shores (Aguilera and Navarrete, 2011; Chapman and Underwood, 1996; Coleman, 2010; Grayson and Chapman, 2004; Moisez et al., 2020; Montecinos et al., 2020). Even so, the high levels of such patchiness for varied species on the Veraval shore was striking. This suggests that the processes causing patchiness on other shores are acting strongly here, or other processes are involved. For some intertidal gastropods, patchiness may be caused by aggregation in areas of abundant food (Lauzon-

Table 1 List of total numbers of macrofaunal taxa found in January 2020 during the sampling at two sites on the intertidal rock platforms at Veraval.

Phylum	Class	Order	Family	Species/common name	Authority	Site 1	Site 2
Mollusca	Gastropoda	Caenogastropoda	Cerithiidae	*Clypeomorus moniliferus*	Kiener, 1841	831	2531
				Cerithium caeruleum	G. B. Sowerby II, 1855	224	369
				Cerithium zonatum	W. Wood, 1828	0	6
				Rhinoclavis sinensis	Gmelin, 1791	0	2
		Neogastropoda	Muricidae	*Murex brunneus*	Link, 1807	1	0
				Purpura panama	Röding, 1798	1	1
			Conidae	*Conus cumingii*	Reeve, 1848	0	1
				Conus figulinus	Linnaeus, 1758	0	1
			Melongenidae	*Tylothais savignyi*	Deshayes, 1844	2	1
		Cycloneritida	Neritidae	*Nerita albicilla*	Linnaeus, 1758	2	0
		Systellommatophora	Onchidiidae	*Paronia verruculata*	Cuvier, 1830	1	1
		Patellogastropoda	Nacellidae	*Cellana karachiensis*	Winckworth, 1930	3	0
		Trochida	Turbinidae	*Lunella coronata*	Gmelin, 1791	13	70
		Sacoglossa	Limapontiidae	*Placida* sp.	—	4	0
		Siphonariida	Siphonariidae	*Siphonaria* spp.	—	21	42
		Nudibranchia	Plakobranchidae	*Elysia* sp.	—	0	11
	Polyplacophora	Chitonida	Chitonidae	*Rhyssoplax peregrina*	Thiele, 1909	2	2
Arthropoda	Malacostraca	Stomatopoda	Squillidae	*Gonodactylaceus* sp.	—	0	2
		Decapoda	Pilumnidae	*Pilumnus vespertilio*	Fabricius, 1793	2	0
			Plagusiidae	*Plagusia squamosa*	Herbst, 1790	0	1
			—	Unidentified hermit crabs	—	143	155
Annelida	Polychaeta	Sabellida	Sabellidae	*Sabella pavonina*	Savigny, 1822	0	6
Cnidaria	Anthozoa	Actiniaria	Actiniidae	*Aulactinia veratra*	Drayton in Dana, 1846	1	0
				Gyractis sesere	Haddon & Shackleton, 1893	0	3

Table 2 Statistical details from the one-sample Kolmogorov-Smirnov goodness-of-fit tests done on two cerithiid gastropod species at two sites on the Veraval coast. Gastropod distributions among quadrats were compared to Poisson distributions expected if distributions are random, with significant values representing population over-dispersion.

Species	Site	Max. deviation D	Kolmogorov-Smirnov test statistic ks	P
Clypeomorus	1	0.80	5.06	<0.001
moniliferus	2	0.38	2.37	<0.001
Cerithium	1	0.75	4.74	<0.001
caeruleum	2	0.56	3.56	<0.001

Table 3 ANCOVA on abundances of two intertidal gastropods testing effects of topographic habitat complexity (continuous variable) and random site (categorical variable). PERMDISP tests showed that variances were homogenous.

Species	Source	DF	MS	F	P
Clypeomorus	Habitat complexity covariate	1	46.44	0.11	>0.5
moniliferus	Site	1	4294.30	10.32	<0.001
	Residual	37	416.20		
Cerithium	Habitat complexity covariate	1	0.51	0.00	>0.75
caeruleum	Site	1	31.24	1.32	>0.25
	Residual	37	23.60		

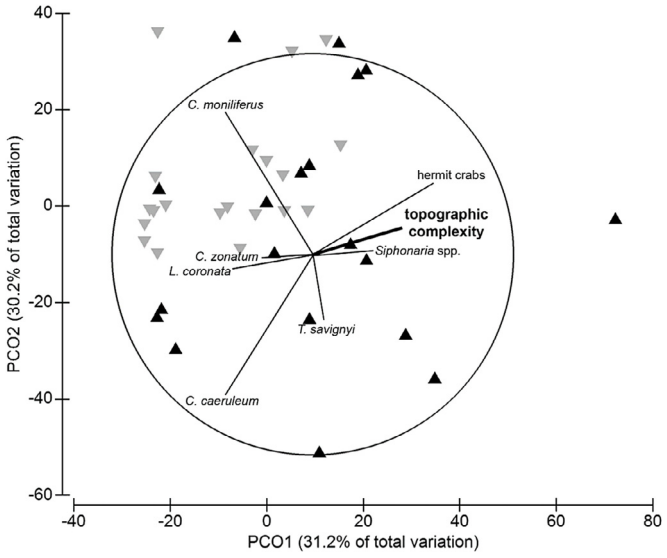

Figure 3 PCO ordination showing the structure of macroinvertebrate assemblages in quadrat samples of intertidal rock platforms at two sites near Veraval (Site 1 has black symbols, Site 2 grey). Vectors are included showing the macroinvertebrate taxa with strongest correlations to sample points (Pearson correlation $R^2 > 0.25$) and the sampling points associated with the measured environmental variable (topographic complexity, highlighted in bold); the vector length represents the strength of the correlation.

Guay and Scheibling, 2009). The cerithiids here have a highly generalised diet including microalgae and detritus that can be taken from surfaces such as on rocks, mud, seaweeds, or seagrasses (Ayal and Safriel, 1982). Here we did not quantify these potential food sources but their generalised nature may be considered to result in a relatively even spread over rock platforms such as at Veraval, so we considered that food supply may not be a feature of priority to test for explaining this small-scale clustering. There was evidence that habitat complexity, in the form of unevenness of the rock topography, was to a limited extent structuring the invertebrate assemblage as a whole. Based on the current results, however, it may be ruled out that such habitat complexity is involved in the strong patterns of cerithiid aggregation at the scale of complexity we measured, although further studies may consider testing if complexity of the rock surface at different scales may still affect cerithiid aggregation.

Highly uneven topography may involve the presence of beneficial crevices and other shelters that produce some tendency for processes resulting in aggregation (e.g. Chapman and Underwood, 1994). However, gastropods may still acquire such shelter using the presence of conspecifics. For example, although crevices and pits may protect from

temperature/desiccation (Stafford and Davies, 2005) or predation (Garrity and Levings, 1981), similar protection may also occur for individuals within dense aggregations (Ray and Stoner, 1994; Rojas et al., 2013) even on flat rock. In the case of cerithiid aggregations, the latter situation may be occurring.

Observations of intertidal cerithiid behaviour in other regions have shown that while feeding at high tide they are not aggregated, and that cluster formation occurs shortly before low tide. Clustering possibly occurs via initiation of the thigmotactic response while moving (Moulton, 1962), although it has been unclear whether thigmotaxis is directed to features of the rock substratum or to surrounding conspecifics. Our evidence suggests this situation may likewise be occurring for *Clypeomorus moniliferus* and *Cerithium caeruleum* in our study location, and that features of the rock substratum are not involved. Thus, regardless of variability in topographic complexity, aggregations likely develop in response to the presence of other gastropods. Individuals of *Austrolittorina unifasciata*, a similar aggregating intertidal gastropod studied by Chapman (1995, 1998), follow each other's trails, and chemotaxis is a potential mechanism to allow gastropod individuals to contact each other during the aggregation forming process. Other features of *A. unifasciata* do not, however, relate to the cerithiids studied here, such as the association of *A. unifasciata* with complex rock topography (Chapman and Underwood, 1994). Informal observations of cerithiids done by Moulton (1962) suggested a process of desiccation and temperature stress reduction may occur within cerithiid aggregations, but the study by Stafford et al. (2012) should also be considered that discussed the difficulties of confirming any such process.

Although there was no evidence that cerithiids were affected by habitat topography, the multivariate analysis indicated such an effect may occur for hermit crabs and limpets of the genus *Siphonaria*. This is similar to results from Loke et al. (2019) who found that a related limpet in Singapore, *Siphonaria atra*, is also associated with uneven intertidal topography. They may be acquiring predation, temperature or desiccation protection by using features of uneven rocky topography. Snyder-Conn (1979) found that hermit crabs can have aggregation patterns similar to cerithiids (i.e. dispersed distributions during high tide immersion followed by aggregation at low tide emersion; Moulton, 1962). However, hermit crab aggregation was clearly controlled by topographic features such as crevices and boulders (Snyder-Conn, 1979). The lack of evidence for such topographic control in the cerithiids we studied highlights the importance of testing correlations or effects of substratum features to understand intertidal invertebrate aggregation, as explanations clearly cannot be extrapolated from one taxon to another, even if the biotic patterns have close similarity.

Shelter seeking aggregation behaviours may be used by macroinvertebrate prey on the Veraval coast due to large abundances of intertidal crab and whelk predators (Bhadja et al., 2014) and the potential for extreme regional summer temperatures (Azhar et al., 2014). Also, while topographic complexity appears largely ineffectual, other environmental factors unexplored in this study may be contributing to gastropods aggregating in certain areas. For cerithiids, there may be implications from aggregation for survivorship from harsh environmental conditions or predators, but also for processes such as parasitism (Cannon, 1979). In addition, for some cerithiids, factors affecting their populations may in turn have consequences for the wider ecological system, e.g. via changes to biochemical cycling (Nicolaidou and Nott, 1999). These results can guide further research on factors affecting cerithiid aggregation. Our results indicate plausibility of aggregation being affected not by topography, but more likely by the alternative explanation of the presence of conspecifics. This could be tested experimentally, with aggregation levels measured following manipulation of densities of conspecific cerithiids or artificial mimics of cerithiids. Overall, the current study along with any further related observational or experimental research will inform our understanding of causes for and consequences of aggregation behaviour in intertidal invertebrates.

Declaration of competing interest

The authors declare that they have no known competing financial interests or personal relationships that could have appeared to influence the work reported in this paper.

Acknowledgements

This research was supported by a National Fellowship for OBC from the University Grants Commission, Statutory Body of the Government of India. K.L. was funded by a Senior Research Grant from the Malacological Society of London.

References

Aguilera, M.A., Broitman, B.R., Thiel, M., 2014. Spatial variability in community composition on a granite breakwater versus natural rocky shores: Lack of microhabitats suppresses intertidal biodiversity. Mar. Pol. Bull. 87, 257—268. https://doi.org/10.1016/j.marpolbul.2014.07.046

Aguilera, M.A., Navarrete, S.A., 2011. Distribution and activity patterns in an intertidal grazer assemblage: influence of temporal and spatial organization on interspecific associations. Mar. Ecol. Prog. Ser. 431, 119—136. https://doi.org/10.3354/meps09100

Anderson, M.J., Gorley, R.N., Clarke, K.R., 2008. PERMANOVA+ for PRIMER: Guide to Software and Statistical Methods. PRIMER-E, Plymouth. http://updates.primer-e.com/primer7/manuals/PERMANOVA+_manual.pdf

Ayal, Y., Safriel, U.N., 1982. Role of competition and predation in determining habitat occupancy of Cerithiidae (Gastropoda: Prosobranchia) on the rocky, intertidal, Red Sea coasts of Sinai. Mar. Biol. 70, 305—316. https://doi.org/10.1007/BF00396849

Azhar, G.S., Mavalankar, D., Nori-Sarma, A., Rajiva, A., Dutta, P., Jaiswal, A., Sheffield, P., Knowlton, K., Hess, J.J., 2014. Heat-related mortality in India: Excess all-cause mortality associated with the 2010 Ahmedabad heat wave. PLoS One 9 (3), e91831. https://doi.org/10.1371/journal.pone.0091831

Beck, M.W., 1998. Comparison of the measurement and effects of habitat structure on gastropods in rocky intertidal and mangrove habitats. Mar. Ecol. Prog. Ser. 169, 165—178. https://doi.org/10.3354/meps169165

Bhadja, P., Poriya, P., Kundu, R., 2014. Community structure and distribution pattern of intertidal invertebrate macrofauna at some anthropogenically influenced coasts of Kathi-

awar peninsula (India). Adv. Ecol. 2014 Article ID 547395. https://doi.org/10.1155/2014/547395.

Button, C.A., 2008. The influence of density-dependent aggregation characteristics on the population biology of benthic broadcast-spawning gastropods: pink abalone (Haliotis corrugata), red abalone (Haliotis rufescens), and wavy turban snails (Megastraea undosa) PhD thesis. University of California, San Diego.

Cannon, L.R.G., 1979. Ecological Observations on *Cerithium moniliferum* Kiener (Gastropoda: Cerithiidae) and its trematode parasites at Heron Island, Great Barrier Reef. Aust. J. Mar. Fresh. Res. 30, 365—374. https://doi.org/10.1071/MF9790365

Chapman, M.G., Underwood, A.J., 1994. Dispersal of the intertidal snail, *Nodilittorina pyramidalis*, in response to the topographic complexity of the substratum. J. Exp. Mar. Biol. Ecol. 179, 145—169. https://doi.org/10.1016/0022-0981(94)90111-2

Chapman, M.G., 1995. Aggregation of the littorinid snail *Littorina unifasciata* in New South Wales. Australia. Mar. Ecol. Prog. Ser. 126, 191—202. https://doi.org/10.3354/meps126191

Chapman, M.G., Underwood, A.J., 1996. Influences of tidal conditions, temperature and desiccation on patterns of aggregation of the high-shore periwinkle, *Littorina unifasciata*, in New South Wales, Australia. J. Exp. Mar. Biol. Ecol. 196, 213—237. https://doi.org/10.1016/0022-0981(95)00131-X

Chapman, M.G., 1998. Variability in trail-following and aggregation in *Nodilittorina unifasciata* Gray. J. Exp. Mar. Biol. Ecol. 224, 49—71. https://doi.org/10.1016/S0022-0981(97)00169-X

Chapperon, C., Le Bris, C., Seuront, L., 2013. Thermally mediated body temperature, water content and aggregation behaviour in the intertidal gastropod *Nerita atramentosa*. Ecol. Res. 28, 407—416. https://doi.org/10.1007/s11284-013-1030-4

Coleman, R.A., 2010. Limpet aggregation does not alter desiccation in the limpet *Cellana tramoserica*. J. Exp. Mar. Biol. Ecol. 386, 113—118. https://doi.org/10.1016/j.jembe.2010.02.011

Denadai, M.R., Amaral, A.C.Z., Turra, A., 2004. Biology of a tropical intertidal population of *Cerithium atratum* (Born, 1778) (Mollusca, Gastropoda). J. Nat. Hist. 38, 1695—1710. https://doi.org/10.1080/0022293031000156330

Fairweather, P.G., 1988. Predation creates haloes of bare space among prey on rocky seashores in New South Wales. Aust. J. Ecol. 13, 401—409. https://doi.org/10.1111/j.1442-9993.1988.tb00988.x

Garilli, V., Galletti, L., Parrinello, D., 2018. Distinct protoconchs recognised in three of the larger Mediterranean *Cerithium* species (Caenogastropoda: Cerithiidae). Molluscan Res. 38, 105—118. https://doi.org/10.1080/13235818.2017.1396633

Garrity, S.D., Levings, S.C., 1981. A predator-prey interaction between two physically and biologically constrained tropical rocky shore gastropods: direct, indirect and community effects. Ecol. Monogr. 51, 267—286. https://doi.org/10.2307/2937274

Grayson, J.E., Chapman, M.G., 2004. Patterns of distribution and abundance of chitons of the genus *Ischnochiton* in intertidal boulder fields. Aust. J. Ecol. 29, 363—373. https://doi.org/10.1111/j.1442-9993.2004.01375.x

Green, J.L., Ostling, A., 2003. Endemics—area relationships: the influence of species dominance and spatial aggregation. Ecology 84, 3090—3097. https://doi.org/10.1890/02-3096

Hallier, J.P., Gaertner, D., 2008. Drifting fish aggregation devices could act as an ecological trap for tropical tuna species. Mar. Ecol. Prog. Ser. 353, 255—264. https://doi.org/10.3354/meps07180

He, H.S., DeZonia, B.E., Mladenoff, D.J., 2000. An aggregation index (AI) to quantify spatial patterns of landscapes. Landscape Ecol. 15, 591—601. https://doi.org/10.1023/A:1008102521322

Ishakani, A.H., Joshi, N.H., Ayaz, M., Sumara, K., Vadher, K.H., 2016. Assessment of seaweed diversity at Veraval coast, Gujarat. J. Exp. Zool. India 19 (2), 863—868.

Lapointe, V., Sainte-Marie, B., 1992. Currents, predators, and the aggregation of the gastropod *Buccinum undatum* around bait. Mar. Ecol. Prog. Ser. 85, 245—257 https://www.jstor.org/stable/24829760

Lauzon-Guay, J.S., Scheibling, R.E., 2009. Food dependent movement of periwinkles (*Littorina littorea*) associated with feeding fronts. J. Shellfish Res. 28, 581—587. https://doi.org/10.2983/035.028.0322

Loke, L.H., Heery, E.C., Lai, S., Bouma, T.J., Todd, P.A., 2019. Area-independent effects of water-retaining features on intertidal biodiversity on eco-engineered seawalls in the tropics. Front. Mar. Sci. 6, 16. https://doi.org/10.3389/fmars.2019.00016

Meager, J.J., Schlacher, T.A., Green, M., 2011. Topographic complexity and landscape temperature patterns create a dynamic habitat structure on a rocky intertidal shore. Mar. Ecol. Prog. Ser. 428, 1—12. https://doi.org/10.3354/meps09124

Misra, S., Kundu, R., 2005. Seasonal variations in population dynamics of key intertidal molluscs at two contrasting locations. Aquat. Ecol. 39, 315—324. https://doi.org/10.1007/s10452-005-1779-9

Moisez, E., Spilmont, N., Seuront, L., 2020. Microhabitats choice in intertidal gastropods is species-, temperature- and habitat-specific. J. Therm. Biol. 94, 102785. https://doi.org/10.1016/j.jtherbio.2020.102785

Montecinos, C., Riera, R., Brante, A., 2020. Site fidelity and homing behaviour in the intertidal species *Chiton granosus* (Polyplacophora) (Frembly 1889). J. Sea Res. 164, 101932. https://doi.org/10.1016/j.seares.2020.101932

Moulton, J.M., 1962. Intertidal clustering of an Australian gastropod. Biol. Bull. 123, 170—178. https://doi.org/10.2307/1539513

Nicolaidou, A., Nott, J.A., 1999. The role of the marine gastropod *Cerithium vulgatum* in the biogeochemical cycling of metals. In: Biogeochemical Cycling and Sediment Ecology, 59. Springer, Dordrecht, 137—146. https://doi.org/10.1007/978-94-011-4649-4_7

Ray, M., Stoner, A.W., 1994. Experimental analysis of growth and survivorship in a marine gastropod aggregation: balancing growth with safety in numbers. Mar. Ecol. Prog. Ser. 105, 47—59.

Rojas, J.M., Castillo, S.B., Escobar, J.B., Shinen, J.L., Bozinovic, F., 2013. Huddling up in a dry environment: the physiological benefits of aggregation in an intertidal gastropod. Mar. Biol. 160, 1119—1126. https://doi.org/10.1007/s00227-012-2164-6

Rohde, K., Sandland, R., 1975. Factors influencing clustering in the intertidal snail *Cerithium moniliferum*. Mar. Biol. 30, 203—215. https://doi.org/10.1007/BF00390743

Schmitt, R.J., 1987. Indirect interactions between prey: Apparent competition, predator aggregation, and habitat segregation. Ecology 68, 1887—1897. https://doi.org/10.2307/1939880

Snyder-Conn, E., 1979. Tidal clustering and dispersal of the hermit crab *Clibanarius digueti*. Mar. Behav. Physiol. 7, 135—154. https://doi.org/10.1080/10236248009386977

Stafford, R., Davies, M.S., 2005. Spatial patchiness of epilithic biofilm caused by refuge-inhabiting high shore gastropods. Hydrobiologia 545, 279—287. https://doi.org/10.1007/s10750-005-3320-5

Stafford, R., Davies, M.S., Williams, G.A., 2008. Self-organization of intertidal snails facilitates evolution of aggregation behavior. Artif. Life 14, 409—423. https://doi.org/10.1162/artl.2008.14.4.14401

Stafford, R., Davies, M.S., Williams, G.A., 2012. Misinterpreting the potential benefits of aggregation for reducing desiccation in the intertidal: a simple analogy. Mar. Ecol. 33, 512—515. https://doi.org/10.1111/j.1439-0485.2012.00513.x

Stoll, P., Prati, D., 2001. Intraspecific aggregation alters competitive interactions in experimental plant communities. Ecology 82, 319—327.

https://doi.org/10.1890/0012-9658(2001)082[0319:IAACII]2.0.CO;2

Thivakaran, G.A., Sawale, A.K., 2016. Mangrove macrofaunal diversity and community structure in Mundra and Kharo, Kachchh, Gujarat. Indian J. Geo-Mar. Sci. 45, 1584—1592. http://nopr.niscair.res.in/handle/123456789/38600

Underwood, A.J., 2004. Landing on one's foot: small-scale topographic features of habitat and the dispersion of juvenile intertidal gastropods. Mar. Ecol. Prog. Ser. 268, 173—182. http://doi.10.3354/meps268173

Underwood, A.J., Chapman, M.G., 1989. Experimental analyses of the influences of topography of the substratum on movements and density of an intertidal snail, *Littorina unifasciata*. J. Exp. Mar. Biol. Ecol. 134, 175—196. https://doi.org/10.1016/0022-0981(89)90068-3

Underwood, A.J., Chapman, M.G., Connell, S.D., 2000. Observations in ecology: you can't make progress on processes without understanding the patterns. J. Exp. Mar. Biol. Ecol. 250, 97—115. https://doi.org/10.1016/S0022-0981(00)00181-7

Yamaguchi, M., 1977. Shell growth and mortality rates in the coral reef gastropod *Cerithium nodulosum* in Pago Bay, Guam, Mariana Islands. Mar. Biol. 44, 249—263. https://doi.org/10.1007/BF00387706

Yu, Z., Hu, Z., Song, H., Xu, T., Yang, M., Zhou, C., Zhang, T., 2020. Aggregation behavior of juvenile *Neptunea cumingii* and effects on seed production. J. Oceanol. Limnol. 38, 1590—1598. https://doi.org/10.1007/s00343-020-0042-5

Oceanologia 64 (2022) 396—403

Available online at www.sciencedirect.com

ScienceDirect

journal homepage: www.journals.elsevier.com/oceanologia

SHORT COMMUNICATION

Algal bloom, hypoxia, and mass fish kill events in the backwaters of Puducherry, Southeast coast of India

Pravakar Mishra[a], Subrat Naik[a,*], P. Vipin Babu[b], Umakanta Pradhan[a], Mehmuna Begum[a], Thanamegam Kaviarasan[a], Athan Vashi[a], Debasmita Bandyopadhyay[a], P. Ezhilarasan[a], Uma Sankar Panda[a], M.V. Ramana Murthy[a]

[a] *National Centre for Coastal Research (NCCR), Ministry of Earth Sciences, NIOT Campus, Pallikaranai, Chennai, India*
[b] *Puducherry Pollution Control Committee (PPCC), Puducherry, India*

Received 13 March 2021; accepted 22 November 2021
Available online 5 December 2021

KEYWORDS
Algal bloom;
Hypoxia;
Fish kill;
Water quality;
Puducherry;
India

Abstract The Chunnambar backwater of Puducherry experienced changes in water quality over a period. The most significant impact was the sudden mass fish kill event coincided with the *Pseudo-nitzschia* bloom. On 25th September 2019, a mass fish kill event was reported, i.e. about a 0.25 metric ton (MT) floating on the water surface. On 29th September 2019, a much larger (~1 MT) than the earlier incident had occurred. Sampling was carried out to assess the causes thereof. The results indicate that high organic matter and bacterial loads accumulated in the water and sediment due to the closure of the river mouth for an extended period. High ammonia (61.4 μM) and phosphate (6.2 μM) levels attributed to eutrophic conditions in the water column and hypoxemia due to low dissolved oxygen (1.62 mg/L at St.1 and 2.4 mg/L at St.5) and algal bloom were the proximate cause of these sudden fish kills. We recommend periodic dredging to facilitate proper water exchange between the backwater and the sea.

* Corresponding author at: National Centre for Coastal Research (NCCR), Ministry of Earth Sciences, NIOT Campus, Pallikaranai, Chennai 600 100, India. Phone: +91-44-66787086;+91-9444865125.
E-mail addresses: subrat@nccr.gov.in, naiksubrat@gmail.com (S. Naik).
Peer review under the responsibility of the Institute of Oceanology of the Polish Academy of Sciences.

Production and hosting by Elsevier

https://doi.org/10.1016/j.oceano.2021.11.003

The mass fish kill in the rivers, lakes, estuaries, and coastal waters are (Hoyer et al., 2009; La and Cooke, 2011), usually triggered by abrupt changes in environmental parameters, i.e., salinity, temperature, pH, and dissolved oxygen (DO), and the introduction of chemicals, toxicants or pollutants, toxic algal blooms and pathogens (Eissa et al., 2013; Meyer and Barclay, 1990). These changes can hinder coastal and marine environments and influence the local economy, i.e., loss of tourism, fisheries, aesthetic value, and negatively impact the food web dynamics and nutrient balance (Holmlund and Hammer, 1999). In many cases, the primary reasons attributed to mass fish kill are natural and anthropogenic hypoxia (Ram et al., 2014). The other important factor that triggers fish kill is toxic algal blooms (Kangur et al., 2005). Certain species of diatom like the genus *Pseudo-nitzschia* produce neurotoxin domoic acid (DA) is responsible for the neurological disorder known as amnesic shellfish poisoning (ASP) (Pulido, 2008), can affect fish and other organisms (Galvao et al., 2009). Excess nutrient input is a primary concern in many coastal areas (Carpenter et al., 1998; Rabalais et al., 2002) and induce the growth of phytoplankton, some harmful algal blooms, high organic matter, hypoxic or anoxic conditions, and mass mortality of biota (Anderson et al., 2008; Glasgow and Burkholder, 2000). Various developmental activities introduce a significant amount of organic matter and nutrients, typically untreated or partially treated sewage released into the rivers and estuaries, accelerate hypoxia and the eutrophication processes (Villate et al., 2013). Coastal hypoxia (DO $<$ 2.0 mg/L, or approximately 30% saturation) is a major threat to coastal ecosystems globally (Ram et al., 2014; Zhang et al., 2010). Mortality occurs if oxygen levels drop below a critical concentration depending on the fish species. Fishes in the water bodies likely evade adverse environmental conditions to overcome the harmful surroundings. However, if a large proportion of the water bodies are suddenly affected, fishes cannot absorb the ecological stress and relocate, resulting in mass mortality. In the past, mass fish kill events in the Indian coastal waters have been reported, i.e., Tapti Estuary of Gujarat (Ram et al., 2014), Kokilamedu, Ennore, and Adyar estuary of Tamil Nadu (Raja et al., 2019; Sachithanandam et al., 2017; Venugopalan et al.,1998).

Puducherry, a union territory (UT) coastal city, is one of India's most visited tourist destinations, surrounded by the Bay of Bengal on the eastern side and Tamil Nadu state on the other three sides. A backwater known locally as Chunnambar lies in the southern part of the city adjacent to the popular Paradise Beach, attracts many tourists for recreational activities, i.e., swimming, sailing, boating, sunbathing, and wading. The city has a population of around 735,000 (as per the 2011 census). There are six major industries in the UT of Puducherry manufacturing paper, alcoholic beverages, chemicals, and pharmaceuticals. Around 40 million liters per day (MLD) of domestic sewage is being generated, of which 31 MLD is treated in situ and the remaining 9 MLD is lost into the drains and rivers (Govt. of Puducherry, 2019). The region experiences a tropical sub-humid climate with an annual mean temperature of 25°C and average yearly precipitation of 1200 mm (Solai et al., 2010).

On 25th September 2019, the Puducherry Pollution Control Committee (PPCC) was informed by the locals about the incident of a large number of dead fishes floating near the boathouse (St.1) of Chunnambar backwater (Figure 1). To assess the immediate cause of the fish kill incident, PPCC carried out a field survey and surface water sampling at four locations (St.1 to St.4) on 26th September 2019 (Figure 1). On 29th September 2019, another fish kill incident larger than the previous one occurred at a different location in the backwater at St.5 (Figure 1). On 1st October 2019, National Centre for Coastal Research (NCCR), Chennai, took cognizance of the incident and sampled water and sediment from 6 locations between 9 AM and 1 PM. The sampling locations are spatially distributed i.e., St.1 to St.5 in the Chunnambar backwater, and St.6 at the shore, covering about 1.8 km^2 of backwater area (Figure 1). Surface water samples were collected in pre-cleaned polyethylene bottles using a 5L Niskin's water sampler, then preserved in an icebox and transported to the laboratory for analysis. A mercury thermometer measured the temperature with an accuracy of $\pm$ 0.1°C. The water quality probe (*In Situ* AQUA TROLL, USA) measured pH and oxygen saturation. The dissolved oxygen and biochemical oxygen demand (BOD) were estimated following Winkler's titration method. Salinity was determined by Mohr Knudsen's titration method (Grasshoff et al., 2009). Millipore membrane, 47 mm diameter filter (porosity 0.45 μm) was used for gravimetric determination of total suspended matter (TSM). Dissolved inorganic nutrients (NO_3^--N, NO_2^--N, NH_4^+-N, PO_4^{3-}-P, SiO_4^{4-}-Si, TN, and TP) and the analytical precision of each nutrient parameters such as (nitrate+nitrite $\pm$ 0.02 μM, ammonium $\pm$ 0.02 μM, phosphate $\pm$ 0.01 μM and silicate $\pm$ 0.02 μM) was adopted by following the standard protocol (Grasshoff et al., 2009). One liter of water sample for Chl-*a* and pheophytin were filtered through Whatman GF/F, 47-mm-diameter filter (porosity 0.7 mm), and pigment extraction was performed using 90% acetone. Chlorophyll-*a* (Chl-*a*) and pheophytin concentrations were measured by using a UV-visible spectrophotometer (Strickland and Parsons, 1972). One liter of phytoplankton sample was collected and preserved with Lugol's iodine solution. The samples were settled for 48 hours after that, the supernatant was siphoned to the volume of approximately 250 ml. 1 ml of an aliquot of the sample was taken in a Sedgewick-Rafter counting chamber for enumeration of cells under a phase-contrast microscope (Nikon ECLIPSE N*i*), and species were identified following standard identification manuals (Desikachary, 1987; Sournia, 1970; Subrahmanyan, 1971). The microbial density from the surface waters was analyzed by the spread plating method on selective medium plates with 0.1ml of suitable dilutions. The final counts were expressed in the colony-forming unit (CFU/mL) followed by APHA (1998). Statistical analyses included Factor Analysis (FA) and Canonical Correspondence Analysis (CCA) on the present water quality data to understand the relationships between variables. FA and CCA were carried out by using *Past 3* statistical software.

The spatial variations of physicochemical and biological parameters are shown in Table 1. Automatic weather station (AWS) data on air temperature, rainfall, wind speed, and direction for the period 20th to 30th September 2019 provided by PPCC were analysed to understand local meteorological influence. The wind speed was in the range of 0.5 to 4 m/s with an average of 2.2 m/s, and wind direction varied from 200° to 250°, predominantly south-westerly. About

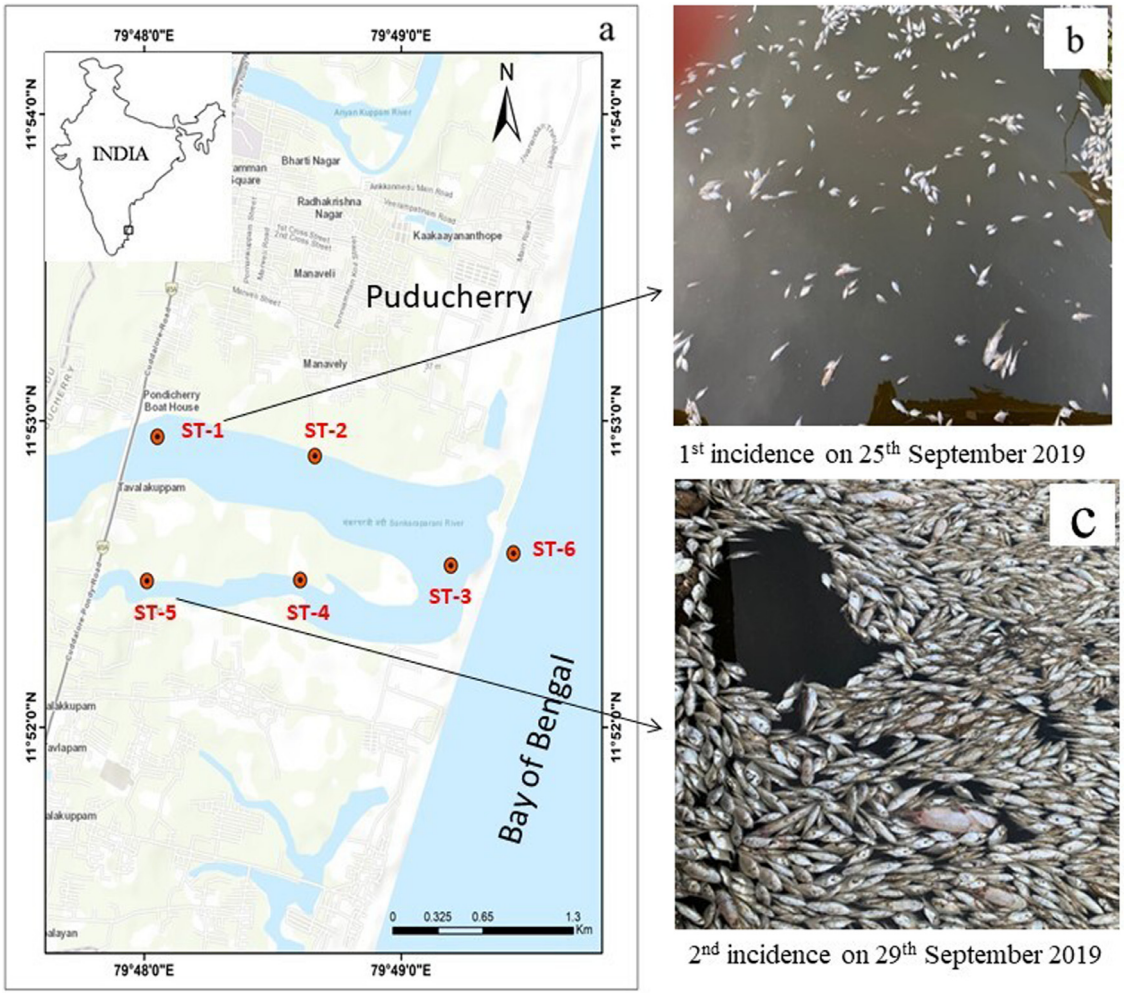

Figure 1 a) Study map with sampling locations; b— c) Fish kill incidents.

15 mm rainfall was recorded on 26th September 2019. The daily air temperature followed high and low values consistent with the diurnal variations, between 28 to 32°C except for two days (22nd and 23rd September 2019) with the minimum value of more than 30°C. Water temperature varied from 28.6 to 32.9°C. Maximum temperature was recorded at St.5 during second fish kill incident (Table 1). The pH ranged from 6.9 to 8.4; the lowest and highest pH was noticed at St.1 on 26th September and 1st October 2019, respectively (Table 1). Salinity ranged from 26 to 34.9 PSU, and the highest salinity was observed at St.6 (shore). Total suspended matter (TSM) varied from 42 to 201.2 mg/L; high values were observed during the first fish kill incident. The DO ranged from 1.62 to 10.5 mg/L were recorded during the study period. Low DO (1.62 mg/L) was recorded at St.1 in the first fish kill incident whereas, DO was 2.4 mg/L at St.5 in the second incident (Table 1). The maximum DO (10.5 mg/L) was recorded at St.4 might be due to high oxygen saturation (177.1%) in the water column (Table 1). Nitrite concentration ranged from 0.2 to 0.5 μM, with an average of 0.33 μM. Nitrate and ammonia ranged from 1.2 to 4.7 μM and 2.5 to 61.4 μM, respectively. The maximum value was recorded at the mass fish kill location (St.5, Table 1). High nitrate and ammonia values revealed the degradation and decomposition of fishes after the fish kill incident. Similarly, phosphate values varied from 1.2 to 6.2 μM, and the maximum was observed at St.5 (Table 1). High phosphate characterizes the decomposition process, and the adjacent location at St.4 (4.35 μM) signifies the impact of the incident. Silicate varied from 4.9 to 148.2 μM, and the maximum value was recorded at St.5 (Table 1), indicating the riverine input of silica into the water.

During the sampling period, a prominent discolouration of the surface water was noticed, attributed to the bloom of *Pseudo-nitzschia,* resulting in long, dense golden-brown patches (Figure 2a,b,c) spreading over about 1 km^2 in the backwater. Phytoplankton density ranged from 94,800 Nos/L to 589,600 Nos/L (Table 1). A total of 31 species of phytoplankton belonging to four groups, such as diatoms, dinoflagellates, green algae, and cyanobacteria, were recorded. Diatoms (67%) constituted the most dominant group, followed by dinoflagellates (17%), green algae (11%), and cyanobacteria (5%). Eutrophic waters consequently favor algae proliferation, causing algal bloom and the onset of hypoxic and anoxic conditions (Karim et al., 2002). The bloom of *Pseudo-nitzschia* contributed 75% of the total abundance and was widely distributed in all locations in the backwater except at St.6 shore water (Table 2).

Table 1 Physicochemical and biological parameters in the study area.

Parameters	Backwater (BW)									Shore (SH)
	St.1		St.2		St.3		St.4		St.5	St.6
	I	II	I	II	I	II	I	II	II	II
Depth (m)	-	1.4	-	2.6	-	1.3	-	2.5	1.2	-
AT (°C)	28	29.5	28	32	29	30.6	28.5	31.2	30.6	30
WT (°C)	29	28.6	29.5	30.8	31	29.7	30.5	31.7	32.9	28.8
pH	6.9	8.4	7.1	8.2	7.7	8.2	7.8	8.2	7.6	8.0
Salinity (PSU)	29	28.7	32	28.8	28	28.9	26	29.2	29.5	34.9
TSM (mg/L)	164.7	50	164.3	54.0	201.2	50.0	167.7	42.0	52.0	42.0
DO (mg/L)	1.62	8.3	2.91	6.2	3.90	9.8	4.11	10.5	2.4	6.2
Oxygen Sat %	-	149.4	-	98.7	-	153.3	-	177.1	39.3	99.1
BOD (mg/L)	-	3.7	-	2.9	-	3.5	-	4.5	2.2	3.0
NO_2 (μM)	-	0.3	-	0.2	-	0.3	-	0.4	0.3	0.3
NO_3 (μM)	-	4.4	-	2.9	-	1.2	-	1.9	4.7	4.1
NH_4 (μM)	-	6.8	-	8.2	-	4.9	-	2.5	61.4	2.8
PO_4 (μM)	-	2.9	-	2.4	-	2.8	-	4.3	6.2	1.2
SiO_4 (μM)	73.6	9.3	80.2	73.8	66.4	90.8	62.0	113.1	148.2	4.9
Chl-*a* (mg/m^3)	-	188.8	-	210.9	-	203.0	-	98.9	43.2	34.7
Phaeo (mg/m^3)	-	46.9	-	15.6	-	10.7	-	11.8	1.4	4.1
Phytoplankton ($\times 10^5$ Nos/L)	-	3.82	-	5.90	-	4.85	-	3.33	4.57	0.95
THB ($\times 10^5$CFU/mL)	-	3.44	-	5.28	-	8.54	-	4.6	4.36	3.96
TC ($\times 10^3$CFU/mL)	-	9.5	-	1.3	-	15.6	-	6.1	3.1	9.2
FC ($\times 10^1$ CFU/mL)	-	5.0	-	ND	-	2.0	-	13.0	ND	9.0
ECLO ($\times 10^2$ CFU/mL)	-	9.0	-	ND	-	2.0	-	ND	14.0	3.0
SHLO ($\times 10^4$ CFU/mL)	-	1.08	-	2.04	-	1.24	-	3.32	1.38	2.0
VPLO ($\times 10^4$ CFU/mL)	-	1.12	-	0.38	-	6.4	-	1.56	9.3	1.92

I — Fish kill incident on 25.09.2019; Sampling date: 26.09.2019.
II — Fish kill incident on 29.09.2019; Sampling date: 01.10.2019.

Some species of phytoplankton had occurred commonly in both shore and backwater. The common species such as diatoms *Rhizosolenia setigera, Navicula longa,* and green algae *Chlorella marina* were recorded. A high density of *Pseudo-nitzschia* cells were found in the backwater and the gills of the dead fishes. The presence of many cells might have suffocated the fish by clogging or irritating the gills leading to asphyxiation. Samples of six fish kill species were collected and identified (Figure 3a—f). DO levels were below 3 mg/L during fish kill events, and low DO (<2 mg/L) can cause suffocation of fish and one of the common causes of fish kills. The decay of algae exhausted the oxygen, and the decomposition process depleted the available DO result in massive fish kill (San Diego-McGlone et al., 2008). The Chl-*a* ranged from 34.7 to 210.9 mg/m^3, and the highest was recorded at St.2 in concomitant with high phytoplankton population density (Table 1). The values of pheophytin in the study area varied between 1.4 and 46.9 mg/m^3, and the highest pheophytin concentration was recorded at St.1 (Table 1).

High microbial abundance recorded in the backwater was attributed to the enrichment of organic matter associated with sewage effluent. Total heterotrophic bacteria (THB) ranged from 3.44 to 8.54 $\times 10^5$ CFU/mL, and the maximum density was encountered at St.3. Total coliform (TC) and Faecal coliform (FC) varied from 1.30 to 15.60 $\times 10^3$ CFU/mL and ND (not detected) to 13.0 $\times 10^1$ CFU/mL, respectively. The pathogenic bacteria such as *Vibrio parahaemolyticus* like organisms (VPLO) varied from 0.38 to 9.30 $\times 10^4$ CFU/mL, *Shigella* like organisms (SHLO) from 1.08 to 3.32 $\times 10^4$ CFU/mL and, *Escherichia coli* like organisms (ECLO) from ND to 14.0 $\times 10^2$ CFU/mL, respectively. Maximum counts of VPLO and ECLO were found at St.5 (Table 1). In the present case, oxygen depletion in the backwater might have occurred due to the increasing uptake of available dissolved oxygen by bacteria during the breaking down of high organic matter.

The factor analysis was carried out to elucidate the pattern of variation existing in the dataset. Four significant factors (eigenvalue>1) indicate the total variance of 85.14% (Table 3). Factor 1 explains 39.52% of the total variance and strong positive loadings of PO_4, NH_4, SiO_4, and TN moderate positive loading of water temperature. High phosphate and nitrogenous substances specify the sewage pollution re-

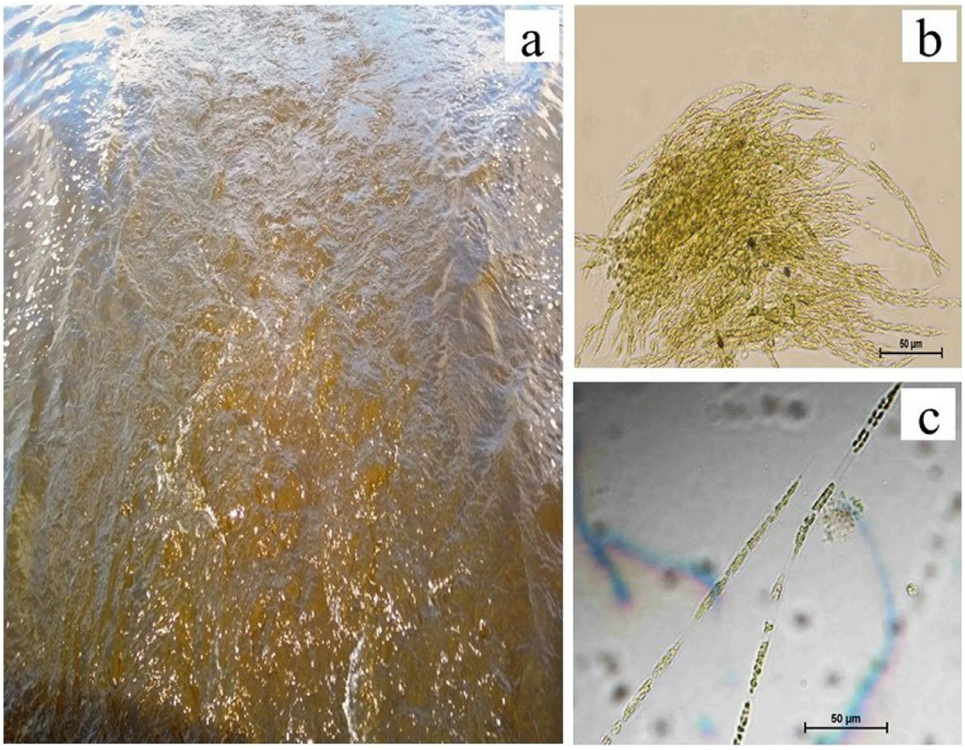

Figure 2 a) Discoloration of backwater; b—c) microscopic images of *Pseudo-nitzschia*.

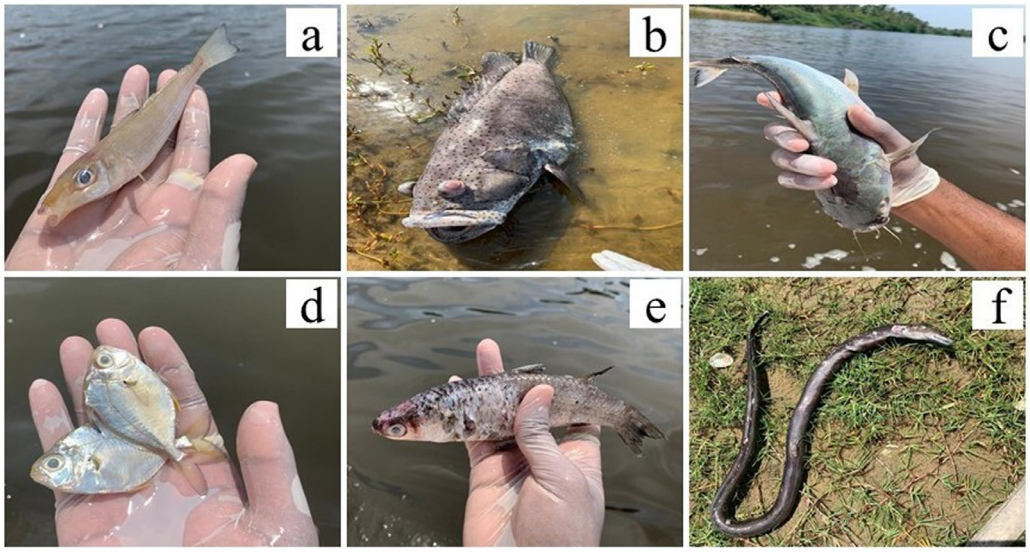

Figure 3 a—f) Six fish species killed; a) *Silago sihama*, b) *Cephalopholis sonerrati*, c) *Arius arius*, d*) Leiognathus equidens*, e) *Mugil cephalus* and, f) *Strophiodonsathate*.

sulting from the untreated sewage drained into the backwater. Factor 2 explains the 25.71% of the total variance with strong positive loading of NH_4, and NO_3, whereas negative loading of DO%, DO, BOD, and pH. Depletion of DO and increase of BOD indicate the eutrophic condition in the water column due to mostly land and agricultural runoff, domestic and urban sewage. Factor 3 explained 19.91% of the total variance and detected strong positive loading of phytoplankton, Chl-*a*, and TP. In contrast, a negative salinity load indicates the presence of excess nutrients, and favorable water temperature supports the phytoplankton growth in the backwater. The tri-plot of CCA was performed to understand the relationship between the phytoplankton and environmental variables are presented in Figure 4. The first three axes explained about 99% of the relationship between the environmental variables. Axis-1 accounted for 75.85% of the total variation, was positively correlated with salinity and pheophytin but negatively correlated with WT, NO_2, SiO_4, and phytoplankton. Axis-2 explained about 16.43% of the total variation, and it was positively correlated with

Table 2 Phytoplankton taxa (Nos/ml) in the Chunnambar backwater.

Sl.No.	Taxa	Backwater (BW)					Shore (SH)	% Comp.	
		St.1	St.2	St.3	St.4	St.5	St.6	BW	SH
1	*Asterionellopsis glacialis*	X	X	X	X	X	56	0.0	11.8
2	*Bacteriastrum hyalinum*	X	X	X	X	25	X	0.4	0.0
3	*Ceratium furca*	X	X	32	29	42	X	1.8	0.0
4	*Ceratium tripos*	X	X	X	46	X	X	0.8	0.0
5	*Chaetoceros curvisetus*	X	56	X	X	X	X	1.0	0.0
6	*Chaetoceros diadema*	X	X	X	64	X	X	1.1	0.0
7	*Chlamydomonas* sp.	X	X	34	X	X	X	0.6	0.0
8	*Chlorella marina*	X	X	X	X	78	34	1.3	7.2
9	*Chlorella salina*	30	84	X	X	X	X	1.9	0.0
10	*Coscinodiscus centralis*	X	X	X	X	X	72	0.0	15.2
11	*Dinophysis caudata*	X	X	X	X	X	28	0.0	5.9
12	*Gonyaulax minima*	29	X	X	X	56	X	1.4	0.0
13	*Guinardia striata*	X	X	X	X	X	24	0.0	5.1
14	*Leptocylindrus danicus*	X	X	X	31	X	X	0.5	0.0
15	*Lyngbya elegans*	X	X	X	35	X	X	0.6	0.0
16	*Navicula clavata*	X	X	X	X	X	19	0.0	4.0
17	*Navicula longa*	24	X	X	X	X	38	0.4	8.0
18	*Odontella mobiliensis*	X	X	42	X	X	X	0.7	0.0
19	*Oocystis* sp.	X	36	45	X	X	X	1.4	0.0
20	*Oscillatoria australis*	28	X	X	X	X	X	0.5	0.0
21	*Peridinium pentagonum*	X	X	18	X	X	X	0.3	0.0
22	*Pinnularia alpina*	X	X	X	X	X	26	0.0	5.5
23	*Planktoniella sol*	X	X	23	X	X	X	0.4	0.0
24	*Prorocentrum micans*	X	X	X	20	X	X	0.3	0.0
25	*Pseudo-nitzschia*	729	1026	956	572	1135	X	**75.1**	0.0
26	*Rhizosolenia alata*	X	X	X	X	X	43	0.0	9.1
27	*Rhizosolenia setigera*	57	106	75	128	92	76	7.8	16.0
28	*Skeletonema costatum*	X	X	X	X	X	58	0.0	12.2
29	*Thalassionema nitzschioides*	12	X	X	X	X	X	0.2	0.0
30	*Thalassiothrix longissima*	X	X	52	X	X	X	0.9	0.0
31	*Triceratium reticulum*	X	32	X	X	X	X	0.5	0.0
	Total taxa	**909**	**1340**	**1277**	**925**	**1428**	**474**	**100.0**	**100.0**

NO_3, NH_4, PO_4, turbidity, and TSM and negatively correlated with pH, DO, DO%, BOD, and Chl-*a*. The study revealed that the anthropogenic nutrients and salinity were the most important environmental factors influencing the phytoplankton bloom and hypoxic conditions in the water column resulted in the mass fish kill.

Usually, fish kills incidents are a major cause of concern for the coastal water quality and ecosystem health. Our study demonstrates the impact of untreated sewage load in the backwater declined the water quality as THB counts were overall high in the water column. Pollution indicators such as FC and TC were several folds above the permissi-

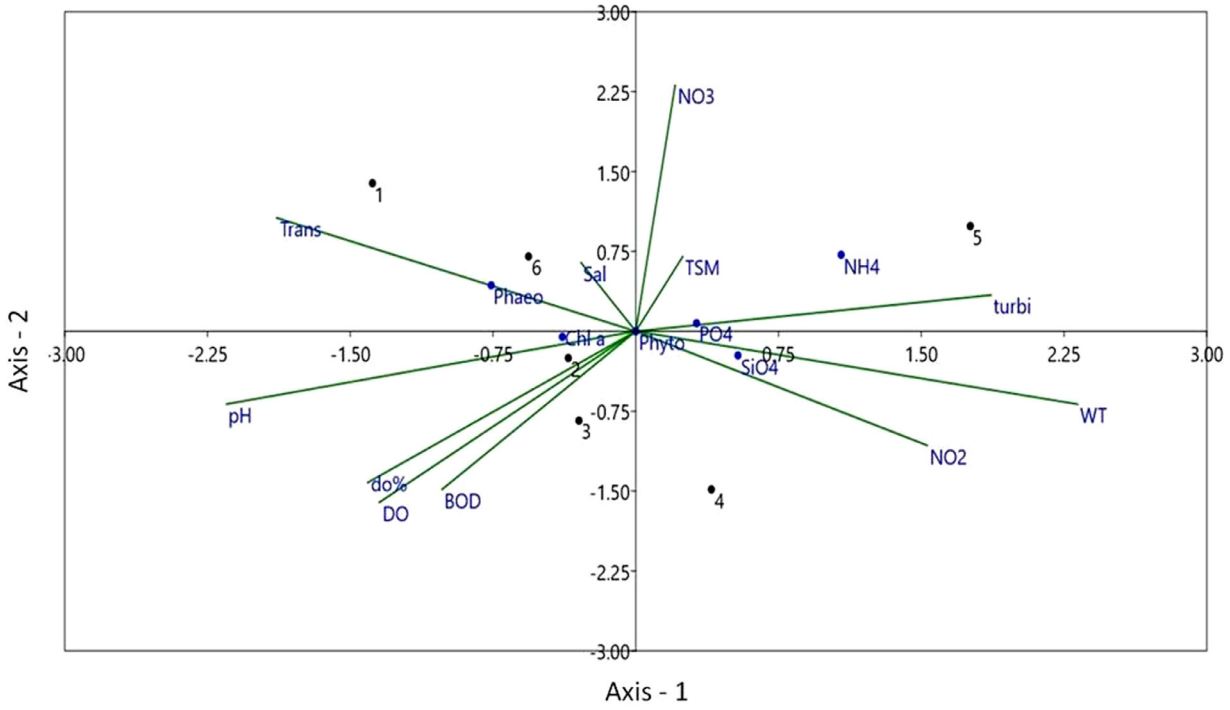

Figure 4 Canonical Correspondence Analysis (CCA) for environmental variables.

Table 3 Factor Loadings > 0.650000 (Varimax normalized). Extraction: Principal Component Analysis.

Variables	F-1	F-2	F-3
AT	0.08	0.03	0.3
WT	**0.79**	0.31	0.02
pH	−0.49	**−0.75**	0.41
DO%	−0.1	**−0.99**	0.11
salinity	−0.48	0.22	**−0.84**
DO	0.01	**−0.85**	−0.21
BOD	0.04	**−0.98**	−0.01
PO_4	**0.96**	0.23	0.09
NO_2	**0.65**	−0.36	−0.2
NO_3	−0.05	**0.69**	−0.17
SiO_4	**0.84**	0.16	0.12
NH_4	**0.88**	**0.75**	0.01
TP	0.21	0.51	**0.73**
TN	**0.83**	−0.08	0.45
Chl-*a*	−0.3	−0.36	**0.87**
Phaeo	−0.23	−0.35	0.55
Phyto	0.27	0.14	**0.89**
Eigenvalue	7.11	4.63	3.58
% of Variance	39.52	25.71	19.91
Cumulative %	39.52	65.23	85.14

ble level [100 CFU/100ml, Central Pollution Control Board (CPCB), New Delhi], and the variability of pathogenic and vibrio forms was more pronounced during the study. There is a dire requirement to develop a framework for safe backwater use for amusement, contact sports, and fishing. The intrusion of a huge load of nutrients, *viz.*, nitrate, ammonia, and phosphate levels, were associated with sewage discharge and other anthropogenic and recreational activities in the backwater. High nitrate, phosphate, ammonia, and silicate were recorded at the location of the major fish kill. In addition to this, the algal bloom of *Pseudo-nitzschia*, high bacterial loads, and the hypoxic conditions (1.62 mg/L) attributed to the episodic mass fish kill events in the Chunnambar backwater.

The present study demonstrates that the discharges from nearby residential hamlets, tourism activities, untreated point sources such as Sankaraparani River waters must be maintained as per CPCB water quality criteria and guidelines. Even though several measures have been implemented by the local administration and pollution control agencies, it is still necessary to focus on long-term solutions. It is suggested that appropriate water exchange between the backwater and the sea through periodic dredging and maintenance of the inlet, proper wastewater treatment facilities, and installation of good aeration systems are some of the immediate measures that need to be implemented for improving the Chunnambar backwater quality. The regulatory authorities need to regularly monitor the water bodies to assess the changes happening in the water bodies to prevent pollution.

Declaration of competing interest

The authors declare that they have no known competing financial interests or personal relationships that could have appeared to influence the work reported in this paper.

Acknowledgments

We are thankful to the Secretary, Ministry of Earth Sciences, Govt. of India, for facilitating the study at the National Centre for Coastal Research (NCCR), Chennai. The authors are thankful to Smitha R., Chairperson, PPCC, Puducherry, for extending necessary administrative support. Dr. Anil Mohapatra, ZSI, Gopalpur, is duly acknowledged for the identification of fish species. This manuscript has NCCR contribution no. NCCR / MS 378.

References

Anderson, D.M., Burkholder, J.M., Cochlan, W.P., Glibert, P.M., Gobler, C.J., Heil, C.A., Kudela, R.M., Parsons, M.L., Rensel, J.E.J., Townsend, D.W., Trainer, V.L., Vargo, G.A., 2008. Harmful algal blooms and eutrophication: examining linkages from selected coastal regions in the United States. Harmful Algae 8 (1), 39—53. https://doi.org/10.1016/j.hal.2008.08.017

APHA, 1998. Standard Methods for the Examination of Water and Wastewater, 20th Edn., American Public Health Association, Washington DC.

Carpenter, R.S., Caraco, N.F., Correll, D.L., Howarth, R.W., Sharpley, A.N., Smith, V.H., 1998. Nonpoint pollution of surface waters with phosphorus and nitrogen. Ecol. Appl. 8 (3), 559—568. https://doi.org/10.1890/10510761(1998)008[0559:NPOSWW]2.0.CO;2

Desikachary, T.V., 1987. Atlas of diatoms, fascicle III and IV. Madras Science Foundation, Madras 222—400.

Eissa, A.E., Tharwat, N.A., Zaki, M.M., 2013. Field assessment of the mid winter mass kills of trophic fishes at Mariotteya stream, Egypt: Chemical and biological pollution synergistic model. Chemosphere 90, 1061—1068. https://doi.org/10.1016/j.chemosphere.2012.09.010

Galvao, J.A., Oetterer, M., Bittencourt-Oliveira, M.C., Gouvea-Barros, S., Hiller, S., Erler, K., Luckas, B., Pinto, E., Kujbida, P., 2009. Saxitoxins accumulation by freshwater tilapia (Oreochromis niloticus) for human consumption. Toxicon 54, 891—894. https://doi.org/10.1016/j.toxicon.2009.06.021

Glasgow, H.B., Burkholder, J.M., 2000. Water quality trends and management implications from a five-year study of a eutrophic estuary. Ecol. Appl. 10 (4), 1024—1046. https://doi.org/10.1890/1051-0761(2000)010[1024:WQTAMI]2.0.CO;2

Government of Puducherry, 2019. State Environment Plan. U.T. Puducherry, Depart. Sci. Tech. Environ., 116 pp.

Grasshoff, K., Kremling, K., Ehrhardt, M., 2009. Methods of seawater analysis. John Wiley & Sons., 632 pp.

Holmlund, C.M., Hammer, M., 1999. Ecosystem services generated by fish populations. Ecol. Econom. 29 (2), 253—268. https://doi.org/10.1016/S0921-8009(99)00015-4

Hoyer, M.V., Watson, D.L., Wills, D.J., Canfield Jr, D.E., 2009. Fish kills in Florida's canals, creeks/rivers, and ponds/lakes. J. Aquat. Plant Manage. 47, 53—56.

Kangur, K., Kangur, A., Kangur, P., Laugaste, R., 2005. Fishkill in Lake Peipsi in summer 2002 as a synergistic effect of a cyanobacterial bloom, high temperature, and low water level. Proc. Estonian Acad. Sci. Biol. Ecol. 54 (1), 67—80.

Karim, R.M., Sekine, M., Ukita, M., 2002. Simulation of eutrophication and associated occurrence of hypoxic and anoxic condition in a coastal bay in Japan. Mar. Pollut. Bull. 45, 208—285. https://doi.org/10.1016/S0025-326X(02)00098-X

La, V.T., Cooke, S.J., 2011. Advancing the Science and Practice of Fish Kill Investigations. Rev. Fish. Sci. 19 (1), 21—33. https://doi.org/10.1080/10641262.2010.531793

Meyer, F.P., Barclay, L.A, 1990. Field manual for the investigation of fish kills (No. 177). US Department of the Interior, Fish and Wildlife Service. US Dept. Interior.

Pulido, O.M., 2008. Domoic acid toxicologic pathology: A review. Mar. Drugs 6, 180—219. https://doi.org/10.3390/md20080010

Rabalais, N.N., Turner, R.E., Dortch, Q., Justic, D., Bierman Jr., V.J., Wiseman Jr., W.J., 2002. Nutrient-enhanced productivity in the northern Gulf of Mexico: past, present and future. Hydrobiologia 475 (476), 39—63. https://doi.org/10.1023/A:1020388503274

Raja, S.U.K., Ebenezer, V., Kumar, A., Sanjeevi, P., Murugesan, M., 2019. Mass mortality of fish and water quality assessment in the tropical Adyar estuary, South India. Environ. Monit. Assess. 191 (8), 512. https://doi.org/10.1007/s10661-019-7636-4

Ram, A., Jaiswar, J.R.M., Rokade, M.A., Bharti, S., Vishwasrao, C., Majithiya, D., 2014. Nutrients, hypoxia and mass fish kill events in Tapi Estuary, India. Estuar. Coast. Shelf Sci. 148, 48—58. https://doi.org/10.1016/j.ecss.2014.06.013

Sachithanandam, V., Mageswaran, T., Sridhar, R., Arumugam, K., Purvaja, R., Ramesh, R., 2017. Rapid assessment on mass mortality of fishes in Ennore estuary of Tamil Nadu, India. Rapid assessment on mass mortality of fishes in Ennore estuary of Tamil Nadu. India. Indian J. Mar. Sci. 46, 1647—1650.

San Diego-McGlone, M.L., Azanza, R.V., Villanoy, C.L., Jacinto, G.S., 2008. Eutrophic waters, algal bloom, and fish kill in fish farming areas in Bolinao, Pangasinan, Philippines. Mar. Pollut. Bull. 57, 295—301. https://doi.org/10.1016/j.marpolbul.2008.03.028

Solai, A., Gandhi, M.S., Sriram, E., 2010. Implications of physical parameters and trace elements in surface water off Pondicherry, Bay of Bengal, South East Coast of India. Int. J. Environ. Sci. 1, 529—542.

Sournia, A., 1970. Les Cyanophyctesdans le planctonmarin. Ann. Biol. 49, 63—76.

Strickland, J.D.H., Parsons, T.R., 1972. A practical handbook of seawater analysis. Fisheries Research Board of Canada, 310 pp.

Subrahmanyan, R., 1971. The Dinophycaes of Indian Seas, Part II. Peridiniaceae. Mar. Biol.Assoc. India, 134 pp.

Venugopalan, V.P., Nandakumar, K., Rajamohan, R., Sekar, R., Nair, K.V.K., 1998. Natural eutrophication and fish kill in a shallow freshwater lake. Curr. Sci. 74, 915—917. https://www.jstor.org/stable/24101100

Villate, F., Iriarte, A., Uriarte, I., Intxausti, L., de la Sota, A., 2013. Dissolved oxygen in the rehabilitation phase of an estuary: influence of sewage pollution abatement and hydro-climatic factors. Mar. Pollut. Bull. 70 (1—2), 234—246. https://doi.org/10.1016/j.marpolbul.2013.03.010

Zhang, J., Gilbert, D., Gooday, A.J., Levin, L., Naqvi, S.W.A., Middelburg, J.J., Scranton, M., Ekau, W., Pena, A., Dewitte, B., Oguz, T., 2010. Natural and human-induced hypoxia and consequences for coastal areas: synthesis and future development. Biogeosciences 7 (5), 1443—1467. https://doi.org/10.5194/bg-7-1443-2010